Experimental and Theoretical Investigation of Tetrel Clathrates for Li-ion Batteries:

Electrochemistry, Structure and Applications

by

Andrew Dopilka

A Dissertation Presented in Partial Fulfillment
of the Requirements for the Degree
Doctor of Philosophy

Approved July 2021 by the
Graduate Supervisory Committee:

Candace K. Chan, Chair
Karl Sieradzki
Xihong Peng
Houlong Zhuang

ARIZONA STATE UNIVERSITY

August 2021

ABSTRACT

Current Li-ion battery technologies are limited by the low capacities of the electrode materials and require developments to meet stringent performance demands for future energy storage devices. Electrode materials that alloy with Li, such as Si, are one of the most promising alternatives for Li-ion battery anodes due to their high capacities. Tetrel (Si, Ge, Sn) clathrates are a class of host-guest crystalline structures in which Tetrel elements form a cage framework and encapsulate metal guest atoms. These structures can form with defects such as framework/guest atom substitutions and vacancies which result in a wide design space for tuning materials properties. The goal of this work is to establish structure property relationships within the context of Li-ion battery anode applications. The type I $Ba_8Al_yGe_{46-y}$ clathrates are investigated for their electrochemical reactions with Li and show high capacities indicative of alloying reactions. DFT calculations show that Li insertion into the framework vacancies is favorable, but the migration barriers are too high for room temperature diffusion. Then, guest free type I clathrates are investigated for their Li and Na migration barriers. The results show that Li migration in the clathrate frameworks have low energy barriers (0.1-0.4 eV) which suggest the possibility for room temperature diffusion. Then, the guest free, type II Si clathrate (Na_1Si_{136}) is synthesized and reversible Li insertion into the type II Si clathrate structure is demonstrated. Based on the reasonable capacity (230 mAh/g), low reaction voltage (0.30 V) and low volume expansion (0.21 %), the Si clathrate could be a promising insertion anode for Li-ion batteries. Next, synchrotron X-ray measurements and pair distribution function (PDF) analysis are used to investigate the lithiation pathways of Ba_8Ge_{43}, $Ba_8Al_{16}Ge_{30}$, $Ba_8Ga_{15}Sn_{31}$ and $Na_{0.3}Si_{136}$. The results

show that the Ba-clathrates undergo amorphous phase transformations which is distinct from their elemental analogues (Ge, Sn) which feature crystalline lithiation pathways. Based on the high capacities and solid-solution reaction mechanism, guest-filled clathrates could be promising precursors to form alloying anodes with novel electrochemical properties. Finally, several high temperature (300-550 °C) electrochemical synthesis methods for Na-Si and Na-Ge clathrates are demonstrated in a cell using a Na β’’-alumina solid electrolyte.

ACKNOWLEDGEMENTS

There are many individuals who have helped and supported my work in this dissertation and this section will acknowledge their contributions.

First, I want to acknowledge and thank my advisor, Professor Candace K. Chan, for accepting me into her lab group and her belief and support in my research activities.

Next, I acknowledge and thank Professor Svilen Bobev. His support and collaboration have been pivotal for the completion of this dissertation.

I acknowledge and thank the contributions of Amanda Childs, who was vital in helping prepare many of the clathrate samples for synthesis and for conducting measurements at the Diamond beamline.

I acknowledge and thank the contributions of Dr. Alexander Ovchinnikov, who conducted and helped with Rietveld refinements and synthesis of clathrate compounds and was a great mentor during my visit to the University of Delaware.

I acknowledge and thank the contributions by Dr. Ran Zhao who provided the basis for the initial clathrate experiments and mentored me during the start of my PhD.

I acknowledge and thank the contributions of Professor Xihong Peng, who taught and enabled me to perform density functional theory calculations which have been crucial for this dissertation.

I would like to thank the members of the Chan Lab group for providing a welcoming and warm environment during my doctoral studies.

I acknowledge and thank the contributions of Dr. J. Mark Weller, who performed transmission electron microscopy experiments and who also was a great coworker who I shared many enjoyable discussions and coffee breaks with.

I want to acknowledge the Diamond Light Source (Didcot, UK) for access to beamline I15-1 (proposal no. CY23152) and T. Forrest and D. Keeble for assistance with synchrotron measurements.

I want to acknowledge the Deutsches Elektronen-Synchrotron (Hamburg, Germany) for access to beamline P02.1 (proposal no. I- 20180707), and J. Tseng for assistance with the XRD measurements.

I acknowledge the use of the APS at Argonne National Laboratory through the 11-BM mail in program (Proposal-63359, 66690) supported by the U.S. Department of Energy, Office of Science, Office of Basic Energy Sciences, under Contract No. DE-AC02-06CH11357

I acknowledge the use of the services from the Instrumental Design and Fabrication Core Facility at Arizona State University for construction of the stainless-steel reactors.

I acknowledge the use of the Research Computing at Arizona State University for providing high-performance computing resources that have contributed to the research results reported within this dissertation.

I am also extremely grateful for the financial support provided by the ASU Fulton Schools of Engineering Dean's Fellowship throughout my studies.

I acknowledge and thank Professor Peter A. Crozier for letting me join his group as an undergraduate, his great classes, and his support of my PhD studies at ASU.

I acknowledge and thank Professor Houlong Zhuang for participating on my dissertation committee and being a valuable resource when I had computational related questions.

I acknowledge and thank Professor Mary Laura Lind for allowing me to join her research group as an undergraduate and creating an environment that sparked my interest in scientific research.

I acknowledge and thank Professor George Wolf for his extremely insightful classes and helping me gain the confidence to tackle difficult scientific concepts.

I acknowledge and thank Tobias Schultz for all his assistance with the lab during his visit and his initial ideas for the stainless-steel reactors used in this dissertation.

I gratefully acknowledge the use of facilities within the Eyring Materials Center at Arizona State University supported in part by NNCI-ECCS-1542160.

I want to gratefully acknowledge the funding from NSF DMR-1710017 and DMR-2004514.

TABLE OF CONTENTS

Page

CHAPTER Page

CHAPTER Page

APPENDIX Page

LIST OF TABLES

Table Page

Table Page

Table Page

Table Page

Table Page

LIST OF FIGURES

Figure Page

Figure Page

Figure Page

Figure Page

Figure Page

Figure Page

Figure Page

Figure Page

Figure Page

Figure Page

Figure Page

Figure Page

Figure Page

Figure Page

PREFACE

This dissertation contains a large fraction of my published work in addition to some unpublished work that has gone through the proof-of-concept stage. The dissertation is divided into 6 chapters: Introduction and Background, Experimental and Theoretical Methods, Clathrates as Insertion Anodes, Clathrates as Alloying Anodes, and High Temperature Electrochemical Synthesis of Silicon and Germanium Clathrates.

Chapter 1, **Introduction and Background** will give a brief introduction into Li-ion batteries as a technology and the important theory behind understanding their electrochemical and structural properties. A short introduction into Tetrel clathrates will also be given along with a literature review of work published prior to the beginning of my PhD work.

Chapter 2, Experimental and Computation Methods, introduces the experimental and computation techniques used in this work. First, the electrochemical methods will be discussed followed by the materials characterization used. Then a brief introduction into density functional theory will be given followed by certain methods to calculate properties relevant for Li-ion batteries.

Chapter 3, **Clathrates as Insertion Anodes**, contains three publications focused on evaluating clathrates within the context of the Li-ion insertion mechanism. This is focused on applications where Li is reversibly inserted into the clathrate framework without destruction of the original host lattice. The first section is an experimental and computational work published in the American Chemical Society journal – Applied

Materials and Interfaces called “Experimental and Computational Study of the Lithiation of $Ba_8Al_yGe_{46-y}$ Based Type I Germanium Clathrates.”

The second section is a computational work published in the American Chemical Society journal—Journal of Physical Chemistry C entitled: ”Ab *Initio* Investigation of Li and Na Migration in Guest-Free, Type I Clathrates.”

The third and last section is an experimental and computational work published by Wiley-VCH GmbH in the journal – Advanced Energy & Sustainability Research entitled: “Structural Origin of Reversible Li Insertion in Guest-Free, Type-II Silicon Clathrates.”

Chapter 4, Clathrates as Alloying Anodes, contains one published article and two articles that are currently under review and seeks to investigate how the alloying reactions (i.e. phase transformations) of clathrates differ from their elemental analogues. The articles that are currently under review are presented in their submitted version so the published version might differ from the version presented within this dissertation. The first section is an experimental work published in the American Chemical Society journal—Chemistry of Materials and is titled: “Understanding the Amorphous Lithiation Pathway of the Type I Ba_8Ge_{43} Clathrate with Synchrotron X-Ray Characterization.”

The second section is the adapted from a manuscript that is under revision in the American Chemical Society journal- Applied Materials and Interfaces and is titled “Structural and Electrochemical Properties of Type VIII $Ba_8Ga_{16-\delta}Sn_{30+\delta}$ Clathrate ($\delta \approx 1$) during Lithiation.”

The third section is adapted from a manuscript that is under revision in the American Chemical Society journal- Journal of Physical Chemistry C and is titled "Electrochemical Lithium Alloying Behavior of Guest-Free, Type II Silicon Clathrates."

Chapter 5, High Temperature Electrochemical Synthesis of Silicon and Germanium Clathrates includes one published article and two unpublished reports of demonstrating the use of high temperature (300 – 550 °C) electrochemical methods to synthesize Na-Si and Na-Ge clathrates. The first section is published by IOP Publishing in the Journal of the Electrochemical Society and is titled: "Solid-State Electrochemical Synthesis of Silicon Clathrates Using a Sodium-Sulfur Battery Inspired Approach."

The second section is unpublished work and is titled "Electrochemical Synthesis of Type II $Na_xSi_yGe_{136-y}$" and the third section is titled "Electrochemical Na-Sn Flux Synthesis of Na-Si Clathrates". The results for these sections have not been as thoroughly edited as the previous sections and will be prepared into manuscripts for future publication.

Chapter 6, Summary, gives a recap of the results presented in this dissertation and gives a brief outlook for future experiments and directions to pursue.

The **Appendix** includes the supporting information for the publications and manuscripts.

1. INTRODUCTION AND BACKGROUND

1.1. Li-ion Batteries

1.1.1. Introduction

The ability to store and transfer large amounts of energy on demand is a vital commodity and resource to human societies. Perhaps the most transformative form of stored energy is the fossil fuel, in which energy is stored in organic molecules that have formed over millions of years. Upon combustion, the fuels release large amounts of heat that can be used or converted into other forms of energy (i.e. mechanical/electrical). When refined, these fuels can have very large energy densities which is important for utilizing them for transportation and portability.[1] These fossil fuels have been essential for the development of modern society and currently 80% of the world's energy consumption originates from these fuels, but there are several limitations and concerns with their long-time use.[2,3] First, the supply of fossil fuels is limited. As the terminology "fossil" implies, the compounds are formed over millions of years from the decomposition of organisms. This means that the reserves of fossil fuels will eventually be depleted, and other alternative means will be needed to supply energy for societies. The other major concern is that the combustion of organic fossil fuel releases CO_2 into the atmosphere which results in the warming of the global atmosphere.[2,3] Finally, the emissions from combustion reactions can have detrimental health effects on humans via pollution.[4] Due to the large dependence of human society on fossil fuels and their potential downsides, alternatives to store and convert energy are desperately needed.

One of the most important alternatives for energy storage is the galvanic cell (or battery) which allows for the conversion between chemical and electrical energy.

Batteries have existed for centuries but generally their energy density relative to other fuel sources (i.e. gasoline) is much lower meaning that they are only useful for niche applications.[1] This changed dramatically when the first Li-ion battery was commercialized by Sony in 1990.[5] The battery had an operating cell voltage of 4 V and an energy density (80 Wh/kg, 200 Wh/L) three times higher than that of the current best Ni-Cd rechargeable battery (1.2 V).[5] The dramatic increase in the energy density and the high reversibility of the chemistry led to a revolution for batteries and their applications in portable electrical devices. The handheld phone, laptops and other common electrical devices are all enabled by the high energy density and reversibility of the Li-ion battery. This importance was highlighted by the Nobel prize in chemistry in 2019 being awarded to the three key developers of the modern Li-ion battery.[6] Considering the need for alternatives for fossil fuels to store and deliver energy, the Li-ion battery has been a contender for several other applications other than portable electronics. Most notably, electric vehicles[7] and grid storage applications[8] are gaining interest in the recent years in response to attempts to move away from fossil fuels. However, current Li-ion batteries are either too expensive or do not perform well enough to meet the demands of these new applications.[9] Thus, there is a large impetus to develop batteries that utilize new chemistries that can meet these challenging demands for the future.

1.1.2. Parts of a Li-Ion Battery

A Li-ion battery is an electrochemical cell comprised of three main components: the anode, the cathode, and the electrolyte. When the battery is discharged (i.e. operated as a galvanic cell), the anode is oxidized while the cathode is reduced. On charging, (i.e. operated as an electrolytic cell), the anode is reduced while the cathode is oxidized. Since

anode and cathode refer to which electrode is being reduced or oxidized, technically, the anode and cathode are switched when operated as an electrolytic cell (upon charging). Despite this, most researchers refer to the anode and cathode based on when the cell is discharging or acting as a galvanic cell. Some researchers refer to each electrode as negative/positive which resolves the naming discrepancy. In this work, the negative electrode will be generally referred to as the anode and the positive electrode as the cathode. **Figure 1.1.1** shows a schematic of a modern Li-ion battery cell showing crystal model schematics of both anode and cathodes and the movement of lithium upon discharge.

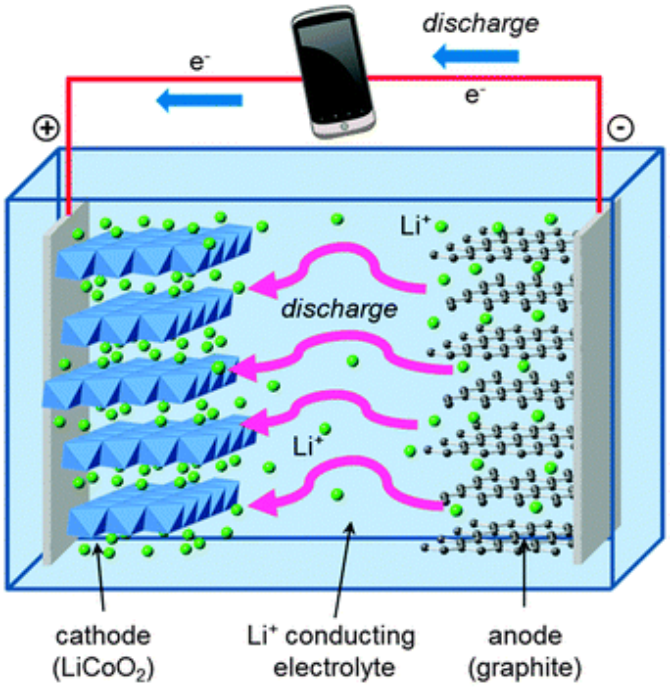

Figure 1.1.1 Schematic of a Li-ion battery. Li-ions are in green, Co oxide octahedra in blue, and carbon atoms in black.[10]

During the charging and discharging of a Li-ion battery, Li ions are shuttled through an electrically insulating electrolyte between two layered compounds with large differences in chemical potential for Li-ions. The cathode is typically comprised of a crystalline layered Li metal oxide ($LiMO_2$ M= Ni, Co, Mn). In such materials, the metal ions are octahedrally coordinated by oxygen anions which form edge sharing layers as depicted by the blue polyhedral in **Figure 1.1.1**. During charge and discharge, the Li-ions move in and out of these metal oxide layers. In a similar manner, the anode, crystalline graphitic carbon, undergoes a similar reaction by which Li moves in and out of the hexagonal carbon layers upon discharge and charge. In between the anode and cathode is a separator soaked with a Li conducting electrolyte. This serves to maintain the difference of electric potential by being electronically insulating while also allowing the transport of Li-ions between the anode and cathode. The separator is comprised of a porous polymetric material while the electrolyte is a Li salt dissolved in a carbonate-based electrolyte. Finally, the two electrodes are connected via an external circuit which allows electrons to pass between the electrodes. The half reaction of the cathode upon discharge can be written as such:

$$Li_{1-x}CoO_2 + xLi^+ + xe^- \leftrightarrow LiCoO_2 \ (4.35\ V\ vs\ Li/Li^+)$$

where x refers to the amount of Li in the crystal structure of $LiCoO_2$. The half reaction for graphite upon discharge is as follows:

$$LiC_6 \leftrightarrow C_6 + Li^+ + e^- \ (0.10\ V\ vs\ Li/Li^+)$$

As can be seen by the large difference in potential vs Li/Li^+, assembling these two electrodes together in a full cell would result in a full cell voltage of 4.25 V, typical of Li-

ion batteries. The origin of the large difference of the voltages is related to the electronic structure of each host material and the chemical environment of the Li. In the case of $LiCoO_2$, the charge from the Li atom is stored on the transition metal orbitals bonded with oxygen resulting in the oxidation state of the Co atom changing from +4 to +3 upon discharge.[11] In the case of graphite, the charge is stored in the π^* antibonding orbitals of the carbon layers resulting in a maximum of one Li stored for every six carbon atoms resulting in the LiC_6 compound.[12] Thus, the electronic structure of host materials and the resulting potential couple with Li will determine if an electrode material is an anode or a cathode. Generally, anodes have a low reaction voltage vs Li/Li^+ (potential of Li metal) while cathodes have a higher voltage and the difference between them determines the maximum operating voltage of the Li-ion battery.

Li-ion batteries are more complex than the simple schematic in **Figure 1.1.1**. Typically, the anode and cathode particles are mixed with a polymeric binder and a conductive additive to form a porous composite electrode. This composite electrode is then put on to a metallic current collector (Cu for anode, Al for cathode) which serves as a path for electrons to move through the external circuit. The purpose of the composite electrode is to ensure that all anode or cathode particles are connected ionically and electronically to the electrolyte and the current collector, respectively.

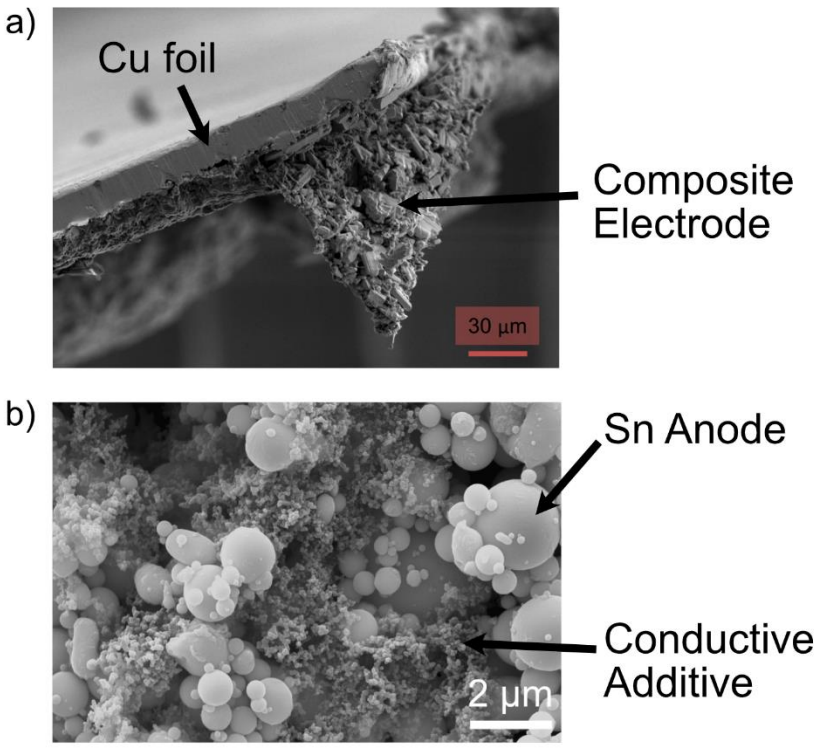

Figure 1.1.2 (a) SEM micrograph of a cross section of a battery electrode.[13] (b) Plane view of a composite electrode comprised of Sn particles as the active material, carbon black as the conductive additive and PVDF as the binder.

Figure 1.1.2 shows scanning electron microscope images of a cross section and plan view of two different composite electrodes. As can be seen in the cross-section image in **Figure 1.1.2a**, the composite electrode forms a porous film that is attached to the Cu foil current collector. The composite film is typically formed by first mixing, the active material, the conductive additive, and a polymeric binder in a solvent to form a viscous slurry. The slurry is then cast upon the metal foil and heated to remove the solvent. **Figure 1.1.2b** shows a plan view of a composite electrode comprised of Sn particles, carbon black, and polyvinylidene (PVDF). The large spherical particles are the

Sn which represents the active material, while the smaller nanosized particles are carbon black which serve to connect everything electronically.

Once both composite anode and cathode are adhered onto the metal current collectors, the electrodes can be now assembled into a full electrochemical cell. To achieve this, the two electrodes are soaked in the liquid electrolyte and pressed together with a polymeric separator that is soaked with electrolyte in between the two electrodes. This is illustrated in the schematic in **Figure 1.1.3** showing a fully assembled Li-ion battery with composite anode and cathode, metal current collectors and separator.

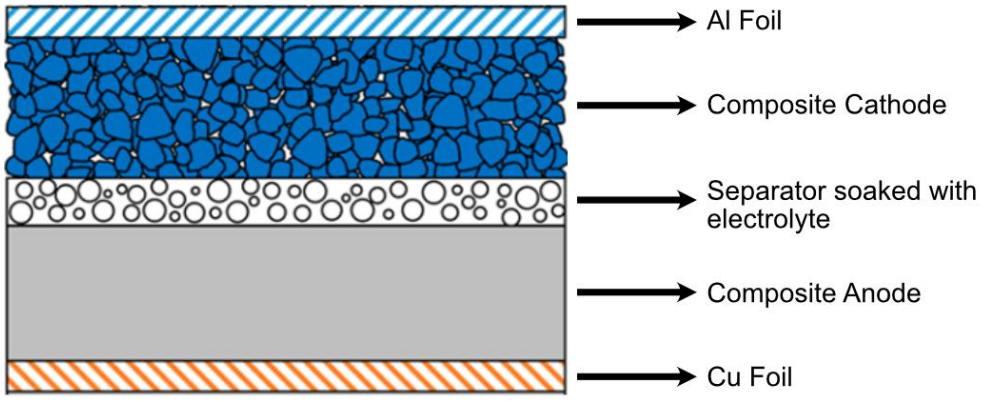

Figure 1.1.3 Schematic of a full Li-ion battery cell.[14]

Once this layered cell is assembled, it is sealed under an inert gas or vacuum sealed in some type of packing that allows it to maintain its inert atmosphere as several cell components are highly air and moisture sensitive. Common packaging types are coin cells and pouch cells. Coin cells, as the name implies, are flat cylindrically shaped cells that contain the cell components in a stainless-steel housing.[15] The cell is assembled

under an Argon atmosphere and then crimped under pressure to ensure the seal. The applied pressure also ensures that the electrodes maintain contact with the current collectors and separators. A pouch cell is a type of cell that using some sort of flexible packaging material. Generally, pouch cells can achieve higher energy densities due to the lighter packaging material but can have more challenges related to lifetime due to leaks or gas evolution within the cell.[16] Once the packaging is sealed, the battery can then be used as an energy storage device. The performance of the battery depends heavily on the choice of anode, cathode, and the electrolyte components.

1.1.3. Metrics for Li-ion Batteries

This section will introduce the various quantities and figures of merit used for evaluating the performance of Li-ion batteries. These figures help guide researchers in optimizing materials properties. First, the Ragone plot is presented which depicts the energy density and power density of various energy store devices against each other on a logarithmic scale.

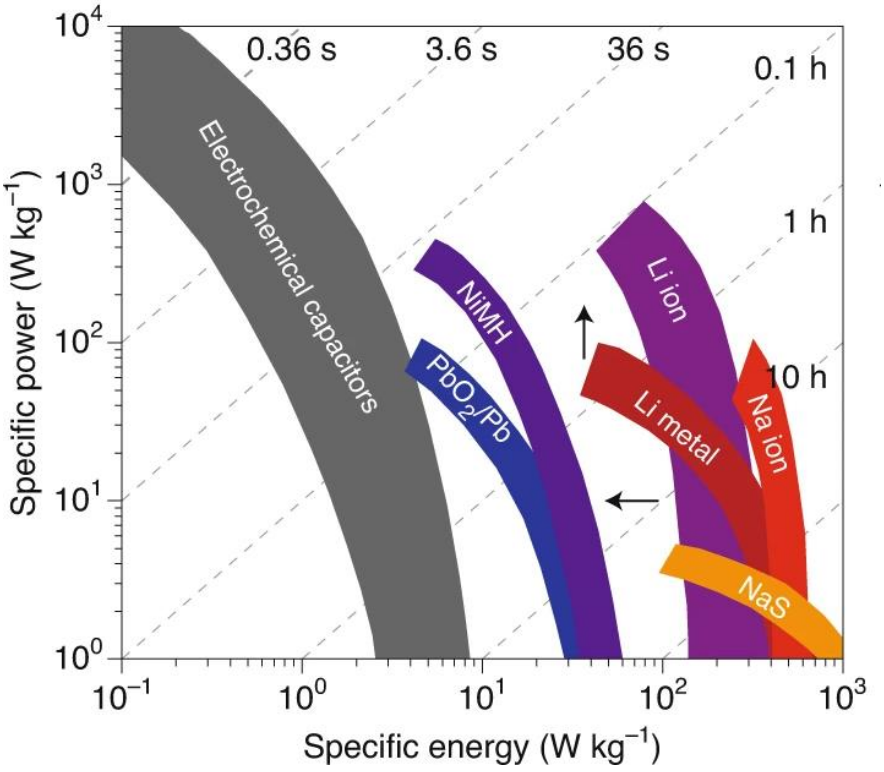

Figure 1.1.4 Ragone plot which plots the Specific power and Specific energy ranges of various electrochemical storages devices.[17]

In **Figure 1.1.4**, the ranges of specific energy and specific power are plotted for each type of electrochemical storage device. Ideally, an energy storage device will be designed to maximize both specific energy and power resulting in it moving to the top right of the plot. However, as the specific power increases for all devices, the specific energy decreases dramatically. This demonstrates the common trade-off between energy and power density when designing electrochemical storage devices. As discussed earlier, Li-ion batteries were a significant upgrade in performance on both metrics when compared to previous battery technologies (NiMH and PbO_2/Pb). These metrics are especially important for electric vehicles as the specific energy affects the range while the specific power affects the possible acceleration and recharging time. For instance, the

United States Advanced Battery Consortium (USABC) has made for goals for battery packs for electric vehicles at 235 Wh/kg and 470 W/kg.[18] To achieve these higher metrics, much work is going into developing novel materials and battery architectures.

The origin of these metrics is determined by the choice of electrode, electrolyte, current collectors, and packaging materials. In general, to maximize the specific energy (aka as energy density), the space that does not store energy (i.e. not the electrodes) is minimized. This means that the amount of electrolyte, current collectors, and packaging materials are minimized while the relative amount of electrode materials (i.e. graphite / $LiCoO_2$) are maximized. The theoretical limit of a Li-ion battery electrode is determined by the maximum amount of Li that reacts with the material. For example, the most lithiated form of graphite is a composition of LiC_6. The following equation can be used to calculate the specific capacity (mAh/g) of an electrode material based on the composition of Li:[19]

$$C_G = \frac{xF}{3.6M_W}$$

where C_G is the specific capacity of the electrode in terms of mAh/g, x is the number of Li per formula unit of the host, F is Faraday's constant (96485.332 C/mol) and M_w is the molecular weight of the host material (not including the Li). For instance, if we set x =1 and the M_w is equal to C_6 (72.06 g/mol), the theoretical capacity for graphite is calculated to be 372 mAh/g. This calculation can be done to estimate the capacity of new materials and compare experimental capacities with the theoretical. To obtain the specific energy of a material, the specific capacity is multiplied by the voltage of the full cell:

$$E_G = C_G * V$$

where E_G is the specific energy of the electrode and V is the voltage of the full cell couple. If a full cell voltage of 4.25 V is assumed for a graphite/$LiCoO_2$ cell, then specific energy of graphite would be 1581 Wh/kg. This is notably higher than the specific energy of a full Li-ion battery (~250 Wh/kg) and this is because the cathode does not have as high as a capacity as graphite. The specific energy will typically also include the weight components of the electrolyte, current collectors, and packaging materials which do not contribute to energy storage.

Another important point is that the specific capacity of an electrode will sometimes be less than that of the theoretical capacity due to various factors involving the structural transformations of the host material. For example, $LiCoO_2$ has a theoretical specific capacity of 274 mAh/g if all the Li is removed but in commercial cells only a capacity of 140 mAh/g was used.[20] Because each electron that passes through the electrochemical cell corresponds to a Li moving between electrodes, the capacity can be used to estimate the composition of the host material. In this case, 140 mAh/g corresponds to around a composition of $Li_{0.5}CoO_2$ where only half of the Li in the structure is used for energy storage. This limitation originates from irreversible reactions that occur past a certain voltage cutoff which result in poor long-term cycling of the cell.[20] Much Li-ion battery research is related to boosting the usable capacities of the electrode materials while maintaining the high reversibility and calendar life of the battery. In this work, specific capacity will be a common metric used to characterize the

reaction of electrode materials with Li ions. This metric allows for the determination of the # of Li that react and comparison to other electrode materials.

In addition to capacity and amount of energy stored, the rate at which the energy can moved (i.e. power) is also an important metric. For batteries, the power capability affects the time it takes for a battery to charge or discharge and relates to the quantity known as the C-rate. The C-rate (i.e. charge rate) is commonly used in the battery field to describe the time in which it take a battery to fully charge/discharge. The units of C-rate are inverse hours (hr^{-1}). For example, a C-rate of 1 C corresponds to a charge/discharge time of one hour, while a C-rate of 0.1 C corresponds to a charge/discharge of 10 hours. This metric allows researchers to compare electrode materials at different rates and characterize the energy vs power curve that is shown in **Figure 1.1.4**. To calculate the C-rate, the specific capacity and current need to be known. The current is controlled galvanostatically which means the charge and discharge is performed at a constant current. Capacity is often represented as mAh, which gives researchers a convenient way to calculate the C-rate and the time required for charge and discharging. For instance, if an electrode has a capacity of 400 mAh/g and a charge rate of 40 mA/g is used, the time in hours required for the full capacity to be reached is simply the capacity (mAh/g) divided by the charge rate (mA/g). This would result in 10 hours for the charge/discharge time. Taking the inverse of this is the C-rate (0.1 C).

As mentioned briefly before, there is generally a trade-off between specific energy and the specific power. As a higher current is provided by the battery, there is less capacity for the battery to provide. This section briefly introduces the origin of this

phenomenon. In a composite battery electrode, there is an electrolyte, active material, and a current collector. Each part is responsible for transporting a certain charged species for completing the desired electrochemical reaction. The electrolyte is responsible for transporting Li ions while the current collector is responsible for transporting the electrons from the external circuit. The active material (electrode material) however requires the transportation of both electrons and ions for the bulk electrochemical reactions to occur. This is notably different from traditional three-electrode solution-based electrochemistry where dissolved ions or molecules solution react at the interface of conducting electrode (i.e. platinum) and then diffuse away back into solution. In a battery electrode material (i.e. graphite), the electrochemical interface is dynamic and occurs at the surface and centers of particles as opposed to the only the surface as in the solution-based cell. This mixed ion and electron conducting behavior is the origin of the high energy storage capabilities of battery materials.[21] This also means that the active material for Li-ion batteries must also be good electron and ion conductors. As the Li diffusion coefficients in electrode active materials are much lower than the Li-ion conductivity of the electrolyte, different sized particles and geometries are used to reduce the Li diffusion lengths in the active particles to achieve certain current rates.[21]

Figure 1.1.5 depicts two examples of different battery electrode geometries with different lengths needed for ions and electrons to reach the furthest length of the active particle. In **Figure 1.1.5a**, the active material (green) are wires connected to a metal current collector (grey) and immersed in the electrolyte (blue). M^{z+} and e^- refer to the insertion of metal ions and electrons, respectively into the active material while L_{ion} and L_{eon} represent the respective lengths each charge species must travel to complete the

reaction. [22] In the case of the wires, the diffusion length for the metal ions is the radius of the wire, while the diffusion length of the electrons is the whole length of the wires. **Figure 1.1.5b** demonstrates that by modifying the size of the particles and the electronic contacts that these characteristic lengths can be modified. B represents a more typical electrode where spherical particles are surrounded by each other with a conductive additive (**Figure 1.1.2**). The reason these types of composite electrodes are used is to reduce the L_{ion} and L_{eon} to achieve better rate performance (i.e. higher C-rate).

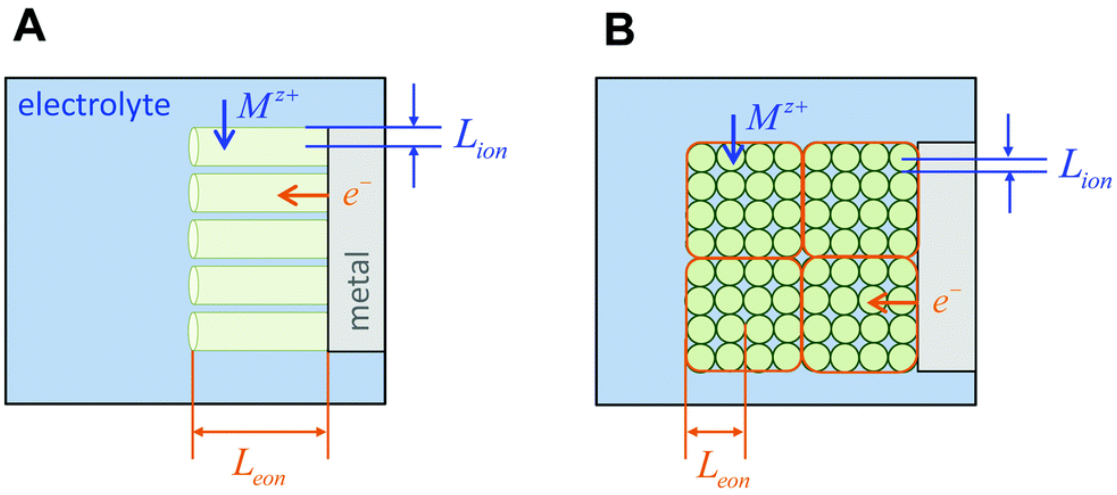

Figure 1.1.5 (a) Schematic of a battery electrode comprised of wire active material connected to the metal current collector and (b) battery electrode comprised of spherical active particles surrounded by a conductive additive. L_{ion} and L_{eon} correspond to the diffusion lengths for ionic and electronic transport in the cell, respectively.[22]

The rate performance of a battery is directly related to the diffusion coefficient, diffusion lengths of the active energy storage phase and the conductivities of the electrolyte and current collector. Thus, the observed rate dependence on the capacity for all batteries (as seen in **Figure 1.1.4**) is related to the fact that at a certain current rate, the

bulk diffusion in the active materials is not high enough (or diffusion length is too long) to operate at the same time scale as the desired current rate. This results in high polarizations or resistance in the electrochemical cell that results in a loss of voltage to operate the battery as a galvanostatic cell. Increasing the power capability of a cell is quite straightforward: the diffusion coefficients in the active particles need to increase or the diffusion lengths need to decrease. One common strategy to increase the rate capability is to decrease the particle size of the active material, but this comes with a sacrifice to the specific energy. Smaller particles require more pore space for the electrolyte to reach them which in turn limits how dense the composite electrode can pack which decreases the energy density. This is a common trade-off in electrode design and the resulting battery design depends on the required specific power and energy requirements of the device.

1.1.4. Single Phase and Two-Phase Reactions

The thermodynamics of a battery electrode are observable by the potential difference between a reference electrode and the active electrode phase. The voltage is related to the difference of chemical potentials between two electrodes by the Nernst equation:[23]

$$\mathrm{V} = -\frac{\left(\mu_{Li}^{cathode} - \mu_{Li}^{anode}\right)}{e}$$

Where V is the voltage, $\mu_{Li}^{cathode}$ and μ_{Li}^{anode} are the chemical potentials in terms of eV/mol for the cathode and anode, respectively and e is the charge of an electron in Coulombs. The chemical potential varies as a function of the Li content according to:[23]

$$\mu_{Li} = \frac{\partial \mathrm{g}}{\partial \mathrm{x}}$$

Where ∂g is the Gibbs free energy function as a function of x. **Figure 1.1.6** shows various forms of the Gibbs free energy function, g(x) as a function of x, which represents the Li content in a host material, MA. MA represents the host material (e.g. CoO_2, C_6). If one of electrodes has a fixed chemical potential as a function of Li content (e.g. Li metal), then the voltage of the cell represents the changes in the chemical potential of a single electrode. The chemical potential is the slope of the Gibbs free energy curve and thus the corresponding voltage profile depends on the shape of the g(x) curve. In **Figure 1.1.6a**, the Gibbs free energy is a single parabola with a minimum at x = 0.3. The corresponding voltage profile (**Figure 1.1.6b)**, shows a continuously decreasing voltage with increasing Li content demonstrating how the chemical potential of the electrode continuously increasing with the incorporation of more Li. This situation where there is a single minimum in the g(x) is referred to as a single-phase reaction and sometimes a solid solution mechanism. A typical example of this reaction mechanism is in the Li_xTiS_2

system which shows a smooth sloping voltage profile.[24]

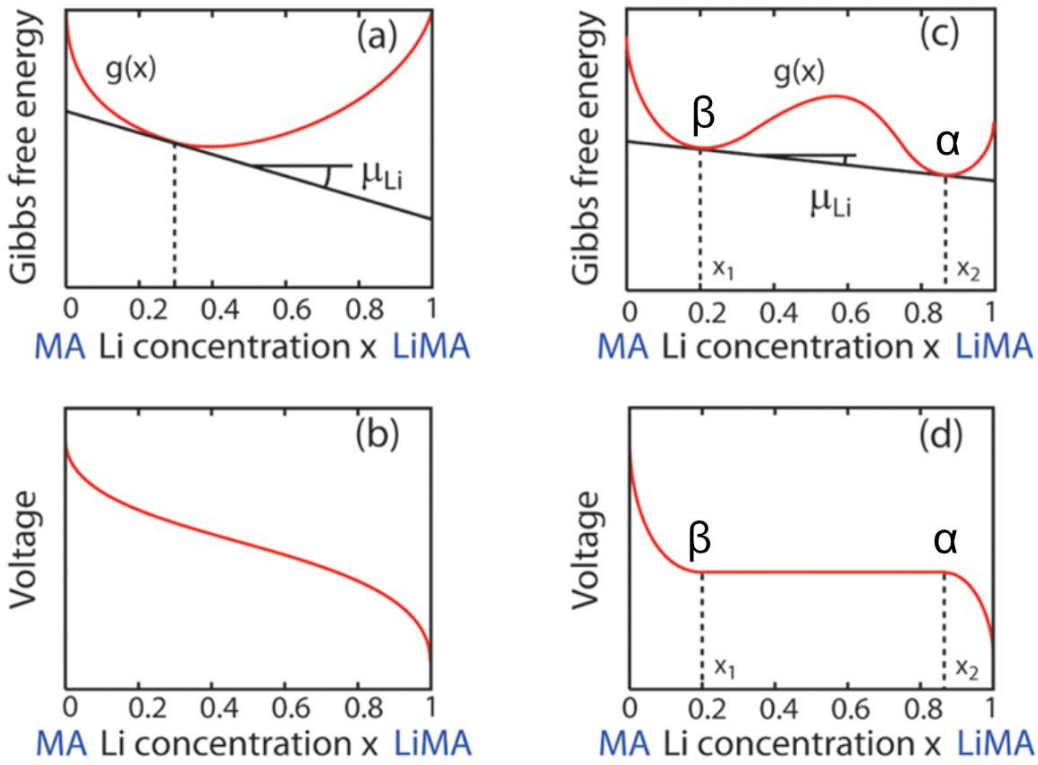

Figure 1.1.6 Graph of the Gibbs free energy vs composition and corresponding voltage profile for a (a)(b) single phase reaction (c)(d) and two phase reaction.[23]

In the case where there are two minima in the g(x) curve, a two-phase reaction occurs between the minima of the parabolas. As seen in **Figure 1.1.6c**d, its more energetically favorable to have an α and β phase in coexistence with one another then to vary the Li content in each phase. Due to this, the slope is fixed between the α and β phases and thus the voltage is fixed between the minimum of each phase in g(x). This is referred to as a two-phase reaction mechanism and is seen in many electrode materials, with $LiFePO_4$ being a typical example of having a very flat two-phase reaction at 3.5 V

vs Li/Li^+. The origin of a two-phase reaction plateau is also explained by the Gibbs phase rule which is shown in the following equation:

$$F = C - P + 2$$

Where F is the number of degrees of freedom, C is the number of elemental components in the system, and P is the number of phases. For a two component system with two phases present and the temperature and pressure are specified, the degrees of freedom are equal to zero. This means that the potential must be fixed when the two-phases are present.

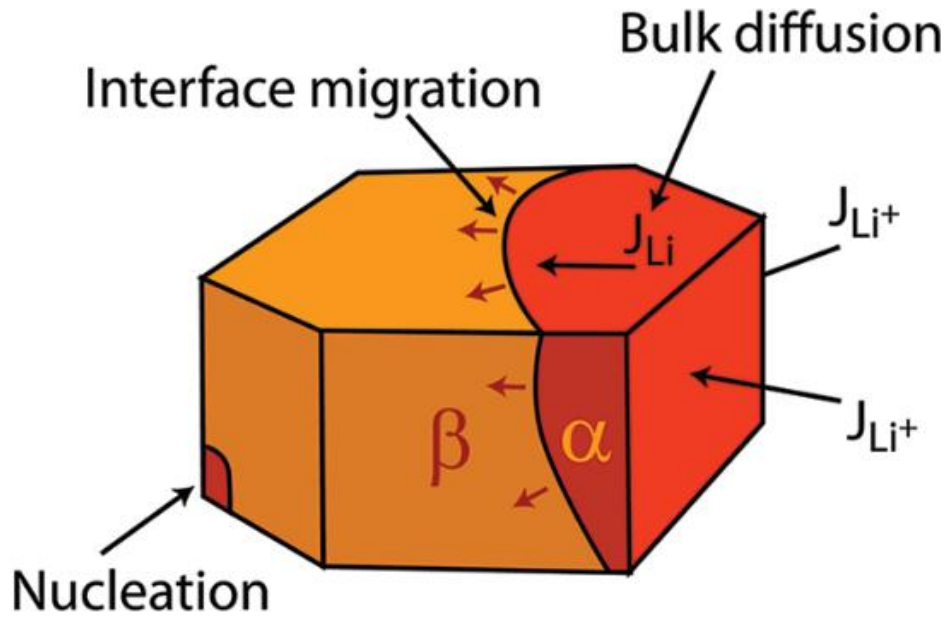

Figure 1.1.7 Schematic of a single active particle during a two phase reaction between Li-rich α phase and Li-poor β phase. J_{Li+} represents the flux of Li^+ in the electrolyte going toward the interface with the active particles. J_{Li} represents the flux of Li inside the Li-rich α phase which is required to have the two phase reaction proceed.[23]

A schematic representation of a two-phase reaction in a single particle is shown in **Figure 1.1.7**. As Li enters the electrode, the system wants to put the Li in a phase that

results in the lowest free energy. In a two-phase system, this first begins with nucleation of the lithium rich phase (α). Once nucleation has occurred, growth of this new phase can occur. As the nominal Li content increases in the total particle, the relative fractions of the α and β phases change until reaching the final composition of the Li-rich phase. For the situation in **Figure 1.1.6cd**, the α phase would fully consume the β at a Li composition of x = 0.85. This reaction proceeds through interface migration and there is a clearly defined phase front that moves throughout the particle. For this reaction to occur, the newly nucleated α phase must be able to provide bulk diffusion of Li to the interface. This is represented by the J_{Li} which indicate the flux of Li atoms through the α phase toward the interface. In a single-phase reaction, the Li content of the whole particle changes as a function of the total system Li concentration and there is no interphase migration.

Since the voltage profile as function of Li content of an electrode material is readily obtained from experiments, voltage plateaus are often a signature of a two-phase reaction and allows electrochemists to characterize the electrochemical reactions occurring in the system. Understanding the reaction mechanism of electrode materials is important as it establishes structure property relationships. Since a battery's usefulness is its current-voltage relationships, the underlying causes of these properties are of importance to boost the performance of these devices. At the core of a battery is the atomistic storage of the active charge species in a host material, and an understanding of this process relies on a thorough characterization of the atomistic structure of the material to connect it to its electrochemical properties. Much of this work will be devoted to

connecting the voltage profile of new electrode materials to their structural phase transformations to establish the link being structure and electrochemical properties.

1.2. Li-ion Battery Anodes

This section will introduce two types of Li-ion battery anodes that are classified based on their corresponding reaction mechanism. An electrode material is defined as an anode based on its potential relative to Li/Li^+ (typically 0 V- 2 V) and its application as the negative electrode in a full Li-ion battery cell. A list of the desirable properties for an anode for a Li-ion battery are listed as follows:

- Low reaction potential
- High capacity (volumetric and gravimetric)
- Good rate capability
- Minimal irreversible first cycle reactions
- Low volume expansion
- High electron and ionic conductivity
- High cycling stability
- Low voltage hysteresis

Finding an anode with all these properties is a challenge and many times certain parameters are correlated against each other. For instance, capacity and volume expansion are intrinsically linked by the space Li atoms occupy. Thus, choosing an anode is often dependent on the voltage-current characteristics needed for a specific application. The following discussion will highlight some of the major anode chemistries and briefly discuss high level trades offs that occur based on the electrode material.

The first section is about insertion anodes which includes graphite and is the most widely used type of anode currently used in Li-ion batteries.[9] The second section will

discuss alloying anodes in which the electrode undergoes phase transformations with the electrochemical incorporation of Li to form high-capacity Li-rich phases. These anodes are very promising for next-generation batteries due to their high capacities. Insertion and alloying anodes are the main focus of this work. Conversion anodes are another type of anode that undergo phase transformations with high capacities.[25] Another type of anode that has gained renewed popularity in recent years is the Li metal anode, which is considered the holy-grail of Li-ion battery anodes.[26] Due to different mechanism of Li storage, I will defer the reader to pertinent reviews for this system.

1.2.1. Insertion

The topotactic insertion (also known as intercalation) of Li atoms into a host material is the key development that enabled the revolutionary electrochemical properties of a Li-ion battery. This process involves the bulk diffusion of Li into a host structure without significantly altering the original structure of the host. The lack of structural transformations during the lithiation and delithiation process results in very high reversibility of the electrochemical reactions which is beneficial for the long lifetime of a battery. Generally, insertion anodes have good cycling stability but are limited in capacity due to their host framework. Two examples of widely used commercial anodes will be highlighted here: graphite and $Li_{4/3}Ti_{5/3}O_4$ (LTO).[27]

Graphite is the most used anode material for Li-ion batteries.[9] It has a high capacity (for insertion anodes), low reaction potential, made of an abundant element, good electric/ionic conductivity, and high cycling stability. These set of properties make

graphite an ideal Li-ion battery anode and has resulted in the widespread success of the material.

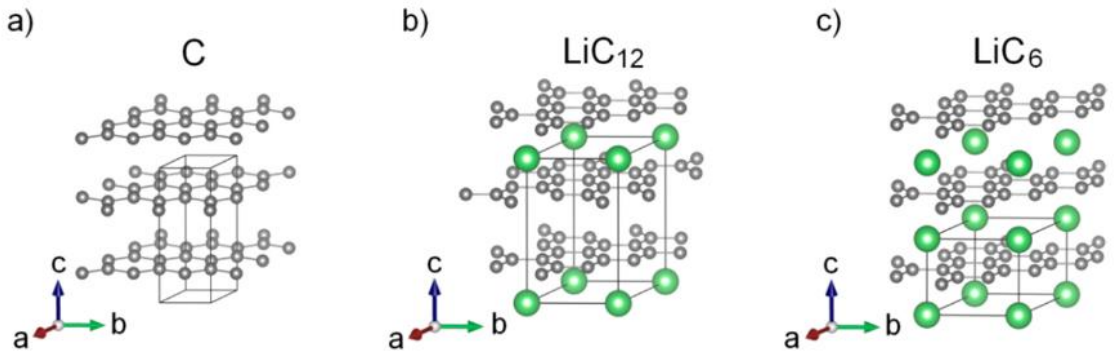

Figure 1.2.1 Crystal structure of (a) pristine graphite, (b) LiC_{12}, and (c) LiC_6.[28]

During electrochemical lithiation, graphite undergoes goes a series of phase transformations between different Li_xC_6 "stages". Pristine graphite is comprised of carbon sheets and is described by the hexagonal $P6_3/mmc$ space group. **Figure 1.2.1** shows crystal model schematics of pristine graphite, LiC_{12} and LiC_6. LiC_{12} and LiC_6 are the two major lithium intercalation compounds that form during electrochemical lithiation. The voltage profile for the 2nd cycle for graphite is shown in **Figure 1.2.2**. Note that since capacity of a cell is related to the amount of Li reacting with the electrode, voltage profiles can be shown in terms of the composition which allows for a more direct connection to the structural/electrochemical property relationship. The voltage profile shows a series of plateaus and slopes on lithiation (red curve) and a similar mirrored behavior on delithiation (blue). The voltage difference between lithiation and delithiation is known as the voltage hysteresis and is dependent on the current rate (ohmic drop) and

the thermodynamics of the system. Insertion anodes generally have a low hysteresis due to the similarities of the structures upon lithiation and delithiation. This is another benefit of insertion electrodes as a low hysteresis results in a higher energy storage efficiency.

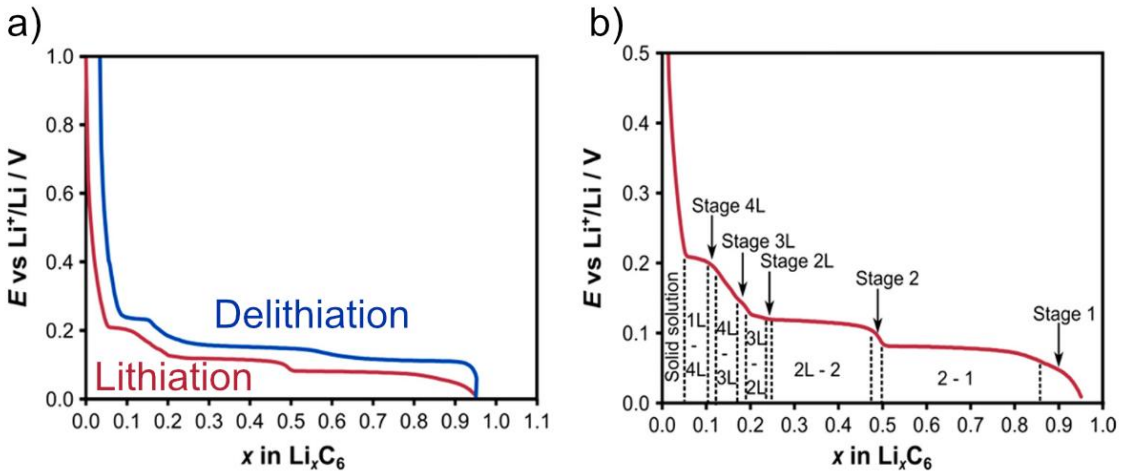

Figure 1.2.2 (a) Voltage profile of the lithiation and delithiation of graphite during the 2nd cycle. (b) Voltage profile of the lithiation of graphite with labels corresponding to the phases present during lithiation at a specific composition and voltage. [28]

Based on the voltage plateaus during lithiation and delithiation, it is expected that the Li_xC_6 is going through various phase transformations during lithiation. **Figure 1.2.2b** shows the lithiation profile with the labelled lithium stages and the two-phase and single phase regions. The number of each stage refers to number of unoccupied graphite layers between two occupied layers. The energy landscape for lithiated graphite is quite complex and is a good example of how single phase and two-phase regions can occur as the Li content is changed. Upon full lithiation to $Li_{0.95}C_6$, a total volume expansion of ~13% has been reported.[28]

The lithium titanium oxide ($Li_{4/3}Ti_{5/3}O_4$, LTO) spinel structure is another successful and commercialized anode that has attractive properties as a Li insertion anode.[27] The voltage profile of the lithiation and delithiation of LTO is shown in **Figure 1.2.3a**.[29] Unlike the many phase transformations in graphite, LTO undergoes a two-phase reaction with a flat voltage plateau at 1.55 V with a capacity of ~155 mAh/g. The Li-poor phase consists of a defect spinel structure where Li and Ti occupy the octahedral 16d sites and Li occupy the tetrahedral 8a sites (**Figure 1.2.3b**).[30] During lithiation a two-phase reaction occurs between the original phase and a Li-rich rock salt phase in which Li reside in the 16c octahedral sites (**Figure 1.2.3c**). The phase transformation does not result in a change in the lattice parameter between the two phases which results in a very low volume change between the lithiated and deithiated phases. The low volume change and high reaction potential result in LTO having exceptional cycling stability. However, the high reaction voltage (1.55 V) and low capacity (155 mAh/g) mean that the energy density of a full cell with LTO will have lower energy density compared to a full cell using graphite. LTO cells generally have very long calendar lives and can be safely charged more quickly than graphite-based cells.

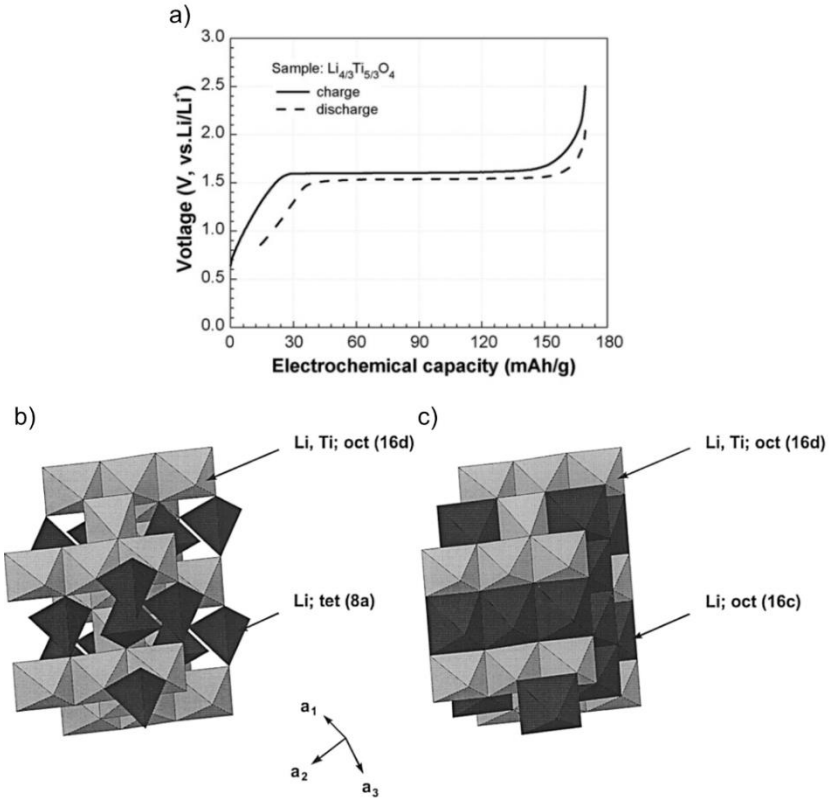

Figure 1.2.3 (a) Voltage profile of the lithiation and delithiation of $Li_{4/3}Ti_{5/3}O_4$ (LTO). [29] Crystal structure of (b) $Li_{4/3}Ti_{5/3}O_4$ and (c) the fully lithiated state, $Li_{7/3}Ti_{5/3}O_4$.[30]

Overall, anodes based on topotactic insertion reactions have very good reversibility and lifetime but are limited in their capacities due to the host material taking up space. Two examples of insertion anodes were given to introduce concepts related to the operation and electrochemistry of insertion anodes. Based on the different voltage profiles and their corresponding structural transformations, each anode has a different use case depending on the requirements for the battery. For high energy density applications such as portable electronics, graphite is the preferred anode due to its high capacity and low reaction voltage. For fast charging and long calendar life, LTO is optimal due to its very good cycling stability despite having a lower capacity and energy density.

1.2.2. Alloying

In contrast to the minimal structural changes of insertion anodes, alloying anodes undergo significant phase changes with large volume expansion. As a result, alloying anodes have much higher capacities than insertion anodes. Alloying refers to the process in which Li forms multicomponent phases starting from an unlithiated phase. For instance, a general reaction can be written as:

$$xLi + M \rightarrow Li_xM$$

where x is the number of Li and M is an elemental phase that can form binary compounds with Li. This is notably similar to graphite where x = 0.1667 however for other elements, Li can react with up to x = 4.4 which results in a much higher capacity than graphite. To illustrate this point, **Figure 1.2.4** shows the volumetric and gravimetric capacities of various elements.

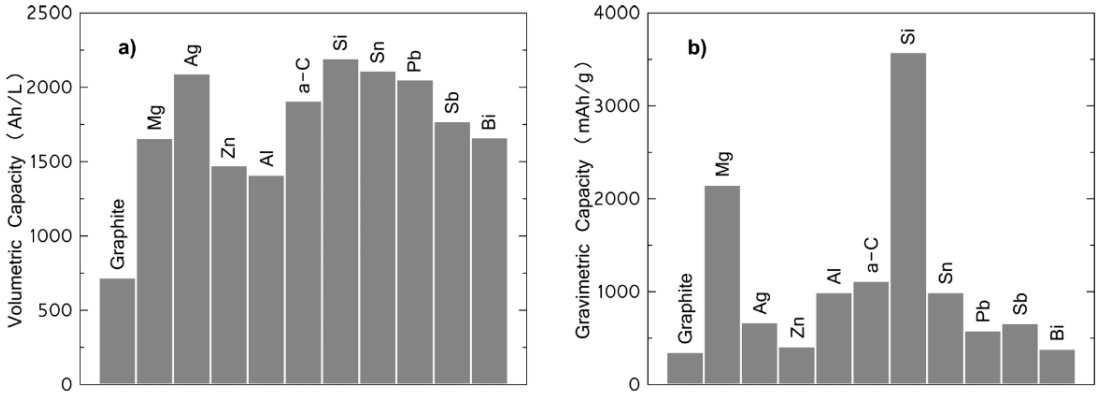

Figure 1.2.4 The (a) volumetric and (b) gravimetric (specific) capacity of the fully lithiated states of different elements.[14]

Compared to graphite, Li alloys show improved volumetric and gravimetric capacities. Notably, Si has both the highest capacities in both categories by forming a

$Li_{3.75}Si$ phase at the end of lithiation. Using pure Si as an anode would result in around a 10x increase in gravimetric capacity when compared to graphite. This large increase in capacity has motivated much interest in alloying anodes, particularly Si, for next generation batteries. However, the large volume expansion associated with the alloying reaction is detrimental for cycling stability and results in low Coulombic efficiencies. Columbic efficiency refers to the ratio of capacities upon charge and discharge and is important for the lifetime of a battery. **Figure 1.2.5** shows a plot of the energy density vs the percent volume expansion of several alloying anodes. Compared to the ~13% volume expansion of graphite after lithiation, the 200-300% expansion for alloying anodes serves as a significant challenge for designing electrodes that can withstand the large volume changes upon charging and discharging.

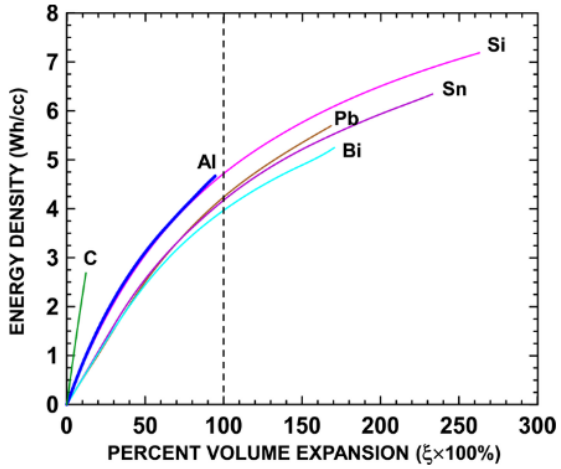

Figure 1.2.5 Energy density vs the % volume example for different elements. [14]

Generally, the reaction mechanism for alloying anodes is not as simple as single reaction step and typically follow various phase transformations between crystalline and

amorphous phases. To illustrate this concept, the Li reaction pathways of Si at high and low temperatures will be discussed.

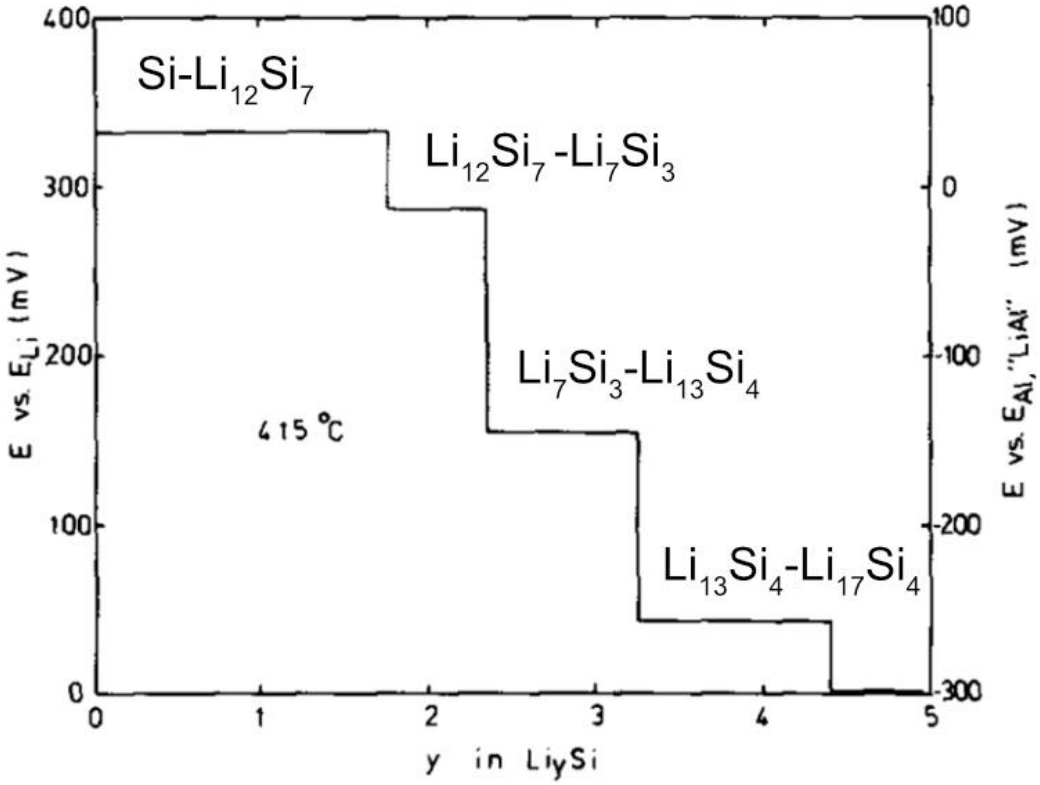

Figure 1.2.6 Coulombic titration curve of the lithiation at 415 °C showing the phases present in each plateau. [31]

Figure 1.2.6 shows a coulometric titration cure of the lithiation of Si at 415 °C. The coulometric titration curve involves current pules with time for relaxation at open circuit voltage which allows for the observation of the system without any polarization. The curve in **Figure 1.2.6** represents the equilibrium potentials obtained from the periods at open circuit voltage. The lithiation of Si at elevated temperatures involves many phase transformations between crystalline Li-Si phases. As described before, voltage plateaus indicate two-phase reactions where the phase fraction of each phase changes as a function

of the Li content. For instance, at 325 mV vs Li/Li^+, diamond cubic Si (α-Si) undergoes a two-phase reaction to form $Li_{12}Si_7$. At a composition of $Li_{1.7}Si$, $Li_{12}Si_7$ is the only phase present in the system. As more lithium is added, a new two-phase region begins at 290 mV between $Li_{12}Si_7$ and Li_7Si_3. Phase transformations to higher Li content phases occur until the potential of the Li_xSi reaches the potential of Li metal (at 0.0 V vs Li/Li^+)

Crystal models of the phases that are formed during lithiation are shown in **Figure 1.2.7**. These intermetallic Li-Si phases are part of a family of compounds known as Zintl phases. Zintl phases are compounds in which electropositive cations donate their electrons to electronegative anions which allows for a completion of their valence. In most cases, the electronegative anion is a cluster comprised of intermetallic elements. In the case of the of the compounds shown in **Figure 1.2.7**, Si forms clusters with different amounts of Si atoms which result in different charges for anion. The Si clusters will have covalent bonding between Si-Si bonds while the Li-Si interactions will be mostly ionic in nature. At the bottom of each model lists the type of Si anions present in the phase. As the Li content increases, the Si needs to accommodate more electrons and thus forms anions with fewer Si-Si bonds. At the highest lithiated phases, Si single atoms are surrounded by Li atoms, as in the $Li_{17}Si_4$ phase.

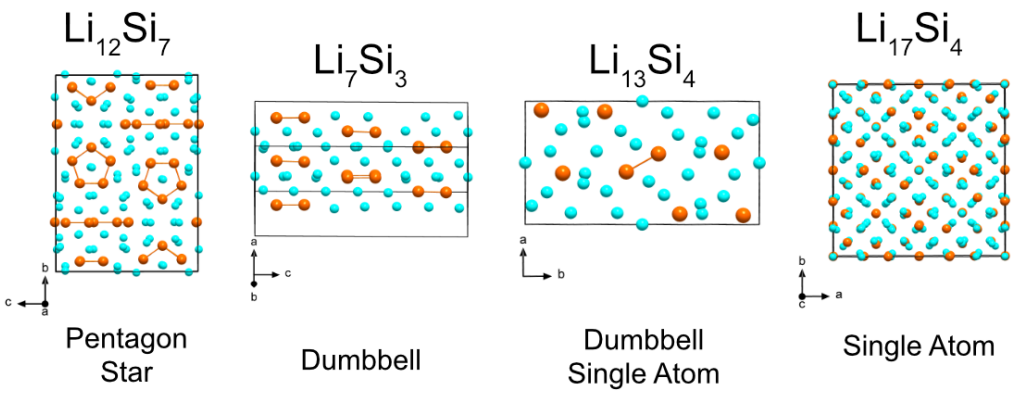

Figure 1.2.7 Crystal structures of the Li-Si phases formed during the lithiation of Si at 415 °C. Li atoms are cyan and Si atoms are orange. The text below each structure lists the type of Si clusters present in the structure.

The important distinction between the insertion mechanism and alloying mechanism is that the original host structure is significantly transformed from its original state during lithiation. If we start with diamond cubic Si and compared it to $Li_{12}Si_7$, the lithiated phase is structurally different and many Si-Si bonds have been broken. Such large structural transformations typically occur via two-phase reactions and voltage plateaus. Although, graphite and LTO also undergo two-phase reactions, the structural similarity between the different lithiated phases is the defining feature of an insertion/topotactic mechanism.

Figure 1.2.6 shows a voltage profile that is obtained at 415 °C which is much higher than typical Li-ion battery temperatures. This means that any kinetically limited reactions are bypassed during the phase transformations which allows the system to reach equilibrium by forming the most energetically favorable set of phases. In the case of Si at high temperatures, the coulometric titration closely follows the binary Li-Si phase

diagram if the Li content is modulated. However, at room temperature there are significant kinetic barriers during the formation of alloying phases with lithiation that result in non-equilibrium pathways. The most important example of this behavior is the lithiation of diamond cubic and amorphous Si at room temperature.[32]

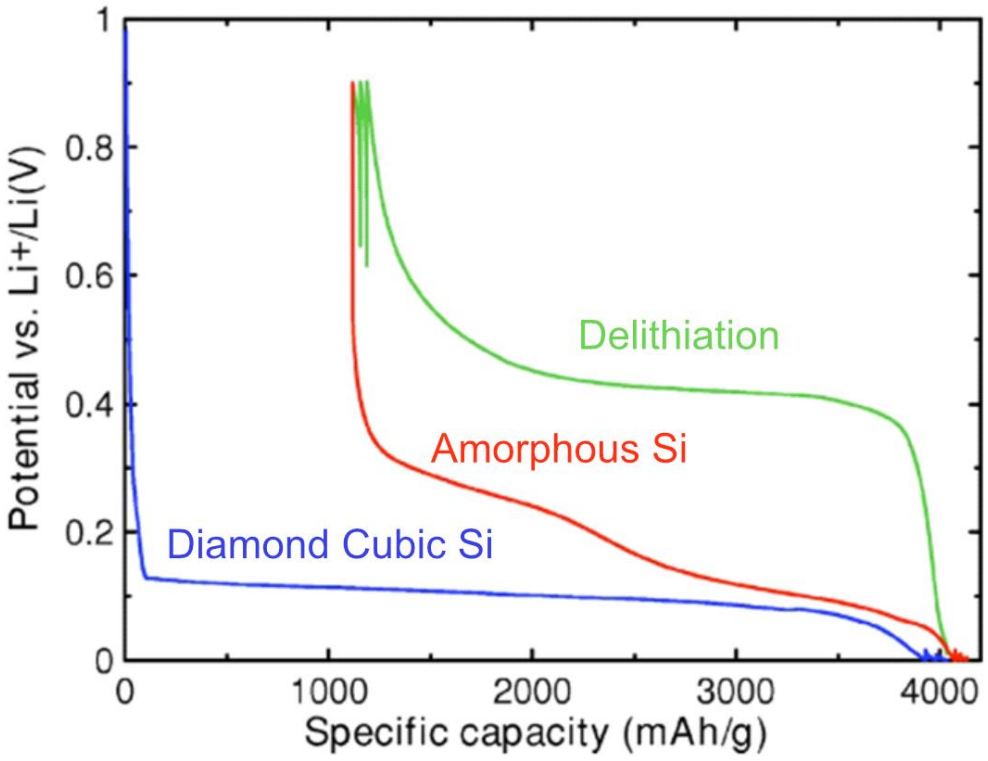

Figure 1.2.8 Voltage profile of the room temperature lithiation and delithiation of diamond cubic Si and the amorphous Si that forms in the 2nd cycle lithiation. [33]

Instead of the many voltage plateaus seen in the lithiation at 415 °C, the lithiation of diamond cubic Si at room temperature shows a single voltage plateau around 0.10-0.15 V (**Figure 1.2.8**) which then slopes off reaching a capacity of 4000 mAh/g (Li_4Si).[33] The structural origin of this plateau has been assigned to a two-phase reaction between diamond cubic Si and an amorphous Li_xSi where x is estimated to be 3.5.[33] After the full

conversion of Si to an amorphous phase and reaching a potential of around 50-60 mV, the amorphous phase crystallizes into a metastable $Li_{15}Si_4$ phase.[33] Notably, all of the cyrstalline phases described above in the high temperature lithiation process are bypassed in lieu of amorphous and metastable phases suggesting that there are kinetic limitations occurring during the lithiation. During delithiation, there is a voltage plateau related to the phase transformation between $Li_{15}Si_4$ and an amorphous Li_xSi where x is estimated to be 2.[33] After one full charge and discharge, the originally crystalline Si is converted into an amorphous Si phase. The 2nd cycle (starting with amorphous Si) shows a significantly different behavior upon lithiation with a more sloped features that start at higher potentials. However, similar to the first lithiation, $Li_{15}Si_4$ forms at low potentials. After amorphous Si is formed, it follows a similar reaction pathway for subsequent cycles.[34]

The non-equilibrium amorphous lithiation pathway of diamond cubic Si highlights an important factor of room temperature lithiations in that kinetic limitations can dominate the local phase space. For Li-Si, the Li atoms are expected to be significantly more mobile than the Si at room temperature which explains why crystallization of the Li-Si phases cannot occur, as a large amount of Si rearrangements would need to happen for them to crystallize. At higher temperatures (e.g. 415 °C), the Si kinetics are not a limiting factor and thus the system can assume the equilibrium state of crystalline phases at a certain composition.

The structures of the amorphous Li_xSi phases are more difficult to determine due to the materials not containing long-range order. This means that methods that characterize the local structure are needed. Using nuclear magnetic resonance

spectroscopy and pair distribution function analysis, the structure of the amorphous Si during lithiation and delithiation has been proposed and is shown in **Figure 1.2.9**.[35] As discussed before, Si during lithiation is kinetically limited and is unable to form equilibrium crystalline phases. However, the crystalline phases are useful as a reference for discussing and comparing to the structure of the amorphous phases. It can be seen in **Figure 1.2.9** at 100 mV, that the lithium containing phase coexisting with the diamond cubic Si consist of different types of Si clusters such as trimers, dimers and single atoms. Similar to the crystalline phases, the amorphous phase is found to be comprised of some type of Si clusters surrounded by Li atoms. At full lithiation (0 mV), the sample is comprised mostly of isolated Si atoms, similar to the $Li_{17}Si_4$ phase that forms at 415 °C. In general, all alloying anodes undergo a similar reaction process in which the original structure is broken up until Li atoms occupy most of the space and surround the original host atoms. Which type of crystalline or amorphous phases form and what types of clusters are present during the lithiation and delithiation is important to understand as these intermediate phases determine the properties of the anode during charge and discharge.

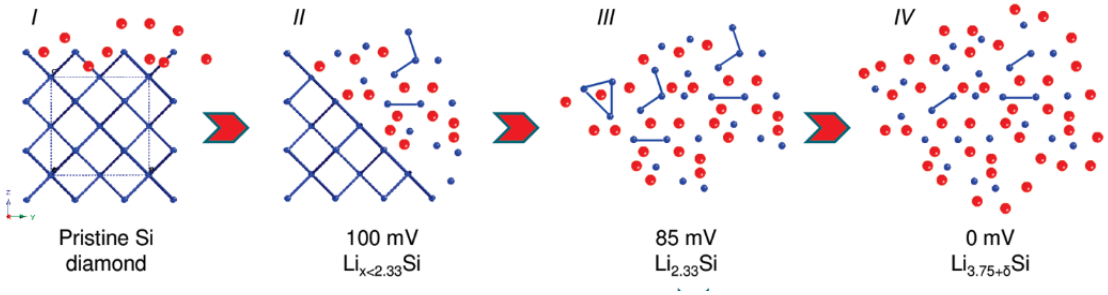

Figure 1.2.9 Schematic of a proposed lithiation mechanism of diamond cubic Si at room temperature.[35] Si atoms are blue and Li atoms are red.

The main issue with implementation of these high-capacity alloying anodes is the large irreversible capacities that occur over cycling when using traditional electrode construction. **Figure 1.2.10** shows a schematic of when silicon is cycled as a film or as particles.[36] If the film or particles are too large, the volume expansion and contraction associated with the alloying reaction creates large stress fields that result in particle fracture. The fractured particles reveal fresh reactive surfaces to the electrolyte which then results in continuous irreversible solid electrolyte interphase formation. The volume expansion also can result in particles becoming unconnected from the current collector which results in quick capacity fade.

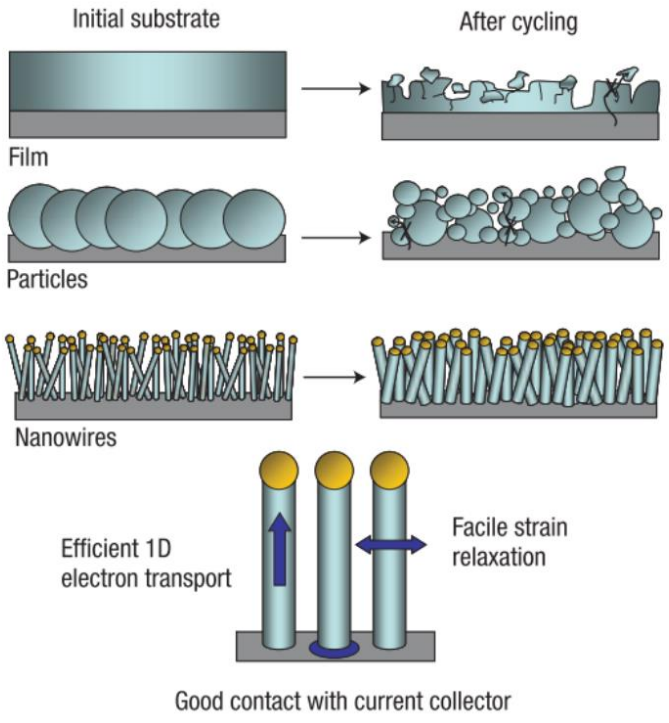

Figure 1.2.10 Schematic showing how Si electrodes with film and particle geometries result in fracture and electronic disconnection from the substrate. Nanowires, however, are able to buffer the volume expansion that occurs during lithiation/delithiation and stay connected after cycling.[36]

Many strategies have been developed to solve these issues but the most widespread one is the implementation of nanostructured materials which allows the volume expansion to be buffered. **Figure 1.2.10** shows that Si nanowires (~90 nm diameter) can be used effectively as an anode with high reversibly by allowing for the large 300% volume expansion of Si to occur without fracture or without loss contact with the current collector.[36] Many reports of Si and alloyed anode nanostructures have been reported with excellent performance.[32,37–39] However, it's important to note that the high surface area of nanostructures reduces the energy density of the electrode and increases the surface area for more side reactions with the electrolyte which is detrimental for the life time of a battery.

1.3. Tetrel Clathrates

Tetrel clathrates are host-guest crystalline structures that form a cage framework of group IV (Si, Ge, Sn) elements and host alkali-metal and alkali-earth metal atoms. The clathrate structure was first observed as a hydrate with gas molecules encapsulated in a framework of water atoms. The first Tetrel clathrate structures based on Na and Si were solved by Kasper et al. in 1965 [40] which sparked wide interest in discovering other compositions of intermetallic clathrates.[41] Since then, a large number of compositions and structural types have been synthesized and their properties investigated.[42] An excellent book detailing the structure, chemistry and properties of Tetrel clathrates is titled "The Physics and Chemistry of Inorganic Clathrates" published by Springer.[43] The following section will briefly some important structural characteristics of Tetrel clathrates that will be important to understand for the proceeding chapters.

1.3.1. Structural Types

Tetrel clathrates form different repeating units of framework and guest atom arrangements. These different structures are referred to as "types" and each different type describes a particular crystalline structure. The type I structure is the most common Tetrel clathrate and has the general formula M_8Tt_{46} where M refers to the guest atom, typically a alkali metal or alkaline earth metal and Tt refers to a group IV elements such as Si, Ge, and Sn. The structure is described by the $Pm\bar{3}n$ (223) space group. A crystal model schematic is presented in **Figure 1.3.1** of the Na_8Si_{46} with Si as the framework atoms and Na sitting in the middle of the structure. Clathrate types are commonly described by the types of polyhedra, or cages, the structure forms, and the connections between them.

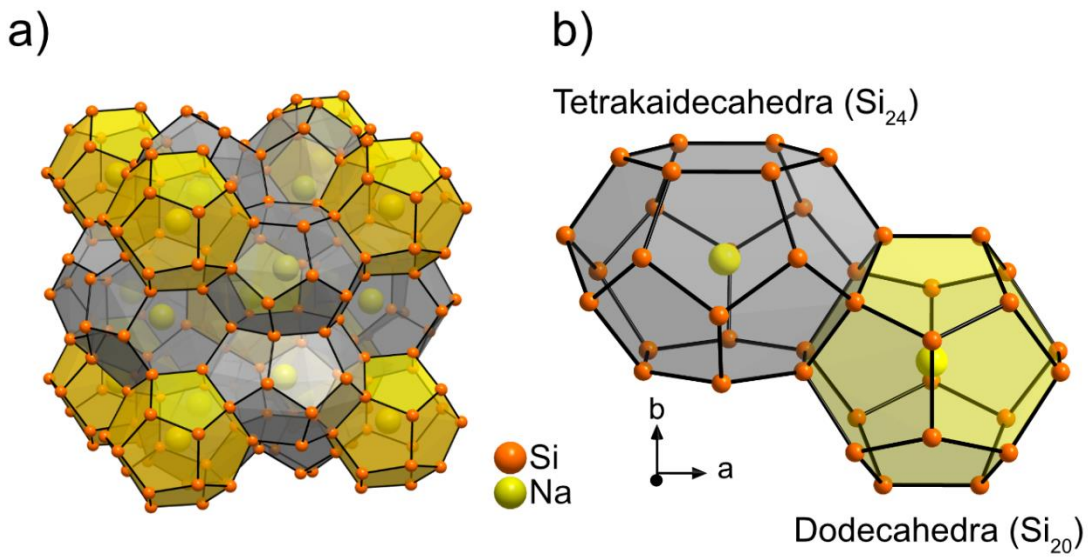

Figure 1.3.1 (a) Crystal model schematic of the expanded unit cell of type I Na_8Si_{46} clathrate with dodecahedra (Si_{20}) shaded in yellow and tetrakaidecahedra (Si_{24}) shaded in grey. (b) Schematic of the two types of polyhedral cages that comprised the type I clathrate structure.

In **Figure 1.3.1**, the two different types of polyhedra are shaded in grey and yellow. and a close up of the two of the polyhedra are shown connected by a pentagonal face in **Figure 1.3.1b**. The main distinguishing feature between the polyhedra is the amount of hexagonal and pentagonal faces that comprise the polyhedra. The tetrakaidecahedra are comprised of 12 pentagonal faces and 2 hexagonal faces while the dodecahedra are only comprised of 12 pentagonal faces. The number of hexagonal faces in the polyhedra determines the size of the cages, therefore the Tt_{24} cage has a larger free volume than the Tt_{20} cage. In the Na_8Si_{46} structure, the center of each of these cavities is occupied by a Na atom. Since there are six Si_{24} cages and two Si_{20} cages in a single unit cell and each guest atom position is symmetrically unique. The formula can also be written as $Na_6Na_2Si_{46}$ where the occupancy of each guest atom position is split based on the amount of polyhedra per formula unit. Because the size of each cage is different,

metal atoms prefer to occupy different types of cages. For instance, the $Ba_6Na_2Si_{46}$ can be synthesized where the Ba atoms prefer to occupy the larger Si_{24} cages while Na occupy the smaller Si_{20} cages.[44]

There are many types of clathrates with their own unique characteristics and this first example serves to introduce the concept and description of the structure. The type I structure is the most prominent example of the clathrate structure with an estimated ~200 compositions synthesized.[42] The following chapters will introduce the structures of other clathrate types that are investigated such as the type II and type VIII structures.

1.3.2. Defects

This section will briefly introduce some of the defects that clathrates form in deviation from their general formula. Guest atom vacancies and framework vacancies and substitutions will be discussed and clathrates as Zintl phases will be introduced.

A Zintl phase is an intermetallic compound whereby electropositive atoms donate electrons to electronegative atoms in order to complete valency rules.[45] Typically, alkali metals and alkaline earth metals donate their electrons to clusters of p-group elements. Typically, "true" Zintl phases are closed-shell compounds where the number of electrons allows for complete covalent bonding of the p-group elements. For instance, consider the prototypical Zintl compound: Na_4Si_4.[46] In this structure, the Si form tetrahedral clusters which accept 4 electrons from the Na atoms resulting in an electronically balanced structure.

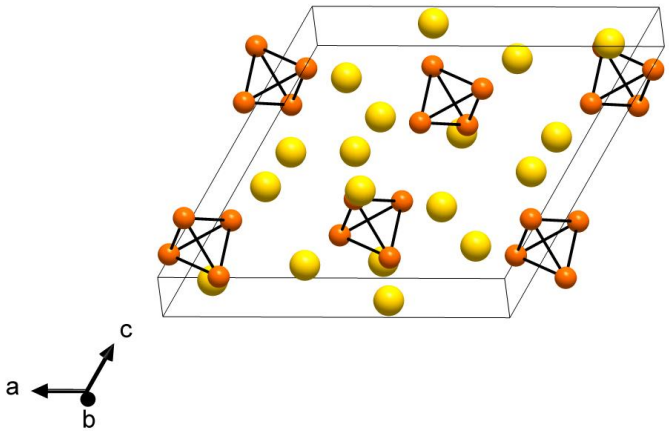

Figure 1.3.2 Crystal model schematic of Na_4Si_4 with Na in yellow and Si in orange.[46]

A crystal model schematic of Na_4Si_4 is shown in **Figure 1.3.2**. Counting the electrons in the Si tetrahedra results in 16 electrons from the 4 Si atoms. Based on achieving a fully closed octet for the tetrahedra, this would require 20 electrons. Therefore 4 more electrons are needed by the cluster, and these are provided by the 4 Na atoms for each tetrahedra. Based on this electronic configuration, a closed shell can be completed.[45]

Tetrel clathrates are often viewed in a similar type of bonding picture whereby the electropositive guest atoms donate their electrons to the host framework of Tetrel elements.[47] Considering Na_8Si_{46} described above, Na donates their electrons to the conduction band of the Si framework thus resulting in metallic behavior for the clathrate due to the free electrons from the Na atoms. This situation is referred to as a metallic Zintl phase where free electrons are delocalized in the structure.[45]

To compensate for the excess charge from the electropositive atoms, the clathrate structure can form with defects on the framework sites that reduce the overall electron count of the system.[47] There are two main forms of charge compensation: framework substitutions and framework vacancies. **Figure 1.3.3** shows density of states for type I clathrates $K_8B_8Si_{38}$[48] and $Ba_8Ge_{43}\square_3$[43] with the electron accounting below each plot. In the case of $K_8B_8Si_{38,}$ the B atoms substitute for Si on the framework sites. Boron is a group III elements which means it has one less electron than Si. This means that the 8 e^- of excess charge from the K atoms will be compensated by the one less electron from the eight boron atoms resulting in an electron balanced system. This is reflected in density of states of the material which shows the Fermi level (E_f) in the gap which is indicative of semiconducting behavior. The electron accounting show how each element in the structure can be assigned a charge in terms of the total electron balance. The K atoms have a positive charge which represent the charge transfer to the framework atoms. The Si atoms have a no charge because they can form 4 bonds (4b) with themselves while remaining neutral. The B atoms also form 4 bonds but require an extra electron to do so and thus are assigned a negative charge. Overall, the system is balanced as the amount of electrons donated by the K are balanced by the B.

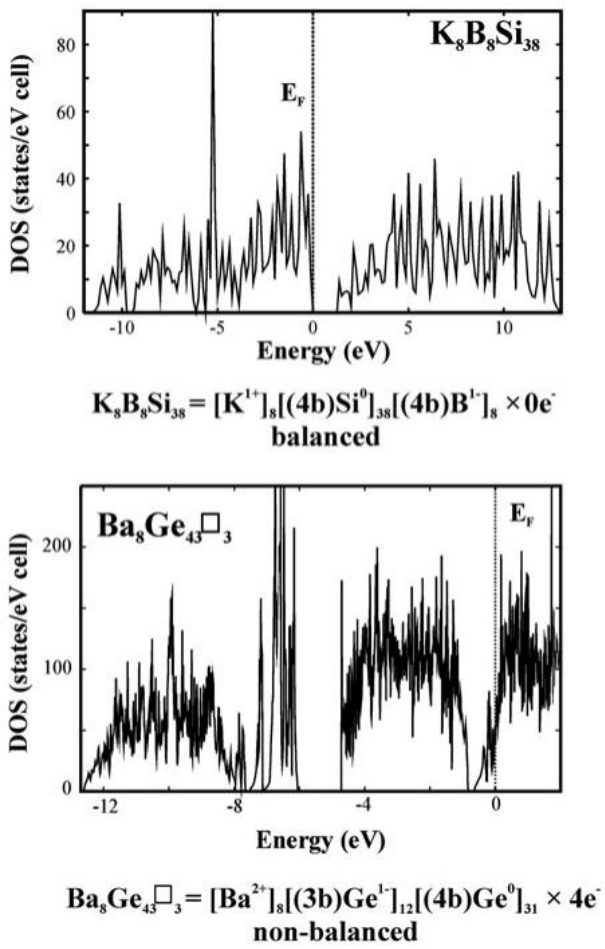

Figure 1.3.3 Calculated density of states (DOS) and electron accounting for the type I (a) $K_8B_8Si_{38}$ and (b) $Ba_8Ge_{43}\square_3$ clathrates.[43]

For $Ba_8Ge_{43}\square_3$, the type I structure forms with Ge vacancies which serve to reduce the total electron count of the system to compensate for the electrons from the Ba guest atoms. Similar to the previous case, the Ba atoms are expected to donate their electrons to the host framework for a total of 16 e^-. When there are framework vacancies, the four surrounding Ge atoms only make 3 bonds (3b) and then take an electron from the Ba to achieve a compete shell. This results in 12 electrons from the Ba atoms

compensating for dangling bonds of the Ge atoms surrounding the vacancies. The 4 excess electrons result in a non-balanced accounting and are the origin of the metallic electronic behavior. This is reflected in the calculated density of states where the Fermi level is in the conduction band. The electron accounting for $Ba_8Ge_{43}\square_3$ is shown below the density of states plot.

The guest atom, framework atom, and atom substitutions result in a wide design space for tuning the properties of clathrates structures. **Figure 1.3.4** shows a periodic table showing the major and minor clathrate-forming elements.[42] Notably, the Tetrel elements and alkali metals comprise the main clathrate-forming elements. Although the thermoelectric performance of clathrates has been studied extensively in relation to the defects of clathrates,[42] comparatively little work has been done considering their possible electrochemical reactions with Li. Considering the large interest in Tetrel elements for Li-ion battery anodes, the investigation into the wide design space of clathrates is warranted. The following section will overview the previous literature regarding the electrochemical performance of Tetrel clathrates and some other related materials.

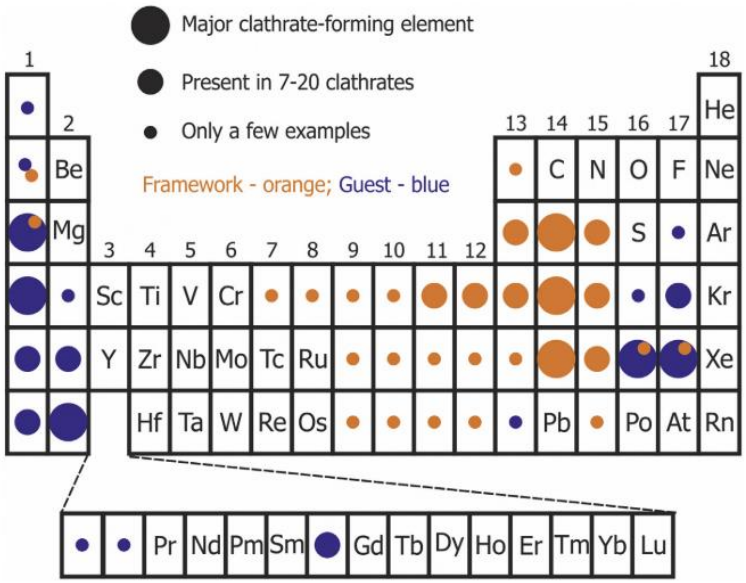

Figure 1.3.4 Periodic table showing the major and minor clathrate forming elements for the framework and guest atoms.[42]

1.4. Literature of Previous Applications of Tetrel Clathrates for Li-ion Batteries

In 2012, Langer et. al reported the synthesis, characterization and electrochemical lithiation of Type II Si clathrate.[49] The Type II Si clathrate was synthesized via the thermal decomposition of Na_4Si_4 under dynamic vacuum at 450 ºC for 5 days resulted in Type II Si clathrate with minor Type I Si impurities. The Na content of the clathrate was estimated by Rietveld refinement from powder diffraction data and resulted in a composition of $Na_{1.3}Si_{136}$. This suggests that most of the cages of the clathrate are empty. Half-cells with Li metal were used to test the electrochemical properties and one full lithiation is reported with ex-situ XRD at different points in lithiation. **Figure 1.4.1** shows the voltage profile from the $Na_{1.3}Si_{136}$ from Langer et. al and the voltage profile from diamond cubic Si.[50] Note that the first lithiation of diamond cubic silicon shows a flat voltage plateau without much sloping until the end of lithiation.

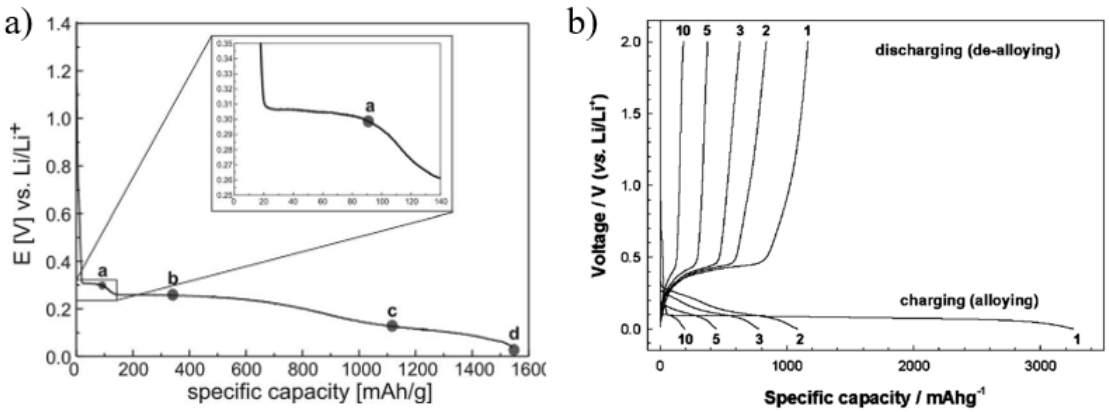

Figure 1.4.1 (a) Voltage profile of $Na_{1.3}Si_{136}$ with an enlarged inset of the plateau corresponding to insertion of Li.[49] (b) Voltage profile of cycles 1,2,3,5 and 10 of diamond cubic Si.[50]

Ex-situ NMR was performed on electrode at the point "a" (**Figure 1.4.1a**) to assess the local Li environment. The authors found from ^{7}Li NMR, chemical shifts at 412 and 433 ppm in a 2:1 ratio from the ^{7}Li NMR analysis. They attribute the two resonances to Li occupation inside the clathrate structure because the chemical shifts are higher than that for Li metal (270 ppm). This is analogous to the situation in Na_xSi_{136} where Na resonates at a chemical shift higher than Na metal which indicate strongly metallic bonding character of the Li/Na atoms in the clathrate cages.

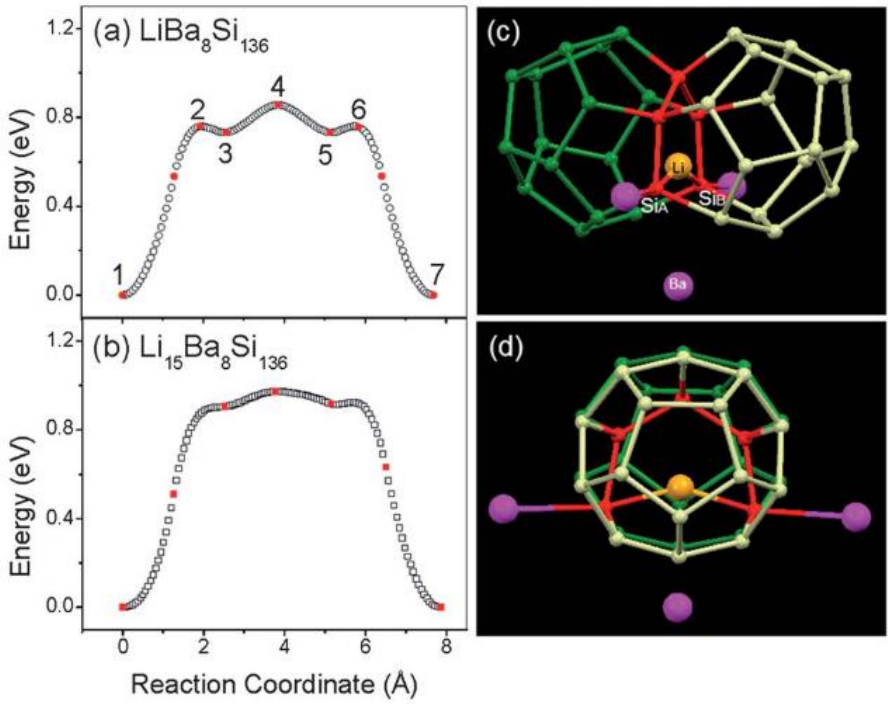

Figure 1.4.2 Nudged elastic band (NEB) calculations showing the energy vs reaction coordinate of Li migration between two Si_{20} cages where a Si-Si is broken and then reformed.[51]

In 2013, Yang et al. published an article titled "Silicon clathrates as anode materials for lithium ion batteries?" and evaluated Type II Si clathrates for Li-ion anode applications with first principles density functional theory (DFT) calculations.[51] The

formation energy, voltage, volume expansion and band structure of $Ba_{6-8}Si_{136}$ at various states of Li insertion were evaluated. In addition, the migration of Li between the cages were considered by using the nudged elastic band (NEB) method. The authors found that Li insertion into the small Si_{20} cages of Ba_8Si_{136} resulted in flat voltage profile at 0.4 V, small volume change, and metallic character. The NEB calculations found that the lowest migration barrier for Li was through a hexagonal face (0.33 eV) and that moving Li moving through a pentagonal face involved breaking and reforming a Si-Si bond with a barrier of 0.73-85 eV. **Figure 1.4.2** shows the NEB energies vs reaction coordinate (**Figure 1.4.2ab**) and the transition states of the bond breaking pathway (**Figure 1.4.2cd**) for Li in $LiBa_8Si_{136}$ and $Li_{15}Ba_8Si_{136}$.

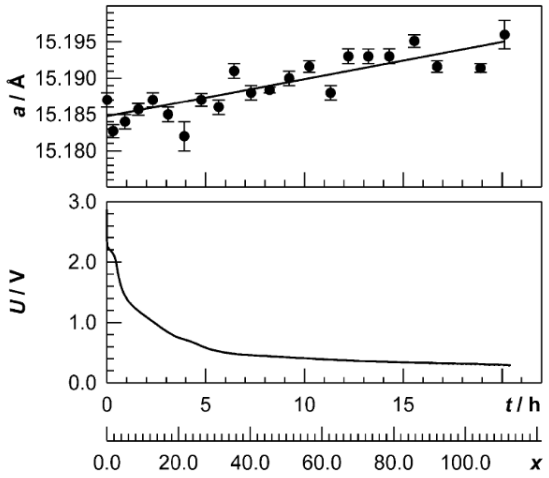

Figure 1.4.3 The measured lattice constant and voltage of Ge_{136} as a function of Li content where $Li_xGe_{136.}$ [52]

In 2014, a brief communication investigated the lithiation of guest free Type II Ge clathrate, Ge_{136} with in-situ powder X-ray diffraction.[52] The lattice constant of the Ge clathrate phase was monitored as a function of lithiation (**Figure 1.4.3**). The authors

attributed the increase of the lattice constant during increasing Li as evidence of Li occupation of the clathrate cages.

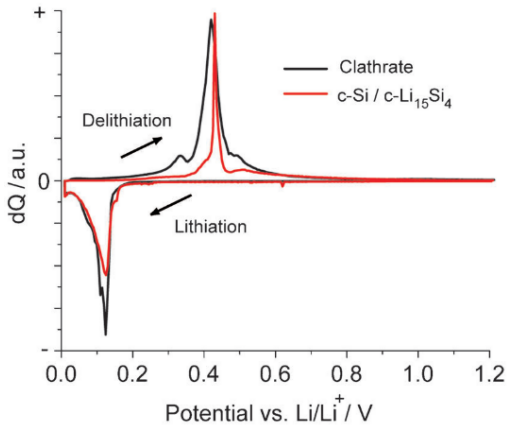

Figure 1.4.4 Normalized dQ plot showing that the reactions of $Na_{24}Si_{136}$ and diamond cubic Si are similar.[53]

In 2014, Wagner et al investigated the electrochemical cycling of sodium-filled silicon clathrates.[53] The investigated material was mixture of 80% Type II $Na_{24}Si_{136}$ and 20% Type I Na_8Si_{46}. The authors found that the electrochemical reactions of this mixture of clathrates behaved very similarly to diamond cubic Si (c-Si) which is shown in **Figure 1.4.4**. *Ex situ* XRD after full lithiation of the Si clathrate detected the presence of $Li_{15}Si_4$, which is typical of the full lithiation of diamond cubic Si. DFT calculations were also performed to investigate the energetics of potential Li insertion sites into the $Na_{24}Si_{136}$ by calculating the formation energy. Authors evaluated the composition $Li_{16}Na_{24}Si_{136}$ with three different Li configurations in the cage structure and concluded that with the negative formation energies, these configurations were potentially accessible.

In 2015, Li et. al reported the synthesis and characterization of the Type I $Ba_8Al_ySi_{46}$-y clathrate synthesized by thermal annealing and arc-melting.[54] Electrochemical cycling, nuclear magnetic resonance spectroscopy, X-ray diffraction, and X-ray photoelectron spectroscopy were used to evaluate the structural and electrochemical properties. The authors found that reversible capacities of 499 mAh/g at 5 mA/g could be obtained without destruction of the clathrate lattice, as evidenced by ex-situ XRD and NMR. The electrochemical voltage profile is also distinctly different than that of diamond cubic Si showing a sloped reaction with a much lower capacity, as shown in **Figure 1.4.5**. The NMR spectroscopy showed no changes in the ^{29}Si chemical shift, suggesting no changes to the Si clathrate lattice. The ^{7}Li showed a resonance similar to LiSi and different than the resonances of Li in the Type II Si clathrate suggesting a different chemical environment for Li based on the occupation of Ba in the clathrate cages.

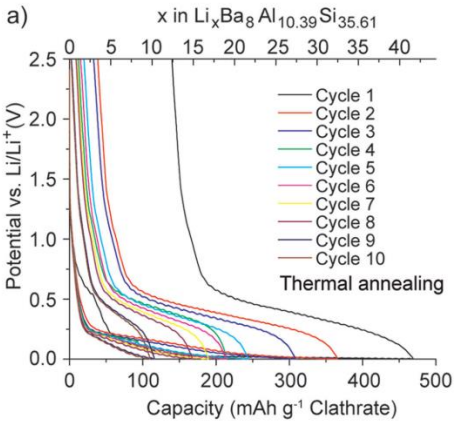

Figure 1.4.5 First 10 cycles of $Ba_8Al_{10.39}Si_{34.61}$ Type I Clathrate synthesized by thermal annealing.[54]

In 2015, Peng et al. reported a DFT investigation of the lithiation of Ba-doped Si clathrate, Ba_8Si_{46}.[55] Various Li positions inside the Type I clathrate crystal structure were investigated and evaluated by calculating the formation energies and voltages with respect to Li metal. The structural distortion and band structure from Li insertion were also analyzed.

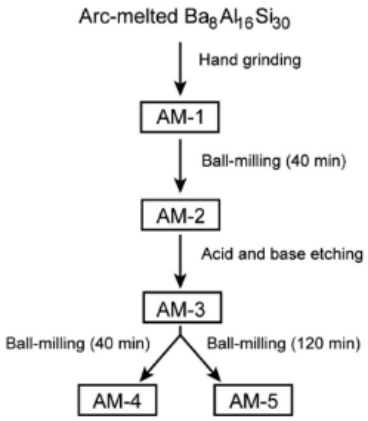

Figure 1.4.6 Processing step investigated for the Type I clathrate, $Ba_8Al_{16}Si_{30}$.[56]

In 2017, Zhao et al. investigated the role of processing on the surface properties and the electrochemical behavior of the Type I Si clathrate, $Ba_8Al_{16}Si_{30}$.[56] In the previous work by Li et. al, various processing steps were applied to the clathrate powder before electrochemical evaluation including ball-milling and acid/base treatment. Zhao et al. performed electrochemical and structural characterization in between each of these processing steps. **Figure 1.4.6** shows the different processes applied to the clathrate. The authors found that the surfaces of the ball-milled powder (AM-2, AM-4, AM-5) exhibited significant amorphous surfaces surrounding a crystalline clathrate core from the transmission electron microscopy imaging. This was correlated to electrochemical

performance as the powder with the thicker amorphous surface had a higher capacity. The authors concluded that the $Ba_8Al_{16}Si_{30}$ clathrate powders were electrochemically inactive to Li unless defects were introduced by ball-milling.

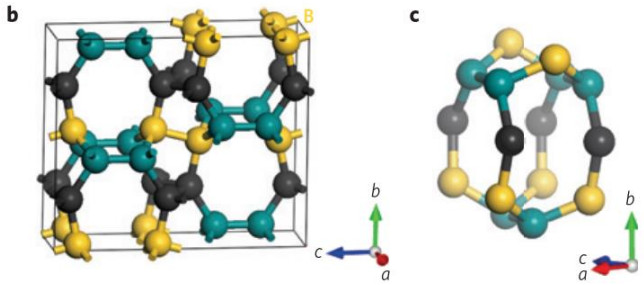

Figure 1.4.7 Crystal structure of the recently discovered Si polymorph, Si_{24}, with a crystal structure similar to clathrates and predicted to have high Li mobility.[57]

That concludes the clathrate literature related to applications for batteries. A summary of two papers evalulating a recently discovered Si polymorph Si_{24} for Li-ion battery and Na-ion battery applications is given in the following dicussion. The Si_{24} material is an open cage framework of Si obtained from Na_4Si_{24} by heating under vacuum similar to the way Si_{136} is obtained.[57] A picture of the crystal structure is shown in **Figure 1.4.7**. In 2017, Arrieta et. al investigated sodium intercalation in the Na_xSi_{24} for Na-ion anodes with DFT calculations.[58] By using cluster expansions to generate possible Na_xSi_{24} supercell configurations the authors evalulated 235 different configurations to generate a realtionship between formation energy and Na content. The voltage profile dervied from this suggested a solid solution mechansim for Na intercalation. NEB calculations were also performed resulting in 0.7-0.8 eV barriers for Na hopping. In 2018, He et al investigated Si_{24} for Li-ion and Na-ion anode applications with DFT.[59] For both Li and

Na, the voltage, volume expansion, electronic structure, and diffusivity were evalulated. The authors found that Li and Na insertion into the structure resulted in small volume changes and both structures had had high diffusion of Li and Na based on ab-inito molecular dyanamics calculations.

1.5. Goals of Research

Overall, the literature related to Tetrel clathrates has been limited to Si clathrates with one brief experimental work related to Ge clathrates. Ge and Sn clathrates represent a large design space for Tetrel clathrates and since Si, Ge, and Sn are all promising alloying anode materials with high capacities, understanding how their Li-alloying reactions differ is of interest for Li-ion batteries. Furthermore, from the evidence of Li insertion in Si_{136} and the DFT calculations regarding Si_{136} and Si_{24}, it seems that Li insertion into empty frameworks of Tt elements could have interesting properties. However, there has been no report of reversible insertion of Li into these structures without guest atoms. The main goal of this work is to develop relationships between the clathrate structures and their electrochemical properties which to date has mainly been limited to Si clathrates. From the review it can be seen that the electrochemistry is similar to the host elements and in some other cases very different. This work hopes to shed light on to why these similarities and differences occur and what implications they have for Li-ion batteries.

Based on these considerations, this dissertation is split into three parts: Clathrates as Insertion Anodes, Clathrates as Alloying Anodes, and High Temperature Electrochemical Synthesis of Si and Ge Clathrates. The first section investigates the open structure of Tetrel clathrates as topotactic insertion anodes where Li is able to reversibly diffuse in and out of the clathrate lattice upon electrochemical bias. To investigate this a combination of density functional theory and experimental methods will be used to identify structural features that are amenable to bulk Li diffusion. The second section investigates how the clathrate structure affects the Li alloying pathways of Ge, Sn and Si

clathrates with a comparison to the common elemental analogue (i.e. diamond cubic Ge/Si). The goal is to give a clearer understanding of how the structural features of clathrates can be used to modify the subsequent lithiation pathways which is important for optimizing the performance of Li-ion battery anodes. To do this, synchrotron X-ray diffraction and pair distribution function analysis is used to investigate the long and short range order of the clathrates at different Li compositions. Finally, the last section demonstrates the viability of using high temperature electrochemistry to synthesize the metastable Na-Si and Na-Ge clathrates. Since these clathrates are of technological interest, developing more controllable synthesis methods will aid in understanding their structure-property relationships. This section focuses on using an electrochemical cell with Na β''-alumina solid electrolyte to desodiate the Na_4Tt_4 (Tt= Si, Ge) Zintl phases at 300-550 °C, which under some conditions result in the synthesis of the Tetrel clathrates.

2. EXPERIMENTAL AND COMPUTATIONAL METHODS

2.1.Electrochemical Characterization

2.1.1. Electrode and Cell Construction for Li-ion Batteries

In this work, powdered samples of clathrate materials are investigated in two electrode half-cells with Li metal to investigate their electrochemical reactions with Li. Li metal is used as both the reference and counter electrode because the potential of Li metal does not change as the state of charge changes. The reference allows the composition dependent potential changes of the materials to be investigated.

The composite electrodes for the clathrate and comparison active materials are constructed in the following way. First, the clathrate material is grinded up so that a suitable slurry can be made. In some cases, the clathrate material is already a powder with sufficiently small particles size and no intermediate grinding is needed. Grinding is done either via ball-milling or by hand grinding with a mortar and pestle. After the powder is ready, the clathrate active material, carbon black conductive additive, and polyvinylidene fluoride (PVDF) binder is mixed in an 80/10/10 weight% ratio. Then N-Methyl-2-pyrrolidone (NMP) is added to the solids and mixed with a stir bar until the slurry reaches a desirable consistency. Sometimes to facilitate dissolving the PVDF in the NMP, the slurry is heated to 50-75 °C during vigorous stirring. Generally, the amount of active material was quite low (0.2-0.3 g) and thus a small vial (20-50 mL) could be used to form the slurry.

Once the slurry has been evenly mixed, the slurry is cast upon dendritic copper foil with a Mayer rod. To control the thickness of the film, different layers of scotch tape

were used. Then the film was dried at 120 ºC on a hotplate to evaporate the NMP for 4-5 hours. Now the electrode film can be cut into 15 mm disc electrodes and evaluated in electrochemical cells.

Figure 2.1.1 Labelled parts of a coin cell including the spring, circle electrode, positive case, negative case, and spacers.

Two types of cells are used in this work: coin cells and pouch cells. Coin cells were generally used for longer term cycling experiments while pouch cells were used for samples that needed to be extracted for *ex situ* characterization (e.g. XRD/SEM). Coin cells are comprised of stainless-steel casing and are then crimped to seal the coin cell. **Figure 2.1.1** shows the parts used to construct the coin cell. There is a spring that is used to maintain pressure after crimping, the electrode (in the case of a half-cell with Li metal as the counter electrode, the other electrode is considered the cathode), the spacers, and

the negative and positive case. In addition, there is the circular Li metal chip which acts as the counter/reference electrode, the separator, and the electrolyte. Then these components are assembled in the following order:

1) Negative case
2) Spring
3) 2 Spacers
4) Copper anode
5) Place 3-5 drops or a measured amount of electrolyte (~20-40 µL) on top the electrode so it appears evenly wetted.
6) Place the polymer separator (Celgard) on top of the electrode so it covers it
7) Place 2 more drops of electrolyte on top of the separator and place the Li metal foil on top so it is concentric with the composite electrode.
8) Positive case
9) Crimp the coin cell to seal it.

Then the coin cell is ready for electrochemical testing.

For pouch cells, the cell is assembled in a similar way, but the packaging is a polyfoil bag and is heat sealed. The current collector leads are strips of Cu foil. The cell is assembled in the following order:

1) Cu lead (leading to outside the polyfoil bag)
2) Place a small drop of electrolyte next to the lead and place to copper anode electrode on top with the active side facing up. This creates a good adhesion for the electrode to make the cell construction easier.

3) Place 3-5 drops or a measured amount of electrolyte (~20-40 µL) on top the electrode so it appears evenly wetted.
4) Place the polymer separator (Celgard) on top of the electrode so it covers it
5) Place 2 more drops of electrolyte on top of the separator and place the Li metal foil on top so it is concentric with the composite electrode.
6) Place the 2nd copper lead on top of the Li metal.
7) Seal both sides of the polyfoil bag where the Cu leads come out.

2.1.2. Galvanostatic Measurements

Once a half-cell has been constructed, the cell can be charged and discharged with a potentiostat. A potentiostat allows for the precise control and measurement of the voltage and current of an electrochemical cell. Biologic VMP3 and MPG potentiostats are mainly used in this work to conduct the galvanostatic current with potential limits (GCPL) technique. This technique forces a constant current charge or discharge on the cell and the voltage of the cell is changed in order to achieve the constant current measurement. Constant current measurements are standard for testing battery materials, and they allow for straightforward calculations of the current rate needed for a desired C-rate. For instance, if the capacity of the material is 200 mAh/g, then a constant current of 200 mA/g will charge/discharge the cell in one hour (i.e. C-rate of 1). The active mass of the electrode is measured by subtracting away the mass contribution of the Cu current collector and then multiplying the mass by the ratio used in the slurry (usually 80wt%). Typically, potential limits are used during constant current to maintain the electrode in

voltage ranges where the materials are stable. In this work the typical voltage range for measurements is 0.01 V – 2.5 V vs Li/Li^+. However, this can be altered depending on the specific voltage ranges that are interesting for investigation.

Once a cell is constructed and is being charged and discharged with the potentiostat, a voltage profile is obtained which relates the potential to the extent of the reaction. Since constant current measurements are used, the time of applied current is proportional to the capacity via the magnitude of the applied current. As described earlier, the capacity can be converted into a number of Li as well which is often useful for directly connecting the chemistry of the system to specific electrochemical reactions.

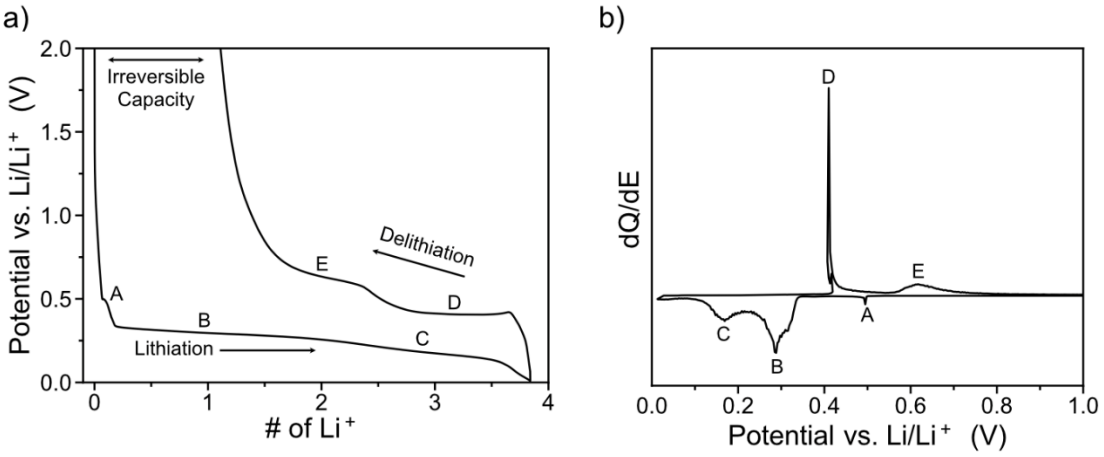

Figure 2.1.2 Voltage profile and corresponding dQ/dE plot of diamond cubic Ge showing the first lithiation and delithiation.

Figure 2.1.2 shows an example of a voltage profile obtained from the lithiation of diamond cubic Ge powder in a two electrode half-cell with Li metal. **Figure 2.1.2a** shows the voltage profile in terms of Potential vs. Li/Li^+ versus the # of Li^+ per Ge atom. Typically, adding lithium to the composite electrode will decrease the potential of the cell

until it reaches the lower voltage cutoff of 0.01 V. Since 0.00 V corresponds to the energy of Li metal, low reaction voltage corresponds to higher energy states, while high potentials correspond to lower energy states. When the current is reversed and lithium is moved away from composite electrode, the potential of electrode increases relative to Li metal. This is shown for the part of the curve labelled delithiation which refers to the removal of Li from the active material. In the voltage profile of diamond cubic Ge, there are various features such as plateaus and sloped regions. From the previous discussion, observing these features is important for identifying the electrochemical reactions occurring within the material. **Figure 2.1.2** labels significant features upon lithiation and delithiation.

Figure 2.1.2b shows a plot of the derivative, dQ/dE, versus the potential. This type of plot called a dQ plot or a dQ/dE plot is an alternative way to view the information contained in the voltage profile. This is a useful way to view the information because it emphasizes features in the voltage profile with high dQ/dE (or plateaus). The corresponding dQ/dE plot shows plateaus as peaks and allow for the convenient assignment of electrochemical reactions based on the peak position. For instance, the plateau during lithiation labelled “D”, corresponds to a sharp peak in the dQ/dE plot. The higher the magnitude of the peak, the flatter the plateau.

Another feature of the voltage profile is being able to quantify the irreversible capacity, which is the difference in charge between the lithiation and delithiation. This quantity is related to the Coulombic efficiency and is an important parameter for measuring the amount of irreversible reactions in an electrochemical cell. As can be seen

in **Figure 2.1.2a**, there is an irreversible capacity of around 1 Li^+ between lithiation and delithiation. Notably, this is not obviously apparent in the dQ/dE plot where the capacity can be measured by integrating the curves in terms of the potential. For this reason, the voltage profile is useful for observing changes in capacity over time while the dQ/dE plot is insightful for monitoring changes in the electrochemical features during the reaction. Understanding the structural origin of the electrochemical plateaus (e.g. B, C D, E) is the main goal for a battery researcher as it allows for the connection of the electrochemical properties to the structure of the material as a function of state of charge.

2.1.3. Electrochemical Impedance Spectroscopy (EIS)

Electrochemical Impedance Spectroscopy is a useful electrochemical technique that utilizes AC potentials to measure the frequency dependent impedance of an electrochemical cell. Since different electrochemical impedances occur in different times scales, or frequency ranges, this method allows for the characterization of quantities related to charge transfer resistance, capacitance, resistance, and diffusion. The measurement is implemented by applying a sinusoid perturbation (current or potential) at a certain frequency and measuring the corresponding response of the system. Like traditional AC circuits, the system will have a certain response based on type of circuit elements present. The impedance of the system is represented by the following equation:

$$Z(\omega) = \frac{E}{I} = Z_0 \exp(j\phi) = Z_0 \exp(cos\phi + jsin\phi)$$

Where $Z(\omega)$ is the impedance of the system as a function of the frequency, E is the voltage, I is the current, Z_0 is the magnitude of the impedance, and ϕ is the phase shift. An electrochemical cell can be modeled as an equivalent circuit which allows for the modelling of the features of the EIS experiment. For instance, a resistor and parallel in parallel shows up as a semicircle in the Nyquist plot, which shows the negative imaginary impedance vs the real impedance. This resistor and capacitor in parallel represent an electrochemical interface where charge transfer can occur. The equivalent circuit model can be used to describe the impedance response of a battery and gain quantitative data about the impedance of the system.

2.1.4. Galvanostatic Intermittent Titration Technique (GITT)

The Galvanostatic Intermittent Titration Technique is an electrochemical technique that involves constant current pulses in between periods of open circuit voltage relaxation.[60] After a current pulse is applied, the state of charge of the system changes and during relaxation the new open circuit voltage contains information about the kinetics and thermodynamics of the electrochemical system. This method can be used to estimate the diffusivity of an electroactive ion in a solid solution electrode material and observe how the polarization of a cell changes as a function of charge. In this work, the latter application will be used. **Figure 2.1.3** shows a plot of the current, and voltage vs time to demonstrate the voltage current relationship during the measurement.

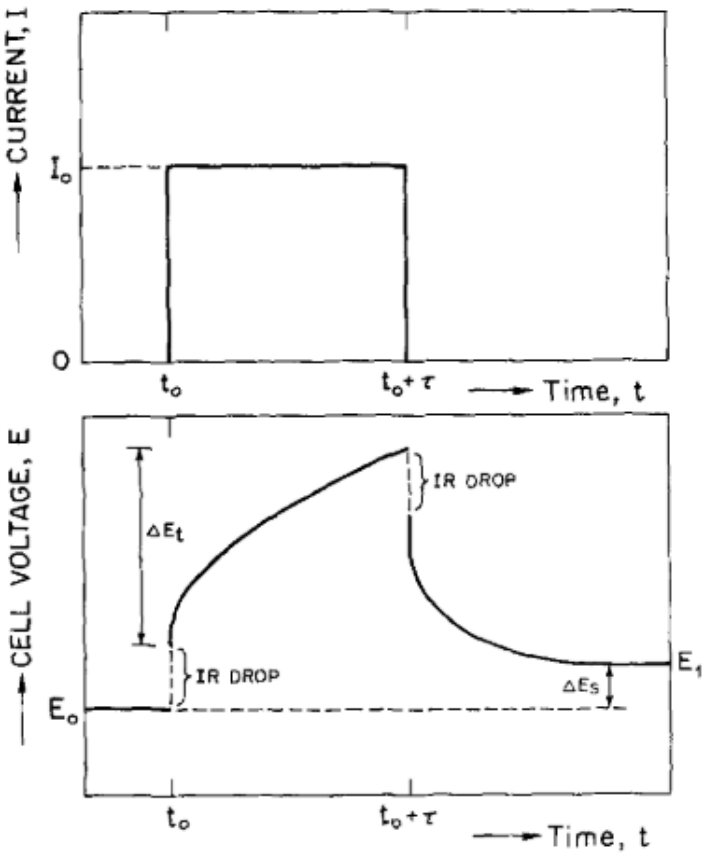

Figure 2.1.3 Plot of the current and voltage vs time for a single current pulse of the galvanostatic intermittent titration technique.[60]

This method is useful for several situations because it allows for the open circuit voltage to be viewed as a function of charge. Sometimes the voltage response to a constant applied current is dominated by polarizations that are not related to the equilibrium behavior of the system. By allowing the system to relax, the kinetic effects on the potential can be mitigated and better understanding of the capacity dependent effects on the potential can be elucidated.

2.1.5. High Temperature Electrochemical Cells

The 5th chapter of this dissertation will explore the high temperature electrochemical synthesis Si and Ge clathrates. This section will briefly go over the construction of the housing of these cells and their implementation. The specifics of the cell construction will be discussed within each of the sections of Chapter 5.

The standard Li-ion cells that are tested in this work are all measured at room temperature. However, many times the sluggish kinetics at room temperature result in non-equilibrium pathways. For example, the previously described amorphous Si phase transformation is an excellent example of how room temperature lithiation results in a non-equilibrium reaction pathway. There has been various work done in performing electrochemical experiments at higher temperatures which have been useful for revealing the equilibrium behavior of certain systems. Since the commonly used organic electrolyte, separator and binder in Li-ion batteries are not stable up to higher temperatures (200-600 °C) alternative electrolytes and components need to be used to achieve stable electrochemistry. For this reason, the high temperature cells investigated in this work use Na β’’-alumina solid electrolytes to shuttle Na atoms for the synthesis of Si/Ge clathrates.

Another challenge is the housing used to contain the electrochemical cell. The housing must have the following requirements for practical use:

- Stable under high temperatures
- Creates an effective seal to maintain a closed volume.

- Allows for a current collector that is electronically isolated from another current collector
- Easy to open and close after operation

High temperature electrochemical experiments are often done in a glovebox which is inconvenient as it requires a custom setup for heating and performing the measurements. To perform the high temperature electrochemical measurements, a stainless-steel housing reactor comprised of commonly available high vacuum parts is used to perform electrochemical experiments outside of the glovebox in common lab furnaces.

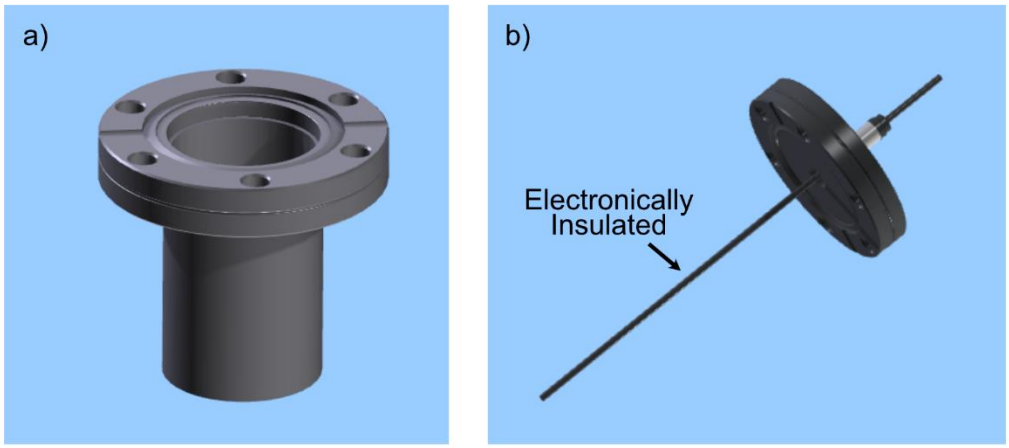

Figure 2.1.4 Images of the high temperature cell parts: (a) stainless steel half nipple (Kurt J. Lesker, HN-0275) and (b) stainless-steel electrical feedthrough (Kurt J. Lesker, EFT0512093)

The electrochemical reactor is comprised of a stainless-steel half nipple with a stainless-steel cap welded to the bottom of it. The machine and electrical shop in the Instrument Design and Fabrication Core Facility at ASU were used for the welding. The

electronically insulated part is an electrical feed through with a stainless-steel current collector and alumina insulation. Pictures of these parts from the supplier website are shown in **Figure 2.1.4**. To assemble the cell, the parts are brought into the glovebox and the electrochemical cell is placed inside the housing and then the electrical feedthrough is sealed together with the half-nipple with a copper O-ring and tightened with screws and bolts. Wires can then be attached to the main body of the housing and the top of the feedthrough which correspond to the two current collectors for the negative and positive terminals of the cell. The housing is then placed in an oven and then hooked to a potentiostat. **Figure 2.1.5a** shows a photograph of the housing in the glovebox prior to assembly with the Cu O-ring in place. **Figure 2.1.5b** shows the housing sealed and outside the glovebox with the stainless-steel wires coming from the different terminals. **Figure 2.1.5c** shows a photograph of the cells after they are placed in the furnace. The stainless-steel wiring surrounded by Alumina bead insulation comes out of the edge of the furnace door so that it can connect to the potentiostat terminals.

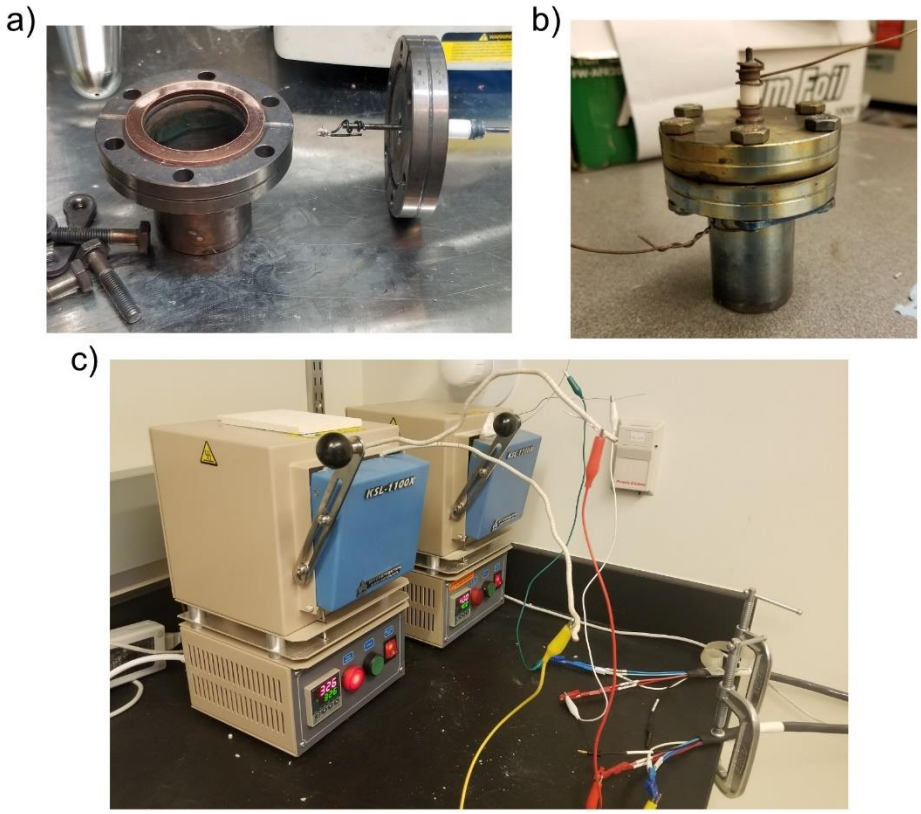

Figure 2.1.5 (a) Photograph of the high temperature cell housing prior to assembling in the glove box. (b) Photograph of the high temperature cell housing after assembly with the stainless-steel wires connected to the two terminals. (c) Photograph of the furnace used for the high temperature electrochemical experiments with the leads coming out and connecting to the potenitostat leads.

The stainless-steel housing has been tested to up to 450 °C in air and shows stable operation after long periods of heating. Temperatures above 450 °C result in more significant oxidation of the housing parts and make it difficult to open the cell because the screws and bolts seize where the screws are unable to be screwed off. If this happens the bolt itself needs to be fractured. To operate at temperatures higher than 450 °C, it is recommended that the cell be heated inside a glovebox with an inert, oxygen free atmosphere which results in less oxidation to the housing. Overall, this housing for high temperature electrochemical cells has been proven to allow for a sealed oxygen free

environment and significantly simplifies the requirements for operating cells at high temperatures.

2.2.Materials Characterization

2.2.1. Powder X-ray Diffraction (PXRD)

X-ray diffraction (XRD) is a widely used non-destructive technique to characterize the long-range order in solid materials. Powder XRD refers to the method by which powders comprised of many crystallites are investigated which result in smooth rings in a diffraction pattern. An X-ray source provides X-rays of a wavelength on a similar length scale as the separation of atoms in the material. This allows for the constructive and deconstructive interference of X-rays as they scatter off the electrons of the atoms. At certain angles and spacing between atoms, constructive interference occurs, and reflections can be observed which correspond to specific spacings between atoms in a crystalline lattice. The relationship between atomic plane distance (d), angle (θ), and wavelength (λ) is described by Braggs' law:

$$n\lambda = 2dsin\theta$$

Based on this equation, a relationship between the position of reflections as a function of angle can be related to the spacing of the lattice in a crystalline material. A more detailed derivation and description of PXRD can be found in a book on the subject.[61]

Figure 2.2.1 shows an overview of the information content of a powder pattern.[61] For this work, PXRD will be commonly used to identify crystalline structures and refine their atomic positions and parameters using the Rietveld refinement technique (see below). Since many Li anode materials are originally crystalline, PXRD will be an important tool for identifying the structural transformations at intermediates points of

lithiation. It is important to emphasize that Bragg diffraction only gives information about structures that have long-range order, and many times materials undergo disordered phase transformations. For this reason, pair distribution function (PDF) analysis will be used in conjunction with Bragg diffraction to give a complete picture of the structure of the lithiation intermediates.

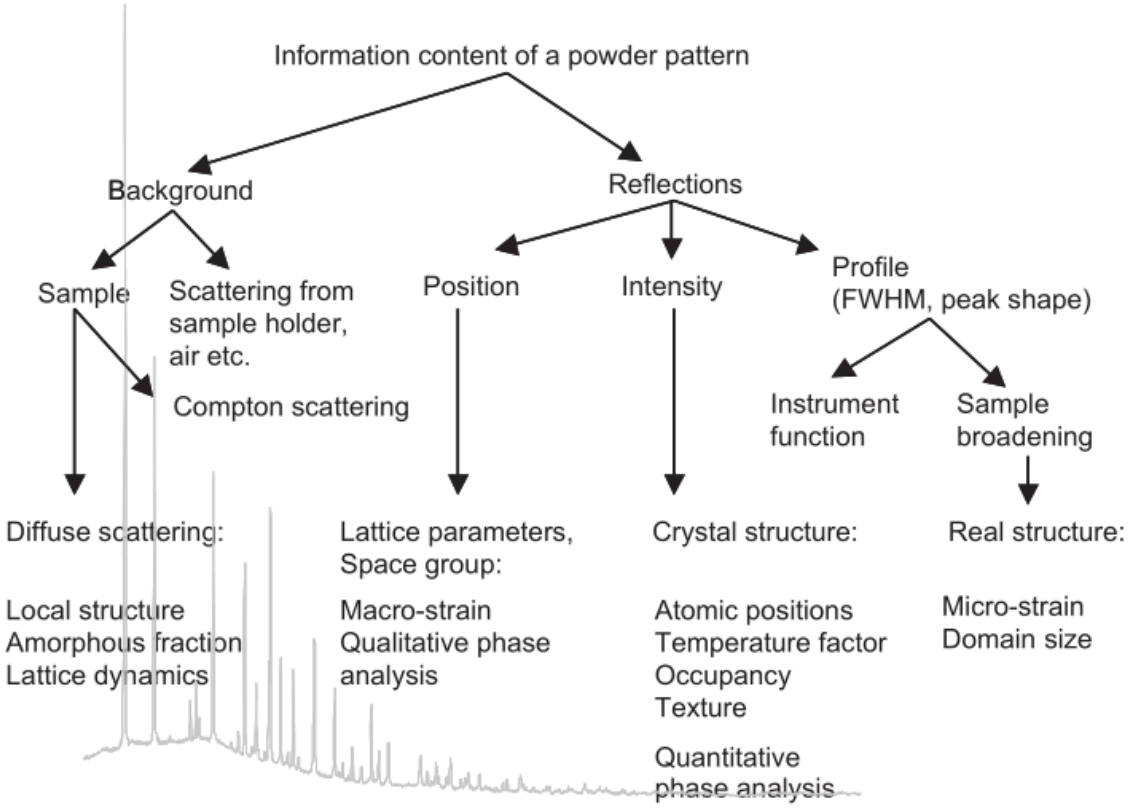

Figure 2.2.1 Schematic that shows the information contained in the different parts of a PXRD pattern.[61]

2.2.2. Rietveld Refinement

Rietveld refinement is a method to simulate a PXRD pattern and fit it to an experimental PXRD pattern in order to obtain quantitative structural information.[62,63] The

method involves a least squares regression to minimize the difference between the experimental and simulated patterns. The method is only applicable to crystalline structures and requires a structural model to refine the experimental pattern. The PXRD pattern is not just influenced by the structure of the sample but also the characteristics of the instrumental setup. The Rietveld refinement method models both structural and instrumental parameters which allow for the full description of the patterns. For instance, the peak shapes of the Bragg peaks are modelled by the pseudo-Voigt function and the background is modelled with Legendre polynomials. Once the instrumental features are sufficiently modelled, then the structural features that affect the pattern can be refined to obtain quantitative structural information such as atomic positions, atomic displacement parameters and partial occupancies. Obtaining quantitative structural information is important for drawing conclusions between the electrochemical profiles and the corresponding structural changes. A more detailed introduction into this method can be found in the following references. For this work, the JANA2006[64] is used to perform the refinements of PXRD from either lab X-ray sources or synchrotron X-ray sources.

2.2.3. Total X-ray Scattering and Pair Distribution Function (PDF) Analysis

The structural investigation of amorphous materials is a great challenge for the scientific community. The typical X-ray diffraction method based on Bragg diffraction used to characterize crystalline structures is not applicable and a method that probes the local structure is necessary to establish structure property relationships. Total X-ray scattering is used to obtain a PXRD pattern of a material out to very high scattering

angles. The diffuse scattering out to high angles contains information about the structure of a material and be viewed by creating a pair distribution function (PDF) plot which is a function of real space.[65] Due to the high scattering angle requirement to achieve quality data, these measurements are often performed at a Synchrotron light source which are very bright and have high-energy X-rays compared to laboratory sources.[66] **Figure 2.2.2** shows a schematic of a material sample being illuminated with high-energy X-rays and the resulting PXRD ring pattern on the flat X-ray detector. The resulting PXRD contains both Bragg peaks (if crystalline) and diffuse scattering which is why it is referred to as total scattering. By correcting the pattern for the background, multiple scattering, and adsorption and then taking a Fourier transform, the result is the generation of PDF plot. As seen in **Figure 2.2.2a**, a PDF of amorphous SiO_2 is shown demonstrating how structural information can be obtained from an amorphous material. **Figure 2.2.2b** shows the experimental setup for the PDF measurements conducted at the Diamond Light Source in Didcot, UK. **Figure 2.2.2c** shows a photograph of the sample contained in a glass capillary, sample holder, X-ray source, and heater. The X-rays are shot through the center of the glass capillary and the scattering is recorded on the X-ray detector. The glass capillary is spun at high speeds to compensate for any orientation related artifacts in the powder.

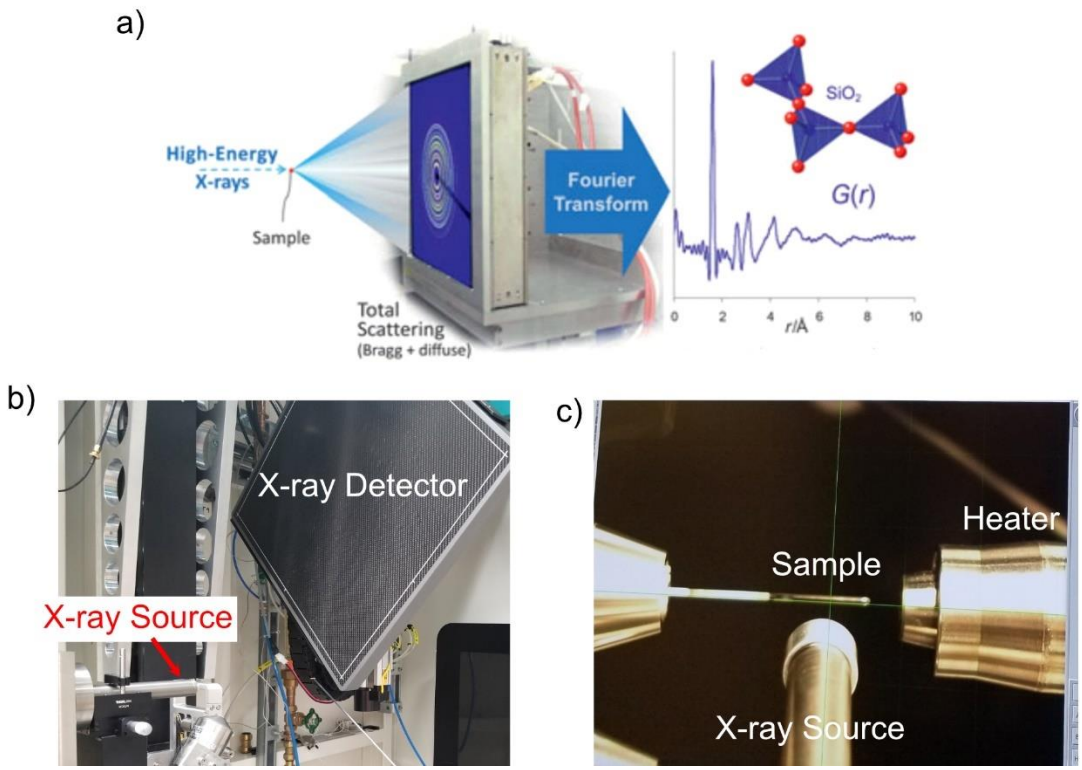

Figure 2.2.2 (a) Schematic of the process of acquiring a PDF using a high-energy X-ray source.[66] (b) Photograph of the X-ray source and detector at the PDF beamline at the Diamond Light Source. (c) Photograph of the sample holder, capillary, X-ray source and heater at the Diamond Light Source.

Once the PDF plot is obtained local bonding information can be obtained and modelled. **Figure 2.2.3** shows a schematic of a 2D hexagon carbon lattice with the corresponding simulated PDF pattern. If circles are drawn from a center atom corresponding to each of the next closest distance atom to the center, a series of circles can be created that correspond to certain atom-atom distances within the material. The PDF plot is a histogram that corresponds to these specific atom-atom distances within a material. For instance, **Figure 2.2.3b** shows the PDF with G(r) as a function of distance in angstroms. At 1.42 Å, there is a peak present in the PDF which matches with the first

circle drawn from the center atom in **Figure 2.2.3a**. Similarly, there are peaks at 2.46 and 2.84 Å which correspond to the 2nd closest and 3rd closest atom from the center atom. If the material is an infinite crystal, these peaks, referred to as correlations, continue out to infinity. However, if the material is disordered, then these correlations will become broad and end at a certain distance depending on the amount of similar atom-atom distances. This can be seen in **Figure 2.2.2a** which shows the correlations in the PDF plot of SiO_2 ending around 10 Å. The important characteristic of the PDF analysis is that both crystalline and amorphous structures can be analyzed with the same technique which gives a more complete view of the structure of the investigated material.

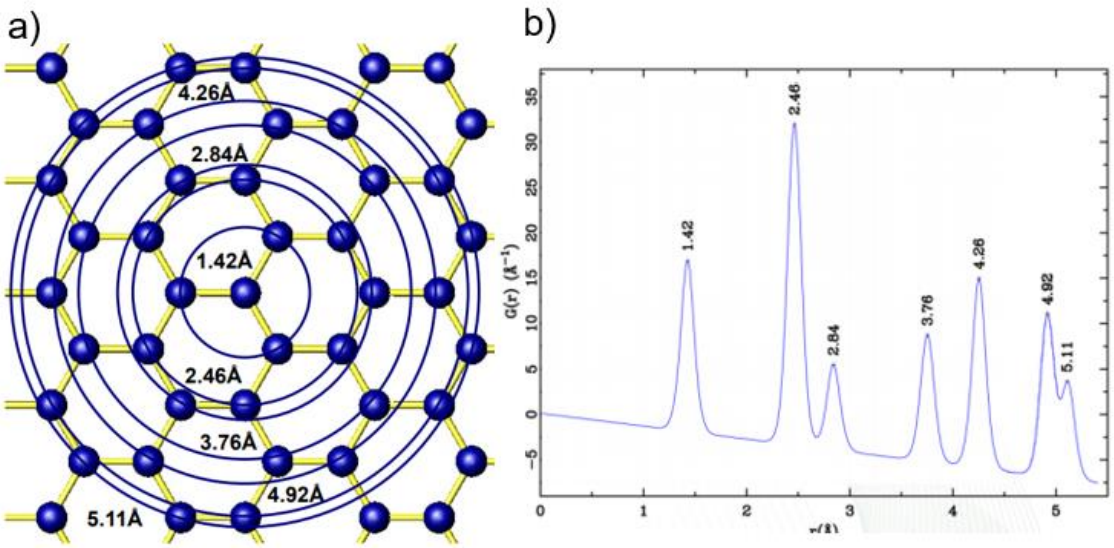

Figure 2.2.3 Schematic of 2D hexagonal carbon lattice with the atomic coordination spheres drawn and distance labelled from the center carbon atom. (b) Corresponding PDF pattern from the structure in (a).[67]

Similar to the Rietveld refinement method for PXRD patterns, the PDF plot can be simulated and refined to an experimental pattern by reducing the least squares error. [68] This allows materials that are crystalline to be fit a structural model and quantitative structural data can be extracted. An example of a refined PDF plot is presented in **Figure 2.2.4** which shows the experimental, simulated and difference curves for the PDF of the type I Ba_8Ge_{43} clathrate. A quantitative structural model for amorphous structures is more difficult to achieve to the massive increase in possible positional parameters of the atomic positions. This is typically achieved by using the reverse Monte Carlo method (RMC) which fits a super cell of atoms to the PDF pattern.[69] This method is out of the scope of the current work and generally, a qualitative analysis of amorphous PDF is achieved by comparison with crystalline patterns. The refinement of the PDF plots is done with PDFgui program.[68] More details of mathematical transformations done to the total scattering data and details about the PDF refinements can be found in the supporting information of Chapter 4 where PDF is used to analyze the amorphous phase transformations of Tetrel clathrates. In addition, the book titled "Underneath the Bragg Peaks: Structural Analysis of Complex Materials" is recommended for the theory and derivation for the PDF method.[65]

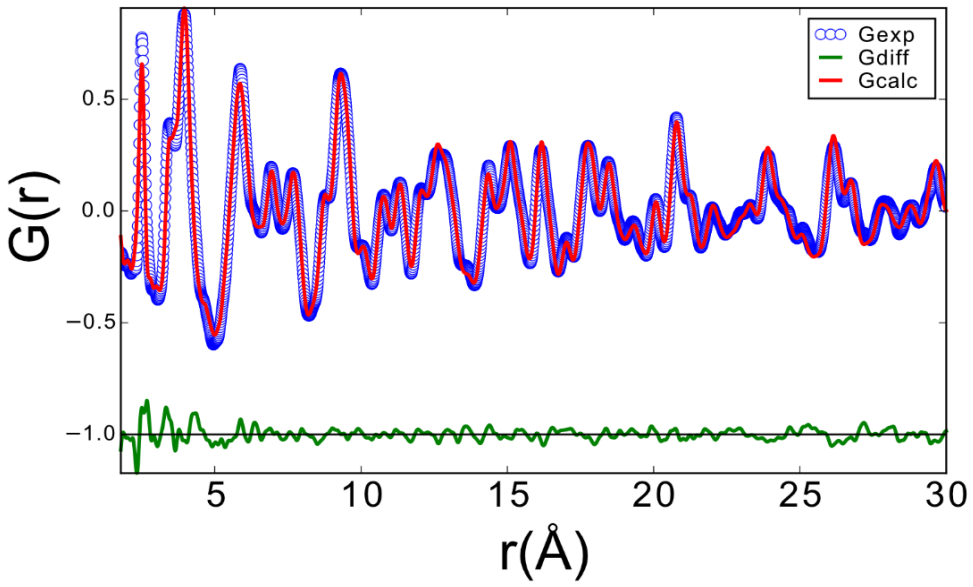

Figure 2.2.4 PDF refinement of a polycrystalline sample of Ba_8Ge_{43}. The blue circles represent the experimental pattern, the red curve is the simulated pattern, and the green curve is the difference curve between the experimental and simulated.

2.2.4. Scanning Electron Microscopy (SEM)

Scanning electron microscopy is a technique that characterizes the morphology of solid materials. In the microscope, an electron source is focused on to the sample with a series of electron optics and the focused beam of electrons is rastered across an area of the sample to form the image. As this occurs, the sample emits secondary electrons which are detected by an electron detector. The number of electrons detected at each pixel determines the intensity of the pixel and forms image as the beam is scanned over the area. The secondary image detector mode gives a topographic based image of the sample which is useful for characterizing the shape and size of features in the sample. In this work, SEM is used to characterize the morphology and particle sizes of synthesized

materials. An FEI Nova 200 Nanolab SEM and a Phillips XL-30 ESEM are used for the SEM images in this work.

2.2.5. Transmission Electron Microscopy (TEM)

TEM is a microscopy technique that uses a high energy beam of electrons to characterize the morphology and structure of thin material samples. The method requires transmission of electrons through the sample; thus, the sample must be thin enough to be electron transparent. As electrons are transmitted through the sample, the electrons interact in various ways which can give structural and morphological information of the sample. One of these interactions is electron diffraction which can be used to characterize the local crystallinity of materials. Electron diffraction is similar to X-ray diffraction and gives information about the long-range order in the sample. The ability to differentiate regions of amorphous and crystalline components of a material on a local scale is of great value especially for properties that rely heavily on interfacial reactions like Li-ion batteries. The TEM in this work was conducted using an aberration corrected FEI Titan microscope operated at 300 kV.

2.2.6. Energy Dispersive Spectroscopy (EDS)

Energy dispersive spectroscopy (EDS) is a method for characterizing the elemental composition of materials and is often implemented inside SEM and TEM instruments. In an electron microscope, the sample is bombarded with electrons which excites core electrons to higher energy levels. When the excited electron relaxes to a lower energy state, the energy is released in the form of an X-ray which is detected by an energy dispersive spectrometer. Since the energies of these transitions are characteristic

of each element, this method can be used to quantify and identify the elemental composition present the sample. Notably, in the electron microscope only the area that is hit with electrons excites X-ray meaning that the compositional information can be obtained in a spatial resolution of the microscope electron beam. In this dissertation, EDS is often used to compliment other materials characterization tools to confirm the suspected composition based on X-ray diffraction structural information. EDS is also useful for identifying spatial dependent compositional inhomogeneities that can occur in materials which do not show up in bulk characterization techniques.

2.2.7. X-ray Photoelectron Spectroscopy (XPS)

X-ray photoelectron spectroscopy (XPS) is a technique based on the photoelectric effect that is surface sensitive and provides information about the composition and chemical nature of the sample. In an XPS instrument, a focused beam of X-rays is shot at the sample which results in electrons being ejected from various core atomic states in the material. A detector then calculates the energy of the ejected electrons and compares it with the original energy of the incident X-rays. The difference of these values is termed the binding energy which refers to the energy required to eject the electron from the core atomic states. The binding energy of the electron is determined by the atomic composition and the type of chemical environment the atom is in. Therefore, this technique provides quantitative compositional information and details of the chemical states of the atoms (i.e. oxidation states). However, the detection depth of the instrument is often restricted to ~10 nm within the surface making it primarily used for surface analysis. The XPS used in this work was a VG ESCALAB 220i-XL with Al Kα anode

(1486.6 eV) operating at 63 W and 12 kV. Fitting of the XPS data was performed with casaXPS.

2.3.Density Functional Theory (DFT)

2.3.1. Brief Introduction

Density functional theory (DFT) is a widely used computational method to approximate and solve the many-body Schrodinger equation. The origins of DFT arise from the Hohenberg-Kohn theorems.[70] The first theorem states that the electronic structure of a many-electron system is defined by its electron density which can be mapped to three spatial coordinates. This is a key point as the most common method, Hatree-Fock, for solving the Schrodinger equation involved the orbitals and spatial coordinates of each electron. As a result, the computational scaling of a the common Hartree-Fock method is N^4 where N is the number basis functions used while, DFT scales with N^3.[71]The improved computational scaling allows for the calculation of systems with a larger number of atoms. The next Hohenberg-Kohn established an energy functional that is defined in terms of the charge density.

From these theorems, Kohn and Sham developed the widely used method for calculating the many-body problem in an analogous way to the Hatree-Fock method whereby a non-interacting electron gas interacts with an external potential and the correlation and exchange effects appear as additional effective potentials.[72] The exchange-correlation functional is the key approximation for the DFT theory and has been a key area of determining different types of DFT. The simplest approximation is the local density approximation (LDA) which is based on the exact exchange energy and parameterized correlation for a homogeneous electron gas.[72] This functional performs well with metallic systems where, the electron density is spread out but the suffers when the electron density is more localized. To improve this other more computational demanding functionals have

been developed and are now the most widely used functionals. The functional used in this work is the Perdew, Burke, and Ernzerhof (PBE) functional[73] which is classified as generalized gradient approximation (GGA) functional[74] and is a standard functional used for bulk solids. The GGA functional adds additional terms to compensate for the non-homogeneity of the true electron density which significantly improves the results of systems that are defined by more localized electron densities. More detailed descriptions of the theory of DFT and electronic calculations can be found in the following books by Martin[75] and Cramer[71]. I also recommend the review article by Van der Ven et al. for DFT calculations related to battery materials.[76] To carry out the DFT calculations in this work, the Vienna Ab initio Simulation Package (VASP)[77] was used with the PBE functional[73], the projector augmented wave potentials[78] with a plane-wave basis set. The more specific details of the calculations can be found in the computational methods section of the following chapters or in the corresponding Appendices. The following section will go over the property calculations used frequently in this dissertation.

2.3.2. Formation Energy

The formation energy refers to the energy difference of a multicomponent compound with respect to its elemental forms. To calculate this with DFT, the energies of the multicomponent are subtracted from the energies of the elemental form on a per atom basis. The equation for a hypothetical two-component system, XY, would be:

$$E_{form} = \frac{E(XY) - E(X) - E(Y)}{2}$$

where E(XY), E(X), and E(Y) is the energy from the DFT calculation and then divided by the total number of atoms to obtain the energy per atom. This calculation gives an

estimate of the stability of a compound relative to its elemental forms however it does not consider other competing multicomponent phases.

2.3.3. Average Voltage

The voltage of an electrochemical reaction can be estimated based on simple DFT energy calculations.[11] The voltage of a battery is determined by the difference of the chemical potential between the two electrodes. For a Li-ion battery this was described earlier as:

$$\mathrm{V(x)} = -\frac{\left(\mu_{Li}^{cathode}(x) - \mu_{Li}^{anode}(x)\right)}{e}$$

where Φ is the voltage, $\mu_{Li}^{cathode}$ and μ_{Li}^{anode} are the chemical potentials in terms of eV/mol as a function of the Li content (x) for the cathode and anode, respectively and e is the charge of an electron in Coulombs. Then by considering only the end member Li compositions of $\mu_{Li}^{cathode}$, the average lithiation voltage between these two Li compositions can be written in terms of the changes in Gibbs free energy of reaction:

$$\mathrm{V(x)} = \frac{-\Delta G_r}{(x_2 - x_1)e}$$

where x_2 and x_1 are the Li compositions of the two end members. Take for example, a general Li metal oxide, $LiMO_2$. The fully lithiated phase is $LiMO_2$ and the delithiated phase is MO_2. The average lithiation voltage would then be:

$$\mathrm{V(x)} = -\frac{\mathrm{E(LiMO_2)} - E(\mathrm{MO_2}) - E(Li)}{(1-0)e}$$

where $\mathrm{E(LiMO_2)}, E(\mathrm{MO_2}), \text{and } E(Li)$ are the DFT energies. The important assumption here is that the 0 K DFT energy is a good approximation for the Gibbs free energy. ΔG_r is equal to $\Delta E_r + P\Delta V_r - T\Delta S_r$ and the P and T terms are predicted to be sufficiently small compared to internal energy of ΔE_r so that. $\Delta G_r \approx \Delta E_r$. Therefore, the internal energy obtained from the DFT calculations can be used to estimate the average voltage between two lithiated end members.[11]

Essentially, the volage calculation evaluates the energy of two difference of two different Li compositions with respect to Li metal. The important difference between this and the formation energy is that the formation energy is relative to all elemental forms while the voltage is relative to Li metal. In electrochemical cells, often the electrode can achieve metastable states with respect to the elemental forms but is stable relative to Li metal.[79] Thus for predicting the electrochemical properties of a Li host, the voltage calculations is often more useful.

2.3.4. Nudged Elastic Band (NEB) Method

As mentioned in the previous sections, Li diffusion is a key component to the operational of a Li-ion battery. In insertion materials, Li hops between difference lattice sites randomly and in response to a chemical gradient. The kinetics of this hop are important for the speed at which Li-ion batteries can be charged and discharged and is often a limiting factor of materials in this respect. Therefore, computational methods that can be used to estimate the energy barrier of this hop are important for evaluating new electrode materials.

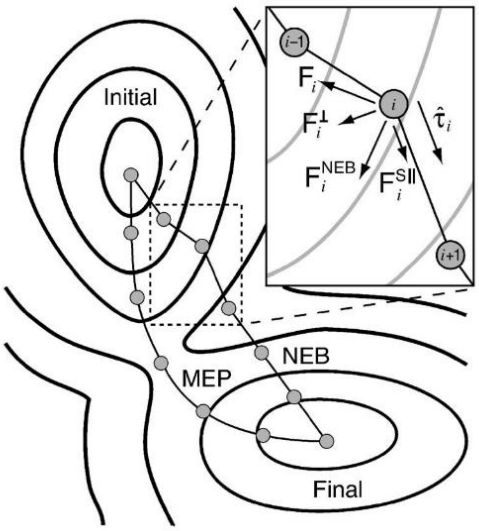

Figure 2.3.1 Schematic of the NEB method where the initial band of positions is moved to the minimum energy path by minimizing the perpendicular force of the NEB. [80]

The nudged elastic band (NEB) method constructs a set of different positions, called images, between two local minimum and calculates the minimum energy path between them.[81] Each image is connected by spring forces so that the distance between each image is maintained. The minimum energy path is found by minimizing the perpendicular force to the band. **Figure 2.3.1** shows a scheme of a two-dimension energy landscape with the initial and final positions in the basin of two energy wells. The original band (NEB) is not at the minimum energy path (MEP) so the calculations converge this original set of positions to reach the MEP. The highest energy position is the saddle point and corresponds to the transition state energy. This is the key value that for evaluating Li diffusion. The diffusion of Li can be thought of a similar way as in the **Figure 2.3.1**, however the energy of the system is a variable of the position of the host

atoms that surround the Li and the position of Li. The host atoms and Li will move in a way that minimizes the energy between the local minimum positions.

This method has been useful for developing an atomic scale model of the Li movement in intercalation materials and is simple and not very computationally demanding.[23,82–84] The downside is that the positions of the Li and the pathway have to be decided by the user and it becomes difficult to evaluate all the possible combination of pathways in some cases. In the case of simple systems, the migration barrier for Li hopping can be calculated simply and gives a reasonable estimate of whether or not Li migration through a lattice will be possible. This method is mainly used for evaluating the mobility in insertion reactions due to generally highly crystalline structures.

The NEB method is implemented in VASP as the Climbing image NEB[85] within the Transition State Tools for VASP (VTST) package.

3. CLATHRATES AS INSERTION ANODES

3.1. Experimental and Computational Study of the Lithiation of $Ba_8Al_yGe_{46-y}$ Based Type I Germanium Clathrates

Reproduced with permission from Dopilka, A.; Zhao, R.; Weller, J. M.; Bobev, S.; Peng, X.; Chan, C. K. Experimental and Computational Study of the Lithiation of $Ba_8Al_yGe_{46-y}$ Based Type I Germanium Clathrates. *ACS Appl. Mater. Interfaces* **2018**, *10*, 37981–37993. Copyright 2021 American Chemical Society.

3.1.1. Introduction

Clathrates[41,86] are known for their unique cage-like structures and their potential as promising superconducting[87–91], thermoelectric[92–98], magnetic[41,99,100], hydrogen storage[101,102], and hard materials[103,104]. Recently, clathrates have also been investigated as potential electrode materials for Li-ion batteries[49,52,53,55,56,105–108] . We have previously investigated the electrochemical properties of ternary type I clathrates based on $Ba_8Al_ySi_{46-y}$ in great detail[56,106]. In our group's prior work, we found that off-stoichiometric silicon clathrates ($8 < y < 12$) displayed capacities corresponding to insertion of ~40 Li^+ per formula unit[106], whereas materials close to the Zintl condition ($y \approx 16$) displayed very low capacities unless disordered/amorphous surface layers were introduced via ball-milling[56]. Based on these results, we hypothesized that Li^+ insertion at defects or vacancies could play an important role in the electrochemical properties of clathrates. Interestingly, for all silicon clathrate compositions studied, no electrochemically-induced amorphization of the material was observed, and there were

no discernable changes to the lattice constant of the bulk structure. This is distinctly different from what occurs during electrochemical lithiation of diamond cubic silicon (c-Si), where a more than 300% change in volume and transformation to amorphous lithium silicide phases are observed[109].

In order to further elucidate the electrochemical properties of clathrates, herein we extend our studies to type I clathrates based on $Ba_8Al_yGe_{46-y}$ and explore the effect of defects in the clathrate structure on the lithiation behavior using experimental and first-principles density functional theory (DFT) investigations. Similar to the aforementioned silicon clathrates studied previously, these germanium clathrates are made up of two pentagonal dodecahedra (Ge_{20}) and six tetrakaidecahedra (Ge_{24}) per unit cell (**Figure 3.1.1**), crystallizing in the $Pm\bar{3}n$ (223) space group. Each Ge_{20} cage is composed of 12 pentagonal faces, while the Ge_{24} cages are made up of 12 pentagonal and 2 hexagonal faces. The Ba guest atoms are found at the 6*d* and 2*a* sites in the center of the Ge_{24} and Ge_{20} cavities, respectively, while the Ge and Al atoms occupy the framework sites at the 6*c*, 16*i*, and 24*k* positions as described by Wyckoff symmetry notation[110,111]. The framework substitution of Ge by Al atoms enables the structure to be rationalized by the Zintl concept, where each element achieves a (nearly) closed-shell electronic configuration[112].

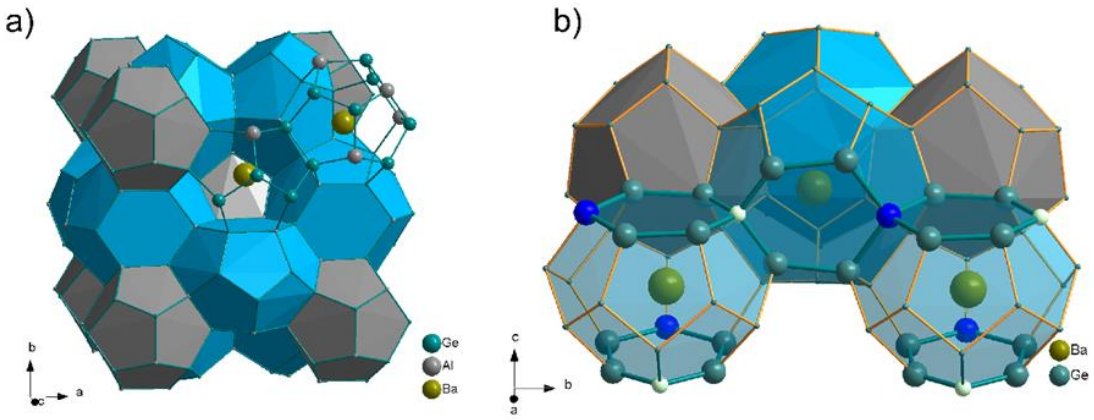

Figure 3.1.1 (a) Crystal structure $Ba_8Al_{16}Ge_{30}$. The blue polyhedra are the tetrakaidecahedra with two hexagonal faces and the dodecahedra are shaded grey. (b) Crystal structure of Ba_8Ge_{43} showing the chains of connected hexagons containing vacancies. The dark blue atoms are Ge atoms occupying 6*c* positions and the white atoms represent the positions of the vacancies, also at the 6*c* sites.

Ge clathrate frameworks have been shown to be able to accommodate vacancies and even Li atoms. For example, to compensate the excess electrons donated to the framework from the Ba atoms, Ba_8Ge_{46} (but not Ba_8Si_{46}) can spontaneously form three vacancies in the 6*c* positions to form $Ba_8Ge_{43}\square_3$, where $\square$ is a vacancy (from now on referred to as Ba_8Ge_{43})[113] (**Figure 3.1.1b**). Framework vacancies have also been reported in the ternary $Ba_8Al_yGe_{46-y}$ ($4 \leq y \leq 16$) clathrates[111]. Electrochemical Li insertion into these framework vacancies has to our knowledge, not been reported, but clathrate compounds containing Li framework substitution, e.g. $K_8Li_yGe_{46-y}$ ($0 \leq y \leq 2.3$), have been synthesized[114–116]. Li framework substitution is particularly interesting because it suggests that there are defined, stable Li positions in the clathrate structure; however, if Li movement between these positions is possible has yet to be addressed. In this work, we investigate the electrochemical properties of $Ba_8Al_yGe_{46-y}$ (y = 0, 4, 8, 12, 16)

clathrates synthesized by arc-melting. We find that all of the compositions undergo two-phase reactions to form Li-rich amorphous phases, similar to the transformations seen in diamond structured Si (c-Si) and certain forms of diamond Ge (c-Ge) [117–120]. This is distinctly different from the Si clathrate analogues, which do not transform to amorphous phases during electrochemical reaction. A composition dependence on the capacity and reaction voltage is seen with changes in Al framework substitution. It is also found that ball-milling significantly amorphized the clathrate structure as determined using X-ray diffraction (XRD) and transmission electron microscopy (TEM). Si clathrates subjected to the same ball-milling conditions did not display as much amorphous phase formation[56], suggesting that the Ge framework is less structurally stable. Electrochemical impedance spectroscopy is used to confirm the presence of Warburg diffusion of Li^+ in the amorphous phases by inspection of the Bode plots in the low frequency region.

Finally, we investigate the possibility of Li insertion into the clathrate structure prior to the two-phase reaction with XRD and first-principles DFT calculations. Single crystal XRD results indicate the presence of vacancies in clathrates with low Al content. From DFT calculations, we find that Li insertion into the 3 framework vacancies in Ba_8Ge_{43} is energetically favorable at a calculated lithiation voltage of 0.77 V vs. Li/Li^+. However, the calculated energy barrier for Li diffusion between vacancies is 1.6 eV, which is too high for significant room temperature diffusion. If Ba is removed from the Ge_{24} cage, the activation barrier decreases to 0.5 eV, indicating that the guest atom impedes Li motion. DFT also predicts an increase in lattice constant after insertion of the 3 Li into the vacancies; however *ex situ* XRD shows no increase in lattice constant before or during the onset of the two-phase reaction, suggesting no Li incorporation into the

vacancies. These results show that framework vacancies are unlikely to have a significant impact on the capacity of the clathrates but do suggest that guest atom vacancies could open diffusion paths for Li, allowing for empty framework positions to be occupied.

3.1.2. Experimental and Computational Methods

3.1.2.1 Synthesis of $Ba_8Al_yGe_{46-y}$ Clathrates

A series of clathrates with composition of $Ba_8Al_yGe_{46-y}$ (y = 0, 4, 8, 12, 16) were synthesized using arc-melting (**Appendix A.1**). The samples were named according to Al*y*, where *y* represents the nominal amount of Al, e.g. Al16 means y = 16 or $Ba_8Al_{16}Ge_{30}$. The as-made, arc-melted ingots were processed further: HG-Al*y* refers to the sample ground by hand using a mortar and pestle, while BM-Al*y* refers to the HG-Al*y* sample after ball-milling.

3.1.2.2 Material Characterization

The Ge clathrates were characterized using single-crystal (SCXRD) and powder X-ray diffraction (PXRD), X-ray photoelectron spectroscopy (XPS), scanning electron microscopy (SEM) and transmission electron microscopy (TEM). Composite electrodes containing the clathrate powders, carbon black, and binder on copper foils were evaluated in half cells with Li metal counter electrodes and nonaqueous electrolyte. More details about the materials and electrochemical measurements are described in **Appendix A.2.**

3.1.2.3 Computational Methods

First-principles density-functional theory (DFT) calculations were performed in a similar manner as in our previous work[55] and are described in more detail in **Appendix A.7**. The formation energies, Gibbs free energy change, and average lithiation voltages were calculated as described previously[55]. The climbing image nudged elastic band (NEB) method was used to calculate the Li diffusion barriers[85].

3.1.3. Results and Discussion

3.1.3.1. Structural Characterization

PXRD patterns were taken on the synthesized Ge clathrates samples before and after ball-milling. All of the hand ground samples displayed crystalline peaks (**Figure 3.1.2a**) matching the reflections for Ba_8Ge_{43} clathrate (PDF 01-073-5638)[113], and in excellent agreement with the simulated PXRD patterns from the refined structures via single-crystal XRD methods. For the Al containing samples, the reflections were shifted to lower angles and least-squares refinement showed the lattice constant increased from 10.653 Å for Al0 to 10.835 Å for Al16 (**Table A.1**). These cell parameters match closely with those previously reported[111] as well as the SCXRD results (**Table 3.1.1**). Crystalline diamond cubic Ge (c-Ge), identified by the (111) reflection, was noticeable in the PXRD patterns for Al0 and Al4, but the phase fraction determined from the refinement showed that the quantity was very small (**Table A.1**). No other crystalline peaks were observed. The powder after ball-milling (**Figure A.1a**) also displayed a crystalline clathrate structure without any change of the cell parameter and impurities, but the PXRD

diffraction intensities decreased and the peaks were broader, which is consistent with a smaller particle size in the ball-milled samples.

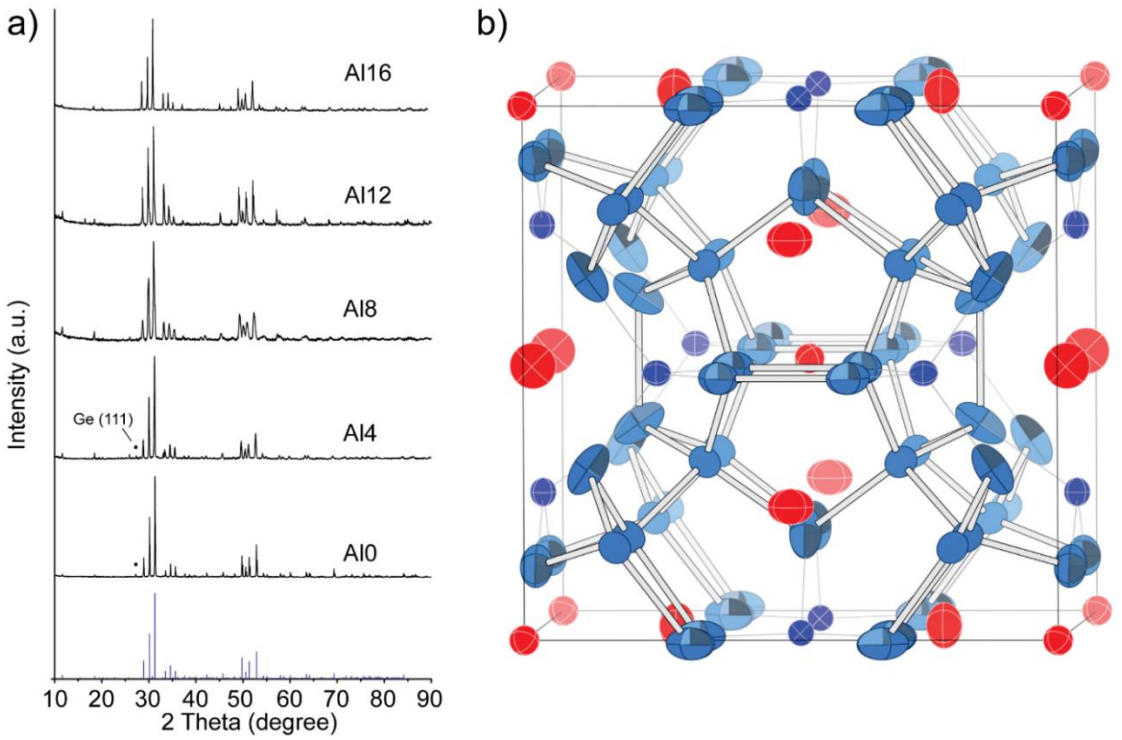

Figure 3.1.2 (a) PXRD patterns of hand ground Ge clathrates with reference pattern PDF 01-073-5638 corresponding to Ba_8Ge_{43} on the bottom; (■) c-Ge. (b) Representation of the $Ba_8Al_yGe_{46-y}$ (y = 4) structure with anisotropic displacement parameters. The thermal ellipsoids are drawn at the 90% probability level, where the Ba atoms are colored in red and the Ge/Al framework positions are differentiated as follows: 24*k* sites are represented with light blue ellipsoids with octant shading; the 16*i* sites are shown as light blue outline ellipsoids, and the 6*c* sites are in dark blue (with the principal ellipses shown). The data are obtained from the single-crystal refinement for sample Al4. The distinctive shape of the ellipsoid of the atoms occupying the 24*k* sites is indicative of small positional disorder – a direct consequence of vacancies present at the neighboring 6*c* sites.

SCXRD was performed on the as-synthesized clathrate samples by extracting small crystallites from the crushed arc-melted ingots. The lattice parameters and Ge:Al

ratios obtained from the SCXRD data are shown in **Table 3.1.1** and the crystallographic information files can be found in **Appendix A.2**. Standard deviations on the occupancies were 1% or better. The four samples with the highest Al content (Al8 – Al16) showed unit cell parameters in the narrow range of 10.8008(5) to 10.8425(6) Å and refined compositions of $Ba_8Al_{11.4(1)}Ge_{34.6(1)}$ to $Ba_8Al_{15.6(1)}Ge_{30.4(1)}$.

Table 3.1.1 Lattice parameter and Ge:Al ratio on each framework site (6*c*, 16*i*, and 24*k*) as determined from single crystal XRD studies (*: the balance to 100% occupancy is attributed to vacancies)

Sample Name	Nominal Composition	a-parameter (Å) from SCXRD	Ge:Al Ratio		
			6*c*	16*i*	24*k*
Al0	Ba_8Ge_{43}	10.6335(15)	--	--	--
Al4	$Ba_8Al_4Ge_{42}$	10.7411(10)	5.4 : 61.3*	9 : 1	~100 : 0
Al8	$Ba_8Al_8Ge_{38}$	10.8008(5)	1 : 99	69 : 31	98 : 2
Al12	$Ba_8Al_{12}Ge_{34}$	10.8385(17)	8 : 92	60 : 40	92 : 18
Al14	$Ba_8Al_{14}Ge_{32}$	10.8425(6)	18 : 82	62 : 38	86 : 14
Al16	$Ba_8Al_{16}Ge_{30}$	10.819(3)	30 : 70	69 : 31	74 : 26

The structure refinements for almost all prepared clathrates showed excellent agreement between the nominal (loading) and final composition, which is indirect proof for the homogeneity of the samples. The unit cell volumes subtly decrease with the decrease of the Al-content, corresponding to the small difference in the elemental radii (Al is 1.248 Å while Ge is 1.242 Å), but the variations in the unit cell volume were not

monotonic. Since Al and Ge atoms scatter X-rays in a significantly different way, the refinements of the occupancies of Al on the 3 framework positions was possible and confirmed the preference of Al for the 6*c* site. This is in contrast to the $Ba_8Al_ySi_{46-y}$ clathrates, where the exact Al:Si ratios on the individual framework sites cannot be reliably established using X-rays[121,122]. The ratios are in agreement with the literature on other type I clathrates, where the preference for the 6*c* site is well documented [123,124].

For the sample with the lowest Al content (Al4), the 24*k* site appeared to contain no measurable amount of Al; the 16*i* site was co-occupied by Ge and Al in a ratio of 9:1, and for the first time, the 6*c* site in a Ba-Al-Ge clathrate system was found to be under-occupied – when freed, the site occupation factor of this position was less than 100%, suggesting that the atom(s) located at 6*c* is almost 1/4 lighter than Al. This, together with the drastic decrease in the unit cell parameter (a = 10.741 Å) is an indicator of vacancies at the 6*c* site. The diffraction data can then be modeled with ca. 2 vacancies at the 6*c* site. This results in a refined composition of $Ba_8Al_{\sim 6}Ge_{\sim 38}$, which is in good, but not excellent agreement with the nominal composition of $Ba_8Al_4Ge_{42}$. This structural description is consistent with the interatomic distances within the framework, which for the Al-rich samples show Ge/Al (6*c*) – Ge/Al (24*k*) bond lengths exceeding 2.51-2.53 Å (recall that the 6*c* site is mostly occupied by Al, which is spatially more demanding than Ge), while for Al4, the corresponding bond distance is 2.4660(9) Å.

The anisotropic displacement parameters of the Ge atoms neighboring the vacancies (i.e, in the 24*k* sites) are also worthy of a mention – instead of spherical, the mean square atomic displacements (0.0273 $Å^2$, 0.0141 $Å^2$, and 0.0140 $Å^2$) show that one

of the principal directions is nearly twice as large as the other two. This is also readily seen in **Figure 3.1.2b**, where the nearest Ge/Al neighbors at the 24*k* site are strongly affected by the vacancy, causing the ellipsoid to be elongated in the direction of the Ge/Al (6*c*) – Ge/Al (24*k*) bond.

Exactly the same phenomenology concerning the bond distances and anisotropic displacement parameters is also seen in the structure refinements for Al0, Ba_8Ge_{43}. The unit cell parameter decreased sharply to 10.6335(15) Å with the 6*c* site being vacant nearly 50% of the time. As a result, the unrealistically short Ge–Ge distance of 2.354(1) Å is avoided. The anisotropic displacement parameter of the Ge atoms neighboring the vacancies is also clear indication that these atoms are "vibrating" around their equilibrium positions – the principal direction is nearly three times as large as the other two, as evident from the principal mean square displacements of 0.0510 $Å^2$, 0.0160 $Å^2$, and 0.0153 $Å^2$. The latter is a sign that the structural description of the Al0 clathrate in the same space group as the others leads to a structurally-deficient compound and alternatives must be sought. Other groups have shown that using an 8-times larger unit cell volume with cell edge in excess of 21 Å and body-centered cubic symmetry might resolve these problems[113,125,126], although the diffraction patterns of our arc-melted samples did not show reflections that violate the presumed symmetry.

3.1.3.2. XPS Characterization

XPS was used to further characterize the surfaces of the hand ground and ball-milled clathrate electrodes. Deconvolution of the high resolution Ge 2*p* spectrum (**Figure**

A.2a), showed characteristics typical for GeO_2, GeO, and Ge-Ge at binding energies of 1220.8 eV, 1219.2 eV and 1217.8 eV, respectively[127]. From the fitting procedure, the amount of Ge-Ge signal was found to be 9% for Al0 and 15% for Al16 in both HG and BM cases (**Table A.2**). To serve as a reference, c-Ge powder was ball-milled and characterized by XPS; the Ge-Ge contribution was 21% of the total Ge 2*p* signal (**Table A.2**). This suggests that the oxide layer on the Ge clathrates is thicker than the native oxide layer on c-Ge. A similar observation was made in epitaxially grown Ge clathrate, where only the Ge oxide signals were seen in the Ge 2*p* XPS spectrum taken from the surface[128]. The high resolution XPS profile for Al 2*p* (**Figure A.2b**) showed a single peak at 75.44 eV and 75.07 eV for BM-Al16 and HG-Al16 respectively. These binding energies are in the range for aluminum oxide[129]. Due to the care taken to minimize oxygen contamination during the arc-melting synthesis, the oxidized surfaces likely formed from the exposure of the germanium clathrates to atmospheric oxygen.

3.1.3.3. SEM and TEM Characterization

SEM was used to characterize the morphology of the pristine electrodes prepared from hand ground (**Figure A.3**) and ball-milled clathrates (**Figure A.4**). The SEM micrographs of the HG samples show large shards (greater than 3 μm) of clathrate particles covered in carbon black. The BM samples contained spherically-shaped particles generally around 1 μm or smaller in diameter, demonstrating that ball-milling changed the morphology and particles sizes. No morphological differences were observed between the clathrates of varying Al substitution.

TEM was used to characterize the surfaces and crystallinity of the hand ground and ball-milled Al0 and Al16 samples (**Figure 3.1.3**). Selected area electron diffraction (SAED) was also used to assess the crystallinity of an entire particle. Similar to our previous work with the $Ba_8Al_ySi_{46-y}$ clathrates, we find that ball-milling has a considerable effect on the crystallinity of the samples, particularly at the surface. For HG-Al0, distinct lattice fringes and a spot pattern in the fast Fourier transform (FFT, inset) were observed, indicating crystalline clathrate in the center of the particle, although with a thick amorphous layer (up to ~15 nm) on the surface (**Figure 3.1.3a**). The amorphous layer on the surface of the particles is consistent with the oxide layer observed in the XPS results. From the TEM image, small crystalline regions could be seen in the BM-Al0 particles, but the SAED pattern showed diffuse rings, indicating that the particle lacked long range order and contained large amorphous content (**Figure 3.1.3b**). This indicates that the ball-milling process significantly amorphized the Al0 clathrate particles, which is consistent with the lower and broader intensities from the PXRD patterns of the ball-milled powders (**Figure A.1a**).

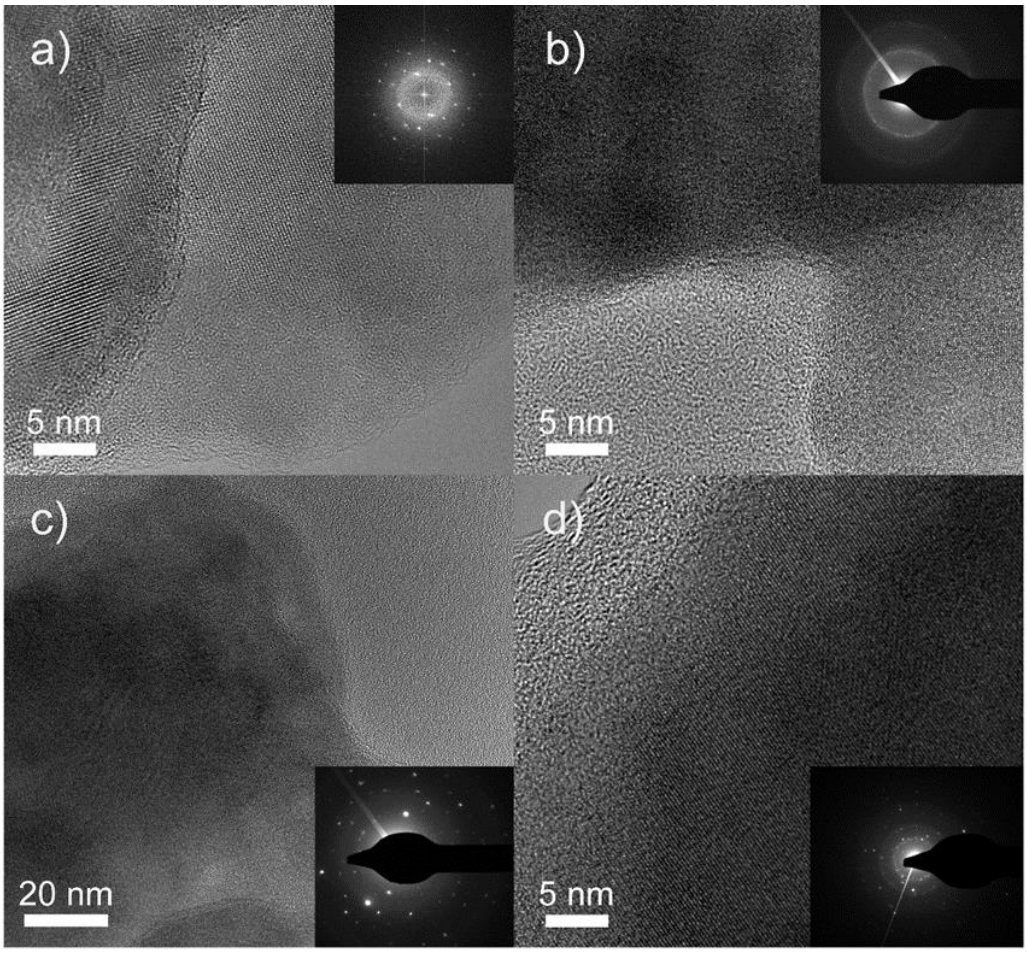

Figure 3.1.3 High resolution TEM and SAED of Ge clathrates (a) HG-Al0, (b) BM-Al0, (c) HG-Al16, and (d) BM-Al16.

For the Al16 samples, a similar trend is seen whereby HG-Al6 (**Figure 3.1.3c**) is more crystalline than BM-Al16 (**Figure 3.1.3d**) based on the SAED patterns of the particles. The BM-Al16 sample appears to have retained more of its crystallinity after the ball-milling based on the decreased amount of amorphous background in the SAED compared to BM-Al0. This is consistent with the XRD pattern (**Figure A.1a**) where BM-Al16 had sharper and more intense reflections than the BM-Al0 pattern, suggesting a higher crystallinity for BM-Al16.

3.1.3.4. Galvanostatic Measurements

To study the electrochemical properties of the Ge clathrate samples, galvanostatic cycling was performed between 0.01 – 2.5 V vs. Li/Li^+ at 25 mA/g. The first charge (lithiation) and discharge (delithiation) voltage curves are shown in **Figure 3.1.4**. As indicated by the voltage plateaus observed during charging, the clathrates undergo two-phase conversion reactions[130] to form Li-rich phases, with a large amount of Li reacted per clathrate formula unit (f.u.), as designated by the numbers next to each voltage profile. For example, HG-Al0 (Ba_8Ge_{43}) reacted with 173 Li per f.u. in the first charge, which corresponds to 4 Li/Ge (assuming all of the charge went towards the lithiation reaction with the clathrate). However, due to the irreversible capacity loss in the first cycle, there is likely substantial solid electrolyte interphase (SEI) formation from electrolyte reduction and the actual Li/Ge ratio is much lower.

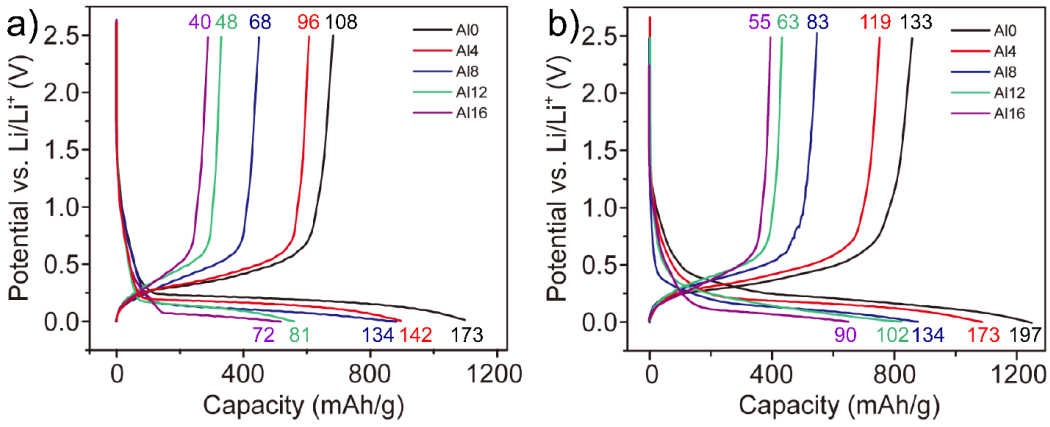

Figure 3.1.4 Galvanostatic voltage curves obtained from the first cycle for (a) HG and (b) BM samples. Numbers indicate the equivalent number of Li per formula unit of clathrate.

It is well known that c-Ge will react with Li to form a series of amorphous and crystalline Li-Ge phases, accompanied by a large volume expansion[118]. In contrast to c-Ge, which reacts at ~350 mV vs. Li/Li^+ [118,131,132], we find that the reaction potential for the clathrates occurs at a lower voltage (~160 – 200 mV for HG-Al0) and decreases with increasing amount of Al content. The capacity of the first charge also decreases with increasing Al content, suggesting that framework substitution of Al alters the properties of the two-phase reaction. The voltage profiles are more sloped in the ball-milled samples (**Figure 3.1.4b**) than in the hand ground ones (**Figure 3.1.4a**), which is consistent with the higher amount of amorphous content in the ball-milled powders, since lithium is expected to react with the amorphous clathrate phase in a solid-solution mechanism, similar to lithiation of amorphous Si and Ge[132,133].

The delithiation voltage profiles for the HG and BM samples are similar and show a gradually sloping voltage profile, indicating a single-phase reaction. The voltage profiles of the subsequent cycles were also sloped (as shown in **Figure A.5a** for HG-Al0). These observations are similar to those found in lithiation of c-Si and c-Ge, whereby amorphous lithium silicide/germanide phases grow at the expense of the unlithiated crystalline phase as the electrochemical reaction proceeds in the first charge, but subsequent cycling involves lithium insertion/deinsertion into the amorphous phases in a solid-solution mechanism. XRD of the electrodes at the end of the first charge (**Figure A.1b**) showed no reflections, which suggest that the phases after lithiation are amorphous. This is different from the lithiation of Ge and type II $Na_{24}Si_{136}$ clathrates, where the formation of Li containing crystalline phases is observed at low voltages[53,118]. These *ex situ* XRD results suggest that the presence of Ba and Al seem to impede the

formation of these phases in Ge clathrates, although *operando* studies would be more suitable for detecting the presence or absence of transient Li-Ge phases[39]. The capacities also increase after ball-milling, which can be attributed to enhanced lithiation in the smaller particle sizes due to the decreased diffusion length, as observed in the SEM images (**Figure A.3** and **Figure A.4)**.

The differential capacity (dQ) plots for Al0 and Al16 (**Figure 3.1.5**), derived from galvanostatic cycling, are presented to elucidate the differences between the HG and BM voltage profiles. The reduction peaks are attributed to the two-phase reaction between the unlithiated Ge clathrate and the amorphous Li germanide phases. The HG-Al0 dQ plot (**Figure 3.1.5a**) displayed two sharp reduction peaks at 0.16 and 0.12 V vs. Li/Li^+, suggesting the formation of a series of Li germanide phases with different compositions. This potential-dependent redox behavior is distinctly different from that in c-Ge, where peaks at ~0.35 V and ~0.18 V are seen in dQ plots during lithiation[118,132]. The BM-Al0 sample, however, shows a much broader voltage profile with the reactions starting at ~0.4 V in contrast to ~0.2 V for HG-Al0. This is consistent with the large amount of amorphous content in BM-Al0, as seen in the TEM results (**Figure 3.1.3b**) and the tendency for amorphous materials to display a much wider reaction window due to a larger distribution of possible Li reaction site energies[134]. Upon delithiation, both BM and HG-Al0 show similar behavior with an oxidation peak at 0.3 V, suggesting that the phases created at the end of lithiation are similar. The dQ plots for HG and BM-Al16 match closely with each other (**Figure 3.1.5b**), indicating that the ball-milling did not significantly affect the electrochemical properties. This is consistent with the TEM and XRD results showing that the BM-Al16 retained more of its crystallinity than BM-Al0.

The reaction begins at 0.08 V in the Al16 samples, demonstrating a decrease in reaction voltage as the Al content increases. The delithiation of Al16 is characterized by a broad peak stretching from 0.15 to 0.6 V, which contrasts with the sharper profile observed in Al0. We attribute this to the distribution of Al over many possible configurations in the amorphous phase, which would result in the reaction voltage to be more spread out, reflecting the different possible chemical environments for Li. The dQ plots of subsequent cycles (**Figure A.6)** showed little change in the potential-dependence behavior, with broad reaction peaks characteristic of the lithiation of amorphous phases.

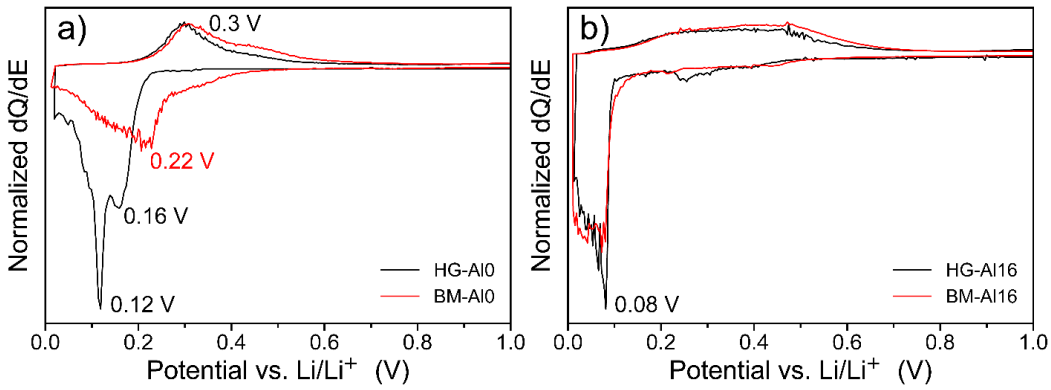

Figure 3.1.5 Differential capacity plots of the first cycle of (a) ball-milled and hand ground Al0 and (b) ball-milled and hand ground Al16 from galvanostatic cycling at 25 mA/g.

The capacity retention plots for the HG samples (**Figure A.5b**) showed that the capacity of the Al0, Al4, and Al8 clathrates quickly decreased to less than 5% of their initial lithiation capacity while Al12 and Al16 retained 10% and 20%, respectively, of the initial capacity after 20 cycles. The results also show that Al16 showed the highest

capacity retention, but lowest charge capacity in the first cycle. Al12 and Al16 react with the least amount of Li and thus suffer less from the volume expansion induced capacity degradation during cycling. The Coulombic efficiency (CE) of the first cycle for the BM and HG samples (**Figure A.5c**) decreases with increasing Al content, and is also higher for the ball milled samples.

This quick capacity fade is typical of unoptimized Si and Ge electrodes and arises due to large volume changes during charge and discharge, which can cause particle decrepitation/pulverization and detachment from the current collector[50,109,135]. Our electrode preparation (**Appendix A.5**) is not optimized for large volume expansion, as generally more conductive additives are used to maintain electronic contact[136]. Ge powder that was ball-milled was also tested and a similar capacity fade was observed (**Figure A.7**). Therefore, this low capacity retention could be due to the pulverization and particle detachment of the clathrate materials after the amorphization reaction and hence could be improved with subsequent modification of the electrode formulation and particle sizes.

The composition dependence of the capacity can be rationalized by considering the electrochemical behavior of Li with Ge vs. Al. Al reacts with 1 Li to form the LiAl phase at room temperature[137], while Ge can react with up to 4.4 Li[132]. This means that replacing Ge with Al will decrease the capacity of the resulting amorphous phase. In **Table A.3**, the theoretical and observed experimental capacities are compared assuming reaction of 4.4 Li/Ge. Note that in order to understand the effect of composition to the observed capacities, the contribution of charge to SEI formation is not considered. Al0

shows the closest correspondence to the theoretical values, but as the Al content increases, the difference between theoretical and experimental values increases. Previous studies on amorphous Si-Al sputtered thin films[138] have suggested that the formation of ternary phases, such as LiAlSi [139], may trap Li and limit the lithiation. LiAlGe also exists, but its electrochemical properties have not been investigated. The formation of a kinetically trapping phase could also explain the lower CE found for the clathrates with higher Al content (**Figure A.5c**). However, no other crystalline phases are detected after lithiation **(Figure A.1b)**, indicating that if present, any crystalline regions are too small to detect via XRD. Different SEI formation properties could also contribute to this trend in the CE. The presence of Ba in these amorphous phases further complicates the analysis and more detailed studies would be needed to understand the properties and formation of the amorphous phases.

3.1.3.5. Post-Mortem Characterization

As discussed previously, PXRD of the electrodes after the first charge showed that the reflections associated with the clathrates had all disappeared, suggesting the amorphization of the material and a conversion reaction mechanism (**Figure A.1b**). Comparing the morphology of the clathrate electrodes before and after the first lithiation (**Figure A.4**) showed indication of particle volume expansion and coating of the electrode with an SEI layer, which explains the fast decay of the capacities (**Figure A.5b**) and generally low Coulombic efficiencies (**Figure A.5c-d**).

These results confirm that the reaction mechanism of Li with the Ge clathrates is a conversion reaction to a Li-rich phase like that seen in the electrochemical lithiation of c-Si and c-Ge. However, the question of whether Li insertion into the crystal structure is possible is still yet to be answered. The voltage region before the start of the voltage plateau is considerably more sloped for the BM samples, indicating a single-phase reaction[130]. *Ex situ* PXRD was performed for the BM and HG samples before and after the beginning of this region, which corresponds to 40 and 60 Li inserted per f.u. (with the assumption that all the charge went towards Li insertion), to assess the crystallinity at these points in the lithiation process. The voltage profiles and corresponding XRD results from these experiments are shown in **Figure 3.1.6a-b.**

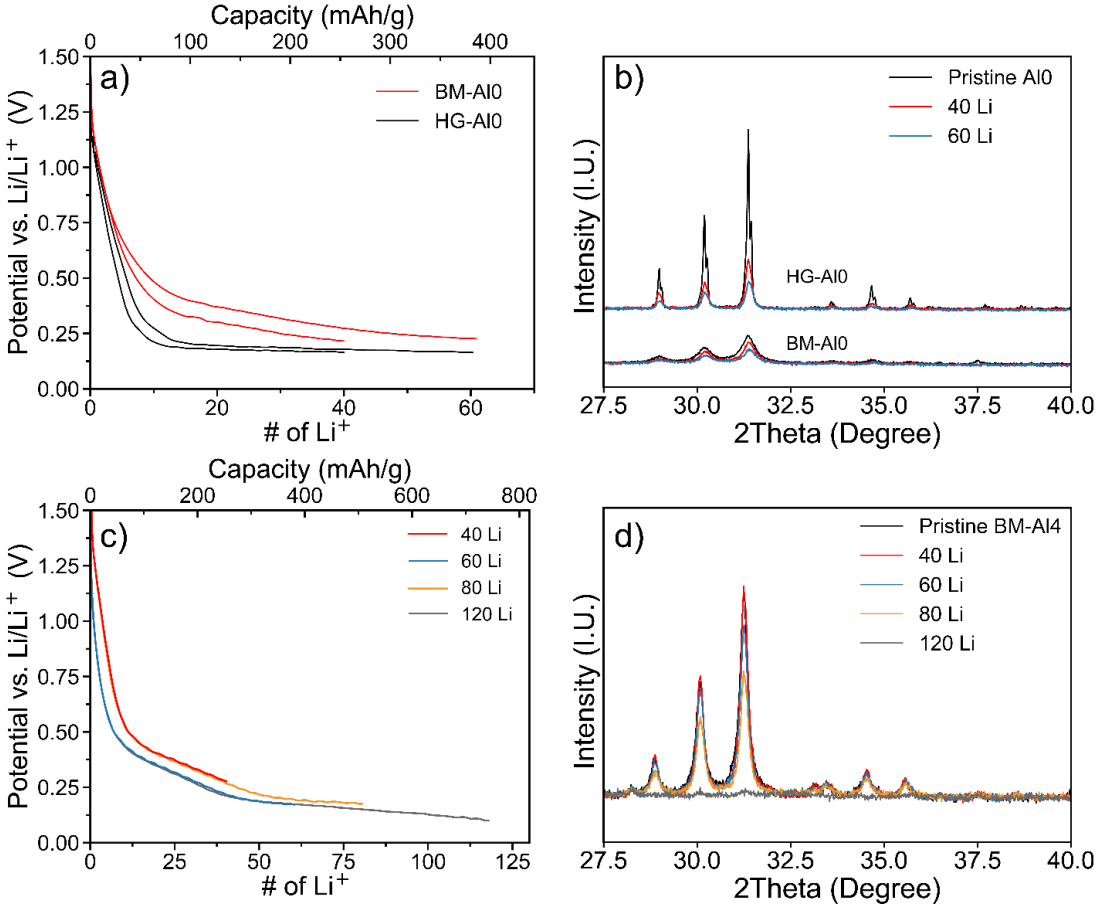

Figure 3.1.6 Voltage profiles (galvanostatic charging at 25 mA/g) of the electrodes to specific degrees of lithiation (left) and corresponding PXRD patterns obtained after the lithiation (right) for (a)(b) HG and BM-Al0, (c)(d) BM-Al4.

For the pristine (unlithiated) electrodes, the HG-Al0 sample is more crystalline when compared to the BM sample, as seen by the higher intensity and sharper reflections. This is also consistent with the TEM characterization results (**Figure 3.1.3**). After insertion of 40 Li per f.u., the intensities of the clathrate peaks in the XRD decreased in both Al0 samples, but by different amounts. The intensity of the reflections in HG-Al0 decreased by more than half, while that for BM-Al0 decreased to ~75% of those in the pristine sample. After insertion of 60 Li, the reflections decreased more for both samples. The larger decrease in peak intensity for HG-Al0 suggests that the Li being inserted is participating in the two-phase conversion reaction between the Ge clathrate and the Li-rich amorphous phase, thus decreasing the amount of crystalline clathrate. This is corroborated by the flat voltage profile at this point in the first lithiation step (**Figure 3.1.6a)**. The voltage profile for BM-Al0, however, is more sloped indicating a solid-solution insertion into an amorphous phase[133,140], which in this case is the amorphous clathrate phase that was formed during ball-milling. BM-Al4 was investigated in a similar manner (**Figure 3.1.6c-d**). After insertion of 40 Li per f.u., no decrease in the intensity of the clathrate reflections was detected. This suggests that these Li were not participating in a two-phase conversion of the crystalline clathrate, but a reaction with the amorphous surfaces (i.e., the surface oxides, the amorphous layer formed from ball-milling). As more Li was inserted, the clathrate structure was completely converted to the amorphous phase at around 120 Li per f.u.. No significant change in peak positions was

seen after the insertion of these different amounts of Li, suggesting that the clathrate structure was maintained without large change in lattice constant until the conversion reaction.

The PXRD results were confirmed with SCXRD measurements on samples after lithiation. Al0 powders were chemically lithiated using direct contact with Li foil, but the refinement results showed no statistically significant differences from the lattice constant and formula of the as-synthesized Al0 (**Appendix A.2**).

3.1.3.6. Electrochemical Impedance Spectroscopy

In our previous investigation of Si clathrates, electrochemical impedance spectroscopy (EIS) was used to identify the mechanism of lithiation as being confined to the surface of the particles in a pseudocapacitive-Faradaic process, primarily by inspection of the Bode plots[56]. The same galvanostatic pulse protocol we used in that study was applied to both the hand ground and ball-milled Al0 and Al16 Ge clathrate samples (**Appendix A.6, Figure A.8-A.11**). In the Bode plot, the low frequency phase angle close to -45^{o} is an indication of Warburg-type, solid-state diffusion of Li into the electrode, while a phase angle close to -90^{o} would indicate a blocking electrode or surface adsorption of Li[141]. As shown in **Figure 3.1.7**, the low frequency angle moved towards -45^{o} for all samples as the state-of-charge (SOC) increased, which is consistent with the conversion of the crystalline clathrate into amorphous phases that can react with lithium. When comparing the Bode plots for HG-Al0 (**Figure 3.1.7a**) with HG-Al16 (**Figure 3.1.7b**), we see that the phase angles for HG-Al16 remained less than -60^{o}, indicating a

more blocking character. This is also consistent with the increased crystallinity of the pristine sample as observed by TEM, as well as the lower lithiation capacities obtained in the galvanostatic cycling. On the other hand, the phase angle at low frequencies remained close to -80^{o} for silicon clathrates lacking an amorphous surface layer[56], indicating the blocking character of the structure. We attribute the Warburg feature to Li diffusion in the amorphous phases present in the Ge clathrates, which originate from the decreased structural stability of the Ge clathrates to atmospheric oxygen, ball-milling, and also to electrochemically-induced amorphization, while the blocking character of the electrodes originate from the crystalline clathrate domains.

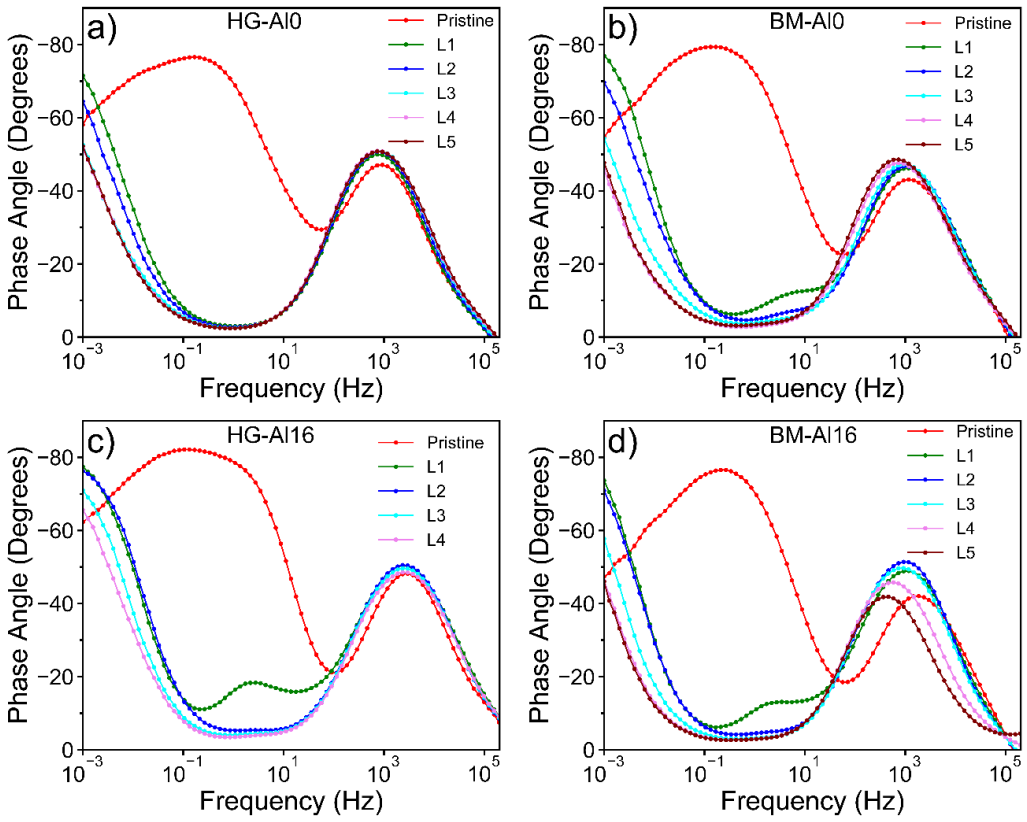

Figure 3.1.7 Bode plots showing the phase angle vs. frequency for (a) HG-Al0, (b) BM-Al0, (c) HG-Al16, (d) BM-Al16 obtained at different SOC, where L1 is the lowest SOC and L5 is the highest. The lithiation capacities for each SOC are shown in **Figure A.8**.

The reaction mechanism for the hand ground and ball-milled Ge clathrate samples can thus be summarized as follows. After reduction (presumably) of the surface oxide species and formation of the SEI layer, the Li reacts with the HG clathrate in a two-phase reaction between the unlithiated crystalline clathrate and a Li-rich amorphous germanide phase. For the BM samples, lithium insertion into the amorphous layer on the outside of the crystalline cores (presumably arising from the damage caused by ball-milling) precedes the two-phase reaction. For both cases, full lithiation results in complete amorphization, with subsequent lithium cycling occurring through a single-phase, amorphous solid-solution.

3.1.3.7. Theoretical Calculations

DFT was used to theoretically investigate the lithiation voltages and diffusion barriers (**Appendix A.7**) for the Al0 and Al16 Ge clathrates to rationalize why Li insertion into the clathrate structure is not observed experimentally unless it is amorphous. The framework vacancies can occupy the 6*c* position in a random or ordered arrangement depending on the synthesis conditions and heat treatment[90,113]. For arc-melted Ba_8Ge_{43}, it has been reported that there is an absence of vacancy ordering[90] and this is consistent with single crystal refinements of the arc-melted Al0 clathrates synthesized in this work (**Appendix A.2**). For this reason, we chose to model Ba_8Ge_{43} with randomly chosen vacancies at the 6*c* positions in the conventional unit cell. For the Al16 clathrate, we followed previous calculations showing that the lowest energy

configuration consists of 3 Al at the 6*c* sites, 1 Al at a 16*i* site, and 12 Al in the 24*k* sites, with no Al-Al bonds[111,142]. The formation energy and lattice constants for the unlithiated structures are shown in **Table 3.1.2**. The lattice constants match well with the experimental results and show the increase of lattice constant with substitution of 16 Ge with Al.

Table 3.1.2 Calculated formation energies, Gibbs free energy changes, voltages, and lattice constants of unlithiated and lithiated compounds. Parentheses after the composition indicate the site(s) occupied by the Li.

Composition	**Formation Energy (eV/atom)**	**Gibbs Free Energy Change (eV)**	**Average Lithiation Voltage (V)**	**Lattice Constant (Å)**
$Ba_8Ge_{43}\square_3$	-0.216	--	--	10.83
$Ba_8Ge_{43}\square_2Li_1$ (6*c*)	-0.228	-0.85	0.85	10.88
$Ba_8Ge_{43}Li_3$	-0.247	-2.31	0.77	11.02
$Ba_8Ge_{43}\square_3Li_1$ (6*b*)	-0.203	0.48	-0.48	10.90
$Ba_8Ge_{43}Li_3Li_1$ (6*c* + 6*b*)	-0.241	0.10	-0.10	11.05
$Ba_8Al_{16}Ge_{30}$	-0.303	--	--	10.95
$Ba_8Al_{16}Ge_{30}Li_1$ (6*b*)	-0.288	0.53	-0.53	10.98
$Ba_8Al_{16}Ge_{30}Li_1$ (Off pentagon in Ge_{24})	-0.286	0.63	-0.63	10.99

For Li insertion to occur in a material, there must be favorable positions in the crystal structure for Li to reside and a low energy pathway between these positions for bulk diffusion. The formation energies, Gibbs free energy change, average lithiation voltages, and lattice constants of simulated lithiated compositions are displayed in **Table**

3.1.2 and schematics of these structures in **Figure A.12** and **Figure A.13.** The composition $Ba_8Ge_{43}\square_3$ means that the 6*c* framework vacancies are unoccupied while $Ba_8Ge_{43}\square_2Li_1$ means that 1 Li occupies one of the 6*c* sites in place of the vacancy. The $Ba_8Ge_{43}\square_2Li_1$ structure (**Figure A.12a**) is found to be energetically favorable, resulting in a decrease in the formation energy and a high average lithiation voltage of 0.85 V vs Li/Li^+. Filling the three vacancies with Li (i.e., $Ba_8Ge_{43}Li_3$, **Figure A.12b**) is also favorable with an average lithiation voltage of 0.77 V. The formation energy of these compounds also decreases with Li incorporation, indicating a stabilization of Li in the clathrate structure with respect to bcc Li. This is consistent with experiments findings that type I clathrates can be synthesized with Li in the framework positions[114,143], suggesting that Ba_8Ge_{43} could also be synthesized with Li in these positions. Further, according to the results in **Table 3.1.2**, a lattice parameter increase is calculated with framework Li incorporation, which is consistent with experimental results reported by others. For example, the lattice constants of K_8Ge_{44} and $K_8Li_2Ge_{44}$ are 10.677 and 10.735 Å, respectively[115]. The calculated lattice parameter increase is ~0.2 Å for Li filling all three vacancies in $Ba_8Ge_{43}\square_3$, which should be detectable by XRD. However, no lattice constant increase was observed in our PXRD measurements at different points in lithiation **(Figure 3.1.6b**), suggesting no bulk incorporation of Li into the vacancies. Further, single crystal XRD measurements of lithiated samples showed no changes in lattice constant or any of the refined metrics (**Appendix A.2**).

Next, the nudged band elastic band (NEB) method was used to assess potential pathways for bulk Li diffusion within the $Ba_8Ge_{43}\square_2Li_1$ structure through the estimation of energy barriers for Li migration. The vacancy positions reside on the hexagonal faces of the Ge_{24} cages and are rotated by 90 degrees relative to adjacent hexagonal faces. One possible pathway, denoted as Path 1 in **Figure 3.1.8a**, is for Li to move to the next closest vacancy along the same chain of connected hexagons. This path involves Li moving through the hexagonal face of the Ge_{24} cage until it reaches the center position, which is the 6*b* site; then the Li traverses through a pentagonal face connecting the Ge_{24} cages and follows a symmetrical pathway to the 6*c* site in the adjacent Ge_{24} cage that houses the other vacancy position, also via a 6*b* site. Another pathway, which is more direct and denoted as Path 2 in **Figure 3.1.9a**, is for Li to move within a Ge_{24} cage to the vacancy site on the other hexagonal face.

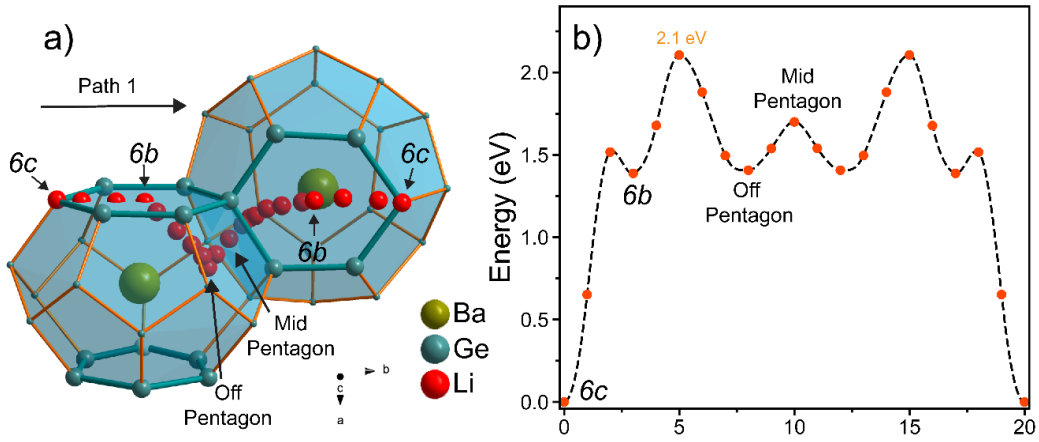

Figure 3.1.8 (a) Schematic of two connected tetrakaidecahedra showing the Li positions of Path 1 where the starting and ending points consist of Li in vacancies at the 6*c* position (white atom indiciates unfilled vacancy). (b) NEB energies of Path 1.

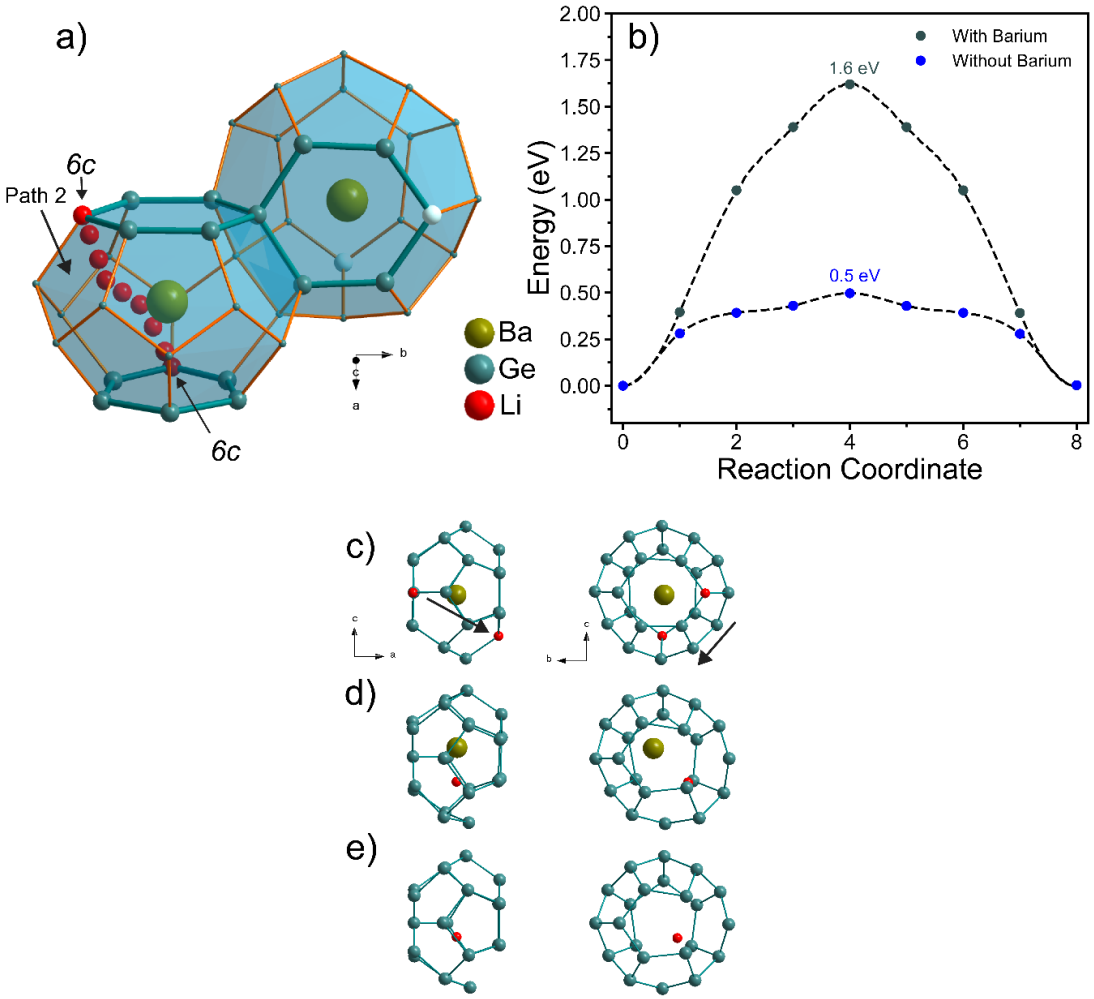

Figure 3.1.9 (a) Schematic of two connected tetrakaidecahedra showing the Li positions of Path 2 between vacancy positions within a single tetrakaidecahedron (white atom represents unfilled vacancy) (b) NEB energies of Path 2 from one vacancy to another vacancy in the $Ba_8Ge_{43}\square_2Li_1$ with and without barium inside the Ge_{24} cage (c) Schematic of a single tetrakaidecahedron with the two vacancies in each hexagonal face filled with Li (red atoms) showing the ending and starting images of the NEB calculation of Path 2. Arrows show the direction of Li movement. (d) Schematic of the highest energy image in (b) with Ba in the Ge_{24} cage. (e) Schematic of the highest energy image in (b) when Ba is not in the Ge_{24} cage.

The calculated energy barriers for Path 1 and Path 2 are presented in **Figure 3.1.8b** and **Figure 3.1.9b** respectively, with the images for each pathway labelled in

Figure A.14 according to each respective reaction coordinate number. We find that the highest energy barrier between two Li vacancy sites via Path 1 is 2.1 eV. There is a local energy minimum when Li is at the 6*b* site; the highest energy barrier is found when Li is moved to a position off a pentagon inside the Ge_{24} cage (image 5 in **Figure A.14a**). For Path 2, the energy barrier between the two vacancy sites is 1.6 eV, where the saddle point occurs when the Li is above a Ge-Ge bridge position between two pentagons (image 4 in **Figure A.14b**). Both paths involve the movement of Li around the Ba guest atom inside the Ge_{24} cage, and the highest energy positions arise in both when Ba is displaced from its favorable position in the center of the cavity, incurring a high energetic cost. **Figure 3.1.9c** shows a single Ge_{24} cage looking down the b-axis (left) and a-axis (right) with Li (red atoms) in the 6*c* vacancy sites and the arrow indicating Path 2. **Figure 3.1.9d** shows the structure corresponding to the highest energy image from the NEB calculation, where the displacement of the Ba from the center is clearly seen. If, however, the Ba atom is absent from the cage center, the energy barrier for Li movement between the vacancies decreases to 0.5 eV (**Figure 3.1.9b**) and the Li is positioned closer to the cage center (**Figure 3.1.9e**). As the Li diffusion barrier in c-Si is 0.47 eV [144,145] and that for c-Ge is 0.35 eV [145], these results suggest that Li movement through the clathrate structure could be feasible, but that guest atoms in the cage cavities impede lithium movement between framework vacancies. Despite lithiation into the vacancies at the 6*c* positions being energetically favorable, the high energy barrier between them (1.6 eV or 2.1 eV, depending on the pathway) would prevent these positions from being occupied through electrochemical lithiation at room temperature.

Other Li positions aside from the framework vacancies in Ba_8Ge_{43} and $Ba_8Al_{16}Ge_{30}$ were also considered and shown in **Table 3.1.2**. For the Ba_8Si_{46} clathrates, the most favorable position for Li was found to be the 6*b* site, where the Li is centered within the hexagonal plane separating two Si_{24} cages[55]. This is also found to be the lowest energy position in the Al0 and Al16 Ge clathrates (**Figure A.13**). However, the formation energy relative to the starting structure increased when placing Li in the 6*b* site, and the calculated lithiation voltages were negative. This indicates that lithiation relative to metallic Li is not energetically favorable. This was also seen in the Ba_8Si_{46} case[55], but with a lower voltage of -1.23 V compared to -0.48 V for the Al0 Ge clathrate.

Much like the high energy transition state between two vacancies, the instability of these positions can be rationalized by unfavorable guest atom displacements. When Li is relaxed at the 6*b* position in $Ba_8Al_{16}Ge_{30}$ (**Figure A.13a**), the two Ba atoms in the adjacent cages are pushed 0.35 Å away from the cage center, resulting in a 3.1 Å Ba-Li distance. The other local minimum position found was in the Ge_{24} cage off-plane of the pentagon adjacent to the Ge_{20} cage (**Figure A.13b**). This configuration had 0.1 eV higher energy than Li in the 6*b* position, and resulted in the Ba atom to be pushed 0.78 Å off center, resulting in a 3.07 Å Ba-Li distance. In contrast, Li in the framework vacancies in Ba_8Ge_{43} results in no Ba displacement from the center and a Ba-Li distance of 3.84 Å. When Li is added to the 6*b* site in $Ba_8Ge_{43}Li_3$, the relaxed structure has large distortions in the framework as seen in **Figure A.12d.** The voltage (-0.10 V) is higher than when the vacancies are not filled (-0.48 V) suggesting that the framework distortions are more energetically favorable. This Li-induced framework distortion could lead to eventual framework destruction with the introduction of more Li where Ge-Ge bonds are broken

to form the phase front of the amorphous transition, similar to what has been predicted in c-Si [146].

It is interesting to note that Li insertion at the 6*b* site in Ge clathrate does seem to be more favorable than the Si clathrate case as the voltage is higher (-0.48 V vs -1.23 V). This could suggest that the Ge framework more favorably accommodates Ba displacements (resulting from Li insertion) due to the larger cage size or different framework stiffness. Previously, *ab initio* molecular dynamics studies have shown that Ge atoms migrate significantly during lithiation of diamond cubic Ge, while Si atoms remain in a static position during lithiation[147,148]. The structural rigidity of Si frameworks and limited of migration during lithiation compared to Ge could also explain the significant difference of lithiation between Si clathrates and Ge clathrates. This is consistent with our experimental XPS, XRD, and TEM results showing that Ge clathrates are less structurally stable than the Si analogues. Overall, we find that unfavorable Li positions in the Ge clathrates and high energy barriers between vacancies suggest that Li insertion into the crystal structure is not feasible, which is consistent with experimental results.

3.1.4. Conclusions

We investigated a series of $Ba_8Al_yGe_{46-y}$ (y = 0, 4, 8, 12, 16) type I clathrates as Li-ion battery anodes for the first time. Similar to diamond cubic Si and Ge, but different from the silicon clathrate analogues we investigated in our previous studies, the Ge clathrates underwent conversion reactions to Li-rich amorphous phases. Increasing the amount of Al substitution for Ge in the clathrate resulted in an decrease in framework

vacancies, a decrease in the lithiation capacity, and a reduction in the two-phase reaction voltage. Ba_8Ge_{43} reacted at ~0.2 V vs. Li/Li^+ with a capacity of 1098 mAh/g and $Ba_8Al_{16}Ge_{30}$ reacted at 0.08 V with a capacity of 518 mAh/g. Ball-milling the hand ground powders resulted in significant amorphization of the Ge clathrates, which led to more sloped voltage profiles characteristic of electrochemical lithiation of amorphous phases. Galvanostatic cycling demonstrated capacity fading typical of unoptimized Li-alloy electrodes, consistent with large volume changes and particle decrepitation during the reactions. The EIS analysis at low frequency support the presence of a Warburg diffusion mechanism, which we attribute to bulk Li diffusion in the amorphous phases. DFT calculations were used to determine whether Li insertion and diffusion in the bulk structure is feasible. It was found that Li insertion at framework vacancies of Ba_8Ge_{43} at the 6*c* position is energetically favorable, but a high energy barrier (1.6 eV) would prevent Li diffusion between vacancies unless the Ba guest atom is absent. A lattice constant increase is calculated for $Ba_8Ge_{43}Li_3$ but not observed experimentally during lithiation, suggesting no Li incorporation into the bulk clathrate structure. Overall, the bulk type I $Ba_8Al_\delta Ge_{46-\delta}$ clathrates seem to be electrochemically inactive until they are converted to amorphous phases.

These results are similar to the type I Si clathrates that we previously investigated. However, the Si clathrates did not undergo a two-phase reaction to an amorphous phase, indicating that the structure is stable under these potentials. Future studies will explore the origin of the electrochemically-induced amorphization observed in the type I Ge clathrates, but it could be due to the apparent greater instability of the Ge structures (e.g. to air oxidation, ball-milling) compared to the Si analogues. It could also be due to the

higher stabilization of Li in Ge phases compared to Si (as indicated by higher reaction voltages for Ge). Understanding the nature of the amorphous phase transition in these intermetallic-type compounds could aid in the identification of new, stable Li-ion anodes that do not suffer from larger volume expansions due to electrochemical alloying with lithium.

3.2. *Ab initio* Investigation of Li and Na Migration in Guest-free, Type I Clathrates

3.2.1. Introduction

To meet the stringent power and energy density requirements for next-generation batteries, there has been considerable attention given to the search for materials with high ionic mobility, an important connection to the diffusion coefficient, which contributes to the rate capability of a battery electrode. The energy landscape of the migrating ion is a key factor in determining the ionic mobility in solid materials. In general, fast ion conductors are characterized by diffusing ions in a "frustrated" or flat energy landscape, where there is considerable disorder on the intercalant sites, leading to small kinetic barriers for transport[13,149].

Intermetallic clathrates have cage structures that host guest atoms and exhibit interesting characteristics including superconductivity[87–91], hydrogen storage[101,102], tunable optical properties[150] and thermoelectricity[92–96,98]. The origin of such properties is the unique interaction between the sp^3 bonded host framework with the guest atoms and the defects associated with this structural type. Recently, there has been much interest in the mobility of ions within clathrates and the potential of this class of materials to be used as anodes in lithium-ion batteries[49,52–56,105,107,151,152]. However, more investigation is

needed to identify the structural features of the unique cage framework that are suitable for ion conduction. Understanding the mobility of guest atoms within clathrates is relevant not only for battery insertion electrodes that rely on bulk ion diffusion, but also for the synthesis of clathrates and other novel polymorphs[153] (e.g., Si_{136}[40,154,155], Si_{24}[57], Si_6H_6[156], Ge_{136}[150,157], allo-Ge[158], germanane[159]), where the removal of the alkali metal guests via thermal evaporation or oxidative deintercalation at the surface are possible paths to obtaining the desired structures.

Our group has thoroughly investigated the electrochemical reactions of Tetrel (Tt) clathrates with Li and has found that type I clathrates based on Ba_8Tt_{46} (Tt = Si, Ge) do not intercalate Li atoms, with the observed reactions mainly confined to the surface or occurring through bulk, electrochemically induced conversion processes to amorphous phases[54,56,152]. In our recent study on Ba_8Ge_{43} clathrates, density functional theory (DFT) calculations suggested that it was energetically feasible for Li to occupy vacancies on the framework sites, but the migration energy barrier between them was found to be too high for room temperature lithiation due to the presence of Ba atoms in the cages[152]. If the Ba atom was absent, the calculated migration barrier decreased dramatically, suggesting the need for guest atom vacancies to enable Li migration.

To further investigate the mobility of ions in clathrates, herein we use first principles DFT methods to calculate the migration pathways of Li and Na in guest free, type I clathrates Tt_{46} (Tt = Si, Ge, and Sn) and to explore how the energy barrier varies with the type of framework atom. The preferred Li and Na atom positions were calculated based on the Gibbs free energy change of reaction; the nudged elastic band

(NEB) method was used to estimate migration barriers for different pathways within and between cages to evaluate the ionic mobility. We find that Li migration in guest free, type I clathrates is accompanied by low energy barriers comparable to those in state-of-the-art Li-ion conductors, which suggests the possibility of facile Li migration through the clathrate frameworks. This is attributed to the destabilization of Li in the large Tt_{24} cages, since the lowest energy sites are not in the center of the cage cavity, resulting in considerable disorder. The energy barrier is dependent on the cage size, with Ge_{46} displaying the lowest Li migration barrier of 0.13 eV. For Na migration, the migration barriers are significantly higher between cages, suggesting limited Na mobility through the clathrate frameworks. These results will help guide researchers in the design and experimentation of clathrates and other open framework intermetallic compounds as potential anodes for Li and Na ion batteries.

3.2.2. Computational Methods

The first-principles DFT calculations were performed to explore Li (Na) insertion and migration in guest free type I clathrates using a similar manner as in our previous work[55,152]. The calculations were carried out using the VASP code[77,78], the PBE functional[73], and projector augmented wave (PAW) potentials with a plane wave basis set[78]. In the PAW potentials, the Si 3s and 3p, Ge 4p and 3d, Sn 5p and 4d, Li 1s and 2s, Na 3s and 2p, Mg 3s and 2p, Ba 5s and 5p electrons were treated as valence electrons. The kinetic energy cutoff for the plane wave basis set was chosen to be 400 eV and the reciprocal space was sampled with the Monkhorst pack meshes $3 \times 3 \times 3$ centered at Γ.

The cubic Tt_{46} unit cell ($Pm\bar{3}n$ space group) was used in all calculations. The convergence criteria for the electronic and ionic relaxations were set to be 0.01 and 0.1 meV, respectively. These criteria resulted in relaxed structures with residual forces below 0.03 eV/Å. The geometric optimization was performed in two steps. First, the unit cell volume was optimized without the constraint of the cubic symmetry. Then the relaxed lattice constant, taken from the relaxed volume, was used in a second step where only ionic relaxation was allowed under the cubic symmetry constraint. The crystal structures with the ionic positions of the second step are reported.

The Gibbs free energy change of reaction (ΔG_r) and the average voltage were calculated as described previously[55,152]. The formulas used for calculating the Gibbs free energy change and average voltage for insertion of Li in Tt_{46}, for example, are shown in equation (1) and (2), respectively:

$$\Delta G_r = E(LiTt_{46}) - E(Li) - E(Tt_{46}) \quad (1)$$

$$V(x) = -\frac{\Delta G_r}{x}, x = \#\ of\ Li \quad (2)$$

where $E(LiTt_{46})$ and $E(Tt_{46})$ are the total free energies for the clathrate systems with and without the Li atom, and $E(Li)$ is the energy per atom for Li metal. The calculated values for $E(Li)$ and $E(Na)$ are -1.904 eV/atom and -1.311 eV/atom, respectively. A negative ΔG_r (i.e. positive voltage) represents a spontaneous reaction relative to Li (or Na) metal, suggesting the feasibility of lithiation (sodiation) in a half cell with Li (Na) metal as the counter electrode. The formation energies for the clathrate structures were obtained using the equations described in our previous work[55,152]. The elemental energies used for Si, Ge, and Sn were -5.419, -4.621, and -3.912 eV/mol from the diamond cubic

(Si, Ge) and tetragonal (Sn) structures. All crystal structure figures were created with Diamond 4.5.3.

The climbing image nudged elastic band (NEB) method was used to calculate the Li and Na migration barriers[85]. All NEB calculations used a linear interpolation as a starting band with 7 intermediate images between the beginning and ending images. The images were converged until the force on each image was below 0.03 eV/Å.

3.2.3. Results

3.2.3.1. Tt_{46} Structures

The type I clathrate structure crystallizes in the $Pm\bar{3}n$ space group and has a general formula of M_8Tt_{46}, where M is the guest atom hosted inside a framework of Tt (Tt = Si, Ge, and Sn) atoms[40]. The structure is composed of two types of polyhedra, six Tt_{24} (tetrakaidecahedra) and two Tt_{20} (dodecahedra), that host the guest atom, M (**Figure 3.2.1a**). The Tt_{24} cage is composed of 12 pentagonal and 2 hexagonal faces while the Tt_{20} cage is composed of 12 pentagonal faces. This is highlighted in **Figure 3.2.1a-b**, where a hexagon and pentagon are colored in red and blue, respectively. The type I structure can be visualized as one dimensional (1D) channels of Tt_{24} cages connected by shared hexagonal faces oriented in the three perpendicular directions, while the Tt_{20} cages fill the space between them. This is shown in **Figure 3.2.1c**, where two Tt_{24} in each perpendicular direction are shaded in different colors representing the three 1D channels. The related type II clathrate structure ($Fd\bar{3}m$ space group, general formula $M_{24}Tt_{136}$) is

composed of 16 dodecahedral cages (Tt_{20}) and 8 larger hexakaidecahedra (Tt_{28}), in which the Tt_{28} cages are connected in a tetrahedral network via hexagonal faces[40].

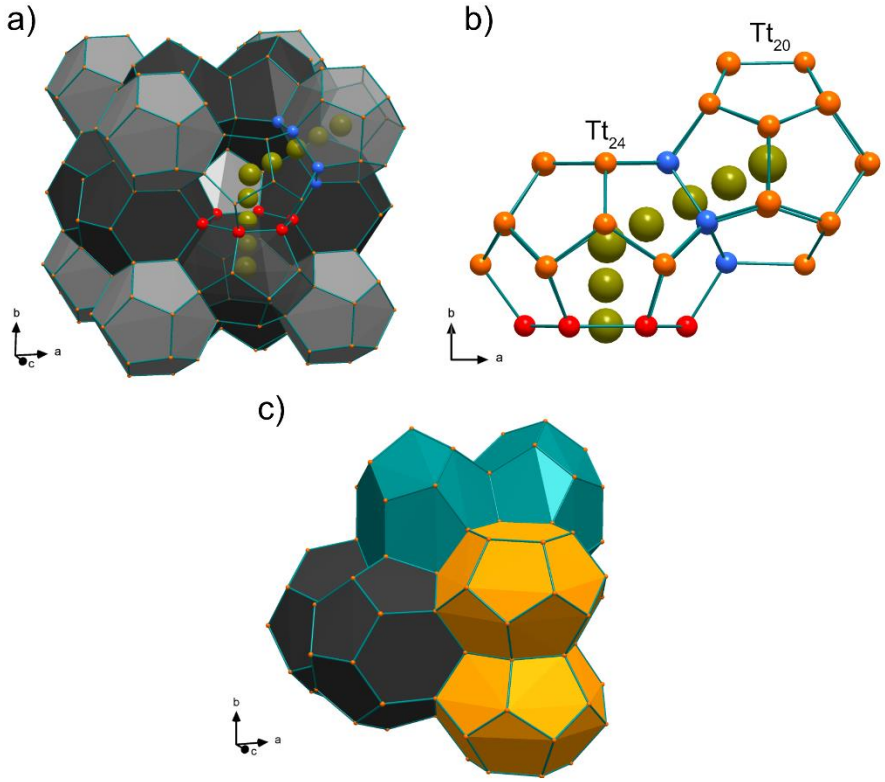

Figure 3.2.1 Crystal structures of type I clathrate Tt_{46}. The orange atoms represent Tt framework atoms (Tt = Si, Ge, Sn). The olive colored atoms represent the positions of the M guest atom (M = Li, Na) as it migrates through Tt atoms in the hexagonal and pentagonal faces between connected cages (indicated by red and blue atoms, respectively). (a) Polyhedral view, with the black polyhedra representing the tetrakaidecahedra (Tt_{24} cages) and the gray polyhedra representing the dodecahedra (Tt_{20} cages). (b) Ball-and-stick view of a Tt_{24} and Tt_{20} cage viewed down the [001]. (c) Polyhedral view with the three perpendicular channels of interconnected Tt_{24} cages (i.e., via connected hexagons) shaded in different colors.

The formation energies and lattice constants of the calculated Tt_{46} structures are presented in **Table 3.2.1**. To our knowledge, there have been no reports on the phase pure synthesis of these empty type I clathrate structures; this is likely due to the distortion of the Tt atoms from the ideal tetrahedral configuration found in their bulk phases. This is

supported by the positive formation energies in **Table 3.2.1** indicating that these structures are metastable with respect to their lower energy, bulk analogues. The lattice constants match well with previous calculations[55,160,161] and their experimental structures (e.g., a = 10.197 Å for Na_8Si_{46}, a = 10.686 Å for K_8Ge_{44}, and a = 12.03 Å for K_8Sn_{44})[162–164].

Table 3.2.1 Formation energy and optimized lattice constants of the guest-free Tt_{46} (Tt = Si, Ge, Sn) clathrate structures.

Composition	Formation Energy (eV/atom)	Lattice Constant (Å)
Si_{46}	0.057	10.230
Ge_{46}	0.031	10.720
Sn_{46}	0.152	12.380

3.2.3.2. Li Positions in Empty Type I Clathrates

To determine the most favorable lithium sites in the type I clathrate crystal structure, a Li atom was placed in various initial positions in either the Tt_{24} or Tt_{20} cages of a single Tt_{46} unit cell as described in our previous study[55]. The Gibbs free energy change of reaction (ΔG_r) and corresponding voltage were calculated after relaxation of the unit cell. **Figure 3.2.2a** shows the calculated results for the four Li sites representing positions of local minima in the three Tt_{46} structures: 1) the center of the Tt_{24} cage, 2) the center of the Tt_{20} cage; inside the Tt_{24} cage, coordinated off of the 3) hexagonal face (Off Hex), or the 4) pentagonal face (Off Pent). The relaxed Li positions are shown in **Figure 3.2.2b-d**, where the [001] view of two Tt_{24} cages and one Tt_{20} cage is depicted. A negative Gibbs free energy change (positive voltage) indicates a favorable reaction with

respect to Li metal, which is a useful metric for predicting whether materials can be electrochemically lithiated in a half-cell with Li metal.

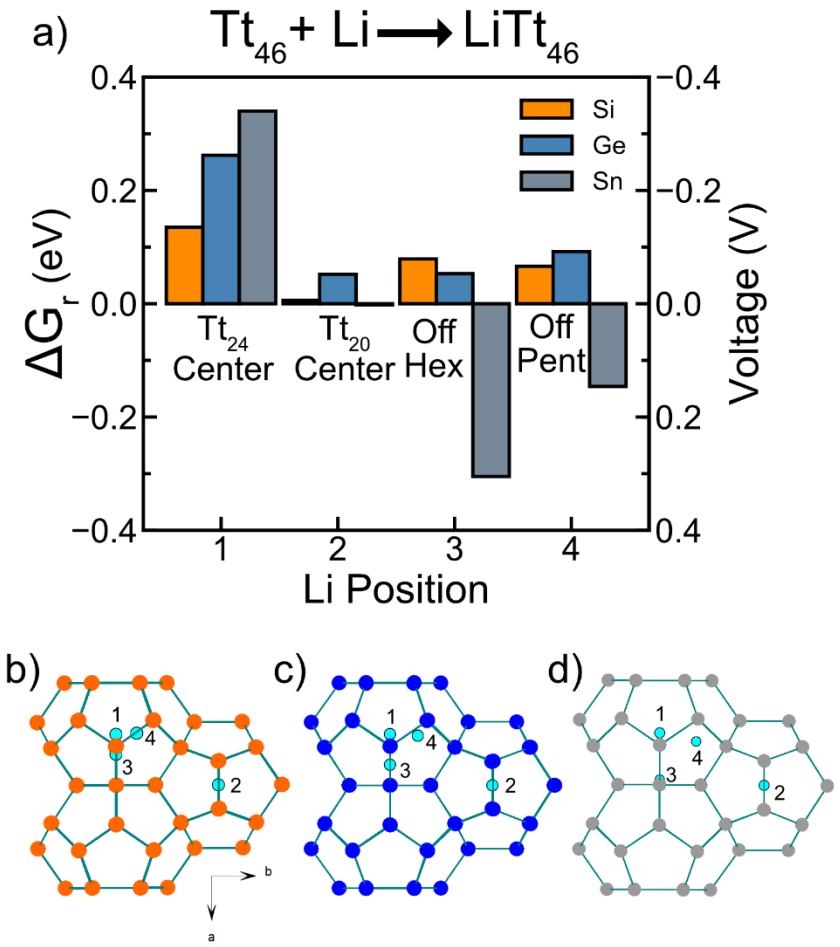

Figure 3.2.2 a) Gibbs free energy change of reaction (ΔG_r) and voltage vs. Li/Li^+ for the reaction Tt_{46} + Li → $LiTt_{46}$, where Tt = Si, Ge, Sn, for each of the 4 Li positions. Schematic with two Tt_{24} cages and one Tt_{20} cage for b) Si_{46}, c) Ge_{46}, and d) Sn_{46} showing the 4 Li positions after relaxation when viewed down the [001] direction. Li = cyan, Si = orange, Ge = blue, Sn = grey.

The results show that when a Li atom is relaxed in the Tt_{24} cage center (position 1), ΔG_r is positive and increases when increasing the size of the framework atom (**Figure 3.2.2a**). On the other hand, it is more favorable for Li to occupy the Tt_{20} cage center (position 2), as indicated by the lower ΔG_r values. This site also has similar energies

regardless of the framework atom. Based on these results, it appears that the size and the geometry/shape of the cage are important for the energetics of the Li insertion sites. The lower energy of the Li position at the Tt_{20} cage center compared to the Tt_{24} center can be attributed to the smaller cage volume and more symmetric cage geometry (since the Tt_{20} cage is made solely of pentagonal faces), which better accommodate the small Li atom. For Sn_{46}, however, we find that Li will prefer an off-center position where it is coordinated by a pentagonal face in the Sn_{20} cage because of the larger cage sizes compared to Si_{46} and Ge_{46} (shown in **Figure B.1**). Indeed, ΔG_r = -0.181 eV for this off-centered position in the Sn_{20} cage, which is much lower than that for the Sn_{20} center position (ΔG_r = -1.6 meV) as well as the Off Pent position in the Sn_{24} cage. From this, we can see that Li will still prefer an off-center position if the Tt_{20} cage is large enough.

Considering Li inside a Tt_{24} cage, the results show that for all three Tt_{46} compositions, Li prefers to be coordinated off of a hexagonal (position 3, Off Hex) or pentagonal (position 4, Off Pent) face instead of occupying the Tt_{24} cage center. Due to the similar energies of these off-center positions, this suggests that Li inside a Tt_{24} cage will display positional disorder. The Li-Tt bond lengths and lattice parameters for the relaxed structures containing Li in each of the 4 positions are presented in **Table B.1.** For the Off Hex and Off Pent positions for the three Tt_{46} compositions, the Li-Tt distance range was around 2.8 – 3.0 Å, suggesting that this is the energetically favored Li-Tt bond length. The most favorable Li site in both Ge_{46} and Sn_{46} is position 3 (Off Hex), where Li resides closer to the hexagonal face than the cage center (**Figure 3.2.2c-d**). In Sn_{46}, the relaxed Off Hex Li position is very close to the center of the hexagonal face with a Li-Sn distance of 2.90 Å, meaning that the hexagon in Sn_{46} is large enough for Li to favorably

reside near the center. For Si_{46}, Li position 4 (Off Pent) is the most favorable site but the energy is only slightly lower (13 and 69 meV, respectively) to those for Li position 3 (Off Hex) and Li position 1 (Tt_{24} Cage center). As the size of the Tt_{24} cage increases from Si to Sn clathrates, not only does the cage center position become more unfavorable, but Li prefers to be coordinated near the hexagonal face instead of the pentagonal one, likely due to the increased amount of interaction with six Tt atoms compared to five. The ΔG_r values for the reaction of Li with Ge_{46} and Si_{46} are both slightly positive, suggesting that these reactions would not be favorable in a half cell with Li metal. A more detailed study investigating the energies of various compositions and considering the ordering of Li would be needed to estimate the exact reaction voltages[58,165,166].

3.2.3.3. Li Migration Pathways in Empty Type I Clathrates

Because each cage in the clathrate structure is composed of several different faces (pentagonal or hexagonal), the ionic mobility between cages is expected to be impacted by the geometry of these faces. If the initial position of M (M = Li, Na) is near the center of a cage, it must traverse through either a hexagonal or pentagonal face to reach an adjacent cage, unless it goes through a Tt-Tt bond. These possible intercage pathways (presented via the atomic positions used in the NEB calculations) are illustrated in **Figure 3.2.1a-b**.

The NEB results to evaluate Li mobility within the clathrate structure are presented in **Figure 3.2.3. Figure 3.2.3a** shows the NEB calculations for Li migration between two Tt_{24} cages through the interconnecting hexagonal face for Tt = Si and Ge (Tt

= Sn is not included because the center of the hexagon is a local energy minimum in $LiSn_{46}$ and thus not a saddle point in the Li migration pathway between Sn_{24} cages). The migration barriers for Li movement through the hexagonal face in Si_{46} and Ge_{46} are 0.35 eV and 0.09 eV, respectively. Previous estimates have suggested that ionic migration barriers should be, at most, in the range of 0.525-0.65 eV for materials to be effective as battery electrodes[167]. The NEB results for Li movement between adjacent Tt_{20} and Tt_{24} cages through the interconnected pentagonal face are presented in **Figure 3.2.3b**, with a schematic of the Li pathway for Si_{46} in the inset (**Figure B.2** shows the analogous schematics for Ge_{46} and Sn_{46}). Ge_{46} shows a very shallow local minimum at reaction coordinate 1, an indication of the flat energy landscape inside the Ge_{20} cage for Li. The energy barriers for Li moving through the pentagonal face are 2.05 eV, 1.28 eV, and 0.54 eV for Tt = Si, Ge, and Sn, respectively. Previously, calculations performed on the type II Si clathrate showed that the barrier for Li and Na migration through a pentagonal face is much higher than that through a hexagonal face[105,168]. This is consistent with our findings in type I clathrates, despite the slightly different structures between type I and II clathrates.

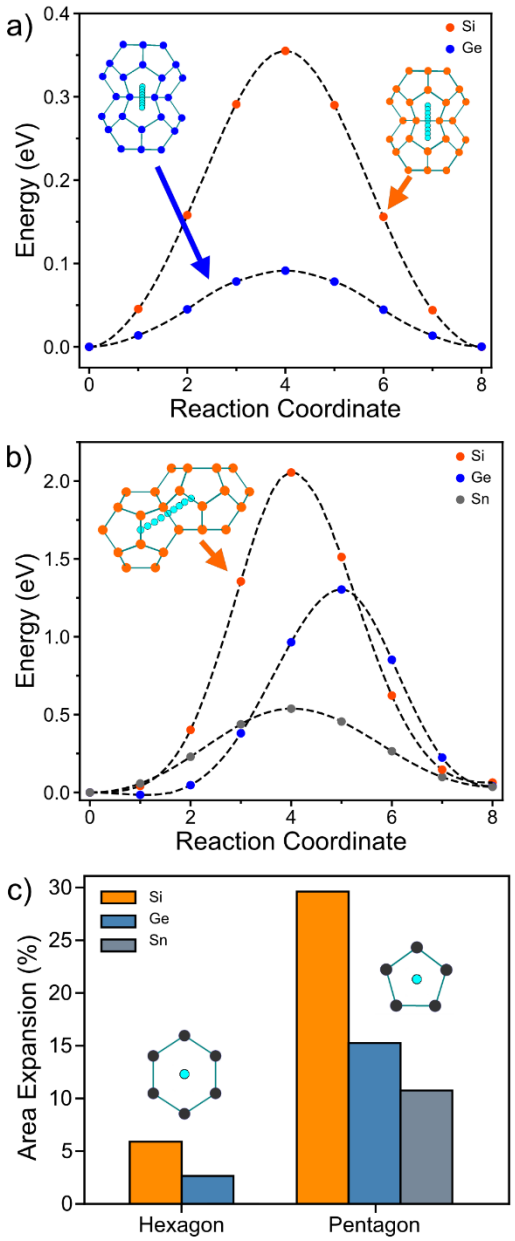

Figure 3.2.3 a) NEB calculated minimum energy path for Li (cyan) migration in Si_{46} and Ge_{46} between the Off Hex positions in two adjacent Tt_{24} cages through a hexagonal face. b) NEB calculated minimum energy path for Li migration between the Tt_{20} and Tt_{24} cages through a pentagonal face. c) Percentage of the area expansion of the hexagonal and pentagonal faces at the highest energy position for the two pathways in a) and b) relative to the starting size of the hexagon/pentagon.

The calculated results also indicate that Li intercage diffusion causes distortion of the Tt atoms bonded within the faces. When Li moves through the hexagonal face, the Tt

atoms expand outwards away from the Li as it passes through the center. A similar result is observed when Li moves through the pentagonal face, but the atoms are moved more significantly away from their initial positions due to the smaller initial area of the pentagon. This is illustrated in **Figure 3.2.3c,** which shows the increase in the area of the face (as a percentage of the initial area) at the highest energy image for Li migration through the hexagonal and pentagonal faces. There is more expansion of the hexagonal face for Si_{46} compared to Ge_{46} (5.9% vs. 2.6%), demonstrating that the amount of expansion is related to the height of the migration barrier. The lower area expansion and transition state energy for Ge_{46} suggests that the larger starting size of the hexagon allows for Li transport with less structural perturbation, leading to a lower energy barrier. In contrast, the expansion of the pentagonal face is much higher, reaching almost 30% for Si. The higher energy barriers for Li migration through the pentagonal face can be rationalized by the much larger displacement of the surrounding Tt atoms and shorter Tt-Li lengths during migration. The Tt-Li bond lengths are presented in **Table B.2** and a schematic of the initial and transition states are shown in **Figure B.3**. These data show that the shorter Tt-Li bond lengths at the transition state also correlate with the higher transition state energy. As the pentagon/hexagon expands to move away from the Li, the distortion of the surrounding framework from the tetrahedral configuration will also raise the energy. The saddle point will be pinned by these two competing mechanisms. From these results, we see that the energy barrier decreases significantly when increasing the size of the framework atom for both types of intercage Li migration pathways. This can be explained by the longer Li-Tt bonds at the transition state, less structural perturbation, and the higher propensity for Ge and Sn to accommodate framework distortions away

from the ideal tetrahedral structure. The results are similar to those found in another study that calculated the migration barriers for Li in diamond cubic Si, Ge and Sn, where the migration barrier was also found to decrease as the Tt atom size increased[145].

For the Ge and Sn frameworks, the most favorable position for Li insertion was found to be close to the hexagonal face (position 3 in **Figure 3.2.2**), far from the cage center position, which suggests that transport within a Tt_{24} cage should also be considered. Si_{46} is not included because the lowest energy position, the Off Pent position, is closer to the cage center. **Figure 3.2.4a-b** shows the NEB calculations for Li movement between two Off Hex positions in Ge_{46} and Sn_{46} via two pathways: through the center or along the cage side. The lower energy pathway involved Li migrating along the side of the cage to the local minimum position at the Off Pent site (position 4 in **Figure 3.2.2**), then moving to the other Off Hex position on the other side of the Tt_{24} cage. The highest energy along this pathway was 0.13 eV for Ge and 0.37 eV for Sn. Movement through the cage center resulted in higher energy barriers (0.2 eV and 0.65 eV for Ge and Sn, respectively) demonstrating that Li prefers to stay near the cage side. In general, Li in the lower energy (i.e., off-centered) positions inside the Tt_{24} cage have a Tt-Li distance of around 2.8-3.0 Å (**Table B.1**). When Li is at the center of the Tt_{24} cage in Ge_{46} and Sn_{46} clathrates, the Li-Tt distance increases to 3.60 Å and 4.17 Å, respectively. The latter bond length is much longer than the lower energy Li-Tt distances, which results in a higher energy barrier for intracage movement of Li within Sn_{46} through this pathway.

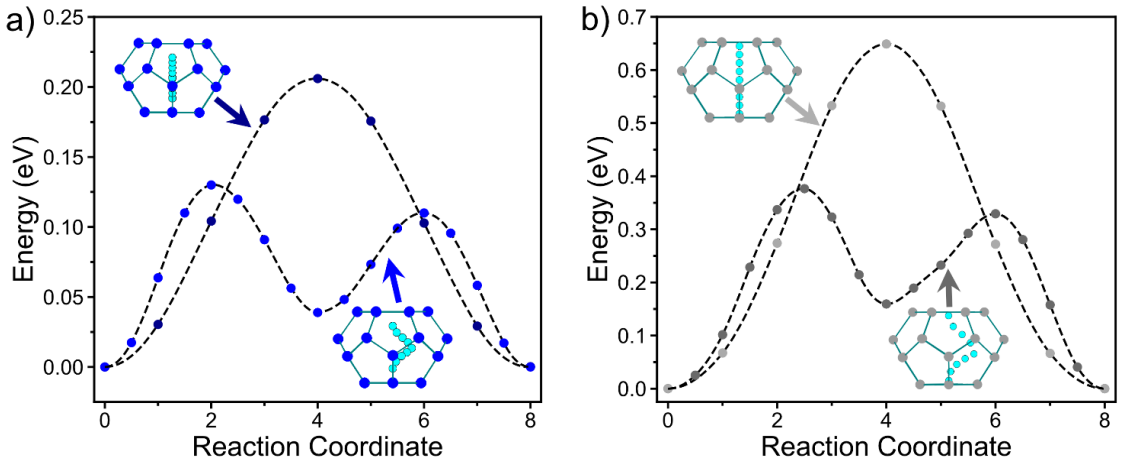

Figure 3.2.4 NEB calculated minimum energy paths for Tt_{24} intracage migration of Li (cyan) in a) Ge_{46} and b) Sn_{46}. The pathway is between Off Hex positions through the center of the cage or along the side of the cage.

Previously, calculations by Tse *et al*. showed that Li diffusion between Si_{20} cages in the type II Si clathrate structure was affected by the presence of nearby Ba guest atoms[105]. If Ba was in an adjacent cage (which would be a Si_{28} cage in type II clathrates), the lower energy pathway for Li migration between Si_{20} cages was to break a Si-Si bond rather than going through the center of the pentagonal face. To investigate the possibility of this type of cooperative Li migration in the type I clathrates, the NEB calculation for Li migration between the Si_{20} and Si_{24} cages was performed in Si_{46} with all Si_{24} cages filled with Li in the Off Pent positions (i.e., Li_6Si_{46}). The results (**Figure 3.2.5a**) show that when Li occupies the other Si_{24} cages, the migrating Li will break a Si-Si bond instead of migrating through the center of the pentagonal face, since the former process is accompanied by a much lower energy barrier (0.77 eV vs. 2.0 eV). **Figure 3.2.5b-c** show crystal models of one Si_{20} cage and two Si_{24} cages at reaction coordinate 0 and at reaction coordinate 4 (the transition state). The Si atoms in black indicate the three pentagons that

share the bond that becomes broken in the transition state. The Si-Si bond originally has a bond length of 2.4 Å (**Figure 3.2.5c**); at the transition state, the Li atom (cyan) moves between the Si atoms and the Si distance increases to 5.0 Å, demonstrating that the Si-Si bond is replaced by Li-Si interactions. During Li migration from Si_{20} to Si_{24}, the Li occupying the adjacent Si_{24} cage (blue atom) moves 1.13 Å closer to the broken bond from its original position. The possibility for two Li atoms to stabilize the transition state is similar to results by Zhao *et al*. showing that as more Li surround the Si atoms during lithiation of diamond structured Si, it becomes more favorable to break the Si-Si bonds in favor of Li-Si bonds[146]. When repeating the calculation first reported by Tse *et al*.[105] for the migration of Li between Si_{20} cages in type II clathrate $LiBa_8Si_{136}$ (**Figure B.4**), we found that during the transition, the Ba atom moves 0.57 Å towards the broken Si-Si bond as well. These results suggest that cooperative motion between electroactive ions or guest atoms can result in a unique diffusion mechanism for accessing the Tt_{20} cages of clathrates, namely by breaking and reforming a Tt bond.

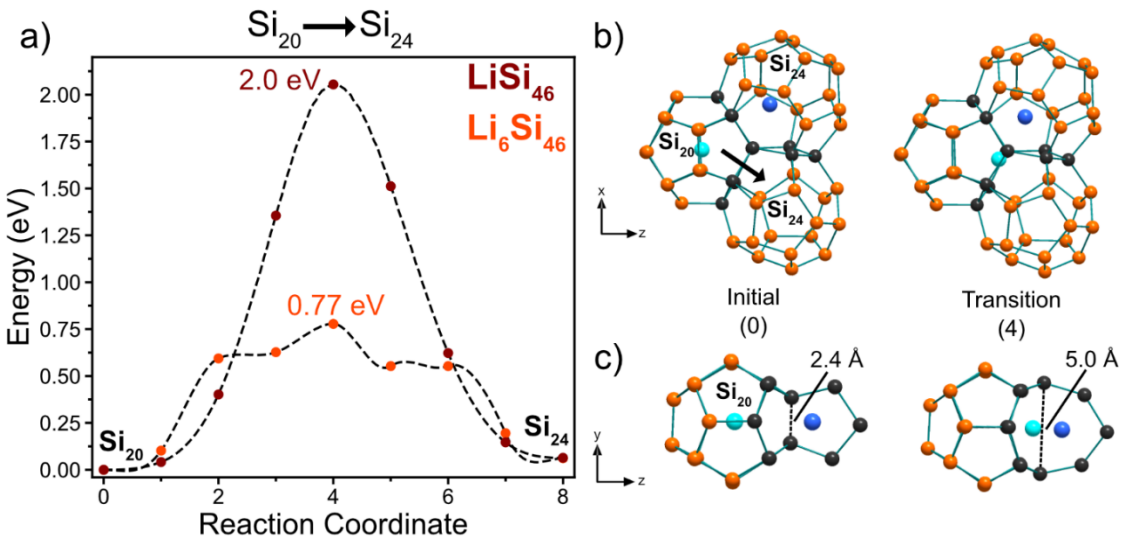

Figure 3.2.5 a) NEB calculated minimum energy paths for Li migrating from the Si_{20} cage to the Si_{24} cage with and without the adjacent Si_{24} cages filled with Li. b) Crystal models of the intersection of two Si_{24} cages and one Si_{20} of the initial positions and the transition state positions for the minimum energy path in Li_6Si_{46}. Si atoms are orange, the cyan atom is the mobile Li, and the blue atom is Li in the adjacent Si_{24} cage. The Si atoms in black are from the three pentagons that share the bond which is broken in the transition state. c) Crystal model viewed down the x-axis relative to b) showing the Si-Si bond that is broken (dashed line).

The overall Li diffusion pathways in the type I clathrate frameworks can thus be described as follows. For Li in empty Si_{46}, the diffusion will be dominated by Li hopping between Si_{24} cages via hexagonal faces with a migration barrier of 0.35 eV. The high energy barrier (2.05 eV) for Li diffusion through pentagonal faces means that accessing the Si_{20} cage is unlikely in the dilute Li regime. If Li is already present in the other Si_{24} cages, the Si_{20} cages could be accessible to Li through a cooperative migration mechanism that involves Si bond breaking and results in a lower migration barrier of 0.77 eV. The Si_{24} cages will be preferentially occupied and 1D diffusion can occur through the 3 perpendicular channels of Si_{24} cages connected by hexagonal faces. Ge_{46} shares a

similar trend as Si_{46} where intercage migration through the hexagonal face has the lowest energy barrier of 0.09 eV. However, intracage migration in the Ge_{24} cage has a higher energy barrier of 0.13 eV. The 1.28 eV barrier for intercage migration through the pentagonal face to the Ge_{20} cage will restrict access in the dilute Li regime. For Sn_{46}, the cage size becomes large enough that intracage migration in Sn_{46} is the major limiting factor, with a migration barrier of 0.37 eV. Li occupation of the Sn_{20} cage is feasible in this case as well, with a migration barrier of 0.54 eV through the pentagonal face.

In summary, the Li diffusion in empty type I clathrates is predicted to be determined by movement between Tt_{24} cages via the hexagonal faces. As the cage size increases from Si_{46} to Sn_{46}, Li prefers to be closer to the side of the cage and intracage diffusion begins to be a more important factor for the migration barriers. Ge_{46}, with the lowest barrier of 0.13 eV, has a cage size that minimizes the intercage and intracage migration barriers, resulting in a flat energy landscape with regards to the possible Li positions. When the cage is smaller (e.g. Si_{46}), intercage transport via the hexagonal face is limiting, and when the cage is larger (e.g. Sn_{46}), intracage transport is limiting.

3.2.3.4. Na Positions and Migration Pathways in Empty Type I Clathrates

To find the most favorable Na positions in the empty type I clathrate structure, a treatment similar to the one used to study Li diffusion was applied by placing the Na in four positions: 1) Tt_{24} center, 2) Tt_{20} center, 3) Off Hex, and 4) Off Pent. The ΔG_r for Tt_{46} with one Na is presented in **Figure 3.2.6**, with the associated crystal structures showing the position of Na after relaxation. **Table B.3** shows the Tt-Na bond lengths and lattice parameters of the relaxed structures.

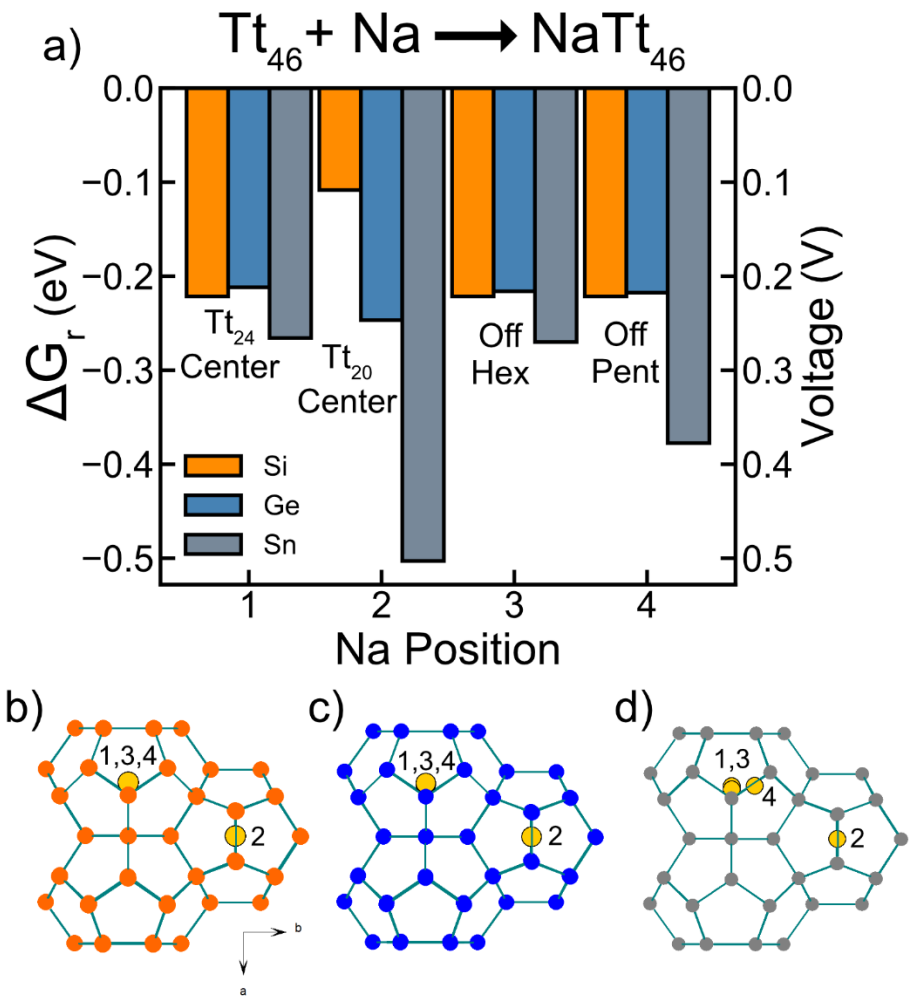

Figure 3.2.6 a) Gibbs free energy change of reaction (ΔG_r) and voltage vs. Na/Na^+ for the reaction Tt_{46} + Na → $NaTt_{46}$, where Tt = Si, Ge, Sn, for each of the 4 Na positions. Schematic of two Tt_{24} cages and one Tt_{20} cage for b) Si_{46}, c) Ge_{46}, and d) Sn_{46} showing the 4 Na positions after relaxation viewed down the [100] direction. Na = yellow, Si = orange, Ge = blue, Sn = grey.

For $NaSi_{46}$, Na occupation is favorable inside both the Si_{20} and Si_{24} cages as shown by the negative ΔG_r values calculated for the relaxed positions When the initial positions are off-center of the hexagonal or pentagonal faces in the Si_{24} cage, the Na moves to the center after relaxation. Different from the Li case, Na prefers the center

position of both Si_{24} and Si_{20} cages. This is consistent with well-documented experimental evidence that shows Na occupation in both cage center positions of Na_8Si_{46} with low thermal displacement parameters[164,169,170], indicating low disorder on the Na site. For $NaGe_{46}$ and $NaSn_{46}$, the calculations show that it is also favorable for Na to occupy both cages, as shown by the negative ΔG_r values. Similar to the case for Si_{46}, Na prefers the center of the Ge_{24} cage when relaxed from the initial Off Hex and Off Pent positions. The Off Pent site is the most favorable position for Na inside the Sn_{24} cage. This position is similar to the off-centered positions reported for K and Ba in Sn_{24} cages, where splitting in the anisotropic thermal displacement parameters show disorder in the directions parallel to the hexagonal faces[162,171]. Despite the energetic favorability for occupation of Na in Ge_{46} and Sn_{46}, to our knowledge, no Na containing, type I Ge and Sn clathrates have been synthesized, although Na containing, type II Ge clathrates have been prepared via thermal decomposition of Na_4Ge_4[150]. The negative ΔG_r values for all of the investigated Na positions in the Tt_{46} clathrates also suggest that the electrochemical sodiation of all compositions is energetically favorable if the kinetics allow it.

Next, the NEB calculations for Na migration between Tt_{24} cages through the hexagonal face and then from the Tt_{20} cage to the Tt_{24} cage are presented in **Figure 3.2.7a-b**. The migration barriers for Na through the hexagonal face (**Figure 3.2.7a**) for Si, Ge, and Sn are 2.42, 1.48, and 0.45 eV, respectively. Na migration in Sn_{46} is slightly different from that in Si_{46} and Ge_{46} as the initial (i.e., lowest energy position) is the Off Pent position (Na Position 4 in **Figure 3.2.6d);** a crystal model schematic of the NEB pathway is shown in the inset of **Figure 3.2.7a.** The local minimum at reaction coordinate 2 is an intracage transition from an Off Pent to Off Hex position within the

Sn_{24} cage. Similar to the case of Li migration, Na is found to move through the center of the hexagonal face and forces the six Tt atoms to move away from the Na atom, resulting in an increase in the area of the hexagon of 15.6 %, 15.1 % and 9.6 % for Si, Ge, and Sn, respectively (**Figure 3.2.7c**)**.** Compared to Li migration, the area expansion of the hexagonal face and the migration energies for Na migration are higher. This can be attributed to the larger size of Na and longer Tt-Na interaction distances, which is evident from the preference of Na for the Tt_{24} cage center. The Tt-Na distances for the hexagonal transition states are provided in **Table B.4**. Initially, the Na-Tt distances are 3.44-3.65 Å. At the transition state, the Na-Tt bond lengths decrease dramatically (i.e., 2.52 Å for the Si_{46} case), which correlates with the high migration barrier.

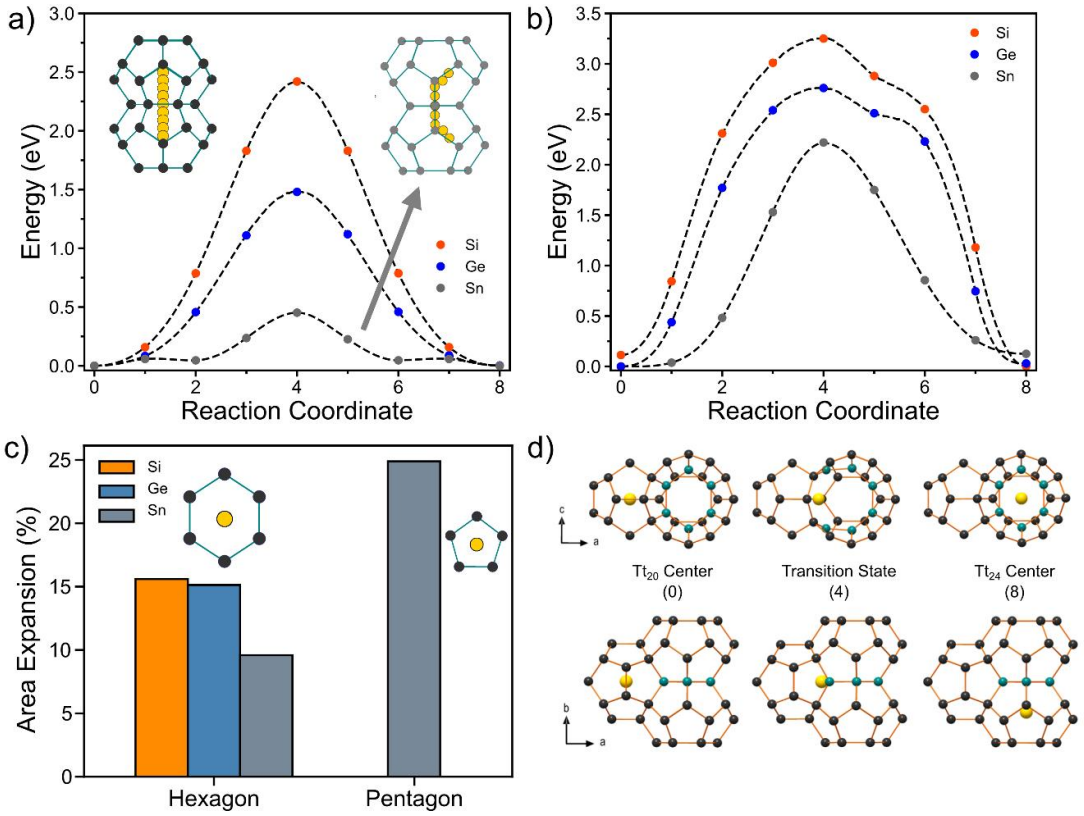

Figure 3.2.7 a) NEB calculated minimum energy paths for Na (yellow) migration in Si_{46} and Ge_{46} (black), and Sn_{46} (grey) through the hexagonal face. b) NEB calculated minimum energy paths for Na migration between the Tt_{20} and Tt_{24} cages for Tt_{46} through a pentagonal face. c) Percentage of areal expansion of the hexagonal and pentagonal face in the type I clathrate structure at the highest energy position (reaction coordinate 4) in a) and b) relative to the starting size of the hexagon/pentagon. d) Crystal models of $NaSi_{46}$ and $NaGe_{46}$ at the 0, 4, and 8th reaction coordinate of b) viewed down the b and c axis. Teal atoms indicate those in the hexagonal face.

Figure 3.2.7b shows the NEB results for Na migration between Tt_{20} and Tt_{24} cages. The migration barriers are 3.25 eV, 2.76 eV and 2.22 eV for Si, Ge and Sn, respectively. For Si_{46} and Ge_{46}, when migrating from a Tt_{20} to Tt_{24} cage, Na will preferentially break a Tt bond instead of passing through the center of the pentagonal face. The increased asymmetry in the NEB minimum energy path in **Figure 3.2.7b** is a result of this Tt bond breaking. The reaction path is illustrated in **Figure 3.2.7d,** showing

the crystal structures of reaction coordinate 0, 4, and 8 in the NEB calculation from two viewing directions. At the transition state, the Tt bond is broken as the Na migrates between the two Tt atoms. This mechanism is similar to that which was previously described for the Li case in Si_{46} (**Figure 3.2.5**). However, no other guest or Na atom is needed in an adjacent Tt_{24} cage to allow the system to converge to this minimum energy path. This could be explained by considering the extremely unfavorable transition of Na moving through a Tt pentagonal face, which would likely cause large perturbation to the position of the Tt atoms and result in very short Na-Tt distances. This bond breaking pathway is then favored by significantly perturbing two Tt atoms and stabilizing the broken bonds with the Na atom. For $Sn_{46,}$ the minimum energy path does not converge to this Na migration pathway and instead the Na passes through the pentagonal center. This is possibly because the Sn pentagon is large enough to sustain framework distortions while maintaining longer Sn-Na distances during the transition state. Since Na migration from Si_{20} cages is relevant for the thermal desodiation of Na_xSi_{136} under vacuum, a synthetic approach to access guest-free type II clathrates[154,155,168,172], a calculation for Na diffusion from a Si_{20} to a Si_{28} cage was also performed to see if this bond breaking phenomenon occurs. **Figure B.6** shows the NEB minimum energy path and crystal structures of this path; the results show that this Na migration pathway in the type II clathrate does indeed result in the breaking of a Si-Si bond, but with a lower activation energy of 2.48 eV (vs. 3.25 eV in type I Si_{46} clathrate).

The overall diffusion pathways for Na in Tt_{46} frameworks can now be summarized. The lowest energy migration paths involve transport through the hexagonal face between Tt_{24} cages through the 1D channels. Accessing the Tt_{20} cages involves a

higher energy transition state via a bond breaking mechanism for Si_{46} and Ge_{46}. For room temperature diffusion, the energy barriers are too high in Si_{46} (2.42 eV) and Ge_{46} (1.48 eV) for any significant Na ionic mobility[167]. On the other hand, for Sn_{46}, the lower barrier of 0.45 eV could allow Na hopping between Sn_{24} cages. Overall, when compared to Li, Na has much lower mobility in guest free, type I clathrate frameworks due to its larger atomic size and preference for longer bond distances to the Tt atoms.

A similar analysis for Mg guest atoms was also calculated and the Gibbs free energy change of reaction values are shown in **Figure B.5**. The ΔG_r for all four positions were positive, with values above 0.5 eV for the three Tt compositions investigated, suggesting that these reactions are unfavorable. This is consistent with no known reports of clathrates containing Mg guest atoms.

3.2.4. Discussion

4.1.4.1 Comparison of Li Migration in Clathrates vs. Diamond Structure and Other Open Frameworks

The Li environment in guest free, type I clathrates is distinctly unique to that in diamond structured analogs. The tetrahedral "cavities" that are known to be the stable Li positions in the diamond structure are much smaller than the cavities in the clathrate cages and are more densely packed[145,173]. The Li tetrahedral position allows for symmetric interaction with the four surrounding Tt atoms, resulting in a minimum in the energy landscape for the Li interstitial. Transport between these tetrahedral interstitial positions is through a hexagonal-like ring of Tt atoms which have Li migration barriers

previously calculated as 0.62 eV, 0.44 eV, and 0.39 eV for Si, Ge, and Sn, respectively[145].

For the clathrates, Li can also traverse through a hexagonal ring between Tt_{24} cages but with lower energy barriers of 0.35 eV and 0.09 eV for Si_{46} and Ge_{46} (**Figure 3.2.3a**), respectively. This difference can be attributed to the destabilization of the Li site energies inside the Tt_{24} cages. The Tt_{24} cages are too large for favorable Li-Tt interactions when Li is in the cage center, which results in Li preferring to be close to the cage side near one of the hexagonal or pentagonal faces. This site preference removes the favorable Li-Tt symmetric interaction from all sides (such as that in the tetrahedral position in the diamond structure) and frustrates the Li energy landscape when it occupies the Tt_{24} cage. This results in multiple Li positions with similar energies. In other words, the open framework structure of the clathrates smooths out the energy landscape for a Li intercalant by removing highly symmetric positions that act as low-energy minima. This has the effect of decreasing the relative difference between Li resting sites and the transition state, leading to lower energy barriers for Li migration through the hexagonal face (0.35 eV and 0.09 eV for Si_{46} and Ge_{46}, respectively) compared to those seen in the diamond structures (0.62 eV and 0.44 eV for Si and Ge, respectively).

Among the Tt_{46} clathrates investigated here, the Ge_{46} clathrate displays the lowest Li migration energy barriers. The energy difference among the different Li positions in the Tt_{24} cage is low (~0.2 eV) and the hexagonal face is large enough to enable facile Li migration between Tt_{24} cages (0.09 eV barrier). This balance between the size of hexagonal face and Tt_{24} cage leads to the lowest Li migration barrier among the

compositions investigated here. This concept is summarized in **Figure 3.2.8**, where two adjoining Tt_{24} cages are labelled with the relative intracage (red arrows) and intercage (black arrows) migration barriers. When the cage size is smaller, as is the case of Si_{46}, the highest energy position is the transition state at the center of the hexagonal face, which leads to a higher energy barrier for intercage diffusion (0.35 eV). When the cage is larger, as in the case of Sn_{46}, unfavorable Tt-Li interactions at the cage center lead to a larger relative energy difference among the possible Li sites and a higher migration barrier for intracage diffusion (0.37 eV). Ge_{46} is the intermediate case between these two extremes, with relatively low barriers for both intracage and intercage migration. These results suggest that the size of the cage (and by extension, the channels through which the guest atoms diffuse) are the primary factors for determining the migration barriers and hence could potentially be tuned by creating alloys of these Tt_{46} compounds.

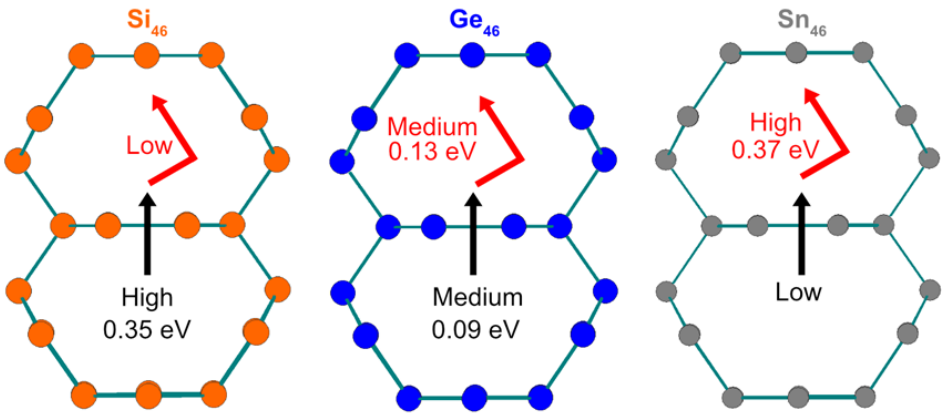

Figure 3.2.8 A scheme summarizing the relative energy barriers for Li intracage (red arrows) and intercage (black arrows) migration through two adjoining Tt_{24} cages (shown in cross-section) connected by a hexagonal face. As the cage size increases, the intracage barrier increases while the intercage barrier decreases.

Recent theoretical studies investigating a new Si polymorph (Si_{24})[57] with similar structural features as clathrates reported a low migration barrier of 0.14 eV for Li hopping and high room temperature conductivity from *ab initio* molecular dynamics calculations[58,59]. The Si_{24} structure is composed of channels of hexagonal-like rings in which Li is predicated to migrate, similar to the results found here. The calculated migration barriers for type I clathrates and Si_{24} are similar to those of Li-ion superionic conductors, which have activation barriers of around 0.2-0.3 eV[82], suggesting that Li migration would be facile. Hence, open, covalently bonded frameworks of Tt atoms appear to have promising ionic mobility for Li if there are no guest atoms present.

4.1.4.2 Comparison of Li and Na Migration in Clathrates

Compared to Li, Na intercalation appears to be severely limited by the fact that it is relatively difficult to squeeze the larger Na atom size through the hexagons and pentagons connecting adjacent clathrate cages. Except in the case of Sn_{46}, the calculated Na migration barriers suggest that the diffusion of Na between cages would be limited. This is well supported by the experimental evidence that Na evaporation from Na_xSi_{136} occurs in the temperature range of 370-450 ^oC under vacuum[40,155,164,172], indicating that the migration barriers for Na diffusion from the bulk to the surface are much higher than those that would enable significant room temperature diffusion. The type I clathrate Na_8Si_{46} does not exhibit Na loss via evaporation under similar conditions as Na_xSi_{136}, suggesting that Na migration in type I clathrates is even more limited. Effectively, the diffusion channels are too narrow to allow for facile Na migration. This is in contrast

with Li, which has close to the ideal size (Tt-Li length of 2.8-3.0 Å) for migrating through hexagonal faces composed of Tt atoms. Only in Sn_{46}, which has larger sized hexagons compared to Si_{46} and Ge_{46}, can the Na atom diffuse with a migration barrier of 0.45 eV, pointing to the possibility of Na intercalation in guest free Sn clathrates.

The unique bond-breaking migration mechanism for Na migration to and from the Tt_{20} cage highlights the highly unfavorable pathway of intercalants squeezing through the Tt pentagons. Unlike Li migration, the pentagonal transition state in the case of Na migration is obtained without cooperative motion and is likely due to the very high energy of the pentagonal pathway in comparison to breaking a Tt-Tt bond. This mechanism is particularly interesting for explaining the Na diffusion in type II Si clathrates, where it has been suggested that Na moves from the Si_{20} to Si_{28} cages through a pentagonal face[168]. As seen in **Figure B.5**, when migrating from the Si_{20} to Si_{28} cages, Na will cleave and reform a Si-Si bond instead of moving through the center of the pentagon face, which has an energy barrier of 2.48 eV. These results could help explain the diffusion mechanism of Na evaporation from type II Si clathrates during thermal treatment under vacuum.

3.2.5. Conclusions

In summary, DFT calculations were used to evaluate the preferred insertion positions and migration pathways for Li and Na in guest free, type I clathrate frameworks composed of Si, Ge, and Sn. Because of the size mismatch between Li and the Tt_{24} cages, Li prefers a more off-center position inside the Tt_{24} cage as the size of the cage increases

in Si to Sn clathrates. In the smaller Tt_{20} cages, it is more energetically favorable for Li to be closer to the center position of the cage. The diffusion paths for Li in the structures is determined by the connectivity of the cages via hexagonal faces. The barrier for Li to migrate through a hexagonal face is much lower (0.35 eV for Si_{46}) than diffusing through a pentagonal one (2.05 eV), meaning that Li hopping between Tt_{24} cages will dominate the Li migration. Li insertion into the Tt_{20} cage would be kinetically restricted due to the high migration barrier in the dilute regime. However, we find that a lower energy pathway characteristic of cooperative migration (barrier of 0.77 eV) is possible where the Li breaks a Si-Si bond at the transition state if Li atoms are present in adjacent cages. The cage size for Ge_{46} results in a flat energy landscape for the Li positions, leading to a lower barrier of 0.13 eV for migration, which is comparable to barriers in current superionic conductors. The low migration barriers for Li in the Tt_{46} structures suggest the possibility of Li insertion and thus possible applications for Li-ion batteries.

In contrast to the low migration barriers for Li, there are high barriers for Na migration (2.5 eV for Si_{46}) through the hexagonal face between Tt_{24} cages. This is attributed to the larger size of the Na atom and its longer Na-Tt bond distance (~ 3.5 Å) compared to the Li-Tt distances (~ 3.0 Å). Movement of Na to the Tt_{20} cage results in a similar bond breaking mechanism as seen in the Li case, but without the need for cooperative motion of another metal atom in the adjacent cage. This points to the unfavorablity of Na moving through a Tt pentagon and the general sluggishness of Na migration. In the case of Sn_{46}, the migration barrier through the hexagon is 0.45 eV, suggesting the feasibility of Na insertion into Sn clathrates. Although the ion mobility is high in some cases, the difficulty to synthesize guest free, type I clathrates currently

preclude experimental support of these results. However, the insights presented here are informative for understanding the synthesis of guest free materials via chemical deintercalation routes, and may be helpful for the design of novel synthetic methods for these open framework materials.

3.3. Structural Origin of the Reversible Li Insertion in Guest-free, Type II Silicon Clathrates

3.3.1. Introduction

Tetrel (*Tt* = Si, Ge, Sn) clathrates are host-guest materials comprising cage frameworks of *Tt* elements that encapsulate alkali metal and alkali-earth metal guest atoms. Well known as promising candidates for thermoelectric materials,[42] clathrates also have interesting properties for optoelectronics[174–176] and superconducting[44,89,177] applications. Due to the large interest in *Tt* elements as high capacity Li-ion battery anodes, the electrochemical properties of *Tt* clathrates have also been investigated in recent years, revealing properties distinct from those of diamond cubic structured analogues[49,52–56,105,152,178–180]. For instance, the reaction of Li with the type I clathrate $Ba_8Al_{16}Si_{30}$ is dominated by surface rather than bulk reactions,[56] while the $Ba_8Al_yGe_{46-y}$ ($0 < y < 16$) clathrate undergoes bulk phase transitions to form amorphous Li-Ba-Ge phases with local structures similar to those in Li-Ge crystalline phases.[152,178] For the type II clathrate $Na_{24}Si_{136}$, the lithiation profile is similar to that for diamond cubic Si,[53] while $Na_{1.6}Si_{136}$ displays one more similar to that of amorphous Si.[49] Due to the wide range of possible clathrate structures and compositions,[42] we are interested in establishing a better

understanding of the structure-property relationships of clathrates within the context of Li-ion battery applications.

The type II clathrate is described by the $Fd\bar{3}m$ space group and has a general formula of $M_{24}Tt_{136}$ where *M* are alkali metal or alkaline earth metals (*e.g.* Na, K, Cs, Ba).[40] In a single unit cell, the structure is composed of eight Tt_{28} cages (hexakaidecahedra) and sixteen Tt_{20} cages (dodecahedra). The *Tt* atoms reside at the vertices of the polyhedra and form hexagonal or pentagonal faces while the guest atoms occupy the center positions. **Figure 3.3.1a** shows a model of a Si_{20} cage (yellow) and Si_{28} (black) cage occupied by Na guest atoms from the structure of a Na-filled type II silicon clathrate. In this structure, the Si_{28} cages, composed of 4 hexagons and 12 pentagons, form a face-sharing tetrahedral network connected by the four hexagonal faces (**Figure 3.3.1b**). The Si_{20} cages, composed of 12 pentagons, fill the space between the Si_{28} cages by forming perpendicular channels, which can be seen in the [011] direction (**Figure 3.3.1c**). **Figure 3.3.1d** shows a larger polyhedral model to illustrate the connectivity between the two types of cages. Deviation from the general formula of $M_{24}Tt_{136}$ is often observed in clathrates with guest atom vacancies ($M_{24-x}Tt_{136}$),[40,181,182] and framework substitutions ($M_{24}A_xTt_{136-x}$, *A* = another element substituting *Tt*),[116,183,184]. These defects or combination of defects result in a wide structural landscape for controlling the materials properties of *Tt* clathrates.

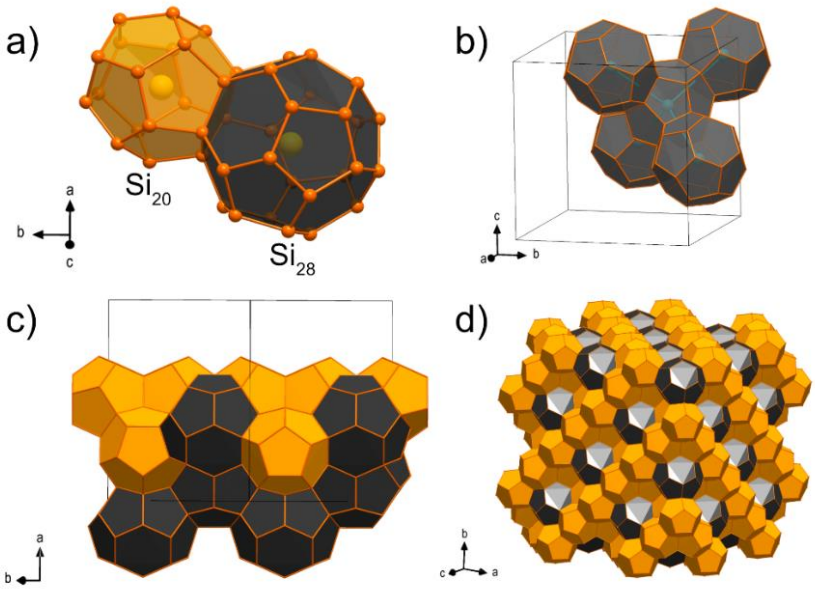

Figure 3.3.1 (a) Crystal model showing the two types of polyhedra in the type II clathrate $Na_{24-x}Si_{136}$ ($0 < x < 24$) structure: the dodecahedra (Si_{20}) in yellow and the hexakaidecahedra (Si_{28}) in black. **(b)** Polyhedral model showing the network of Si_{28} cages connected by shared hexagonal faces. The blue spheres and bonds indicate the tetrahedral arrangement of the connected Si_{28} cages. Polyhedral view of the type II clathrate structure **(c)** viewed down the [011] direction and **(d)** 2 x 2 x 2 supercell showing both Si_{20} and Si_{28} cages.

The type II clathrate $Na_{24-x}Si_{136}$ [40,164,185] is notable for having a tunable Na content. For Li-ion battery applications, the removal of Na from the cages provides the opportunity for using the guest-free clathrates as Li-ion battery electrodes. Langer *et al.* used nuclear magnetic resonance spectroscopy (NMR) to demonstrate that electrochemical insertion of Li into $Na_{1.6}Si_{136}$ takes place at 0.30 V vs. Li/Li^+.[49] However, the reversibility of this insertion process was not evaluated and the Li positions and migration pathways within the cages were not resolved.

Herein, we undertake a detailed investigation to establish the structural origin of mechanism for Li insertion into type II Si_{136} clathrates with low Na content. Using electrochemical analysis, synchrotron X-ray diffraction (XRD), and density-functional theory (DFT) calculations, a reversible topotactic Li insertion process was identified in nearly guest-free clathrate $Na_{0.9}Si_{136,}$ which is accompanied by a volume expansion of 0.22 % after Li occupation of both Si_{20} and Si_{28} cages. The Li positions in the larger Si_{28} cages are significantly off-center, pointing to the possibility of high disorder and the presence of multiple Li atoms inside the Si_{28} cages. DFT calculations show that the Li positions predicted to be most favorable match closely with those found from XRD refinement. Nudged elastic band calculations are used to investigate the Li migration pathways and show that Li migration should be dominant through the interconnected network of Si_{28} cages due to the low migration barrier of 0.20 eV. Li migration into Si_{20} cages is predicted to be kinetically limited unless there is a neighboring Li atom which enables an alternative bond-breaking pathway with a lower energy barrier of 0.65 eV. Overall, the results show how Li insertion into the vacant cages of the type II Si clathrate structure can be promising for Li-ion anodes due to the low reaction voltage (0.3 V vs. Li/Li^+), and negligible volume expansion (0.22 %) coupled with a suitable capacity (~230 mAh/g). We identify Li migration through the hexagonal faces between interconnected cages as an important condition for bulk Li diffusion. Based on this structural feature, other open Tetrel frameworks are identified that could have analogous Li insertion/de-insertion behavior.

3.3.2. Experimental and Computational Methods

The $Na_{0.9}Si_{136}$ (Na1) and $Na_{10.7}Si_{136}$ (Na11) clathrates were synthesized by thermal decomposition of Na_4Si_4 under vacuum using methods modified from previous reports.[40,155] The clathrates were prepared into electrodes on Cu foil with carbon black as a conducting additive and polyvinylidene difluoride (PVDF) as a binder. The electrodes were lithiated galvanostatically in half-cells with lithium metal and then extracted for *ex situ* powder XRD (PXRD) measurements. Cycling experiments were conducted in CR2032 coin cells using lithium metal as the counter electrode. Synchrotron X-ray diffraction measurements were performed at the 11-BM beamline at the Advanced Photon Source (APS) at Argonne National Laboratory (λ = 0.41284 Å for analysis of as-synthesized samples and λ = 0.412781 Å for analysis of samples after lithiation) and the P02.1 powder diffraction beamline (λ = 0.20733 Å) at PETRA III at the Deutsches Elektronen-Synchrotron (DESY). The first-principles DFT calculations were performed in a similar manner to our previous work[55,152,179] and are described in more detail in the **Appendix C.1**. The Gibbs free energy change and average lithiation voltages were calculated as described previously.[55] The climbing image nudged elastic band (NEB) method was used to calculate the Li migration barriers.[85] More detailed descriptions of the synthesis, electrochemical and synchrotron measurements, and refinements are in the **Appendix C.1**.

3.3.3. Results and Discussion

3.3.3.1. Structural Characterization of As-Synthesized $Na_{24-x}Si_{136}$ Samples

To understand the role of guest atom occupancy on the electrochemical reaction of Li with type II Si clathrates, two samples with different Na content were prepared (see **Appendix C.1** and **Figure C.1**) and then characterized with synchrotron powder XRD (PXRD). The first sample was heated under vacuum for 5 days to lower the Na content to near guest-free concentrations. The PXRD pattern of this sample confirms that the sample contains predominately the type II clathrate phase with small impurities from the type I clathrate phase (**Figure 3.3.2a**). The Rietveld refinement (**Table C.1**) of this sample resulted in a composition of $Na_{0.9(1)}Si_{136}$ with a lattice parameter of 14.6460(1) Å, so this sample will be referred to as "Na1" from now on. The second sample was heated under vacuum for 30 hours to target a type II Si clathrate sample with intermediate Na content. The Rietveld refinement (**Figure 3.3.2b, Table C.2**) of this sample resulted in a composition of $Na_{10.7(1)}Si_{136}$ (hence, we refer to this as the "Na11" sample) with a lattice parameter of 14.6544(2) Å and 1.4 wt% impurity of Na_8Si_{46}. The lattice constants, atomic coordinates, and displacement parameters match well with previous PXRD and single crystal XRD refinements of type II Si clathrates with different Na content.[186,187] For Na11, the large Si_{28} cages were found to be preferentially occupied by Na over the Si_{20} cages, consistent with previous X-ray diffraction analyses.[49,164,186,187]

Scanning electron microscopy (SEM) imaging showed that the clathrate particles were comprised of particles (3 – 11 micron) decorated with smaller protrusions (**Figure C.2a-b**). Transmission electron microscopy (TEM) showed that the clathrate particles are polycrystalline, with the selected area electron diffraction (SAED) pattern showing reflections corresponding to different orientations of crystalline domains (**Figure C.2c**) and high resolution TEM (HRETM) imaging revealing the type II cage structure (**Figure**

3.3.2c). Energy dispersive X-ray spectroscopy (EDS) conducted in the TEM detected signals from O, Na, Si and Cu (from the TEM grid) for both Na1 and Na11 samples (**Figure 3.3.2d-e**), consistent with the presumed composition of the samples based on the XRD patterns. For Na11, the Na composition varied depending on the area of interest (**Figure 3.3.2e**). When an EDS spectrum was collected from a small particle, the Na content was similar to that of the Na1 sample. When the EDS spectrum was collected from a thicker area near the center of a larger particle, the Na content was higher than in the Na1 sample, which is consistent with the higher average Na content of Na11. This variation of the Na content based on the particle size is likely due to Na evaporation during the synthesis under vacuum, where smaller particles are expected to lose Na more quickly because of the higher surface area and shorter diffusion lengths.

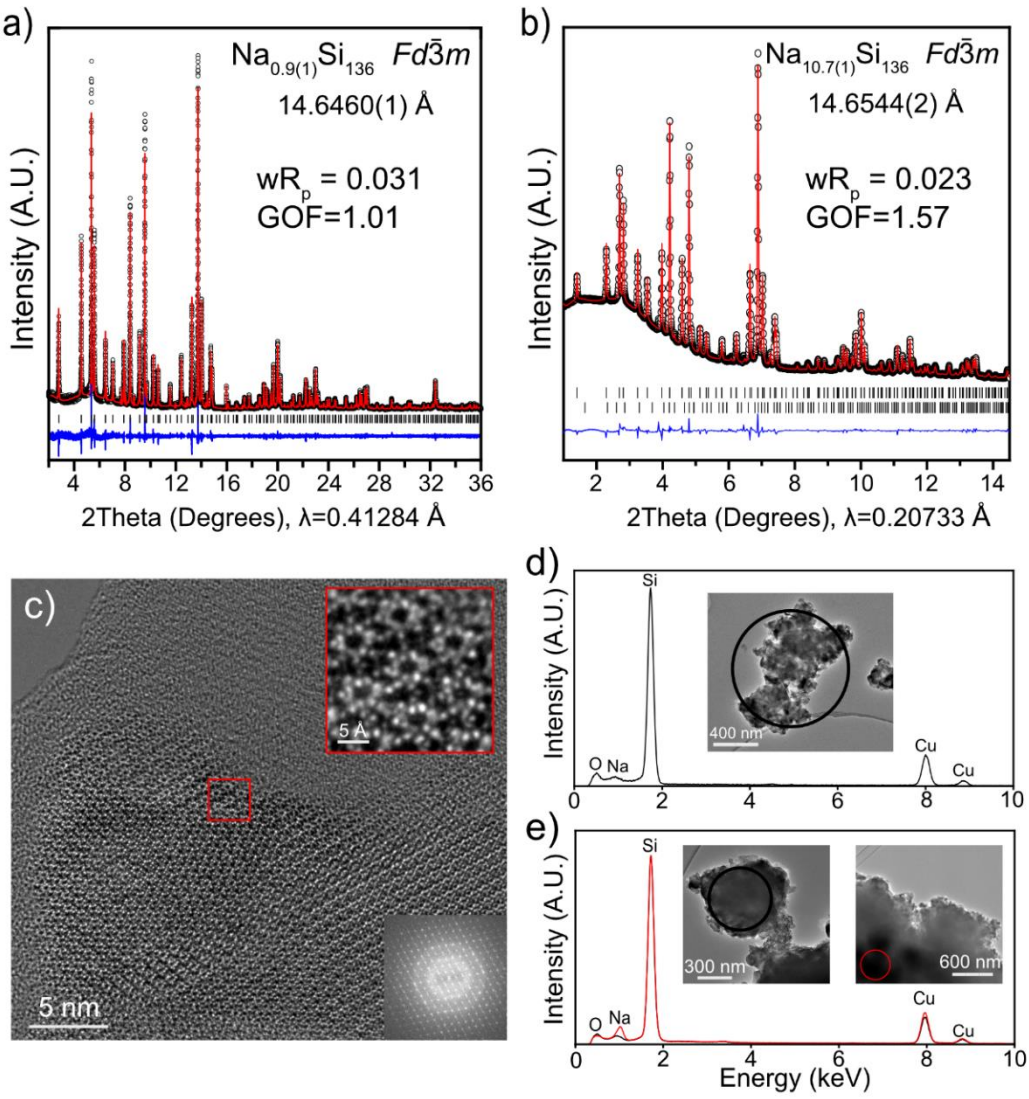

Figure 3.3.2. Rietveld refinement of the PXRD patterns of the **(a)** Na1 and **(b)** Na11 samples. The black circles represent the experimental pattern, the red curve represents the calculated pattern, and the blue curve represents the difference curve. Tick marks indicate the reflection positions. In (b), the top set of marks correspond to the type II phase, while the bottom ticks correspond to the type I clathrate phase. The refined atomic positions, occupancies, and atomic displacement parameters can be found in **Table C.1-2 (c)** HRTEM image of Na1 along the [110] zone axis with inset showing the characteristic cage structure of the type II Si clathrate of the region indicated with the red box. Bottom right inset is a fast Fourier transform (FFT) of the image showing the spot pattern of the [110] zone axis. **(d)** TEM-EDS data from Na1 (taken from area indicated by black circle) and **(e)** two areas in the Na11 sample (the red curve is the EDS spectrum from the middle of a thicker part of the particle as indicated by the red circle). The Cu signal is from the copper TEM grid.

3.3.3.2. Electrochemical Li Insertion into Si_{136}

Voltage profiles corresponding to the first full lithiation of Na1 and Na11 type II Si clathrates are shown in **Figure 3.3.3**. The voltage profile for Na1 displayed plateaus at 0.30, 0.25, 0.10 and 0.05 V vs. Li/Li^+, which are more clearly discerned as peaks in the dQ/dE plot (**Figure 3.3.3** inset). The plateau at 0.30 V was attributed to the insertion of Li into the cage structure by Langer *et. al* through NMR analysis, while amorphization of the Si framework was determined to begin at 0.25 V from XRD analysis.[49] The process at 0.05 V is attributed to transformation of the amorphous Li_xSi alloy to crystalline $Li_{15}Si_4$.[35,117,188] The broad peak at 0.10 V is typically not observed during lithiation of diamond Si, but rather during lithiation of amorphous Si,[35,117,189] suggesting that a similar phase transformation could be occurring in the type II clathrate at this voltage. The lithiation capacity (3700 mAh/g) for Na1 is comparable to that seen in diamond or amorphous Si electrodes and corresponds to a Li-Si ratio close to the composition expected for formation of $Li_{15}Si_4$ (3586 mAh/g).

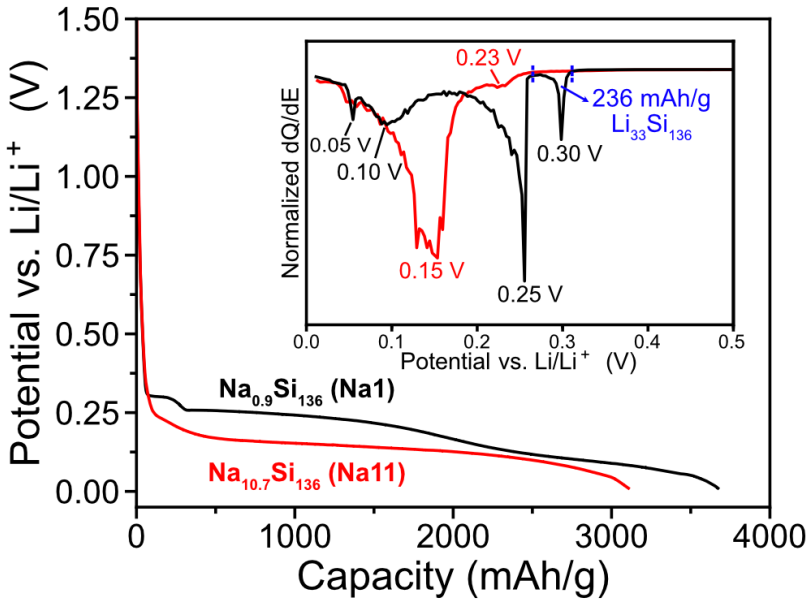

Figure 3.3.3 Voltage curve for galvanostatic lithiation of type II clathrate with compositions of $Na_{0.9}Si_{136}$ (Na1, black trace) and $Na_{10.7}Si_{136}$ (Na11, red trace) at 25 mA/g with a 0.01 V vs. Li/Li^+ cutoff. The inset is the normalized dQ/dE plot derived from the voltage profiles. The blue dashed lines indicate the voltage range attributed to Li insertion into Si_{136}.

The voltage profile for Na11 is distinctly different from that for Na1 and is dominated by a sloping curve (seen as a broad peak centered at 0.15 V in the dQ/dE plot). The plateau at 0.30 V attributed to Li insertion into the clathrate framework is not present in the voltage profile of Na11, suggesting that this lithiation process observed in Na1 does not occur in Na11. The small peak at 0.23 V is similar in voltage to the peak at 0.25 V in the Na1 sample, which we attribute to the presence of clathrate with low Na-content as an impurity phase in the Na11 sample. This hypothesis is supported by the observed variation in Na content in small vs. large particles by EDS (**Figure 3.3.2e**), where a small particle of Na11 was found to have a similar Na content to that of the Na1 sample. The

broad peak at 0.15 V in the dQ/dE plot, attributed to the beginning of an amorphization reaction, is found at a lower voltage than the amorphization of Na1 (0.25 V) but is similar to the voltage for the amorphization of $Na_{24}Si_{136}$ (0.120 V).[53] It is interesting to note that the amorphization potential for Na1 is around 0.15 V higher than that for diamond cubic Si, which reacts at 0.10 V,[34] indicating that there is a significant thermodynamic or kinetic difference in the Li-Si amorphous phase conversion.

To assess the number of Li inserted into the clathrate cage structure, the capacity was measured from 0.32 – 0.26 V to remove possible contributions from formation of solid electrolyte interphase (SEI) or reactions with the carbon black additive, as well as to avoid charge associated with the amorphization reactions. This voltage range is indicated by the blue dashed lines in the normalized dQ/dE plot in the inset of **Figure 3.3.3**. The resulting capacity of 236 mAh/g corresponds to a composition of $Li_{33}Si_{136}$ when attributing all of the charge transferred in this voltage region to Li insertion into the clathrate cages. This amount of capacity is notable because it results in a larger number of guest atoms than expected for the typical type II clathrate stoichiometry of $M_{24}Tt_{136}$, which assumes that one guest atom occupies each of the 24 cages in the unit cell. This suggests that either multiple Li are occupying the cages of the clathrate structure (which has been suggested before for Li_xGe_{136}[52]) or there is another reaction mechanism occurring that is contributing to the capacity. Previously, the synthesis of $Na_{30.5}Si_{136}$ was demonstrated where two Na atoms were shown to occupy a single Si_{28} cage.[190] Considering the smaller size of Li atoms, we speculate that multiple Li atoms occupying a single Si_{28} cage could also be possible. To further investigate this possibility, synchrotron PXRD measurements were performed of lithiated type II clathrate samples.

3.3.3.3. Synchrotron X-ray Powder Diffraction of Lithiated Si_{136}

To obtain insight into the Li positions in the clathrate structure, synchrotron PXRD was conducted on the Na1 sample after electrochemical lithiation. Lithiation was performed with a cutoff voltage of 0.26 V vs. Li/Li^+ to prevent the start of the two-phase amorphization reaction. The voltage profile and corresponding dQ/dE plot are presented in **Figure 3.3.4a**, with a capacity of around 207 mAh/g (corresponding to a composition of $Li_{29}Si_{136}$) attributed to Li insertion into the clathrate cages only.

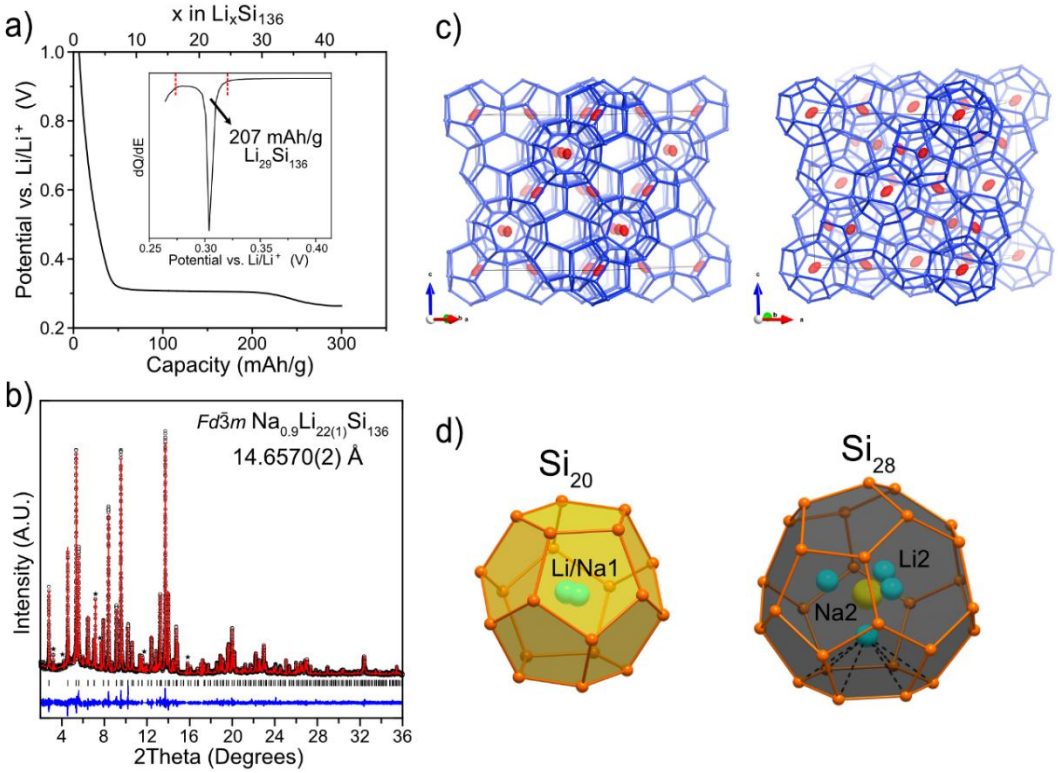

Figure 3.3.4 Analysis of Li insertion into Na_1Si_{136} (Na1) **(a)** Galvanostatic voltage profile and corresponding dQ/dE plot of a Na1 electrode lithiated at 10 mA/g. The red lines indicate the voltage range (0.27 – 0.32 V) in which the dQ/dE plot was integrated to determine an approximate composition of $Li_{29}Si_{136}$ after lithiation. **(b)** Synchrotron PXRD (λ = 0.412781 Å) of the lithiated clathrate (black = observed, red = simulated, blue = difference curve, tick marks = positions of reflections; the stars mark an unknown impurity phase present in the XRD pattern which was omitted for the refinement. **(c)** Residual electron density peaks (isosurface level 0.8 e $Å^{-3}$) from the difference Fourier mapping in the small Si_{20} cages from the pattern in (b). The blue atoms represent Si while the red surfaces represent the isosurface of the residual electron density. **(d)** Atomic positions used in the refinement for Na (yellow) and Li (cyan) guest atoms in the Si_{20} and the Si_{28} cages. The black dotted lines are the Li-Si bonds between the off-center Li to the Si atoms comprising the hexagonal face.

The PXRD pattern for the lithiated clathrate Na1 sample is shown in **Figure 3.3.4b** and was refined to a larger lattice parameter of 14.6570(2) Å compared to that in the as synthesized, unlithiated sample (**Figure 3.3.2a**), corresponding to a 0.22 % volume

expansion. This indicates a small expansion in the Si framework after electrochemical lithiation. To analyze the possible Li positions in the clathrate, the pattern was fit to the guest-free Si_{136} structural model and then difference Fourier mapping was used to identify residual electron density in the clathrate cages. The results show significant electron density shifted slightly off the center of the Si_{20} cages (**Figure 3.3.4c**). When the electron density was modeled as pure Na, this position refined to an occupancy of 9%, which is much larger than the value found for this site in the pristine Na1 (≈ 2 %). Even without considering the Si_{28} cages, a 9% occupation of this position by Na would result in a higher Na content than what was present in the unlithiated clathrate. This finding suggests that the electron density in the Si_{20} cages originates from the presence of both Na and Li. To properly handle the mixed occupation and underoccupation, the occupancy of Na was set to the value refined in the unlithiated clathrate, while the occupancy of Li (located in the same site) was allowed to vary.

In addition, the larger Si_{28} cages were found to accommodate well-structured residual electron density with a maximum located close to the center of the cage and four maxima shifted from the center toward the hexagonal faces in the form of a tetrahedron. A small occupation of the central position in the Si_{28} cages was detected for the pristine Na1 clathrate as well. Furthermore, the absolute value of the residual electron density in this position for the lithiated clathrate corresponds to the same occupancy by Na as in the unlithiated Na1. Therefore, this position was treated as pure Na. The four peaks situated closer to the hexagonal faces were refined as partially occupied Li sites, based on the distances to the adjacent Si sites.

The positions of the Na and Li atoms used in the refinement are shown in **Figure 3.3.4d**. The Li position in the Si_{20} cage refined to an occupation of 0.33, which corresponds to 10.88 Li within the sixteen Si_{20} cages, while the Li site in the Si_{28} cage refined to an occupation of 0.34, corresponding to 10.8 Li in the eight Si_{28} cages and suggesting the possibility of multiple Li atoms within the larger cages. This resulted in a final composition of $Na_{0.9}Li_{22(1)}Si_{136}$. The atomic positions and occupancies from the refinement can be found in **Table C.3**. The refined composition contains less Li (22) than that expected based on the capacity from the voltage profile (29 Li). The electrochemical lithiation was repeated with another nearly Na-free clathrate sample prepared in a similar fashion and additional PXRD experiments were conducted at a different beamline to confirm this result; **Figure C.3** and **Table C.4-5** shows the electrochemical voltage profile, PXRD pattern and refinement parameters before and after lithiation. The results are similar to those shown in **Figure 3.3.4**, with a small increase in lattice parameter and higher electron density attributed to Li occupation of both Si_{28} and Si_{20} cages after lithiation, confirming that the observed electrochemical reactions from 0.3 – 0.26 V vs. Li/Li^+ correspond to Li insertion into the vacant cages of the type II clathrate structure. These results are also consistent with previous NMR spectroscopy measurements which showed two distinct chemical shifts for Li, corresponding to different Li environments in the clathrate cages and chemical shift values that were higher than that for Li metal,[49] similar to what is seen for Na NMR analysis of $Na_{24-x}Si_{136}$.[191] Future neutron diffraction experiments would be insightful for more accurately characterizing the Li positions and occupancies in the clathrate structure.

3.3.3.4. DFT Calculations to Determine Li Positions in Si_{136}

Next, DFT calculations were used to form a theoretical basis for understanding the preferred Li positions in the type II Si clathrate structure and the diffusion pathways between them. Similar to our previous study investigating Li migration in guest-free clathrates that adopt the type I structure,[179] several possible Li sites were considered and the Gibbs free energy of reaction (ΔG_r)[11] was evaluated as the metric for assessing the favorability of a Li position (see **Appendix C.1** for more details). **Figure 3.3.5a** shows a portion of the type II Si clathrate structure where a Si_{28} cage is shared via a pentagonal face to a Si_{20} cage, along with the Li positions identified as local energy minima from the DFT calculations – Positions 1 and 2 are found at the centers of the Si_{20} and Si_{28} cages, respectively, while Positions 3 and 4 are coordinated off the hexagonal ("Off Hex") and pentagonal ("Off Pent") faces, respectively, inside of the Si_{28} cages. **Figure 3.3.5b** shows additional views of the Li sites at Positions 3 and 4 with selected Si–Li bond lengths indicated.

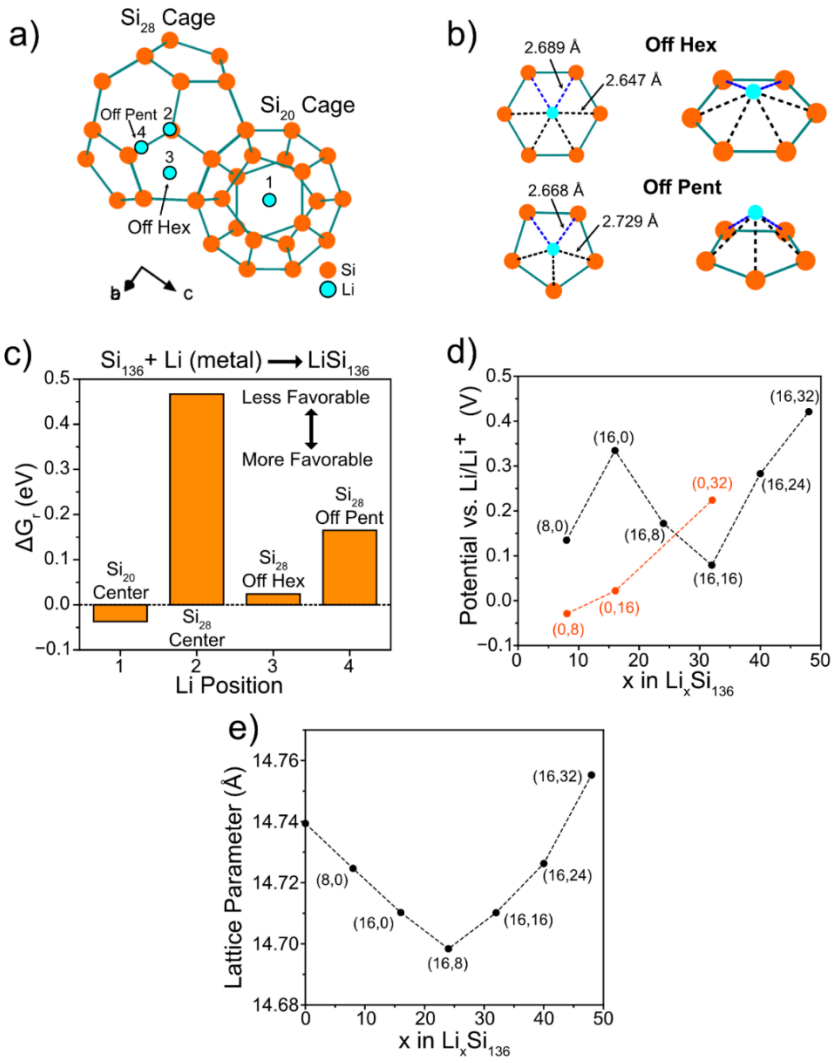

Figure 3.3.5 DFT calculations of Li positions in Si_{136} **(a)** Schematic of a Si_{28} cage connected with a Si_{20} cage showing the DFT calculated Li positions viewed down the [110] direction. **(b)** Schematic of the "Off Hex" and "Off Pent" Li positions with select bond lengths. The blue colored bonds are provided to help visualize the change in orientation. **(c)** Gibbs free energy of reaction (ΔG_r) for the reaction Si_{136} + Li (metal) → $LiSi_{136}$ for each different Li position. **(d)** Average lithiation voltage as a function of the Li content (x) in Li_xSi_{136} where each point is identified by indices (a, b) where a = number of Li in the Si_{20} cage center (16*c* Wyckoff site) and b = the number of Li in the "Off Hex" position within the Si_{28} cages (32e Wyckoff site) **(e)** DFT calculated lattice constants for different amounts of Li in the Si_{136} lattice as shown in (d).

Figure 3.3.5c shows the calculated change in the Gibbs free energy of reaction considering Li inserted into each of the four positions in the Si_{136} structure, where a negative value indicates a favorable reaction for the formation of $LiSi_{136}$ with respect to Li metal and Si_{136}. The results show that Li occupation in the center of the smaller (Si_{20}) cage (Position 1) was favorable with a slightly negative Gibbs free energy of reaction (ΔG_r) of –36 meV. Among the possible sites within the Si_{28} cage, Li in the center of the cage (Position 2) was very unfavorable (ΔG_r = +0.467 eV) compared to the other positions. From these results, it is expected that Li occupation of the Si_{28} cage would result in Li being off-center due to the relatively high energy of the centered position, while Li in the Si_{20} cage would favor being closer to the center of the cages. These results are in good agreement with our previous calculations on the preferred Li positions in Tetrel (*Tt*) clathrate cages with the type I structure, which is made up of Tt_{20} and Tt_{24} cages. In that study,[179] we found that if the clathrate cage is sufficiently large (*e.g.*, in the case of the Tt_{24} cages in type I clathrates), then the lowest energy position for Li was to be coordinated off the hexagonal face with a Li–*Tt* (*Tt* = Si, Ge, and Sn) bond distance of 2.7 – 2.9 Å rather than at the cage center. The DFT calculated positions in **Figure 3.3.5a** are in good agreement with those determined from the PXRD refinement (**Figure 3.3.4d**). In both cases, Li is found near the center of the Si_{20} cages while coordinated off of the hexagonal faces in the Si_{28} cages. The refined Li-Si distances from the PXRD analysis was 2.86 – 2.9 Å for Li in the "Off Hex" position, which are slightly longer than that calculated using DFT (2.65 – 2.69 Å).

To evaluate the most favorable Li site in the clathrate lattice during electrochemical lithiation, the average lithiation voltage was calculated from the change

in Gibbs reaction energy as a function of total Li content (**Figure 3.3.5d**) for select structures. This analysis does not consider the many possible orderings of Li within Li_xSi_{136}, which would require a cluster expansion analysis to simulate the 0 K voltage profile.[58,76] Rather, we seek to understand the energetic differences between Li occupation of the Si_{20} and Si_{28} cages. In **Figure 3.3.5d-e**, the indices next to each point identify the number of Li in the Si_{20} cage center or in the "Off Hex" position within the Si_{28} cages (corresponding to the first and second number, respectively, in the indices). When adding eight Li to the "Off Hex" positions in the Si_{28} cages, the Li is divided evenly between the eight Si_{28} cages, meaning that (0,8) and (0,16) correspond to one and two Li occupying a single Si_{28} cage, respectively. When comparing the calculated voltages in Li_xSi_{136} for x = 8 and 16, it is more favorable for Li to occupy the Si_{20} cages, *i.e.*, points (8, 0) and (16, 0), than the Si_{28} cages, *i.e.*, points (0, 8) and (0, 16) based on the higher voltages calculated for the former case (which corresponds to a lower ΔG_r). However, after the sixteen Si_{20} cages are each filled with a single Li in the center position, adding eight Li to the Si_{28} cages in the "Off Hex" position (corresponding to (16, 8) at x = 24) is favorable, on account of the positive voltage vs. Li/Li^+. This suggests that Li occupation of the Si_{28} cages is more favorable if the Si_{20} cages are filled with Li. Interestingly, as eight Li are subsequently added to the Si_{28} "Off Hex" positions (for x = 40, 48), the voltage increases again, indicating the energetic feasibility for multiple Li to occupy a single Si_{28} cage. The composition of $Li_{48}Si_{136}$ corresponds to a single Li occupying the centers of each of the sixteen Si_{20} cages, and four Li occupying each of the eight Si_{28} cages in the "Off Hex" positions. Even without Li occupation of the Si_{20} cages, $Li_{32}Si_{136}$ (corresponding to the point (0, 32)) has a positive voltage of 0.22 V, further

suggesting that multiple Li occupation of the Si_{28} cage is more favorable than occupation by a single Li atom. In short, the theoretical voltage calculations indicate an energetic preference for Li to occupy the Si_{20} cages over the Si_{28} cages and suggest that it is energetically favorable for multiple Li to occupy a single Si_{28} cage.

The calculated lattice constants of the crystal structures for the black curve in **Figure 3.3.5d** are presented in **Figure 3.3.5e**. For the structure where Li only occupies each of the Si_{20} cage centers at (16, 0), the lattice parameter decreases when compared to empty, guest-free clathrate (from 14.74 to 14.71 Å). This result is similar to what has been reported for $Na_{24-x}Si_{136}$, where the Si_{136} framework contracts when Na occupies the Si_{28} cages, and is consistent with our previous calculations for $Li_{24}Si_{136}$.[53,186] As Li is added to the "Off Hex" positions in the Si_{28} cages, the lattice parameter increases until reaching a value of 14.76 Å at a composition of $Li_{48}Si_{136}$, where all 32 possible "Off Hex" positions are filled. The PXRD results (**Figure 3.3.4b**) show an increase in the lattice parameter of around ~0.01 Å after lithiation, while a decrease in lattice parameter of ~0.03 Å is predicted by the calculation at the estimated composition of x = 29 – 32 Li. Therefore, both experimental and DFT results suggest that Li insertion into the Si_{136} lattice results in a very small volume change. More *ab initio* modeling and structural characterization, particularly *in operando*, will be needed to better elucidate the Li composition dependence on the clathrate lattice parameter.

From the combination of the electrochemical, structural, and computational results, we can therefore summarize the structure of Si_{136} after lithiation. **Figure 3.3.6** presents the guest-free, type II Si clathrate structure before and after electrochemical

lithiation, showing the proposed Li positions and estimated composition. The composition of $Li_{32}Si_{136}$ is primarily estimated based on the electrochemical voltage profile (*i.e.*, as shown in **Figure 3.3.4a**), as accurately assessing Li occupancy with PXRD is difficult especially when there is possible disorder on the sites. The identified Li positions, near the center of the Si_{20} cage and coordinated off the hexagonal faces in the Si_{28} cage, are supported by the PXRD refinement analysis (**Figure 3.3.4**) and match well with those predicted by DFT calculations (**Figure 3.3.5**). The preferred position of the Li guest atoms is cage-dependent. In the smaller Si_{20} cages composed solely of pentagonal faces, the Li atom prefers to be close to the cage center, with the PXRD analysis suggesting disorder on this position. In the larger Si_{28} cages comprised of pentagonal and hexagonal faces, the Li atom is predicted by DFT to be coordinated off the hexagonal faces of the cage ("Off Hex") due to the lower energy of this position compared to the cage center or coordination off of a pentagonal face ("Off Pent").

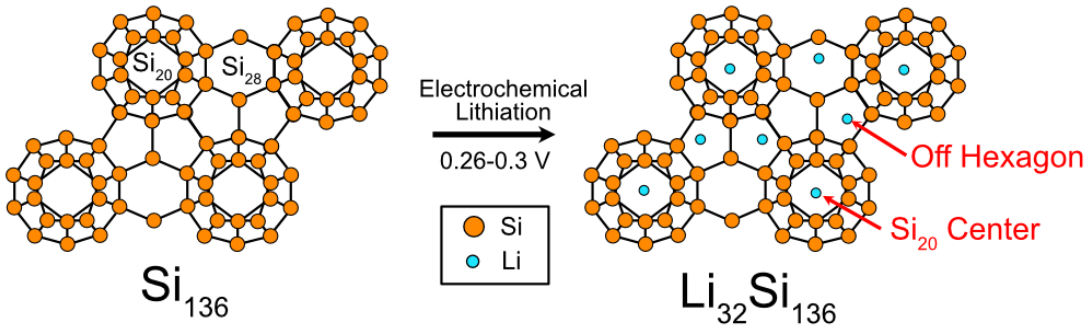

Figure 3.3.6 Schematic showing the lithium positions after electrochemical lithiation of Si_{136}. The Li atoms are proposed to occupy both Si_{20} and Si_{28} cages. In the Si_{28} cages, multiple Li reside in a single cage while occupying positions off of the hexagonal faces.

3.3.3.5. Li Migration Pathways in Si_{136}

To identify the diffusion pathways for Li within the Si_{136} bulk structure, the climbing image NEB method[85] was used. In our previous study, we investigated the migration barriers of Li in guest-free, type I clathrate frameworks and found that Li migration between cages is mediated by the connection of hexagonal faces because of the lower migration barrier through these faces compared to the pentagonal ones.[179] NEB calculations for Li migration between cages (*i.e.*, intercage migration) are presented in the guest-free, type II Si clathrate structure shown in **Figure 3.3.7a**.

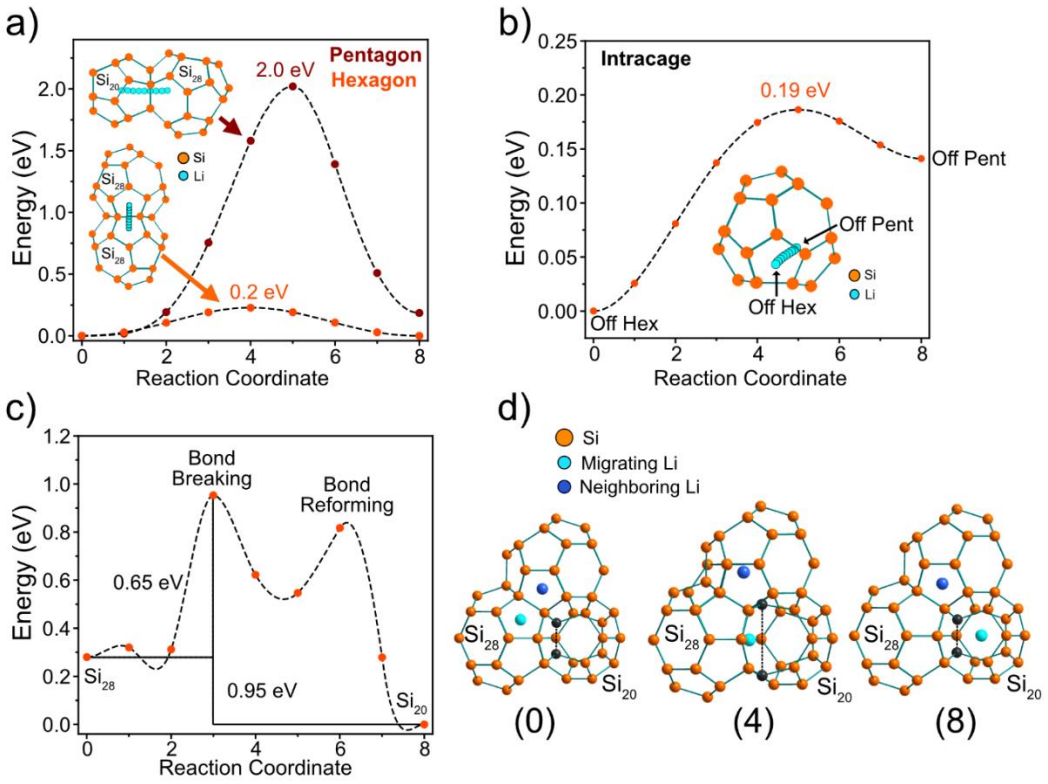

Figure 3.3.7 (a) NEB-calculated minimum energy paths for migration of Li (cyan) in Si_{136} between the Si_{20} and Si_{28} cages through a shared pentagonal face (Pentagon path) and between the Si_{28} and Si_{28} cages through a shared hexagonal face (Hexagon path). **(b)** NEB-calculated minimum energy path for Li between Off Hex and Off Pent positions in the Si_{28} cage; inset shows a schematic of the Si_{28} cage with the Li positions in the pathway. **(c)** NEB-calculated minimum energy path for Li migrating from Si_{28} cage to the Si_{20} cage through a shared pentagonal face with a Li in the adjacent Si_{28} cage. **(d)** Crystal model showing reaction coordinates 0, 4, and 8 of the NEB calculation in (c); the migrating Li is shown in cyan, the neighboring Li is in dark blue, and the Si atoms of the broken bond are in black.

Consistent with previous calculations, Li migration from the Si_{20} cage to the Si_{28} cage through a pentagonal face results in a higher energy barrier[105,179] compared to Li migration between Si_{28} cages through a hexagonal face (2.0 vs 0.2 eV, respectively). In both paths, the transition state involves the expansion of the pentagonal or hexagonal face as Li passes through the face center. The height of the barrier is correlated to the Li-Si

distance at the transition state and the degree to which the Si atoms bonded in the pentagonal/hexagonal face must move from their original positions in order to accommodate the migrating Li atom. As the hexagonal face has a larger cross-sectional area, acceptable Li–Si distances can be maintained with minimal disruption to the positions of the surrounding Si atoms as the Li passes through the hexagonal face, which results in a lower migration barrier. In contrast, the pentagonal transition state requires shorter Li-Si distances and a larger degree of movement of Si atoms, which results in a higher energy barrier for Li migration. Intracage migration (*i.e.*, Li movement within the cage) was also considered for the Si_{28} cage due to the preference of Li to adopt an off-center position. The calculation showed a migration barrier of only 0.19 eV when Li moved from the "Off Hex" position to the "Off Pent" position (**Figure 3.3.7b**), meaning that Li would prefer to move along the side of the Si_{28} cage rather than through the center.

From these calculations, Li diffusion through the clathrate framework is predicted to be dominated by Li movement between the Si_{28} cages through the hexagonal faces, while diffusion into the Si_{20} cages from the Si_{28} cages is expected to be limited due to the high migration barrier of 2.0 eV (Pentagon path in **Figure 3.3.7a**). However, the PXRD refinement results (**Figure 3.3.4b** provide support for Li occupation of the Si_{20} cages, meaning that there must be another possible pathway for Li insertion into the Si_{20} cages other than the aforementioned 2.0 eV pathway. Since the Si_{20} cage is composed of only pentagonal faces, the low energy pathway through a hexagonal face (Hexagon path in **Figure 3.3.7a**) is not possible.

In our previous DFT study focused on guest-free type I clathrates, we found that Li could migrate into the Si_{20} cage of the type I Si_{46} clathrate through a different pathway that involved temporary Si–Si bond breaking.[179] If a Li atom were present in an adjacent cage, it could help to stabilize a transition state in which a Si–Si bond could lengthen to the extent that Li could migrate into the Si_{20} cage with a lower energy barrier than if it were to migrate through the center of the pentagonal face.[179] To assess the feasibility of a similar mechanism in the type II Si_{136} clathrate, the DFT calculation was repeated for Li migration from a Si_{28} to Si_{20} cage, but with the addition of a Li atom to an adjacent Si_{28} cage in the "Off Hex" position. The energy profile of this bond-breaking migration path is shown in **Figure 3.3.7c** and the crystal schematic of the reaction coordinates 0, 4, 8 are shown in **Figure 3.3.7d** (migrating Li atom shown in cyan). The reaction path starts with the migrating Li in the "Off Hex" position in the Si_{28} cage and the ending position is the center of the Si_{20} cage. The results show that the lowest energy pathway for the migrating Li to enter the Si_{20} cage was not through the center of the pentagonal face, consistent with the high energy barrier of 2.0 eV, but rather "through" the bond connecting two of the Si atoms in the pentagonal face (indicated by the black atoms in **Figure 3.3.7d**). This pathway, which effectively involves breaking and reformation of the Si–Si bond, has a migration barrier of only 0.65 eV, which is feasible for room temperature diffusion.[167] As Li moves through the center of the Si–Si bond, those Si atoms move away from the Li towards adjacent Si_{28} cages. It is interesting to note that the energetics of this migration process are asymmetric. When Li moves into the Si_{20} cage, the barrier is 0.65 eV, while it is 0.95 eV for the reverse process. This reflects the site preference for Li to be inside the Si_{20} cage, as shown in **Figure 3.3.5d.**

3.3.3.6. Reversible Li Insertion in Si_{136}

As the NEB calculations indicated the possibility of asymmetric energy barriers between Li insertion and deinsertion from the Si_{20} cages, the full lithiation and delithiation characteristics of the Na1 material were further investigated with electrochemical analysis. Previous studies conducted on guest-free Si_{136} only reported the lithiation characteristics;[49] our previous study investigating both lithiation and delithiation was performed on Na-containing Si_{136} (*i.e.*, $Na_{24}Si_{136}$) over a voltage range in which the clathrate structure transformed to amorphous phases.[53] Therefore, the reversibility of the lithiation process within the potential window where the clathrate structure is intact has not been fully evaluated.

To investigate this, the Na1 electrode was cycled at 25 mA/g from 2.5 V to a voltage cutoff of 0.26 V vs. Li/Li^+ to allow lithium insertion only into the clathrate structure (*i.e.*, preventing the Li alloying reaction below 0.25 V). The voltage profiles over the full potential range for the first three cycles are shown in **Figure C.4a**, while the zoomed in region from 0.5 – 0.2 V is shown in **Figure 3.3.8a** for the first two cycles. A voltage cutoff of 0.26 V was chosen for cycle 1 and 2 to investigate only the Li insertion process (*i.e.*, to prevent the amorphous phase transition). As evidenced by the very similar voltage profiles for the first two cycles, the Li insertion/deinsertion process into Si_{136} is presumed to take place in a reversible manner. The lower observed specific capacity in the 2^{nd} cycle is likely due solid electrolyte interphase (SEI) formation. The different shapes of the lithiation vs. delithiation curves, however, is an indication that

these processes involve different Li reaction pathways. During lithiation, a voltage plateau (labeled as A) followed by a sloped region (B) are observed (**Figure 3.3.8a**). The voltage profile for delithiation is characterized by three distinct regions (labeled as C, D, and E), including a small peak (indicated by the asterisk), where the potential decreases and then increases again as Li is removed. This is unusual, as the potential typically only increases as the Li content is decreased. In the corresponding dQ/dE plot (**Figure 3.3.8b**), a broad peak centered at 0.32 V is observed during delithiation, corresponding to the sloped voltage region C in **Figure 3.3.8a**, along with two sharper peaks at 0.34 and 0.36 V that correspond to the two quasi-plateaus in region D and E, respectively.

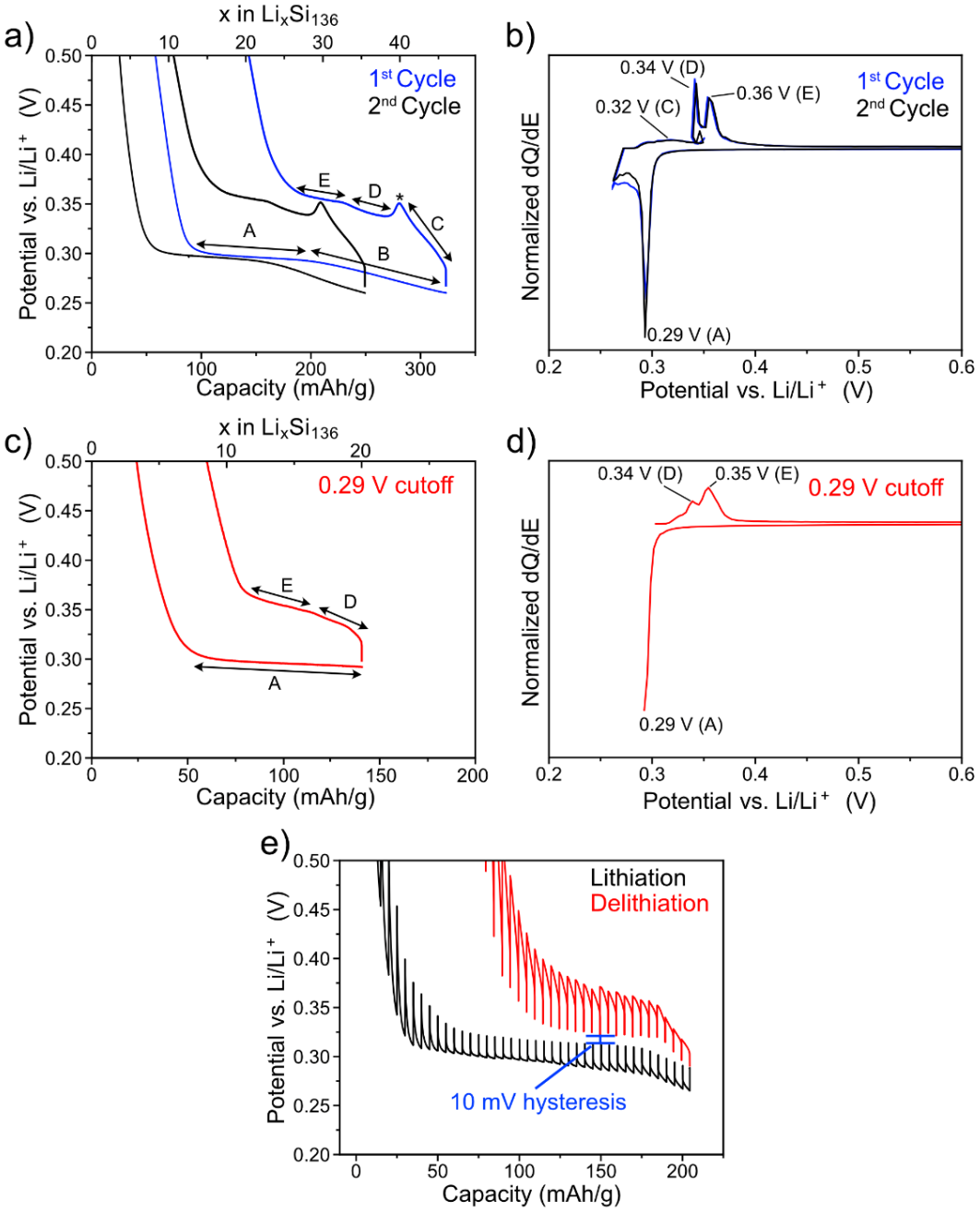

Figure 3.3.8 The lithiation and delithiation voltage profile of Na1 cycled with lithiation cutoff voltage of **(a)** 0.26 V (Cycle 1 and 2) and **(c)** 0.29 (Cycle 3) at 25 mA/g with distinct voltage regions labelled with letters. **(b, d)** Normalized dQ/dE derived from the voltage profiles with features corresponding to the regions in (a) and (c) labelled accordingly. **(e)** GITT profile of the lithiation and delithiation of Na1 at a current density of 10 mA/g with 30 min current pulses and 5 hours relaxation time. The cell was cycled 2 times from 0.27 – 2.5 V prior to the GITT experiment. Zoomed-out versions of these plots can be found in **Figure C.4**.

To better understand these observations, the cutoff voltage for lithiation in the third cycle was increased to 0.29 V (**Figure 3.3.8c**) so that the process associated with the sloped region B that was observed in the first two cycles was prevented. Notably, the sloped region C and corresponding peak in the dQ/dE plot (**Figure 3.3.8d**) were absent in the subsequent delithiation profile. This suggests that the processes associated with region C during delithiation correspond to the reverse of reaction B in the lithiation profile. Overall, these results provide strong support that the observed plateau at 0.30 V (region A) corresponds to a reversible reaction with a reproducible, albeit, asymmetric voltage profile with two distinct regions of Li insertion.

To obtain a better understanding of the energetics of the lithiation and delithiation pathways, the galvanostatic intermittent titration technique (GITT)[192] was used to observe the polarization of the lithiation and delithiation reactions in Na1 (**Figure 3.3.8e**, an expanded view is shown in **Figure C.4b**; here polarization refers to the difference in potential in the cell during galvanostatic vs. open circuit conditions). Most notably, the voltage hysteresis after relaxation between lithiation and delithiation is around 10 mV, which is similar to the hysteresis seen in traditional insertion electrode materials (i.e. $LiFePO_4$, $LiCoO_2$).[193] The low voltage hysteresis is strong support of a topotactic insertion reaction, as it shows that the electrode is in a similar structural state after the current pulses during both lithiation and delithiation. Another notable point is that the polarization is higher during delithiation (40 – 60 mV) than lithiation (20 mV). We speculate that this could indicate different kinetics for lithiation and delithiation, which could be related to the origin of the asymmetric voltage profile and is also supported by the asymmetric migration barriers observed in the NEB calculations (**Figure 3.3.7c**).

The GITT profile also shows an irreversible capacity loss of 22% between the lithiation and delithiation charge capacities. Note that two galvanostatic cycles (without rest periods) were performed prior to the GITT measurement to ensure the formation of the SEI and in general, the clathrate shows high Coulombic efficiencies after the first cycle loss (>95 %). The origin of this behavior is currently unknown but could be related to larger amounts of SEI formation as the electrode spends much longer times at the low potentials than in a regular cycling experiment (see GITT profile in terms of time, **Figure C.4c-d**). It has been previously shown that the SEI growth on Si clathrates can be problematic depending on the processing conditions of the clathrate.[54,180] Another potential explanation for the irreversible capacity is the trapping of Li during relaxation, which could be related to the higher polarizations found for delithiation. The hypothesis is supported by the lack of the peak labelled with the asterisk (**Figure 3.3.8a**) in the GITT voltage profile (**Figure 3.3.8e**) for delithiation suggesting that the periods of relaxation are affecting the delithiation pathway.

Next, galvanostatic cycling experiments were conducted to evaluate the long-term cycling stability of the Na1 clathrate with two voltage cutoffs for lithiation (the delithiation cutoff voltage was fixed at 2.5 V). For the cell with 0.26 V cutoff (**Figure 3.3.9a**), the initial capacity was 275 mAh/g (first cycle efficiency of 68%), which decreased to 200 mAh/g in the 2nd cycle. The capacity then increased to 225 mAh/g over 10 cycles and then began to decrease to 100 mA/g after 50 cycles. The Coulombic efficiency reached >98.5% past cycle 10 and continued to increase during cycling (**Figure 3.3.9b**). For the cell with 0.28 V cutoff, the cycling stabilized around 90 mAh/g and reached 60 mAh/g after 50 cycles. Analysis of the voltage profiles for the cell with

0.26 V cutoff (**Figure 3.3.9c**) showed that the shape of the delithiation curves changed with cycling. At cycle 10 and 20, the plateau attributed to clathrate delithiation at 0.34 – 0.36 V decreased in favor of a sloped feature around 0.5 – 0.6 V. This sloped feature is similar to the voltage reported for the delithiation of amorphous Si.[117,189] We speculate that when the lithiation voltage cutoff is too low, some of the clathrate could be converted to an amorphous Li_xSi phase through an alloying reaction, as evidenced by its different delithiation voltage profile indicated in **Figure 3.3.9c**. Analysis of the cell with 0.28 V cutoff (**Figure 3.3.9d**) shows that the shape of the voltage curve is retained during cycling, suggesting that using the higher voltage cutoff circumvented the suspected amorphization reaction. On this basis, we suspect the better capacity retention obtained when using the 0.28 V cutoff is due to mitigation of the amorphous phase transformation (*i.e.*, preventing transformation of crystalline Li_xSi_{136} to amorphous Li_xSi). PXRD of the electrodes after 50 cycles (**Figure C.5**) showed that reflections from the type II Si clathrate were still present when using both voltage cutoffs, suggesting that the majority of the crystalline clathrate phase structure was retained despite the suspected amorphous phase formation in some of the sample, and further supporting a topotactic mechanism.

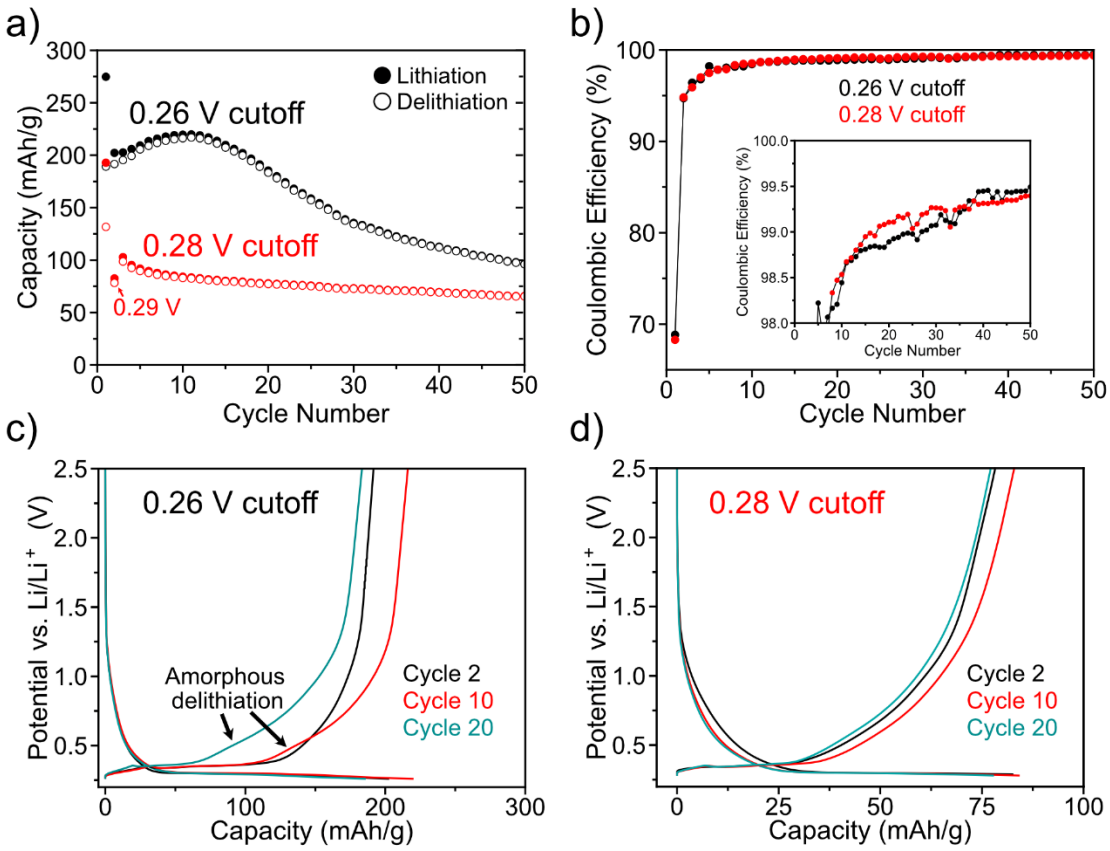

Figure 3.3.9 (a) Voltage profile of Na1 cycled at 25 mA/g with a voltage cutoff of 0.26 and 0.28 V. **(b)** Coulombic efficiency vs. cycle number; **(c)** Voltage profiles of the 2^{nd},10^{th} and 20^{th} cycle with a 0.26 V voltage cutoff showing the increase of amorphous reactions at longer cycles. **(d)** Voltage profile of Na1 cycled at 25 mA/g with a voltage cutoff of 0.28 V.

3.3.3.7. Structural Origins of Li insertion in Clathrate Materials

For topotactic Li insertion to occur, there must be facile migration between Li sites in the host crystal. Based on the observed and calculated Li positions from the PXRD and DFT analysis, the possible Li diffusion pathways in the cage structure can be postulated. First, we point out the importance having a low enough Na content in the cages in order to observe the Li insertion plateau at 0.30 V. This is demonstrated in

Figure 3.3.3, where this feature is absent from the $Na_{10.7}Si_{136}$ (Na11) electrode. Because the Na guest atoms preferentially occupy the large Si_{28} cages in $Na_{24-x}Si_{136}$, this means that in $Na_{10.7}Si_{136}$, the eight Si_{28} cages are occupied by Na atoms while most of the sixteen Si_{20} cages are unoccupied. The fact that this Li insertion plateau at 0.30 V is not observed when the Si_{28} cages are occupied by Na implies that the presence of unoccupied Si_{28} cages is an important condition for the reversible Li insertion process to occur.

Considering the NEB calculations presented in **Figure 3.3.7a**, it is evident that Li diffusion into the Si_{28} cages compared to the Si_{20} cages is favored due to the lower energy barrier for the hexagonal transition state (0.2 eV). Since the Si_{28} cages form a tetrahedral network of hexagonal face sharing cages (**Figure 3.3.1b**), the lowest energy pathway for Li to migrate through the bulk structure would be through this Si_{28} cage network. On the basis of the high migration barrier for Li diffusion through the pentagonal face (2.0 eV), one would expect that Li could not occupy the Si_{20} cages (composed of only pentagonal faces) because the barrier to enter the cage is too high for room temperature migration. However, the PXRD results (**Figure 3.3.4b**) show significant Li occupation in the Si_{20} cages, meaning that a different pathway must be taken for Li to enter the Si_{20} cages. As described previously, a pathway involving temporary bond-breaking allows Li to enter the Si_{20} cage with a much lower activation barrier of 0.65 eV. This bond-breaking migration path has been calculated previously in several other situations, such as Li migration in $LiBa_8Si_{136}$ and Li_6Si_{46} and for Na migration in the Si_{20} cages of Si_{46} and Si_{136}.[51,179] In the case of Li, the pathway is energetically feasible if there is another guest atom in cage adjacent to the transition state. Yang *et al.* posited that the extra electron density from the neighboring guest atom could

aid in stabilizing the transition state, thus allowing access to the bond breaking pathway.[51] We agree with this hypothesis and speculate that a cooperative migration mechanism involving multiple Li could be important for Li to access the Si_{20} cages of the clathrates by bypassing the pentagonal transition state.

Another notable aspect of the bond-breaking migration pathway is the observed energetic asymmetry when Li migrates between the Si_{28} and Si_{20} cages. Migration from the Si_{28} cage to the Si_{20} has a barrier of 0.65 eV, while moving in the reverse pathway would have a barrier 0.95 eV (**Figure 3.3.7c**). If we assume that the prominent pathway for Li to occupy a Si_{20} cage is by migration from a Si_{28} cage (as opposed to migration from Si_{20} to Si_{20}), it is expected that there will be an asymmetry in the migration barrier due to the difference in site energies within Si_{20} and Si_{28} cages, which is shown in **Figure 3.3.5d**. We speculate that this asymmetry could be related to the asymmetry seen in the delithiation voltage profile (**Figure 3.3.8a,b**) and the GITT polarization (**Figure 3.3.8e**). According to the DFT calculations, Li occupation of the Si_{20} cages is most energetically favorable (**Figure 3.3.5d**), which means that these sites should be filled first upon lithiation. However, for Li to enter the Si_{20} cage is expected to be kinetically difficult and requires a cooperative Li migration path with Li in the Si_{28} cages. If the Si_{28} cages were not the main Li pathway, then it is expected that the Na11 electrode (where Si_{28} cages are filled by Na) would display electrochemical voltage characteristics similar to those in Na1. Since this is not the case (**Figure 3.3.3**), we can presume that Li first travels through the Si_{28} cages and then migrates into the Si_{20} cages.

On the basis of the structural, electrochemical, and DFT analyses described above, we therefore summarize the Li migration pathway through the Si_{136} type II clathrate structure as illustrated in **Figure 3.3.10** with the red arrow showing the continuous Li migration pathway through the Si_{28} cages connected via hexagonal faces (atoms in the hexagon shown in yellow). Along the migration "highway", Li can migrate into the Si_{20} cages, possibly via the bond-breaking pathway depicted in **Figure 3.3.7d**. During delithiation, Li will also need to leave via the Si_{28} "Li highway," but the barrier to go back into the Si_{28} cage is predicted to be higher via the bond-breaking mechanism because of the higher site energy of the Si_{28} cage. We speculate that the unusual delithiation voltage profile could be related to this need for Li to travel through the Si_{28} cages for bulk diffusion, which results in different Li structuring than during lithiation. More detailed *ab intio* modeling and *in situ* characterization would be required for elucidating the exact mechanism.

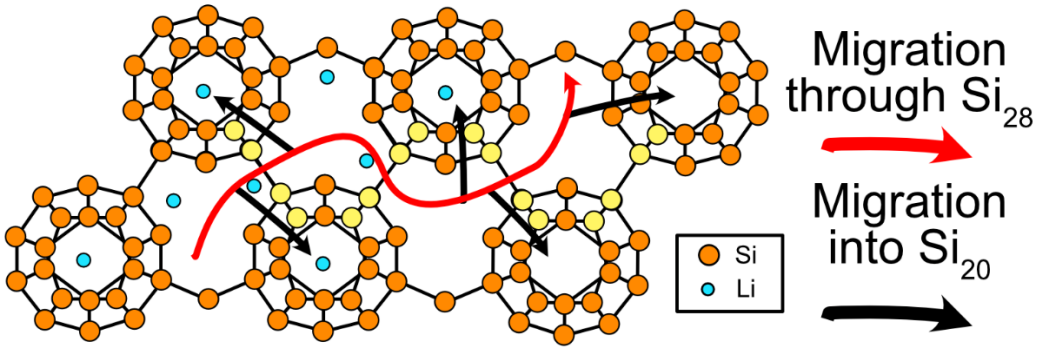

Figure 3.3.10 Schematic showing the proposed Li pathways through the type II Si_{136} clathrate structure. Li migration would primary occur through the interconnected Si_{28} cages via the hexagonal transition states (Si atoms in the hexagons are shown in yellow) due to the low energy barrier of 0.2 eV. In order for the Li to access the Si_{20} cages, it must first travel to an adjacent Si_{28} cage and then enter the Si_{20} cage via the bond-breaking mechanism illustrated in **Figure 3.3.7d**.

From our analysis, we conclude that topotactic Li insertion into guest free, type II Si clathrates is feasible due to the fulfillment of two important requirements: 1) stable Li positions in the structure, and 2) facile Li diffusion into the host structure. If considering α-Si with the diamond cubic structure, Li insertion into the tetrahedral position is energetically unfavorable due to expansion of the surrounding Si atoms,[145] but Li diffusion between these positions shows a reasonable calculated migration barrier of 0.62 eV.[145,194] In contrast, the larger cavities of the guest-free type II Si clathrate allow the Li to be inserted without perturbing the Si framework, resulting in more favorable lithiation energetics. Another important factor is that the distance between adjacent Li positions is larger in the clathrate structure than in α-Si. As described by Zhao *et al*., as Li enters adjacent tetrahedral positions in α-Si, it becomes more favorable for Li to surround and then break a Si-Si bond, which could lead to the beginning of amorphization.[146] Based on the low energy migration pathways in Si_{136} and the larger distance between adjacent Li positions (4.85 – 5.43 Å), we hypothesize that the amorphization reaction is kinetically bypassed because Li atoms are able to spread throughout the lattice and fill the vacant cages without surrounding the Si–Si bonds. Only after the lattice is filled with Li does it become feasible for the conversion reaction to begin and form amorphous Li_xSi. The analysis presented here demonstrate how the cage structure of Si clathrates results in novel electrochemical properties originating primarily from low energy barrier Li migration throughout the bulk structure.

Now that the structural framework for enabling Li insertion has been established, we can consider other Tetrel clathrate-like materials within this framework. In our previous DFT study focused on type I clathrates, we concluded that Li diffusion would be

preferred within the 1D channels of Si_{24} cages connected by hexagonal faces.[179] Based on the results reported here for the type II clathrates, we expect to see similar insertion behavior in Si_{46} as in Si_{136}, although this is difficult to experimentally verify due to the synthetic challenges of obtaining guest-free Si_{46} of high purities and quantities. Notably, Si_{46} with type I clathrate structure has a higher ratio of hexagon containing polyhedra to Si_{20} polyhedra (6:2), suggesting that the hypothesized bond-breaking pathway for Li to enter the Si_{20} cage may play less of a role on the insertion properties. A recently discovered Si clathrate-like polymorph, Si_{24},[57] was reported with low calculated Li migration barriers (0.1 eV) through 1D hexagon-like channels[59] and is expected to demonstrate Li insertion characteristics based on the results here. Guest-free type II Ge (Ge_{136})[181] has been previously been investigated for battery applications and a continuous increase in the lattice parameter was observed with increased lithiation,[52] thus implying the occupation of Li within the framework. Since Ge_{136} shares the same structure as Si_{136}, we expect to see Li insertion behavior but with more off-center Li positions and lower migration barriers due to the larger Ge cage sizes.

For all of these materials, it is also important to consider the possibility of alloying/conversion reactions that occur in a similar voltage range to Li insertion. The competition between insertion and conversion/alloying reactions is determined by a close interplay between kinetics and thermodynamics. As described by Hannah *et al.*, insertion is expected to occur prior to a conversion reaction if the voltage for Li insertion is higher than the voltage for conversion and if the kinetics are favorable for insertion.[79] Thus, it is important for the Li site energy in the Tetrel framework to be stable enough (at high enough voltage vs. Li/Li^+) and accompanied by facile diffusion in order to be competitive

with possible alloying reactions. In the case of Si_{136}, Li insertion is observed at 0.30 V while the alloying reaction occurs at 0.25 V, confirming that this requirement is satisfied for the type II Si-clathrate. However, based on the higher voltage of the alloying reaction for Si_{136} (0.25 V) compared to that in α-Si and $Na_{10.7}Si_{136}$ (0.10 – 0.15 V), we suspect that Li insertion through the bulk clathrate enables an alternative alloying pathway that is more similar to what occurs in lithiation of amorphous Si. Future work will be dedicated towards understanding the structural differences between alloying reactions in the type II Si clathrate and other Si structures to understand the amorphous phase formation mechanisms.

3.3.3.8. Implications for Li-ion Battery Anodes

Given the Li insertion characteristics for the type II Si clathrate discussed above, we now discuss the potential implications for using these materials as Li-ion battery anodes. If a capacity of 231 mAh/g (468 Ah/L) is assumed based on the composition $Li_{32}Si_{136}$ that forms at a reaction of voltage of 0.30 V vs. Li/Li^+, then the electrochemical properties are competitive with other insertion anode materials. For instance, spinel $Li_4Ti_5O_{12}$ (LTO) has a capacity of 175 mAh/g (500 Ah/L)[27] at 1.55 V vs. Li/Li^+, meaning that the clathrate would have a higher energy density due to the comparable capacity but lower reaction voltage of 0.30 V, which would result in a larger cell voltage when partnered with a cathode in a full cell. Another notable feature of Li insertion into Si_{136} is the very small volume expansion of ~0.2%, meaning that the insertion process could be considered “zero strain,” similar to LTO. In addition, the voltage profile between

lithiation and lithiation displays low hysteresis, which is advantageous for high energy efficiency. Although only a composition of $Li_{32}Si_{136}$ was achieved experimentally, DFT calculations suggested that $Li_{48}Si_{136}$ would be energetically favorable with a low predicted volume expansion of 0.31% (**Figure 3.3.5d,e**). If this structure ($Li_{48}Si_{136}$) could be achieved, it would have a capacity of 346 mAh/g (703 Ah/L), which would be comparable to graphite (372 mAh/g, 719 Ah/L) but with much lower predicted volume expansion (0.31% vs 13% for graphite[28]). Based on these reasons, guest-free type II Si clathrates could be very promising Li-ion insertion anodes and further research into their electrochemical properties is warranted.

For practical applications, there are several obstacles that still need to be overcome. Most notably, the voltage range for the Li insertion process (0.26 – 0.30 V vs. Li/Li^+) is close to the potential at which the conversion reaction to the Li_xSi amorphous phase takes place (0.25 V) and therefore the cutoff voltage must be carefully controlled. From our cycling experiments, we found that if the voltage cutoff was too close to the potential at which the conversion reaction initiated, the amorphous phase transition could partially take place and result in poorer capacity retention. The irreversible capacity loss due to SEI formation, particularly in the first cycle, also needs to be addressed, possibly through previously established methods used for other anode materials, such as electrode pre-treatment or electrolyte additives.[195] More studies will be needed to investigate the long-term cycling behavior and stability of Si-clathrates as a host for Li.

3.3.4. Conclusions

In this work, the structural origins of the electrochemical properties of type II Si clathrate were investigated with synchrotron X-ray characterization and density functional theory calculations. Type II Si clathrate samples with compositions of $Na_{0.9(1)}Si_{136}$ (Na1) and $Na_{10.7(1)}Si_{136}$ (Na11) were synthesized and synchrotron PXRD patterns refined to determine the starting Na content and structure after lithium insertion. The lithiation of the Na1 and Na11 are accompanied by distinctly different voltage profiles, demonstrating the importance of the Na content on their electrochemical properties. In the nearly guest-free Na1 clathrate, topotactic Li insertion is observed, which is a unique characteristic since Tetrel elemental compounds typically undergo Li alloying reactions. The voltage plateau at 0.30 V vs. Li/Li^+ was attributed to Li insertion into both Si_{20} and Si_{28} cages, likely with multiple guest atoms within the larger Si_{28} cages, as supported by Rietveld refinement of synchrotron PXRD measurements and DFT calculations. Na11 does not show the same insertion behavior, suggesting that vacant Si_{28} cages are key to enabling Li insertion (as opposed to conversion reactions to amorphous phases). For the first time, we demonstrate the reversible cycling of Li in the type II Si clathrate, which shows a reproducible voltage profile that is asymmetric but features low hysteresis. NEB calculations show that Li migration barriers between interconnected Si_{28} cages are low (0.2 eV) through the center of the hexagonal face. In contrast, Li migration through the center of a pentagonal face for movement between Si_{20} and Si_{28} cages has a high energy barrier of 2.0 eV unless Li is present in an adjacent Si_{28} cage, which can facilitate a lower energy pathway (0.65 eV) that involves temporary Si-Si bond breaking. The latter pathway may be responsible for the asymmetry observed in the voltage profile. In summary, we attribute the structural origin of Li insertion in Si_{136} to the energetically

favorable Li insertion sites in the Si-clathrate cages and facile diffusion paths throughout the bulk structure. Importantly, we identify the migration pathway through Si hexagonal faces as an important condition for enabling bulk Li diffusion. On the basis of this structural feature, we speculate that other open Tetrel frameworks such as Si_{46}, Si_{24} and Ge_{136} could also demonstrate reversible Li insertion with low volume expansion, which could be promising for possible applications as Li-ion battery anodes.

4. CLATHRATES AS ALLOYING ANODES

4.1. Understanding the Amorphous Lithiation Pathway of the Type I Ba_8Ge_{43} Clathrate with Synchrotron X-ray Characterization

4.1.1. Introduction

Tetrel elements (Tt = Si, Ge, Sn) are potential candidates for next generation Li-ion battery anodes due to their intrinsically high capacities originating from a series of complex phase transformations. While the room temperature lithiation of diamond structured Si (α-Si) proceeds through the formation of amorphous phases until crystallization of $Li_{15}Si_4$ at high degrees of lithiation,[117,196] Ge and Sn readily crystallize at intermediate Li compositions to form various Li-Tt binary compounds.[120,135,197] The phases that form have direct consequences on the electrochemical properties such as the voltage, rate capability, and stress evolution. Understanding how these properties are affected by the initial host structure and its subsequent lithiated intermediates is important for optimizing the performance of alloying anodes. Much work has been conducted on the role of nanostructuring on the alloying reactions of the elemental Tetrels,[37,198–202] but other than comparisons between amorphous and diamond structured Si (or Ge)

electrodes[117,132,198,203–207], less focus has been given to understanding the effect of the initial crystal structure on the subsequent lithiation pathways.

To further this understanding, our group and others have been investigating Tetrel clathrates[49,51–56,152,179,180] and other polymorphs[59,158,208] for their electrochemical properties for Li-ion batteries. The type I Ba-Ge clathrate, Ba_8Ge_{43}, deviates from the M_8Tt_{46} stoichiometry due to the presence of vacancies on Ge sites, which compensate for the excess electrons contributed from the Ba atoms. Substituting group III elements (Al, Ga, In) for Ge allows for further charge compensation of the Ba and results in the ability to tune the materials properties of the clathrate. For instance, the electron precise $Ba_8Al_{16}Ge_{30}$ clathrate is a semiconductor[111], while Ba_8Ge_{43} displays metallic like behavior due to the excess electrons from the Ba[209]. The structure of Ba_8Ge_{43} (**Figure 4.1.1**) is composed of two dodecahedra (Ge_{20}) and six tetrakaidecahedra (Ge_{24}) per formula unit, where all Ge atoms are in slightly distorted tetrahedral configurations. Much work has gone into understanding how the clathrate structure and defects affect the thermoelectric[42,210,211] and superconducting[88,89,177,212] properties of these materials, however their role on the electrochemical and Li ion alloying properties is less understood. Our goal in this work is to establish structure-property relationships for clathrates within the context of Li-ion battery applications.

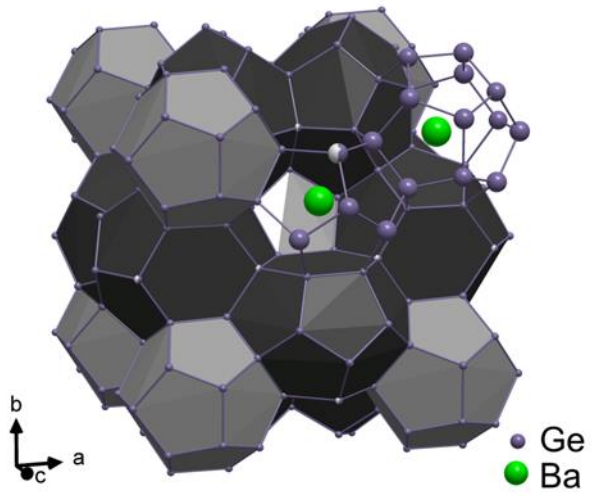

Figure 4.1.1 Crystal structure of type I Ba_8Ge_{43} clathrate (from ref.[152]). The purple spheres represent the Ge atoms, white spheres represent vacancies and the green spheres represent the Ba atoms. The Ge_{20} and Ge_{24} polyhedra are shaded in gray and black, respectively.

Because of the similar covalent bonding within the cage-like framework in Tetrel clathrates and their elemental analogs, the clathrates are expected to undergo similar alloying reactions with lithium. However, previous work shows that in some situations this is not the case. For example, using laboratory X-ray diffraction analysis, we found previously that the type I $Ba_8Al_yGe_{46-y}$ ($0 < y < 16$) clathrates proceed through an amorphous pathway different from the crystalline phase transformations typically seen in lithiation of α-Ge.[152] On the other hand, Si clathrates with type II structure (Na_xSi_{136}, $0 < x < 24$) reacted with Li similarly to α-Si;[53] however, if the Na occupancy of the cages was low, the voltage profile looked similar to that in amorphous Si.[49] From these studies, it appears that the guest atom type and occupancy in the clathrate are important parameters for determining their electrochemical properties. However, the formation of amorphous phases in the reaction intermediates precludes the use of Bragg diffraction for structural

characterization, necessitating local structure characterization methods to understand the nature of the amorphous phases during the lithiation of clathrates.

Atomic X-ray pair distribution function (PDF) analysis has proven to be a vital tool in elucidating the alloying pathways of Tetrel elements with alkali metals.[35,120,213–216] The PDF is derived from the total X-ray scattering pattern and provides information about the probability of finding atomic pairs at certain distances.[217] This technique enables the local structure of amorphous and crystalline materials to be investigated, thus, allowing for a better picture of the lithiation intermediates to be attained. From this, differences in electrochemistry between clathrates and the elemental phases can be corroborated by differences in the structures formed during the lithiation reactions. In addition, PDF analysis with *in situ* heating of electrochemically obtained amorphous phases can illuminate how the amorphous phases that form are related to known crystalline phases. For example, heating experiments on electrochemically synthesized amorphous Li_xSi resulted in crystallization to Li-Si phases, implying a similar local structure of the two phases.[218,219] Obtaining PDFs during this crystallization process could provide insights into how the amorphous structure relates to the crystalline structures.

In this work, the lithiation pathways of the type I clathrate Ba_8Ge_{43} are investigated in more detail with *ex situ* synchrotron X-ray PDF analysis and X-ray diffraction and compared to α-Ge at similar states of lithiation. The PDF results confirm that Ba_8Ge_{43} proceeds through an amorphous pathway during lithiation, with no atomic correlations associated with long-range order observed beyond 10 – 30 Å. This contrasts

with the crystalline phase transformations observed during lithiation of α-Ge micron-sized particles, which are characterized by long range order in both the XRD and PDF results. The local structure of the lithiated $Ba_8Al_{16}Ge_{30}$ clathrate, where Al is substituted on the Ge site, is found to be very similar to that seen in Ba_8Ge_{43} after reaction with lithium. *In situ* heating during XRD and PDF measurements were conducted to evaluate the thermal stability of the amorphous phases and identify crystallization events and the phases formed. Heating of the lithiated clathrate materials caused the amorphous Li-Ba-Ge phases to crystallize to Li-Ge binary compounds at low temperatures (350 – 420 K), suggesting structural relationships between the amorphous and crystalline phases. Our results show that analysis of the lithiation pathway of type I Ba_8Ge_{43} clathrate and comparison to the elemental analogue can provide an understanding of the effects of guest atoms and framework atoms on the lithiation pathways and its implications for Li-ion battery anodes.

4.1.2. Experimental Methods

The Ba_8Ge_{43} and $Ba_8Al_{16}Ge_{30}$ clathrates were synthesized and prepared into electrodes in a similar manner as described in our previous work.[152] The electrodes were lithiated galvanostatically in half-cells with lithium metal and then extracted for *ex situ* measurements. Synchrotron X-ray pair distribution (PDF) measurements were conducted at Diamond Light Source (Didcot, United Kingdom) at the I15-I dedicated PDF beamline with $\lambda = 0.161669$ Å. The atomic PDF, $G(r)$ as defined by Billinge *et al.*[220], was generated from the total scattering data using PDFgetx3 within the xPDF suite software

package[221,222]. Synchrotron X-ray diffraction measurements were performed at the P02.1 powder diffraction beamline at PETRA III at the Deutsches Elektronen-Synchrotron (DESY) with $\lambda = 0.20733$ Å. More detailed descriptions of the synthesis, electrochemical and synchrotron measurements, and PDF analysis are in the **Appendix D**

4.1.3. Results

4.1.3.1. *Ex situ* XRD and PDF analysis

To evaluate the local and long-range order of the lithiation intermediates, the Ba_8Ge_{43} and α-Ge electrodes were electrochemically lithiated to different compositions and then subjected to *ex situ* synchrotron XRD and PDF measurements at room temperature. Scanning electron microscopy (SEM) of the electrodes showed that the Ba_8Ge_{43} sample was composed of irregularly shaped, micron-sized particles (2 – 10 μm) with some larger shards (>20 μm) and the α-Ge sample was composed of similarly irregularly shaped, micron-sized particles (**Figure D.1**). Therefore, we assume there are no nano-size effects on the structural or electrochemical observations made here. The voltage profiles and differential charge (dQ/dE) plots for the first lithiation of Ba_8Ge_{43} and α-Ge are shown in **Figure 4.1.2** with blue, orange and green points representing the compositions (as a ratio of Li to Ge) at which XRD and PDF samples were taken. The voltages and capacities of the cells at each of these points is presented in **Table D.1**. The lithiation of Ba_8Ge_{43} is characterized by a plateau at 0.2 V vs. Li/Li^+ (seen as a large cathodic peak in the dQ/dE plot) and then a sloped decrease in voltage, consistent with our previous work.[152] In contrast, the voltage profile of α-Ge has a higher reaction

voltage starting around 0.3 V vs. Li/Li^+ and the dQ/dE plot shows a small peak at 0.5 V and two peaks corresponding to plateaus at 0.31 and 0.18 V, which represent a series of separate phase transformations.[120] Ba_8Ge_{43} has a broad peak around 0.25 – 0.3 V in the dQ/dE plot which is attributed to impurity α-Ge in the sample (shown later). Notably, both electrodes enable a reaction of 3.75 Li per Ge atom but the lower reaction voltage of Ba_8Ge_{43} suggests a difference in phase transformations during lithiation.

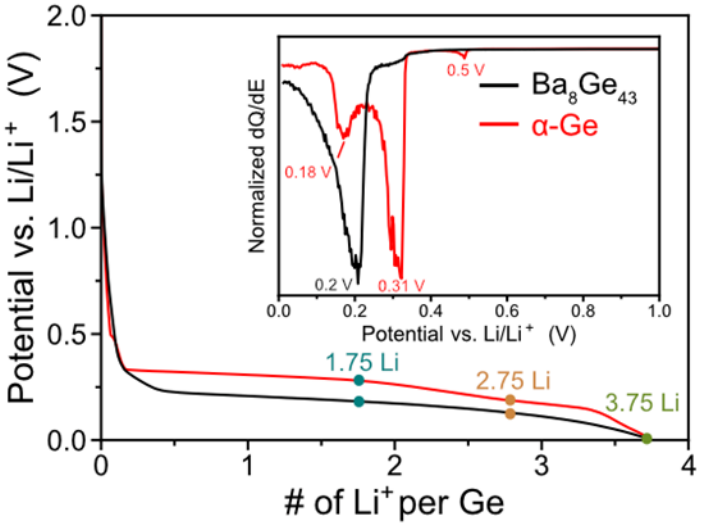

Figure 4.1.2 Voltage profile and corresponding dQ/dE plot of the lithation of Ba_8Ge_{43} and α-Ge at 25 mA/g (corresponding to C-rates of C/41 for Ba_8Ge_{43} and C/55 for α-Ge) with a voltage cutoff of 10 mV vs. Li/Li^+. The blue, orange, and green circles represent the compositions at which cells were disassembled for *ex situ* PDF and XRD measurements.

To understand the origin of the differences in these electrochemical features, the XRD and PDF patterns of α-Ge and Ba_8Ge_{43} were compared at various degrees of lithiation at room temperature. The XRD and PDF results for the lithiation of α-Ge are shown in **Figure 4.1.3a-b** with reference patterns corresponding to Li_5Ge_2[223] and $Li_{15}Ge_4$[224]; the results for the Ba_8Ge_{43} samples at similar Li compositions are shown in **Figure 4.1.3c-d**. Overall, the results for lithiation of α-Ge are fairly consistent with those

reported by Jung *et. al*,[120] although therein different voltage cutoffs were used to prepare the various samples rather than specific amounts of Li. (We acknowledge that there is substantial inconsistency in the literature[119,135,200,225,226] on the nature of the phases that form upon electrochemical lithiation of α-Ge at room temperature, the results of which may be affected by the Ge particle size, current density used, as well as the characterization technique. For the sake of consistency with the literature, we have chosen to only compare our results to those reported by Jung *et al*.,[120] wherein X-ray PDF was also used for analysis of micron-sized α-Ge.) Following a reaction of 1.75 equiv. Li per Ge atom, a nominal composition referred to as $Li_{1.75}Ge$ hereafter, the XRD pattern shows reflections corresponding to α-Ge and a lithium germanide phase we have tentatively identified as Li_5Ge_2 with $R\bar{3}m$ symmetry, indicating a two-phase reaction. This is supported by a Rietveld refinement analysis (**Figure D.2a,Table D.2**) fitting the Li_5Ge_2 and α-Ge structures with a phase fraction of 83% and 17% respectively. In the work by Jung *et. al*,[120] Li_7Ge_3 (reported as having $P32_12$ symmetry but this is likely an error, as there is no such space group and it is likely intended to be $P3_212$) was identified as a major intermediate phase during lithiation of α-Ge and first principles calculations suggested the energetic feasibility of this phase[223]. Li_7Ge_3 and Li_5Ge_2 have very similar structures in which Ge_2 dumbbells are arranged parallel to one another with slightly different numbers of Li surrounding them. As a result, XRD and PDF patterns are nearly identical, making them difficult to differentiate. The XRD results show that further lithiation of α-Ge to an overall composition $Li_{2.75}Ge$ resulted in the almost complete disappearance of the α-Ge phase, as well as a decrease and broadening of the reflections attributed to Li_5Ge_2. A reflection at $2\theta = 5.4°$ was also present in the diffraction pattern at

this stage of the lithiation in the work by Jung *et. al*[120] and therein attributed to a disordered Li_7Ge_2-like phase. The XRD pattern of $Li_{3.75}Ge$ shows reflections corresponding to crystalline $Li_{15}Ge_4$ and was fit well by Rietveld refinement analysis (**Figure D.2b,Table D.3**) with a lattice parameter of 10.7763(4) Å, consistent with previously reported results and the PDF pattern obtained here.

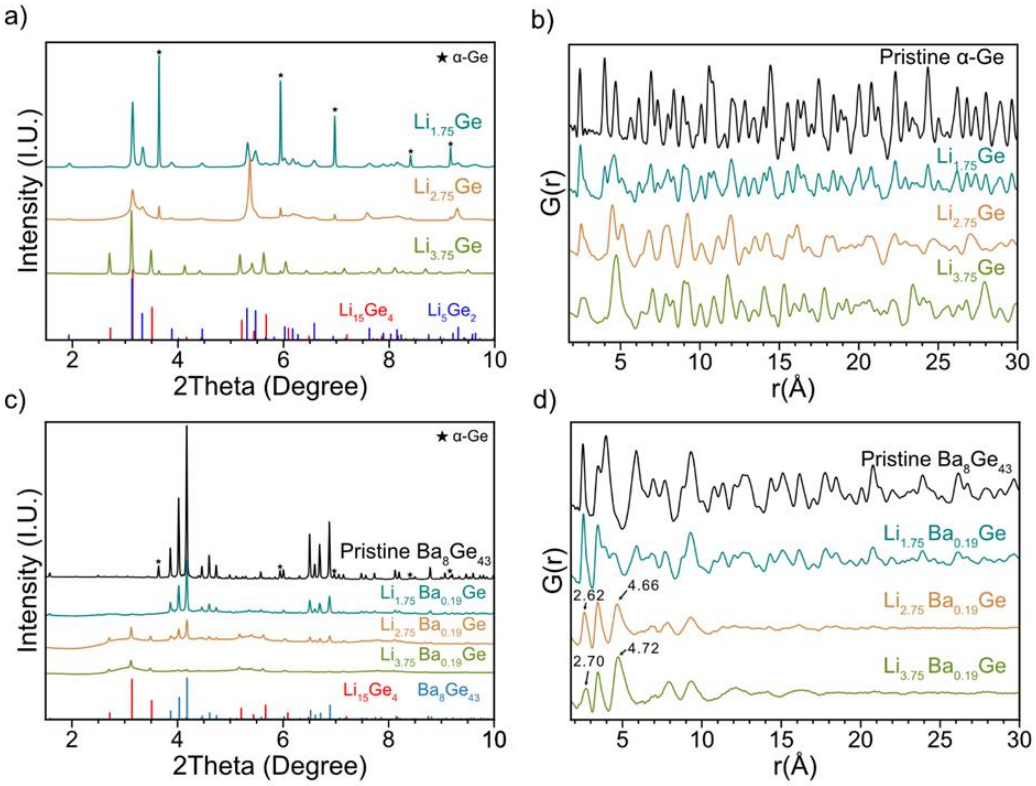

Figure 4.1.3 Synchrotron XRD (λ = 0.20733 Å) (a,c) and PDF (b,d) results for **(a,b)** pristine α-Ge, $Li_{1.75}Ge$, $Li_{2.75}Ge$, and $Li_{3.75}Ge$ and **(c,d)** pristine Ba_8Ge_{43}, $Li_{1.75}Ba_{0.19}Ge$, $Li_{2.75}Ba_{0.19}Ge$, and $Li_{3.75}Ba_{0.19}Ge$.

The details of the PDF refinements for the lithiation of the α-Ge samples in **Figure 4.1.3b** are shown in **Figure D.3**. The PDF of the pristine Ge particles could be refined with a good fit to the α-Ge phase with a R_w = 8.26% (**Figure D.3a**). Lithiation to a composition of $Li_{1.75}Ge$ and voltage of 0.28 V resulted in a PDF pattern containing α-

Ge correlations with decreased intensity and the emergence of new correlations indicative of the presence of another phase. Refinement of the PDF was attempted using the structures of α-Ge and several highly lithiated Li-Ge compounds commonly referred to as "dumbbell phases," (*e.g.*, Li_7Ge_3, Li_5Ge_2, Li_9Ge_4, Li_7Ge_2)[223,227,228] wherein parallel Ge-Ge dumbbells are surrounded by slabs of Li atoms. Calculated PDF patterns and crystal structures for these phases are presented in **Figure D.4** and **S5**, respectively. The best fit for the PDF from $Li_{1.75}Ge$ (R_w = 19%) was obtained with 9.5 mol% α-Ge and 90.5 mol% Li_5Ge_2 (**Figure D.3b, Table D.4)**. Fitting with Li_7Ge_3 and Li_9Ge_4 instead of Li_5Ge_2 resulted in similar phase fractions and R_w values (19.7% for Li_7Ge_3 and 22.3% for Li_9Ge_4), which is consistent with the nearly identical arrangement of Ge-Ge dumbbells in these phases (see **Figure D.5**). At a composition of $Li_{2.75}Ge$ and a voltage of 0.17 V, the best fit attained was from a combination of $Li_{13}Ge_5$ (64.3%) and Li_7Ge_2 (35.7%) (**Figure D.3c, Table D.5**), similar as the results reported by Jung *et. al*,[120] wherein multiple combinations of Ge-Ge dumbbells phases resulted in comparable fits. We found that fitting to Li_7Ge_3 and Li_5Ge_2 also resulted in decent fits (**Table D.5**), which suggests that the Ge_2 dumbbells are the dominant local feature present in the electrode at this point in the lithiation process. The fact that the PDF for $Li_{2.75}Ge$ can be fit comparably to multiple phases, as well as the broadness of the reflections in the XRD pattern, suggests that the structure is disordered but maintains a local structural motif of Ge-Ge dumbbells and isolated Ge atoms. At a composition of $Li_{3.75}Ge$, the PDF could be fit to $Li_{15}Ge_4$ with R_w = 22.6%, the structure of which consists of isolated Ge atoms surrounded by Li. The addition of a Li-Ge dumbbell phase resulted in a better fit (R_w = 11.9%) with 85.7 mol% $Li_{15}Ge_4$ and 14.3 mol% Li_7Ge_3 (**Figure D.3d, Table D.6**). The modest improvement in

the fitting is suggesting that the Li-Ge dumbbell phases have been mostly consumed by the addition of more Li, and the Li-reduction causes the breaking of the Ge-Ge bonds in the structure, which were the primary structural motifs identified prior to this point. These observations are consistent with the results from Jung *et al.*,[120] wherein it was suggested that $Li_{15}Ge_4$ could decompose before the *ex situ* PDF measurement was performed. Alternatively, there still could be residual Ge-Ge bonding in the material. A similar observation was made after lithiation of α-Si,[35] where $Li_{15}Si_4$ crystallizes at full lithiation but Si-Si bonds can still be observed in the PDF.

The synchrotron XRD patterns of the Ba_8Ge_{43} samples are shown in **Figure 4.1.3c** with reference patterns for $Li_{15}Ge_4$ and Ba_8Ge_{43}[152]. The XRD pattern for the as-synthesized Ba_8Ge_{43} clathrate shows a small amount of α-Ge as secondary phase, possibly resulting from Ba loss via evaporation during the clathrate synthesis. After addition of 1.75 Li per Ge atom (*i.e.*, to a composition of $Li_{1.75}Ba_{0.19}Ge$ and voltage of 0.175 V vs. Li/Li^+), the reflections corresponding to the Ba_8Ge_{43} phase decrease in intensity without any new reflections appearing, confirming that the Ba_8Ge_{43} converts to an amorphous phase upon lithium insertion, consistent with our previous observations using laboratory XRD.[152] Subsequent lithiation to a composition of $Li_{2.75}Ba_{0.19}Ge$ results in a further decrease in Ba_8Ge_{43} reflections and the appearance of reflections corresponding to $Li_{15}Ge_4$. At this point in the reaction, the cell has reached a voltage of 0.11 V vs. Li/Li^+ (**Table D.1**), which is below the point where α-Ge can be converted to $Li_{15}Ge_4$.[120] Therefore, we attribute the origin of $Li_{15}Ge_4$ to the reaction of Li with the α-Ge impurity phase, not the clathrate phase. Upon further lithiation to $Li_{3.75}Ba_{0.19}Ge$, the

XRD pattern only shows reflections attributed to $Li_{15}Ge_4$ formed from the impurity phase reaction, confirming that the lithiated clathrate phase is amorphous.

The corresponding PDF patterns for Ba_8Ge_{43} at different degrees of lithiation are shown in **Figure 4.1.3d**. The X-ray PDF measurement is sensitive to the atomic scale correlations between pairs of atoms, giving insight to the local structuring of Ge, Li and Ba atoms. The intensity of the correlations is dependent on the atomic number and concentration of the elements, meaning that Ge correlations (Ge-Ge, Ge-Li, Ge-Ba) are expected to contribute the most to the observed patterns in the clathrate. Refinement of the PDF for the pristine clathrate showed that there was a minimal amount (4.4 mol%) of α-Ge as a secondary phase (**Figure D.6a, Table D.7**), confirming the XRD results. In the low-r region, the PDF shows correlations at ca. 2.51 Å, 3.50 Å, 3.96 Å and 5.92 Å (**Figure 4.1.3d**). Inspection of the simulated partial PDFs (**Figure D.4a**) show that these correlations correspond to direct Ge-Ge bonding, Ba-Ge correlations, next nearest neighbor Ge-Ge distances, and 3rd nearest neighbor Ge-Ge distances, with minimal contributions from Ba-Ba correlations due to the large separation distance of the Ba atoms (~6 Å) in the clathrate structure (**Figure D.4a**).

By observing how these correlations change with increasing amounts of lithium addition to Ba_8Ge_{43}, the average local structure of the lithiated intermediate phases can be determined. After addition of 1.75 Li per Ge, the PDF shows that the correlations decrease in intensity relative to the pristine sample. Significant changes are seen at low r-values, while the pattern at high-r values (10 – 30 Å) resembles that for the pristine clathrate. Refinement of the pattern to the Ba_8Ge_{43} structure from $10 < r < 30$ Å confirms

that the high-r correlations match reasonably well with those for pristine clathrate (**Figure D.6b, Table D.7**). The difference curve of the refinement from 2 < r < 30 Å reveals correlations at 2.62 Å, 3.42 Å and 4.50 Å (**Figure D.6c**) but no other features at r > 10 Å, suggesting that these low-r correlations arise from an amorphous, lithium-containing phase that coexists with the pristine clathrate.

Upon addition of lithium to reach the composition of $Li_{2.75}Ba_{0.19}Ge$ (at 0.11 V vs. Li/Li^+), it is apparent that the Ba_8Ge_{43} starting material has been completely reacted and the PDF lacks noticeable features at r > 10 Å, indicating the absence of long-range order. The PDF for $Li_{2.75}Ba_{0.19}Ge$ (**Figure 4.1.3d**) displays features very similar to those in the difference plot obtained in the refinement for $Li_{1.75}Ba_{0.19}Ge$ to the Ba_8Ge_{43} structure (**Figure D.6d**). The first peak at 2.62 Å is similar in position to that found in Li-Ge dumbbell phases, wherein the Ge-Ge (~2.4 – 2.6 Å) and Li-Ge correlations (~2.7 – 2.8 Å) contribute to the first peak in the PDF (**Figure D.4**). The second peak at 3.44 Å is typical of Ba-Ge distances (*e.g.,* such as that in $BaGe_2$)[229] but slightly shorter than the 3.5 –3.9 Å lengths for these Ba-Ge distances in the pristine clathrate phase (**Figure D.4a**). The third peak at 4.66 Å is similar to the distance separating Ge dumbbells from each other (4.4 – 5.2 Å) in Li-Ge dumbbell phases.

Further lithiation to a composition of $Li_{3.75}Ba_{0.19}Ge$ (voltage of 10 mV) results in a PDF that is very similar to the one seen for $Li_{2.75}Ba_{0.19}Ge$ but with slightly shifted correlations and intensities (**Figure 4.1.3d**). The peak at 2.62 Å for $Li_{2.75}Ba_{0.19}Ge$ related to Ge-Ge and Li-Ge bonds is less intense and is shifted to 2.70 Å in $Li_{3.75}Ba_{0.19}Ge$, suggesting that fewer direct Ge-Ge bonds are present. The peak at 4.66 Å is shifted to

4.72 Å and is more intense relative to the peak at 2.70 Å, suggesting an increase in correlations arising from separated Ge atoms relative to the correlations from the Ge-Ge bond in the dumbbells. As the Li content increases relative to Ge, it is expected that more isolated Ge atoms surrounded by Li will be present compared to Ge dumbbells, as seen in the $Li_{15}Ge_4$ ($Li_{3.75}Ge$) phase where no dumbbells are present (**Figure D.4f**). Overall, the PDFs of the Ba_8Ge_{43} samples after reaction with lithium suggest that the lithiation proceeds through a two-phase conversion of the pristine, crystalline clathrate into an amorphous phase, corroborating the presence of a constant voltage plateau in the voltage profile. The amorphous phase has similar local structures as those found in Li-Ge phases, with the addition of a correlation at 3.44 Å from Ba-Ge bonds.

PDF analysis of the Ba_8Ge_{43} sample after one full lithiation/delithiation cycle was also performed and is shown in **Figure D.7** along with the corresponding voltage profile and dQ/dE plot (**Figure D.7ab**). The lithiation/delithiation voltage profile of α-Ge is provided as well to demonstrate that the delithiation pathway is different for Ba_8Ge_{43}. In α-Ge, there are two plateaus during delithiation (at 0.41 V and 0.62 V vs. Li/Li^+) consistent with previous reports,[213] while the delithiation of Ba_8Ge_{43} showed a broad peak in the dQ/dE plot at 0.3 V with a gradually sloped voltage profile. The PDF of Ba_8Ge_{43} after full lithiation and delithiation showed no long-range correlations at $r > 10$ Å, indicating that the delithiated Ba_8Ge_{43} is amorphous (**Figure D.7c**). There is a correlation centered at 2.51 Å corresponding to Ge-Ge bonding, and a broad peak at 3.43 Å from Ba-Ge correlations with a broad shoulder at ~3.96 Å, which is close to the next nearest neighbor Ge distance in Ba_8Ge_{43}. Comparing the PDF for pristine, crystalline Ba_8Ge_{43} with that of the amorphous Ba_8Ge_{43} after delithiation (**Figure D.7d**) shows

similarities in peak positions of the observed features, implying very similar local structures. This suggests that although the clathrate structure undergoes an amorphous phase transformation after addition of lithium, the local structure of the subsequent amorphous phase after lithium is removed resembles that seen in the original crystalline structure. In other words, despite the crystalline-to-amorphous transition, the local structural features of the clathrate are retained after one cycle.

The Al-substituted clathrate, $Ba_8Al_{16}Ge_{30,}$ was also subjected to PDF analysis after full lithiation to an amount of 1.9 Li per (Al + Ge) atom. The voltage profile and corresponding dQ/dE plot are presented in **Figure D.8** along with the PDF refinement (**Table D.8**) of the pristine $Ba_8Al_{16}Ge_{30}$ and PDF after reaction with 1.9 Li to a total composition of $Li_{1.9}Ba_{0.17}Al_{0.35}Ge_{0.65}$. Consistent with our previous work[152], the Al substituted clathrate reacted at a lower voltage of 0.06 V vs Li/Li^+ compared to 0.2 V of Ba_8Ge_{43} but with less capacity than Ba_8Ge_{43}. The PDF plot at the most lithiated composition (**Figure D.8c**) showed a significant amount of crystalline fraction present, which was fit well to the pristine $Ba_8Al_{16}Ge_{30}$ structure meaning that the original clathrate phase was not fully reacted. Similar to the $Li_{1.75}Ba_{0.19}Ge$ refinement (**Figure D.6c**), the difference pattern of the refinement for $Li_{1.9}Ba_{0.17}Al_{0.35}Ge_{0.65}$ revealed an amorphous phase with correlations at 2.64 Å, 3.45 Å, and 4.57 Å, suggesting the formation of a similar amorphous phase as that seen in the lithiation of Ba_8Ge_{43}. This suggests that the lithiation of $Ba_8Al_{16}Ge_{30}$ proceeds in a similar manner to Ba_8Ge_{43}; however, the presence of Al in the amorphous phase results in a lower reaction voltage and capacity compared to $Ba_8Ge_{43.}$

4.1.3.2. *In situ* heating PDF studies

As described in the previous section, visual comparison of the PDFs for Ba_8Ge_{43} and α-Ge after lithiation show similarities in peak positions at low-r values (2 – 5 Å), suggesting similar local structures for the Li and Ge atoms. However, the assignment of the broad peaks from 6 – 10 Å in the lithiated clathrate samples is less obvious and could originate from Ge-Ge, Ba-Ge, and Li-Ge correlations. To identify the origin of these correlations, variable temperature PDF measurements were conducted to evaluate the lithiated Ba_8Ge_{43} structures upon moderate heating and their relationship to the original amorphous structure. **Figure 4.1.4a-b** shows PDFs of Ba_8Ge_{43} lithiated to compositions of $Li_{2.75}Ba_{0.19}Ge$ and $Li_{3.75}Ba_{0.19}Ge$ acquired during *in situ* heating from room temperature to 450 and 420 K, respectively. The corresponding false colormaps are shown underneath in **Figure 4.1.4c-d**, where the light blue and dark blue shading indicates regions of higher and lower intensities, respectively. For $Li_{2.75}Ba_{0.19}Ge$ (**Figure 4.1.4a,c**), there is little change in the PDF pattern until reaching a temperature of 410 K, where the broad peaks from 6 – 10 Å begin to sharpen and noticeable long-range correlations begin to appear out to 30 Å, indicating that crystallization is occurring. After heating to 450 K, the peaks sharpen further, suggesting a higher degree of ordering. In the case of $Li_{3.75}Ba_{0.19}Ge$ (**Figure 4.1.4b,d**), crystallization occurred at a lower temperature of 350 K, as seen by the appearance of correlations at r > 10 Å. As in $Li_{2.75}Ba_{0.19}Ge$, the broad peaks originally around 2 – 10 Å begin to sharpen as the crystallization occurred.

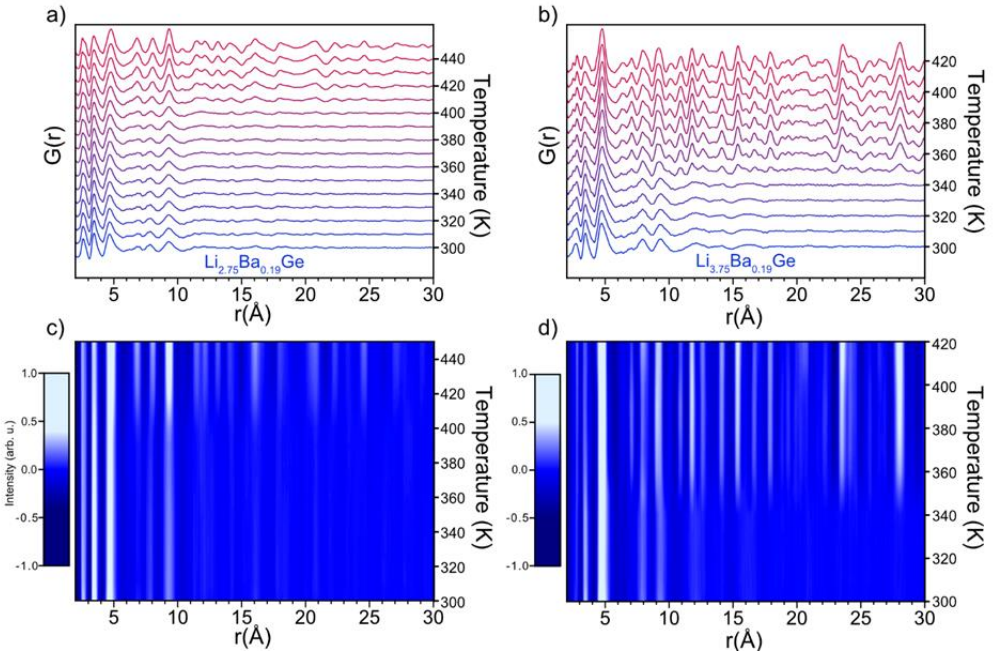

Figure 4.1.4 (a) *In situ* PDF measurements of heating the lithiated Ba_8Ge_{43} ($Li_{2.75}Ba_{0.19}Ge$) from 300 to 450 K. (b) *In situ* PDF measurements of heating the fully lithiated Ba_8Ge_{43} ($Li_{3.75}Ba_{0.19}Ge$) from 300 to 420 K. PDF scans were taken for 10 minute intervals with the temperature held at every 10 K; patterns are y-offset for clarity. (c) and (d) show corresponding false colormaps for $Li_{2.75}Ba_{0.19}Ge$ and $Li_{3.75}Ba_{0.19}Ge$; a linear interpolation was used between measured data points.

To better illustrate the structural features, the PDFs of the lithiated clathrate samples before and after heating are shown in **Figure 4.1.5**, along with the PDF of the α-Ge sample lithiated to the same composition for comparison. Visual inspection shows that the PDFs contain similar features, indicating that the heat-induced crystallization process produced a structure in the lithiated clathrate that was similar to that found in the Li-Ge phases that evolved from lithiation of α-Ge at room temperature. This is supported by comparison of structure functions of the same sets of samples, wherein Bragg peaks in comparable positions are present, suggesting similarities in the crystalline phases in each sample (**Figure D.9**).

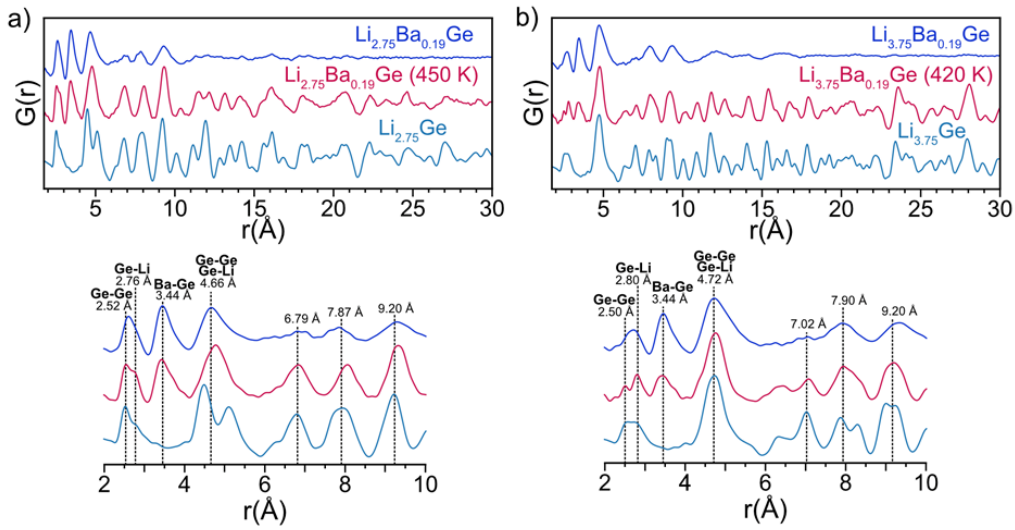

Figure 4.1.5 (a) Comparison of PDFs of $Li_{2.75}Ba_{0.19}Ge$: unheated (blue), heated to 450 K (pink), and lithiated, unheated α-Ge (light blue). (b) Comparison of PDFs of $Li_{3.75}Ba_{0.19}Ge$: unheated (blue), heated to 420 K (pink), and lithiated, unheated α-Ge (light blue). Enlarged regions of 2 < r < 10 Å are shown below. Patterns are y-offset for clarity.

For the $Li_{2.75}Ba_{0.19}Ge$ PDFs (**Figure 4.1.5a**), three correlations are present from 2 – 5 Å while two sets are present in the $Li_{2.75}Ge$ PDF. The correlation centered at 3.44 Å is present only in the Ba-containing samples and is assigned to Ba-Ge correlations. The correlation at 4.66 Å remains a single peak after heating, while two peaks at slightly lower and higher r-values are present in $Li_{2.75}Ge$. The origin of the doublet can be attributed to the different 2nd sphere Ge-Ge separations in the "dumbbell" phases (**Figure D.10a**). The fact that the PDF for $Li_{2.75}Ba_{0.19}Ge$ has a single peak instead of a doublet could suggest the presence of more isolated Ge atoms (*i.e.* as in Li_7Ge_2, **Figure D.5d**) or more disorder in the orientation between dumbbells. A similar phenomenon was observed in the *in situ* PDFs obtained during lithiation of Ge nanoparticles, wherein a single broad peak around 4.5 – 4.6 Å was observed as opposed to the split peak seen in the PDF of dumbbell phases.[213] The broad correlations from 6 – 10 Å in the amorphous sample

become sharper and more intense after the heat treatment, suggesting that these interatomic interactions become more ordered upon annealing. Refinement of the pattern obtained after heating to the structure of Li_7Ge_2 from resulted in a fit with $R_w = 55\%$, which was improved to $R_w = 28.6\%$ by restricting the fit range to 6 – 30 Å to exclude the Ba-Ge correlation at 3.44 Å (**Figure D.11ab, Table D.9**). The fairly good fit at higher r-values suggests that the long-range order in $Li_{2.75}Ba_{0.19}Ge$ phase after heating to 450 K is similar to that found in Li_7Ge_2, implying the presence of dumbbells and isolated Ge atoms. The largest discrepancy in the pattern was at low-r values (2 – 6 Å), suggesting the presence of an amorphous phase probably related to the Ba present in the sample. The correlations around 6 – 10 Å are fit well by the Li_7Ge_2 refinement, meaning that the broad peaks in the lithiated sample prior to heating are related to the correlations in the crystalline phase formed after heating. In the Li_7Ge_2 PDF pattern, the correlations from 6 – 10 Å represent next nearest neighbor Ge-Ge correlations (either between single atoms or dumbbells), as illustrated in **Figure D.10b**. Since major correlations die out past 10 Å in the unheated $Li_{2.75}Ba_{0.19}Ge$ sample, it can be presumed that a similar, albeit disordered, structuring of Ge atoms is present in the amorphous sample.

In the PDFs of the fully lithiated samples shown in **Figure 4.1.5b**, the correlations from 2 – 5 Å in the clathrate-derived samples have three main correlations, while there are only two in the $Li_{3.75}Ge$ sample (**Figure 4.1.5b**) due to the absence of Ba-Ge bonding. The broad correlations from 6 – 15 Å in $Li_{3.75}Ba_{0.19}Ge$ become sharper after heating, an indication of an increased ordering and suggesting that the amorphous and crystalline structures are related. On the other hand, *in situ* PDF measurements during heating from 310 – 420 K for the fully lithiated α-Ge sample (composed predominately of $Li_{15}Ge_4$)

was also conducted; however, the pattern showed little change, indicating temperature stability over this range (**Figure D.12**).

Refinement of the PDF from $Li_{3.75}Ba_{0.19}Ge$ after heating to 420 K showed that the high-r features of the PDF could be reasonably captured by the $Li_{15}Ge_4$ phase (**Figure D.11c,Table D.9**), suggesting the long-range order present is from $Li_{15}Ge_4$ correlations. All PDFs have a peak around 4.72 Å, which is attributed to the combination of non-bonded Ge-Ge correlations (centered at 4.68 Å) and Li-Ge correlations (shoulder at ~5 Å) found in the crystalline $Li_{15}Ge_4$ phase (see calculated PDF in **Figure D.10c**). The significant discrepancy in the difference curve of the refinement for the heated sample (**Figure D.11c**), suggests the presence of another phase. Due to the decrease in intensity of the Ba-Ge peak at 3.44 Å after heating, the other phase is likely a Ba-containing amorphous phase. Similar to the $Li_{2.75}Ba_{0.19}Ge$ sample, the fact that the features from 6 – 10 Å in the PDF of the heated $Li_{2.75}Ba_{0.19}Ge$ sample can be connected to correlations from the $Li_{15}Ge_4$ crystalline phase suggests that the original features in the unheated sample can be assigned to similar structural features as those found in the crystalline phase.

4.1.3.3. Thermal Stability and Crystalline Phase Evolution During Heating

To probe the thermal stability and phase evolution of the amorphous phases formed during electrochemical lithiation of the Ba_8Ge_{43} clathrate, *in situ* XRD heating experiments were conducted. A heating ramp from 300 to 480 K was performed in 20 K intervals with a 6 min hold at each temperature and scans taken every 2 min. While

heating the amorphous $Li_{3.75}Ba_{0.19}Ge$ sample (**Figure 4.1.6a**), no changes to the pattern were seen until reaching 380 K, at which point reflections corresponding to $Li_{15}Ge_4$ started to appear, consistent with the PDF *in situ* heating results. There were few additional changes to the XRD pattern with continued heating up to 480 K. Rietveld refinement analysis showed that the reflections after heating fit well to the $Li_{15}Ge_4$ structure model (**Figure D.13**) and showed a linear increase in lattice parameter from 10.8119(1) at 360 K to 10.8350(5) at 480 K. In contrast, when performing a similar heat treatment for the $Li_{3.75}Ge$ derived from α-Ge, the XRD pattern transformed from $Li_{15}Ge_4$ into a series of different reflections between 420 – 440 K (**Figure 4.1.6b**).

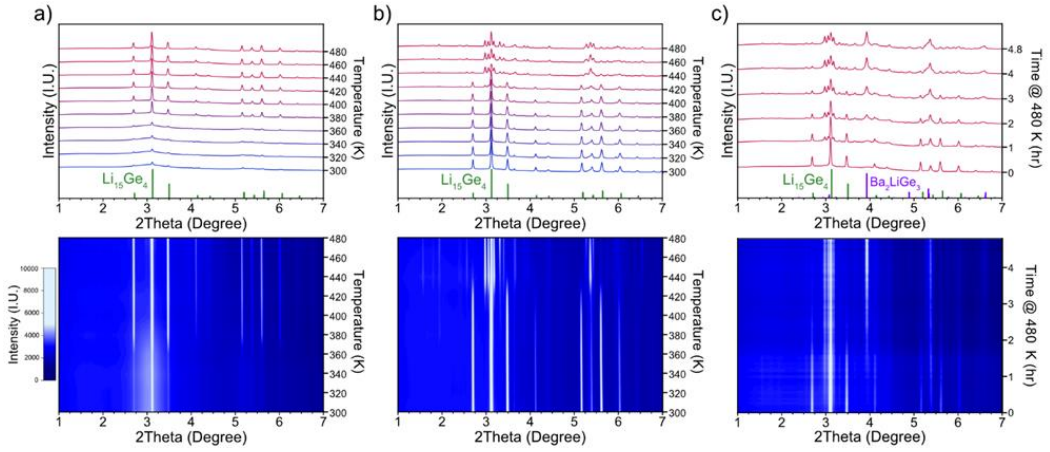

Figure 4.1.6 Synchrotron XRD results obtained during *in situ* heating (a,b) XRD patterns (top) and false colormap (bottom) obtained during heating ramp to 480 K for (a) fully lithiated Ba_8Ge_{43} ($Li_{3.75}Ba_{0.19}Ge$) and (b) fully lithiated α-Ge ($Li_{3.75}Ge$); (c) XRD pattern (top) and false colormap (bottom) of $Li_{3.75}Ba_{0.19}Ge$ during extended heating at 480 K.

To further probe the kinetics of the phase transformations in $Li_{3.75}Ba_{0.19}Ge$, the sample was held at 480 K and XRD scans were collected every 2 min. As shown in **Figure 4.1.6c**, many small reflections and a major reflection at $2\theta = 3.9°$ started to appear

with further heating as the $Li_{15}Ge_4$ reflections decreased in intensity. **Figure 4.1.7** compares the XRD patterns for $Li_{3.75}Ge$ and $Li_{3.75}Ba_{0.19}Ge$ after heating at 480 K for 6 min and 396 min (6.6 h), respectively, with identification of the reflections from crystalline phases from the literature. For the $Li_{3.75}Ba_{0.19}Ge$ sample, the $Li_{15}Ge_4$ transformed to numerous crystalline Li-Ge phases and a Li-Ba-Ge phase with extended heating at 480 K. The phases identified include: LiGe, Li_7Ge_2, Li_7Ge_3, Li_9Ge_4, $Li_{15}Ge_4$, and Ba_2LiGe_3. A plot with the reference patterns of the identified compounds is presented in **Figure D.14.** The main reflection for Ba_2LiGe_3 (at $2\theta = 3.9°$) appeared after around 2 hours and continued to grow during the 6.6 hour hold time, while the reflections from $Li_{15}Ge_4$ transformed completely into the Li-Ge phases after 4 hours. In contrast to the Ba-containing sample, the $Li_{3.75}Ge$ sample needed less heating to transform to a similar set of Li-Ge phases. From comparison to the reference patterns, the $Li_{3.75}Ge$ sample (which showed $Li_{15}Ge_4$ reflections at room temperature) appeared to transform into LiGe, Li_7Ge_2, Li_7Ge_3, and Li_9Ge_4 after the one hour heating ramp from 300 to 480 K. Notably, no reflections from Ba_2LiGe_3 were present, consistent with the presumed composition of the sample. The similar reaction products observed in both heating experiments suggest that $Li_{15}Ge_4$ decomposition underwent a similar pathway in both $Li_{3.75}Ba_{0.19}Ge$ and $Li_{3.75}Ge$ samples; however the time needed to achieve the decomposition of $Li_{15}Ge_4$ was longer for the sample derived from lithiation of the Ba_8Ge_{43} clathrate, suggesting a difference in the reaction kinetics.

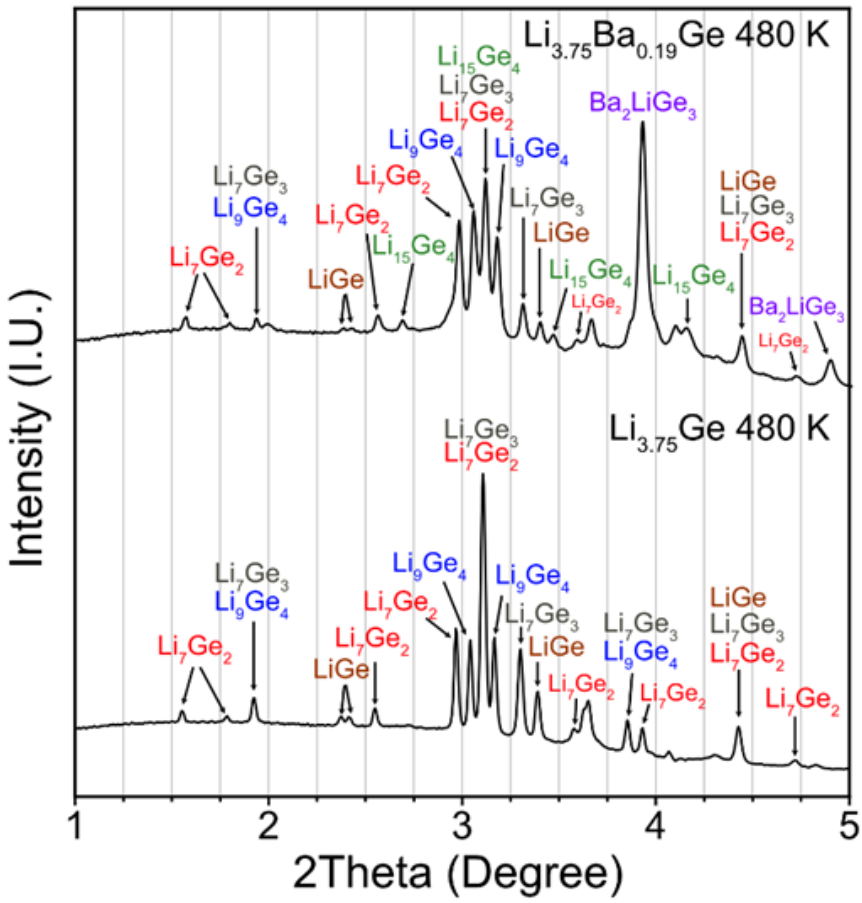

Figure 4.1.7 Synchrotron XRD patterns of $Li_{3.75}Ba_{0.19}Ge$ after heating at 480 K for 6.6 hours and $Li_{3.75}Ge$ after heating ramp to 480 K.

The thermal decomposition of $Li_{15}Ge_4$ is unexpected as it is a thermodynamically stable phase and melts congruently at 750 ºC.[230] Our results show that $Li_{15}Ge_4$ decomposed into Li-Ge dumbbell phases at 150 ºC, implying that the Li content decreased to the extent that $Li_{15}Ge_4$ was not the preferred phase. Previously, heating studies on electrochemically synthesized $Li_{15}Si_4$, which is metastable, showed that $Li_{15}Si_4$ decomposed to Li_7Si_3 and $Li_{13}Si_4$ instead of $Li_{17}Si_4$ and $Li_{13}Si_4$ as expected based on the phase diagram.[218] The authors hypothesized that reactions between Li and the solid

electrolyte interphase (SEI) at the electrode/electrolyte interphase or with the electrode binder could reduce the overall Li available in the system to react with Si. This is supported by a study showing that $Li_{15}Si_4$ synthesized via ball-milling (*i.e.*, no SEI present) decomposed into the expected products,[231] suggesting that the residual electrolyte and SEI play an important role in the thermal stability of the material. In this work, the *in situ* heating experiments were conducted in sealed capillaries made of borosilicate, which could also react with Li. However, conducting the same heat treatment using a Ta boat under argon resulted in similar XRD patterns (**Figure D.15**), suggesting that this was not a factor. We conclude that the thermal decomposition of $Li_{15}Ge_4$ at 150 ºC is likely related to reactions with SEI, binder or residual electrolyte causing a decrease in the net Li content and leading to the formation of Li-Ge dumbbell phases. Interestingly, the decomposition of $Li_{15}Ge_4$ in the clathrate-derived, Ba-containing phase takes place over a longer period of time than the decomposition of $Li_{15}Ge_4$ derived from lithiation of α-Ge, implying that the presence of Ba slows these Li-Ge phase transformations.

Considering the final state of the system after the heat treatment, the presence and crystallization of Ba_2LiGe_3 from the $Li_{3.75}Ba_{0.19}Ge$ sample indicates that the initial system was far from equilibrium. There are few reported crystalline phases in the Li-Ba-Ge system; thus, when the Ba is evenly dispersed between Li and Ge atoms in the amorphous phase, the kinetic barrier to form the set of crystalline phases with the lowest energy is high as this requires a large degree of Ba migration. In addition, the Ba_2LiGe_3 phase features hexagonal Ge rings (**Figure D.5f)** that would require Ge-Ge bond formation, which is expected to have a higher energy barrier than solely Li

rearrangements.[219] Only after 2-3 hours of heating at 480 K does the Ba and Ge have enough time to coalesce to form Ba_2LiGe_3, the presumed Ba-containing equilibrium phase at this composition.

Based on the results from the PDF, XRD, and *in situ* heating experiments, the lithiation of Ba_8Ge_{43} appears to be heavily influenced by the presence of Ba in the reaction intermediates. In contrast to the crystalline phase transformations for α-Ge, the clathrate proceeds through lithiation by formation of amorphous intermediates with local structures similar to those in Li-Ge crystalline phases. The PDF heating experiments demonstrate that the amorphous phases that form initially after lithiation have structural relationships to the Li-Ge crystalline phases, evidenced by the ease in which they undergo crystallization at low temperatures. *In situ* XRD heating experiments for the $Li_{3.75}Ba_{0.19}Ge$ and $Li_{3.75}Ge$ samples show that the $Li_{15}Ge_4$ phase that is formed either electrochemically, or by heating the amorphous Ba-containing phase, is unstable at 480 K and decomposes to other Li-Ge phases.

4.1.4. Discussion

4.1.4.1. Lithiation Mechanism of Ba_8Ge_{43}

Overall, the lithiation of Ba_8Ge_{43} is influenced by the presence of Ba in the reaction intermediates and results in an amorphous lithiation pathway. From the PDF analysis and *in situ* heating experiments, we determine that the amorphous reaction intermediates of Ba_8Ge_{43} share a local structure like that of the Li-Ge crystalline phases. Therefore, we propose that the Ba atoms act as “pillars” to prevent the bulk nucleation

and growth of Li-Ge crystalline phases during lithiation by physically separating smaller "pockets" of Li-Ge atoms with local structure similar to that in the Li-Ge phases.

Figure 4.1.8 illustrates the proposed lithiation pathway for the Ba_8Ge_{43} clathrate. Initially, the pristine clathrate has Ba atoms distributed evenly throughout the Ge cage matrix (**Figure 4.1.8a**). As Li enters the system, a two-phase reaction begins with nucleation of an amorphous phase, which is presumed to have similar composition and structure as those seen in the crystalline Li-Ge dumbbell phases. However, the long-range parallel alignment of the Ge-Ge dumbbells (see e.g., **Figure D.5a-c**) is prevented due to the presence of the Ba atoms. Therefore, the amorphous phase is proposed to consist of Ge-Ge dumbbells surrounded by Li atoms and in between Ba atoms. This is depicted in **Figure 4.1.8b**, which shows a two-phase interface between an amorphous phase (with randomly oriented Ge-Ge dumbbells) and the pristine Ba_8Ge_{43}. As more Li enters the system, the pristine clathrate continues to be consumed and is eventually completely converted to a Li-Ba-Ge amorphous phase. The exact composition is not known but our results suggest that the conversion is complete by the time the total composition reaches $Li_{2.75}Ba_{0.19}Ge$. As seen in the PDF plot of $Li_{2.75}Ba_{0.19}Ge$ (**Figure 4.1.3a**), the local order extends to ~10 Å, suggesting that the regions of Li-Ge order (indicated by the circled region in **Figure 4.1.7c**) are on this length scale. Considering that $Li_{2.75}Ba_{0.19}Ge$ sample crystallized into a structure resembling Li_7Ge_2 during the *in situ* heating measurement (**Figure 4.1.4a**), we expect that both dumbbells and isolated Ge atoms are present at this point in the lithiation.

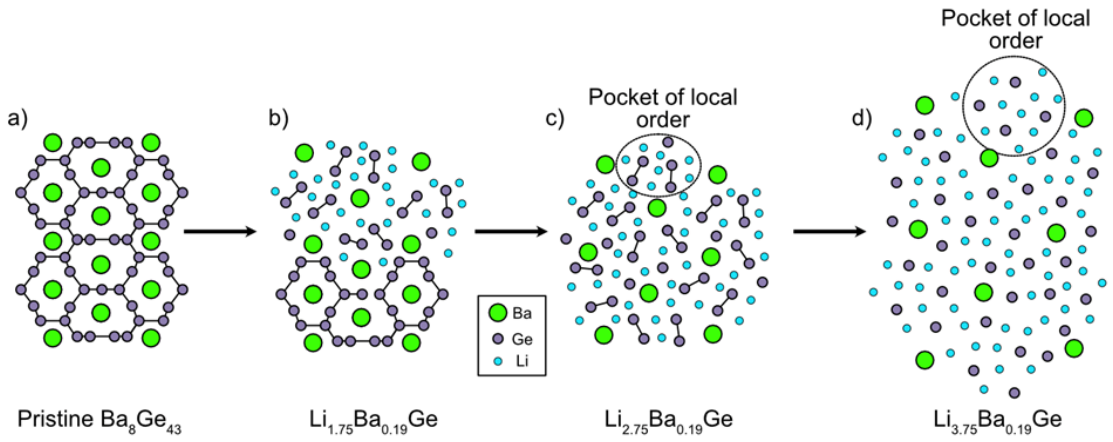

Figure 4.1.8 Proposed electrochemical lithiation mechanism of Ba_8Ge_{43}. (a) In the pristine Ba_8Ge_{43}, Ba atoms are spread periodically throughout a framework of Ge atoms. (b) Once lithiation proceeds, an amorphous phase nucleates and begins to grow at the expense of the unlithiated crystalline Ba_8Ge_{43}. (c) After about 2.75 Li per Ge are inserted, complete conversion of the Ba_8Ge_{43} has occurred, resulting in an amorphous phase composed of pockets of Li-Ge local order between Ba atoms. (d) At full lithiation, the amorphous phase is composed of pockets of Li-Ge with Ge single atoms surrounded by Li.

With the incorporation of more Li atoms, Ge-Ge dumbbells are broken up in favor of isolated Ge atoms surrounded by Li, as depicted in **Figure 4.1.8d** for the composition $Li_{3.75}Ba_{0.19}Ge$. At this composition, the local structuring extends further to ~15 Å based on the PDF analysis. This increase suggests the growth of the Li-Ge pocket of local order, which is consistent with the expected volume expansion as more Li enters the system. At this stage, the local structure is similar to that in the $Li_{15}Ge_4$ phase, which is supported by the crystallization of the amorphous phase to $Li_{15}Ge_4$ at 350 K. We note that more detailed modeling of the amorphous phases presented here would require the reverse Monte Carlo method and/or density functional theory calculations and will be reserved for future work.

We conclude that the lithiation pathway for Ba_8Ge_{43} follows an amorphous, metastable phase evolution because of the kinetic differences between the host atoms and the electroactive Li atoms. This is similar to the lithiation of α-Si, which goes through an amorphous pathway instead of crystallizing to the equilibrium Li-Si phases.[117,196] Because the Si atoms have low mobility at room temperature, phases that rely on Li movement are kinetically favorable.[32,117] Ge has higher mobility at room temperature compared to Si,[148] which accounts for why Li-Ge crystalline phases are kinetically favored to form in some circumstances. In the case of Ba_8Ge_{43}, the mobility of Ba is limited at room temperature, which kinetically traps the Ba in the amorphous phase and prevents the formation of a more thermodynamically favorable (i.e., crystalline) phase under these compositions. This conclusion is supported by the *in situ* XRD heating experiments showing the formation of Ba_2LiGe_3 after heating at 480 K for multiple hours. On the basis that the Ba_2LiGe_3 phase is more Ba dense than the Li-Ba-Ge amorphous phase formed after lithiation, a significant amount of Ba migration is needed for Ba_2LiGe_3 to form. Thus, the presence of the Ba between the Li-Ge pockets kinetically frustrates the phase landscape at room temperature, resulting in the formation of amorphous phases.

The fact that Ba_8Ge_{43} undergoes this amorphous lithiation pathway has several effects on its electrochemical profile when compared to that of α-Ge. Most notably, the voltage of the two-phase reaction for the clathrate is 0.1 V lower than that of the lithiation of α-Ge (**Figure 4.1.2**). It is well known that amorphous phases will have higher energies than crystalline phases at the same composition.[145,232,233] Because of the dependence of the chemical potential on the energy of the system,[11] the phase with a higher energy will

have a lower voltage. Considering that the local environment around Li in the Li-Ba-Ge amorphous phase is similar to that in the Li-Ge crystalline phases, it is expected that the energy will be higher for the amorphous phase, which is consistent with the lower reaction voltage seen for Ba_8Ge_{43}. The presence of Ba in the amorphous phase is expected to further increase the energy of the system due to the donation of electrons from the Ba to Ge and thus increasing the electron-density on Ge. *Ab inito* calculations would be needed to understand the contributions of these two separate effects.

In addition to the lower voltage, the lithiation of Ba_8Ge_{43} is characterized by a single voltage plateau in contrast to the two plateaus for α-Ge. Voltage plateaus originate from the presence of two phases with discreet Li compositions. However, due to the amorphous nature of the intermediates formed upon lithiation of Ba_8Ge_{43}, the crystalline Li-Ge phases typically seen during lithiation of α-Ge are no longer kinetically accessible, leading to a wider range of possible structures with variable Li content for the clathrate case. After complete conversion of Ba_8Ge_{43} to a Li-Ba-Ge amorphous phase via a two-phase reaction, the Li content in the amorphous phase is allowed to vary continuously as evidenced by the sloped voltage profile, which is indicative of a solid solution mechanism. We liken the lithiation mechanism of Ba_8Ge_{43} to be more similar to that in α-Si, which first displays a voltage plateau corresponding to a two-phase transformation between the diamond structure and a highly lithiated amorphous phase; after the full conversion of α-Si, it can be reversibly cycled between amorphous Si and amorphous Li-Si phases[34]. However, in the case of Ba_8Ge_{43}, bulk $Li_{15}Ge_4$ is not formed at the end of lithiation due to the presence of the Ba atoms impeding the long-range order of the Li-Ge pockets.

The voltage profile and corresponding PDF of $Li_{3.75}Ba_{0.19}Ge$ after delithiation both suggest that the material remains amorphous after the lithium is removed (**Figure D.7**). The voltage profile from delithiation of $Li_{15}Ge_4$ derived from micron sized α-Ge is characterized by two plateaus attributed to discreet phase transformations between $Li_{15}Ge_4$ and Li_7Ge_3 at 0.41 V and Li_7Ge_3 to amorphous Ge at 0.62 V.[213] In contrast, the delithiation of $Li_{3.75}Ba_{0.19}Ge$ shows a single broad peak at 0.3 V in the dQ/dE plot with a sloped profile, implying solid solution behavior rather than discrete phase transformations. The PDF of the fully delithiated Ba_8Ge_{43} has similar peak positions to the PDF of the pristine clathrate phase (**Figure D.7d**) suggesting that after the removal of Li, a cage-like structure is preserved in this amorphous phase. Future PDF measurements will be needed to further investigate the delithiation mechanism and how the structure evolves with further lithiation cycles.

4.1.4.2. Implication for Li-ion Battery Anodes

Our results indicate several clear differences in fundamental electrochemical and structural properties for the Ba_8Ge_{43} clathrate compared to α-Ge which could have advantages in the context of potential use-scenarios as anodes in lithium-ion batteries. It is important to note that the crystalline clathrate phase would serve as a precursor to an amorphous phase, which would remain amorphous in subsequent cycles (similar to the lithiation/delithiation of diamond Si). The first potential advantage is that lithiation of Ba_8Ge_{43} proceeds through amorphous solid solutions as opposed to crystalline phase transformations, and bulk crystallization of the thermodynamically stable $Li_{15}Ge_4$ phase is inhibited due to the presence of Ba atoms. Generally, avoiding transformations

between crystalline phases can be beneficial for cycling stability by decreasing the tendency for particle damage due to localized stresses, large volume changes, and/or crystallography-related anisotropy in the lithiation strain[14,32,117,234,235]. Future studies will be needed to understand the stress evolution and cycling stability of the amorphous Ba-Ge that forms after the first cycle.

Another benefit of the amorphous lithiation pathway is the decreased reaction voltage of ~ 0.1 V for lithiation and delithiation of Ba_8Ge_{43} compared to that for α-Ge. This voltage decrease could lead to increases to the energy density of a full cell. Ba_8Ge_{43} and α-Ge both react with a similar amounts of Li per Ge atom (**Figure 4.1.2**), suggesting that the presence of the Ba in the clathrate does not significantly hinder the electrochemical storage. The heavy Ba atoms will lower the gravimetric capacity (1025 mAh/g at $Li_{3.75}Ba_{0.19}Ge$) compared to α-Ge (1386 mAh/g at $Li_{3.75}Ge$); however we do not expect the volumetric capacity to be significantly different, suggesting that a 0.1 V decrease in reaction potential and a solid solution mechanism could be potentially attractive. In addition, we speculate that the presence of Ba could improve electronic conductivity of the amorphous phase and aid the breaking of Ge-Ge bonds during lithiation due to the excess electrons donated by the Ba.

Tetrel clathrates represent a wide design space where the materials can form with different guest atoms, frameworks and framework substitutions. Herein, we demonstrate how the presence of the Ba atoms prevent the crystallization of Li-Ge phases during electrochemical lithiation. However, there are many more possible compositions of clathrates. For example, type I Ge clathrates have been reported to form with Na,[236]

K,[237,238] Sr,[239] Rb,[240] and Cs[238] guest atoms and framework substitutions including Al,[152] Zn,[236] Cd,[238] Ga,[239] and Cu.[241] The large number of compositional and structural possibilities suggest that clathrates could act as precursors to atomically mix elements in a way that result in lithiated amorphous phases with desirable electrochemical properties. For example, substitution of Al for Ge in $Ba_8Al_yGe_{46-y}$ ($0 < y < 16$) was found to result in a decrease in reaction voltage as the amount of Al increased, with the lowest voltage observed at a composition of $Ba_8Al_{16}Ge_{30}$.[152] **Figure D.8** shows that $Ba_8Al_{16}Ge_{30}$ only required insertion of 1.9 Li to reach full lithiation at 0.06 V vs. Li/Li^+ (compared to 3.75 Li for Ba_8Ge_{43}), suggesting possible trade-offs between capacity and voltage for Al substitution. However, PDF analysis showed that $Ba_8Al_{16}Ge_{30}$ underwent an amorphization pathway similar to that seen in Ba_8Ge_{43} (**Figure D.8c**), confirming that the voltage profile corresponding to lithiation can be modified (without large changes in local structure to the resulting amorphous phase) by altering the initial clathrate structure. Future work will need to be conducted to further understand if electrochemical amorphization is unique to the Ba clathrates and which structural conditions result in amorphization.

4.1.5. Conclusions

The lithiation pathway of the type I clathrate Ba_8Ge_{43} was investigated with synchrotron PDF and XRD analysis. Based on the PDF results, Ba_8Ge_{43} proceeds through an amorphous phase transition without any detectable crystalline phases forming, although future *in situ* electrochemical studies would be needed to confirm this. Analysis of the PDFs of Ba_8Ge_{43} after lithiation show that the local order extends to ~10-15 Å with similar structural features as those in crystalline Li-Ge phases of analogous composition.

This is supported by *in situ* heating experiments showing that the amorphous Li-Ba-Ge phases crystallized into Li-Ge crystalline phases of similar composition. PDF analysis of $Ba_8Al_{16}Ge_{30}$ after lithiation showed the clathrate transformed to an amorphous phase similar to the one formed upon lithiation of Ba_8Ge_{43}, suggesting that the substitution of Ge with Al on the clathrate framework has little effect on the local structure changes during the reaction.

We propose that the amorphous pathway seen in these clathrates is caused by the presence of the Ba atoms which act as "pillars" to prevent the crystallization of the Li-Ge domains. The Ba atoms have low mobility at room temperature and are unable to reorder to the more thermodynamically favorable crystalline phases resulting in a metastable pathway where only significant Li migration is possible. The amorphous reaction mechanism results in a single-phase reaction with a decreased reaction voltage and the suppression of crystallization of Li-Ge phases which could have beneficial effects on cell performance. Characterization of the clathrate electrodes after lithiation and delithiation shows that despite the crystalline-to-amorphous transition, the local structural features of the original clathrate structure are retained after cycling. Thus, Tetrel clathrates have potential use as precursors to atomically mix elements that form an amorphous alloying phase with desirable electrochemical properties. The wide design space for clathrates provides opportunities for optimizing alloying anodes by modification of their initial structure.

4.2. Structural and Electrochemical Properties of Type VIII $Ba_8Ga_{16-\delta}Sn_{30+\delta}$ Clathrate ($\delta \approx 1$) during Lithiation

4.2.1. Introduction

Chapter 4.1 showed the used X-ray pair distribution function (PDF) analysis to evaluate the local and long range structure of the intermediates that form during room temperature lithiation of Ba_8Ge_{43} and $Ba_8Al_{16}Ge_{30}$ clathrates, which both adopt the type I structure but contain vacancies or Al atoms, respectively, on the Ge framework.[178] The PDF analysis showed that the lithiation of the clathrates proceeded through amorphous phase transformations, different from those in diamond cubic Ge (α-Ge), which often progress through crystalline phases.[120] We hypothesized that during the lithiation process, the Ba atoms act as "pillars" that kinetically prevent long-range ordering of the regions rich in Li-Ge bonding, which results in suppression of crystalline phase formation. In these regions, the amorphous Li-Ge phases showed similar local structuring to Li-Ge crystalline phases of comparable composition, which was supported by the low temperature amorphous-to-crystalline transformation observed with *in situ* PDF heating studies. Despite the destruction of the crystalline clathrate structure after lithiation, the PDF analysis showed that the cage-like local structure is preserved after delithiation. A consequence of this amorphous phase transformation is that lithium reacts via a solid-solution mechanism and at a lower voltage vs. Li/Li^+ relative to α-Ge, which are both beneficial properties for Li-ion battery anodes.

To further understand how the clathrate structure and composition affects its electrochemical reactivity with Li, herein we investigate the lithiation of the type VIII clathrate, which has a different but closely related structure than the previously investigated Ba-Ge clathrates with type I structure (**Figure 4.2.1a**). Both clathrate polymorphs can be described with the same general formula, M_8Tt_{46} (M = guest atom such as Na, Ba, *etc.*), but display different crystal chemistry.[242] The type VIII clathrate structure is described by the $I\bar{4}3m$ space group and is composed of face-sharing distorted dodecahedra (Tt_{20+3}) filled by M-atoms, and smaller empty cubic voids (**Figure 4.2.1b**).[243] This is notably different than the type I structure, which is composed of six larger tetrakaidecahedra (Tt_{24}) and two pentagonal dodecahedra (Tt_{20}) per formula unit.[210] The polyhedra of the type VIII clathrate can be described as a strongly distorted version of the perfect dodecahedra found in the type I structure.[242] Different from the Tt_{20} dodecahedra in type I clathrates, which contain only pentagonal faces, the Tt_{20+3} distorted dodecahedra in type VIII clathrates contain both pentagonal and hexagonal faces. In our previous studies, we identified Li migration through hexagonal faces as being associated with much lower energy barriers compared to migration through pentagonal faces.[179] Therefore, investigating the possibility of topotactic Li insertion through the hexagonal faces of the distorted dodecahedra in the type VIII clathrate structure is of interest. In addition, the empty voids of the type VIII structure could provide a unique access point for Li into the polyhedral network, which has previously not been investigated.

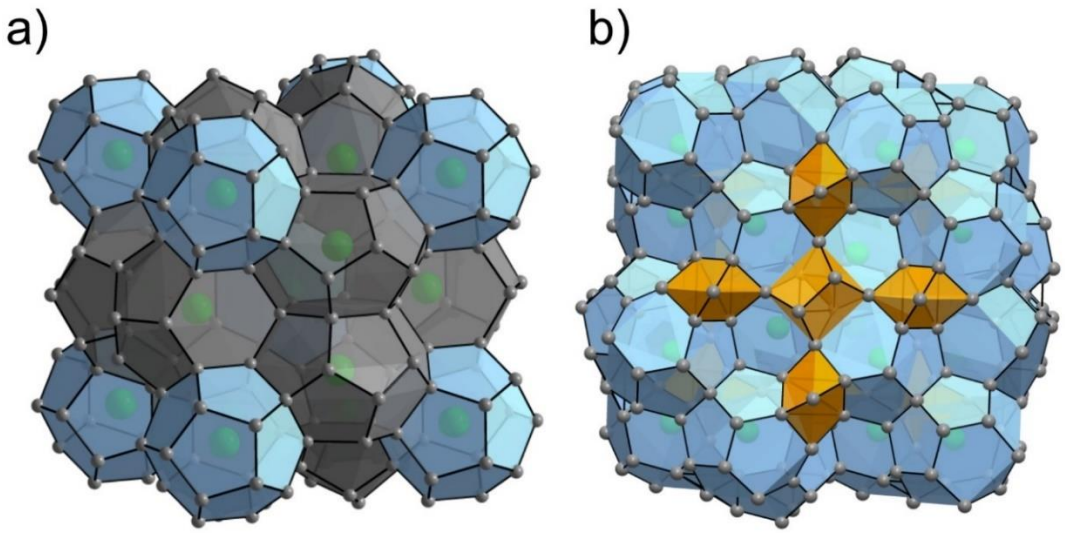

Figure 4.2.1 Crystal structures of **(a)** type I and **(b)** type VIII clathrates with general formulas M_8Tt_{46}. The grey atoms represent the *Tt* framework atoms and green atoms represent the *M* guest atoms. The dodecahedra (Tt_{20}) and distorted dodecahedra (Tt_{20+3}) are shaded in blue, the tetrakaidecahedra (Tt_{24}) in the type I structure are shaded in grey, and the cubic empty voids in the type VIII structure are shaded in orange.

Herein, we investigate the properties of type VIII clathrate $Ba_8Ga_{16-\delta}Sn_{30+\delta}$ ($\delta \approx 1$), where a partial substitution of Sn for Ga atoms occurs on all framework sites. In an extension of our previous analysis comparing the lithiation properties in type I clathrate $Ba_8Ge_{43}\square_3$ ($\square$ = vacancy) and $Ba_8Al_{16}Ge_{30}$ with those of α-Ge, herein we report a comparative study of the lithiation properties of type VIII clathrate with β-Sn. We find that the type VIII clathrate decomposes during the reaction with Li to from a highly lithiated amorphous phase, and displays electrochemical properties distinct from those formed during lithiation of the Sn and Ga elemental phases. As a result of the amorphous phase transformation, the type VIII clathrate exhibits similar capacities (~700 mAh/g), but a lower reaction voltage (0.25 V vs. Li/Li^+) compared to β-Sn (0.45 V). Most notably,

the solid-state phase transformations to binary Sn(Ga)-Li crystalline compounds with low Li content are circumvented in favor of the formation of an amorphous $Li_x(Ga,Sn)$ phase with high Li content ($x \sim 2$), suggesting that the formation of equilibrium phases is kinetically frustrated due to the presence of the Ba atoms and mixing of Sn/Ga on the framework sites. Galvanostatic cycling experiments for the type VIII clathrate and β-Sn electrodes demonstrate that the amorphous solid-solution mechanism for lithiation into the clathrate was retained after the first cycle and resulted in better capacity retention compared to the β-Sn electrodes. To assess the possibility of Li insertion into the type VIII clathrate structure prior to amorphization, DFT calculations were performed on $Ba_8Ga_{15}Sn_{31}$ and show that the Li positions are relatively high in energy, suggesting that Li insertion would not be favorable, consistent with the experimental results. The assembly of Ga and Sn into the clathrate structure with Ba guest atoms results in significantly different electrochemical behavior compared to that seen in elemental Sn and Ga, suggesting the possibility for novel alloying amorphous phases originating from clathrate precursors for anode materials.

4.2.2. Experimental and Computational Methods

The clathrate was prepared in a Sn flux using conditions that favor the type VIII over type I clathrate structure as described previously[243] and the composition was confirmed using single crystal X-ray diffraction (XRD). More details can be found in the **Appendix E**. Slurries containing the active material (type VIII clathrate or commercially obtained β-Sn powder), carbon black, and binder were prepared and coated onto copper

foil (see **Appendix E**). These composite electrodes were then lithiated galvanostatically in half-cells with lithium metal and then extracted for *ex situ* measurements. Synchrotron X-ray pair distribution (PDF) measurements were conducted at Diamond Light Source (Didcot, United Kingdom) at the I15-I dedicated PDF beamline with $\lambda = 0.161669$ Å. The atomic PDF, $G(r)$ as defined by Billinge *et al*.[220], was generated from the total scattering data using PDFgetx3 within the xPDF suite software package.[221,222] The first principles DFT calculations were performed in a similar manner to our previous work[55,152,179,244] and are described in more detail in the **Appendix E**. The Gibbs free energy change, average lithiation voltages, formation energy were calculated as described previously.[55,152,179] The climbing image nudged elastic band (NEB) method was used to calculate the Li migration barriers.[85] More detailed descriptions of the synthesis, electrochemical, synchrotron measurements, PDF analysis, and DFT calculations are in the **Appendix E**.

4.2.3. Results

Single crystal XRD analysis of the products of the flux reaction (see **Table E.1-2** for refinement and structural details) confirmed the synthesized materials adopted the type VIII clathrate crystal structure with a refined composition of $Ba_8Ga_{14.9}Sn_{31.1(1)}$; for simplicity $Ba_8Ga_{15}Sn_{31}$ is used as the composition for the subsequent electrochemical characterization. A close up view of the crystal structure of $Ba_8Ga_{15}Sn_{31}$ is shown in **Figure 4.2.2a**.

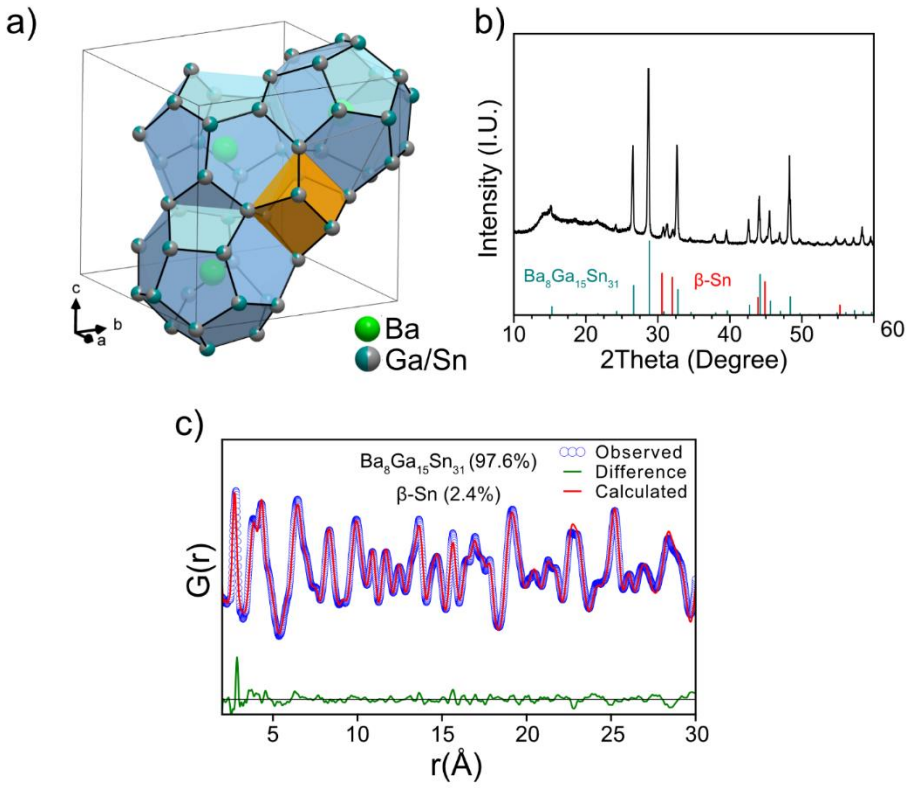

Figure 4.2.2 (a) Crystal structure of type VIII $Ba_8Ga_{15}Sn_{31}$ clathrate derived from the single crystal refinement (**Table E.1-2**). The relative fractions of gray/blue spheres represent the occupancy of Sn/Ga atoms on framework sites and the green spheres represent the Ba atoms. The distorted dodecahedra are shaded in blue while the empty void is shaded in orange. **(b)** Lab powder XRD of crushed single crystals of the clathrate sample with the simulated diffraction patterns for type VIII $Ba_8Ga_{15}Sn_{31}$ (from single crystal diffraction, **Table E.1-2**) and β-Sn. The background from $15° < 2\theta < 25°$ is from the Kapton film that was used to protect the sample from oxidation during the measurement. **(c)** PDF refinement (R_w =15.1%) of pristine $Ba_8Ga_{15}Sn_{31}$ using the structural model derived from the single crystal refinement (**Table E.1-2**). Phase fractions are in terms of mol%.

Laboratory powder XRD (PXRD) was performed on the synthesized clathrate powders obtained after crushing the single crystals. The XRD pattern (**Figure 4.2.2b**) confirms that the bulk of the sample comprised type VIII clathrate, but the pattern also contained some low intensity reflections from β-Sn, likely from residual Sn flux that was not fully removed after the synthesis. Synchrotron PDF analysis was used to quantify the amount of β-Sn impurity in the clathrate sample. The PDF refinement of the pristine

clathrate (**Figure 4.2.2c** and **Table E.3**) showed that the PDF fit the structural model derived from single crystal structural refinements presented herein (**Table E.1-2**) with a small fraction of β-Sn (2.4 mol %).

To investigate the structures of the lithiated type VIII clathrate and β-Sn, electrodes were electrochemically lithiated to similar amounts of Li per Sn/Ga and then subjected to total scattering experiments to obtain structure factor and PDF plots. Scanning electron microscopy (SEM) imaging of the electrodes prior to lithiation (**Figure E.1**) showed that the type VIII clathrate was composed of irregularly shaped particles 2 – 20 μm in size with small spherical β-Sn impurities, while the β-Sn electrode prepared for comparison was composed of 1 – 5 μm spherical particles.

The voltage profiles and corresponding dQ/dE plots of the first lithiation of β-Sn and $Ba_8Ga_{15}Sn_{31}$ are presented in **Figure 4.2.3** with blue, orange, and green points representing the compositions at which samples were collected for total scattering measurements. The voltages and capacities of the cells at these points in the lithiation process are presented in **Table E.4**. Note that the number of Li added to each electrode is normalized to the amount of Sn or (Ga + Sn) atoms in each starting compound.

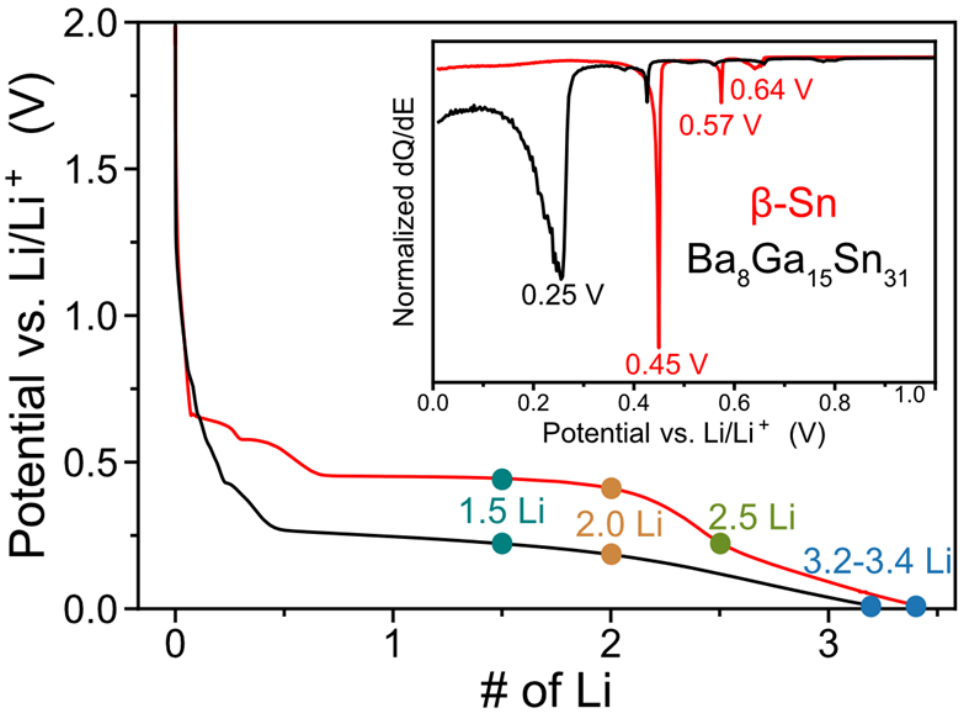

Figure 4.2.3 Voltage profile and corresponding dQ/dE plot of the lithiation of $Ba_8Ga_{15}Sn_{31}$ (black) and β-Sn (red) at 12.5 mA/g and 25 mA/g, respectively with a voltage cutoff of 10 mV vs. Li/Li^+. The blue, orange, and green circles represent the points which cells were disassembled for *ex situ* total scattering measurements. The # of Li is normalized to the amount of non-alkali/alkaline earth metal atoms.

The room temperature voltage profile of β-Sn is characterized by three voltage plateaus and then a sloped curve until reaching the cutoff voltage of 10 mV vs. Li/Li^+. The plateaus at 0.64 V and 0.57 V vs. Li/Li^+ (represented as peaks in the dQ/dE plot) have been assigned to the formation of Li_2Sn_5[245] and LiSn[246], respectively.[197,214,247–250] The plateau at 0.45 V has been previously assigned to an amorphous transition on the basis of *in situ* XRD analysis,[247,249] while an *in operando* NMR study of the lithiation of Sn nanoparticles recently assigned this plateau to the conversion of LiSn to Li_7Sn_3 and then $Li_{13}Sn_5$.[214] After the plateau at 0.45 V, the voltage profile is more sloped and reaches

a final composition of 3.4 Li per Sn, which contains less Li than the theoretical maximum based on the most Li-rich compound (previously $Li_{22}Sn_5$, but later identified as $Li_{17}Sn_4$[251]) from the Li-Sn phase diagram, but is similar to previous experimental reports.[197,250] It has been proposed that disordered $Li_{17}Sn_4$ forms in this sloped voltage region[252,253] by X-ray diffraction analysis, as well as Li_7Sn_2 via NMR measurements.[214]

The lithiation of the type VIII clathrate is characterized by a voltage plateau starting at 0.25 V (seen as a peak in the dQ/dE plot) and then a sloping profile. We assign the process occurring at 0.25 V to the lithiation of the type VIII clathrate phase. The sample reacts with around 3.2 Li per (Ga + Sn) atom, which suggests that the clathrate is being converted into a phase containing high Li content. We note that this composition is an overestimate due to the presence of β-Sn as impurity (which is identified by the small peaks from 0.40 – 0.64 V in the dQ/dE plot that match those in the β-Sn electrode). Additionally, there is likely formation of a solid electrolyte interphase (SEI) due to electrolyte reduction in the first lithiation; both of these processes are expected to consume lithium.

Structure function patterns, S(Q), derived from the total scattering patterns for the β-Sn and $Ba_8Ga_{15}Sn_{31}$ electrodes before and after lithiation are presented in **Figure 4a** and **4c**, respectively. The structure function plots allow for the observation of Bragg peaks at low scattering angles and to tentatively identify the major crystalline phases present in the sample by comparison with calculated reference patterns. To aid comparison, the plots for the lithiated electrodes are labelled at the compositions indicated by the points in **Figure 4.2.3**, *i.e.* Li_xSn (x = 1.5, 2.0, 2.5, 3.4) for the lithiated

β-Sn compositions and $Li_xBa_{0.17}Ga_{0.33}Sn_{0.67}$ (x = 1.5, 2.0, 3.2) for the lithiated clathrate compositions (Li amounts are normalized to the amount of non-alkali/alkaline earth metal atoms). **Figure 4b,d** show the structure factor patterns with the calculated reference patterns of the identified phases. For the β-Sn electrodes (**Figure 4.2.4a**), reflections corresponding to β-Sn disappear and a series of other reflections appear as the Li composition increases during lithiation. At a composition of $Li_{1.5}Sn$, reflections corresponding to LiSn ($P2/m$)[246] are present, as seen by the comparison of the calculated reference pattern with the structure function (**Figure 4.2.4b**). In the $Li_{2.0}Sn$ pattern, the reflections corresponding to LiSn ($P2/m$)[246] decrease in favor of another set of reflections that are assigned to Li_7Sn_3 ($P2_1/m$),[254] which suggests that a two-phase reaction is occurring in this part of the lithiation process. Crystal structures of LiSn and Li_7Sn_3 are shown in **Figure 4.2.4ef** and demonstrate how the Sn square units in LiSn are broken up to form Sn trimers in the Li_7Sn_3 phase. At a composition of $Li_{2.5}Sn$, the sample appears to be mainly composed of Li_7Sn_3 based on the comparison to the calculated pattern (**Figure 4.2.4b**). For the electrode with composition $Li_{3.4}Sn$, the pattern is similar to the one for $Li_{2.5}Sn$, suggesting that Li_7Sn_3 is still present, but with slight changes to some of the intensities of the reflections. Overall, the structure factor patterns confirm that the lithiation of β-Sn proceeds through highly crystalline phase transformations.

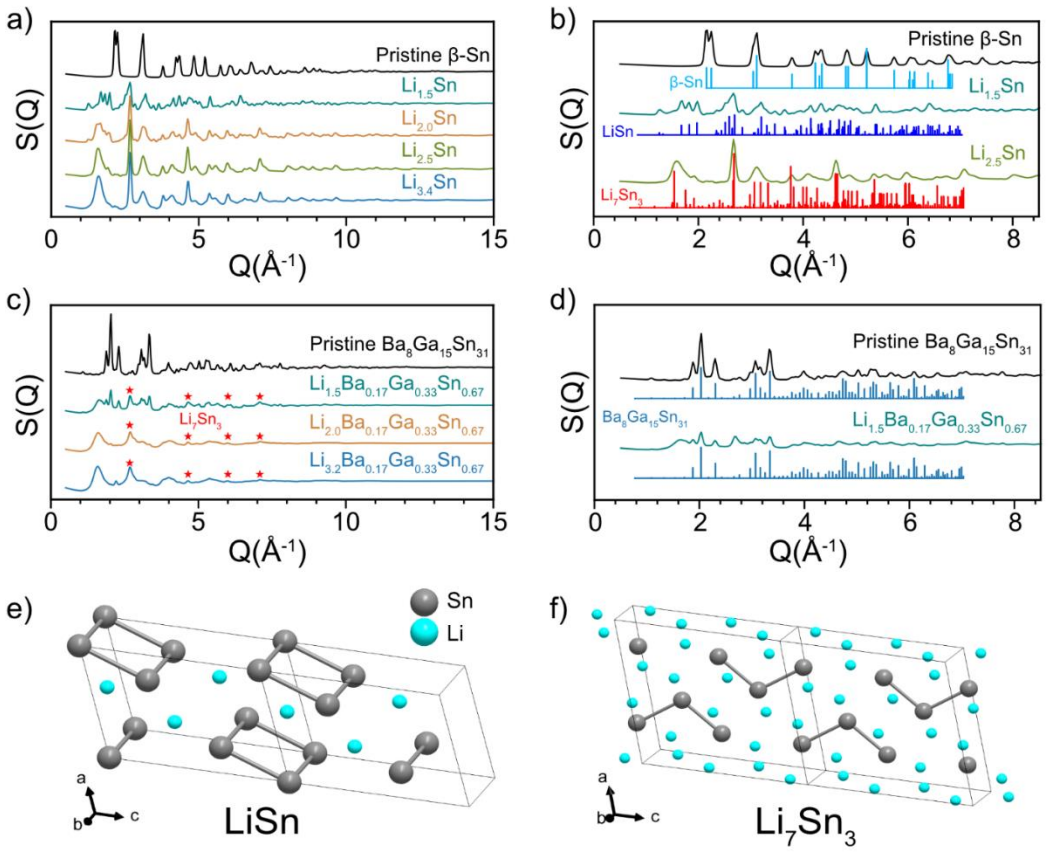

Figure 4.2.4 (a) Structure function plots for pristine β-Sn and lithiated β-Sn electrodes. **(b)** Comparison of structure function plots for β-Sn, $Li_{1.5}Sn$, and $Li_{2.5}Sn$ with calculated reference patterns for β-Sn, LiSn, and Li_7Sn_3. **(c)** Structure function plots for pristine $Ba_8Ga_{15}Sn_{31}$ and lithiated clathrate electrodes. **(d)** Comparison of structure function plots for pristine clathrate and $Li_{1.5}Ba_{0.17}Ga_{0.33}Sn_{0.67}$ with reference pattern for $Ba_8Ga_{15}Sn_{31}$ (from single crystal refinement, see **Table E.1-2**). Crystal structures of intermediate phases identified in the lithiation of β-Sn, **(e)** LiSn (from ref.[246]) and **(f)** Li_7Sn_3 (from ref.[254]).

For the structure function patterns of the type VIII clathrate (**Figure 4.2.4c**), the pristine (unlithiated) sample shows reflections matching the calculated pattern for the type VIII $Ba_8Ga_{15}Sn_{31}$ structure obtained from the single crystal refinement (**Figure 4.2.4d**), consistent with the lab PXRD results. Lithiation to a composition of $Li_{1.5}Ba_{0.17}Ga_{0.33}Sn_{0.67}$ resulted in a decrease in the intensity of reflections corresponding

to $Ba_8Ga_{15}Sn_{31}$ and the emergence of several broad peaks. No other significant reflections are present, suggesting that that the broad peaks originate from an amorphous phase. At a composition of $Li_{2.0}Ba_{0.17}Ga_{0.33}Sn_{0.67,}$ the pattern only displays the broad reflections associated with the amorphous phase and there are no significant reflections past 5 $Å^{-1}$, suggesting that the type VIII clathrate has been fully converted into the amorphous phase. Low intensity reflections (**Figure 4.2.4c**, marked as red stars) are observed that match reflections in the calculated pattern for Li_7Sn_3; the presence of these reflection is attributed to the lithiation of the β-Sn impurity phase to form Li_7Sn_3. For $Li_{3.2}Ba_{0.17}Ga_{0.33}Sn_{0.67}$, the structure function pattern is similar to the pattern for $Li_{2.0}Ba_{0.17}Ga_{0.33}Sn_{0.67}$ but with slightly shifted intensities for the broad peaks. Analysis of the structure function patterns of the intermediates formed during reaction of Li with $Ba_8Ga_{15}Sn_{31}$ suggests that lithiation proceeds through the conversion of the clathrate phase to an amorphous phase.

By taking a Fourier transform of the reduced structure functions, the total scattering data can be analyzed in real space and allows for the observation of local structural changes through the pair distribution function (PDF).[220] The PDF plot provides a weighted histogram of all atom-atom distances within a material and has been used to great effect to understand electrochemical alloying reactions.[35,120,178,213,215,216] The calculated PDF patterns for $Ba_8Ga_{15}Sn_{31}$ and Li-Sn crystalline phases discussed herein are presented in **Figure E.2** and **Figure E.3**, respectively.

Ex situ PDF plots for the lithiated β-Sn and the type VIII clathrate electrodes are presented in **Figure 4.2.5ab**. The PDF refinement for the pristine β-Sn sample fit the

structural model well, suggesting phase-pure starting material (**Figure E.4**). The PDFs of the β-Sn after lithiation were refined (**Figure E.5**, parameters in **Table E.5**) from 2 – 15 Å to LiSn, Li_7Sn_3, and Li_7Sn_2 based on the expected reaction products from the structure function plots (**Figure 4.2.4ab**) and from previously reported assignments.[197] The PDF for the electrode lithiated to a composition of $Li_{1.5}Sn$ was fit to LiSn and Li_7Sn_3, the expected products at this composition, and resulted in a relatively good fit (R_w = 15.9%) with phase fractions of 73.5 mol% LiSn and 26.5 mol% Li_7Sn_3 (**Figure E.5a**). For the $Li_{2.0}Sn$ sample, the PDF was fit to 82.8 mol% Li_7Sn_3 and 18.2 mol% LiSn with a R_w of 11.5% (**Figure E.5b**). The $Li_{2.5}Sn$ pattern was fit well by considering Li_7Sn_3 as the sole phase (R_w = 13.9%, **Figure E.5c**), while the $Li_{3.4}Sn$ PDF was fit well to a mixture of 52.6 mol% Li_7Sn_3 and 47.4 mol% Li_7Sn_2 (R_w = 19.9%, **Figure E.5d**). Interestingly, when the fit range was increased to 30 Å, the fit was worse for PDFs containing Li_7Sn_3 (see **Figure E.5e**), with the high-r correlations from 20 – 30 Å not captured well by the Li_7Sn_3 model. Other studies showed that Li_7Sn_3 synthesized via ball-milling and annealing showed a good fit of the PDF to the Li_7Sn_3 structure from 2 – 30 Å[213], suggesting that the deviation from the Li_7Sn_3 structural model observed in our results (**Figure E.5e**) might be related to the electrochemical formation of Li_7Sn_3 at room temperature. Overall, the PDF analysis shows that the lithiation of β-Sn proceeds through crystalline phase transformations in which the Sn clusters in LiSn (**Figure 4.2.4e**) are transformed into smaller units until Sn dumbbells/trimers and single Sn atoms surrounded by Li atoms (as seen in Li_7Sn_3 and Li_7Sn_2, see **Figure 4.2.4f** and **Figure E.5f,** respectively) are the dominant features present at the end of lithiation.

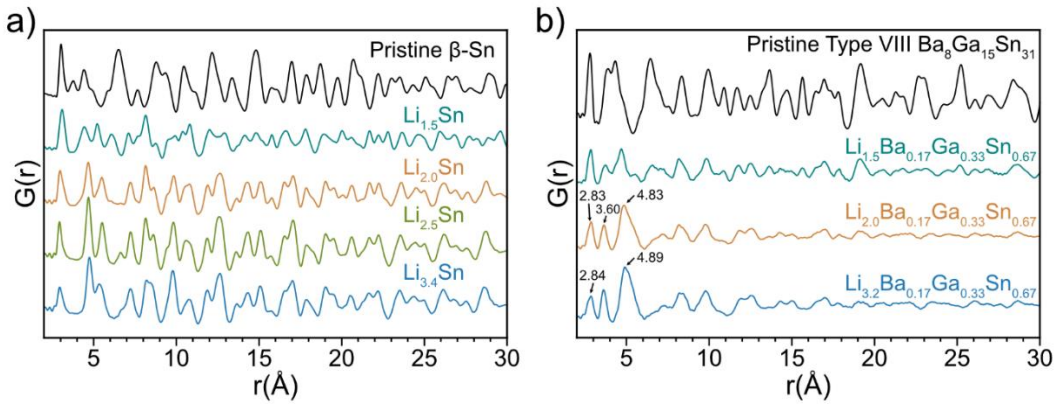

Figure 4.2.5 (a) *Ex situ* X-ray PDFs for pristine β-Sn, $Li_{1.5}Sn$, $Li_{2.0}Sn$, $Li_{2.5}Sn$ and $Li_{3.4}Sn$. **(b)** *Ex situ* X-ray PDFs for pristine $Ba_8Ga_{15}Sn_{31}$, $Li_{1.5}Ba_{0.17}Ga_{0.33}Sn_{0.67}$, $Li_{2.0}Ba_{0.17}Ga_{0.33}Sn_{0.67}$, and $Li_{3.2}Ba_{0.17}Ga_{0.33}Sn_{0.67}$.

In the case of the clathrate samples, since the intensity of X-ray PDF correlations is dependent on the atomic number of the elements, the Sn atomic correlations are expected to contribute the most to the observed PDF patterns. The higher contribution of the Sn–Sn and Sn–Ga correlations to the total PDF pattern for $Ba_8Ga_{15}Sn_{31}$ can be readily seen in the calculated pattern in **Figure E.2**. Inspection of this PDF shows that the first, second, and third correlations in the total PDF pattern correspond to direct Sn/Ga–Sn/Ga bonding, Ba–Sn/Ga distances, and next-nearest neighbor Sn/Ga distances, respectively. The PDF results for the lithiation of the type VIII $Ba_8Ga_{15}Sn_{31}$ (**Figure 4.2.5b**) show that lithiation of the clathrate results in PDFs with decreased intensities and significant shifts in the correlations, which is indicative of phase transformations. Refinement of the PDF from $Li_{1.5}Ba_{0.17}Ga_{0.33}Sn_{0.67}$ showed that correlations corresponding to the pristine type VIII clathrate are still present, but the refinement could not capture all of the correlations at high-r values (10 – 30 Å) (**Figure E.6a**). Adding Li_7Sn_3 to the refinement as a second phase results in a better fit with 30.6 mol% clathrate and 69.4 mol % Li_7Sn_3 (**Figure**

E.6b, Table E.6). We attribute the presence of Li_7Sn_3 to originate from the lithiation of the β-Sn impurity in the clathrate sample. Li_7Sn_3 was chosen as a second phase for the refinement because it is the expected product from the lithiation of β-Sn at the voltage of this particular electrode (0.17 V); furthermore, the Bragg peaks in the structure factor pattern of this sample showed reflections from both the clathrate and Li_7Sn_3 structures (**Figure 4.2.4c**). After fitting the PDF pattern to the clathrate and Li_7Sn_3 phases, three peaks appear in the difference plot at r values of 2.88, 3.60, and 4.70 Å (**Figure E.6b**). We attribute the origins of these correlations to the lithiated amorphous phase that forms when lithium reacts with the clathrate. This result is similar to our previous PDF analysis of type I clathrate Ba_8Ge_{43} after lithiation, where a similar treatment of the refinement revealed an amorphous phase with three peaks at low-r values in the difference plot.[178] Based on the similar result and absence of other Bragg peaks appearing in the structure factor pattern (**Figure 4.2.4c**), we attribute the peaks in the difference plot to an amorphous Li-Ba-Ga-Sn phase that coexists with the pristine (unlithiated) clathrate phase at this stage of the lithiation process.

Further lithiation of the type VIII clathrate to a composition of $Li_{2.0}Ba_{0.17}Ga_{0.33}Sn_{0.67}$ resulted in further decreases in the intensity of the high-r correlations ($10 < r < 30$ Å), suggesting the complete conversion of the crystalline $Ba_8Ga_{15}Sn_{31}$ by this point, consistent with the structure factor plots (**Figure 4.2.4c**). At low-r values ($2 < r < 5$ Å), three main correlations are present at 2.83, 3.60, and 4.83 Å. These correlations are at similar distances to those attributed to the amorphous phase in the PDF for $Li_{1.5}Ba_{0.17}Ga_{0.33}Sn_{0.67}$ (**Figure E.6b**), suggesting that the amorphous phase continues to grow at the expense of the pristine clathrate phase. The low intensity of

correlations past 15 Å indicates the absence of long-range order in the sample, consistent with the broad peaks in the structure factor pattern (**Figure 4.2.4c**). Further lithiation to $Li_{3.2}Ba_{0.17}Ga_{0.33}Sn_{0.67}$ shows a similar PDF pattern as the one for $Li_{2.0}Ba_{0.17}Ga_{0.33}Sn_{0.67}$, but the first correlation at 2.84 Å has a lower intensity relative to the correlation at 4.89 Å, an indication that Sn/Ga-Sn/Ga bonds are being broken to form more Sn/Ga single atoms. Furthermore, the presence of low intensity correlations from 15 – 30 Å in both PDF patterns suggests the presence of small amount of crystalline phase; we attribute this to possible Li-Sn crystalline phases formed from the reaction of the β-Sn impurity present in the clathrate starting material as described previously.

From these results, it appears that the Li-Sn crystalline phases that form upon lithiation of the β-Sn impurity contribute substantially to the PDF of the lithiated clathrate electrode, especially at high r values. To better elucidate the local structure of the amorphous phases formed upon lithiation of the clathrate, the contribution of the residual crystalline Li-Sn compounds was removed by subtracting the appropriate experimental Li_xSn PDF from the PDFs of the lithiated clathrates. The results of this process are shown in **Figure 4.2.6a**. For the PDF of $Li_{2.0}Ba_{0.17}Ga_{0.33}Sn_{0.67,}$ the subtraction was performed using the PDF taken from the $Li_{2.5}Sn$ electrode because both cells were lithiated to a similar voltage (**Table E.4**). The experimental PDF was scaled to fit over the high-r correlations and then subtracted from the clathrate PDF. The correlations from the experimental $Li_{2.5}Sn$ PDF, which was refined to 100% Li_7Sn_3 (**Figure E.5c**), matched the high-r correlations of the type VIII clathrate well, as seen by the low intensity in the difference curve from 15 < r < 30 Å (**Figure 4.2.6a**). A similar process was conducted for the PDF of $Li_{3.2}Ba_{0.17}Ga_{0.33}Sn_{0.67}$ but using subtraction of the PDF from $Li_{3.4}Sn$. Attempts

were made to refine the experimental patterns of $Li_{2.0}Ba_{0.17}Ga_{0.33}Sn_{0.67}$ and $Li_{3.2}Ba_{0.17}Ga_{0.33}Sn_{0.67}$ to the structure of Li_7Sn_3 (**Figure E.6cd**). The results showed a similar difference plot from 2 – 10 Å as the ones shown in **Figure 4.2.6a**, but the high-r (20 – 30 Å) correlations were not fit as well, consistent with the poor fit to Li_7Sn_3 observed in the refinement of the $Li_{2.5}Sn$ PDF from 20 – 30 Å (**Figure E.5e**). The contributions from the impurity Li-Sn crystalline phases were dominant in the PDF above 6 Å and by subtracting them from the clathrate PDFs, it gives a clearer picture of the features originating from the lithiated amorphous phase formed upon reaction of lithium with the clathrate.

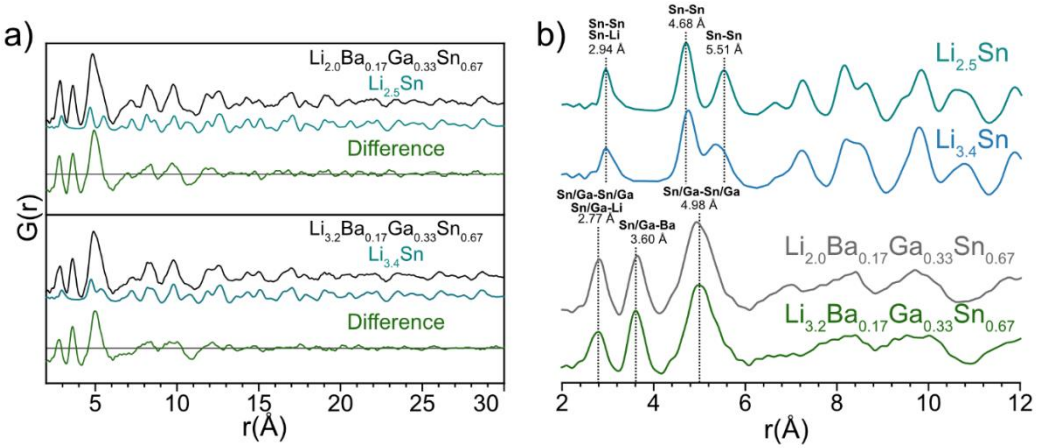

Figure 4.2.6 (a) Subtracting the Li-Sn impurity crystalline phase from the amorphous clathrate PDF. **(b)** Comparison between the lithiated PDFs of β-Sn and the type VIII clathrate. From the refinements, $Li_{2.5}Sn$ was determined to contain Li_7Sn_3, while $Li_{3.4}Sn$ contained a mixture of Li_7Sn_3 and Li_7Sn_2.

In **Figure 4.2.6b**, the PDF patterns for the β-Sn and type VIII clathrate samples after lithiation are compared. The lowest r-values are at 2.94 and 2.77 Å, respectively. In many binary Li-Sn compounds, the first correlation is a combination of direct Sn–Sn bonding and Li–Sn correlations (**Figure E.3**). The Sn–Sn bond length in Li_7Sn_3 and

Li_7Sn_2 is 3.00 Å and 2.95 Å, respectively, which matches the correlation at 2.94 Å and is slightly shorter than the Sn–Sn bond length in β-Sn of 3.11 Å. In comparison, the first correlation seen in the lithiated clathrate with composition of $Li_{3.2}Ba_{0.17}Ga_{0.33}Sn_{0.67}$ (2.77 Å) is much shorter than the first correlation distances in β-Sn, Li_7Sn_3, and Li_7Sn_2 while slightly larger than the Sn–Ga bond length in the pristine type VIII clathrate structure (2.642–2.764 Å).[171] This suggests that the Ga atoms are participating in bonding with Sn in the amorphous lithiated phase and thus results in a lower average bond length when compared to pure Sn–Sn bonding. The next correlation occurs at 3.60 Å for the clathrate derived lithiated phases, which is similar to the Ba–Ga/Sn distances in the pristine clathrate phase (3.632–3.852 Å).[171] The absence of this peak in the PDFs of the Li-Sn reference compounds (**Figure E.3**) as well as the lithiated β-Sn samples confirms that it is associated with Ba–Ga/Sn correlations. This Ba correlation is also notably similar to the Ba–Ge distance (3.44 Å) we observed previously in the PDFs of amorphous Li-Ba-Ge phases formed after lithiation of type I Ba-Ge clathrates.[178] The correlations at 4.68 and 5.51 Å in the $Li_{2.5}Sn$ PDF are associated with two different next-nearest neighbor Sn–Sn correlations in the Li_7Sn_3 phase (**Figure E.3b**). In the clathrate sample, a single correlation is centered at 4.98 Å. The splitting of this peak into two correlations is a consequence of the parallel alignment of two different next-nearest neighbor distances of Sn–Sn units (Sn trimers in the case of Li_7Sn_3, see **Figure 4.2.4f** and **Figure E.7**), while it becomes a single peak as the amount of isolated Sn atoms increases (as in Li_7Sn_2, see **Figure E.3c** and **Figure E.5f**). The peak at 4.98 Å for the clathrate sample is expected to correspond to a similar type of next nearest neighbor correlation; however, the peak is not split which could be due to disorder between Sn/Ga–Sn/Ga units in the amorphous phase

or the presence of more isolated single atoms. We note that this single peak at 4.98 Å is a feature similar to one observed in the PDFs of amorphous lithiated Ba_8Ge_{43}[178] and in lithiated nanoparticles of amorphous Ge and has been attributed to the absence of parallel alignment of adjacent dumbells.[213] Another notable feature in the PDFs for both β-Sn and the clathrate materials is the decrease in intensity of the first correlation (2.7 – 2.9 Å) relative to the correlations from 4.7 – 5.2 Å as the Li content increases. This behavior is indicative of a breaking of direct Sn/Ga bonds resulting in more isolated Sn/Ga atoms surrounded by Li, which manifests as a single peak around 5 Å. This is seen in the PDF of $Li_{3.4}Sn$ (**Figure 4.2.5a**) where instead of completely two split peaks (as seen in $Li_{2.5}Sn$ at 4.68 and 5.51 Å), these correlations are starting to merge, which is an indication that the Sn trimers are being broken up in favor of single Sn atoms. Since a similar trend is observed for the clathrate sample, we suspect that Sn/Ga–Sn/Ga bonds are being broken in an analogous manner albeit via a more disordered arrangement.

Finally, after the subtraction of the Li-Sn contribution to the PDF pattern, broad peaks at around 6 – 12 Å are present in the PDFs of the lithiated clathrate electrodes at similar positions to the correlations in the PDFs of the Li-Sn compounds, suggesting the presence of analogous but disordered structures in the amorphous phases. We made a similar observation when comparing the PDFs of crystalline Li-Ge binary compounds with those of amorphous phases formed after lithiation of Ba_8Ge_{43} in our previous work.[178] There we found from PDFs taken during *in situ* heating at 420 – 450 K that the amorphous lithiated Ba_8Ge_{43} phases crystallized into binary Li-Ge phases. With *in situ* PDF, we demonstrated that the broad correlations from 6 – 10 Å in the amorphous sample were disordered analogues of similar correlations in the crystalline Li-Ge phases.

We performed *in situ* PDF heating experiments from 300 – 420 K (**Figure E.8**) of the amorphous $Li_{3.2}Ba_{0.17}Ga_{0.33}Sn_{0.67}$, but no significant crystallization events were observed over this temperature range, possibly due to the need for a higher temperature or the complication of Ga being present. Overall, the PDF results show that the local structure of the amorphous Li-Ba-Ga-Sn phase have similarities to those in the crystalline Li-Sn phases. The main difference of the structures is the lack of long-range order and the presence of the Ba–Ga/Sn peak at 3.60 Å, suggesting that the Ba atoms are intermixed between regions of Li–Ga/Sn.

Next, the effect of different lithiation mechanisms on cycling performance for β-Sn and the type VIII clathrate are compared. **Figure 4.2.7** shows the voltage profiles, capacity, and Coulombic efficiency (CE) for the two materials for 10 cycles. For β-Sn, the cycling performance is quite poor with a first cycle CE of 55% and low capacity retention, with loss of almost all of the initial capacity by the third cycle. In contrast, the type VIII $Ba_8Ga_{15}Sn_{31}$ clathrate shows much better cycling and CE over the 10 cycles. For the clathrate electrode, the capacity begins at 670 mAh/g and decreases to 75 mAh/g after the 30^{th} cycle while the CE begins at 75% and then stabilized greater than 95% for the remaining cycles (**Figure E.9**). While detailed investigation of electrolyte reduction processes on the type VIII clathrate surface is out of scope for this work, low CE and insufficiently passivating solid electrolyte interphases (SEI) have been observed before in type I silicon clathrate electrodes[106,180] and may also be the case for the Sn clathrate. We expect, however, that optimization of the electrolyte and electrode construction will allow these materials to have better cycling performance to be competitive with other alloying anode materials.

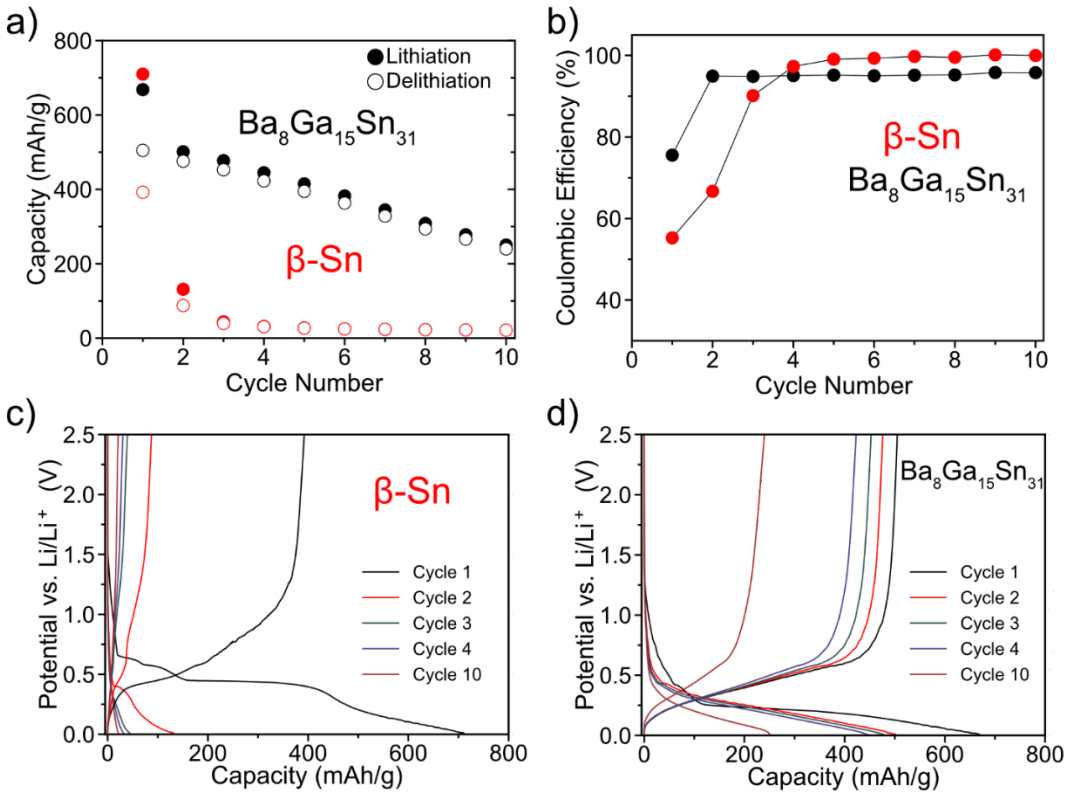

Figure 4.2.7 (a) Capacity and **(b)** Coulombic efficiency vs. cycle number for β-Sn and type VIII $Ba_8Ga_{15}Sn_{31}$ clathrate electrodes in half-cells cycled at 12.5 mAh/g with a voltage range of 0.01 – 2.5 V vs. Li/Li^+. Voltage profiles for **(c)** β-Sn and **(d)** type VIII $Ba_8Ga_{15}Sn_{31}$ clathrate.

The voltage profile for the first cycle of β-Sn (**Figure 4.2.7c**) shows the characteristic plateaus described by crystalline phase transformations during lithiation as described before. However, during the first delithiation, the voltage profile shows a more sloped profile as well as a lower capacity, resulting in a low CE. Based on the low capacity in subsequent cycles, we presume that the capacity fade originates from electronic disconnection of the β-Sn particles from the current collector due to volume contraction of Li_xSn during the first delithiation. Previously, an *in operando* NMR study showed that the capacity fade of Sn nanoparticles originated from the disconnection of

Li_7Sn_3 during delithiation;[214] we expect this effect to be exacerbated in our case due to the use of larger sized Sn particles. In contrast, the type VIII clathrate shows a more reversible voltage profile with much better cycling stability, despite the larger particle size (**Figure E.1**). The voltage profile of the first delithiation shows a gradually sloped profile from 0.01 – 0.60 V vs. Li/Li^+ with a much higher CE of 75%. In the second cycle, the lithiation curve shows a sloped profile ranging from 0.45 – 0.01 V vs. Li/Li^+ cutoff that mirrors the delithiation profile. In subsequent cycles, the electrode appears to be following the same reaction path due to the similar shape of the voltage profiles, suggesting that after the amorphization of the clathrate in the first cycle, the resulting amorphous phase cycles reversibly. There is still notable capacity fade during electrochemical cycling of the clathrate electrode, which could be due to volume expansion or unstable SEI formation.

Since both electrodes were prepared similarly, the difference in cycling behavior is attributed to differences in the properties of the β-Sn and clathrate active materials. We attribute the better electrochemical performance of the clathrate phase to the amorphous structural transformation. After the $Ba_8Ga_{15}Sn_{31}$ is converted into an amorphous lithiated phase in the first cycle, subsequent delithiation and lithiation cycles go through solely amorphous solid-solutions, which are known to reduce the stress[32,117,235] experienced by the electrode during lithiation and delithiation, resulting in higher cycling stabilities.

The aforementioned electrochemical and structural analysis showed that the lithiation process of the type VIII clathrate could be described as a conversion/alloying reaction to an amorphous phase. To assess the possibility of Li insertion into the type

VIII $Ba_8Ga_{15}Sn_{31}$ structure prior to electrochemical amorphization, we performed DFT calculations to evaluate the Li site energies and migration barriers between possible Li positions. The type VIII structure is comprised of hexagonal-face containing polyhedra, which are potentially favorable structural features for Li insertion based on our previous calculations and experiments,[55,152,179,244] as well as empty voids, which could potentially serve as access points for Li to enter the larger polyhedra. To evaluate the energetic favorability of Li insertion, the Gibbs free energy of reaction (ΔG_r) was calculated for several Li positions where a negative ΔG_r represents a favorable reaction relative to the unlithiated $Ba_8Ga_{15}Sn_{31}$ and Li metal. The pristine clathrate was calculated using the experimental type VIII $Ba_8Ga_{15}Sn_{31}$ unit cell; the Ga substitutions on Sn sites were determined by the occupancy fraction derived from the single crystal refinement while minimizing Ga–Ga bonds. The resulting structure has a lattice parameter of 11.838 Å (experimental = 11.588 Å) and a formation energy of –0.179 eV/atom. The hypothetical type VIII Ba_8Sn_{46} structure was also computed and resulted in a much higher formation energy of –0.051 eV/atom, demonstrating how the framework substitution of Ga stabilizes the structure. Then, single Li atoms were placed in the $Ba_8Ga_{15}Sn_{31}$ lattice and relaxed to find the local minimum positions for $LiBa_8Ga_{15}Sn_{31}$. Four Li positions were determined as local minima based on this procedure and are shown in the pristine structure in **Figure 4.2.8ab** which displays a cubic void (shaded orange) connected to the distorted dodecahedra (shaded light blue).

Li position 1 represents Li in the center of the void which forms in between the distorted dodecahedra (as shown more clearly in **Figure 4.2.1b** and **Figure 4.2.2a**). The Gibbs free energy of reaction (ΔG_r) of this position is shown in **Figure 4.2.8c** as Li

position “1” with a value of 0.62 eV, suggesting that this position does not result in a favorable reaction. Observation of the Li distances between the unrelaxed (Li–Sn/Ga = 2.22 Å) and relaxed structures (Li–Sn/Ga = 2.54 Å) suggests that the high energy originates from the expansion of the void to maintain acceptable Li–Sn/Ga distances, resulting in significant disturbance of the surrounding Sn/Ge framework. Due to the positive ΔG_r of this position, we conclude that the voids in the type VIII structure are too small to be occupied by Li.

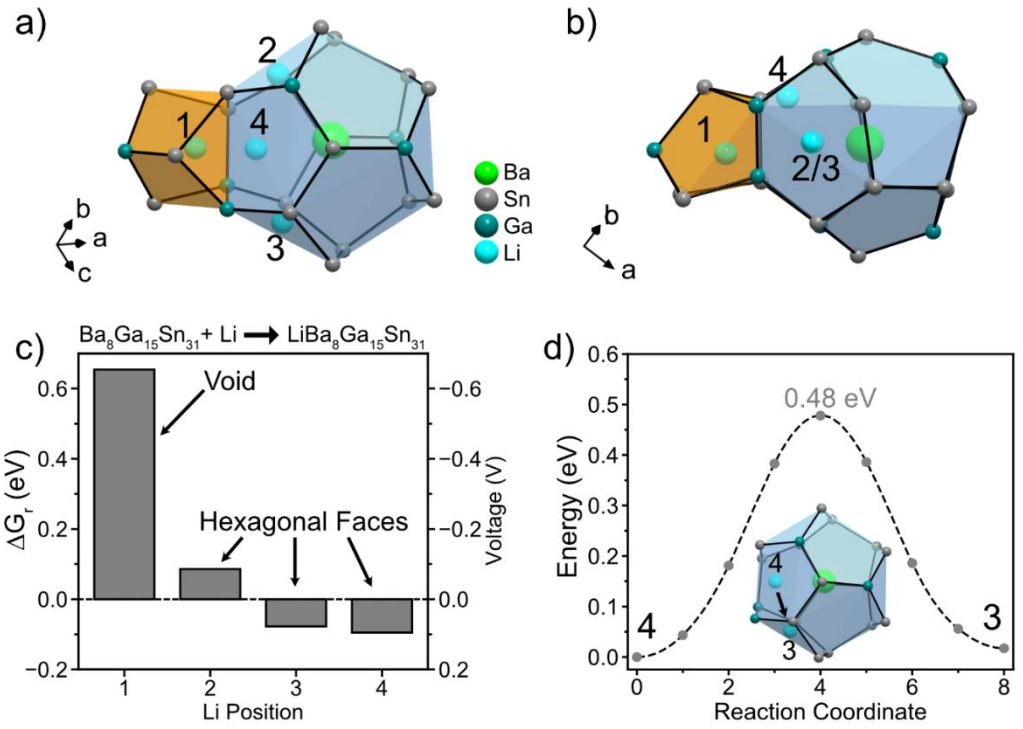

Figure 4.2.8 (a,b) Schematics of an empty void (orange) connected to a distorted dodecahedra (blue) in the calculated type VIII $Ba_8Ga_{15}Sn_{31}$ structure with investigated Li positions viewed in two perpendicular directions and labelled 1-4. **(c)** Gibbs free energy of reaction (ΔG_r) for the reaction $Ba_8Ga_{15}Sn_{31}$ + Li → Li $Ba_8Ga_{15}Sn_{31}$ for each different Li position. The corresponding potential (V vs. Li/Li^+) is shown on the right axis. **(d)** NEB-calculated minimum energy paths for migration of Li (cyan) between positions 4 and 3 in the distorted dodecahedra.

In our previous studies, we identified hexagonal faces as important features for Li to coordinate to or migrate through.[179,244] In particular, for the guest-free, type I Sn clathrate (Sn_{46}), the center of the hexagonal face was determined as a favorable Li position. Due to large size of the hexagon comprised of Sn atoms,[179] appropriate Li–Sn distances (2.7-2.8 Å) can be maintained. Therefore, we chose to investigate the Li positions in the center of the Sn/Ga hexagonal faces in the distorted dodecahedra in the type VIII structure. The energies of the hexagonal face positions are represented by positions 2 and 3; the two positions are distinct because of the different positioning of the adjacent Ga atoms in the hexagonal face (*i.e.*, Position 2 has two Ga atoms on opposite sides of the hexagonal face, while Position 3 has two Ga bonded together next to the void). The ΔG_r for Li in these positions are +0.06 and –0.087 eV, respectively, suggesting that the local positions of the Ga atoms in the hexagon affect the Li site energy. These energies are lower than if Li was placed in the void (Position 1), but higher than Li insertion into the Sn_{46} hexagon (–0.30 eV).[179] After relaxation, there is a slight rearrangement of the hexagonal face and the Ba atom in the adjacent cage is perturbed from its original position, suggesting that these disturbances might be the origin of the higher relative energy. Position 4 is also close to a hexagonal face, but this hexagonal face is distorted because part of it forms the empty void. Similar to Position 3, this position has a Gibbs free energy of reaction (ΔG_r) of –0.093 eV, suggesting that the hexagonal-like faces have similar energies for Li insertion.

Next, climbing image nudged elastic band (NEB) calculations were used to estimate the Li migration barrier between adjacent Li positions within the distorted dodecahedra. The NEB energy reaction path between position 4 and 3 is presented in

Figure 4.2.8d with the inset showing the beginning and ending Li positions in the cage. The pathway for the migration involves Li moving along the side of the cage while the Ba atom in the cage moves slightly to maintain its distance from the migrating Li atom. This pathway results in a barrier of 0.48 eV which is reasonable for room temperature diffusion, suggesting that Li migration could be feasible within the structure between the two hexagonal faces of the distorted dodecahedra.

The DFT results suggest that Li insertion is energetically feasible as it predicts Li insertion positions with negative Gibbs free energy (positive voltage vs. Li/Li^+) with a reasonable migration barrier (0.48 eV) for bulk diffusion. However, whether this process is seen experimentally depends on competing reactions that can occur in a similar voltage range. Since the potential for the alloying reaction of $Ba_8Ga_{15}Sn_{31}$ to form the Li-rich amorphous phase is at 0.25 V vs. Li/Li^+ (**Figure 4.2.3**), we do not expect Li insertion into the clathrate lattice to occur since this is a higher voltage reaction compared to the insertion reactions (*e.g.*, Li insertion into Position 3 or 4 at ~0.10 V vs. Li/Li^+ per **Figure 4.2.8c**) as the Li content increases. We attribute the relatively high Li site energies in the $Ba_8Ga_{15}Sn_{31}$ structure to the presence of the Ba guest atoms since our previous calculations showed that guest-free Sn clathrate (Sn_{46}) has a favorable Li site energy of –0.30 eV. To accommodate the Li atom, the Ba atoms move from their favorable positions in the center of the dodecahedral cages, which incurs an energetic cost to the system and results in a higher energy Li position compared to if the Ba was not present. If guest-free type VIII structures could be obtained, they would be particularly interesting for insertion electrodes due to large amount of hexagonal faces in the polyhedra. Unfortunately, there

have been few reports of Tetrel clathrates forming with the type VIII structure, all which have full guest atom occupancy.[255–257]

4.2.4. Discussion

4.2.4.1. Comparison of the lithiation mechanisms of Ba_8Ge_{43} and $Ba_8Ga_{15}Sn_{31}$

The structural transformation of the type VIII clathrate $Ba_8Ga_{15}Sn_{31}$ during lithiation is very similar to those observed in our study on type I Ge clathrates[178]. To illustrate this, the voltage profiles, dQ/dE plots, and PDFs of the fully lithiated structures of $Ba_8Ga_{15}Sn_{31}$ and Ba_8Ge_{43} are presented in **Figure 4.2.9**. Both clathrate voltage profiles show a plateau (seen as a large peak in the dQ/dE plot) followed by a sloped region until the end of lithiation. This shape of voltage profile suggests that upon lithiation, the clathrate phase undergoes a two-phase reaction to form a lithiated amorphous phase, which is further lithiated via a solid-solution mechanism. The PDFs of the fully lithiated amorphous phases derived from Ba_8Ge_{43} and $Ba_8Ga_{15}Sn_{31}$ show similar peak shapes and positions up to 15 Å, with the peaks for $Li_{3.2}Ba_{0.17}Ga_{0.33}Sn_{0.67}$ shifted to slightly higher r-values due to the longer bond lengths of Ga and Sn atoms.

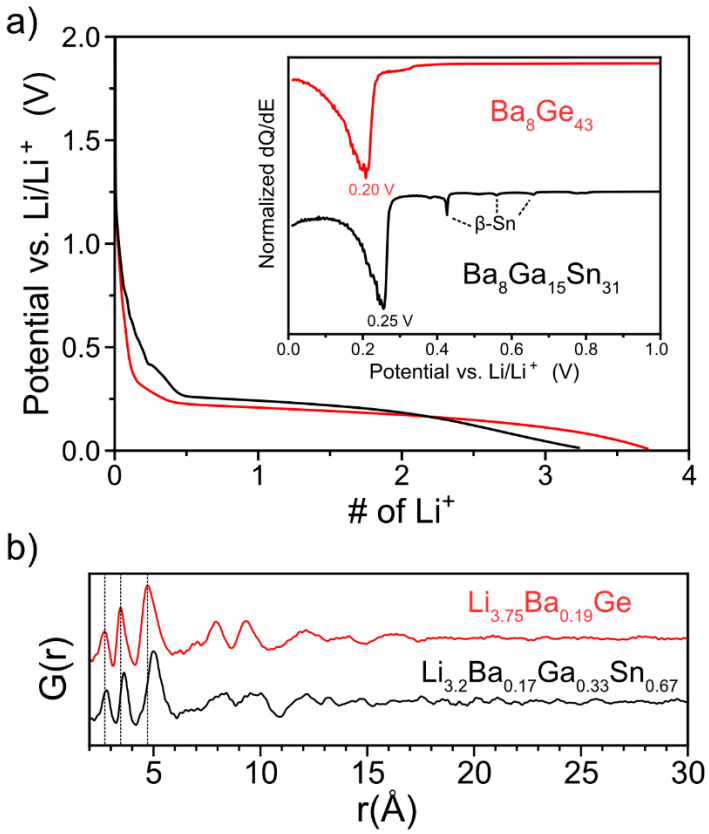

Figure 4.2.9 (a) Voltage plot for Ba_8Ge_{43} and $Ba_8Ga_{15}Sn_{31}$ and corresponding dQ/dE plots. **(b)** Comparison of the PDFs of the most lithiated phases of the Ba_8Ge_{43} clathrate and the $Ba_8Ga_{15}Sn_{31}$ clathrate. The compositions are normalized to the amount of non-alkali/alkaline earth metal atoms. The data for Ba_8Ge_{43} are reproduced from ref.[178].

The close similarity of the structures and reaction mechanisms for Ba_8Ge_{43} and $Ba_8Ga_{15}Sn_{31}$ during lithiation reveals several important characteristics for the lithiation of Ba-filled clathrates. First, the composition and local structure of the clathrate seems to be more important for the Li alloying reaction rather than the initial crystal structure. While the Ba_8Ge_{43} clathrate is described by the type I and $Ba_8Ga_{15}Sn_{31}$ by the type VIII structure, the spacing of Ba atoms and the local structures are relatively similar. This is illustrated in **Figure 4.2.10**, which shows a schematic of the local structure around Ba atoms that is common to both clathrate structure types with select Ba-Ba distances

labeled (**Figure 4.2.10a**), as well as a unit cell of the Ba sublattice in the type VIII (**Figure 4.2.10b**) and type I (**Figure 4.2.10c**) clathrate structure. The common local feature of the Ba sublattice comprises two face-sharing tetrahedra which then combine in face-sharing and corner-sharing arrangements in the type VIII structure, and in face-sharing arrangements for the type I structure. Both Ba sublattices have similar Ba-Ba distances of around 6 Å, but the distances in Ba_8Ge_{43} show a wider spread as a result of the different Ba sites in the type I structure (corresponding to the centers of the Ge_{20} and Ge_{24} cages). When the clathrate structure is eventually converted to an amorphous phase via electrochemical lithiation, the similar local structuring of Ba within the framework structure has a larger effect on the structures of the resulting amorphous phases compared to the small differences in the arrangement of framework/guest atoms in the original clathrate structure.

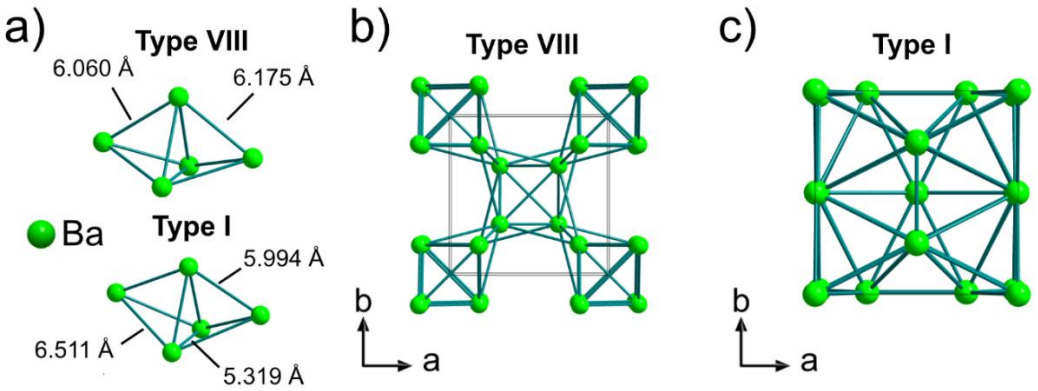

Figure 4.2.10 (a) Schematic of the common local Ba feature in the type VIII $Ba_8Ga_{15}Sn_{31}$ and type I Ba_8Ge_{43} clathrate Ba sublattices. Ba sublattice of the **(b)** type VIII $Ba_8Ga_{15}Sn_{31}$ clathrate and **(c)** type I Ba_8Ge_{43} clathrate.

Another important consideration is that despite differences in composition, both clathrates react through a similar mechanism, as supported by the similar shaped voltage

curves and PDFs after lithiation (**Figure 4.2.9**). The PDF of the framework-substituted, type I clathrate $Ba_8Al_{16}Ge_{30}$ also displayed similar features to the one for Ba_8Ge_{43}[178] and $Ba_8Ga_{15}Sn_{31}$ after lithiation. The shared reaction mechanism between the Ba-filled clathrates with different compositions is interesting as elemental Ge,[120] Sn,[197] Al,[137] and Ga[258] all have distinctly different lithiation pathways at room temperature and involve crystallization to Li binary phases. Furthermore, alloys of Sn, such as SnSb[259,260] and GaSn,[261] show electrochemical features during lithiation that can be traced back to the lithiation of the constituent elemental phases, suggesting that significant demixing and crystallization occurs during the lithiation process despite the alloyed state of the starting material. We attribute the distinct electrochemical properties of the clathrates to the unique structure where Ba guest atoms and framework atoms form an atomically mixed amorphous phase after lithiation, which kinetically prevents demixing of the constituent elements.

The origin of this amorphous pathway in the lithiation of type VIII clathrate can be attributed to kinetic limitations of the lithiation of the host structure. The Ba atoms are presumed to act as "pillars" which serve to break up long-range order and prevent the bulk crystallization of Li-Sn/Ga phases. This is similar to what we observed in the Ba_8Ge_{43} system,[178] but the lack of known binary Ba-Sn clathrate phases (*i.e.*, Ba_8Sn_{43}) precludes a direct comparison to Ba_8Ge_{43}. In contrast, β-Sn undergoes phase transformations at low Li content to form crystalline phases (*e.g.*, Li_2Sn_5, LiSn) that follow the binary phase diagram. Comparison of the crystal structures of β-Sn, Li_2Sn_5, and LiSn (**Figure E.10**) show a common square Sn unit that is progressively broken up as the Li content increases. It has been suggested that this common feature in the Li-Sn

crystalline phases enables kinetically facile phase transformations with good reversibility.[247,249] In the case of the clathrate, the original crystal structure is unrelated to Li-Sn or Li-Ga binary phases, which means that a significant amount of rearrangement and demixing of Ba/Sn/Ga would be required to form crystalline binary phases, a process that is highly unlikely at room temperature. As a result of these kinetic limitations, the phases that form are amorphous with the mobile Li ions driving the structural changes.

The amorphous lithiation pathway of $Ba_8Ga_{15}Sn_{31}$ has significant effects on the voltage profile relative to that in β-Sn. Most notably, the voltage of reaction with lithium is lower for the clathrate (0.25 V vs. Li/Li^+) than for β-Sn (0.45 V), which is consistent with the formation of a higher energy amorphous phase. In addition, the presence of Ba and Ga substitution in the clathrate is expected to further increase the Gibbs free energy of the lithiated phase (*i.e.*, lower the voltage) as seen in our previous study on the $Ba_8Al_yGe_{46-y}$ ($0 < y < 16$) clathrates, which demonstrated that increasing Al substitution decreased the reaction potential compared to Ba_8Ge_{43}.[152] We speculate that Ga substitution could have a similar effect on the reaction potential. We also note that the clathrate reacts with a lower amount of Li compared to β-Sn (3.2 Li for the clathrate, 3.4 Li for β-Sn), which was also a notable effect when increasing the degree of Al substitution in $Ba_8Al_yGe_{46-y}$.

After the initial conversion of the clathrate to an amorphous phase in the first cycle, the delithiation profile is sloped, showing no distinct plateaus corresponding to phase transformations. This sloped behavior suggests that delithiation of the $Li_xBa_{0.17}Ga_{0.33}Sn_{0.67}$ phase goes through a solid-solution mechanism where the Li content

varies continuously during the reaction. After one lithiation and delithiation cycle, the originally crystalline clathrate is suspected to now be amorphous, similar to the what occurs for diamond cubic Si.[32,117] Based on the PDF analysis of Ba_8Ge_{43} after full lithiation and delithiation, the local structure was similar to that of the original pristine crystalline clathrate but did not exhibit long-range order. Based on the similar reaction mechanisms of the Ba clathrates, we expect the delithiated $Li_xBa_{0.17}Ga_{0.33}Sn_{0.67}$ phase to have a similarly structured amorphous phase. During cycling, the shape of the voltage profile does not change significantly, suggesting that the amorphous phase formed in the first cycle is able to be reversibly cycled. However, future PDF characterization after cycling or *in situ* measurements will be needed to confirm this.

4.2.4.2. Design Strategies for Li-ion battery applications

On the basis that Ba_8Ge_{43}, $Ba_8Al_{16}Ge_{30}$, and $Ba_8Ga_{15}Sn_{31}$ all undergo amorphous phase transformations upon reaction with Li, we presume that this amorphous reaction mechanism might be a general feature of the Li-alloying of clathrates with guest atoms. An exception to this trend is the type I clathrate $Ba_8Al_{16}Si_{30}$, which we found to display electrochemical reactions dominated by surface reactions rather than bulk alloying reactions.[56,106] Notably, the presence of guest atoms is important as clathrates with type II structures that can be synthesized without guest atoms (*i.e.* vacant cages) can go through topotactic insertion reactions *without* transforming to amorphous phases at low degrees of lithiation. This has been observed in Si_{136}[49,244] and also likely occurs in Ge_{136},[52] but amorphous phase transformations are observed if the type II clathrates are prepared with guest atoms[53] or overlithiated.[16] On the basis of the DFT calculations presented herein

(**Figure 4.2.8**) and our previous calculations, we conclude that clathrates with occupied cages will favor amorphous phase transformations over insertion reactions since the energies for the Li sites (for insertion processes) and migration barriers increase if the cages are already occupied.[55,152,179] By assuming a common amorphous reaction mechanism among clathrates containing guest atoms, we can propose a general strategy for designing clathrates to serve as alloying anodes which could be helpful in directing future research. First, it is important to emphasize that the initial crystalline clathrate structure will be converted into an amorphous phase in the first lithiation process and later cycles will involve lithiation/delithiation of amorphous phases. This is similar to the electrochemical reaction of Li with diamond cubic Si, where the diamond structure is not recovered after Li is removed.[32,34,117] Next, the guest atoms (*i.e.*, Ba) in the clathrate structure serve as electrochemically inactive but structurally important components, with the role of kinetically frustrating the formation of crystalline phases. Suppressing the formation of crystalline phases mitigates large changes in volume, which can lead to better cycling retention. Then, substitution of elements on Tetrel framework sites (*i.e.*, with Ga or Al) allows for tuning of the reaction voltage and lithiation capacity of the amorphous phase.

In terms of the guest atom selection, the optimal choice is the lightest atom possible to maintain a high gravimetric specific capacity while still having the benefit of serving as "pillar" to suppress crystalline phase transformations. In this regard, the lightest reported guest atom (other than Li) for clathrates is Na.[42] However, our previous studies investigating the properties of Na-filled Si clathrates in batteries suggest that the Na guest atom does not suppress crystalline phase transformations, as the formation of

crystalline $Li_{15}Si_4$ was observed after full lithiation of both type I (Na_8Si_{46}) and type II ($Na_{24}Si_{136}$) clathrates.[53,262] The lithiation of Na-filled Ge clathrates (*e.g.*, $Na_{24-x}Ge_{136}$[182,263], $Na_8Zn_4Ge_{42}$[236],$Na_8Ga_8Ge_{38}$[264]) has yet to be reported but would be promising if phase transformations were disrupted. However, we think this is unlikely as Ge generally shows a higher propensity than Si for to undergo crystalline phase transformations during lithiation when considering the elemental phases with diamond cubic structure. The next lightest guest atom for clathrates is K, with many K-filled Si, Ge, and Sn clathrates reported.[237,265–267] We believe K-filled clathrates are particularly promising due to the significantly larger atomic size of K compared to Na, which might affect the room temperature lithiation pathway significantly while still having a relatively low atomic weight. We have preliminary data of the K containing Ge clathrate, $K_8Li_xGe_{46-x}$,[115] showing that the voltage profile has a single major plateau during lithiation and then a sloped delithiation curve (**Figure E.11ab**), similar to Ba_8Ge_{43} and $Ba_8Ga_{15}Sn_{31}$, suggesting it might also go through an amorphous phase transformation. PXRD after full lithiation showed that the pristine clathrate reflections decreased in intensity without any other phases being detected, further supporting an amorphous phase transformation (**Figure E.11c**). Due to the large particle sizes of the $K_8Li_xGe_{46-x}$ (**Figure E.11de**), we suspect that there could be kinetic limitations during the lithiation which resulted in incomplete conversion of the clathrate. Further structural characterization with PDF analysis of the lithiation intermediates of $K_8Li_xGe_{46-x}$ will be needed to confirm the suspected amorphous phase transformation. Tetrel clathrates have also been reported to form containing Rb, Cs, and Sr guest atoms[41,268–270]; however, these guest atoms are heavier than K and Na and would be less attractive in terms of gravimetric capacity.

More work examining the effect of the size and valency on the guest atom on the subsequent lithiation pathways would be warranted for assessing the viability of heavier guest atoms.

Substitution of framework atoms with other elements is also an interesting design avenue as it allows for tuning of the reaction capacity/voltage while also being able to compensate for the extra mass originating from the guest atoms. In the case of $Ba_8Ga_{15}Sn_{31}$, the molar mass (5829.3 g/mol) is lower than that of pure Sn (6409.8 g/mol) on a per atom basis meaning that the additional mass from Ba atoms is negated by the incorporation of the Ga. This means that despite the lower amount of Li reacting with $Ba_8Ga_{15}Sn_{31}$ (3.2 Li per Sn/Ga vs. 3.4 Li per Sn for β-Sn), both $Ba_8Ga_{15}Sn_{31}$ and β-Sn have similar initial capacities (~700 mAh/g). In addition to the modification of the capacity in terms of weight or amount of reacted Li, our findings suggest that adding substitutions decreases the reaction voltage (also seen when substituting Al for Ge in $Ba_8Al_yGe_{46-y}$)[152,178] which would result in a higher overall cell voltage when the clathrate is coupled with a cathode in a full cell, resulting in a higher energy density. The effect of substitutions on the capacity, reaction voltage, and amount of Li that can react with the electrode means there should be an optimal point at which the energy density is maximized. Considering the K-filled Ge and Sn clathrates, the Al-substituted clathrates $K_8Al_8Ge_{38}$ and $K_8Al_8Sn_{38}$[271] are particularly promising due to the low weight of Al, which could nullify the weight increase from K while also potentially decreasing the reaction voltage with minimal decreases to the amount of Li that reacts. If these clathrates go through amorphous lithiation pathways like the Ba clathrates, then they could be promising alternatives to elemental Ge and Sn anodes for Li-ion batteries.

4.2.5. Conclusions

In this work, the lithiation pathway of the type VIII $Ba_8Ga_{15}Sn_{31}$ clathrate is investigated with electrochemical analysis and total scattering X-ray powder diffraction measurements. $Ba_8Ga_{15}Sn_{31}$ and β-Sn (as a comparison) are lithiated to similar amounts and then subjected to X-ray characterization. The lithiation voltage profile for the type VIII clathrate shows a single plateau at 0.25 V followed by a sloping profile, while the voltage profile of β-Sn has three plateaus corresponding to known phase transformations to Li-Sn crystalline phases. Structure factor patterns at different points in lithiation confirm that β-Sn goes through highly crystalline phase transformations, while the type VIII clathrate undergoes an amorphous phase transition. PDF analysis confirms the phase transformation of the type VIII $Ba_8Ga_{15}Sn_{31}$ clathrate to a highly lithiated amorphous phase that lacks long-range order. The PDF analysis also suggests that the amorphous $Li_xBa_{0.17}Ga_{0.33}Sn_{0.67}$ phases share similar local structure to those in crystalline Li-Sn phases. Galvanostatic cycling experiments showed that the type VIII clathrate resulted in much better cycling and Coulombic efficiency than β-Sn, which is attributed to reduced stresses and deleterious effects of volume expansion/contraction during cycling on account of the solid-solution lithiation/delithiation mechanism in the clathrate. DFT calculations to assess the possibility of topotactic Li insertion into the $Ba_8Ga_{15}Sn_{31}$ clathrate suggest that the Li insertion site energy is too high to be competitive with the amorphous alloying reaction due to the presence of the Ba guest atoms in the cages.

Overall, we find that the lithiation of the type VIII $Ba_8Ga_{15}Sn_{31}$ is very similar to that observed in the type I Ba_8Ge_{43} clathrate investigated in our previous work. The similar reaction mechanism and structure of the amorphous phases is attributed to the unique clathrate structure in which Ba atoms are distributed through the cage framework and act as "pillars" to prevent long-range ordering. The resulting amorphous phase has distinct electrochemical reactions with Li relative to elemental phases and potentially beneficial electrochemical properties such as a lower reaction voltage and better cycling stability due to the solid-solution mechanism. Tetrel clathrates represent a wide design space for tuning the materials properties because of the numerous types of guest atoms, structures, and compositions. Based on the results presented here, we expect that many other clathrate compositions could undergo amorphous alloying reactions with novel and tunable electrochemical properties for Li-ion battery applications.

4.3. Electrochemical Lithium Alloying Behavior of Guest-free, Type II Silicon Clathrates

4.3.1. Introduction

Chapter 4.1 and 4.1 demonstrated the cage structure and accompanying defects result in significantly different electrochemical properties for clathrates compared to the well-studied amorphous and diamond cubic elemental phases. For instance, we have shown that the Ba_8Ge_{43}, $Ba_8Al_{16}Ge_{30}$, and $Ba_8Ga_{15}Sn_{31}$ clathrates undergo solely amorphous phase transformations upon electrochemical reaction with Li rather in contrast to the crystalline phase transformations typically observed in the constituent element phases (*i.e.*, Ge, Al, Ga, Sn).[178,272] Further, the amorphous phases formed after the first lithiation of the clathrates are retained in subsequent cycles and display promising electrochemical properties as alloying anodes for Li-ion batteries due to the solid-solution nature of the lithiation process and lower reaction voltage relative to those in elemental phases.

Given their open framework structure, we have also investigated the possibility of topotactic Li insertion into the cages of guest-free clathrates. We recently reported evidence of reversible Li insertion into nearly guest-free type II Si clathrate ($Na_{24-y}Si_{136}$, $y \sim 23$).[244] In the type II Si clathrate structure, Si dodecahedra (Si_{20}) and hexakaidecahedra

(Si_{28}) are arranged in face-sharing configurations while guest atoms (*i.e.* Na) reside at the centers of each cage.[40] **Figure 4.3.1a** shows a schematic of a Si_{20} (grey) and Si_{28} (blue) cage connected via a pentagonal face and **Figure 4.3.1b** shows a polyhedral model of the clathrate to illustrate the connectivity of the cages. While the Si_{20} cages consist of only pentagonal faces, the Si_{28} cages contain both hexagonal and pentagonal faces. From our *ab initio* analysis of the possible Li diffusion pathways in guest-free Si_{136}, we determined that the large Si_{28} cages, which are connected to each other via hexagonal faces, are predicted to be responsible for bulk Li diffusion through the type II clathrate structure. This is because the calculated Li migration barrier through the hexagonal faces (0.2 eV) was much lower than migration through the pentagonal faces (2.0 eV).[244]

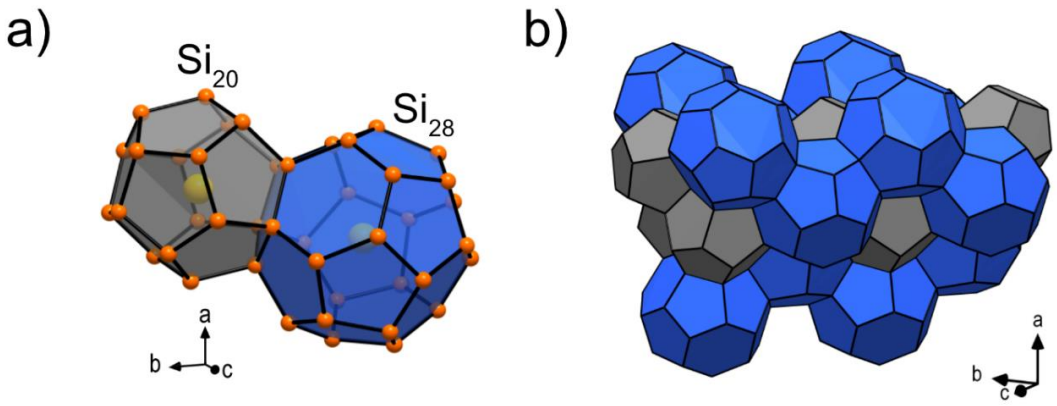

Figure 4.3.1 (a) Crystal model schematic of the dodecahedra (Si_{20}, grey) and the hexakaidecahedra (Si_{28}, blue) that comprise the type II Si clathrate structure with Na guest atoms in the cage centers. Si atoms are orange and Na atoms are yellow. **(b)** Polyhedral model of the type II clathrate Si_{136}.

In our previous investigation of the lithiation properties of type II Si clathrates, we observed that topotactic Li insertion into the structure influenced the subsequent Li alloying behavior that was observed with addition of higher amounts of Li.[244] In nearly

guest-free Si clathrate (Na_1Si_{136}), a voltage plateau at 0.26 – 0.30 V vs. Li/Li^+ was correlated to Li insertion into the vacant cages, resulting in a composition of $Li_{32}Si_{136}$. Immediately upon the incorporation of more Li, the lithiated clathrate phase ($Li_{32}Si_{136}$) then underwent a phase transformation attributed to the formation of an amorphous lithium silicide phase starting at 0.25 V.[49,244] On the other hand, when the Si clathrate cages were filled with Na guest atoms (*i.e.*, as in $Na_{11}Si_{136}$ and $Na_{24}Si_{136}$), no voltage plateaus at either ~0.30 V (from Li insertion) or 0.25 V (from the conversion of crystalline $Li_{32}Si_{136}$ to amorphous lithium silicide) were observed. Rather, a single voltage plateau at 0.12 – 0.15 V was seen,[53,244] which is more similar to the lithiation process seen in diamond cubic Si (α-Si).[33,34]. Based on our analysis of the Li diffusion paths in Si_{136}, we determined that Na occupation of the Si_{28} cages prevents Li insertion by blocking the low energy, Li migration pathway through the hexagonal faces. Since the process at 0.25 V was only observed if preceded by topotactic Li insertion into the clathrate (*i.e.*, to form $Li_{32}Si_{136}$), we speculate that this Li insertion process kinetically enables the formation of an amorphous phase with a lower Li content than what is typically seen in the lithiation of α-Si. To investigate this phenomenon, herein we use synchrotron X-ray total scattering measurements to obtain structure function and pair distribution function (PDF) plots to characterize the local and long-range structure of the amorphous intermediates formed during the electrochemical lithiation of guest-free, type II Si clathrate. By comparing the phases formed upon alloying the clathrate with Li to those seen when reacting diamond cubic Si (α-Si) to similar Li compositions, we aim to rationalize the structural origins of the potential-dependent phase transformations in the clathrate at degrees of lithiation that exceed the topotactic insertion process.

The results show that after Li insertion into the vacant cage of the type II Si clathrate, a two-phase reaction occurs between the clathrate and an amorphous lithium silicide phase that contains a high amount of Si–Si connectivity. In contrast, the PDF analysis confirms that the two-phase reaction during lithiation of α-Si forms an amorphous phase with comparatively fewer Si–Si bonds, higher lithium content, and a local structure more similar to that in $Li_{15}Si_4$. This structural difference in the amorphous phases formed during lithiation allows us to rationalize the voltage differences of these materials (0.25 V vs. Li/Li^+ for clathrate vs. 0.10 V for α-Si), as phases with lower Li content are expected to contain more Si–Si bonds, thus resulting in a phase with a higher voltage. The low energy Li diffusion paths in the type II clathrate structure enable Li to spread throughout the Si matrix in a manner similar to that seen in the lithiation of amorphous, rather than diamond structured, Si. These results demonstrate how the initial host structure of Si can be used to modify the subsequent Li alloying pathways by enabling bulk Li diffusion into the Si matrix.

4.3.2. Experimental Methods

The type II clathrate was synthesized via the thermal decomposition of Na_4Si_4 and prepared into electrodes as described in our previous work.[244] The electrodes were lithiated galvanostatically in half-cells with lithium metal and then extracted for *ex situ* measurements. Synchrotron X-ray pair distribution (PDF) measurements were conducted at Diamond Light Source (Didcot, United Kingdom) at the I15-I dedicated PDF beamline with λ = 0.161669 Å. The atomic PDF, *G*(r) as defined by Billinge *et al*.,[220] was

generated from the total scattering data using PDFgetx3 within the xPDF suite software package.[221,222] Synchrotron X-ray diffraction measurements were performed at the P02.1 powder diffraction beamline at PETRA III at the Deutsches Elektronen-Synchrotron (DESY) with $\lambda = 0.20733$ Å. More detailed descriptions of the synthesis, electrochemical and synchrotron measurements, and PDF analysis are in **Appendix F**

4.3.3. Results

4.3.3.1. Electrochemical lithiation

To investigate the structural origin of the alloying reaction in the type II clathrate electrodes observed beginning at 0.25 V vs. Li/Li^+, *ex situ* synchrotron X-ray total scattering measurements were conducted after different amounts of Li were electrochemically inserted, with similar measurements performed on α-Si electrodes for comparison. The refinement of the as-prepared clathrate showed that the cages were nearly free of Na guest atoms, with a composition of $Na_{0.3(1)}Si_{136}$ and lattice constant of 14.6484(8) Å (**Figure F.1**, **Table F.1**). Therefore, from here on the clathrate sample will be referred to as Na_1Si_{136}. The voltage profiles and corresponding dQ/dE plots for the first lithiation of Na_1Si_{136} and α-Si are presented in **Figure 4.3.2** with teal, orange, green and blue dots showing the points at which samples were collected for *ex situ* total scattering measurements. The capacity and voltage corresponding to each of the colored dots for each sample are shown in **Table F.2**.

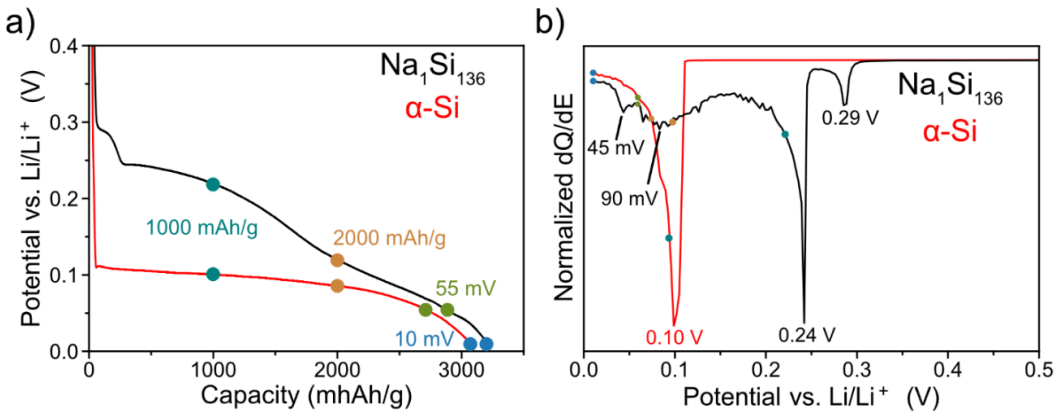

Figure 4.3.2 (a) Voltage profile and corresponding **(b)** normalized dQ/dE plot of the lithiation of Na_1Si_{136} and α-Si at 25 mA/g (~C/120) with a voltage cutoff of 10 mV vs. Li/Li^+. The teal, orange, green and blue dots represent the points at which cells were disassembled for *ex situ* measurements.

The voltage profile and dQ/dE plot for lithiation of crystalline α-Si has already been described in detail in previous work[33,34] and is characterized by a voltage plateau and peak in the dQ/dE plot at 0.10 V vs. Li/Li^+ corresponding to the two-phase, conversion reaction between α-Si and an amorphous lithium silicide phase denoted as a-Li_xSi, where $x \sim 3.5$.[33] In the case of the Na_1Si_{136} electrode, a small voltage plateau and peak in the dQ/dE plot at 0.29 V is observed, which is attributed to the topotactic insertion of Li into the clathrate cages. This process and underlying structural mechanism was described in detail in our previous work.[244] After the topotactic process, a two-phase reaction is seen at 0.24 V vs. Li/Li^+, which is assigned to the conversion of the lithiated clathrate to an amorphous phase.[49] As seen in **Figure 4.3.2**, this alloying reaction occurs at a higher voltage for the Na_1Si_{136} clathrate than for α-Si. It is also a higher voltage than that seen in Na-filled clathrates $Na_{24}Si_{136}$ (type II) and Na_8Si_{46} (type I), which also alloy with Li to form amorphous phases beginning at around 0.10 – 0.15 V vs. Li/Li^+.[53,262]

However, the alloying potential for Na_1Si_{136} is similar to the voltage seen in the lithiation of amorphous Si (0.25 – 0.30 V),[117,207,273–275] suggesting that they may be undergoing similar phase transformations (this will be discussed in further detail later). After the plateau at 0.24 V, the profile for Na_1Si_{136} becomes sloped until reaching the voltage cutoff at 10 mV. In the dQ/dE plot (**Figure 4.3.2b**), there are broad peaks centered at 90 and 45 mV. The broad peak at 90 – 100 mV is often seen in the dQ/dE plots of amorphous Si and is attributed to the breaking up of larger Si clusters in favor of smaller Si units such as Si–Si dumbbells and single atoms.[35,117] The peak at 45 – 50 mV is then attributed to the crystallization of the amorphous Li_xSi phase to crystalline $Li_{15}Si_4$.[117,276] Despite the identical lithiation capacity of 1000 mAh/g, we observe a large difference in reaction potential between the α-Si and Si clathrate electrodes (~90 vs. 220 mV), which implies that the lithium silicide amorphous phases in either case are structurally distinguishable. Therefore, analysis of structure function and pair distribution function plots was conducted to identify the structural differences between these two different amorphous phases.

4.3.3.2. Structure function and pair distribution function (PDF) analysis

The structure function and PDF plots for α-Si and Na_1Si_{136} at the different points in lithiation process indicated in **Figure 4.3.2** are presented in **Figure 4.3.3**. The structure function is derived from the total scattering diffraction pattern and allows for the tentative identification of crystalline and amorphous phases present in the pattern by comparison with calculated reference patterns. **Figure 4.3.3a** shows the structure function plots for the lithiation of α-Si, with the pristine (*i.e.*, unlithiated) material showing reflections that

match the calculated reference pattern of α-Si (**Figure F.2**). At 1000 mAh/g (composition of $Li_{1.05}Si$), the reflections from α-Si are lower in intensity and broad peaks appear at around 1.8 and 2.4 $Å^{-1}$ (marked by blue stars), indicating the growth of a lithiated amorphous Si phase (*i.e.*, a-Li_xSi). Further lithiation to 2000 mAh/g ($Li_{2.10}Si$) shows a larger decrease in α-Si reflections and a growth in the broad peaks attributed to a-Li_xSi. At the 55 mV voltage cutoff (2650 mAh/g, $Li_{2.77}Si$), the pristine α-Si continues to be consumed in the reaction and the broad a-Li_xSi peaks begin to form separate peaks, likely related to the crystallization of $Li_{15}Si_4$. At 10 mV (3201 mAh/g, $Li_{3.35}Si$), the structure function matches that for $Li_{15}Si_4$ ($I\bar{4}3d$),[231] the phase formed upon full lithiation[117], indicating that the α-Si was completely consumed and the a-Li_xSi crystallized into $Li_{15}Si_4$. This behavior is consistent with previously reported *ex situ* and *in situ* XRD analysis of α-Si,[33,117] where a two phase reaction between α-Si and a-Li_xSi was correlated to the plateau at ~0.10 V and the crystallization of $Li_{15}Si_4$ from a-Li_xSi to the process at 50 mV.

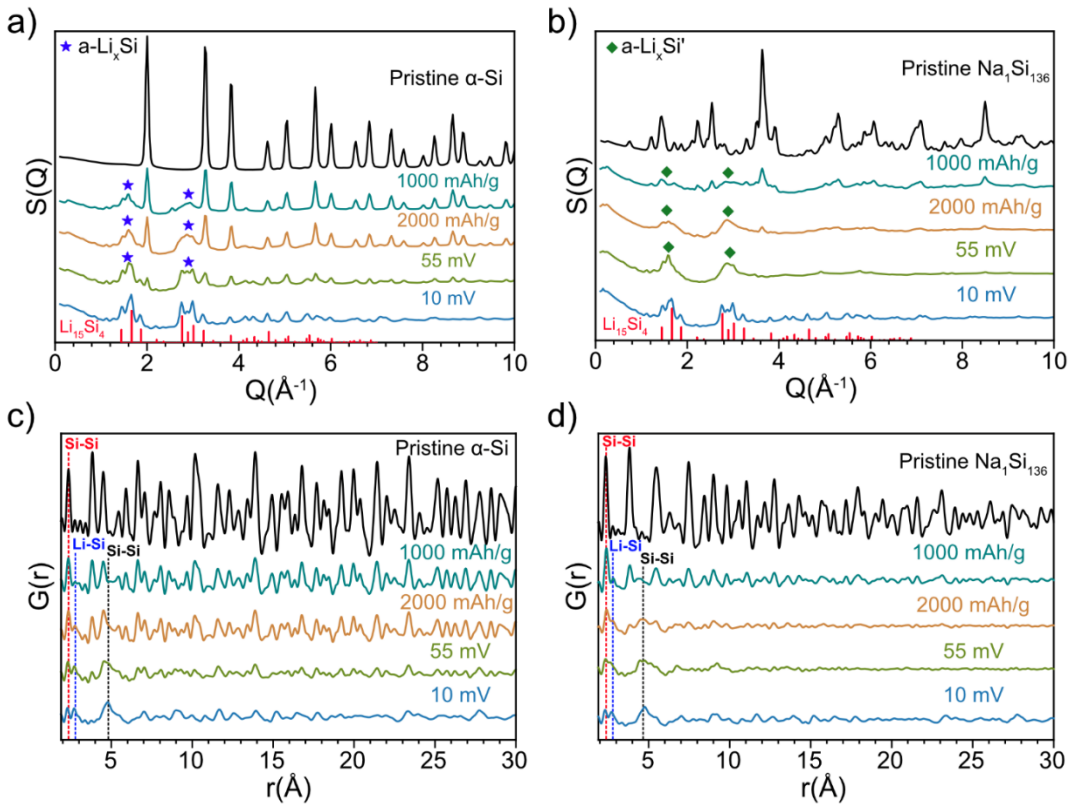

Figure 4.3.3 *Ex situ* structure function and PDF plots of the lithiation of **(a,c)** α-Si and **(b,d)** Na_1Si_{136} at the points marked in **Figure 4.3.2**.

For the guest-free, type II clathrate (Na_1Si_{136}), the structure function plots of the pristine sample (**Figure 4.3.3b**) shows a good match with the calculated reference pattern for the type II Si clathrate (**Figure F.2**). At a capacity of 1000 mAh/g ($Li_{1.05}Si$) and potential of 0.22 V, the reflections corresponding to the pristine clathrate are greatly decreased in intensity and broad peaks appear around 1.8 and 2.4 Å^{-1} (marked by the green diamonds). These peaks, attributed to an amorphous lithium silicde phase (denoted a-Li_xSi' to differentiate from the a-Li_xSi phase that forms upon lithiation of α-Si), are broader than those in the seen in α-Si at 1000 mAh/g, which could be related to structural differences expected from the large observed difference in potential as explained

previously. At 2000 mAh/g ($Li_{2.10}Si$), the pristine clathrate has been almost completely consumed and the peaks associated with a-Li_xSi' increase in intensity. At this point in the lithiation process, the clathrate electrode appears be almostly completely amorphous, which is in contrast to the large fraction of α-Si still present at 2000 mAh/g for the lithiation of α-Si (**Figure 4.3.3a**). At 55 mV (2484 mAh/g, $Li_{2.60}Si$), all the pristine clathrate reflections have disappeared and only broad a-Li_xSi' peaks are present. At 10 mV (3118 mAh/g, $Li_{3.26}Si$), the broad peaks split into sepearate reflections that match with the reference pattern for $Li_{15}Si_4$, confirming that the process observed at 45 mV in the dQ/dE plot (**Figure 4.3.2b**) is related to the crystallization of $Li_{15}Si_4$. In summary, these structure function plots confirm the lithiation mechanism of α-Si and demonstrate that the Na_1Si_{136} clathrate structure, while like α-Si also undergoes a crystalline-to-amorphous conversion reaction, is completely consumed at an earlier stage in the lithiation process relative to that in α-Si. This results in formation of a different type of amorphous lithiated intermediate phase than the one formed from α-Si, although both of these amorphous phases eventually crystallize into $Li_{15}Si_4$ at sufficiently low potentials.

To elucidate the local structural differences of the amorphous phases, the Fourier transform of the reduced structure functions were taken to generate the PDF plots.[220] Generally, the PDF results for the α-Si samples matched those reported in previous studies.[35] The PDF of pristine α-Si (**Figure 4.3.3c**) is well fit by a least-squares refinement of the α-Si structure, confirming the purity of the pristine material (**Figure F.3a** and **Table F.3)**. The first three correlations represent the first three coordination shells in α-Si, *i.e.* from direct Si-Si bonds (2.35 Å), second nearest neighbor (2.83 Å), and third nearest neighbor (4.50 Å) Si-Si distances (identified at 2.35, 3.8, and 4.5 Å by Key

et al.[35]). After lithiation, the intensity of these α-Si correlations decreases, while there are notable changes at low-r values (2 – 5 Å) that originate from the amorphous phase (a-Li_xSi) that is formed at the expense of α-Si as more Li is incorporated into the electrode. Three specific correlations distances are indicated with dotted lines in **Figure 4.3.3c** that correspond to direct Si–Si bonds (2.35 Å, red), Li–Si bonds (2.80 Å, blue) and first non-bonding Si–Si distances (~4.7 Å, black). As Li is incorporated into the system, the silicon lattice is broken up and a decrease in the correlations related to Si–Si bonds is expected, while the correlations from Li–Si bonds and non-bonding Si-Si correlations are expected to increase in intensity. The PDF taken from the electrode after lithiation to 1000 mAh/g looks very similar to that for the pristine α-Si, and these new correlations are very low in intensity therein. However, the new correlations increase in intensity as more lithium is added, consistent with the trend seen in the structure function plots (**Figure 4.3.3a**). For α-Si lithiated to 10 mV, the PDF pattern was refined to crystalline $Li_{15}Si_4$ with a fairly good fit (R_w = 0.254) and lattice parameter of 10.7126 Å (**Figure F.3b**). The PDF of the α-Si electrode lithiated to 10 mV displayed residual Si–Si correlations at 2.28 Å, consistent with the findings from Key *et al*,[35] which were incorporated into the refinement using the α-Si structure with a nanoparticle amplitude correction parameter of 4 Å. On the basis of the similarity of the peak positions between the new correlations that emerged in the PDF of the lithiated α-Si samples with the low-r correlations for $Li_{15}Si_4$ (as seen in the PDF for the 10 mV sample), we posit that these new correlations have a similar origin as those in $Li_{15}Si_4$. In the $Li_{15}Si_4$ structure,[231] the Si atoms are surrounded by Li atoms with a coordination number of 12 (**Figure F.4**), so there are no direct Si–Si bond distances. From inspection of the calculated total and partial PDF patterns for

$Li_{15}Si_4$ (**Figure S4a**), the correlation at 2.73 Å is attributed to the nearest neighbor Li–Si bonds and the correlation at ~4.7 Å to the first nonbonding Si interactions (*i.e.*, next-nearest neighbor). We note that several other non-nearest neighbor correlations are present from 4.5 – 5.5 Å in the partial PDF for Li–Si and so contribute to the relative broadness of the correlation seen at 4.75 Å in the measured PDF. The PDF results confirm the reaction mechanism for lithiation of α-Si, whereby a lithiated amorphous phase forms in a two-phase reaction at the expense of α-Si, with eventual crystallization to $Li_{15}Si_4$ at low potentials near the end of lithiation.

The PDFs for the lithiation of Na_1Si_{136} are shown in **Figure 4.3.3d**. The PDF of pristine Na_1Si_{136} is fit well in the refinement to the type II Si structure model (**Figure F.3c**). Notably, the first two Si–Si distances are similar in α-Si and Na_1Si_{136} while the third-nearest neighbor is 5.45 Å for the clathrate while it is 4.50 Å for α-Si. This longer distance reflects the open cage structure of the type II clathrate. At a lithiation capacity of 1000 mAh/g, the PDF for the clathrate shows a significant decrease in intensity compared to the pristine crystalline material. The low intensity of correlations from $20 < r < 30$ Å suggests a decrease in long-range order and that amorphization is occurring in the sample. As in the α-Si PDFs, correlations at 2.8 Å (Li–Si, blue) and 4.5 – 4.7 Å (Si–Si, black) begin to appear that correspond to Li–Si and non-bonded Si–Si correlations while the correlation related to direct Si–Si bonds (2.35 Å, red) decreases. In the PDF for Na_1Si_{136} lithiated to 2000 mAh/g, the original crystalline clathrate appears to have been almost completely consumed in the reaction, consistent with the structure factor plot (**Figure 4.3.3b**). At 55 mV, the structure is highly disordered with broad peaks around 2.3 – 2.9 Å and 4.6 – 4.9 Å. At 10 mV, correlations at high-r (20 – 30 Å) appear,

evidence of long-range order. As in α-Si, the amorphous phase formed during initial lithiation of the clathrate crystallizes into $Li_{15}Si_4$ at the end of lithiation, which is supported by the PDF refinement (**Figure F.3d**) and observation of $Li_{15}Si_4$ peaks in the structure function plot (**Figure 4.3.3b**). Overall, the PDF plots demonstrate that one of the major structural differences between the lithiation of α-Si and the type II Si clathrate is the Li composition at which host structure is consumed during lithiation. The clathrate becomes completely amorphous earlier in the lithiation process (by 2000 mAh/g or a composition of ~$Li_{2.10}Si$), *e.g.* upon reaction with less Li. This implies that Li is spreading throughout the whole Si matrix and surrounding the Si atoms at an earlier point during lithiation of the clathrate than in α-Si.

To understand how the local structure of the lithiated amorphous phases in the two different polymorphs differ, the PDFs for the lithiated electrodes were fit in the following manner. First, the crystalline contributions of the PDFs were fit to the structures of the pristine, unlithiated starting materials (α-Si and Na_1Si_{136}). On the basis that the lithiation process takes place via a two-phase alloying reaction, the lithiated electrodes should consist of the unreacted crystalline starting phases and amorphous, Li-containing phases; the difference curve of the refinement fit to the crystalline starting phase should therefore reveal the local structure information of the lithiated amorphous phase. These refinements are shown in **Figure F.5** (parameters in **Table F.3-4**) while the difference curves (with crystalline phases removed) are plotted in **Figure 4.3.4ab**. For the Na_1Si_{136} electrode lithiated to 10 mV and 55 mV, the actual PDF (rather than a difference curve), is shown in **Figure 4.3.4b** due to the absence of crystalline α-Si or Na_1Si_{136} phases in these samples.

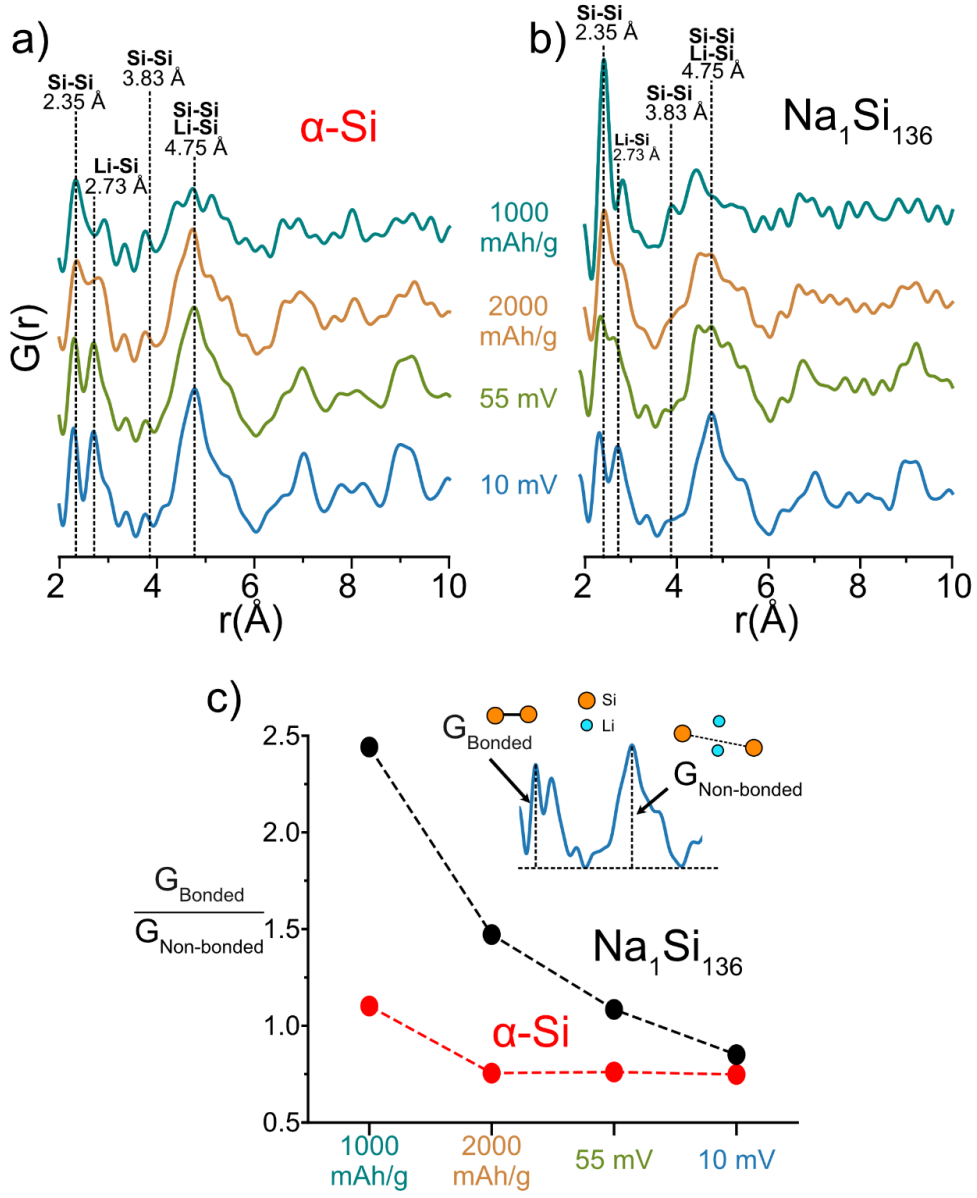

Figure 4.3.4 Difference curves for PDFs for lithiated **(a)** α-Si, **(b)** type II Na_1Si_{136} electrodes after fitting to crystalline α-Si or Na_1Si_{136}, respectively. The plots corresponding to the electrodes lithiated to 10 mV and 55 mV for Na_1Si_{136} are the actual PDF patterns (not difference curves). **(c)** Plot comparing the ratio of the intensity of the direct Si-Si correlations (G_{Bonded}) to the indirect Si-Si correlations ($G_{Non\text{-}bonded}$) at the different stages of lithiation. The higher ratio gives a qualitative indication of a higher amount of Si-Si connectivity within the amorphous phase.

By subtracting away the correlations from crystalline α-Si, the correlations corresponding to the amorphous phases are more evident in the difference curves. For

example, the PDF pattern for α-Si after lithiation to 2000 mAh/g still contains a noticeable amount of α-Si and the correlation around 4.75 Å attributed to the amorphous phase can be barely discerned (**Figure 4.3.3c**). However, the features originating from the amorphous phase are more clearly elucidated in the difference curves (**Figure 4.3.4a**). Due to the low scattering of lithium-rich phases to X-rays, some of the PDFs have noise which manifest as high frequency ripples in the PDF plot. This is most evident in the difference curve for α-Si at 1000 mAh/g, likely due to the small amount of amorphous phase present in the sample. Despite the noise, there are noticeable correlations centered at 2.35, 2.83, and 4.75 Å which, as described earlier, are attributed to Si–Si bonds, Li–Si bonds, and non-bonding Si–Si distances, respectively. The PDFs for the α-Si electrodes at the higher degrees of lithiation (2000 mAh/g, 55 mV, 10 mV) look similar, suggesting a shared common local structure. The main difference between the PDFs is the sharpness of the peaks corresponding to direct Si–Si (2.28 – 2.35 Å) and Li–Si (2.73 – 2.80 Å) bonds. The Si–Si and Li–Si correlations are merged in the 2000 mAh/g sample, while the peaks begin to split as the potential goes from 55 to 10 mV. The broad peaks in the PDF at 2000 mAh/g are expected as this phase is completely amorphous, which results in a broadening of the PDF features due to the larger distribution of different Si and Li atomic environments. The subsequent sharpening of the peaks at lower potentials is consistent with the crystallization of $Li_{15}Si_4$, which results in more defined Li–Si distances. Despite the changes in capacity and voltage, the local structure of the amorphous lithium silicide remains the same; this behavior is consistent with the two-phase reaction mechanism where, as Li enters the system, the lithium silicide phase grows at the expense of the unlithiated phase and the potential remains invariant.[19]

Another important factor is that the correlation related to direct Si–Si bonding at around 2.28 – 2.35 Å decreases in intensity compared to the correlation at 4.75 Å as the lithiation proceeds. The ratio of these correlations is a qualitative indication of the degree to which the Si matrix has been broken up by the incorporation of Li atoms. The larger the intensity of the peak at around 4.75 Å (which we call $G_{Non\text{-}bonded}$) relative to the one at 2.28 – 2.35 Å (G_{Bonded}) means that more Si–Si bonds are being broken to form isolated Si atoms, which is similar to the structure found in crystalline $Li_{15}Si_4$. This ratio of peak intensities is plotted in **Figure 4.3.4c**, which shows the ratio of $G_{Bonded}/G_{Non\text{-}bonded}$ for the different samples. For α-Si (red curve), this ratio starts at 1.2 and then remains at 0.75 until the end of lithiation and crystallization of $Li_{15}Si_4$. The decrease of $G_{Bonded}/G_{Non\text{-}bonded}$ as more Li is incorporated indicates that the amorphous lithiated phase that initially forms has a larger amount of Si clusters with retained Si–Si bonding compared to the amorphous lithiated phase found at higher degrees of lithiation (*i.e.*, two distinct amorphous lithium silicide phases with different local structure). This interpretation is consistent with previous nuclear magnetic resonance (NMR) studies showing two Li chemical shifts corresponding to Li next to Si clusters and Li surrounding isolated Si atoms at the beginning of lithiation of α-Si.[188] As lithiation proceeds, the amount of Si clusters in the amorphous phase eventually decreases while isolated Si atoms increase, consistent with the lower amount of Si–Si bonds observed in the PDFs for α-Si with high Li content (2000 mAh/g, 55 mV, 10 mV).

In contrast, the lithiated amorphous phases formed during lithiation of the clathrate are found to have an evolving local structure. From the difference curves in **Figure 4.3.4b**, the correlation at 2.35 Å, related to direct Si–Si bonds, has a much higher

intensity relative to the correlations from 4 – 5 Å (related to next nearest neighbor Si–Si correlations) found in the PDF of the electrode lithiated to 1000 mAh/g. This indicates that a large amount of Si–Si connectivity from the original clathrate structure was retained in the amorphous phase. This is supported by the $G_{Bonded}/G_{Non\text{-}bonded}$ ratio in **Figure 4.3.4c** showing a much higher ratio of connected Si to unconnected Si compared to the ratio seen for α-Si lithiated at the same capacity (*i.e.*, 2.5 vs. 1.2 at 1000 mAh/g). This indicates that the different Si connectivity is one of the distinguishing features of the amorphous phases formed in α-Si vs. clathrate electrodes at 1000 mAh/g. In addition, there is a notable peak at 3.83 Å in the PDFs of the clathrate samples that is related to the next-nearest neighbor correlations in a Si tetrahedron or Si pentagon, indicating that Si clusters of this size are still in present in the amorphous phase[35]. The noise in the PDF for α-Si lithiated to 1000 mAh/g makes it difficult to distinguish whether or not a similar peak at 3.83 Å is present, but we believe it is possible given the observation of Si clusters in the previous NMR studies.[35,188] The local structure of the amorphous phase formed after lithiation of the clathrate to 2000 mAh/g, the point at which the pristine phase has been almost completely consumed, shows a decrease in intensity in the correlations at 2.35 and 3.83 Å and increase in intensity for the correlations around 4.75 Å, indicating that Si–Si bonds have been broken. Further lithiation to 55 mV shows a similar trend as that seen in α-Si where the $G_{Bonded}/G_{Non\text{-}bonded}$ ratio decreases, suggesting that lithiation proceeds through a continuous breaking of Si–Si bonds with the incorporation of more Li. At 10 mV, the local structure is similar to the one at 55 mV, but with sharper and more defined correlations, consistent with the crystallization of $Li_{15}Si_4$.

To better understand the local structure of the lithiated clathrate at 1000 mAh/g and 2000 mAh/g, the two difference curves from the refinement are plotted with the simulated total and partial PDFs of $Li_{12}Si_7$ (**Figure 4.3.5a**), a crystalline phase comprising Si arranged in "stars" and pentagons (**Figure 4.3.5b**). Since the pristine clathrate structure contains Si atoms in both of these arrangements, and because the composition of the electrode lithiated to 2000 mAh/g ($Li_{2.10}Si$) is similar to that of $Li_{12}Si_7$ ($Li_{1.71}Si$), we believe this comparison could help to elucidate the local structure of the lithiated amorphous phase, a-Li_xSi', present at this point of the lithiation process.

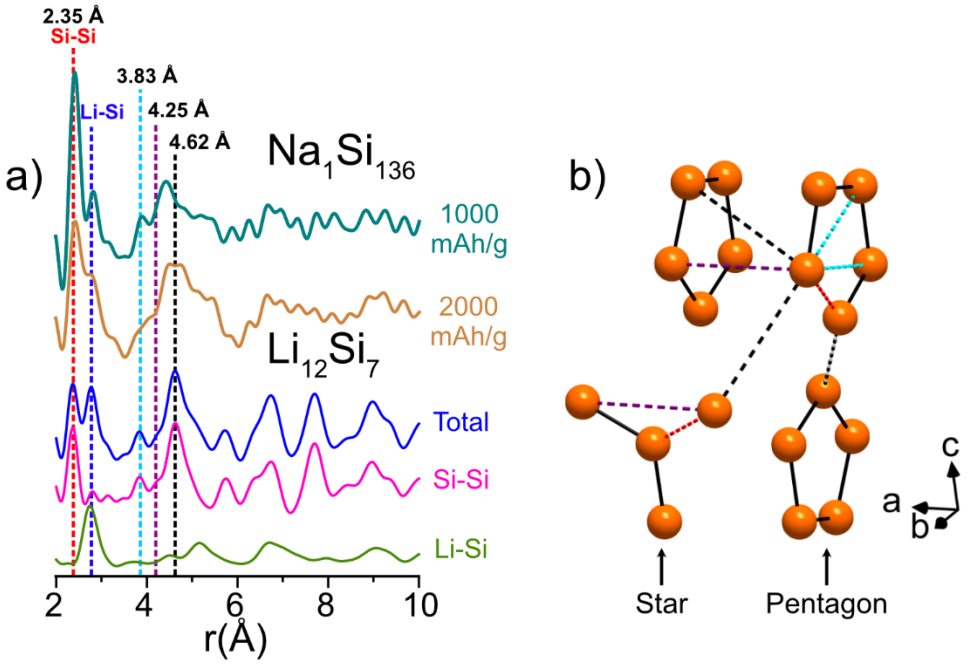

Figure 4.3.5 (a) Difference curves for PDFs for lithiated type II Na_1Si_{136} electrodes after fitting to crystalline Na_1Si_{136}, respectively and simulated total partial PDF of $Li_{12}Si_7$. **(b)** Crystal structure model of $Li_{12}Si_7$ (from ref[277]) displaying only the Si atoms. The dashed colored lines correspond to correlation distances in (a).

As seen in the Si–Si and Li–Si partial PDFs, the two shortest correlations in the total PDF of $Li_{12}Si_7$ correspond to direct Si–Si bonds and Li–Si bonds. Notably, the Li–Si correlations only contribute significantly to the total PDF at around 2.74 Å, while at higher distances, the Si–Si correlations dominate. The three correlations indicated with the dotted lines in the $Li_{12}Si_7$ total PDF (3.83, 4.25, and 4.62 Å) are identified in **Figure 4.3.5b**, with the color of the bond matching the dotted line in **Figure 4.3.5a**. At 3.83 Å (cyan), there is a small peak in the calculated PDF pattern of $Li_{12}Si_7$ corresponding to the next-nearest neighbor distance in the Si pentagon. This correlation appears to be present in the PDFs of the clathrate lithiated to both 1000 and 2000 mAh/g, suggesting that similar Si–Si distances are present in the a-Li_xSi' amorphous phase. Next, there is a small correlation at around 4.25 Å (purple) which manifests as a shoulder to the larger peak at 4.62 Å (black). The former correlation corresponds to the Si-Si distance in $Li_{12}Si_7$ found between parallel Si pentagons as well as the edge of the Si_4 stars (purple). The latter corresponds to Si–Si correlations between the pentagon and star Si clusters (black). This distance matches the correlation seen in the 2000 mAh/g PDF but is larger than that observed in the 1000 mAh/g PDF (4.52 Å). Both of these correlations are shorter than the non-bonding Si–Si correlation at 4.70 Å for $Li_{15}Si_4$ (**Figure F.4a**), suggesting that isolated Si atoms are not the major feature in the lithiated clathrate phases. This is consistent with the high $G_{Bonded}/G_{Non\text{-}bonded}$ ratio seen in **Figure 4.3.4c**. The correlations from ~3.8 – 5.5 Å are broader than those in crystalline $Li_{12}Si_7$, which is expected for disordered amorphous phases. On the basis of the similar correlation distances in the amorphous phase at seen in PDFs at 1000 and 2000 mAh/g as those in $Li_{12}Si_7$ as shown in **Figure 4.3.5a**, and the higher $G_{Bonded}/G_{Non\text{-}bonded}$ ratio indicating more Si–Si bonding

(**Figure 4.3.4c**), we expect that large Si clusters such as pentagons, stars or other larger aggregates are present in the amorphous phase formed during the initial lithiation of the Si clathrate.

The PDF results show that the main structural differences in the amorphous phases formed upon lithiation of α-Si and the type II Si clathrate are related to: 1) the Si–Si connectivity within the amorphous phase, and 2) the amount of Li needed to amorphize the crystalline host. In the case of α-Si, an amorphous phase with high Li content (x in Li_xSi has been estimated to equal 3.5 based on an *in situ* XRD study[33]) is formed that contains a significant fraction of isolated Si atoms. In the type II Si clathrate, the amorphous phase forms with a lower Li content (around Li_2Si) and hence retains more Si–Si bonding. As lithiation proceeds, the amount of Si–Si connectivity continuously decreases until reaching a local structure similar to that in $Li_{15}Si_4$.

4.3.4. Discussion

The electrochemical Li alloying mechanism in the type II Si clathrate can be summarized based on the presented results as follows. After topotactic Li insertion into the vacant cages (from 0.30 to 0.26 V), a flat plateau at 0.24 V is observed which is followed by a sloped voltage profile until the voltage cutoff. The plateau at 0.24 V is assigned to the two-phase reaction between the lithiated clathrate ($Li_{32}Si_{136}$) and the amorphous a-Li_xSi' phase. This is illustrated in **Figure 4.3.6** at a composition of $Li_{1.05}Si$ (corresponding to capacity of 1000 mAh/g), where both the $Li_{32}Si_{136}$ clathrate and the newly nucleated amorphous phase are present. From the PDF analysis, the local structure

of the amorphous phase is proposed to consist of large Si clusters/chains with many direct Si–Si bonds. Considering that the original clathrate structure comprises of Si atoms arranged in pentagons, hexagons, and stars, we believe these Si clusters could be kinetically accessible at room temperature as only a few Si–Si bonds need to be broken to form them. This amorphous structure is notably different than the local structure of the amorphous phase seen in α-Si at 1000 mAh/g (**Figure 4.3.4ac**), which contains fewer Si–Si bonds. Since the chemical potential (and hence electrode potential) of the Li–Si phases are determined by the amount of Li in the phase and size of the Si clusters,[145,204,233,278] the number of Si–Si bonds is expected to correlate with the reaction voltage. We thus identify the large Si clusters in the amorphous clathrate phase as the origin of the higher reaction potential seen in the clathrate (0.22 V) compared to the α-Si (0.09 V) electrodes at the same lithiation capacity of 1000 mAh/g.

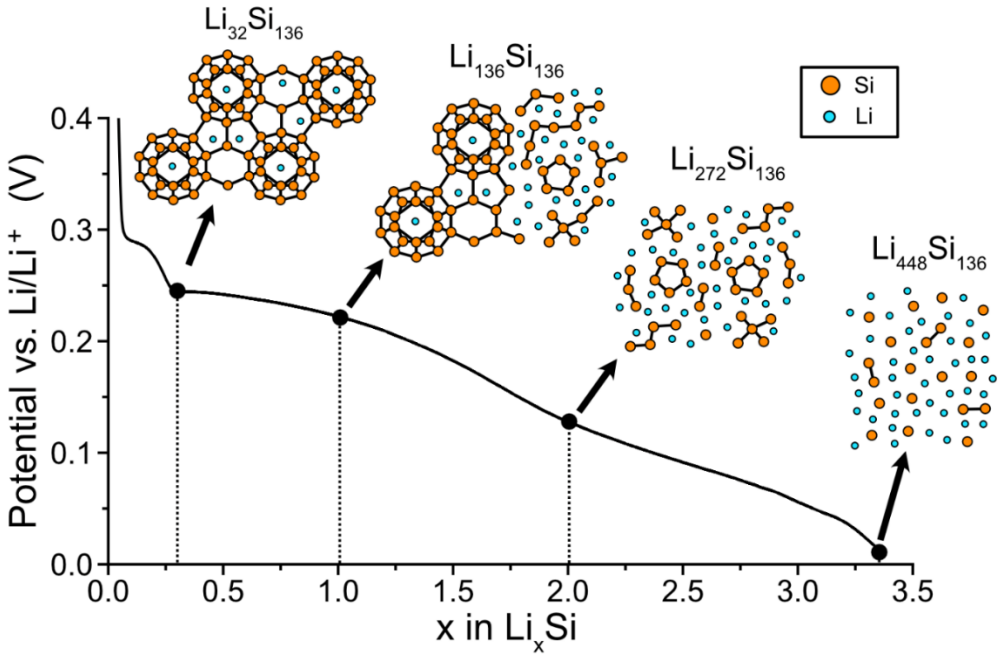

Figure 4.3.6 Proposed lithium alloying mechanism for the guest free type II Si clathrate.

With the introduction of more Li, the pristine clathrate is almost completely consumed at a capacity of 2000 mAh/g (corresponding to a composition of $Li_{2.10}Si$). From the sloped voltage profile, it is expected that the lithiation process occurs as a single-phase reaction where Li atoms distribute throughout the whole sample while continuously breaking Si–Si bonds, which results in a monotonic decrease in the potential. This is supported by **Figure 4.3.4c** showing a decrease in the $G_{Bonded}/G_{Non\text{-}bonded}$ peak ratio upon increasing lithiation. From comparison of the PDF at a composition of $Li_{2.10}Si$ to the simulated PDF of crystalline $Li_{12}Si_7$ (**Figure 4.3.5**), we expect that similar Si clusters (*i.e.*, pentagons and stars) could be present due to the analogous positioning of the Si–Si correlations.

As more Li enters the system to reach a composition of $Li_{3.30}Si$ and potential of 10 mV, the amount of remaining Si–Si bonds decreases until the amorphous phase crystallizes to $Li_{15}Si_4$ with some residual Si–Si bonds remaining (**Figure 4.3.6**). The dQ/dE plot of the clathrate is characterized by a broad peak at 0.10 V vs. Li/Li^+; a similar peak in the dQ/dE plot of the lithiation of amorphous Si has been attributed to the conversion of two distinct amorphous phases (a-$Li_{2.5}Si$ and a-$Li_{3.5}Si$)[35,279]. After isolated Si atoms become the dominate feature, the a-Li_xSi' phase then can undergo the amorphous-to-crystalline phase transformation to form $Li_{15}Si_4$ due to the similar local structures.[280]

Based on these results, we liken the alloying behavior in the type II Si clathrate to be similar to that in amorphous Si. Numerous mechanisms have been proposed for the

first cycle reaction between Li and amorphous Si, with certain analyses showing two-phase reactions between pristine amorphous Si and a distinct amorphous lithium silicide phase,[207,275,281] while others show single-phase behavior,[276,279,282] depending on the sample conditions and electrode parameters. Despite these opposing descriptions, it is generally agreed that lithium insertion into amorphous Si beyond the first cycle follows solid-solution behavior. An example dQ/dE plot of the lithiation of amorphous Si is reproduced in **Figure F.6** and compared to that of the type II Si clathrate. Despite the different processes at high potentials (see **Figure F.6** for more detail), the low potential processes associated with the Li alloying reactions are similar, suggesting that Li is able to spread across the Si matrix and continuously break Si–Si bonds via a single-phase reaction in both materials.

From comparison of the lithiation characteristics of Na_1Si_{136} to those of other clathrates, the effect of bulk Li diffusion throughout the whole Si matrix on the electrochemical profile becomes clear. This point is illustrated in **Figure 4.2.7**, which compares the reported voltage and dQ/dE plots for Na-filled Si clathrates from this and previous works,[53,262] along with those of amorphous Si[33] and α-Si. Upon lithiation, the Na-filled type II clathrates ($Na_{11}Si_{136}$ and $Na_{24}Si_{136}$) display voltage plateaus similar that seen in α-Si and notably at lower potentials than the sloped voltage profiles from amorphous Si and nearly guest-free clathrate (Na_1Si_{136}). When the Si_{28} cages of the type II Si clathrate are filled with Na (as in the case of $Na_{11}Si_{136}$ and $Na_{24}Si_{136}$), Li has low diffusivity throughout the bulk crystal as the Li migration barriers around the Na guest atoms are expected to be high.[244] Similarly, there is low Li diffusivity in α-Si.[283] This low Li diffusivity can explain the two-phase reaction mechanism seen in $Na_{11}Si_{136}$, $Na_{24}Si_{136}$,

and α-Si, whereby lithiation occurs through a moving phase boundary between a lithiated and non-lithiated phase rather than homogenous lithiation through a solid-solution. On the other hand, the topotactic insertion reaction of Li into Na_1Si_{136} allows for Li to spread throughout the Si matrix, forming $Li_{32}Si_{136}$ with Li sites in the Si_{28} cages throughout the electrode, and establishes important diffusion paths that are maintained after amorphization occurs.[244] This allows the nearly guest-free type II Si clathrate to form an amorphous phase with a higher amount of retained Si–Si bonds than those found in the Na-filled clathrates, which is responsible for the higher voltage during the initial part of the lithiation process. Given that the clathrate host becomes amorphous at a composition with comparatively lower Li content, the reaction is then able to proceed through a single-phase reaction similar to that seen in the lithiation of amorphous Si.

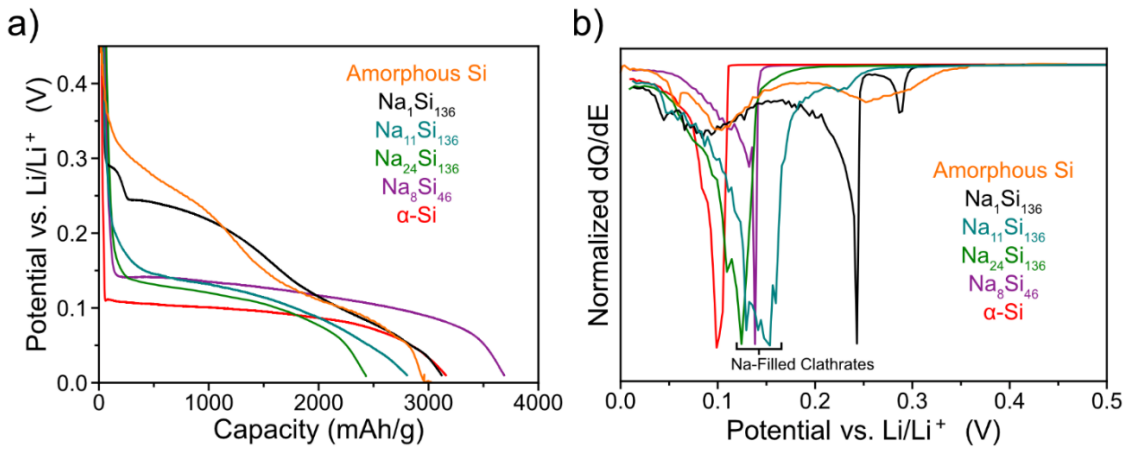

Figure 4.3.7 Comparison of the voltage profiles and dQ/dE plots of various reported Si structures. The data for Na_1Si_{136} and α-Si are from this work, that for $Na_{24}Si_{136}$ from ref. 5, that for $Na_{11}Si_{136}$ from ref 12, that for Na_8Si_{46} from ref.13, and that for amorphous Si from ref.17

Another interesting trend in the Na-filled clathrates ($Na_{11}Si_{136}$, $Na_{24}Si_{136}$, Na_8Si_{46}) is that they all react at a higher voltage (around 0.12 – 0.15 V) compared to that for α-Si (0.10 V) (**Figure 4.3.7**). We speculate that this behavior could originate from the presence of the Na guest atoms within the Si framework, which provide extra electron density that could aid in destabilizing the Si–Si bonds as Li is inserted and the amorphization process begins. Since Si–Si bond breaking is expected to be the most kinetically difficult step of the reaction,[35] the presence of Na atoms could modify the local structure of the amorphous phase, which would change the reaction voltage. Future PDF studies would be insightful for confirming this speculation.

It is also interesting to note that the voltage characteristics of the type I clathrate, Na_8Si_{46},[262] are similar to those of the Na-filled type II clathrate ($Na_{24}Si_{136}$).[53] The type I clathrate structure has a different arrangement of polyhedral cages comprising six tetrakaidecahedra (Si_{24}) and two dodecahedra (Si_{20}) per unit cell. Though the arrangement of Si is slightly different in the type I and type II structures, the local structures are similar. Since both crystal structures become amorphous during electrochemical lithiation, the small differences in the initial crystalline structures are not expected to result in significant differences in the local structure after lithiation, since the properties of the amorphous phases are dominated by local interactions. This is an important point as it suggests that the *composition* of the clathrate is more relevant for determining the electrochemical alloying behavior rather than the *structure* of the clathrate. In this case, we see that the alloying behavior in nearly Na-free clathrate is more similar to the solid-solution process seen in amorphous Si, whereas the Na-filled clathrates all display similar two-phase reactions. As explained earlier, this distinction likely has to do with the

diffusivity of Li through the structure, with the presence of Na decreasing the Li diffusivity and inhibiting the single-phase reaction.

4.3.5. Conclusions

X-ray pair distribution analysis is used to investigate the amorphous alloying pathway of Na_1Si_{136} and compare it with diamond cubic structured α-Si. We find that after the initial insertion of Li into the empty cages, the clathrate goes through a two-phase reaction to form an amorphous phase with a high amount of Si–Si connectivity. Upon incorporation of more Li, the local structure of the amorphous phase changes via the continuous breaking of Si–Si bonds, resulting in a sloped voltage profile. Near the end of lithiation, broad peaks in the dQ/dE plot at 0.10 V and 50 mV are observed, which is similar to those seen in the lithiation of amorphous Si. PDF measurements confirm that observed feature at 50 mV corresponds to the amorphous-to-crystalline phase transformation to form $Li_{15}Si_4$, suggesting that the clathrate behaves similarly to conventional Si electrodes after the initial insertion and two-phase reaction.

The origin of the high voltage, two-phase reaction of the lithiated clathrate ($Li_{32}Si_{136}$) is attributed to the initial topotactic Li insertion process into the clathrate cages that precedes the Li alloying reaction and allows Li to spread throughout the Si matrix, establishing important diffusion paths which allow the crystalline Si clathrate matrix to become amorphous at a lower Li composition and allows the resulting amorphous lithium silicide phase to lithiate via single phase reaction mechanism. These results demonstrate

how initial bulk Li insertion into an alloying anode can lead to modified reaction paths by kinetically enabling the nucleation of amorphous phases with lower Li content.

5. HIGH TEMPERATURE ELECTROCHEMICAL SYNTHESIS OF SILICON AND GERMANIUM CLATHRATES

5.1. Solid-State Electrochemical Synthesis of Silicon Clathrates Using a Sodium-Sulfur Battery Inspired Approach

5.1.1. Introduction

Intermetallic clathrates are a class of materials comprising face-sharing polyhedral cages of Tetrel (Tt, where Tt = Si, Ge Sn) elements that encapsulate alkali or alkaline earth metal guest atoms. With their unique structures and tunable cage sizes, clathrates have received much attention for their thermoelectric,[211,284] superconducting,[44,87,177] optoelectronic,[174,182,285] and electrochemical[49,52,54,56,152,178,179] properties. As many of these properties are modulated by host-guest interactions and the clathrate cage occupancies, synthetic methods that can reliably result in pure-phase materials of the desired polytype are highly important. In particular, the possibility of using silicon and germanium clathrates as potential anodes for Li-ion batteries has attracted substantial research interest in recent years. We recently conducted *ab initio* density functional theory (DFT) calculations on type I clathrates based on Tt_{46} and found

the barriers for Li migration were 0.4 eV or lower, which suggests that these materials could be very promising in battery applications.[179] Through our experimental studies,[53,54,56,152,178] we have further investigated the role of framework structure and defects in clathrates for applications as anodes, with structure-dependent electrochemical properties playing a major role in the lithium insertion or alloying behavior in these materials. As a result, synthetic approaches that can result in phase-pure clathrate materials will greatly benefit the elucidation of relationships between their structure and electrochemical properties.

The clathrates discovered in 1965 by Kasper *et. al* contain Na guest atoms surrounded by different sized Si frameworks, with the type I clathrate (Na_8Si_{46}) composed of Si_{20} and Si_{24} cages and the type II clathrate ($Na_{24}Si_{136}$) composed of Si_{20} and Si_{28} cages.[86] The synthesis of these structures relies on the removal of Na atoms from the Na_4Si_4 Zintl phase, *e.g*. via thermal decomposition,[86,155,170,286–288] reaction with chemical oxidants,[181,289] or spark plasma sintering (SPS),[290–293] after which the tetrahedral Si clusters reform into the clathrate cages under sufficiently high temperatures (350 – 600 ºC). The success of the SPS and kinetically controlled thermal decomposition[170] methods have demonstrated the importance of the rate of reaction (*i.e.*, rate of sodium removal from Na_4Si_4) for obtaining phase-pure Si clathrates with Na guest atoms. However, these techniques do not allow for direct control over the reaction rate; rather, the reaction rate is determined by the reactor characteristics at a certain temperature. For instance, the SPS technique relies on DC current pulses to control the temperature (by Joule heating) and to drive the oxidation of Na_4Si_4. Since the DC current pulses are responsible for heating and oxidation, they are intrinsically coupled and thus can only operate in a limited range to

satisfy the required temperature. Therefore, a technique that allows for direct manipulation of the oxidization rate independently of the temperature could enable greater control of phase selectivity and morphology, which is important for materials property characterization and utilization of clathrates in the aforementioned applications.

To address these issues, we present a new synthetic approach for silicon clathrates using an electrochemical cell inspired by the high temperature sodium-sulfur (Na-S) battery,[294] wherein molten Na and S electrodes are separated by a Na^+ conducting beta alumina solid electrolyte. On the basis of the high Na^+ conductivity in beta alumina materials[295] in the temperature range in which clathrates can form from tetrahedral Si clusters, we propose that an electrolytic cell utilizing β”-alumina and a molten Na electrode can be used to electrochemically oxidize (*i.e.,* desodiate) a working electrode comprised of the Zintl precursor to form the Si clathrate using galvanostatic control over the reaction kinetics. Herein, this cell is used to prepare type I clathrate Na_8Si_{46} from Na_4Si_4 through a solid-state electrochemical oxidation reaction for the first time. The room temperature lithium insertion properties of the Na_8Si_{46} obtained from this synthesis were also evaluated and are reported for the first time. The results show that solid-state electrochemical synthesis by use of a β”-alumina solid electrolyte is effective for obtaining phase-pure type I clathrate materials. The synthetic approach decouples the reaction temperature from the rate of oxidation, leading to opportunities for more controlled crystal growth. In addition, the application of electrochemical analytical methods enables a deeper understanding of the thermodynamic processes involved in the formation of intermetallic clathrate phases. We therefore show that beta alumina, of which the original discovery was deemed by Whittingham and Huggins to be the

"prelude to a revolution in solid-state electrochemistry" for its role in catalyzing the search for ion conducting materials crucial to the development of rechargeable batteries,[296] can also play a key role in enabling solid-state synthesis methods for the preparation of novel electrode materials for these batteries.

5.1.2. Experimental Methods

Preparation of Na_4Si_4 Pellet - In order to prepare Na_4Si_4, Na and Si were combined in a 1.2 : 1 molar ratio and sealed in a Nb tube under argon using arc-welding. The Na and Si were purchased from either Aldrich or Alfa-Aesar with stated purity greater than 99.9 wt % (metals basis) and were used as received. The Nb tube was then sealed in a stainless-steel reactor under an argon environment and then heated at 650 ^oC for 48 hr. Afterwards, the Nb tube was opened in an argon-filled glovebox and the contents were ground with a mortar and pestle into a fine powder. The Na_4Si_4 powder was then pressed into a 12 mm diameter pellet using a pressure of 1000 psi in an argon environment. The pellet of Na_4Si_4 served as the working electrode in all electrochemical experiments. The typical amount of Na_4Si_4 used in an experiment was 100-160 mg.

Assembly of Electrochemical Cell - The housing of the electrochemical cell comprised a stainless-steel 304L half nipple (Kurt J. Lesker, HN-0275) with the bottom welded closed with a stainless-steel cap. This served as the positive electrode current collector in the experiments. A 0.094-inch diameter stainless-steel wire insulated with alumina and mounted on a 2.75-inch feedthrough (Kurt J. Lesker, EFT0512993) served as the negative electrode current collector. During the experiments, the flange with the

electrical feedthrough was connected to the positive current collector using screws and a copper gasket (**Figure G.1**). The solid electrolyte was purchased from Ionotec LTD (B1-50-LNZ, Na β"-alumina tube) and had dimensions of 28 mm (ID) x 50 mm (length) x 1.5 mm (thickness). Metallic Na and Sn were purchased from Sigma-Aldrich. Large excesses of Na and Sn metal was used for the counter electrode. For Na, the mass was around 5 g, while the mass of the Sn metal was 20 g.

A schematic of the assembled cell is shown in **Figure 5.1.1a**. A pressed pellet of Na_4Si_4 serves as the working electrode (WE) and a cup of Na^+ ion conducting, β"-alumina serves as the solid electrolyte[295] and reservoir for containing the liquid metal counter/reference electrode (either molten Na or Sn). This configuration is analogous to a Na-S battery with the Na_4Si_4 pellet in lieu of the molten sulfur cathode.[294] To assemble the electrochemical cell, the Na_4Si_4 pellet was placed at the bottom of the positive current collector reservoir. The β"-alumina cup which contained either Na or Sn metal was then placed on top of the pellet. To apply light pressure, a spring was placed on top of the β"-alumina cup before the feedthrough was placed on top with the copper gasket and sealed. Care was taken to ensure that electrical contact was made between the feedthrough and the Na or Sn CE after either metal was melted. All the above preparations were undertaken in an argon-filled glovebox. For electrochemical measurements, the cell was heated in a furnace that was placed inside an argon-filled glovebox and heated to the desired temperature for electrochemical oxidation. Stainless-steel wire (as seen in **Figure G.1)** was used to make electrical connection from the reactor inside the furnace to the electrical feedthrough in the glovebox that was connected to the potentiostat outside.

Electrochemical Measurements - A Biologic SP-200 potentiostat was used to conduct the electrochemical experiments. Galvanostatic cycling with potential limits (GCPL) was used to perform the galvanostatic intermittent titration technique (GITT). In general, a constant current pulse was used for a set amount of time, followed by relaxation at open circuit for a different amount of time. The current, current pulse time, and open circuit relaxation time can be found in the figure captions associated with the voltage profiles. The current density was chosen so that the desodiation reaction would be completed within several days. When the cell impedance was observed to substantially increase, the current density was adjusted (*i.e.,* decreased).

The theoretical gravimetric specific capacity of Na_4Si_4 was determined using its molecular weight, the stoichiometry of the oxidation reaction, and Faraday's constant, as shown in the following:

$$1\ g\ Na_4Si_4 * \frac{1\ mol\ Na_4Si_4}{204.32\ g} * \frac{38\ mol\ Na^+}{\frac{23}{2}\ mol\ Na_4Si_4} * \frac{1\ mol\ e^-}{1\ mol\ Na^+} * \frac{96485.33\ C}{1\ mol\ e^-}$$

$$* \frac{0.2778\ mAh}{1\ C} = 433\ \text{mAh/g}$$

Post-Synthesis Washing of Reaction Products - After the electrochemical oxidation reaction, the electrochemical cell was opened in an argon-filled glovebox and the powder was removed. To remove residual Na_4Si_4, the powder was removed from the glovebox and transferred to a fume hood. Then, ~10 mL ethanol was introduced rapidly to the powder from a wash bottle. Rapid bubbling would indicate the reaction of Na_4Si_4 with ethanol, since silicon clathrates are stable in air and water.[155] ***Note: Extreme care must be taken and appropriate personal protective equipment must be used when***

working with Na_4Si_4 in ambient conditions due to its high reactivity to both air and water. The powder was then immersed in an ultrasonic bath to break up agglomerates. After the bubbling decreased in intensity, de-ionized water (~10 mL) was introduced to the powder and the resulting suspension was sonicated for additional time. ****Caution: Do not add water directly to the powder containing Na_4Si_4 as it could lead to a fire.*** After all the bubbling had completed, the powder was recovered using vacuum filtration and then dried. The typical mass remaining after the washing procedure was 40-50 mg.

Materials Characterization - Powder X-ray diffraction (PXRD) was performed with a Malvern PANalytical Aeris research edition powder diffractometer with Cu X-rays operated at 40 kV and 40 mA with standard Bragg-Brentano diffraction geometry and Pixel3D detector. For the samples used for Rietveld refinement, data were taken from 10 $^{o} < 2\theta < 110^{o}$ in increments of 0.011 degrees. For air-sensitive samples, the sample was covered with a Kapton film in an argon-filled glovebox prior to diffraction measurements. The Kapton film resulted in a broad background from $15^{o} < 2\theta < 25^{o}$. Rietveld refinement was performed with Jana2006.[64] The peak shapes were described by the pseudo-Voigt function, background fit with Legendre polynomials, and atomic displacement parameters were modeled as isotropic. Initial occupancies were allowed to be refined but were then set to full occupancy if they were within the standard deviation of full occupancy. Scanning electron microscopy (SEM) was performed with a FEI Nova 200 Nanolab. The images were collected at 10 kV and a 0.54 nA spot size. Energy dispersive X-ray spectroscopy (EDS) measurements were taken at 20 kV with a 2.4 nA

spot size at a magnification of 800x. X-ray fluorescence (XRF) spectroscopy was performed with a Bruker S2 PUMA.

Room Temperature Lithiation - The synthesized clathrate materials were prepared into slurries by mixing the samples with 10 wt% carbon black (to serve as conducting additive) and 10 wt% polyvinylidene difluoride (PVDF) (to serve as binder) in N-methyl pyrrolidone (NMP) as solvent. Electrodes were also similarly prepared with Si powder (100 mesh, Sigma Aldrich 99.999%, hand ground before use) for comparison. The slurries were stirred overnight and coated onto Cu foil current collectors using a Meyer rod, and then heated at 120 ^{o}C to remove the solvent. The clathrate composite electrodes were evaluated in pouch cells with Li metal as the counter electrode, Celgard 2500 as separator, and 1.2 M $LiPF_6$ EC/EMC (3:7 v/v) as electrolyte. Electrochemical testing was performed with the GCPL (galvanostatic cycling with potential limits) technique using a Biologic VMP3 galvanostat/potentiostat. After lithiation, the pouch cell was opened in the glovebox and prepared for X-ray diffraction.

5.1.3. Results and Discussion

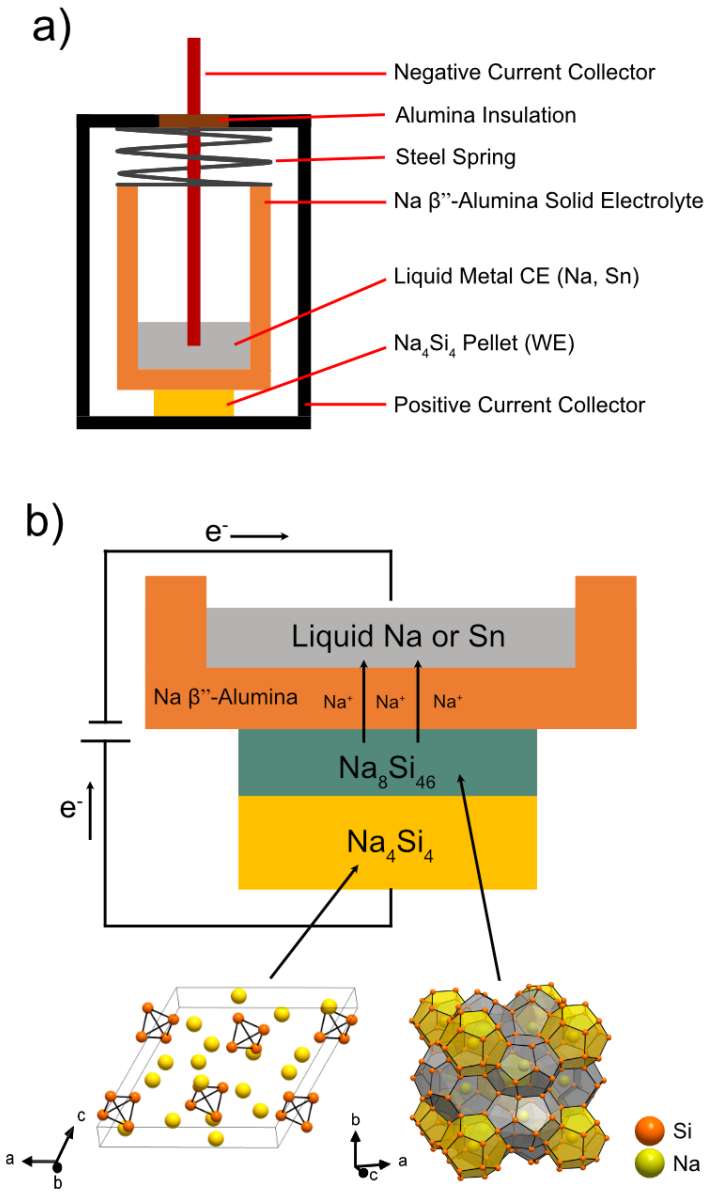

Figure 5.1.1 Schematics of the (a) electrochemical cell and (b) proposed electrochemical reactions. Na_4Si_4 is oxidized to Na_8Si_{46} at the interface with the electrolyte via removal of Na^+ and e^-; the Na^+ ions are reduced at the liquid metal counter electrode to form either Na metal or Na_xSn.

In this proof-of-concept, we show that product formation resulting from Na_4Si_4 decomposition can be controlled using electrochemical oxidation at different temperatures and using different counter electrodes (CE) to control the Na vapor pressure in the system. Removal of Na^+ ions and electrons from Na_4Si_4 results in oxidation of the $[Si_4]^{4-}$ tetrahedra to form new Si-Si bonds that comprise the framework of the Na_8Si_{46} clathrate; the sodium ions travel through the β"-alumina solid electrolyte and recombine with the electrons transferred via the external circuit, becoming reduced on the CE (**Figure 5.1.1b**). These electrochemical reactions, which are analogous to those that take place when charging a Na-S battery,[294] are written as follows:

Working electrode:

$$\left(\frac{23}{2}\right) Na_4Si_4 \rightarrow 38Na^+ + 38e^- + Na_8Si_{46}$$

Counter electrode:

$$Na^+ + e^- \rightarrow Na \quad \text{or} \quad xNa^+ + xe^- + Sn \rightarrow Na_xSn$$

To perform the desodiation of Na_4Si_4, the galvanostatic intermittent titration technique (GITT)[192] was utilized to obtain better understanding of the reaction processes through observation of the voltage under quasi-equilibrium conditions. **Figure 5.1.2a** shows the GITT profile for the oxidation of Na_4Si_4 at 450 ºC using the Na metal CE and low current densities (~1 – 2 mA/cm^2) for desodiation. Before any current was applied, the open circuit voltage was close to 0 V vs. Na/Na^+. The voltage of Na_4Si_4 vs. Na/Na^+ has been predicted by first principles calculations to be 50 mV at 0 K[297] and is expected to decrease with increasing temperature. As constant current was passed through the cell,

Na was removed from the Na_4Si_4 working electrode and the cell potential steadily increased. The difference between the constant current voltage (V_{cc}) and voltage after each relaxation step (V_{oc}) also increased as the reaction progressed, indicating a rise in cell impedance (**Figure 5.1.2**, insets). Despite this rise in cell polarization, the V_{oc} remained relatively constant as the sodium content in the WE decreased. For a two-component system at quasi-equilibrium conditions, a voltage plateau as the composition is varied is indicative of a two-phase reaction mechanism.[19] Therefore, these results suggest that the desodiated products nucleate and grow at the expense of the reacted Na_4Si_4.

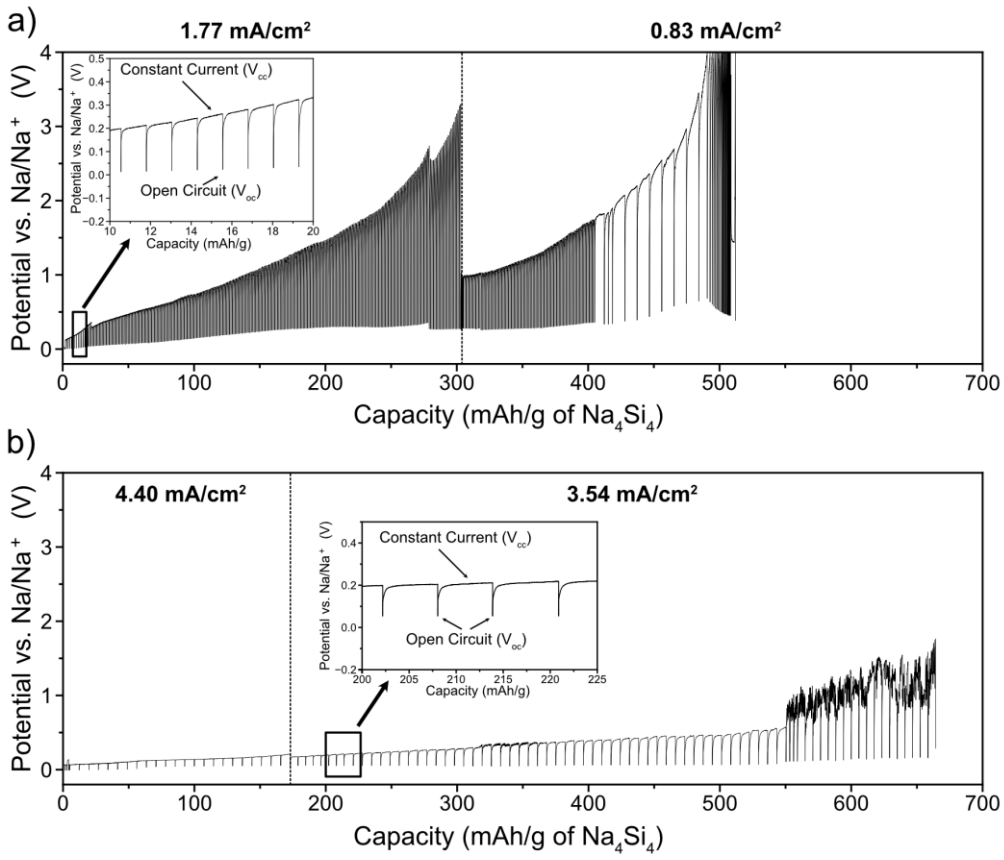

Figure 5.1.2 The galvanostatic intermittent titration technique (GITT) voltage profile for oxidation of Na_4Si_4 using a Na metal counter electrode at (a) 450 ºC (5 min current pulse,

45 s relaxation) and (b) 550 °C (12 min current pulse, 2 min relaxation). The insets demonstrate how the polarization (difference between V_{cc} and V_{oc}) increased during cell operation. For (a), the relaxation time was increased to 1.5 minutes after 280 mAh/g and at 425 mAh/g the curret pulse was increased to 90 minutes.

Due to the cell impedance increasing as desodiation progressed, the applied current density was decreased until the reaction time exceeded two days or when the potential reached 4 V. For the reaction performed at 550 °C using the Na CE (**Figure 5.1.2b**), the cell polarization was much lower than at 450 °C and higher current densities could be realized (3-4 mA/cm^2). The lower polarization of the reaction is likely due to the improved kinetics and conductivities of the components at the higher temperature. In the case of the reactions using the Sn CE (**Figure G.2**), the initial V_{oc} before current was applied was around -0.4 V due to the lower chemical potential of Na in Sn metal. The voltage profile had a similar shape as that obtained with the Na CE. Due to the large excess of Sn compared to the Na_4Si_4 in the cell, we expect the potential of Na_xSn to be relatively constant during the reaction, thus acting as a quasi-reference electrode.

PXRD analysis of the as-obtained products after the reactions (*i.e.*, prior to washing) showed that a significant fraction of residual Na_4Si_4 was still present in the samples when using the Na, but not Sn, liquid metal as CE (**Figure G.3**). Additionally, EDS analysis of the pellets reacted using the Na CE showed a high Na to Si ratio, indicative of the presence of Na_4Si_4 remaining after the reaction (**Figure G.4**). The products were then crushed and washed with ethanol and water to remove residual Na_4Si_4. Significant bubbling upon introduction of ethanol to the powder was only observed when washing the reaction products obtained when using the Na CE, indicating

the presence of Na_4Si_4. The powders obtained from the reactions using the Sn CE showed no bubbling when ethanol was introduced. These observations are consistent with the PXRD patterns of the powders before washing (**Figure G.3**) that show substantial amounts of Na_4Si_4 in the former case but not the latter. In cases where clathrate product was formed, a dark bluish black powder was obtained after drying, which matches the physical description of Na-Si clathrates from previous studies.[290]

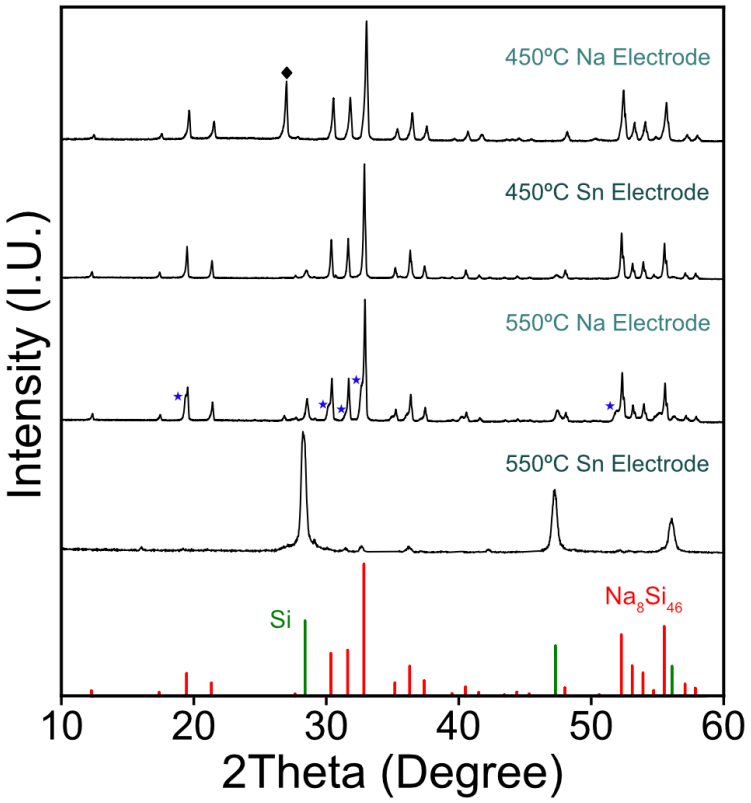

Figure 5.1.3 PXRD patterns of reaction products after washing with ethanol and water. The temperature and counter electrode used are indicated above each pattern. The reflection marked with a diamond is of unknown origin and not seen in any other samples. The blue stars indicate the presence of another type I clathrate unit cell attributed to the $Na_8Ga_ySi_{46-y}$ phase.

The PXRD results after the washing procedure revealed reflections corresponding to the type I clathrate Na_8Si_{46} under all conditions investigated (**Figure 5.1.3**). α-Si with diamond cubic structure was observed as a minority phase for the reaction performed at 550 ºC using the Na CE (8.12 wt%) and 450 ºC with the Sn CE (5.29 wt%), although α-Si was the predominate phase at 550 ºC using the Sn CE. Energy dispersive X-ray spectroscopy (EDS) analysis of the powders containing Na_8Si_{46} after washing (**Figure G.5**) detected the presence of Na and Si, corroborating the PXRD results and confirming the formation of clathrate compounds, which are stable in water or alcohol.[155]

SEM images comparing the morphologies of the Na_8Si_{46} samples obtained under the different reaction conditions are presented in **Figure 5.1.4**. For samples prepared at 450 ºC, agglomerates were observed with primary particles less than 1 micron in size and ligament-like microstructures. The sample prepared at 550 ºC with the Na CE displayed agglomerates with larger primary particle sizes, demonstrating how altering the reaction conditions can result in modified morphologies. The porous, ligament-like morphology could result from the decrease in volume that occurs when converting Na_4Si_4 to Na_8Si_{46} while the particles maintain ionic and electronic contact. Indeed, cross-section SEM imaging of the pellet after oxidation at 550 ºC reveals a porous connected network (**Figure G.4b**), supporting this hypothesis. In all reaction conditions used, the cell impedance increases with progressive conversion of Na_4Si_4 to Na_8Si_{46}, which could be due to the decreased reaction area due to volume contraction.

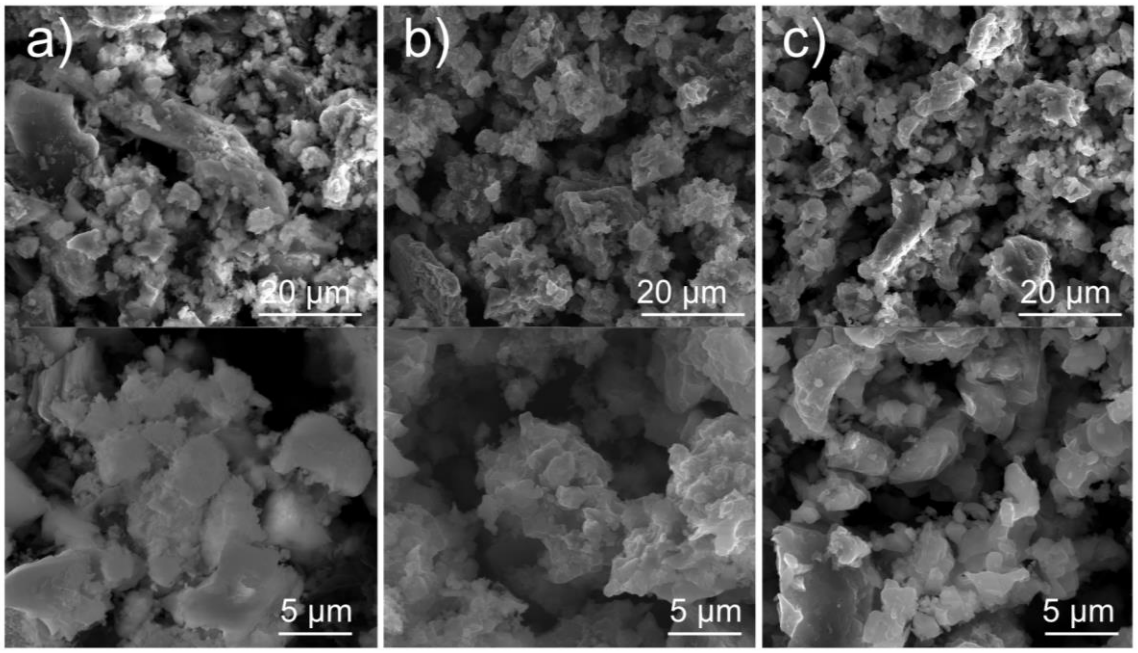

Figure 5.1.4 SEM images of type I Na-Si clathrates obtained at (a) 450 ºC with Na CE, (b) 450 ºC with Sn CE, and (c) 550 ºC with Na CE

Using the available PXRD data, Rietveld refinement was performed, with initial coordinates taken from the type I Na_8Si_{46} clathrate studies by Stefanoski *et al*.[170] The results (**Figure G.6-8, Table G.1-3**) showed that the Na_8Si_{46} structural model (all Na and Si sites occupied) fit well to the experimental pattern and resulted in lattice parameters in the range of 10.2002(4) – 10.2045(6) Å, close to those previously reported.[170,190] Interestingly, no reflections corresponding to the type II Si clathrate (Na_xSi_{136}, $0 < x < 24$) were observed, indicating that the type I phase is favored under these oxidation conditions, possibly due to the unique control over the rate of the reaction. In contrast, other synthetic methods described above typically result in mixtures of type I and type II clathrates.

For the sample synthesized at 550 °C with the Na electrode, closer inspection of the powder pattern revealed broadening of the reflections. The peak-asymmetry, particularly for the reflections at lower Bragg-angles, can be also described as "shoulders" (indicated by the blue stars), as shown in **Figure 5.1.3**. This is an indication of the presence of another type I clathrate phase with a larger unit cell than Na_8Si_{46}. The root-cause for the larger unit cell cannot be ascribed to defects on the Na sites (*i.e.*, Na_xSi_{46}, $0 < x < 8$), nor in the silicon framework (*i.e.*, Na_8Si_{46-x}, $0 < x < 2$), as the cell parameter is approximately 10.29 Å. Introducing the second phase into the refinement greatly improved the fit to the data. In view of the detection of a small amount of Ga in the sample (**Figure G.9**), this second clathrate phase is thought to be $Na_8Ga_ySi_{46-y}$, where Ga atoms are substituting for Si. Such a structure has been previously reported by Urushiyama *et al*.[298] For the refinement of the atomic parameters, the atomic displacement parameters were fixed to 0.005 for the Si/Ga atoms and 0.04 for the Na atoms; unphysical values were obtained when the parameters were not fixed. Then, the Ga content on the 24k site in the clathrate structure was fixed to 2% and the Ga occupancy on the 6c site was allowed to be refined while fixing the number of atoms on the 6c site. The refined lattice constant of 10.2857(6) Å matches well with the expected trend reported by Urushiyama *et al.* for a Ga content of y = 4.[298] We therefore assign this phase to a gallium-substituted silicon clathrate, $Na_8Ga_ySi_{46-y}$ (y = 3.8). The presence of Ga in the sample was confirmed with X-ray fluorescence analysis (**Figure G.9**). This was unexpected, as no Ga was intentionally introduced into the system, so the origin may be from Ga impurities or contamination of raw materials or reactor components. Future work will be done to investigate possible sources of impurities; however, the presence of

the Ga does not affect the major conclusions drawn in this work. This result, moreover, suggests that framework-substituted clathrates may also be accessible using this synthetic approach.

Table 5.1.1 Summary of the reaction products obtained prior to washing, experimental capacity, and percentage of theoretical capacity to form Na_8Si_{46} for the reactions conducted.

Counter Electrode	Temp (°C)	Products Before Washing	Expt. Capacity (mAh/g)	% of Theoretical Capacity
Na	450	Na_8Si_{46} + Na_4Si_4	512	119
Na	550	Na_8Si_{46} + Na_4Si_4 + α-Si (minority)	658	152
Sn	450	Na_8Si_{46} + α-Si (minority)	364	84
Sn	550	α-Si + Na_8Si_{46} (minority)	423	99

To better understand the differences in product formation when using various reaction conditions, the experimental desodiation capacities (determined from the charge transferred) were compared to the theoretical desodiation capacity of 433 mAh/g (based on the starting mass of Na_4Si_4, see **Table G.4**) and summarized in **Table 5.1.1**. The results show that when using the Na CE, the experimental desodiation capacity is greater than the theoretical amount possible calculated based on the starting amount of Na_4Si_4. Excluding corrosion of reactor parts, which is expected to be minimal, an alternative explanation is the presence of a secondary pathway for Na mass transport between electrodes that would allow for the reintroduction of Na to the WE. At these reaction temperatures, we hypothesize that there is sufficient Na vapor pressure to enable its reaction with Na_8Si_{46}, *e.g.*, after diffusion between gaps of the stainless-steel housing and

solid electrolyte. This process (**Figure 5.1.5a**) can be thought of as a "self-discharge" reaction since it reverses the desodiation reactions described earlier. Subsequently, some of the clathrate is transformed back to Na_4Si_4, which can be re-oxidized to Na_8Si_{46} and register as "excess" desodiation capacity with respect to the original mass of Na_4Si_4. In other words, we propose that the Na_4Si_4 detected in the pellet after the reaction was not due to incomplete conversion of Na_4Si_4 to Na_8Si_{46}, but rather from the transformation of the Na_8Si_{46} product back to the reactant. Indeed, *in situ* synchrotron PXRD heating experiments have shown that there is strong structural coherency between certain lattice planes of Na_4Si_4 and Na_8Si_{46}, enabling relatively facile transformation between the two structures as the Na content is modulated.[299]

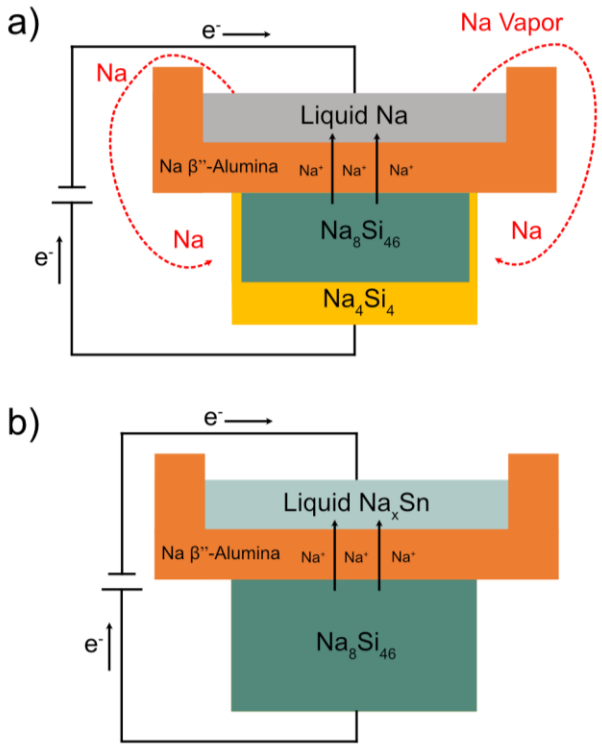

Figure 5.1.5 Schematic illustrating the role of Na vapor during electrochemical oxidation of Na_4Si_4 (a) As Na_4Si_4 is converted to Na_8Si_{46}, Na vapor originating from the Na CE reacts with Na_8Si_{46} to reform Na_4Si_4 on the WE, which can then be re-oxidized. (b) With a Sn CE, there is less Na vapor pressure in the system so the Na_4Si_4 is not reformed on the working electrode.

On the other hand, when Sn is used in place of Na as the CE, we find no excess desodiation capacity and the experimental capacities are lower than the theoretical values (**Table 5.1.1**). Since reflections from Na_4Si_4 were not observed in the PXRD patterns of the as-obtained reaction products (*i.e.*, before washing, see **Figure G.3**), this implies that the Na_4Si_4 was consumed in the electrochemical reaction. When Sn instead of Na is used as the CE, the reduced Na vapor pressure in the system suppresses the back reaction (**Figure 5.1.5b**). This difference is most pronounced for the reaction at 550 ºC using the

Sn CE, where α-Si is the main product. This also suggests that the Na vapor is contributing to the phase formation (which has been shown previously[155]), in this case leading to no clathrate formation. Others have reported the conversion of α-Si to Na_4Si_4 via reaction with Na vapor from 500 – 580 ºC,[175,300] thus confirming the reactivity of Na vapor at these temperatures. Therefore, it is plausible that the reverse reaction (formation of α-Si from Na_4Si_4) can occur under these conditions. Future studies will investigate how the temperature and Na vapor pressure affect the phase selection of the Na-Si clathrates in this system.

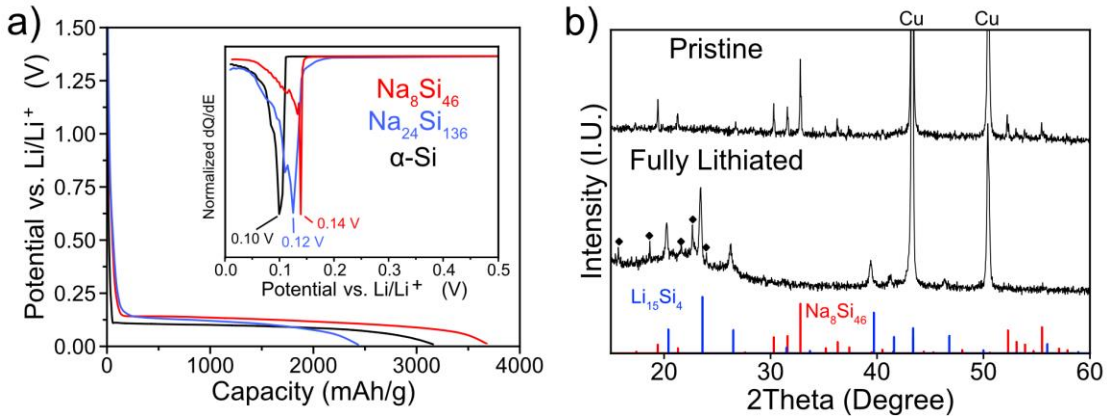

Figure 5.1.6 (a) Room temperature galvanostatic voltage profile and dQ/dE plot (inset) of the lithiation of Na_8Si_{46} synthesized at 450 °C with the Sn counter electrode (40 mA/g) and α-Si (25 mA/g) with a voltage cutoff of 0.01 V vs Li/Li^+. The data for the type II $Na_{24}Si_{136}$ was reproduced from ref. 16 and is obtained from potentiodynamic cycling with a 25 μA/mg threshold current. (b) PXRD patterns of the pristine electrode and after full lithiation with references for $Li_{15}Si_4$[231] and Na_8Si_{46}[170]. The diamonds indicate reflections from an unidentified phase.

Previously, only the electrochemical properties of the type II Na_xSi_{136} or mixed type II/type I phases as anodes for Li-ion batteries have been investigated.[49,53] Due to the phase selective synthesis for the type I silicon clathrate presented here, we are now able

to investigate the electrochemical lithiation of the type I Na_8Si_{46} without contribution from the type II Na_xSi_{136} phase. **Figure 5.1.6a** shows the room temperature voltage profile and dQ/dE plot of the lithiation of the Na_8Si_{46} clathrate synthesized at 450°C using the Sn electrode. Voltage profiles from diamond cubic Si (α-Si) and the mixed type I/II electrode (containing 20% Na_8Si_{46} and 80% $Na_{24}Si_{136}$) from our previous work[53] are shown as comparison. The voltage profile of Na_8Si_{46} is characterized by a plateau at 0.14 V vs. Li/Li^+ represented as a large peak in the dQ/dE plot and reaches a capacity of 3688 mAh/g at the voltage cutoff of 0.01 V. The profile shape of Na_8Si_{46} is similar to that of α-Si, but the clathrate reacts at a slightly higher voltage of 0.14 V vs. Li/Li^+ and displays a higher specific capacity. The voltage profile of Na_8Si_{46} is also similar to that of $Na_{24}Si_{136}$, which has a large voltage plateau around 0.12 V vs. Li/Li^+.[53] PXRD was performed of the electrodes before and after full lithiation (**Figure 5.1.6b**). The results showed that the Na_8Si_{46} reflections disappeared after lithiation, with new reflections corresponding to $Li_{15}Si_4$[41] and an unknown phase (marked by diamonds) observed. The origin of the unknown phase will be investigated in future experiments, possibly with pair distribution function (PDF) analysis, which has been helpful in elucidating the structure of clathrate lithiation intermediates.[178] Our previous work[53] on the mixed type I/II Si clathrate electrode showed that the material turned amorphous during lithium insertion and then subsequently recrystallized into $Li_{15}Si_4$ after full lithiation. The observation of reflections from $Li_{15}Si_4$ in the PXRD pattern of the fully lithiated Na_8Si_{46} suggests that a similar alloying reaction may be occurring in the type I clathrate. This is also interesting as our recent work on the germanium clathrate with type I structure (Ba_8Ge_{43}) showed that the presence of Ba atoms during the Li alloying reaction impeded the formation of crystalline

$Li_{15}Ge_4$.[178] As Na atoms are smaller and more chemically similar to Li than Ba, we suspect that guest atoms larger than Na are needed to prevent long-range ordering during the alloying reactions of clathrates. Overall, the results suggest that Na_8Si_{46} behaves similarly to diamond cubic Si and $Na_{24}Si_{136}$ during lithiation by forming a lithiated amorphous phase until the crystallization of $Li_{15}Si_4$.

These results demonstrate that the bulk conversion of Na_4Si_4 via electrochemical oxidation to Na_8Si_{46} is possible and results in phase-pure materials that can be used for further study as anodes in Li-ion battery systems. We believe that this electrochemical oxidation approach can be broadly applied to other Zintl compound precursors. Our preliminary studies show that Ge clathrates with type II structure can be prepared from Na_4Ge_4 at 350 ºC using the same approach (**Figure G.10**). The success of these methods demonstrates the viability of the solid-state electrochemical approach for synthesis of both Si and Ge clathrates from Na-containing Zintl phases. Compared to other oxidation pathways to obtain intermetallic clathrates, the electrochemical method has distinct advantages. For instance, the rate of oxidation can be controlled independently of the temperature of reaction through tuning of the current density, which could lead to greater control over the reaction products. Due to the flexible nature of the electrochemical synthesis, we expect these results to have important implications for the solid-state synthesis of clathrates for optoelectronic, electrochemical, and thermoelectric applications.

5.1.4. Conclusions

In this work we demonstrate the electrochemical oxidation of Na_4Si_4 at 450 and 550 °C to form the type I Na-Si clathrate phase with a Na β”-alumina solid electrolyte and Na/Sn metal counter electrode. The electrochemical oxidation is performed with the galvanostatic intermittent titration technique (GITT) in order to observe the open circuit voltage at different states of charge. The GITT results show that as more Na is oxidized from Na_4Si_4, the difference between the voltage at constant current and open circuit increases indicating an increase in cell polarization. The relaxed voltage at open circuit is relatively constant during oxidation, suggesting the presence of a two-phase reaction. Based on the XRD analysis after electrochemical oxidation, the Na_4Si_4 phase is converted to the type I Na_8Si_{46} phase, corroborating the electrochemical results. The phase formation is found to be dependent on the temperature and choice of counter electrode (liquid Na or Sn). In the case of the Na counter electrode, the type I Na_8Si_{46} clathrate phase was formed at both 450 and 550 °C while the clathrate phase was only formed at 450 °C when using the Sn counter electrode. Based on the observed excess capacity and residual Na_4Si_4 present when using the Na counter electrode, we propose that the Na vapor pressure plays an important role during the electrochemical reaction by acting as another route for mass transport between electrodes. By decreasing the Na vapor during the reaction through use of the Sn counter electrode, the phase formation and morphology of the clathrate is altered, suggesting possible avenues for further control over the reaction products. Room temperature lithiation of the synthesized Na_8Si_{46} clathrate showed similar Li-alloying reactions to those seen in type II Si clathrate ($Na_{24}Si_{136}$) and α-Si. Overall, the high temperature electrochemical oxidation of Zintl phases with a Na

β”-alumina solid electrolyte is a novel synthetic method with the potential for greater control and understanding of clathrate synthesis.

5.2. Electrochemical Synthesis of Type II $Na_xSi_yGe_{136-y}$

This section is comprised of unpublished work.

5.2.1. Introduction

Type II Ge clathrates are of potential interest for electrochemical[52] and photovoltaic[150] applications. Recently, reversible Li insertion into type II Si clathrates was demonstrated[244] and it is predicted that similar behavior would occur in the type II Ge clathrate due to the same structure. Similar to the Si clathrate, the type II Ge structure can be prepared without guest atoms which is important for enabling the aforementioned applications. However in contrast to the Si clathrates, the synthesis of type II Ge clathrate has been more elusive as the traditional thermal decomposition of the sodium containing Zintl phase (Na_4Tt_4, Tt = Si, Ge) is more difficult for the Ge clathrate.[41] Previous synthesis methods have successfully obtained the type II Ge clathrate but typically with various impurity phases. Using an ionic liquid to oxidize $Na_{12}Ge_{17}$, a guest free type II Ge clathrate was obtained with diamond Ge impurities[157] and this method has been further optimized to rely on the gaseous oxidation by HCl[301]. Thermal decomposition has also been demonstrated to be successful with modified reactors[1c0] and with thin films.[128] Recently, an electrochemical approach based on a molten salt electrolyte synthesized the type II Ge clathrates ($Na_{24-x}Ge_{136}$) from the oxidation of the $Na_{12}Ge_{17}$ Zintl phase along with other impurities.[263] One of the notable impurities is a hexagonal $Na_{1-x}Ge_{3+z}$ phase which has been obtained separately from a thermal decomposition of Na_4Ge_4 at 350-360 ^oC.[302,303] Based on the current reports, there is no established conditions under which the formation of the clathrate phase or hexagonal phase forms and methods for achieving phase purity are needed. To achieve this, better understanding of the reaction conditions

and phase formation in this system is needed to fully realize and establish the properties of this potentially technologically useful material.

Previous synthesis of type II Ge and type II alloyed Si-Ge clathrates demonstrated that alloying Si or Ge into the structure can aid in targeting the type II phase by destabilizing other competing phases.[150] For instance, adding 10% of Ge to Na_4Si_4 resulted in no formation of the type I clathrate phase which is a common byproduct of the thermal decomposition of Na_4Si_4.[155]

Recently, we reported an electrochemical method to synthesize Na-Si clathrates using a Na conducting β-alumina phase with an analogous cell geometry to a Na-S battery. Na_4Si_4 was converted into the type I Na_8Si_{46} clathrate via solid-state two-phase reaction under constant current oxidation conditions. To further evaluate this method for synthesis of clathrates, in this work we investigate the solid-state electrochemical oxidation of Na_4Ge_4 at various temperatures (300-400 °C). To investigate the possibility of achieving better phase purity, the alloyed Na_4Ge_3Si Zintl phase was also synthesized and used as the working electrode in the electrochemical experiments. The electrochemical oxidation method allows for *in situ* observation of the electrode potential during the reaction which can provide better understanding of the reaction mechanisms.

The results show the products of the electrochemical oxidation of Na_4Ge_4 is temperature dependent with the type II phase forming at low temperature, the hexagonal phase at intermediate temperatures, and diamond Ge at higher temperatures. Performing the oxidation with the Si doped $NaGe_3Si_1$ resulted in the formation of pure type II and diamond phases at 350 and 400 °C, respectively suggesting that Si doping removes the

competition from the Na-Ge hexagonal phase. Rietveld refinement is performed on the alloyed type II Ge-Si clathrate and suggests that Na is off-center in the larger cages which is supported by DFT calculations. Overall, this work further demonstrates the viability of using electrochemical methods to synthesize clathrates via the oxidation of the Zintl phase precursors.

5.2.2. Experimental and Computational Methods

5.2.2.1. Preparation of Na_4Ge_4 and $Na_4Ge_3Si_1$ electrodes

In order to prepare Na_4Ge_4, Na and the Ge were combined in a 1.2 : 1 molar ratio and sealed in a Nb tube under argon using arc-welding. The Na and Ge were purchased from either Aldrich or Alfa-Aesar with stated purity greater than 99.9 wt % (metals basis). The Nb tube was heated at 650 °C for 48 hours in a muffle furnace under in an Ar atmosphere with (<0.1 ppm O_2 and H_2O). To prepare $Na_4Ge_3Si_1$, first Ge and Si was ball-milled for 8 hours using a Spex Mixer/Mill 8000M with a stainless-steel jar and balls (SPEX 8007 - Stainless Steel Grinding Vial Set). Then the alloyed Ge-Si powder was combined in a 1.2 :1 molar and heated in a similar manner as the Na_4Ge_4 phase. Afterwards, the Nb tube was opened in the Ar glovebox and the contents were ball-milled in a tungsten carbide lined vial with a tungsten carbide milling ball (SPEX SamplePrep 5004) for 5 minutes to create a homogenous powder. The powders were then pressed under an Argon atmosphere using a 7mm diameter die at 750 psi. The pellet served as the working electrode in all electrochemical experiments. Typical mass of the pellets were around ~30-35 mg which corresponded to capacities of 8-12 mAh.

5.2.2.2. Electrochemical Reactor Assembly

The housing of the electrochemical cell comprised a stainless-steel 304L half nipple (Kurt J. Lesker, HN-0275) with the bottom welded closed with a stainless-steel cap. This served as the positive electrode current collector in the experiments. A 0.094-inch diameter stainless-steel wire insulated with alumina and mounted on a 2.75-inch feedthrough (Kurt J. Lesker, EFT0512993) served as the negative electrode current collector. During the experiments, the flange with the electrical feedthrough was connected to the positive current collector using screws and a copper gasket. All cell assembly was done in a Ar glovebox.

The solid electrolyte was purchased from Ionotec (D11.5-1-LNZ), a cylindrical membrane with a diameter of 11.5 mm and a thickness of 1 mm. The cell is comprised of two boron nitride crucibles. The smaller boron nitride (BN) crucible had dimensions: height of 20 mm, inner diameter of 12 mm and outer diameter of 16 mm. The larger BN crucible had dimensions: height of 18 mm, inner diameter of 16 mm and an outer diameter of 20 mm. In the bottom of the small BN a 10 mm hole was cut in the bottom which serves to create the interface between the solid electrolyte and the Na metal. A metal disc (20 mm diameter, 4 mm height) with a tapped screw hole was screwed into the bottom of the large BN crucible to serve as part of the positive current collector. To assemble the cell, first a 15.5 mm diameter stainless-steel spacer (MTI, EQ-CR20-Spacer-05) was placed in the bottom of the large BN crucible on top of the screw followed by a spring (McMaster Car, 0.5” long, 0.48” OD,9435K115) and then followed by another stainless-steel spacer. Then, the Na_4Ge_4 pellet electrode was placed in the

center of the stainless-steel spacer. Then, the solid electrolyte membrane was placed on top of the pellet electrode. The small BN crucible is then placed on top and into the large BN crucible (they fit snugly together) and pushed down so the spring is applying pressure. Then while pressure is applied, a locking wire is inserted through pre-cut holes in the sides of both crucibles which locks both crucibles under compression of the spring. Then, Na metal is placed in the small BN crucible with the hole in the bottom that is exposed to the solid electrolyte. Prior to sealing in the housing, the cell is heated on a hot plate at 250 °C (in the glovebox) so that the Na metal melts to ensure contact with the solid electrolyte. Then, the cell is placed in the bottom of stainless-steel housing and is sealed with a copper O-ring. In subsequent cell assembly (i.e after heating and a reaction), the Na metal is stuck to solid electrolyte (as seen in **Figure 5.2.1c**) and the solid electrolyte and Na metal are secured to the small BN crucible. The same Na metal electrode was used for all the presented electrochemical experiments. After each reaction, a new spring was used. After a completed reaction, the cell was disassembled inside an Ar glovebox. In general, the working electrode pellet was not adhered to the solid electrolyte. In between the Na_4Ge_4 and $Na_4Ge_3Si_1$ reactions, the solid electrolyte surface was polished with 1000 grit SiC sandpaper.

5.2.2.3. Electrochemical Characterization

The electrochemical reactions were carried out using the galvanostatic intermittent titration technique (GITT) which involves current pulses followed by times for open circuit relaxation. The potentiostat used to carry out the electrochemical

reactions with a Biologic MPG-2 using the galvanostatic charging with potential limits (GCPL) method. Prior to starting the electrochemical oxidation, the cell was heated (in 2 hours) and held at 450 °C for 20 hour and then ramped down to the reaction temperature in 30 minutes with an additional 30 minute equilibration time before any current was passed. The purpose of the hold at 450 °C is to ensure and establish good interfacial contact with the Na and the solid electrolyte. Experiments done without the initial higher temperature hold resulted in poor interfacial wetting and high polarizations.

5.2.2.4. Materials Characterization

Powder X-ray diffraction (PXRD) was performed with a Malvern PANalytical Aeris research edition powder diffractometer with Cu X-rays (K alpha and beta) operated at 40 kV and 40 mA with standard Bragg-Brentano diffraction geometry and Pixel3D detector. For air-sensitive samples, the sample was covered with a Kapton film in an argon-filled glovebox prior to diffraction measurements. The Kapton film resulted in a broad background from $15^{o} < 2\theta < 25^{o}$. Scanning electron microscopy (SEM) was performed with a FEI Nova 200 Nanolab. The images were collected at 10 kV and a 0.54 nA spot size. Energy dispersive X-ray spectroscopy (EDS) measurements were taken at 20 kV or 30 kV at a magnification of 800x or 1500x.

Rietveld refinement was performed with Jana2006.[64] The peak shapes were described by the pseudo-Voigt function, background fit with Legendre polynomials, and atomic displacement parameters were modeled as isotropic.

5.2.2.5. Density Functional Theory (DFT) Calculations

The first-principles DFT calculations were performed to explore Na insertion and migration in guest free type II Ge clathrates using a similar manner as in our previous work[55,152,179,244]. The calculations were carried out using the VASP code[77,78], the PBE functional[73], and projector augmented wave (PAW) potentials with a plane wave basis set[78]. In the PAW potentials, the Ge 4p and 3d and Na 3s and 2p electrons were treated as valence electrons. The kinetic energy cutoff for the plane wave basis set was chosen to be 400 eV and the reciprocal space was sampled with the Monkhorst pack meshes 3 × 3 × 3 centered at Γ. The cubic Ge_{136} unit cell ($Fd\bar{3}m$ space group) was used in all calculations. The convergence criteria for the electronic and ionic relaxations were set to be 0.01 and 0.1 meV, respectively. These criteria resulted in relaxed structures with residual forces below 0.03 eV/Å. The geometric optimization was performed in two steps. First, the unit cell volume was optimized without the constraint of the cubic symmetry. Then the relaxed lattice constant, taken from the relaxed volume, was used in a second step where only ionic relaxation was allowed under the cubic symmetry constraint. The crystal structures with the ionic positions of the second step are reported.

The Gibbs free energy change of reaction (ΔG_r) and the average voltage were calculated as described previously[55,152]. The formulas used for calculating the Gibbs free energy change and average voltage for insertion of Na in Ge_{136}, for example, are shown in equation (1) and (2), respectively:

$$\Delta G_r = E(NaGe_{136}) - E(Na) - E(Ge_{136}) \quad (1)$$

$$V(x) = -\frac{\Delta G_r}{x}, x = \#\ of\ Na \quad (2)$$

where $E(NaGe_{136})$ and $E(Ge_{136})$ are the total free energies for the clathrate systems with and without the Na atom, and $E(Na)$ is the energy per atom for Na metal. The calculated values for $E(Na)$ is -1.311 eV/atom. A negative ΔG_r (i.e. positive voltage) represents a spontaneous reaction relative to Na metal, suggesting the feasibility of sodiation in a half cell with Na metal as the counter electrode. All crystal structure figures were created with Diamond 4.5.3.

The climbing image nudged elastic band (NEB) method was used to calculate the Na migration barriers[85]. All NEB calculations used a linear interpolation as a starting band with 7 intermediate images between the beginning and ending images. The images were converged until the force on each image was below 0.03 eV/Å.

5.2.3. Results and Discussion

In our previous work using β-alumina, a cup of the solid electrolyte was used to hold a liquid metal electrode and placed in contact with a working electrode pellet of the Na_4Si_4 precursor. In this work, a modified reactor was assembled with a solid electrolyte membrane to simplify the cell assembly procedure and provide a more reliable way to apply pressure to the electrodes. **Figure 5.2.1** shows a schematic and photographs of the cell. A detailed description of the cell assembly can be found in the experimental section. Two differently sized boron nitride (BN) crucibles are used as the base of the cell. In the bottom of the large BN crucible is a spring which allows for pressure to be applied when the small BN is placed into the large BN crucible. The $Na_4Si_yGe_{4-y}$ working electrode is placed in the center of stainless-steel spacer followed by the larger diameter solid

electrolyte membrane. Then Na metal, which acts as the reference/counter electrode is placed on top of the solid electrolyte to form the two-electrode cell. Prior to any potential being applied to the cell, the cell was held at 450 °C for 20 hours and then moved to the desired reaction temperature afterwards. Na β''-alumina has notable issues with Na metal wetting at lower temperatures (300 °C) and the hold at 450 °C is used to ensure good wetting of the Na metal with the solid electrolyte.[304] **Figure 5.2.1c** shows the Na metal electrode contacting the solid electrolyte with good wetting after a reaction involving the 450 ºC hold.

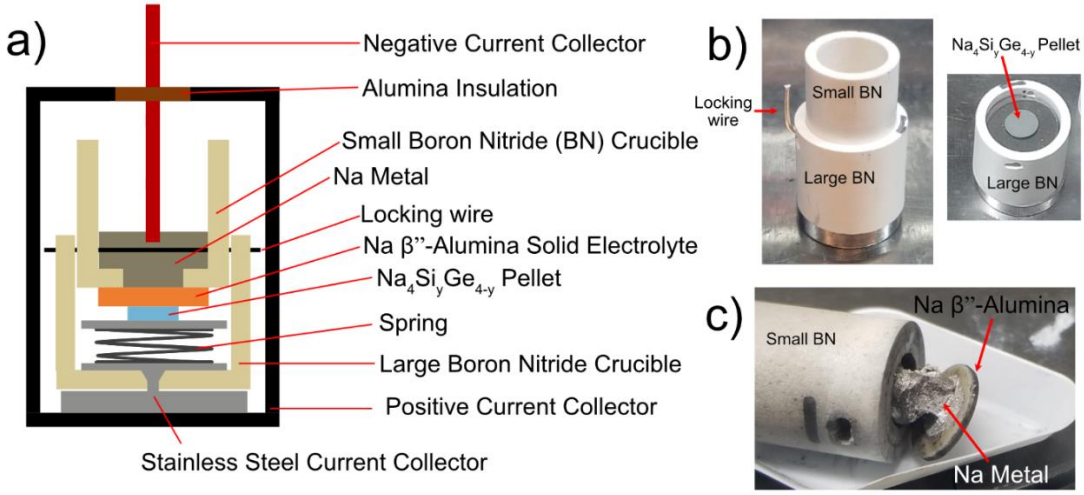

Figure 5.2.1 (a) Schematic of the two-electrode cell used to perform the electrochemical oxidation of the $Na_4Si_yGe_{4-y}$ Zintl precursors (b) Photograph of the cell assembled and the working electrode pellet in the center of the stainless-steel spacer. (c) Photograph of the Na metal and solid electrolyte interface demonstrating good Na wetting of the surface after heating at 450 °C.

To carry out the electrochemical oxidation, the galvanostatic intermittent titration technique (GITT) was used which involves current pulses with time for open circuit relaxation. The purpose of the GITT method is to observe the open circuit potential after

a relaxation time in order to remove the kinetic effects on the potential of the system. The difference between relaxed open circuit potential and the potential during constant current is referred to as the polarization.

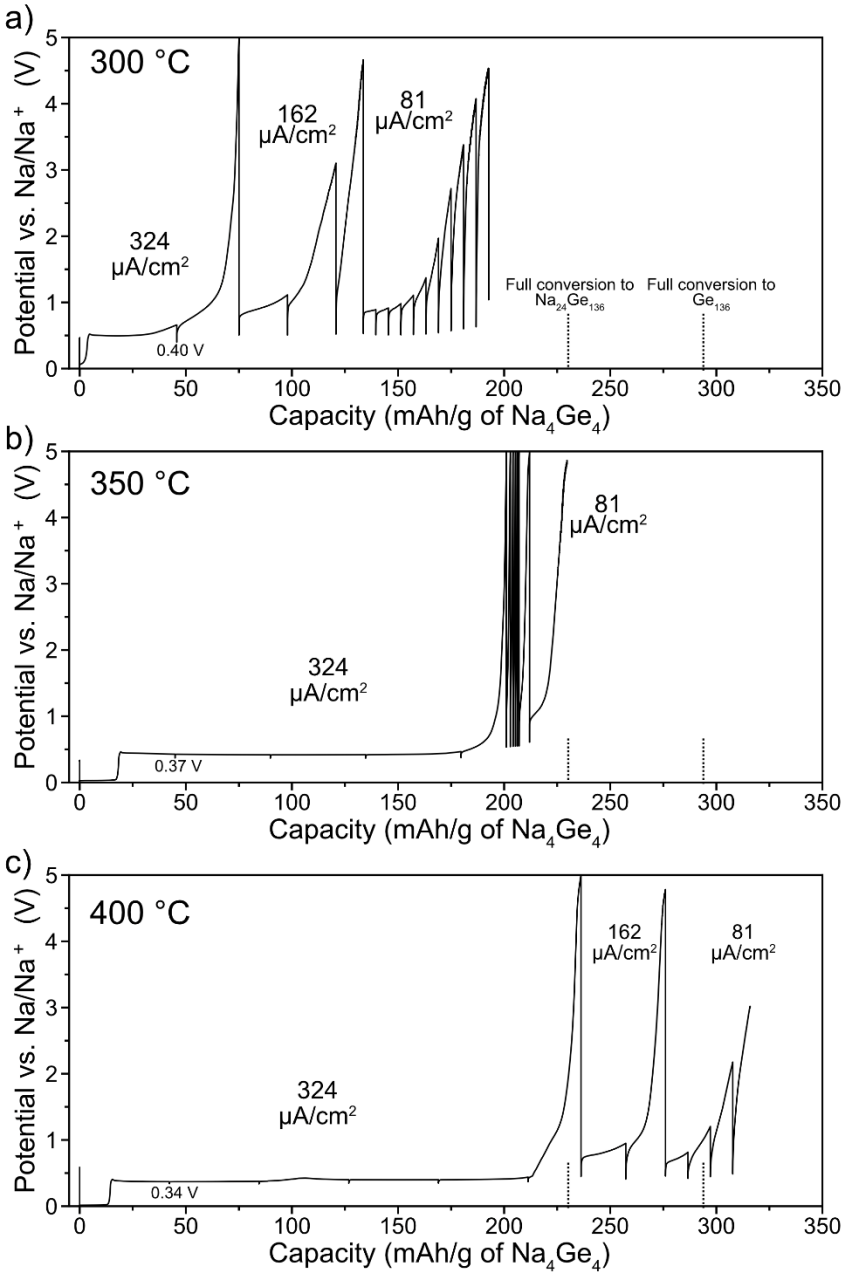

Figure 5.2.2 Galvanostatic intermittent titration technique (GITT) voltage profile of the oxidation of Na_4Ge_4 at (a) 300, (b) 350, and (c) 400 ºC with 12 hour current pulses and 1 hour of relaxation time.

Figure 5.2.2 shows the GITT voltage profiles at 300, 350 and 400 °C with the current densities used in each region for the oxidation of Na_4Ge_4. The current was decreased by half from the previous current starting with 324 μA/cm^2 when the voltage started to increase sharply or reached 5 V. The dotted lines at 231 mAh/g and 281 mAh/g mark the theoretical capacities assuming a starting composition of Na_4Ge_4 and then reaching a composition of $Na_{24}Ge_{136}$ and Ge_{136}, respectively.

Figure 5.2.2a displays the voltage profile for the electrochemical oxidation of Na_4Ge_4 at 300 °C which shows the potential of the cell starts close to 0.0 V vs Na/Na^+ and then shows a sloped region until plateauing at 0.50 V. The sloped region suggests that there could be some variable Na composition (i.e. $Na_{4\pm\delta}Ge_4$) in the Zintl phase as a continuous increasing potential represents a single phase region for a two-component system. The voltage plateau indicates the presence of a two-phase region suggesting that the conversion of Na_4Ge_4 is occurring. The relaxed potential after the first current pulse is 0.40 V which is notably higher than the potential for the conversion of Na_4Si_4 (57 mV at 550 C).[262] The potential of the system quickly rises at the first current density of 324 μA/cm^2 which is then lowered sequentially and eventually reaches a capacity of 190 mAh/g, lower than the capacity needed for full conversion to $Na_{24}Ge_{136}$. The relaxed voltage in between the current pulses is similar suggesting that despite the large rise in cell polarization, a two-phase reaction is occurring, similar to what was observed for the oxidation of Na_4Si_4.[262] **Figure 5.2.2b** shows the GITT voltage profile for the reaction at 350 °C, which shows much lower polarizations and a flat plateau with relaxed voltage of

0.37 V. The beginning of the profile shows a flat plateau near 0.0 V which could occur from excess Na metal from the synthesis as Na metal is expected to react at this potential. The polarization is much lower than at 300 ºC suggesting that the temperature has a large effect on the kinetics of the reaction. The capacity of the cell at 350 ºC reaches 240 mAh/g, which is close to a full conversion to $Na_{24}Ge_{136}$. The reaction at 400 °C is similar to that at 350 °C but with a lower voltage after relaxation of 0.34 V. The cell reaches a higher capacity than what would be expected from full removal of all the Na suggesting that there could be some Na vapor self-discharge as described in our previous work.[262] Although, the two electrodes are sealed from away from each other by a BN/BN interface and a solid electrolyte/BN interface, it is possible that some Na vapor is transporting between them to reform Na_4Ge_4. A Na vapor reaction with Ge to form Na_4Ge_4 has been demonstrated to occur at 400°C suggesting that this could be the cause of the excess capacity.[128]

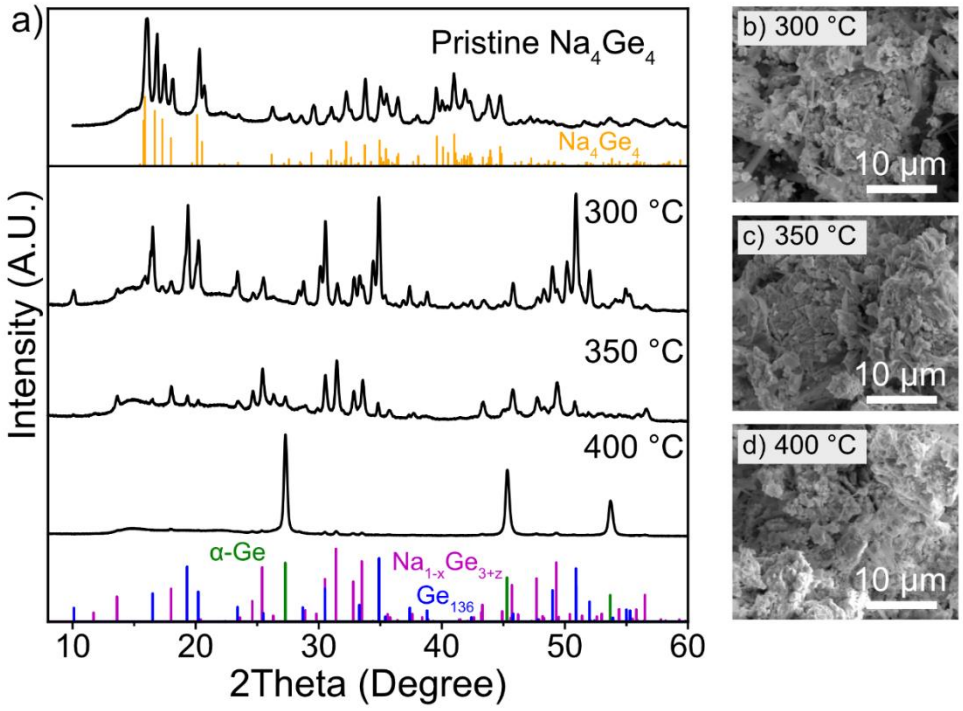

Figure 5.2.3 (a) PXRD of the pristine Na_4Ge_4 and the products of the reaction products synthesized. SEM micrographs of the products after exposure to air at (b) 300, (c) 350, and (d) 400 ºC. The broad background from 15º < 2θ < 25º is from the Kapton film used to protect the sample from oxidation during the PXRD measurement.Na_4Ge_4 reference structure from ref[305], Ge_{136} from ref[157], and $Na_{1-x}Ge_{3+z}$ from ref.[303]

After the reaction was completed, the cell was cooled and then disassembled, and the products were retrieved. PXRD of the pristine Na_4Ge_4 and the product of each reaction without exposure to air (using Kapton film) are presented in **Figure 5.2.3** in addition to SEM images (after exposure to air) at each temperature. The PXRD results show that in all cases the Na_4Ge_4 reflections have been converted into different crystalline phases. At 300 °C, there appears to be a small amount of Na_4Ge_4 present based on the peak at ~16 ° which would be consistent with the capacity being lower than the theoretical to form $Na_{24}Ge_{136}$. The other identified reflections include two Na_xGe_{136}

phases with different lattice parameters (possibility with different Na content) and a small amount of the hexagonal $Na_{1-x}Ge_{3+z}$ phase. Notably, there appears to be no α-Ge impurities at 300ºC which is commonly seen in other synthesis methods.[150,181,263] At 350°C, the major phase is the hexagonal $Na_{1-x}Ge_{3+z}$ phase with Na_xGe_{136} and α-Ge as minor phases, while at 400 °C, the major phase is α-Ge with a minor contribution from the hexagonal $Na_{1-x}Ge_{3+z}$ phase. Based on these assignments, the temperature of the reaction significantly affects the reaction products. At low temperatures, the type II phase is favored which is consistent with the reaction temperatures of other synthesis methods.[128,150,181,263] The formation of the hexagonal phase at 350 °C is also consistent the reported synthesis method of this phase.[302] Based on the voltage profiles in **Figure 5.2.2**, there is no significant voltage difference between the reactions and the effect of the temperature on the potential is not currently known. This suggests that all the phases are at a similar potential and the temperature is the main contributor to the phase formation.

SEM of the reaction products at each temperature are shown in **Figure 5.2.3bcd**. The powders were mainly comprised of agglomerates of smaller particles in addition to particles with wire-like morphology. Interesting, this wire morphology was seen in all the samples and the origin is unknown. The EDS of the powder do not show any obvious elemental impurities (**Figure H.1**), suggesting it is one of the reaction products. Overall, the results demonstrate the solid-state oxidation of Na_4Ge_4 in an electrochemical cell can result in analogous phase formation as other chemical oxidation methods, generally resulting in a multi-phase product. The voltage profiles demonstrate the reactions proceed via two-phase reactions with potentials around 0.34-0.40 V vs Na/Na^+.

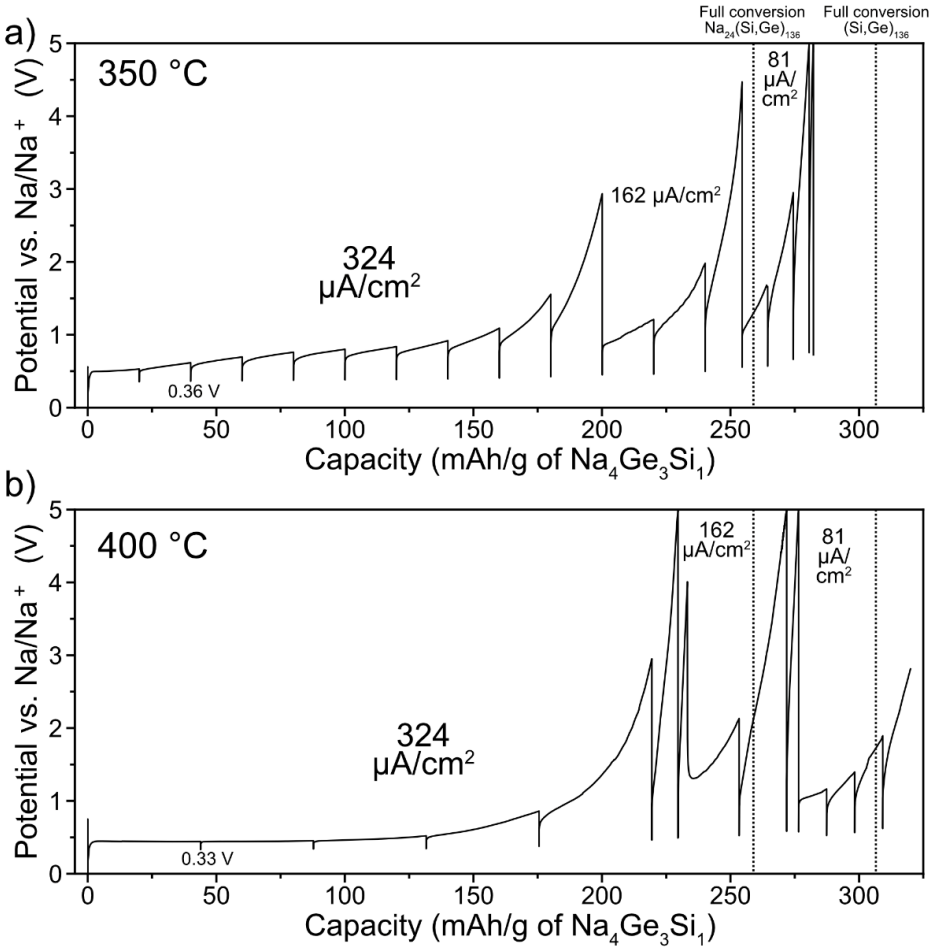

Figure 5.2.4 Galvanostatic intermittent titration technique (GITT) voltage profile of the oxidation of $Na_4Ge_3Si_1$ at (a) 350, and (b) 400 ºC with 12 hour current pulses and 1 hour of relaxation time.

Next, an electrode comprised of $Na_4Ge_3Si_1$ was oxidized in an analogous way as Na_4Ge_4 to investigate whether better phase purity could be achieved. **Figure 5.2.4** shows the voltage profiles of the oxidation of the $Na_4Ge_3Si_1$ Zintl phase at 350 and 400 °C with the dotted vertical lines showing the theoretical capacities for achieving the fully sodiated clathrate phase and to remove all the initial Na. The voltage profiles show similar behavior to those for Na_4Ge_4 with an initial potential starting near 0.00 V and quickly

increasing and then plateauing. There was no initial plateau at 0.00 V for these experiments suggesting that there was possibly less excess Na metal. The relaxed voltages during the plateaus were 0.36 V and 0.33 V for 350 and 400 °C, respectively. These voltages are similar to what was observed for the Na_4Ge_4 precursor at the same temperature suggesting that the Si alloying did not significantly change the reaction voltage. The final capacity at 350 °C was 260 mAh/g which is greater than the capacity of obtaining the composition $Na_{24}Si_{34}Ge_{102}$ while the reaction at 400 °C was 320 mAh/g, higher than the capacity of for removing all the starting Na suggesting that Na vapor might be self-discharging the cell. Overall, the voltage profiles of the oxidation of $Na_4Ge_3Si_1$ show similar behavior to those of the oxidation of Na_4Ge_4.

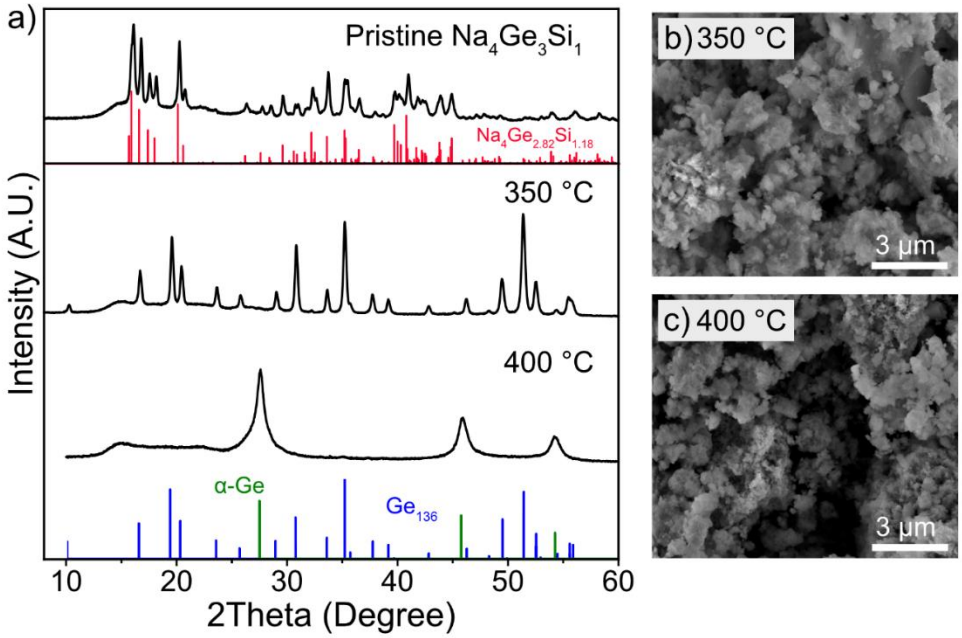

Figure 5.2.5 (a) PXRD of the pristine $Na_4Ge_3Si_1$ and the products of the reactions at 350 and 400 ºC. SEM micrographs of the products after exposure to air at (b) 350 and (c) 400 ºC. The broad background from $15º < 2\theta < 25º$ is from the Kapton film used to protect the sample from oxidation during the PXRD measurement. $Na_4Ge_{2.82}Si_{1.18}$ reference structure from ref[305], Ge_{136} from ref[157]

PXRD of the pristine $Na_4Ge_3Si_1$ reaction products without exposure to air is shown in **Figure 5.2.5** along with corresponding SEM micrographs. The products of the reaction demonstrate that full conversion of the Zintl phase precursor was achieved along with phase pure synthesis of the type II clathrate phase at 350 °C and the α phase at 400 °C. Notably, there is no sign of the hexagonal Na-Ge phase in the PXRD patterns suggesting that the incorporation of Si into the Zintl precursor prevented the formation of this competing Na-Ge phase. SEM micrographs of the products show that the powders are comprised of agglomerates of nanosized particles. The primary particles for the reaction at 400 °C are smaller than the clathrate and are consistent with the broad PXRD peaks which could be due to peak broadening due to nanometer crystallite sizes. The morphology is similar to the previous product of the oxidation of Na_4Si_4 which showed agglomerated powders with a large amount of texture suggesting the presence of many crystallites. Another notable difference between the Na_4Ge_4 oxidation and $Na_4Ge_3Si_1$ is the absence of the particles with wire morphology suggesting that the presence of the Si significantly modified the resulting products.

Rietveld refinement was performed on the PXRD for the clathrate phase synthesized at 350 °C from the $Na_4Ge_3Si_1$ precursor and is shown in **Figure 5.2.6**. First, the pattern was fit with a guest-free $Si_{34}Ge_{104}$ structure assuming homogenous mixing of the Si on the Ge framework sites. The ratio of Si and Ge was fixed to the nominal composition of the precursor and was confirmed based on EDS of the powders (**Figure H.2**). The refined lattice parameter of the structure was determined to be 15.1186(4) Å

which is lower than the lattice parameter of the guest-free Ge_{136} (15.2115(1) Å)[157] and similar to the lattice parameter of the alloyed $Si_{0.25}Ge_{0.75}$ clathrate (15.10 Å),[150] thus confirming the alloying of Si into the Ge clathrate. After the pattern was fit to the guest-free structure, a difference Fourier transform was performed which revealed residual electron density in both $(Ge,Si)_{20}$ and $(Ge,Si)_{28}$ cages. In the smaller cages, a peak was found in the center, which is attributed to Na, while in the larger cages residual electron density was split in a tetrahedron aligned around the four hexagons. The structure was in the refined with Na in the center of the $(Ge,Si)_{20}$ and in the off-center 32e position in the $(Ge,Si)_{28}$ cages with their displacement parameters fixed to equal to the framework site. The refinement resulted in a final composition of $Na_{3.4(1)}Si_{34}Ge_{102}$ suggesting that most of the Na had been removed by the electrochemical oxidation. The atomic parameters and atomic displacement parameters are presented in **Table H.1**.

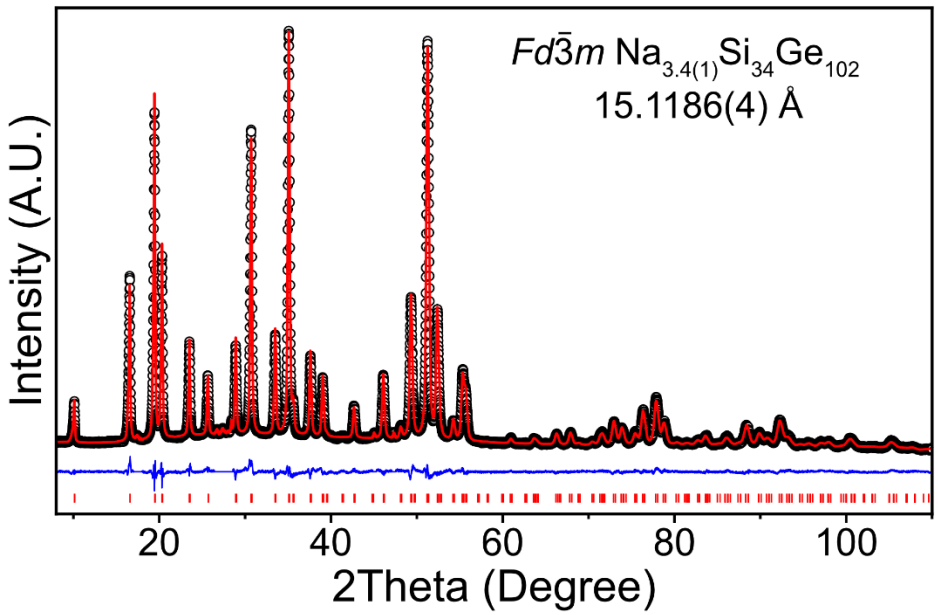

Figure 5.2.6 Rietveld refinement of the PXRD patterns of the products of the oxidation of $Na_4Ge_3Si_1$ at 350 ºC after being exposed to air. The black circles represent the

experimental pattern, the red curve represents the calculated pattern, and the blue curve represents the difference curve. The refined atomic positions, occupancies, and atomic displacement parameters can be found in **Table H.1**. The red tick marks represent the reflections corresponding to $Na_{3.4(1)}Si_{34}Ge_{102.}$ Refinement residuals: χ^2= 2.07, R_p= 0.028, and wR_p= 0.037.

The off-center Na positions aligned with the hexagon faces in the large hexakaidecahedra are similar to our previous refinements of Li in the Si_{28} cages[244] and result from a mismatch between the cage size and the size of the cation. Since Na already has been demonstrated to have a slightly off-center position in the Si_{28} cage,[186,290] this effect is expected to be exacerbated in the larger $(Si,Ge)_{28}$ cages. Although, this disorder has been modelled with off-center positions in the Si_{28} cages, modelling Na with off-center position has yet to be considered for the $Na_{24-x}Ge_{136}$ clathrate.[263,306] Here, we present structural evidence for the off-center positions for Na in the larger Ge cages.

To further investigate the possible Na positions in the Ge_{136} lattice, DFT calculations are used to evaluate separate Na positions. **Figure 5.2.7ab** shows a crystal model schematic of the investigated Na positions and the Gibbs free energy of reaction of each position along with the average sodiation voltage. The four positions investigated were the Ge_{20} center position, the Ge_{28} center position, Ge_{28} coordinated off the hexagonal face (Off Hex) and Ge_{28} coordinated off the pentagonal face (Off Pent). The relaxed off-center positions in the Ge_{28} cage were found to be 1.311 and 1.195 Å off-center for the Off Hex and Off Pent positions, respectively. For comparison, Na in Si_{28} is found experimentally to be 0.54 Å off-center.[290] **Figure 5.2.7b**, shows the Gibbs free energy of reaction for each Na position relative to Na metal and the guest-free Ge_{136} where a more negative Gibbs free energy corresponds to a more favorable reaction.

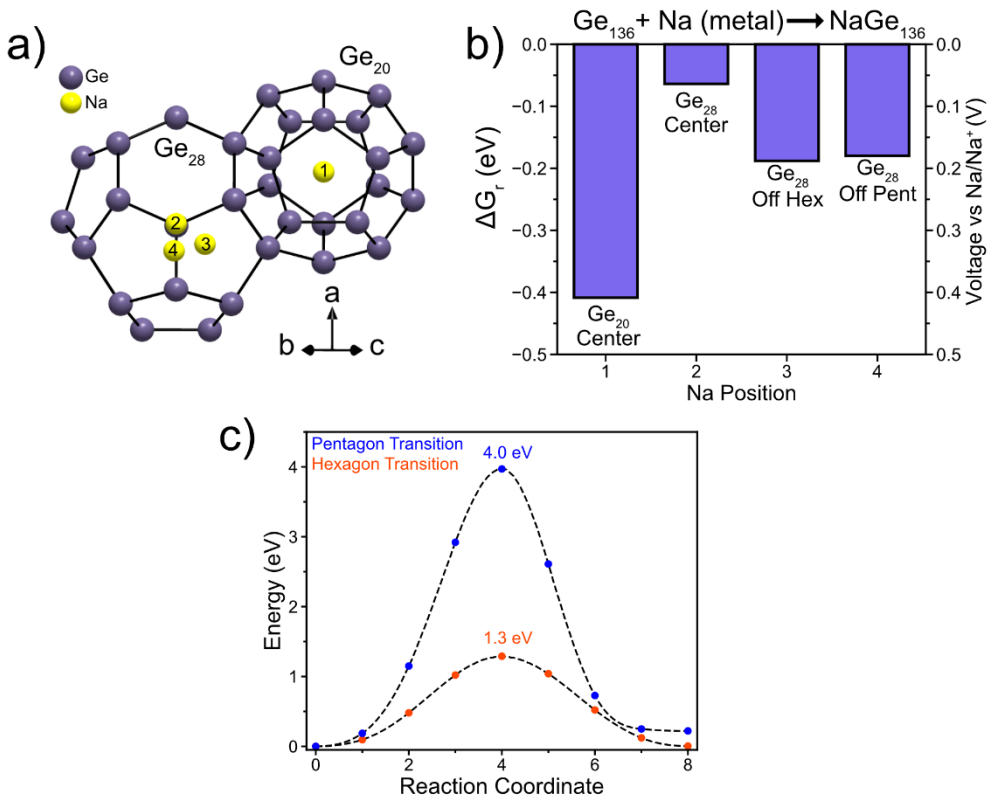

Figure 5.2.7 DFT calculations of Na positions in Ge_{136} **(a)** Schematic of a Ge_{28} cage connected with a Ge_{20} cage showing the DFT calculated Li positions viewed down the [110] direction. **(c)** Gibbs free energy of reaction (ΔG_r) for the reaction Ge_{136} + Na (metal) → $NaGe_{136}$ for each different Na position. **(c)** NEB-calculated minimum energy paths for migration of Na in Ge_{136} between the Ge_{20} and Ge_{28} cages through a shared pentagonal face (Pentagon Transition) and between the Ge_{28} and Ge_{28} cages through a shared hexagonal face (Hexagon Transition).

The results show that the most favorable Na positions in the lattice are the Ge_{20} center and the off-center positions in the Ge_{28} cage. The center Ge_{28} cage position is 0.12 eV higher in energy than the Off Hex positions suggesting that Na would prefer to occupy an off-center position in the large Ge_{28} cages which is consistent with the results from the Rietveld refinement. Though, the results are from the structure in the Rietveld refinement are alloyed with 25% Si, we expect a similar trend as it is primarily based on

the size of the cages. This result is consistent with our previous calculation on the position of Li and Na atoms in clathrate cages as a function of cage size.[179] The stability of the position is primarily determined by size of the clathrate cage and the alkali metal's favorable bond distance. The Ge_{28} cage is too large to maintain the favorable ~3.0 Å Na-Ge distance at the center of the cage and thus the Na atom prefers to be off-center.

Figure 5.2.7c shows the energy vs reaction coordinate plots for nudged elastic band (NEB) calculations performed to investigate the Na migration barriers between the two types of cages. Since, the $Na_{24-x}Ge_{136}$ can have a variable Na content,[263,306] the Na content is expected to be controlled by the bulk diffusion of Na through the clathrate lattice in a similar vein as Si_{136}.[168] Since guest-free clathrates are of more technological interest than the Na-filled ones, understanding the kinetics and pathways of Na migration will be important for obtaining these guest-free structures. The results show that when Na migrates between two Ge_{28} cages through a hexagonal face, the migration barrier is 1.3 eV, similar to our previous results for $NaGe_{46}$ (1.5 eV).[179] For Na migration between the Ge_{28} cage and Ge_{20} cage through a pentagonal face, the migration barrier is much at higher a 4.0 eV. Interestingly, the pathway did not converge to a path that resulted in breaking a Ge-Ge bond to lower migration barrier of the pentagonal transition state. This phenomenon has been observed in a variety of situations for Li and Na migration in clathrates[51,179,244] and seems to be a possible mechanism for alkali metals to move in and out of the small dodecahedra with a lower migration barrier. It is possible that that the transition state is only possible if a Na is in an adjacent cage and is a cooperative mechanism similar to Li in Si_{136} and Si_{46}.[179,244] More calculations and experiments will be needed to elucidate this mechanism and the diffusion of Na within the Ge framework.

The DFT calculations support the finding the Na prefers an off-center position in the hexakaidecahedra and demonstrates that Na migration barriers are expected to be relatively high consistent with the high temperature needed to desodiate the structure.

5.2.4. Conclusions

In this work, the solid-state electrochemical oxidation of Na_4Ge_4 and $Na_4Ge_3Si_1$ Zintl precursors are performed with a two-electrode cell using a Na β''-alumina solid electrolyte. The galvanostatic intermittent titration technique (GITT) is used to perform the oxidation and shows that the synthesis results in a two-phase reaction with constant potentials around 0.34-0.4 V vs Na/Na^+. The oxidation results in full conversion of the Zintl phase precursors which are transformed into different products depending on the temperature. For Na_4Ge_4, the products included the type II Ge clathrate, the hexagonal Na-Ge phase, and α-Ge phase showing a clear low to high temperature (300, 350 ,400 ºC) dependence on the phase formation. For the oxidation of $Na_4Ge_3Si_1$, no hexagonal Na-Ge phase was observed and phase pure alloyed type II clathrate phase and α phase were obtained at 350 and 400 ºC, respectively. Rietveld refinement of the type II alloyed Si-Ge phase resulted in a composition of $Na_{3.4(1)}Si_{34}Ge_{104}$ with a lattice parameter of 15.1184(4) Å in good agreement with previous reports. The Na positions are found to be off-center in the hexakaidechedra based on a difference Fourier transform and is supported by DFT calculations showing that Na energetically prefers an off-center position. Finally, NEB calculations are used to estimate the Na migration barriers which show that migration into the dodecahedra is kinetically difficult with a barrier of 4.0 eV, while Na migration through the hexagonal face between the Ge_{28} cages should is more facile with a barrier of 1.3 eV. These results demonstrate that electrochemical oxidation using a solid electrolyte

can be used to effectively synthesize Ge clathrate materials starting with Zintl phase precursors. Using a Zintl phase precursor alloyed with Si can be used to target the type II phase and achieve better phase purity than the pure Na-Ge precursor.

5.3. Electrochemical Na-Sn Flux Synthesis of Na-Si Clathrates

This section is comprised of unpublished work.

5.3.1. Introduction

Na-Si clathrates are host-guest structures comprised of a Si framework with Na guest atoms and have been recently investigated as Li-ion battery anodes with interesting properties.[49,53,244,262] However, the metastable nature of the structures requires alterative reaction pathways that start with a high energy precursor. All reported syntheses of the type I and type II Na-Si clathrates start with Na_4Si_4 followed by an oxidation of the structure resulting in Na atoms leaving and Si bonds being formed.[40,155,164,170,185,262,290,307–310] The process by which this occurs has been achieved by various oxidation methods including vacuum, chemical oxidants, electrochemical methods. The resulting morphology and size of the Na-Si clathrate crystals depends on whether Si mass transfer is possible at the required reaction temperature. For example, oxidation of Na_4Si_4 under vacuum results in polycrystalline powders while oxidation under applied pressure[170,290] or in a Na-Sn flux resulted in single crystals[309,310]. Due to the volume contraction of Na leaving Na_4Si_4, Si mass transport is required to form large single crystals or else the resulting structure is porous and polycrystalline because there is no mechanism by which Si can diffuse to achieve single crystal growth. This is evident from the SEM and TEM micrographs of the Si clathrates synthesized via the thermal decomposition and electrochemical oxidation of Na_4Si_4 described in Chapter 3.3 and 5.1[244,262]. Further development of the synthesis methods for the Na-Si clathrates will be vital in understanding the structure property relationships of these structures.

Recently, there have been several reports of using Na evaporation with a Na-Sn flux to grow large crystals (1-5 mm) of Na-Si clathrates[309,310] and other ternary[298] and quatnery[311] clathrates. At certain temperature and Na compositions, single crystal growth of type I and type II Si clathrates have been achieved. For example, at 500 °C, a starting mixture of Na:Si:Sn (6:2:1) was subjected to a thermal gradient for 48 hours which resulted in evaporation of 41.7% of the starting Na.[310] These conditions resulted in the growth of type I Na_8Si_{46} single crystals with sizes in the range of 1-2 mm. At a time of 72 hr, 53.3% of Na evaporated and the resulting product were large crystals (5 mm) of type I and type II Na-Si clathrates. From these results, the growth of the Na-Si clathrates is driven by the removal of Na from the Na-Si-Sn mixture resulting in single crystal growth.

As demonstrated in the Chapter 5.1 and Chapter 5.2, electrochemical oxidation of Na can result in analogous reactions to the reactions that rely on Na evaporation[262]. However, electrochemical methods come with the advantage of a larger amount of control over the reaction and an *in situ* observation of the electrode potential which is insightful for understanding the reaction mechanism. To further apply the electrochemical methods to the controlled growth of Na-Si clathrates, this section investigates using electrochemical methods to drive the Na oxidation of a starting mixture of Na-Si-Sn (6:2:1) to perform analogous reactions to the evaporation experiments described by Morito et al.[310] To achieve this, a two-electrode cell is assembled where a cup of the Na β’’-alumina electrolyte is immersed in a pool of Na metal while the inside of the cup contains the Na-Si-Sn flux. The electrochemical cell is then heated to 500 and 550°C and a constant current is applied to the cell which drives Na removal from the Na-Si-Sn flux and promotes the growth of Si clathrates.

5.3.2. Experimental Methods

5.3.2.1. Preparation of Na_4Si_4

In order to prepare Na_4Si_4, first Si was ball-milled for 10 minutes using a SPEX Mixer/Mill 8000M with stainless-steel jar and balls. The purpose of the ball-milling is to make the Si more reactive during its heating with Na metal. Then, Na and the ball-milled Si were combined in a 1.2 : 1 molar ratio and sealed in a Nb tube under argon using arc-welding. The Na and Si were purchased from either Aldrich or Alfa-Aesar with stated purity greater than 99.9 wt % (metals basis). The Nb tube was heated at 650 °C for 48 hours in an Ar glovebox with (<0.1 ppm O_2 and H_2O). Afterwards, the Nb tube was opened in an Ar glovebox and the contents were the ball-milled in a tungsten carbide lined vial with a tungsten carbide milling ball (SPEX SamplePrep 5004) for 5 minutes to create a homogenous powder. This powder was then used as the Na_4Si_4 source for the electrochemical reaction. The purity of the Na_4Si_4 was confirmed with PXRD.

5.3.2.2. Electrochemical Reactor Assembly

The housing of the electrochemical cell comprised a stainless-steel 304L half nipple (Kurt J. Lesker, HN-0275) with the bottom welded closed with a stainless-steel cap. This served as the negative electrode current collector in the experiments. A 0.094-inch diameter stainless-steel wire insulated with alumina and mounted on a 2.75-inch feedthrough (Kurt J. Lesker, EFT0512993) served as the positive electrode current collector. During the experiments, the flange with the electrical feedthrough was connected to the positive current collector using screws and a copper gasket.

The solid electrolyte was purchased from Ionotec (H1-35-LNZ) and was a cup with a height of 35 mm, inner diameter of 20 mm and thickness of 1.5 mm. To assemble the cell, first Na metal (Sigma-Aldrich) was placed in the bottom of a boron nitride crucible (MTI Corporation, EQ-CB-D30H26, 3 0O.D x 24 I.D x 26 H mm). 304 Stainless-steel mesh was placed and wrapped around the bottom of the boron nitride crucible to serve as the negative current collector. Then, the solid electrolyte was placed inside the boron nitride crucible containing Na metal. Then to prepare the reaction, Na_4Si_4 (~127 mg) and Sn powder (~150 mg) (Sigma-Aldrich ,10 micron >99%) were mixed in the bottom of the solid electrolyte cup until the powder looked visually homogeneous. Na metal (120 mg), which was melted and had its oxide layer removed, was placed on top of the powder. The oxide layer was removed by using metal tweezers to skim the oxide layer that is on the surface. As more oxide layers is removed the higher the surface tension of the Na metal becomes which indicates an oxide free surface. The molar ratio of Na:Si:Sn was approximately 6:2:1. Then the housing was sealed in the glovebox with the stainless-steel current collector contacting the powder in the solid electrolyte cup. The electrochemical reactor was heated in a glovebox oven during the electrochemical reaction. **Figure 5.3.1** shows a schematic and photograph of the electrochemical reactor.

5.3.2.3.Electrochemical Characterization

The electrochemical reactions were carried out using the galvanostatic intermittent titration technique (GITT) which involves current pulses followed by times for open circuit relaxation. Details of the current and relaxation times can be found under

the figures with the voltage profiles. The potentiostat used to carry out the electrochemical reactions was a LANHE CT2001A. Prior to starting the electrochemical oxidation, the cell was allowed to rest for 1 hour at the hold temperature (after a 3-hour ramp).

5.3.2.4.Post-Syntheses Washing procedure

To obtain the Na-Si clathrates, the Na-Sn flux was washed away in two steps: the alcohol wash and the acid wash. After the electrochemical reaction, the cell was opened in the Ar glovebox and the product was obtained from the bottom of the solid electrolyte cup. In some cases, the product was stuck to the bottom of the cup and was scraped off using metal tweezers. After a reaction, a metallic looking sheen was present which is attributed to a Na-Sn layer that is known to wet the Na β''-alumina electrolyte well.[304,312] No attempt was made to remove this layer between reactions meaning that there is possibly residual Sn, Na, or Si present during the subsequent reactions.

After obtaining the product in the glovebox, a fraction of the product (~100 mg) was taken outside of the glovebox in a sealed 3-neck flask with rubber stoppers. 20 mL of isopropanol was incorporated into the product with a syringe. Bubbling was observed indicating a reaction of the Na-Sn containing species with the isopropanol. After 20 minutes of reaction, the mixture was transferred to a 50 mL beaker and was then sonicated for 30 minutes (in air). After this time, 10 mL of ethanol was added, and the mixture was sonicated for 30 more minutes. After this time, 5 mL of deionized H_2O was added and sonicated for 1 additional minute. Then the solution was vacuum filtered with a polycarbonate 0.2-micron membrane with a glass frit support while adding additional

20 mL of H_2O. The product was then dried at 70-100 °C for 30 minutes. This concludes the alcohol treatment which results in the removal of the Na in the product.

After the powder was dry, it is introduced into 20 mL glass vial. Then 8 mL of concentrated HCl (38%) is added to the powder and then sonicated for 40 minutes. The goal of the acid treatment is to remove the Sn components which is dissolved as $SnCl_2$. Si clathrates have been shown to be stable in HCl[155,298]. After the 40 minutes of sonication, 10 mL of H_2O is added, and the products are then vacuum filtered using a PVDF membrane and washed with 50 mL of additional H_2O. The products were then dried at 70-100 °C for 30-60 minutes. This concludes the acid treatment which results in the removal of Sn from the products.

5.3.2.5. Materials Characterization

Powder X-ray diffraction (PXRD) was performed with a Malvern PANalytical Aeris research edition powder diffractometer with Cu X-rays (K alpha and beta) operated at 40 kV and 40 mA with standard Bragg-Brentano diffraction geometry and Pixel3D detector. For air-sensitive samples, the sample was covered with a Kapton film in an argon-filled glovebox prior to diffraction measurements. The Kapton film resulted in a broad background from $15^o < 2\theta < 25^o$. Scanning electron microscopy (SEM) was performed with a FEI Nova 200 Nanolab. The images were collected at 10 kV and a 0.54 nA spot size. Energy dispersive X-ray spectroscopy (EDS) measurements were taken at 20 kV with a 2.4 nA spot size.

5.3.3. Results and Discussion

In this proof of concept, a two-electrode cell is assembled and tested to perform the electrochemical oxidation of a mixture containing a molar ratio of 6:2:1 of Na:Si:Sn. The geometry of the electrochemical cell is similar to the Na-S battery[294] where Na serves as the negative electrode inside the a cup of a Na β''-alumina electrolyte and molten sulfur resides in a container in contact with the solid electrolyte. A schematic of the electrochemical cell is presented in **Figure 5.3.1** showing the geometry of the parts. In contrast to the Na-S battery, the electrode that is in contact with the outside of the electrolyte cup is the Na metal which serves as the counter and reference electrode while inside the cup is the Na-Si-Sn flux which serves as the working electrode. The cell is placed into the stainless-steel housing described in Chapter 2.1.5. Stainless-steel mesh is wrapped around the inside and bottom of the boron nitride crucible to provide electronic connection to the Na metal electrode, while stainless-steel wire from the electronic feedthrough establishes the electronic connection to the Na-Si-Sn electrode. **Figure 5.3.1b** shows a photograph of the electrolyte cup inside the boron nitride crucible along with the stainless-steel mesh. To carry out an electrochemical reaction, Na_4Si_4 powder is mixed with Sn powder and a solid Na metal piece is added on top of the powder in an elemental ratio of 6:2:1 (Na:Si:Sn). The reactor is then sealed and placed in a glovebox furnace and heated to the reaction temperature of 500 °C.

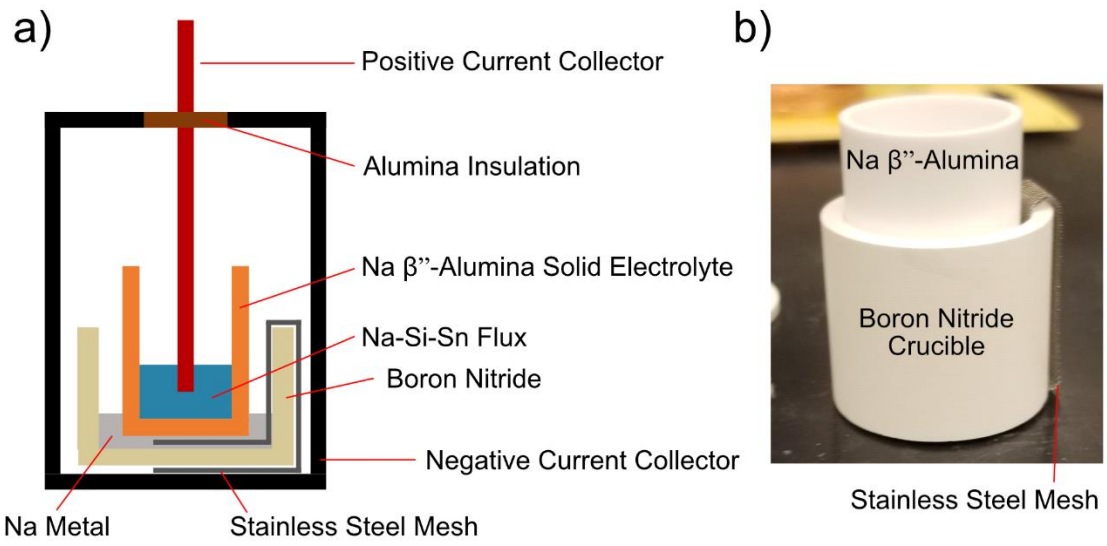

Figure 5.3.1 (a) Schematic of the two-electrode cell. (b) Photograph of the cell prior to use.

Figure 5.3.2 shows the GITT voltage profiles at different amounts of capacity and the PXRD and SEM results after the alcohol and acid washing. As seen in **Figure 5.3.2abc**, the voltage profile has several plateaus and sloped regions which correspond to two-phase and three-phase regions in a three-component system.[19] The capacity has been converted into atomic ratios with the bottom of the graph showing the starting composition of the reactants along with the final composition calculated based on the amount of charge passed through the cell. The final composition has only been calculated based on the electrochemical charge and does not consider possible side reactions or self-discharge due to Na vapor which was discussed in Chapter 5.1. Therefore, the final composition reported is a lower bound and could possibly be higher due to Na vapor self-discharge due to the use of the high temperature and Na counter electrode.

At the start of the reactions, the voltage of the cell relative to Na/Na^+ is around 24 mV and is consistent with the expected products at this composition and temperature.

Based on the Na-Sn phase diagram,[313] at a composition of 4 Na to 1 Sn (assuming 2 Na are with the Si), the Na-Sn should be molten at 500 °C. The positive voltage is consistent with a phase where Sn is dissolved in liquid Na thus increasing the potential relative to pure Na metal (Na/Na^+). Upon constant current electrochemical oxidation, there is a continuous increase in the potential until reaching an open circuit voltage of around 47 mV where there is a plateau corresponding to three-phase coexistence region. Further desodiation results in an increase in the potential and two more plateaus are observed with a larger plateau at 64 mV suggesting the existence of nucleation events. Then, near a composition of $Na_{1.5}Si_{1.9}Sn_{1.0}$, there is a fourth plateau at an open circuit voltage of 91 mV.

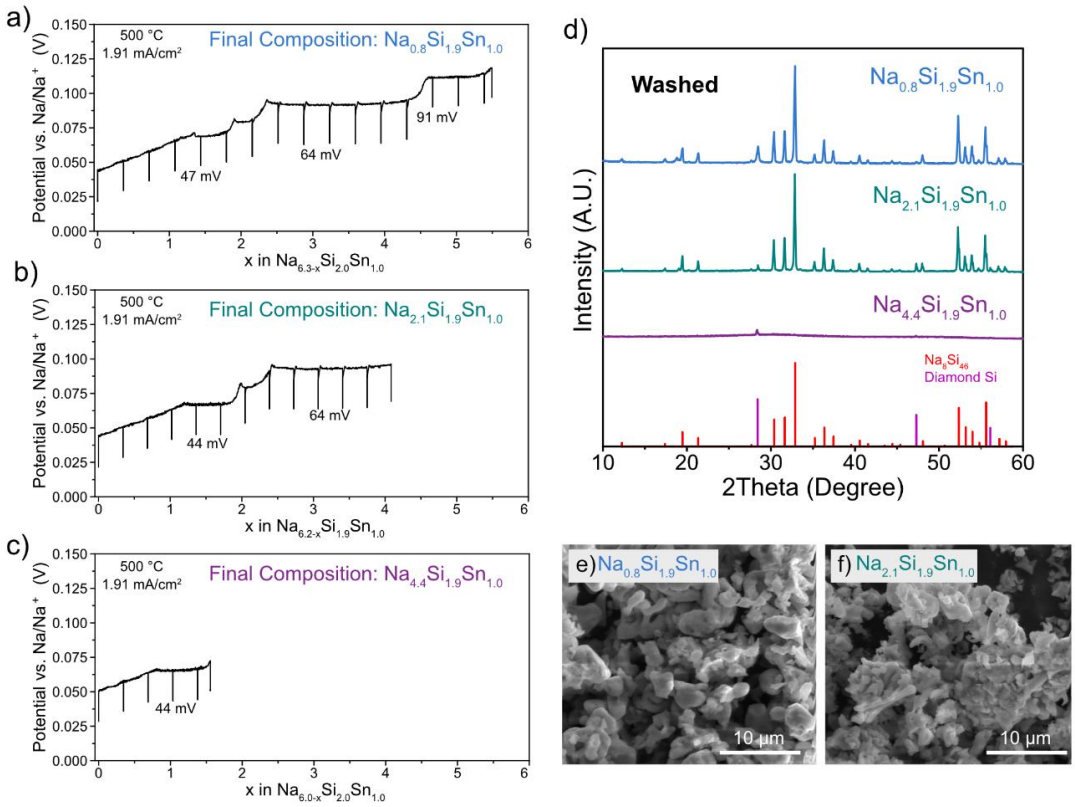

Figure 5.3.2 Galvanostatic intermittent titration technique (GITT) voltage profile at 500 °C with 2 hour 1.91 mA/cm^2 current pulses and 10 mins of relaxation reaching a final composition of (a) $Na_{0.8}Si_{1.9}Sn_{1.0}$, (b) $Na_{2.1}Si_{1.9}Sn_{1.0}$, and (c) $Na_{0.8}Si_{2.0}Sn_{1.0}$. (d) PXRD of the products of the reach after the alcohol and acid wash. SEM micrographs of the washed products reaching a final composition of (e) $Na_{0.8}Si_{1.9}Sn_{1.0}$ and (f) $Na_{2.1}Si_{1.9}Sn_{1.0}$.

After the desodiation, the products are recovered from the cell and washed following previous reports where the Na components are removed via an alcohol wash and the Sn flux is removed with an acid wash.[310] The PXRD patterns after the washing procedures are shown in **Figure 5.3.2d**. For the sample with the final composition of $Na_{0.8}Si_{1.9}Sn_{1.0}$, the PXRD shows reflections matching with the type I Na_8Si_{46} phase along with minor impurities of diamond cubic Si and other unknown phases. For the reaction reaching a composition of $Na_{2.1}Si_{1.9}Sn_{1.0}$, the type I Na_8Si_{46} was also the major product

with minor diamond Si impurities. The PXRD for the washed products of the reaction reaching a composition of $Na_{4.4}Si_{2.0}Sn_{1.0}$, which stops before the voltage plateau at 64 mV, shows that the products are amorphous with a minor presence of diamond Si. The PXRD (**Figure 5.3.2d**) confirms that Na-Si clathrates can be obtained from starting with a mixture of Na-Si-Sn and then driving the Na oxidation with an electrochemical cell. The fact that the products are amorphous before the voltage plateau at 64 mV suggest that this three-phase region at 64 mV could correspond to the nucleation and growth of the type I clathrate phase.

SEM micrographs (**Figure 5.3.2ef**) of the clathrate containing products show that the resulting powder is composed of small particles with ligament-like morphology in the micron size. The particle size appears to be larger for the reaction with a final composition of $Na_{0.8}Si_{1.9}Sn_{1.0}$ compared to $Na_{2.1}Si_{1.9}Sn_{1.0}$, possibly because of the longer time spent at the reaction temperature for the composition of $Na_{0.8}Si_{1.9}Sn_{1.0}$. Notably, this result is in contrast with the previous reports preparing the Na-Si clathrates in a Na-Sn flux which showed single crystal growth at temperatures from 450-600 °C.[310] The small particles of the products suggests that a mechanism for large single crystal growth is not present during the nucleation of the Na-Si clathrates. The ligament-like morphology of the products is similar to the results found in the previous work,[262] suggesting that they might be going through a similar solid-state reaction mechanism.

To further understand the origin on the voltage plateaus in **Figure 5.3.2**, reactions were prepared without NaSi and without Sn and oxidized in an analogous way. The voltage profiles are shown in **Figure 5.3.3** showing the voltage profiles with starting

compositions of $Na_{6.3}Si_{1.9}Sn_{1.0}$ (Na-NaSi-Sn), $Na_{4.0}Sn_{1.0}$ (Na-Sn), and $Na_{6.0}Si_{2.0}$ (Na-NaSi). **Figure 5.3.3a** shows the same voltage profile in **Figure 5.3.2a** for comparison while **Figure 5.3.3b** shows the voltage profile for Na-Sn. Notably, the reaction with only Na and Sn, shows plateaus in similar voltages at the one in **Figure 5.3.3a**, suggesting that these plateaus originate from the Na-Sn part of the electrode. Another important observation is the plateau at 40 mV in the Na-Sn suggests that a two-phase reaction is occurring which implies the crystallization of a solid Na-Sn phase in the previously liquid Na-Sn. Based on the Na-Sn phase diagram, 500 °C the Na-Sn mixture should be liquid until reaching a composition of NaSn with a reported melting point of 578 °C.[313] However, the melting point of Na_9Sn_4 is reported as 478 °C. If there is small discrepancy between the reported melting temperature and the temperature of the furnace, the reaction might result in the nucleation and growth of the Na_9Sn_4 phase which would manifest as a voltage plateau. Furthermore, there's a voltage plateau at 96 mV and the original voltage plateau at 64 mV for the Na-NaSi-Sn system is absent, confirming the previous speculation that the 64 mV plateau corresponds to the nucleation and growth of the type I clathrate phase.

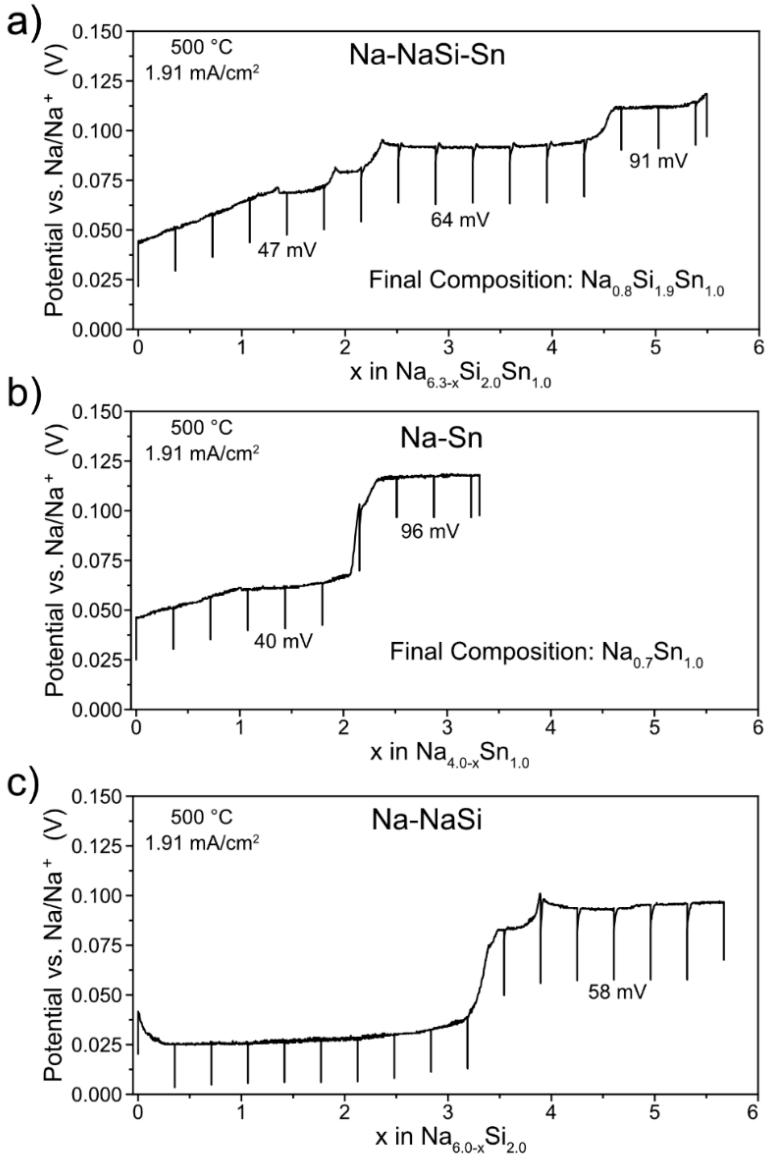

Figure 5.3.3 Galvanostatic intermittent titration technique (GITT) voltage profile at 500 °C with 2 hour 1.91 mA/cm^2 current pulses and 10 mins of relaxation for (a) Na-NaSi-Sn, (b) Na-Sn, and (c) Na-NaSi.

The voltage profile for the Na-NaSi reaction (**Figure 5.3.3c**) shows a low initial starting voltage close to 0 vs Na/Na$^+$ consistent with the larger amount of Na relative to Sn. The initial drop in potential is from the cell not being at equilibrium when the current

pulse started. Oxidation results in a slightly sloped voltage profile until reaching a composition of around $Na_{2.5}Si_{2.0}$ where the potential increases and a voltage plateau at 58 mV occurs. This voltage is similar to that seen corresponding to the type I clathrate nucleation and growth at 64 mV, further confirming this voltage region corresponds to the type I clathrate. PXRD of this reaction confirms that the type I clathrate is nucleated with some other impurities phases, including Na_4Si_4 suggesting it has not been fully converted or there is Na vapor self-discharge (**Figure I.1**). There is also evidence of Sn containing phases suggesting the presence of a small amount of residual Sn from the previous reactions using the same reactor. This behavior for the Na-Si binary is expected, as the two phases are present: Na and Na_4Si_4. As the Na content is decreased, the liquid Na metal will be removed through the cell until only Na_4Si_4 remains. This corresponds to the region from x= 0 to 3 **Figure 5.3.3c.** At this point, the Na_4Si_4 would behave analogous to our previous experiments where the solid-state conversion of Na_4Si_4 would occur to form the type I Na_8Si_{46} clathrate by further decreasing the Na content in the system.[262] The open circuit voltage with the previous study at 550 °C was 56 mV[262] which is close to the observed voltage of 58 mV confirming that an analogous reaction is occurring in this experiment as well.

Based on these comparisons, the role that the Sn plays during the electrochemical reaction becomes clear. If no Sn is present during the reaction, the liquid Na metal will be removed prior to the nucleation of the type I Na_8Si_{46} phase. This is because the potential of the Na metal is lower than the nucleation potential of the type I clathrate. Once all the Na is removed, there is no more liquid flux to promote Si mass transport and results in a solid-state reaction. When Sn is present, the excess Na is present in the form of Na-Sn

solution which is can exists in a wider range of potentials. Notably, the potential corresponding to Na_8Si_{46} is in between two voltage plateaus for the Na-Sn meaning that Na-Sn is still present during the nucleation Na_8Si_{46}. This is important as the Na-Sn component can facilitate mass transport during the nucleation and growth process of the Na_8Si_{46} clathrate.

An important feature of an electrochemical cell is the ability to directly control the current rate independently of the temperature of the reaction system. This is notably not possible during the evaporation of Na as demonstrated by Horito et al which showed that the time it takes for Na to evaporate is dependent on the temperature of the system.[310] To investigate the effect of the current rate on the reaction, **Figure 5.3.4** shows the GITT voltage profiles for two reactions performed at 1.91 and 3.18 mA/cm^2 at 500 °C with the PXRD after washing and the corresponding SEM micrographs.

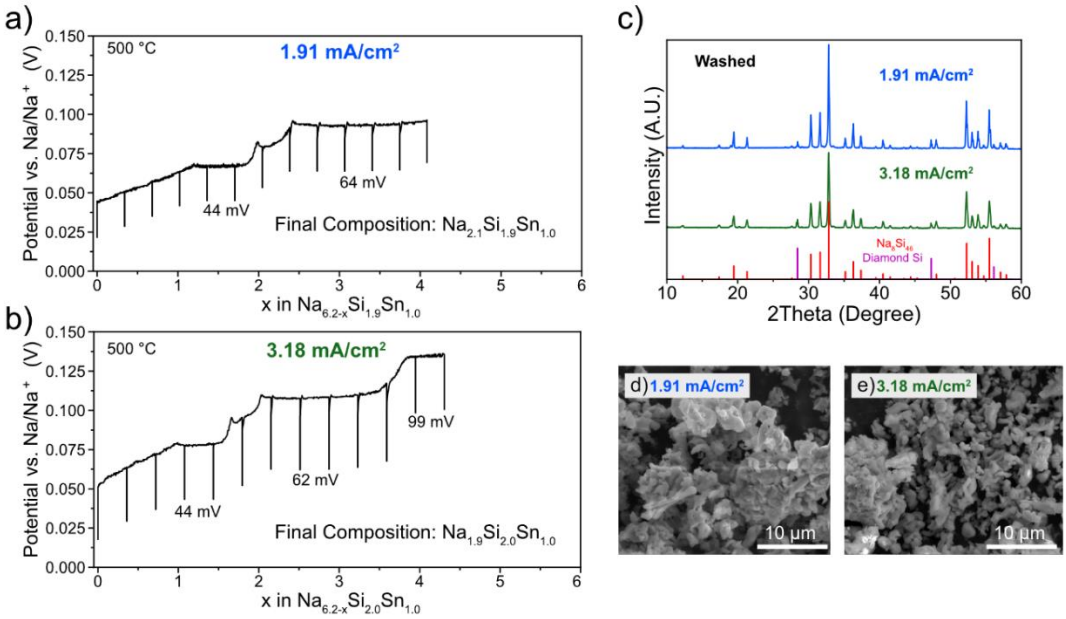

Figure 5.3.4 Galvanostatic intermittent titration technique (GITT) voltage profile at 500 °C with (a) 2 hour 1.91 mA/cm^2 current pulses and (b) 1.2 hour 3.18 mA/cm^2 current pulses with 10 mins of relaxation times. (c) PXRD of the products of the reaction after the alcohol and acid wash. SEM micrographs of the reaction products obtained with a current of (d) 1.91 mA/cm^2 and (e) 3.18 mA/cm^2.

There are several notable differences between the voltage profile in **Figure 5.3.4ab**. First, the voltage profile with the larger current rate of 3.18 mA/cm^2 shows higher polarization (i.e. difference between voltage during applied current and relaxed voltage) which is consistent with the higher ohmic drop as more current is applied in the system. Another difference is the amount of capacity for each plateau/sloped region is less for the higher current meaning that the voltage reaches the 99 mV plateau despite reaching a similar composition as the lower current reaction. This could originate from the Na vapor self-discharge which would have less of an effect on the higher current rate reaction as it spends less time at 500 °C over the course of the reaction. Future experiments will be required to quantify the Na self-discharge. It is also possible to use a

non-Na metal electrode (e.g. Sn) to mitigate the Na vapor pressure as demonstrated earlier in Chapter 5.1.[262] but this complicates the interpretation of the potential of the cell because the potential of the counter Sn electrode would also change over the course of the reaction.

Figure 5.3.4cde shows the PXRD and SEM micrographs of the two products after washing with alcohol and acid. The PXRD show that both conditions result in the synthesis of the type I Na_8Si_{46} with minor diamond Si impurities. From the SEM micrographs, the average particle size of the products synthesized at 3.18 mA/cm^2 is lower than the product synthesized at 1.91 mA/cm^2. This is expected as a higher current rate reduces the time in the Na-Sn flux/solids which will decrease the time for coarsening of nuclei. The higher overpotential required to achieve the larger current rate should also increase the number of nuclei that initially form which leads to a larger number of particles from which to grow from.[314] Overall, by changing the current of the reaction different morphologies of the clathrate particles can be grown which has implications for understanding how the crystallite size of clathrates affects their properties.

In addition to changing the current rate, the temperature can be changed while keeping the same current rate to isolate the effects of temperature on the reaction. The results of this experiment are shown in **Figure 5.3.5** which compare the reactions at a current rate of 1.91 mA/cm^2 at 500 °C and 550 °C. The voltage profiles shown in **Figure 5.3.5ab** demonstrate that the 50 °C change in temperature resulted in a large difference in the electrochemical behavior. At 550 °C, there is a continuously sloped region from the start until reaching a voltage plateau at 57 mV. This contrasts with the voltage plateaus at

500 °C which have been described earlier. The continuous increase of potential suggests that the Na-Sn is fully molten over this composition range which is consistent with the phase diagram.[313] At 57 mV, a plateau is observed which is attributed to the formation of the Na_8Si_{46} clathrate phase. This is supported by the close similarity of voltage plateaus between this experiment (57 mV) and the previous solid-state desodiation at 550 °C (56 mV)[262] that was described previously in Chapter 5.1.

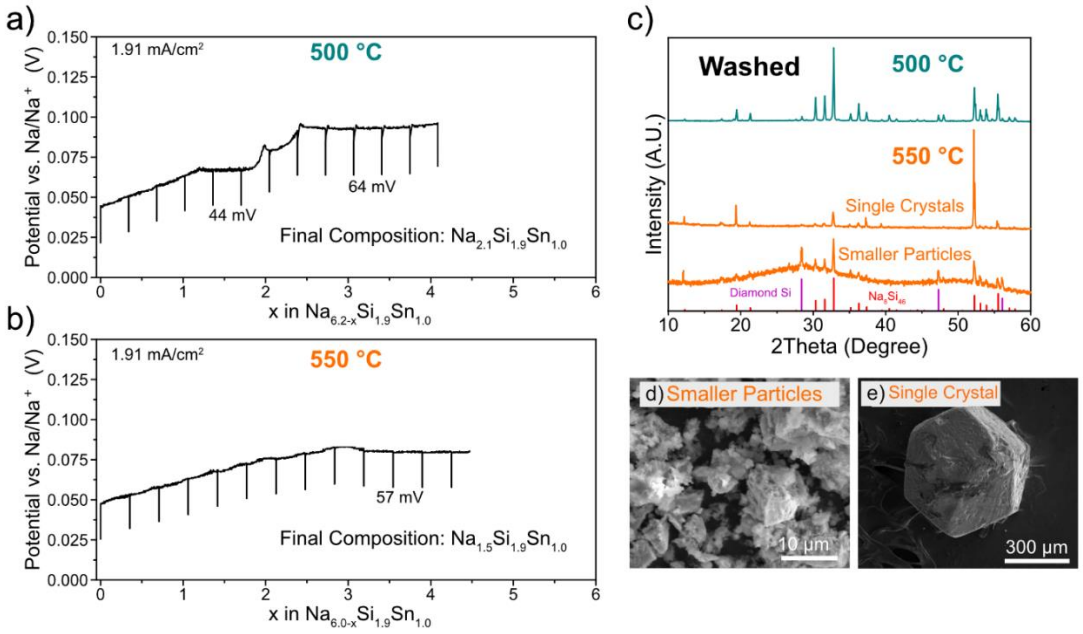

Figure 5.3.5 Galvanostatic intermittent titration technique (GITT) voltage profile at (a) 500 and (b) 550 °C with 2 hour 1.91 mA/cm^2 current pulses and 10 mins of relaxation. (d) PXRD of the products after the alcohol and acid wash. SEM micrographs of the products obtained at 550 °C showing the (d) smaller particles that were decanted during the washing procedure and (e) a Na_8Si_{46} single crystal.

As seen previously, the products at 500 °C resulted in small particles of the type I Na_8Si_{46} phase (**Figure 5.3.2f**). In contrast, the reaction at 550 °C resulted in the growth of single crystals along with an amorphous phase comprised of small particles. During the

washing, the large crystals and smaller particles were separated by decanting the suspended particles which left behind the large single crystals. The PXRD pattern of a small amount of crushed single crystals shows different intensities of the reflections that do not match the PXRD pattern suggesting that there are not enough crystallites to achieve the full PXRD intensity thus confirming the single crystalline nature of the products. The suspended particles were mostly amorphous with small amounts of diamond Si and Na_8Si_{46}. The SEM images of the products at 550 °C show the smaller products (**Figure 5.3.5d**) along with a ~600 micron single crystal (**Figure 5.3.5e**). EDS of the single crystal shows that the composition is consistent with that of a Na-filled Si clathrate with a composition of $Na_{7.6}Si_{46.4}$. (**Figure I.2**). The morphology of the single crystals is similar to that in the work by Moritio et al for the type I clathrate phase[309,310] suggesting that a similar growth mechanism is achieved via electrochemical desodiation of the Na-Sn flux.

The fact that single crystal growth was achieved at 550 °C and not 500 °C is good support to the previous conclusion that the Na-Sn was not fully molten over the full composition range at 500 °C. The molten Na-Sn flux is the key Si mass transport mechanism for obtaining the single crystal growth and since 500 °C results in small particles, it suggests that the Na-Sn component was solid during the growth of the clathrate phase. The voltage plateaus for the Na-Sn at 500 °C (**Figure 5.3.3b**) experiments support this conclusion as the reaction at 550 °C showed no voltage plateaus over the same composition range. These results demonstrate the importance of ensuring that the flux is molten over the range of potentials in which the clathrate phase is nucleated to achieve single crystal growth. In addition, the results show how the

electrochemical method can be used to develop a better understanding of the chemistry occurring during the reaction as *in situ* information is being collected via the potential of the cell. This could lead to a more rational design of fluxes and reaction conditions as opposed to the normal “black box” of synthesis.

5.3.4. Conclusions

In this section, a two-electrode high temperature electrochemical cell was tested and demonstrated to grow type I Na_8Si_{46} clathrate crystals based on a Na β’’-alumina cup with a geometry analogous to the Na-S battery. The working electrode comprised of a mixture of Na:Si:Sn in a 6:2:1 molar ratio and the counter/reference electrode was Na metal. Anodic current was applied to the working electrode to drive the formation of type I Na_8Si_{46} clathrates. The voltage profile of the desodiation reaction was analyzed and a voltage plateau at 62 mV at 500°C was confirmed to correspond to the nucleation and growth of the type I Na_8Si_{46} phase. The effect of current rate and temperature on the reaction products was investigated. Using a temperature of 550 °C resulted in the growth of large single crystals (600 microns) of Na_8Si_{46} in contrast to the smaller particles grown at 500 °C. This difference is attributed to fully liquid nature of the Na-Sn component at 550 °C during the reaction which is important to achieve single crystal growth. Compared to the solid-state method described in the previous work, the flux method has several advantages. First, the polarization was constant and low over the whole course of the reactions, which is beneficial for attaining high current rates and makes it more straight forward to understand the chemistry occurring. Second, the flux synthesis is easier to scale than the solid-state method because there are less diffusion limitations due to Na diffusion not having to occur through a solid-state pellet. Based on these results, I

expect that other alkali metal intermetallic fluxes could be useful for growing intermetallic cage structures. Na-Pb or a Na-Pb-Sn ternary fluxes could be a promising avenue for future research as the melting temperature over the whole composition range is quite low (~400 °C) and could facilitate single crystal growth to a lower temperature range. Overall, the electrochemical flux method is a promising method of growing Si clathrates or other intermetallic structures and provides *in situ* information about the potential of the system which can be useful for developing a deeper understanding of the chemistry that is occurring.

6. SUMMARY AND FUTURE OUTLOOK

In this dissertation, different types of Tetrel clathrates were investigated for their electrochemical and structural properties. Due to the growing and wide interest in Li-ion battery materials, developing a deeper understanding of the structure property relationships will be vital for optimizing the performance of these materials. The relatively unexplored material class of clathrates is interesting due to its wide design space which allows for fine-tuning materials properties. The goal of this dissertation was to significantly expand the understanding of the electrochemical reactions with clathrates and provide understanding of how the initial structure of Tetrel elements affect their electrochemical properties. I will give a summary and thoughts about future work for each chapter in the following paragraphs.

The open structure of clathrates and the possibility for reversible Li-ion insertion has been one of the driving motivations for this work. The key finding in this regard is the structural features of clathrates that enable the electrochemical Li insertion into the clathrate framework. Based on the work presented above, Li insertion requires vacant cages and a diffusion path connected via hexagonal faces. The combination of experimental and computational work has been vital in developing an atomic understanding of the possible Li pathways and which structural features are important. As a result, the type II Si clathrate is demonstrated to have reversible Li-ion insertion and shows very unusual electrochemistry. It is important to note how unusual topotactic Li-insertion is in the electrochemistry of Tetrel elements. Tetrel elements almost always undergo alloying reaction to structurally unrelated phases. Li insertion into type II Si is a testament to the openness of the cages and the fast diffusion paths. The technological

viability of the type II Si clathrate as an anode is of question. The theoretical properties seem promising considering the low volume expansion and elemental abundance of Si. More work will be needed to evaluate the properties of this material, especially the solid electrolyte interphase formation and long-term cycling stability. In addition, developments of synthesis methods need to better control the particle morphology which can elucidate the effect of possible grain-sized effects on the insertion reactions. Overall, Li insertion into Tetrel frameworks could be applied to make anodes with good cycling stability and low reaction potentials.

Alloying anodes based on Li phase transformations to high Li content phases are one of the most promising pathways to boosting the performance of Li-ion batteries. The high capacity of Si can have beneficial effects on the performance of the full cell Li-ion battery compared to a graphite cell. Understanding how the initial structure of these materials affect their lithiation pathways will be vital for optimizing their electrochemical performance. In this dissertation, I demonstrated how the guest atoms of clathrates (e.g. Ba) can promote amorphous phase transformations in systems that typically undergo crystalline phase transformations. Amorphous reaction mechanisms are preferrable to crystalline ones as it reduces the stress the electrode experiences over the course of lithiation. In this view, clathrates that go through the amorphous phase transformation are of interest for Li-ion batteries. The key here is that the clathrate is converted into an amorphous phase and this new amorphous phase is the electrochemically active material in subsequent cycles. Thus, the clathrate serves as a precursor. Due to the large substitutions and guest atom options of clathrates, the properties of the amorphous phases can be tuned which was demonstrated in this work. However, there are several key

properties that need to be investigated to further investigate these materials. Most importantly is the solid electrolyte interphase formation in the first cycle which is critical for achieving a battery with good stability. The guest atom and framework substitution are likely to influence this however little is currently known about the effects. In addition, how the guest atoms affect the Li kinetics in the amorphous phase is not known and is important for the charging rates of the batteries. I believe that the clathrates with K guest atoms warrant investigation due to the higher gravimetric capacities (i.e K_8Sn_{44}, $K_8Al_8Sn_{38}$) and could be very interesting alternatives to pure Sn anodes.

Chapter 5 investigated the possibility of using electrochemical methods to synthesize the metastable Na-Si and Na-Ge clathrates. As mentioned briefly, better synthesis methods are needed for the type II Si clathrate to better understand its electrochemical properties. The traditional synthesis results in fine polycrystalline particles and it is not known how this affects Li insertion. There are other methods to synthesize these structures but, in some cases, they were inaccessible to me at ASU (e.g. spark plasma sintering in a glovebox). Due to this, I was motivated to investigate the electrochemical desodiation of the Na Zintl phases at high temperatures. In general, high temperature electrochemistry is rarely done but shows promise for a wide range of interesting reactions in terms of synthesis. Chapter 5 has two sections focusing on the solid-state synthesis and then the last section discussed the electrochemical flux synthesis. After going through and performing these methods, the flux synthesis method is by far the more interesting and promising method for the growth of clathrates. The main reason is that it is not limited by the poor solid-state Na diffusion in the Si/Ge structures which scales highly with the thickness of the electrode. However, the solid-

state conversion of thin films is a possibly interesting route as the cell will not be limited by the kinetics of the small film. During the bulk synthesis, the polarizations of the cell become too high when an appreciable amount of material is synthesized which complicates the interpretation of the voltage profile. The flux method is easy to scale and can provide much more product without having a dramatic increase in cell polarization. Different fluxes could lower the reaction temperature and reach into the range needed for Ge clathrates. Single crystals of type II Ge crystals have yet to be reported, and this flux method is a possible method for achieving this. The wide possibility of different fluxes, different electrochemical treatments (e.g voltage steps vs constant current), and precursors presents in an interesting design space for growing new clathrate and intermetallic compounds.

REFERENCES

(1) Fischer, M.; Werber, M.; Schwartz, P. V. Batteries: Higher Energy Density than Gasoline? *Energy Policy* **2009**, *37*, 2639–2641.

(2) Mohr, S. H.; Wang, J.; Ellem, G.; Ward, J.; Giurco, D. Projection of World Fossil Fuels by Country. *Fuel* **2015**, *141*, 120–135.

(3) Jackson, R. B.; Friedlingstein, P.; Andrew, R. M.; Canadell, J. G.; Le Quéré, C.; Peters, G. P. Persistent Fossil Fuel Growth Threatens the Paris Agreement and Planetary Health. *Environ. Res. Lett.* **2019**, *14*.

(4) Kampa, M.; Castanas, E. Human Health Effects of Air Pollution. *Environ. Pollut.* **2008**, *151*, 362–367.

(5) Winter, M.; Barnett, B.; Xu, K. Before Li Ion Batteries. *Chem. Rev.* **2018**, *118*, 11433–11456.

(6) Kamat, P. V. Lithium-Ion Batteries and Beyond: Celebrating the 2019 Nobel Prize in Chemistry - A Virtual Issue. *ACS Energy Lett.* **2019**, 2757–2759.

(7) Notter, D. A.; Gauch, M.; Widmer, R.; Wäger, P.; Stamp, A.; Zah, R.; Althaus, H. J. Contribution of Li-Ion Batteries to the Environmental Impact of Electric Vehicles. *Environ. Sci. Technol.* **2010**, *44*, 7744.

(8) Smith, K.; Saxon, A.; Keyser, M.; Lundstrom, B.; Cao, Z.; Roc, A. Life Prediction Model for Grid-Connected Li-Ion Battery Energy Storage System. *Proc. Am. Control Conf.* **2017**, 4062–4068.

(9) Nitta, N.; Wu, F.; Lee, J. T.; Yushin, G. Li-Ion Battery Materials: Present and Future. *Mater. Today* **2015**, *18*, 252–264.

(10) Islam, M. S.; Fisher, C. A. J. Lithium and Sodium Battery Cathode Materials: Computational Insights into Voltage, Diffusion and Nanostructural Properties. *Chem. Soc. Rev.* **2014**, *43*, 185–204.

(11) Aydinol, M.; Kohan, A.; Ceder, G.; Cho, K.; Joannopoulos, J. Ab Initio Study of Lithium Intercalation in Metal Oxides and Metal Dichalcogenides. *Phys. Rev. B - Condens. Matter Mater. Phys.* **1997**, *56*, 1354–1365.

(12) Boesenberg, U.; Sokaras, D.; Nordlund, D.; Weng, T. C.; Gorelov, E.; Richardson, T. J.; Kostecki, R.; Cabana, J. Electronic Structure Changes upon Lithium Intercalation into Graphite – Insights from Ex Situ and Operando x-Ray Raman Spectroscopy. *Carbon N. Y.* **2019**, *143*, 371–377.

(13) Griffith, K. J.; Wiaderek, K. M.; Cibin, G.; Marbella, L. E.; Grey, C. P. Niobium Tungsten Oxides for High-Rate Lithium-Ion Energy Storage. *Nature* **2018**, *559*, 556–563.

(14) Obrovac, M. N.; Chevrier, V. L. Alloy Negative Electrodes for Li-Ion Batteries. *Chem. Rev.* **2014**, *114*, 11444–11502.

(15) Murray, V.; Hall, D. S.; Dahn, J. R. A Guide to Full Coin Cell Making for Academic Researchers. *J. Electrochem. Soc.* **2019**, *166*, A329–A333.

(16) Self, J.; Aiken, C. P.; Petibon, R.; Dahn, J. R. Survey of Gas Expansion in Li-Ion NMC Pouch Cells. *J. Electrochem. Soc.* **2015**, *162*, A796–A802.

(17) Shamberger, P. J. Mapping Design Trade-Offs. *Nat. Energy* **2021**, *6*, 221–222.

(18) Masias, A.; Marcicki, J.; Paxton, W. A. Opportunities and Challenges of Lithium Ion Batteries in Automotive Applications. *ACS Energy Lett.* **2021**, *6*, 621–630.

(19) Huggins, R. A. *Advanced Batteries: Materials Science Aspects*; Springer Science & Business Media, 2008.

(20) Lyu, Y.; Wu, X.; Wang, K.; Feng, Z.; Cheng, T.; Liu, Y.; Wang, M.; Chen, R.; Xu, L.; Zhou, J.; et al. An Overview on the Advances of LiCoO2 Cathodes for Lithium-Ion Batteries. *Adv. Energy Mater.* **2021**, *11*.

(21) Zhu, C.; Usiskin, R. E.; Yu, Y.; Maier, J. The Nanoscale Circuitry of Battery Electrodes. *Science (80-.).* **2017**, *358*.

(22) Usiskin, R. E.; Maier, J. Guidelines for Optimizing the Architecture of Battery Insertion Electrodes Based on the Concept of Wiring Lengths. *Phys. Chem. Chem. Phys.* **2018**, *20*, 16449–16462.

(23) Van Der Ven, A.; Bhattacharya, J.; Belak, A. A. Understanding Li Diffusion in Li-Intercalation Compounds. *Acc. Chem. Res.* **2013**, *46*, 1216–1225.

(24) Whittingham, M. S. Lithium Titanium Disulfide Cathodes. *Nat. Energy* **2021**, *6*, 214.

(25) Bhatt, M. D.; Lee, J. Y. High Capacity Conversion Anodes in Li-Ion Batteries: A Review. *Int. J. Hydrogen Energy* **2019**, *44*, 10852–10905.

(26) Fang, C.; Wang, X.; Meng, Y. S. Key Issues Hindering a Practical Lithium-Metal Anode. *Trends Chem.* **2019**, *0*, 1–7.

(27) Ohzuku, T.; Ueda, A.; Yamamoto, N. Zero-Strain Insertion Material of Li [Li1 / 3Ti5 / 3] O 4 for Rechargeable Lithium Cells. *J. Electrochem. Soc.* **1995**, *142*, 1431–1435.

(28) Schweidler, S.; De Biasi, L.; Schiele, A.; Hartmann, P.; Brezesinski, T.; Janek, J. Volume Changes of Graphite Anodes Revisited: A Combined Operando X-Ray Diffraction and in Situ Pressure Analysis Study. *J. Phys. Chem. C* **2018**, *122*, 8829–8835.

(29) Ma, J.; Wang, C.; Wroblewski, S. Kinetic Characteristics of Mixed Conductive Electrodes for Lithium Ion Batteries. *J. Power Sources* **2007**, *164*, 849–856.

(30) Scharner, S.; Weppner, W.; Schmid-Beurmann, P. Evidence of Two-Phase Formation upon Lithium Insertion into the Li1.33Ti1.67 O 4 Spinel. *J. Electrochem. Soc.* **1999**, *146*, 857–861.

(31) Wen, C. J.; Huggins, R. A. Chemical Diffusion in Intermediate Phases in the Lithium-Silicon System. *J. Solid State Chem.* **1981**, *37*, 271–278.

(32) McDowell, M. T.; Lee, S. W.; Nix, W. D.; Cui, Y. 25th Anniversary Article: Understanding the Lithiation of Silicon and Other Alloying Anodes for Lithium-Ion Batteries. *Adv. Mater.* **2013**, *25*, 4966–4985.

(33) Li, J.; Dahn, J. R. An In Situ X-Ray Diffraction Study of the Reaction of Li with Crystalline Si. *J. Electrochem. Soc.* **2007**, *154*, A156.

(34) Obrovac, M. N.; Krause, L. J. Reversible Cycling of Crystalline Silicon Powder. *J. Electrochem. Soc.* **2007**, *154*, A103–A108.

(35) Key, B.; Morcrette, M.; Tarascon, J.-M.; Grey, C. P. Pair Distribution Function Analysis and Solid State NMR Studies of Silicon Electrodes for Lithium Ion Batteries: Understanding the (De)Lithiation Mechanisms. *J. Am. Chem. Soc.* **2011**, *133*, 503–512.

(36) Chan, C. K.; Peng, H.; Liu, G.; McIlwrath, K.; Zhang, X. F.; Huggins, R. A.; Cui, Y. High-Performance Lithium Battery Anodes Using Silicon Nanowires. *Nat. Nanotechnol.* **2008**, *3*, 31–35.

(37) Su, X.; Wu, Q.; Li, J.; Xiao, X.; Lott, A.; Lu, W.; Sheldon, B. W.; Wu, J. Silicon-Based Nanomaterials for Lithium-Ion Batteries: A Review. *Adv. Energy Mater.* **2014**, *4*, 1300882.

(38) Jin, Y.; Kneusels, N. J. H.; Marbella, L. E.; Castillo-Martínez, E.; Magusin, P. C. M. M.; Weatherup, R. S.; Jónsson, E.; Liu, T.; Paul, S.; Grey, C. P. Understanding Fluoroethylene Carbonate and Vinylene Carbonate Based Electrolytes for Si Anodes in Lithium Ion Batteries with NMR Spectroscopy. *J. Am. Chem. Soc.* **2018**, *140*, 9854–9867.

(39) Park, C. M.; Kim, J. H.; Kim, H.; Sohn, H. J. Li-Alloy Based Anode Materials for Li Secondary Batteries. *Chem. Soc. Rev.* **2010**, *39*, 3115–3141.

(40) Kasper, J. S.; Hagenmuller, P.; Pouchard, M.; Cros, C. Clathrate Structure of Silicon Na8Si46 and NaxSi136 (X. *Science (80-.).* **1965**, *150*, 1713–1714.

(41) Cros, C.; Pouchard, M.; Hagenmuller, P. Sur Une Nouvelle Famille de Clathrates Mineraux Isotypes Des Hydrates de Gaz et de Liquides. Interpretation Des Resultats Obtenus. *J. Solid State Chem.* **1970**, *2*, 570–581.

(42) Dolyniuk, J.; Owens-baird, B.; Wang, J.; Zaikina, J. V; Kovnir, K. Clathrate Thermoelectrics. *Mater. Sci. Eng. R* **2016**, *108*, 1–46.

(43) Nolas, G. S. *The Physics and Chemistry of Inorganic Clathrates*; 2014.

(44) Yamanaka, S.; Enishi, E.; Fukuoka, H.; Yasukawa, M. High-Pressure Synthesis of a New Silicon Clathrate Superconductor, Ba_8Si_{46}. *Inorg. Chem.* **2000**, *39*, 56–58.

(45) Sevov, S. C. Zintl Phases. In *Intermetallic Compounds - Principles and Practice*; John Wiley & Sons, Ltd, 2002; pp 113–132.

(46) Goebel, T.; Prots, Y.; Haarmann, F. Refinement of the Crystal Structure of Tetrasodium Tetrasilicide, Na 4Si4. *Zeitschrift fur Krist. - New Cryst. Struct.* **2008**, *223*, 187–188.

(47) Baitinger, M.; Böhme, B.; Wagner, F. R.; Schwarz, U. Zintl Defects in Intermetallic Clathrates. *Zeitschrift fur Anorg. und Allg. Chemie* **2020**, *646*, 1034–1041.

(48) Jung, W.; Lörincz, J.; Ramlau, R.; Borrmann, H.; Prots, Y.; Haarmann, F.; Schnelle, W.; Burkhardt, U.; Baitinger, M.; Grin, Y. K7B7Si39, a Borosilicide with the Clathrate I Structure. *Angew. Chemie - Int. Ed.* **2007**, *46*, 6725–6728.

(49) Langer, T.; Dupke, S.; Trill, H.; Passerini, S.; Eckert, H.; Pöttgen, R.; Winter, M. Electrochemical Lithiation of Silicon Clathrate-II. *J. Electrochem. Soc.* **2012**, *159*, A1318–A1322.

(50) Ryu, J. H.; Kim, J. W.; Sung, Y.-E.; Oh, S. M. Failure Modes of Silicon Powder Negative Electrode in Lithium Secondary Batteries. *Electrochem. Solid-State Lett.* **2004**, *7*, A306–A309.

(51) Yang, J.; Tse, J. S. Silicon Clathrates as Anode Materials for Lithium Ion Batteries? *J. Mater. Chem. A* **2013**, *1*, 7782–7789.

(52) Böhme, B.; Minella, C. B.; Thoss, F.; Lindemann, I.; Rosenburg, M.; Pistidda, C.; Møller, K. T.; Jensen, T. R.; Giebeler, L.; Baitinger, M.; et al. B1-Mobilstor: Materials for Sustainable Energy Storage Techniques - Lithium Containing Compounds for Hydrogen and Electrochemical Energy Storage. *Adv. Eng. Mater.* **2014**, *16*, 1189–1195.

(53) Wagner, N. A.; Raghavan, R.; Zhao, R.; Wei, Q.; Peng, X.; Chan, C. K. Electrochemical Cycling of Sodium-Filled Silicon Clathrate. *ChemElectroChem* **2014**, *1*, 347–353.

(54) Li, Y.; Raghavan, R.; Wagner, N. A.; Davidowski, S. K.; Baggetto, L.; Zhao, R.; Cheng, Q.; Yarger, J. L.; Veith, G. M.; Ellis-Terrell, C.; et al. Type I Clathrates as Novel Silicon Anodes: An Electrochemical and Structural Investigation. *Adv. Sci.* **2015**, *2*, 1500057.

(55) Peng, X.; Wei, Q.; Li, Y.; Chan, C. K. First-Principles Study of Lithiation of Type I Ba-Doped Silicon Clathrates. *J. Phys. Chem. C* **2015**, *119*, 28247–28257.

(56) Zhao, R.; Bobev, S.; Krishna, L.; Yang, T.; Weller, J. M.; Jing, H.; Chan, C. K. Anodes for Lithium-Ion Batteries Based on Type I Silicon Clathrate $Ba_8Al_{16}Si_{30}$ - Role of Processing on Surface Properties and Electrochemical Behavior. *ACS Appl. Mater. Interfaces* **2017**, *9*, 41246–41257.

(57) Kim, D. Y.; Stefanoski, S.; Kurakevych, O. O.; Strobel, T. A. Synthesis of an Open-Framework Allotrope of Silicon. *Nat. Mater.* **2015**, *14*, 169–173.

(58) Arrieta, U.; Katcho, N. A.; Arcelus, O.; Carrasco, J. First-Principles Study of Sodium Intercalation in Crystalline Na_xSi_{24} ($0 \leq x \leq 4$) as Anode Material for Na-Ion Batteries. *Sci. Rep.* **2017**, *7*, 5350.

(59) He, Y.; Lu, X.; Kim, D. Y. A First-Principles Study on Si_{24} as an Anode Material for Rechargeable Batteries. *RSC Adv.* **2018**, *8*, 20228–20233.

(60) Weppner, W. Determination of the Kinetic Parameters of Mixed-Conducting Electrodes and Application to the System Li[Sub 3]Sb. *J. Electrochem. Soc.* **1977**, *124*, 1569.

(61) Le Bail, A.; Madsen, I.; Cranswick, L. M. D.; Cockcroft, J. K.; Norby, P.; Zuev, A. D.; Fitch, A.; Rodriguez-Carvajal, J.; Giacovazzo, C.; Von Dreele, R. B.; et al. *Powder Diffraction*; Dinnebier, R. E., Billinge, S. J. L., Eds.; The Royal Society of Chemistry, 2008.

(62) Rietveld, H. M. A Profile Refinement Method for Nuclear and Magnetic Structures. *J. Appl. Crystallogr.* **1969**, *2*, 65–71.

(63) Mccusker, L. B.; Von Dreele, R. B.; Cox, D. E.; Louër, D.; Scardi, P. Rietveld Refinement Guidelines. *J. Appl. Crystallogr.* **1999**, *32*, 36–50.

(64) Petrícek, V.; Dušek, M.; Palatinus, L. Crystallographic Computing System JANA2006: General Features. *Zeitschrift fur Kristallographie*. 2014, pp 345–352.

(65) Egami, T.; Billinge, S. J. L. *Underneath the Bragg Peaks: Structural Analysis of Complex Materials*; Elsevier, 2003.

(66) Chapman, K. W. Emerging Operando and X-Ray Pair Distribution Function Methods for Energy Materials Development. *MRS Bull.* **2016**, *41*, 231–238.

(67) Billinge, S. J. L. The Rise of the X-Ray Atomic Pair Distribution Function Method: A Series of Fortunate Events. *Philos. Trans. R. Soc. A Math. Phys. Eng. Sci.* **2019**, *377*.

(68) Farrow, C. L.; Juhas, P.; Liu, J. W.; Bryndin, D.; Boin, E. S.; Bloch, J.; Proffen, T.; Billinge, S. J. L. PDFfit2 and PDFgui: Computer Programs for Studying Nanostructure in Crystals. *J. Phys. Condens. Matter* **2007**, *19*.

(69) Biswas, P.; Atta-Fynn, R.; Drabold, D. A. Reverse Monte Carlo Modeling of Amorphous Silicon. *Phys. Rev. B - Condens. Matter Mater. Phys.* **2004**, *69*, 1–5.

(70) P. Hohenberg, W. K. Inhomogenous Electron Gas. *Phyiscal Rev.* **1964**, *136*, B864-871.

(71) Cramer, C. J. *Essentials of Computational Chemistry: Theories and Models*; John Wiley \& Sons, 2013.

(72) W. Kohn, L. J. S. Self-Consistent Equations Including Exchange and Correlation

Effects. *Phys. Reivew* **1965**, *140*, A1133-1138.

(73) Perdew, J. P.; Burke, K.; Ernzerhof, M. Generalized Gradient Approximation Made Simple. *Phys. Rev. Lett.* **1996**, *77*, 3865–3868.

(74) Langreth, D. C.; Mehl, M. J. Beyond the Local-Density Approximation in Calculations of Ground-State Electronic Properties. *Phys. Rev. B* **1983**, *28*, 1809–1834.

(75) Martin, R. M. *Electronic Structure: Basic Theory and Practical Methods*; Cambridge University Press, 2004.

(76) Van Der Ven, A.; Deng, Z.; Banerjee, S.; Ong, S. P. Rechargeable Alkali-Ion Battery Materials: Theory and Computation. *Chem. Rev.* **2020**, *120*, 6977–7019.

(77) Kresse, G.; Furthmüller, J. Efficient Iterative Schemes for Ab Initio Total-Energy Calculations Using a Plane-Wave Basis Set. *Phys. Rev. B - Condens. Matter Mater. Phys.* **1996**, *54*, 11169–11186.

(78) Kresse, G.; Joubert, D. From Ultrasoft Pseudopotentials to the Projector Augmented-Wave Method. *Phys. Rev. B* **1999**, *59*, 1758–1775.

(79) Hannah, D. C.; Sai Gautam, G.; Canepa, P.; Ceder, G. On the Balance of Intercalation and Conversion Reactions in Battery Cathodes. *Adv. Energy Mater.* **2018**, *1800379*, 1–12.

(80) Sheppard, D.; Terrell, R.; Henkelman, G. Optimization Methods for Finding Minimum Energy Paths. *J. Chem. Phys.* **2008**, *128*, 1–10.

(81) Mills, G.; Jónsson, H. Quantum and Thermal Effects in H2 Dissociative Adsorption: Evaluation of Free Energy Barriers in Multidimensional Quantum Systems. *Phys. Rev. Lett.* **1994**, *72*, 1124–1127.

(82) Ceder, G.; Ong, S. P.; Wang, Y. Predictive Modeling and Design Rules for Solid Electrolytes. *MRS Bull.* **2018**, *43*, 746–751.

(83) Urban, A.; Seo, D. H.; Ceder, G. Computational Understanding of Li-Ion Batteries. *npj Comput. Mater.* **2016**, *2*.

(84) Ceder, G.; Hautier, G.; Jain, A.; Ong, S. P. Recharging Lithium Battery Research with First-Principles Methods. *MRS Bull.* **2011**, *36*, 185–191.

(85) Henkelman, G.; Uberuaga, B. P.; Jónsson, H. Climbing Image Nudged Elastic Band Method for Finding Saddle Points and Minimum Energy Paths. *J. Chem. Phys.* **2000**, *113*, 9901–9904.

(86) Kasper, J. S.; Hagenmuller, P.; Pouchard, M.; Cros, C. Clathrate Structure of Silicon Na_8Si_{46} and Na_xSi_{136} (x < 11). *Science (80-.).* **1965**, *150*, 1713–1714.

(87) Kawaji, H.; Horie, H.; Yamanaka, S.; Ishikawa, M. Superconductivity in the Silicon Clathrate Compound $(Na, Ba)_xSi_{46}$. *Phys. Rev. Lett.* **1995**, *74*, 1427–1429.

(88) Reny, E.; San-Miguel, A.; Guyot, Y.; Masenelli, B.; Mélinon, P.; Saviot, L.; Yamanaka, S.; Champagnon, B.; Cros, C.; Pouchard, M.; et al. Vibrational Modes in Silicon Clathrate Compounds: A Key to Understanding Superconductivity. *Phys. Rev. B* **2002**, *66*, 014532.

(89) Connétable, D.; Timoshevskii, V.; Masenelli, B.; Beille, J.; Marcus, J.; Barbara, B.; Saitta, A. M.; Rignanese, G. M.; Mélinon, P.; Yamanaka, S.; et al. Superconductivity in Doped Sp3 Semiconductors: The Case of the Clathrates. *Phys. Rev. Lett.* **2003**, *91*, 247001.

(90) Fukuoka, H.; Kiyoto, J.; Yamanaka, S. Superconductivity and Crystal Structure of the Solid Solutions of $Ba_{8-\delta}Si_{46-x}Ge_x$ ($0 \leqslant x \leqslant 23$) with Type I Clathrate Structure. *J. Solid State Chem.* **2003**, *175*, 237–244.

(91) Bryan, J. D.; Srdanov, V. I.; Stucky, G. D. Superconductivity in Germanium Clathrate $Ba_8Ga_{16}Ge_{30}$. *Phys. Rev. B* **1999**, *60*, 3064–3067.

(92) Blake, N. P.; Mollnitz, L.; Kresse, G.; Metiu, H. Why Clathrates Are Good Thermoelectrics: A Theoretical Study of $Sr_8Ga_{16}Ge_{30}$. *J. Chem. Phys.* **1999**, *111*, 3133–3144.

(93) Nolas, G. S.; Slack, G. A.; Schujman, S. B. Chapter 6 Semiconductor Clathrates: A Phonon Glass Electron Crystal Material with Potential for Thermoelectric Applications. *Semicond. Semimetals* **2001**, *69*, 255–300.

(94) Tsujii, N.; Roudebush, J. H.; Zevalkink, A.; Cox-Uvarov, C. A.; Jeffery Snyder, G.; Kauzlarich, S. M. Phase Stability and Chemical Composition Dependence of the Thermoelectric Properties of the Type-I Clathrate $Ba_8Al_xSi_{46-x}$ ($8 \leq x \leq 15$). *J. Solid State Chem.* **2011**, *184*, 1293–1303.

(95) Saramat, A.; Svensson, G.; Palmqvist, A. E. C.; Stiewe, C.; Mueller, E.; Platzek, D.; Williams, S. G. K.; Rowe, D. M.; Bryan, J. D.; Stucky, G. D. Large Thermoelectric Figure of Merit at High Temperature in Czochralski-Grown Clathrate $Ba_8Ga_{16}Ge_{30}$. *J. Appl. Phys.* **2006**, *99*, 1–6.

(96) Nolas, G. S.; Cohn, J. L.; Slack, G. A.; Schujman, S. B. Semiconducting Ge Clathrates: Promising Candidates for Thermoelectric Applications. *Appl. Phys. Lett.* **1998**, *73*, 178–180.

(97) Zhang, H.; Borrmann, H.; Oeschler, N.; Candolfi, C.; Schnelle, W.; Schmidt, M.; Burkhardt, U.; Baitinger, M.; Zhao, J.; Grin, Y. Atomic Interactions in the P-Type Clathrate I $Ba_8Au_{5.3}Ge_{40.7}$. *Inorg. Chem.* **2011**, *50*, 1250–1257.

(98) Uemura, T.; Akai, K.; Koga, K.; Tanaka, T.; Kurisu, H.; Yamamoto, S.; Kishimoto, K.; Koyanagi, T.; Matsuura, M. Electronic Structure and Thermoelectric Properties of Clathrate Compounds $Ba_8Al_xGe_{46-X}$. *J. Appl. Phys.* **2008**, *104*.

(99) Mott, N. F. Properties of Compounds of Type Na_xSi_{46} and Na_xSi_{136}. *J. Solid State Chem.* **1973**, *6*, 348–351.

(100) Kawaguchi, T.; Tanigaki, K.; Yasukawa, M.; Kawaguchi, T. Ferromagnetism in Germanium Clathrate: $Ba_8Mn_2Ge_{44}$. *Appl. Phys. Lett.* **2000**, *77*, 3438–3440.

(101) Neiner, D.; Okamoto, N. L.; Condron, C. L.; Ramasse, Q. M.; Yu, P.; Browning, N. D.; Kauzlarich, S. M. Hydrogen Encapsulation in a Silicon Clathrate Type I Structure: $Na_{5.5}(H_2)_{2.15}Si_{46}$: Synthesis and Characterization. *J. Am. Chem. Soc.* **2007**, *129*, 13857–13862.

(102) Neiner, D.; Okamoto, N. L.; Yu, P.; Leonard, S.; Condron, C. L.; Toney, M. F.; Ramasse, Q. M.; Browning, N. D.; Kauzlarich, S. M. Synthesis and Characterization of $K_{8-x}(H_2)_ySi_{46}$. *Inorg. Chem.* **2010**, *49*, 815–822.

(103) San-Miguel, A.; Kéghélian, P.; Blase, X.; Mélinon, P.; Perez, A.; Itié, J.; Polian, A.; Reny, E.; Cros, C.; Pouchard, M. High Pressure Behavior of Silicon Clathrates: A New Class of Low Compressibility Materials. *Phys. Rev. Lett.* **1999**, *83*, 5290–5293.

(104) San-Miguel, A.; Toulemonde, P. High-Pressure Properties of Group IV Clathrates. *High Press. Res.* **2005**, *25*, 159–185.

(105) Yang, J.; Tse, J. S. Silicon Clathrates as Anode Materials for Lithium Ion Batteries? *J. Mater. Chem. A* **2013**, *1*, 7782.

(106) Li, Y.; Raghavan, R.; Wagner, N. a.; Davidowski, S. K.; Baggetto, L.; Zhao, R.; Cheng, Q.; Yarger, J. L.; Veith, G. M.; Ellis-Terrell, C.; et al. Type I Clathrates as Novel Silicon Anodes: An Electrochemical and Structural Investigation. *Adv. Sci.* **2015**, *2*, 1500057.

(107) Chan, K. S.; Miller, M. A.; Liang, W.; Ellis-Terrell, C.; Chan, C. K. First Principles and Experimental Studies of Empty Si46 as Anode Materials for Li-Ion Batteries. *J. Mater. Res.* **2016**, *31*, 3657–3665.

(108) Warrier, P.; Koh, C. A. Silicon Clathrates for Lithium Ion Batteries: A Perspective. *Appl. Phys. Rev.* **2016**, *3*, 040805.

(109) Huggins, R. a.; Nix, W. D. Decrepitation Model for Capacity Loss during Cycling of Alloys in Rechargeable Electrochemical Systems. *Ionics (Kiel).* **2000**, *6*, 57–63.

(110) Gou, W.; Rodriguez, S. Y.; Li, Y.; Ross, J. H. NMR Experiments and Electronic Structure Calculations in Type-I BaAlGe Clathrates. *Phys. Rev. B - Condens. Matter Mater. Phys.* **2009**, *80*, 1–9.

(111) Rodriguez, S. Y.; Saribaev, L.; Ross, J. H. Zintl Behavior and Vacancy Formation in Type-I Ba-Al-Ge Clathrates. *Phys. Rev. B - Condens. Matter Mater. Phys.* **2010**, *82*, 1–6.

(112) Schäfer, H.; Eisenmann, B.; Müller, W. Zintl Phases: Transitions between Metallic and Ionic Bonding. *Angew. Chemie Int. Ed. English* **1973**, *12*, 694–712.

(113) Carrillo-Cabrera, W.; Budnyk, S.; Prots, Y.; Grin, Y. Ba_8Ge_{43} Revisited: A 2a′x2a′x2a′ Superstructure of the Clathrate-I Type with Full Vacancy Ordering.

Zeitschrift fur Anorg. und Allg. Chemie **2004**, *630*, 2267–2276.

(114) Böhme, B.; Bobnar, M.; Ormeci, A.; Peters, S.; Schnelle, W.; Baitinger, M.; Grin, Y. Type-I Silicon Clathrates Containing Lithium. *Zeitschrift für Krist. - Cryst. Mater.* **2017**, *232*, 223–233.

(115) Liang, Y.; Böhme, B.; Ormeci, A.; Borrmann, H.; Pecher, O.; Haarmann, F.; Schnelle, W.; Baitinger, M.; Grin, Y. A Clathrate-I Phase with Li-Ge Framework. *Chem. - A Eur. J.* **2012**, *18*, 9818–9822.

(116) Böhme, B.; Wei, K.; Bobnar, M.; Prots, Y.; Burkhardt, U.; Baitinger, M.; Nolas, G. S.; Grin, Y. A Type-II Clathrate with a Li-Ge Framework. *Zeitschrift fur Kristallographie - Crystalline Materials*. 2017, pp 543–556.

(117) Obrovac, M. N.; Christensen, L. Structural Changes in Silicon Anodes during Lithium Insertion/Extraction. *Electrochem. Solid-State Lett.* **2004**, *7*, A93–A96.

(118) Loaiza, L. C.; Louvain, N.; Fraisse, B.; Boulaoued, A.; Iadecola, A.; Johansson, P.; Stievano, L.; Seznec, V.; Monconduit, L. Electrochemical Lithiation of Ge: New Insights by Operando Spectroscopy and Diffraction. *J. Phys. Chem. C* **2018**, *122*, 3709–3718.

(119) Lim, L. Y.; Liu, N.; Cui, Y.; Toney, M. F. Understanding Phase Transformation in Crystalline Ge Anodes for Li-Ion Batteries. *Chem. Mater.* **2014**, *26*, 3739–3746.

(120) Jung, H.; Allan, P. K.; Hu, Y. Y.; Borkiewicz, O. J.; Wang, X. L.; Han, W. Q.; Du, L. S.; Pickard, C. J.; Chupas, P. J.; Chapman, K. W.; et al. Elucidation of the Local and Long-Range Structural Changes That Occur in Germanium Anodes in Lithium-Ion Batteries. *Chem. Mater.* **2015**, *27*, 1031–1041.

(121) Condron, C. L.; Porter, R.; Guo, T.; Kauzlarich, S. M. Crystal Structures, Raman Spectroscopy, and Magnetic Properties of $Ba_{7.5}Al_{13}Si_{29}$ and $Eu_{0.27}Ba_{7.22}Al_{13}Si_{29}$. *Inorg. Chem.* **2005**, *44*, 9185–9191.

(122) Condron, C. L.; Martin, J.; Nolas, G. S.; Piccoli, P. M. B.; Schultz, A. J.; Kauzlarich, S. M. Structure and Thermoelectric Characterization of $Ba_8Al_{14}Si_{31}$. *Inorg. Chem.* **2006**, *45*, 9381–9386.

(123) Bobnar, M.; Böhme, B.; Wedel, M.; Burkhardt, U.; Ormeci, A.; Prots, Y.; Drathen, C.; Liang, Y.; Nguyen, H. D.; Baitinger, M.; et al. Distribution of Al Atoms in the Clathrate-I Phase $Ba_8Al_xSi_{46-x}$ at x = 6.9. *Dalt. Trans.* **2015**, *44*, 12680–12687.

(124) Roudebush, J. H.; De La Cruz, C.; Chakoumakos, B. C.; Kauzlarich, S. M. Neutron Diffraction Study of the Type I Clathrate $Ba_8Al_xSi_{46-x}$: Site Occupancies, Cage Volumes, and the Interaction between the Guest and the Host Framework. *Inorg. Chem.* **2012**, *51*, 1805–1812.

(125) Aydemir, U.; Candolfi, C.; Borrmann, H.; Baitinger, M.; Ormeci, A.; Carrillo-Cabrera, W.; Chubilleau, C.; Leonir, B.; Dauscher, A.; Oeschler, N.; et al. Crystal Structure and Transport Properties of $Ba_8Ge_{43}\square_3$. *Dalt. Trans.* **2010**, *39*, 978–992.

(126) Okamoto, N. L.; Oh, M. W.; Nishii, T.; Tanaka, K.; Inui, H. Crystal Structure and Thermoelectric Properties of the Type-I Clathrate Compound Ba_8Ge_{43} with an Ordered Arrangement of Ge Vacancies. *J. Appl. Phys.* **2006**, *99*, 1–8.

(127) Prabhakaran, K.; Ogino, T. Oxidation of Ge(100) and Ge(111) Surfaces: An UPS and XPS Study. *Surf. Sci.* **1995**, *325*, 263–271.

(128) Kume, T.; Ban, T.; Ohashi, F.; Jha, H. S.; Sugiyama, T.; Ogura, T.; Sasaki, S.; Nonomura, S. A Thin Film of a Type II Ge Clathrate Epitaxially Grown on a Ge Substrate. *CrystEngComm* **2016**, *18*, 5630–5638.

(129) Alexander, M. R.; Thompson, G. E.; Beamson, G. Characterization of the Oxide/Hydroxide Surface of Aluminum Using X-Ray Photoelectron Spectroscopy: A Procedure for Curve Fitting the O 1s Core Level. *Surf. Interface Anal.* **2000**, *29*, 468–477.

(130) Huggins, R. A. Materials Science Principles Related to Alloys of Potential Use in Rechargeable Lithium Cells. *J. Power Sources* **1989**, *26*, 109–120.

(131) Chockla, A. M.; Klavetter, K. C.; Mullins, C. B.; Korgel, B. A. Solution-Grown Germanium Nanowire Anodes for Lithium-Ion Batteries. *ACS Appl. Mater. Interfaces* **2012**, *4*, 4658–4664.

(132) Graetz, J.; Ahn, C. C.; Yazami, R.; Fultz, B. Nanocrystalline and Thin Film Germanium Electrodes with High Lithium Capacity and High Rate Capabilities. *J. Electrochem. Soc.* **2004**, *151*, A698–A702.

(133) Hatchard, T. D.; Dahn, J. R. In Situ XRD and Electrochemical Study of the Reaction of Lithium with Amorphous Silicon. *J. Electrochem. Soc.* **2004**, *151*, A838–A842.

(134) Liu, C.; Neale, Z. G.; Cao, G. Understanding Electrochemical Potentials of Cathode Materials in Rechargeable Batteries. *Mater. Today* **2016**, *19*, 109–123.

(135) Yoon, S.; Park, C.-M.; Sohn, H.-J. Electrochemical Characterizations of Germanium and Carbon-Coated Germanium Composite Anode for Lithium-Ion Batteries. *Electrochem. Solid-State Lett.* **2008**, *11*, A42–A45.

(136) Klavetter, K. C.; Wood, S. M.; Lin, Y. M.; Snider, J. L.; Davy, N. C.; Chockla, A. M.; Romanovicz, D. K.; Korgel, B. A.; Lee, J. W.; Heller, A.; et al. A High-Rate Germanium-Particle Slurry Cast Li-Ion Anode with High Coulombic Efficiency and Long Cycle Life. *J. Power Sources* **2013**, *238*, 123–136.

(137) Hamon, Y.; Brousse, T.; Jousse, F.; Topart, P.; Buvat, P.; Schleich, D. M. Aluminum Negative Electrode in Lithium Ion Batteries. *J. Power Sources* **2001**, *97–98*, 185–187.

(138) Fleischauer, M. D.; Obrovac, M. N.; Dahn, J. R. Al–Si Thin-Film Negative Electrodes for Li-Ion Batteries. *J. Electrochem. Soc.* **2008**, *155*, A851–A854.

(139) Tillard, M.; Belin, C.; Spina, L.; Jia, Y. Z. Phase Stabilities, Electronic and

Electrochemical Properties of Compounds in the LiAlSi System. *Solid State Sci.* **2005**, *7*, 1125–1134.

(140) Baggetto, L.; Notten, P. H. L. Lithium-Ion (De)Insertion Reaction of Germanium Thin-Film Electrodes: An Electrochemical and In Situ XRD Study. *J. Electrochem. Soc.* **2009**, *156*, A169–A175.

(141) Song, J. Y.; Lee, H. H.; Wang, Y. Y.; Wan, C. C. Two- and Three-Electrode Impedance Spectroscopy of Lithium-Ion Batteries. *J. Power Sources* **2002**, *111*, 255–267.

(142) Ångqvist, M.; Erhart, P. Understanding Chemical Ordering in Intermetallic Clathrates from Atomic Scale Simulations. *Chem. Mater.* **2017**, *29*, 7554–7562.

(143) Liang, Y.; Schnelle, W.; Veremchuk, I.; Böhme, B.; Baitinger, M.; Grin, Y. Synthesis and Thermoelectric Properties of the Clathrate-I Phase $K_8Li_xGe_{44-x/4}\square_{2-3x/4}$. *J. Electron. Mater.* **2015**, *44*, 4444–4451.

(144) Chan, T. L.; Chelikowsky, J. R. Controlling Diffusion of Lithium in Silicon Nanostructures. *Nano Lett.* **2010**, *10*, 821–825.

(145) Chou, C. Y.; Kim, H.; Hwang, G. S. A Comparative First-Principles Study of the Structure, Energetics, and Properties of Li-M (M = Si, Ge, Sn) Alloys. *J. Phys. Chem. C* **2011**, *115*, 20018–20026.

(146) Zhao, K.; Wang, W. L.; Gregoire, J.; Pharr, M.; Suo, Z.; Vlassak, J. J.; Kaxiras, E. Lithium-Assisted Plastic Deformation of Silicon Electrodes in Lithium-Ion Batteries: A First-Principles Theoretical Study. *Nano Lett.* **2011**, *11*, 2962–2967.

(147) Chou, C. Y.; Hwang, G. S. On the Origin of the Significant Difference in Lithiation Behavior between Silicon and Germanium. *J. Power Sources* **2014**, *263*, 252–258.

(148) Chou, C. Y.; Hwang, G. S. On the Origin of Anisotropic Lithiation in Crystalline Silicon over Germanium: A First Principles Study. *Appl. Surf. Sci.* **2014**, *323*, 78–81.

(149) Di Stefano, D.; Miglio, A.; Robeyns, K.; Filinchuk, Y.; Lechartier, M.; Senyshyn, A.; Ishida, H.; Spannenberger, S.; Roling, B.; Kato, Y.; et al. Superionic Diffusion through Frustrated Energy Landscape. *arXiv:1708.02997* **2017**.

(150) Baranowski, L. L.; Krishna, L.; Martinez, A. D.; Raharjo, T.; Stevanović, V.; Tamboli, A. C.; Toberer, E. S. Synthesis and Optical Band Gaps of Alloyed Si–Ge Type II Clathrates. *J. Mater. Chem. C* **2014**, *2*, 3231.

(151) Warrier, P.; Koh, C. A. Silicon Clathrates for Lithium Ion Batteries: A Perspective. *Appl. Phys. Rev.* **2016**, *3*, 040805.

(152) Dopilka, A.; Zhao, R.; Weller, J. M.; Bobev, S.; Peng, X.; Chan, C. K. Experimental and Computational Study of the Lithiation of $Ba_8Al_yGe_{46-y}$ Based Type I Germanium Clathrates. *ACS Appl. Mater. Interfaces* **2018**, *10*, 37981–

37993.

(153) Taylor, P. C. Exotic Forms of Silicon. *Phys. Today* **2016**, *69*, 34–39.

(154) Beekman, M.; Nolas, G. S. Synthesis and Thermal Conductivity of Type II Silicon Clathrates. *Phys. B Condens. Matter* **2006**, *383*, 111–114.

(155) Krishna, L.; Baranowski, L. L.; Martinez, A. D.; Koh, C. A.; Taylor, P. C.; Tamboli, A. C.; Toberer, E. S. Efficient Route to Phase Selective Synthesis of Type II Silicon Clathrates with Low Sodium Occupancy. *CrystEngComm* **2014**, *16*, 3940–3949.

(156) Nakano, H.; Ikuno, T. Soft Chemical Synthesis of Silicon Nanosheets and Their Applications. *Appl. Phys. Rev.* **2016**, *3*.

(157) Guloy, A. M.; Ramlau, R.; Tang, Z.; Schnelle, W.; Baitinger, M.; Grin, Y. A Guest-Free Germanium Clathrate. *Nature* **2006**, *443*, 320–323.

(158) Scherf, L. M.; Hattendorff, J.; Buchberger, I.; Geier, S.; Gasteiger, H. A.; Fässler, T. F. Electrochemical Synthesis of the Allotrope Allo-Ge and Investigations on Its Use as an Anode Material. *J. Mater. Chem. A* **2017**, *5*, 11179–11187.

(159) Cultrara, N. D.; Wang, Y.; Arguilla, M. Q.; Scudder, M. R.; Jiang, S.; Windl, W.; Bobev, S.; Goldberger, J. E. Synthesis of 1T, 2H, and 6R Germanane Polytypes. *Chem. Mater.* **2018**, *30*, 1335–1343.

(160) Bhattacharya, A.; Carbogno, C.; Böhme, B.; Baitinger, M.; Grin, Y.; Scheffler, M. Formation of Vacancies in Si- and Ge-Based Clathrates: Role of Electron Localization and Symmetry Breaking. *Phys. Rev. Lett.* **2017**, *118*, 1–5.

(161) Saito, S.; Oshiyama, A. Electronic Structure of Si_{46} and $Na_2Ba_6Si_{46}$. *Phys. Rev. B* **1995**, *51*, 2628–2631.

(162) Kaltzoglou, A.; Ponou, S.; Fässler, T. F. Synthesis and Crystal Structure of Mercury-Substituted Type-I Clathrates $A_8Hg_4Sn_{42}$ (A = K, Rb, Cs). *Eur. J. Inorg. Chem.* **2008**, *42*, 538–542.

(163) Von Schnering, H. G.; Llanos, J.; Peters, K.; Baitinger, M.; Grin, Y.; Nesper, R. Refinement of the Crystal Structure of $K_8Ge_{44}\square_2$, an Intermetallic Clathrate I. *Zeitschrift fur Krist. - New Cryst. Struct.* **2011**, *226*, 9–10.

(164) Ramachandran, G. K.; Dong, J.; Diefenbacher, J.; Gryko, J.; Marzke, R. F.; Sankey, O. F.; McMillan, P. F. Synthesis and X-Ray Characterization of Silicon Clathrates. *J. Solid State Chem.* **1999**, *145*, 716–730.

(165) Kim, H.; Kim, D. J.; Seo, D. H.; Yeom, M. S.; Kang, K.; Kim, D. K.; Jung, Y. Ab Initio Study of the Sodium Intercalation and Intermediate Phases in $Na_{0.44}MnO_2$ for Sodium-Ion Battery. *Chem. Mater.* **2012**, *24*, 1205–1211.

(166) Van Der Ven, A.; Thomas, J. C.; Xu, Q.; Swoboda, B.; Morgan, D. Nondilute Diffusion from First Principles: Li Diffusion in Li_xTiS_2. *Phys. Rev. B - Condens.*

Matter Mater. Phys. **2008**, *78*, 1–12.

(167) Rong, Z.; Malik, R.; Canepa, P.; Sai Gautam, G.; Liu, M.; Jain, A.; Persson, K.; Ceder, G. Materials Design Rules for Multivalent Ion Mobility in Intercalation Structures. *Chem. Mater.* **2015**, *27*, 6016–6021.

(168) Slingsby, J. G.; Rorrer, N. A.; Krishna, L.; Toberer, E. S.; Koh, C. A.; Maupin, C. M. Dynamic Free Energy Surfaces for Sodium Diffusion in Type II Silicon Clathrates. *Phys. Chem. Chem. Phys.* **2016**, *18*, 5121–5128.

(169) Stefanoski, S.; Martin, J.; Nolas, G. S. Low Temperature Transport Properties and Heat Capacity of Single-Crystal Na_8Si_{46}. *J. Phys. Condens. Matter* **2010**, *22*, 485404.

(170) Stefanoski, S.; Beekman, M.; Wong-Ng, W.; Zavalij, P.; Nolas, G. S. Simple Approach for Selective Crystal Growth of Intermetallic Clathrates. *Chem. Mater.* **2011**, *23*, 1491–1495.

(171) Schäfer, M. C.; Yamasaki, Y.; Fritsch, V.; Bobev, S. Ternary Compounds in the Sn-Rich Section of the Ba–Ga–Sn System: $Ba_8Ga_{16-x}Sn_{30+x}$ ($1.1 \leq x \leq 2.8$) Clathrates of Type-I and Type-VIII, and $BaGa_{2-x}Sn_{4+x}$ ($x \approx 0.2$) with a Clathrate-like Structure. *Crystals* **2011**, *1*, 145–162.

(172) Horie, H. omi; Kikudome, T.; Teramura, K.; Yamanaka, S. Controlled Thermal Decomposition of NaSi to Derive Silicon Clathrate Compounds. *J. Solid State Chem.* **2009**, *182*, 129–135.

(173) Wan, W.; Zhang, Q.; Cui, Y.; Wang, E. First Principles Study of Lithium Insertion in Bulk Silicon. *J. Phys. Condens. Matter* **2010**, *22*, 415501.

(174) Martinez, A. D.; Krishna, L.; Baranowski, L. L.; Lusk, M. T.; Toberer, E. S.; Tamboli, A. C. Synthesis of Group IV Clathrates for Photovoltaics. *IEEE J. Photovoltaics* **2013**, *3*, 1305–1310.

(175) Kume, T.; Ohashi, F.; Sakai, K.; Fukuyama, A.; Imai, M.; Udono, H.; Ban, T.; Habuchi, H.; Suzuki, H.; Ikari, T.; et al. Thin Film of Guest-Free Type-II Silicon Clathrate on Si(111) Wafer. *Thin Solid Films* **2016**, *609*, 30–34.

(176) Fix, T.; Vollondat, R.; Ameur, A.; Roques, S.; Rehspringer, J. L.; Chevalier, C.; Muller, D.; Slaoui, A. Silicon Clathrate Films for Photovoltaic Applications. *J. Phys. Chem. C* **2020**, *124*, 14972–14977.

(177) Hübner, J. M.; Prots, Y.; Schnelle, W.; Bobnar, M.; König, M.; Baitinger, M.; Simon, P.; Carrillo-Cabrera, W.; Ormeci, A.; Svanidze, E.; et al. In-Cage Interactions in the Clathrate Superconductor Sr_8Si_{46}. *Chem. - A Eur. J.* **2020**, *26*, 830–838.

(178) Dopilka, A.; Childs, A.; Bobev, S.; Chan, C. K. Understanding the Amorphous Lithiation Pathway of the Type I Ba8Ge43 Clathrate with Synchrotron X-Ray Characterization. *Chem. Mater.* **2020**, *32*, 9444–9457.

(179) Dopilka, A.; Peng, X.; Chan, C. K. Ab Initio Investigation of Li and Na Migration in Guest-Free, Type I Clathrates. *J. Phys. Chem. C* **2019**, *123*, 22812–22822.

(180) Tarnev, T.; Wilde, P.; Dopilka, A.; Schuhmann, W.; Chan, C. K.; Ventosa, E. Surface Properties of Battery Materials Elucidated Using Scanning Electrochemical Microscopy: The Case of Type I Silicon Clathrate. *ChemElectroChem* **2020**, *7*, 665–671.

(181) Guloy, A. M.; Ramlau, R.; Tang, Z.; Schnelle, W.; Baitinger, M.; Grin, Y. A Guest-Free Germanium Clathrate. *Nature* **2006**, *443*, 320–323.

(182) Baranowski, L. L.; Krishna, L.; Martinez, A. D.; Raharjo, T.; Stevanović, V.; Tamboli, A. C.; Toberer, E. S. Synthesis and Optical Band Gaps of Alloyed Si–Ge Type II Clathrates. *J. Mater. Chem. C* **2014**, *2*, 3231–3237.

(183) Schafer, M. C.; Bobev, S. Tin Clathrates with the Type II Structure. *J. Am. Chem. Soc.* **2013**, *135*, 1696–1699.

(184) Schäfer, M. C.; Bobev, S. New Type-I and Type-II Clathrates in the Systems Cs-Na-Ga-Si, Rb-Na-Ga-Si, and Rb-Na-Zn-Si. *Inorganics* **2014**, *2*, 79–95.

(185) Reny, E.; Gravereau, P.; Cros, C.; Pouchard, M. Structural Characterisations of the Na Si and Na Si Silicon Clathrates Using the Rietveld Method. *J. Mater. Chem.* **1998**, *8*, 2839–2844.

(186) Beekman, M.; Nenghabi, E. N.; Biswas, K.; Myles, C. W.; Baitinger, M.; Grin, Y.; Nolas, G. S. Framework Contraction in Na-Stuffed Si(CF 136). *Inorg. Chem.* **2010**, *49*, 5338–5340.

(187) Stefanoski, S.; Malliakas, C. D.; Kanatzidis, M. G.; Nolas, G. S. Synthesis and Structural Characterization of NaxSi136($0 < x \leq 24$) Single Crystals and Low-Temperature Transport of Polycrystalline Specimens. *Inorg. Chem.* **2012**, *51*, 8686–8692.

(188) Key, B.; Bhattacharyya, R.; Morcrette, M.; Seznéc, V.; Tarascon, J. M.; Grey, C. P. Real-Time NMR Investigations of Structural Changes in Silicon Electrodes for Lithium-Ion Batteries. *J. Am. Chem. Soc.* **2009**, *131*, 9239–9249.

(189) Loveridge, M. J.; Lain, M. J.; Johnson, I. D.; Roberts, A.; Beattie, S. D.; Dashwood, R.; Darr, J. A.; Bhagat, R. Towards High Capacity Li-Ion Batteries Based on Silicon-Graphene Composite Anodes and Sub-Micron V-Doped LiFePO 4 Cathodes. *Sci. Rep.* **2016**, *6*, 1–11.

(190) Yamanaka, S.; Komatsu, M.; Tanaka, M.; Sawa, H.; Inumaru, K. High-Pressure Synthesis and Structural Characterization of the Type II Clathrate Compound Na30.5Si136 Encapsulating Two Sodium Atoms in the Same Silicon Polyhedral Cages. *J. Am. Chem. Soc.* **2014**, *136*, 7717–7725.

(191) He, J.; Klug, D. D.; Uehara, K.; Preston, K. F.; Ratcliffe, C. I.; Tse, J. S. NMR and X-Ray Spectroscopy of Sodium−Silicon Clathrates †. *J. Phys. Chem. B* **2001**, *105*, 3475–3485.

(192) Weppner, W.; Huggins, R. A. Determination of the Kinetic Parameters of Mixed-Conducting Electrodes and Application to the System Li_3Sb. *J. Electrochem. Soc.* **1977**, *124*, 1569.

(193) Dreyer, W.; Jamnik, J.; Guhlke, C.; Huth, R.; Moškon, J.; Gaberšček, M. The Thermodynamic Origin of Hysteresis in Insertion Batteries. *Nat. Mater.* **2010**, *9*, 448–453.

(194) Kim, H.; Kweon, K. E.; Chou, C. Y.; Ekerdt, J. G.; Hwang, G. S. On the Nature and Behavior of Li Atoms in Si: A First Principles Study. *J. Phys. Chem. C* **2010**, *114*, 17954–17959.

(195) Aravindan, V.; Lee, Y. S.; Madhavi, S. Best Practices for Mitigating Irreversible Capacity Loss of Negative Electrodes in Li-Ion Batteries. *Adv. Energy Mater.* **2017**, *7*, 1–17.

(196) Limthongkul, P.; Jang, Y. Il; Dudney, N. J.; Chiang, Y. M. Electrochemically-Driven Solid-State Amorphization in Lithium-Silicon Alloys and Implications for Lithium Storage. *Acta Mater.* **2003**, *51*, 1103–1113.

(197) Courtney, I.; Tse, J. Ab Initio Calculation of the Lithium-Tin Voltage Profile. *Phys. Rev. B - Condens. Matter Mater. Phys.* **1998**, *58*, 15583–15588.

(198) Graetz, J.; A, S. L.; Graetz, J.; Ahn, C. C.; Yazami, R.; Fultz, B. Highly Reversible Lithium Storage in Nanostructured Silicon Highly Reversible Lithium Storage in Nanostructured Silicon. *Electrochem. Solid-State Lett.* **2003**, *6*, A194–A197.

(199) Liu, X. H.; Zhong, L.; Huang, S.; Mao, S. X.; Zhu, T.; Huang, J. Y. Size-Dependent Fracture of Silicon Nanoparticles during Lithiation. *ACS Nano* **2012**, *6*, 1522–1531.

(200) Chan, C. K.; Zhang, X. F.; Cui, Y. High Capacity Li Ion Battery Anodes Using Ge Nanowires. *Nano Lett.* **2008**, *8*, 307–309.

(201) Liang, W.; Yang, H.; Fan, F.; Liu, Y.; Liu, X. H.; Huang, J. Y.; Zhu, T.; Zhang, S. Tough Germanium Nanoparticles under Electrochemical Cycling. *ACS Nano* **2013**, *7*, 3427–3433.

(202) Wang, J.; Fan, F.; Liu, Y.; Jungjohann, K. L.; Lee, S. W.; Mao, S. X.; Liu, X.; Zhu, T. Structural Evolution and Pulverization of Tin Nanoparticles during Lithiation-Delithiation Cycling. *J. Electrochem. Soc.* **2014**, *161*, F3019–F3024.

(203) Bourderau, S.; Brousse, T.; Schleich, D. M. Amorphous Silicon as a Possible Anode Material for Li-Ion Batteries. *J. Power Sources* **1999**, *81–82*, 233–236.

(204) Chevrier, V. L.; Dahn, J. R. First Principles Model of Amorphous Silicon Lithiation. *J. Electrochem. Soc.* **2009**, *156*, A454–A458.

(205) Zhao, L.; Dvorak, D. J.; Obrovac, M. N. Layered Amorphous Silicon as Negative Electrodes in Lithium-Ion Batteries. *J. Power Sources* **2016**, *332*, 290–298.

(206) Liu, X. H.; Huang, S.; Picraux, S. T.; Li, J.; Zhu, T.; Huang, J. Y. Reversible Nanopore Formation in Ge Nanowires during Lithiation- Delithiation Cycling: An in Situ Transmission Electron Microscopy Study. *Nano Lett.* **2011**, *11*, 3991–3997.

(207) Wang, J. W.; He, Y.; Fan, F.; Liu, X. H.; Xia, S.; Liu, Y.; Harris, C. T.; Li, H.; Huang, J. Y.; Mao, S. X.; et al. Two-Phase Electrochemical Lithiation in Amorphous Silicon. *Nano Lett.* **2013**, *13*, 709–715.

(208) Marzouk, A.; Balbuena, P. B.; El-Mellouhi, F. Open Framework Allotropes of Silicon: Potential Anode Materials for Na and Li-Ion Batteries. *Electrochim. Acta* **2016**, *207*, 301–307.

(209) Candolfi, C.; Aydemir, U.; Baitinger, M.; Oeschler, N.; Steglich, F.; Grin, Y. Thermoelectric Properties of the Clathrate I $Ba_8Ge_{43}\square_3$. *J. Electron. Mater.* **2010**, *39*, 2039–2042.

(210) Christensen, M.; Johnsen, S.; Iversen, B. B. Thermoelectric Clathrates of Type I. *Dalt. Trans.* **2010**, *39*, 978–992.

(211) Takabatake, T.; Suekuni, K.; Nakayama, T.; Kaneshita, E. Phonon-Glass Electron-Crystal Thermoelectric Clathrates: Experiments and Theory. *Rev. Mod. Phys.* **2014**, *86*, 669–716.

(212) Bryan, J. D.; Srdanov, V. I.; Stucky, G. D. Superconductivity in Germanium Clathrate $Ba_8Ga_{16}Ge_{30}$. *Phys. Rev. B* **1999**, *60*, 3064–3067.

(213) Jung, H. Solid State NMR and Pair Distribution Function Analysis Studies of Ge and Sn Anodes for Li-Ion Batteries. **2015**.

(214) Lorie Lopez, J. L.; Grandinetti, P. J.; Co, A. C. Phase Transformations and Capacity Fade Mechanism in Li_xSn Nanoparticle Electrodes Revealed by Operando ^{7}Li NMR. *J. Mater. Chem. A* **2019**, *7*, 10781–10794.

(215) Allan, P. K.; Griffin, J. M.; Darwiche, A.; Borkiewicz, O. J.; Wiaderek, K. M.; Chapman, K. W.; Morris, A. J.; Chupas, P. J.; Monconduit, L.; Grey, C. P. Tracking Sodium-Antimonide Phase Transformations in Sodium-Ion Anodes: Insights from Operando Pair Distribution Function Analysis and Solid-State NMR Spectroscopy. *J. Am. Chem. Soc.* **2016**, *138*, 2352–2365.

(216) Stratford, J. M.; Mayo, M.; Allan, P. K.; Pecher, O.; Borkiewicz, O. J.; Wiaderek, K. M.; Chapman, K. W.; Pickard, C. J.; Morris, A. J.; Grey, C. P. Investigating Sodium Storage Mechanisms in Tin Anodes: A Combined Pair Distribution Function Analysis, Density Functional Theory, and Solid-State NMR Approach. *J. Am. Chem. Soc.* **2017**, *139*, 7273–7286.

(217) Billinge, S. J. L.; Kanatzidis, M. G. Beyond Crystallography: The Study of Disorder, Nanocrystallinity and Crystallographically Challenged Materials with Pair Distribution Functions. *Chem. Commun.* **2004**, *4*, 749–760.

(218) Wang, Y.; Dahn, J. Phase Changes in Electrochemically Lithiated Silicon at Elevated Temperature. *J. Electrochem. Soc.* **2006**, *153*, A2314.

(219) Chevrier, V. L.; Dahn, H. M.; Dahn, J. R. Activation Energies of Crystallization Events in Electrochemically Lithiated Silicon. *J. Electrochem. Soc.* **2011**, *158*, A1207.

(220) Farrow, C. L.; Billinge, S. J. L. Relationship between the Atomic Pair Distribution Function and Small-Angle Scattering: Implications for Modeling of Nanoparticles. *Acta Crystallogr. Sect. A Found. Crystallogr.* **2009**, *65*, 232–239.

(221) Juhás, P.; Davis, T.; Farrow, C. L.; Billinge, S. J. L. PDFgetX3: A Rapid and Highly Automatable Program for Processing Powder Diffraction Data into Total Scattering Pair Distribution Functions. *J. Appl. Crystallogr.* **2013**, *46*, 560–566.

(222) Yang, X.; Juhas, P.; Farrow, C. L.; Billinge, S. J. L. XPDFsuite: An End-to-End Software Solution for High Throughput Pair Distribution Function Transformation, Visualization and Analysis. **2014**, arXiv 1402.3163.

(223) Morris, A. J.; Grey, C. P.; Pickard, C. J. Thermodynamically Stable Lithium Silicides and Germanides from Density Functional Theory Calculations. *Phys. Rev. B - Condens. Matter Mater. Phys.* **2014**, *90*, 22–24.

(224) Johnson, Q.; G.S., S.; D., W. The Crystal Structure of $Li_{15}Ge_4$. *Acta Crystallogr.* **1965**, *18*, 131–132.

(225) Tang, W.; Liu, Y.; Peng, C.; Hu, M. Y.; Deng, X.; Lin, M.; Hu, J. Z.; Loh, K. P. Probing Lithium Germanide Phase Evolution and Structural Change in a Germanium-in-Carbon Nanotube Energy Storage System. *J. Am. Chem. Soc.* **2015**, *137*, 2600–2607.

(226) Loaiza, L. C.; Louvain, N.; Fraisse, B.; Boulaoued, A.; Iadecola, A.; Johansson, P.; Stievano, L.; Seznec, V.; Monconduit, L. Electrochemical Lithiation of Ge: New Insights by Operando Spectroscopy and Diffraction. *J. Phys. Chem. C* **2018**, *122*, 3709–3718.

(227) Hopf, V.; Möller, W.; Schäfer, H. Die Strucktur Der Phase Li_7Ge_2. *Zeitschrift für Naturforsch.* **1972**, *27b*, 1157–1160.

(228) Hopf, V.; Möller, W.; Schäfer, H. Die Kristallstruktur Der Phase Li_9Ge_4. *Zeitschrift für Naturforsch.* **1970**, *25b*, 653.

(229) Vaughey, J. T.; Miller, G. J.; Gravelle, S.; Alejandro Leon-Escamilla, E.; Corbett, J. D. Synthesis, Structure, and Properties of $BaGe_2$: A Study of Tetrahedral Cluster Packing and Other Three-Connected Nets in Zintl Phases. *J. Solid State Chem.* **1997**, *133*, 501–507.

(230) Grüttner, A. PhD Thesis, University of Stuttgart, 1982.

(231) Zeilinger, M.; Baran, V.; Van Wüllen, L.; Häussermann, U.; Fässler, T. F. Stabilizing the Phase Li15Si4 through Lithium-Aluminum Substitution in Li15-XAlxSi4 ($0.4 < x < 0.8$) - Single Crystal X-Ray Structure Determination of Li 15Si4 and Li14.37Al0.63Si 4. *Chem. Mater.* **2013**, *25*, 4113–4121.

(232) Aykol, M.; Dwaraknath, S. S.; Sun, W.; Persson, K. A. Thermodynamic Limit for Synthesis of Metastable Inorganic Materials. *Sci. Adv.* **2018**, *4*, 1–8.

(233) Sivonxay, E.; Aykol, M.; Persson, K. A. The Lithiation Process and Li Diffusion in Amorphous SiO_2 and Si from First-Principles. *Electrochim. Acta* **2020**, *331*, 135344.

(234) Liang, W.; Yang, H.; Fan, F.; Liu, Y.; Liu, X. H.; Huang, J. Y.; Zhu, T.; Zhang, S. Tough Germanium Nanoparticles under Electrochemical Cycling. *ACS Nano* **2013**, *7*, 3427–3433.

(235) Hatchard, T. D.; Topple, J. M.; Fleischauer, M. D.; Dahn, J. R. Electrochemical Performance of SiAlSn Films Prepared by Combinatorial Sputtering. *Electrochem. Solid-State Lett.* **2003**, *6*, 6–10.

(236) Stegmaier, S.; Hlukhyy, V.; Fässler, T. F. The Intermetallic Type-I Clathrate Na8Zn4Ge42. *Zeitschrift fur Anorg. und Allg. Chemie* **2020**, *646*, 1073–1078.

(237) Beekman, M.; Nolas, G. S. Transport Properties of the Binary Type I Clathrate $K_8Ge_{44}\square_2$. *Int. J. Appl. Ceram. Technol.* **2007**, *4*, 332–338.

(238) Schäfer, Marion C. Bobev, S. Synthesis and Structural Characterization of the New Clathrates $K_8Cd_4Ge_{42}$, $Rb_8Cd_4Ge_{42}$, and Cs_8 Cd_4Ge_{42}. *Materials (Basel).* **2016**, *9*.

(239) Zhang, Y.; Lee, P. L.; Nolas, G. S.; Wilkinson, A. P. Gallium Distribution in the Clathrates $Sr_8Ga_{16}Ge_{30}$ and $Sr_4Eu_4Ga_{16}Ge_{30}$ by Resonant Diffraction. *Appl. Phys. Lett.* **2002**, *80*, 2931–2933.

(240) Schäfer, M. C.; Bobev, S. On the Possibility for Rb- and Eu-Cation Ordering in Type-I Clathrates: Synthesis and Homogeneity Range of the Novel Compounds $Rb_{8-x}Eu_x(In,Ge)_{46}$ ($0.6 \leq x \leq 1.8$). *Acta Crystallogr. Sect. C Cryst. Struct. Commun.* **2013**, *69*, 1457–1461.

(241) Johnsen, S.; Bentien, A.; Madsen, G. K. H.; Nygren, M.; Iversen, B. B. Copper Containing Germanium Clathrates. *Int. Conf. Thermoelectr. ICT, Proc.* **2005**, *2005*, 211–214.

(242) Shevelkov, A. V; Kovnir, K. Zintl Clathrates. In *Zintl Phases: Principles and Recent Developments*; Fässler, T. F., Ed.; Springer Berlin Heidelberg: Berlin, Heidelberg, 2011; pp 97–142.

(243) Schäfer, M. C.; Yamasaki, Y.; Fritsch, V.; Bobev, S. Ternary Compounds in the Sn-Rich Section of the Ba–Ga–Sn System: Ba8Ga16–XSn30+x ($1.1 \leq x \leq 2.8$) Clathrates of Type-I and Type-VIII, and BaGa2–XSn4+x ($x \approx 0.2$) with a Clathrate-like Structure. *Crystals* **2011**, *1*, 145–162.

(244) Dopilka, A.; Weller, J. M.; Ovchinnikov, A.; Childs, A.; Bobev, S.; Peng, X.; Chan, C. K. Structural Origin of Reversible Li Insertion in Guest-Free, Type-II Silicon Clathrates. *Adv. Energy Sustain. Res.* **2021**, 2000114.

(245) Hansen, D. A.; Chang, L. J. Crystal Structure of Li 2 Sn 5 . *Acta Crystallogr. Sect. B Struct. Crystallogr. Cryst. Chem.* **1969**, *25*, 2392–2395.

(246) Müller, W.; Schäfer, H. Die Kristallstruktur Der Phase LiSn:The Crystal Structure of LiSn. *Zeitschrift fur Naturforsch. - Sect. B J. Chem. Sci.* **1973**, *28*, 246–248.

(247) Courtney, I. A.; Dahn, J. R. Electrochemical and In Situ X-Ray Diffraction Studies of the Reaction of Lithium with Tin Oxide Composites. *J. Electrochem. Soc.* **1997**, *144*, 2045–2052.

(248) Ichitsubo, T.; Yagi, S.; Doi, T.; Yukitani, S.; Hirai, K.; Matsubara, E. Influence of Mechanical Strain on the Electrochemical Lithiation of Aluminum-Based Electrode Materials. *J. Electrochem. Soc.* **2011**, *159*, A14–A17.

(249) Rhodes, K. J.; Meisner, R.; Kirkham, M.; Dudney, N.; Daniel, C. In Situ XRD of Thin Film Tin Electrodes for Lithium Ion Batteries. *J. Electrochem. Soc.* **2012**, *159*, A294–A299.

(250) Chouvin, J.; Olivier-Fourcade, J.; Jumas, J. .; Simon, B.; Godiveau, O. 119Sn Mössbauer Study of LixSn Alloys Prepared Electrochemically. *Chem. Phys. Lett.* **1999**, *308*, 413–420.

(251) Lupu, C.; Mao, J. G.; Rabalais, J. W.; Guloy, A. M.; Richardson, J. W. X-Ray and Neutron Diffraction Studies on "Li4.4Sn." *Inorg. Chem.* **2003**, *42*, 3765–3771.

(252) Dahn, J. R.; Courtney, I. A.; Mao, O. Short-Range Sn Ordering and Crystal Structure of Li4.4Sn Prepared by Ambient Temperature Electrochemical Methods. *Solid State Ionics* **1998**, *111*, 289–294.

(253) Oehl, N.; Schmuelling, G.; Knipper, M.; Kloepsch, R.; Placke, T.; Kolny-Olesiak, J.; Plaggenborg, T.; Winter, M.; Parisi, J. In Situ X-Ray Diffraction Study on the Formation of α-Sn in Nanocrystalline Sn-Based Electrodes for Lithium-Ion Batteries. *CrystEngComm* **2015**, *17*, 8500–8504.

(254) Müller, W. Preparation Und Crystal Structure of Li7Sn3. *Zeitschrift für Naturforsch. B* **1974**, *29*, 304–311.

(255) Kishimoto, K.; Ikeda, N.; Akai, K.; Koyanagi, T. Synthesis and Thermoelectric Properties of Silicon Clathrates Sr 8AlxGa16-X-Si30 with the Type-I and Type-VIII Structures. *Appl. Phys. Express* **2008**, *1*, 0312011–0312013.

(256) Paschen, S.; Carrillo-Cabrera, W.; Bentien, A.; Tran, V. H.; Baenitz, M.; Grin, Y.; Steglich, F. Structural, Transport, Magnetic, and Thermal Properties of Eu8Ga16Ge30. *Phys. Rev. B - Condens. Matter Mater. Phys.* **2001**, *64*, 1–11.

(257) Sasaki, Y.; Kishimoto, K.; Koyanagi, T.; Asada, H.; Akai, K. Synthesis and Thermoelectric Properties of Type-VIII Germanium Clathrates Sr8 Alx Gay Ge46-x-Y. *J. Appl. Phys.* **2009**, *105*, 073702.

(258) Lee, K. T.; Jung, Y. S.; Kim, T.; Kim, C. H.; Kim, J. H.; Kwon, J. Y.; Oh, S. M. Liquid Gallium Electrode Confined in Porous Carbon Matrix as Anode for

Lithium Secondary Batteries. *Electrochem. Solid-State Lett.* **2008**, *11*, A21–A24.

(259) Besenhard, J. O.; Yang, J.; Winter, M. Will Advanced Lithium-Alloy Anodes Have a Chance in Lithium-Ion Batteries? *J. Power Sources* **1997**, *68*, 87–90.

(260) Yang, J.; Takeda, Y.; Imanishi, N.; Yamamoto, O. Ultrafine Sn and SnSb0.14 Powders for Lithium Storage Matrices in Lithium-Ion Batteries. *J. Electrochem. Soc.* **1999**, *146*, 4009–4013.

(261) Wu, Y.; Huang, L.; Huang, X.; Guo, X.; Liu, D.; Zheng, D.; Zhang, X.; Ren, R.; Qu, D.; Chen, J. A Room-Temperature Liquid Metal-Based Self-Healing Anode for Lithium-Ion Batteries with an Ultra-Long Cycle Life. *Energy Environ. Sci.* **2017**, *10*, 1854–1861.

(262) Dopilka, A.; Childs, A.; Bobev, S.; Chan, C. K. Solid-State Electrochemical Synthesis of Silicon Clathrates Using a Sodium-Sulfur Battery Inspired Approach. *J. Electrochem. Soc.* **2021**, *168*, 020516.

(263) Böhme, B. An Electrochemical Approach toward the Metastable Type II Clathrate Germanium Allotrope. *Inorg. Chem.* **2020**, *59*, 11920–11924.

(264) Takeshita, R.; Kishimoto, K.; Asada, H.; Akai, K. Thermoelectric Properties of Type-I Clathrate Na8Ga8Ge38. *J. Solid State Chem.* **2021**, *294*, 121911.

(265) Ramachandran, G. K.; McMillan, P. F.; Dong, J.; Sankey, O. F. K(7.62(1))Si46 and Rb(6.15(2))Si46: Two Structure I Clathrates with Fully Occupied Framework Sites. *J. Solid State Chem.* **2000**, *154*, 626–634.

(266) Møllnitz, L.; Blake, N. P.; Meitu, H. Effects of Morphology on the Electronic and Transport Properties of Sn-Based Clathrates. *J. Chem. Phys.* **2002**, *117*, 1302–1312.

(267) Krishna, L.; Chai, P.; Koh, C. A.; Toberer, E. S.; Nolas, G. S. Synthesis and Structural Properties of Type I Potassium SiGe Alloy Clathrates. *Mater. Lett.* **2015**, *149*, 123–126.

(268) Bobev, S.; Sevov, S. C. Clathrates of Group 14 with Alkali Metals: An Exploration. *J. Solid State Chem.* **2000**, *153*, 92–105.

(269) Kaltzoglou, A.; Hoffmann, S. D.; Fässler, T. F. Order-Disorder Phase Transition in Type-I Clathrate Cs8Sn 44□2. *Eur. J. Inorg. Chem.* **2007**, 4162–4167.

(270) Zhang, Y.; Lee, P. L.; Nolas, G. S.; Wilkinson, A. P. Gallium Distribution in the Clathrates Sr8Ga16Ge30and Sr4Eu4Ga16Ge30by Resonant Diffraction. *Appl. Phys. Lett.* **2002**, *80*, 2931–2933.

(271) Kröner, R.; Peters, K.; Schnering, H. G. Von; Nesper, R.; Zürich, E. T. H.; Chemie, A.; Zürich, C.-. Crystal Structure of the Clathrates K8Al8Ge38 K8Al8Sn38. *Zeitschrift für Krist. - Cryst. Mater.* **1999**, *213*, 675–676.

(272) Dopilka, A.; Childs, A.; Ovchinnikov, A.; Zhao, R.; Bobev, S.; Peng, X.; Chan, C.

K. Electrochemical Amorphization in the Lithiation of the Type VIII Ba8Ga16–DSn30+d Clathrate (d ≈ 1). *Unpublished* **2021**.

(273) Jung, H.; Park, M.; Yoon, Y. G.; Kim, G. B.; Joo, S. K. Amorphous Silicon Anode for Lithium-Ion Rechargeable Batteries. *J. Power Sources* **2003**, *115*, 346–351.

(274) Maranchi, J. P.; Hepp, A. F.; Kumta, P. N. High Capacity, Reversible Silicon Thin-Film Anodes for Lithium-Ion Batteries. *Electrochem. Solid-State Lett.* **2003**, *6*.

(275) Uxa, D.; Jerliu, B.; Hüger, E.; Dörrer, L.; Horisberger, M.; Stahn, J.; Schmidt, H. On the Lithiation Mechanism of Amorphous Silicon Electrodes in Li-Ion Batteries. *J. Phys. Chem. C* **2019**, *123*, 22027–22039.

(276) Hatchard, T. D.; Dahn, J. R. In Situ XRD and Electrochemical Study of the Reaction of Lithium with Amorphous Silicon. *J. Electrochem. Soc.* **2004**, *151*, A838.

(277) Wu, H.; Hartman, M. R.; Udovic, T. J.; Rush, J. J.; Zhou, W.; Bowman, R. C.; Vajo, J. J. Structure of the Novel Ternary Hydrides Li4Tt2D (Tt = Si and Ge). *Acta Crystallogr. Sect. B Struct. Sci.* **2007**, *63*, 63–68.

(278) Chevrier, V. L.; Dahn, J. R. First Principles Studies of Disordered Lithiated Silicon. *J. Electrochem. Soc.* **2010**, *157*, A392–A398.

(279) Li, J.; Smith, A.; Sanderson, R. J.; Hatchard, T. D.; Dunlap, R. A.; Dahn, J. R. In Situ [Sup 119]Sn Mössbauer Effect Study of the Reaction of Lithium with Si Using a Sn Probe. *J. Electrochem. Soc.* **2009**, *156*, A283.

(280) Gu, M.; Wang, Z.; Connell, J. G.; Perea, D. E.; Lauhon, L. J.; Gao, F.; Wang, C. Electronic Origin for the Phase Transition from Amorphous Li $_x$ Si to Crystalline Li $_{15}$ Si $_4$. *ACS Nano* **2013**, *7*, 6303–6309.

(281) McDowell, M. T.; Lee, S. W.; Harris, J. T.; Korgel, B. A.; Wang, C.; Nix, W. D.; Cui, Y. In Situ TEM of Two-Phase Lithiation of Amorphous Silicon Nanospheres. *Nano Lett.* **2013**, *13*, 758–764.

(282) Wang, X.; Singh, S. S.; Ma, T.; Lv, C.; Chawla, N.; Jiang, H. Quantifying Electrochemical Reactions and Properties of Amorphous Silicon in a Conventional Lithium-Ion Battery Configuration. *Chem. Mater.* **2017**, *29*, 5831–5840.

(283) Hüger, E.; Dörrer, L.; Schmidt, H. Permeation, Solubility, Diffusion and Segregation of Lithium in Amorphous Silicon Layers. *Chem. Mater.* **2018**, *30*, 3254–3264.

(284) Christensen, M.; Johnsen, S.; Iversen, B. B. Thermoelectric Clathrates of Type I. *Dalt. Trans.* **2010**, *39*, 978–992.

(285) Himeno, R.; Ohashi, F.; Kume, T.; Asai, E.; Ban, T.; Suzuki, T.; Iida, T.; Habuchi, H.; Tsutsumi, Y.; Natsuhara, H.; et al. Optical Band Gap of Semiconductive Type II Si Clathrate Purified by Centrifugation. *J. Non. Cryst. Solids* **2012**, *358*, 2138–

2140.

(286) Ohashi, F.; Hattori, M.; Ogura, T.; Koketsu, Y.; Himeno, R.; Kume, T.; Ban, T.; Iida, T.; Habuchi, H.; Natsuhara, H.; et al. High-Yield Synthesis of Semiconductive Type-II Si Clathrates with Low Na Content. *J. Non. Cryst. Solids* **2012**, *358*, 2134–2137.

(287) Horie, H.; Kikudome, T.; Teramura, K.; Yamanaka, S. Controlled Thermal Decomposition of NaSi to Derive Silicon Clathrate Compounds. *J. Solid State Chem.* **2009**, *182*, 129–135.

(288) Stefanoski, S.; Nolas, G. S. Synthesis and Structural Characterization of Single-Crystal $K_{7.5}Si_{46}$ and $K_{17.8}Si_{136}$ Clathrates. *Cryst. Growth Des.* **2011**, *11*, 4533–4537.

(289) Böhme, B.; Guloy, A.; Tang, Z.; Schnelle, W.; Burkhardt, U.; Baitinger, M.; Grin, Y. Oxidation of M_4Si_4 (M = Na, K) to Clathrates by HCl or H_2O. *J. Am. Chem. Soc.* **2007**, *129*, 5348–5349.

(290) Beekman, M.; Baitinger, M.; Borrmann, H.; Schnelle, W.; Meier, K.; Nolas, G. S.; Grin, Y. Preparation and Crystal Growth of $Na_{24}Si_{136}$. *J. Am. Chem. Soc.* **2009**, *131*, 9642–9643.

(291) Stefanoski, S.; Blosser, M. C.; Nolas, G. S. Pressure Effects on the Size of Type-I and Type-II Si-Clathrates Synthesized by Spark Plasma Sintering. *Cryst. Growth Des.* **2013**, *13*, 195–197.

(292) Veremchuk, I.; Beekman, M.; Antonyshyn, I.; Schnelle, W.; Baitinger, M.; Nolas, G. S.; Grin, Y. Binary Alkali-Metal Silicon Clathrates by Spark Plasma Sintering: Preparation and Characterization. *Materials (Basel).* **2016**, *9*, 1–10.

(293) Dong, Y.; Nolas, G. S. Crystal Growth through Field-Assisted Electrochemical Redox and Ion-Exchange Reactions: A Case Study of $K_{4.2}Na_{3.8}Si_{46}$ Clathrate-I. *Cryst. Growth Des.* **2015**, *15*, 4731–4734.

(294) Hueso, K. B.; Armand, M.; Rojo, T. High Temperature Sodium Batteries: Status, Challenges and Future Trends. *Energy Environ. Sci.* **2013**, *6*, 734–749.

(295) Stanley Whittingham, M.; Huggins, R. A. Measurement of Sodium Ion Transport in Beta Alumina Using Reversible Solid Electrodes. *J. Chem. Phys.* **1971**, *54*, 414.

(296) Whittingham, M. S. Beta Alumina – Prelude to a Revolution in Solid State Electrochemistry. *ECS Meet. Abstr.* **2019**, *MA2019-02*.

(297) Chevrier, V. L.; Ceder, G. Challenges for Na-Ion Negative Electrodes. *J. Electrochem. Soc.* **2011**, *158*, 1011–1014.

(298) Urushiyama, H.; Morito, H.; Yamane, H.; Terauchi, M. Na-Ga-Si Type-I Clathrate Single Crystals Grown via Na Evaporation Using Na-Ga and Na-Ga-Sn Fluxes. *RSC Adv.* **2018**, *8*, 40505–40510.

(299) Hutchins, P. T.; Leynaud, O.; O'Dell, L. A.; Smith, M. E.; Barnes, P.; McMillan, P. F. Time-Resolved in Situ Synchrotron X-Ray Diffraction Studies of Type 1 Silicon Clathrate Formation. *Chem. Mater.* **2011**, *23*, 5160–5167.

(300) Kume, T.; Iwai, Y.; Sugiyama, T.; Ohashi, F.; Ban, T.; Sasaki, S.; Nonomura, S. NaSi and Si Clathrate Prepared on Si Substrate. *Phys. Status Solidi C* **2013**, *10*, 1739–1741.

(301) Hoffmann, S.; Baitinger, M.; Grin, Y. Application of n - Dodecyltrimethylammonium Chloride for the Oxidation of Intermetallic Phases. **2011**, 230–238.

(302) Beekman, M.; Kaduk, J. A.; Huang, Q.; Wong-Ng, W.; Yang, Z.; Wang, D.; Nolas, G. S. Synthesis and Crystal Structure of Na1-XGe3+z: A Novel Zeolite-like Framework Phase in the Na-Ge System. *Chem. Commun.* **2007**, No. 8, 837–839.

(303) Beekman, M.; Stefanoski, S.; Wong-Ng, W.; Kaduk, J. A.; Huang, Q.; Reeg, C.; Bowers, C. R.; Nolas, G. S. Structure and Thermal Conductivity of Na1-XGe3+z. *J. Solid State Chem.* **2010**, *183*, 1272–1277.

(304) Reed, D.; Coffey, G.; Mast, E.; Canfield, N.; Mansurov, J.; Lu, X.; Sprenkle, V. Wetting of Sodium on B″-Al2O3/YSZ Composites for Low Temperature Planar Sodium-Metal Halide Batteries. *J. Power Sources* **2013**, *227*, 94–100.

(305) Morito, H.; Momma, K.; Yamane, H. Crystal Structure Analysis of Na4Si4-XGexby Single Crystal X-Ray Diffraction. *J. Alloys Compd.* **2015**, *623*, 473–479.

(306) Feng, X. J.; Lerch, S.; Biller, H.; Micksch, M.; Schmidt, M.; Baitinger, M.; Strassner, T.; Grin, Y.; Böhme, B. Reactivity and Controlled Redox Reactions of Salt-like Intermetallic Compounds in Imidazolium-Based Ionic Liquids. *ChemistryOpen* **2021**, *10*, 205–215.

(307) Böhme, B.; Guloy, A.; Tang, Z.; Schnelle, W.; Burkhardt, U.; Baitinger, M.; Grin, Y. Oxidation of M4Si4 (M = Na, K) to Clathrates by HCl or H2O. *J. Am. Chem. Soc.* **2007**, *129*, 5348–5349.

(308) Gryko, J.; Gryko, J.; McMillan, P. F.; McMillan, P. F.; Marzke, R. F.; Ramachandran, G. K.; Patton, D.; Deb, S. K.; Sankey, O. F. Low-Density Framework Form of Crystalline Silicon with a Wide Optical Band Gap. *Phys. Rev. B - Condens. Matter Mater. Phys.* **2000**, *62*, R7707–R7710.

(309) Morito, H.; Shimoda, M.; Yamane, H. Single Crystal Growth of Type I Na–Si Clathrate by Using Na–Sn Flux. *J. Cryst. Growth* **2016**, *450*, 164–167.

(310) Morito, H.; Shimoda, M.; Yamane, H.; Fujiwara, K. Crystal Growth Conditions of Types i and II Na-Si Clathrates by Evaporation of Na from a Na-Si-Sn Solution. *Cryst. Growth Des.* **2018**, *18*, 351–355.

(311) Urushiyama, H.; Morito, H.; Yamane, H. Single Crystal Growth and Structure Analysis of Type-I (Na/Sr)-(Ga/Si) Quaternary Clathrates. *RSC Adv.* **2019**, *9*, 14586–14591.

(312) Wang, C.; Xie, H.; Zhang, L.; Gong, Y.; Pastel, G.; Dai, J.; Liu, B.; Wachsman, E. D.; Hu, L. Universal Soldering of Lithium and Sodium Alloys on Various Substrates for Batteries. *Adv. Energy Mater.* **2018**, *8*, 1–8.

(313) Sangster, J.; Bale, C. W. The Na-Sn (Sodium-Tin) System. *J. Phase Equilibria* **1998**, *19*, 76–81.

(314) Gunawardena, G.; Hills, G.; Montenegro, I.; Scharifker, B. Electrochemical Nucleation. Part I. General Considerations. *J. Electroanal. Chem.* **1982**, *138*, 225–239.

(315) Liu, N.; Hu, L.; McDowell, M. T.; Jackson, A.; Cui, Y. Prelithiated Silicon Nanowires as an Anode for Lithium Ion Batteries. *ACS Nano* **2011**, *5*, 6487–6493.

(316) Wang, D.; Chang, Y. L.; Wang, Q.; Cao, J.; Farmer, D. B.; Gordon, R. G.; Dai, H. Surface Chemistry and Electrical Properties of Germanium Nanowires. *J. Am. Chem. Soc.* **2004**, *126*, 11602–11611.

(317) Ruffo, R.; Hong, S. S.; Chan, C. K.; Huggins, R. A.; Cui, Y. Impedance Analysis of Silicon Nanowire Lithium Ion Battery Anodes. *J. Phys. Chem. C* **2009**, *113*, 11390–11398.

(318) Borkiewicz, O. J.; Shyam, B.; Wiaderek, K. M.; Kurtz, C.; Chupas, P. J.; Chapman, K. W. The AMPIX Electrochemical Cell: A Versatile Apparatus for in Situ X-Ray Scattering and Spectroscopic Measurements. *J. Appl. Crystallogr.* **2012**, *45*, 1261–1269.

(319) Osman, H. H.; Bobev, S. Synthesis, Structural Characterization and Chemical Bonding of Sr7Li6Sn12 and Its Quaternary Derivatives with Eu and Alkaline Earth Metal (Mg, Ca, Ba) Substitutions. A Tale of Seven Li-Containing Stannides and Two Complex Crystal Structures. *Eur. J. Inorg. Chem.* **2020**, *2020*, 1979–1988.

(320) Smakula, A.; Kalnajs, J. Precision Determination of Lattice Constants with a Geiger-Counter X-Ray Diffractometer. *Phys. Rev.* **1955**, *99*, 1737.

(321) Menges, E.; Hopf, V.; Schäfer, H.; Weiss, A. Die Kristallstruktur von LiGe — Ein Neuartiger, Dreidimensionaler Verband von Element(IV)-Atomen. *Zeitschrift fur Naturforschung - Section B Journal of Chemical Sciences*. 1969, pp 1351–1352.

(322) Von Schnering, H. G.; Bolle, U.; Curda, J.; Peters, K.; Carrillo-Cabrera, W.; Somer, M.; Schultheiss, M.; Wedig, U. Huckel Arenes with Ten n Electrons: Cyclic Zintl Anions Si- and Gel6 Isosterie to P4- and As4. *Angew. Chemie (International Ed. English)* **1996**, *35*, 984–986.

(323) Zeilinger, M.; Fässler, T. F. Structural and Thermodynamic Similarities of Phases in the Li–Tt (Tt = Si, Ge) Systems: Redetermination of the Lithium-Rich Side of the Li–Ge Phase Diagram and Crystal Structures of Li17Si4.0−xGex for x = 2.3, 3.1, 3.5, and 4 as Well as Li4.1Ge. *J. Chem. Soc. Dalt. Trans.* **2014**, *43*, 14959–14970.

(324) Karayaylali, P.; Tatara, R.; Zhang, Y.; Chan, K.-L.; Yu, Y.; Giordano, L.; Maglia, F.; Jung, R.; Lund, I.; Shao-Horn, Y. Editors' Choice—Coating-Dependent Electrode-Electrolyte Interface for Ni-Rich Positive Electrodes in Li-Ion Batteries. *J. Electrochem. Soc.* **2019**, *166*, A1022–A1030.

(325) Sheldrick, G. M. SHELXT - Integrated Space-Group and Crystal-Structure Determination. *Acta Crystallogr. Sect. A Found. Crystallogr.* **2015**, *71*, 3–8.

(326) Dolomanov, O. V.; Bourhis, L. J.; Gildea, R. J.; Howard, J. A. K.; Puschmann, H. OLEX2: A Complete Structure Solution, Refinement and Analysis Program. *J. Appl. Crystallogr.* **2009**, *42*, 339–341.

(327) Sheldrick, G. M. Crystal Structure Refinement with SHELXL. *Acta Crystallogr. Sect. C Struct. Chem.* **2015**, *71*, 3–8.

(328) Gelato, L. M.; Parthé, E. STRUCTURE TIDY– a Computer Program to Standardize Crystal Structure Data. *J. Appl. Crystallogr.* **1987**, *20*, 139–143.

(329) Allison, M. C.; Avdeev, M.; Schmid, S.; Liu, S.; Söhnel, T.; Ling, C. D. Synthesis, Structure and Geometrically Frustrated Magnetism of the Layered Oxide-Stannide Compounds Fe(Fe3-XMnx)Si2Sn7O16. *Dalt. Trans.* **2016**, *45*, 9689–9694.

(330) Frank, U.; Müller, W.; Schäfer, H. Die Kristallstruktur Der Phase Li7Sn2. *Zeitschrift fur Naturforsch. - Sect. B J. Chem. Sci.* **1975**, *30*, 6–9.

APPENDIX A

SUPPORTING INFORMATION FOR CHAPTER 3.1

A.1. Materials Synthesis

Metals of Ba, Si and Al (commercial grade materials with stated purity 99.9% wt) were weighed in an Ar-filled glove box (controlled O_2 and moisture atmosphere). An extra amount (5%) of Ba was loaded since Ba is more volatile than other elements. The total weight of the starting materials was ca. 600 mg. Then, the materials were quickly transferred to the chamber of a custom-made arc-melter, which was evacuated to ca. 10^{-4} Torr and backfilled with high purity argon. After the initial melting, the formed ingot was taken out and turned over. The melting process was repeated three times to ensure good homogeneity. HG-Aly samples (y = nominal amount of Al) were hand ground using a mortar and pestle. BM-Aly samples were subjected to ball-milling for 40 min using a Spex Mixer/Mill 8000M with a 2.5 mL stainless steel vial and 6.35 mm stainless steel ball.

A.2. X-ray Diffraction (XRD)

Powder XRD (PXRD) data were collected using a Panalytical X'pert Pro diffractometer with CuKα radiation operating at 40 kV/40 mA. The least-squares refinement was performed using the Panalytical HighScore Plus software and the results are shown in Table A.1. For PXRD measurements on cycled electrodes, the films were rinsed several times with propylene carbonate and dried in an Ar-filled glovebox overnight.

Single crystal XRD (SCXRD) was performed on the as-prepared Al0 sample. Suitable single crystals were selected from the crushed arc-melted button. Under an optical microscope, using a scalpel, the crystals were cut to less than ca. 0.1 mm in all dimensions. The preparation was done in a droplet of mineral oil and the selected crystals were scooped by a MiTeGen micro-loop mount. SCXRD data were collected on a Bruker Smart Apex diffractometer at 200 K using graphite-monochromated Mo-Kα radiation (α = 0.71073 Å). The SMART (SMART NT, Version 5.63; Bruker Analytical X-ray Systems Inc.: Madison, WI, USA, 2003) and SAINTplus (SAINT NT, Version 6.45; Bruker Analytical X-ray Systems Inc.: Madison, WI, USA, 2003) programs were used for

the data collection, integration, and the global unit cell refinement from all data. Semi-empirical absorption correction was applied with SADABS (SADABS NT, Version 2.10; Bruker Analytical X-ray Systems Inc.: Madison, WI, USA, 2001). The structures were refined to convergence by full matrix least-square methods on F^2, as implemented in SHELXTL (SHELXTL, Version 6.12; Bruker Analytical X-ray Systems Inc.: Madison, WI, USA, 2001). All sites were refined with anisotropic displacement parameters. Other refined parameters included the scale factor, the occupation factors of each framework site, and the atomic coordinates. The least-squares fit of the total of 18 variables against ca. 350 observed structure factors produced excellent residuals and flat difference Fourier map. For the specimens devoid of Al, the occupancies of all framework sites were checked, but in the last refinement cycles, only the occupation factor of the 6c position was varied; thus, there are 2 fewer refined parameters in the provided crystallographic information files (CIF) from the structural work.

The CIFs have been deposited with the Fachinformationszentrum Karlsruhe, 76344 Eggenstein-Leopoldshafen, Germany (fax: +49-7247-808-666; Email: crysdata@fiz-karlsruhe.de), with a depository number of CSD-434713 for $Ba_8Al_{15.6(1)}Ge_{30.4(1)}$ (referred to as sample Al16 in the text), CSD-434714 for $Ba_8Al_{14.5(1)}Ge_{31.5(1)}$ (referred to as sample Al14 in the text), CSD-434715 for $Ba_8Al_{13.9(1)}Ge_{32.1(1)}$ (referred to as sample Al12 in the text), CSD-434716 for $Ba_8Al_{11.4(1)}Ge_{34.6(1)}$ (referred to as sample Al8 in the text), CSD-434717 for $Ba_8Al_{6.1(1)}Ge_{37.9(1)}\square_2$ (referred to as sample Al4 in the text; the symbol $\square$ denotes a vacancy), and CSD-434718 for $Ba_8Ge_{42.78(4)}\square_{3.22(4)}$ (referred to as sample Al0 in the text).

The Al0 sample after chemical lithiation was also studied by SCXRD. For the chemical lithiation, the powders were pressed between two discs of Li foil, with and without a few drops of liquid Li-ion battery electrolyte (1 M $LiPF_6$ EC:DMC:DEC, 4:2:4 in volume, LBC 3051C, MTI) for 2 days. This chemical lithiation procedure has been verified to be effective for the lithiation of other anode materials, including clathrates [106,315]. We found that most of the lithiated Al0 material did not diffract and hence were amorphous. For the small crystallites that were identified, the results from the

refinements of the Al0 sample after direct contact with Li foil (without liquid electrolyte) are virtually identical with the ones from the as-synthesized Al0 (Table A.1). Unit cell constant was 10.6352(12) Å and the refined formula was $Ba_8Ge_{42.76(4)}\square_{3.24(4)}$. The Al0 sample after direct contact with Li foil and liquid electrolyte was subjected to SCXRD as well; the results from the structural work show no statistically significant difference with the previously gathered data. The unit cell constant was 10.6352(16) Å and the refined formula was $Ba_8Ge_{42.77(6)}\square_{3.23(6)}$. The CIFs from these refinements are available as electronic supporting information, but have not been assigned separate depository numbers.

Table A.1 Cell parameter and phase percentages for Ge clathrate samples according to the powder XRD least-squares refinement.

Sample	a-parameter (Å)	Clathrate %	Ge %
Al0	10.653	99.7	0.3
Al4	10.694	98.5	1.5
Al8	10.778	100	0
Al12	10.801	100	0
Al16	10.835	100	0

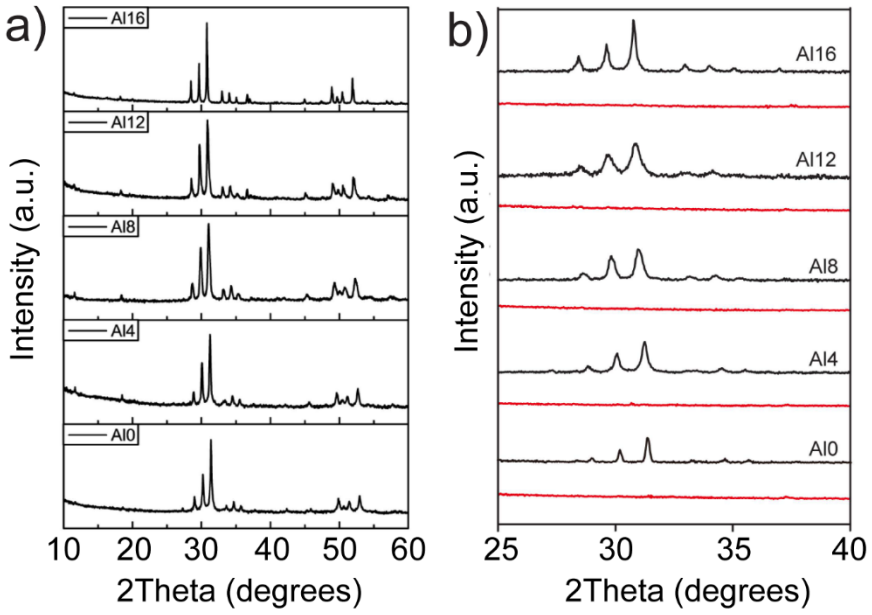

Figure A.1 XRD patterns (a) Ge clathrate powders after 40 minutes of ball-milling, (b) Ge clathrate pristine electrodes (black) and after first lithiation (red).

A.3. X-ray photoelectron spectroscopy (XPS)

XPS was performed using a VG ESCALAB 220i-XL with Al Kα anode (1486.6 eV) operating at 63 W and 12 kV. The X-ray takeoff angle was 45° and the data were acquired from the region about ~400 μm of the surface of the sample. Charge compensation was used. A pass energy of 20 eV was used for high-resolution spectra (energy resolution 0.7 eV). The spectra were calibrated to correct for charging to the hydrocarbon peak at 284.8 eV. Peak fitting was performed using the CasaXPS processing software.

The fitting procedure for the Ge $2p^{3/2}$ peak was done in the following way. First, three peaks were created and the two peaks representing GeO and Ge-Ge had a constraint

to be 1.4 eV and 3 eV lower, respectively, than the GeO_2 peak. These were chosen based on previous literature demonstrating that there is about a 0.75 eV shift for each oxidation state change in Ge[127,316]. These values also matched the spectra of the ball-milled c-Ge powder (BM-Ge) spectra well, as the Ge-Ge peak could be fully resolved clearly in that sample. After the minimization with these constraints, the GeO constraint was lifted and minimized again. The fitting results shown here are after this second step.

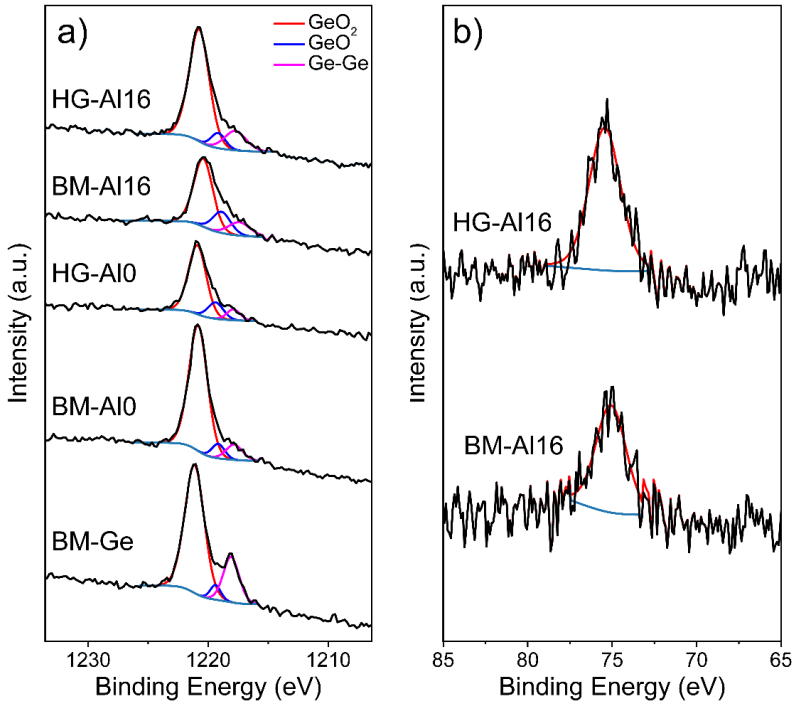

Figure A.2 High resolution XPS of the surface of Ge clathrate electrodes (a) Ge $2p^{3/2}$ spectrum, with ball-milled c-Ge powder (BM-Ge) shown for comparison; (b) Al 2p spectrum.

Table A.2 Ge 2p peak area percentages after the fitting procedure for the Ge clathrates and BM-Ge.

Sample	GeO_2 Area %	GeO Area %	Ge-Ge Area %

HG-Al16	78	7	15
BM-Al16	66	19	15
HG-Al0	75	16	9
BM-Al0	84	7	9
BM-Ge	74	5	21

A.4. Electron microscopy

Scanning electron microscopy (SEM) imaging was performed using an XL 30 ESEM-FEG microscope and a 12 kV electron beam. The electrodes were cut from copper foil and mounted on SEM stubs with carbon tape.

Transmission electron microscopy (TEM) was performed using an aberration correction FEI Titan microscope operated at 300 kV. Powdered samples were dispersed into methanol with ultrasonication for 5 minutes and then dropped onto a copper TEM grid with holey carbon support (Pacific Grid Tech). After all the methanol was evaporated, the grid was loaded onto a single-tilt sample holder and taken into the microscope for examination. The samples were not covered with any conductive coatings. Images and diffraction patterns were recorded using a Gatan UltraScan CCD and Fast Fourier Transforms (FFT) were performed using Gatan Digital Micrograph software.

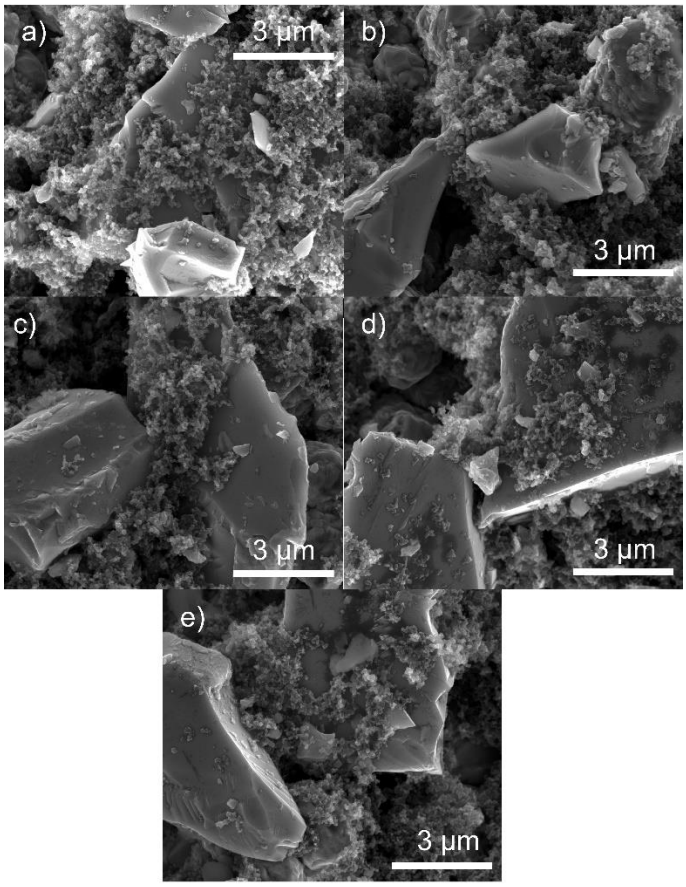

Figure A.3 SEM images of pristine electrodes for the hand ground (a) Al0, (b) Al4, (c) Al8, (d) Al12, and (e) Al16 germanium clathrate samples.

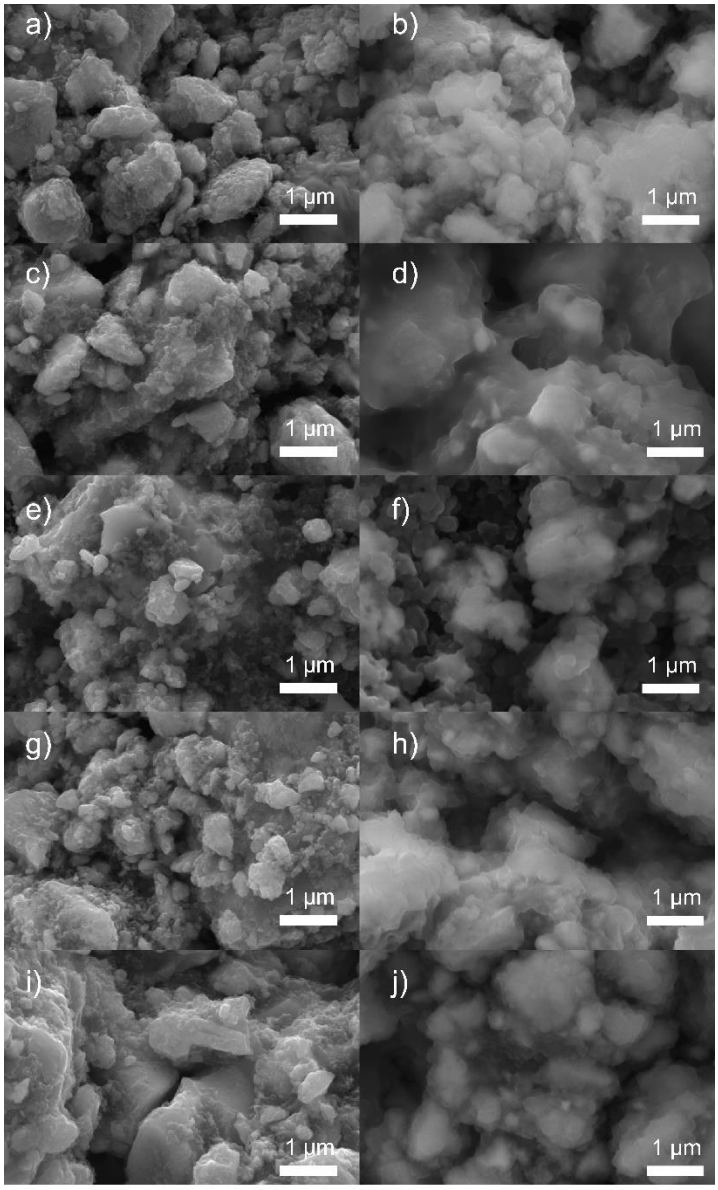

Figure A.4 SEM images pristine (left column) and lithiated (right column) for (a)(b) BM-Al0, (c)(d) BM-Al4, (e)(f) BM-Al8, (g)(h) BM-Al12, (i)(j) BM-Al16.

A.5. Electrochemical characterization

The clathrate powder was prepared into slurries by mixing the clathrate sample with 10 wt% carbon black (TIMCAL Super C45) to serve as conducting additive and 10 wt% polyvinylidene difluoride (PVDF) to serve as binder in N-methyl pyrrolidone (NMP) as solvent. 100 mesh Ge powder (Sigma Aldrich 99.999%) was ball-milled for 40 minutes and prepared in the same fashion as the clathrate powders to use for comparison purposes. The slurries were stirred overnight and coated onto Cu foil current collectors using a Meyer rod, and then heated at 120 ^{o}C to remove the solvent. The clathrate composite electrodes were evaluated in pouch cells with Li metal as the counter electrode, Celgard 2500 as separator, and 1 M $LiPF_6$ (EC:DMC:DEC, 4:2:4 in volume, LBC 3051C, MTI) as electrolyte. Electrochemical testing was performed using a Biologic VMP3 galvanostat/potentiostat. Galvanostatic measurements were performed from 0.01 – 2.5 V vs. Li/Li^+ range using a current density of 25 mA/g. "Charging" is taken to indicate lithiation of the clathrate electrodes, while "discharging" indicates delithiation. Specific capacities were calculated considering only the mass of the clathrates in the composite electrodes.

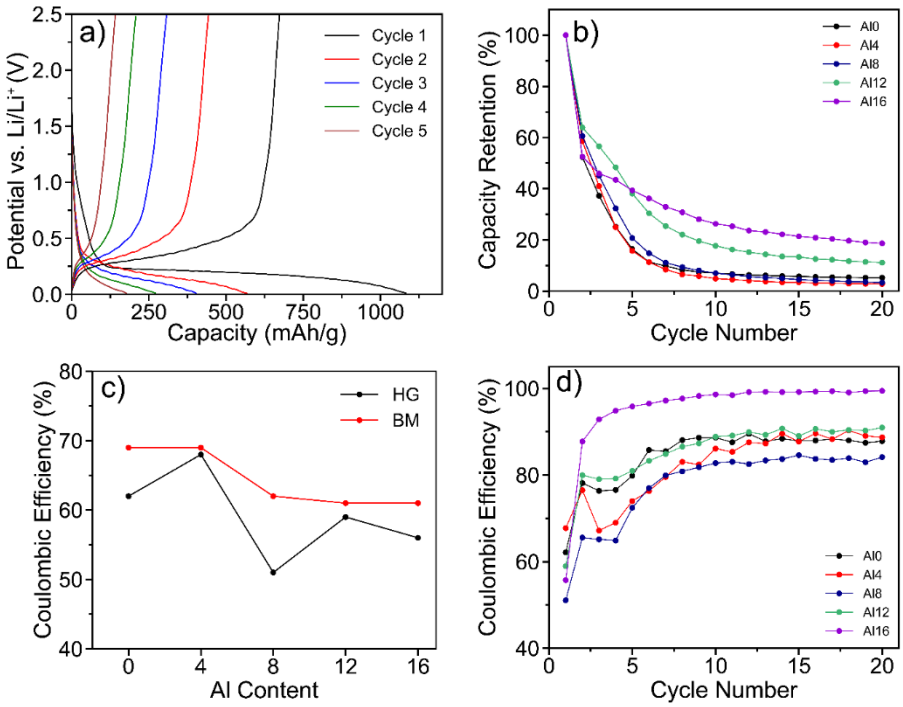

Figure A.5 (a) Galvanostatic cycling (25 mA/g) voltage profiles of the first 5 cycles for HG-Al0 (b) Capacity retention for hand ground Al0-Al16 electrodes, with respect to the initial lithiation capacity (c) Coulombic efficiency of first cycle for hand ground and ball-milled electrodes for different Al content. (d) Coulombic efficiency of hand ground Al0-Al16 electrodes for the first 20 cycles.

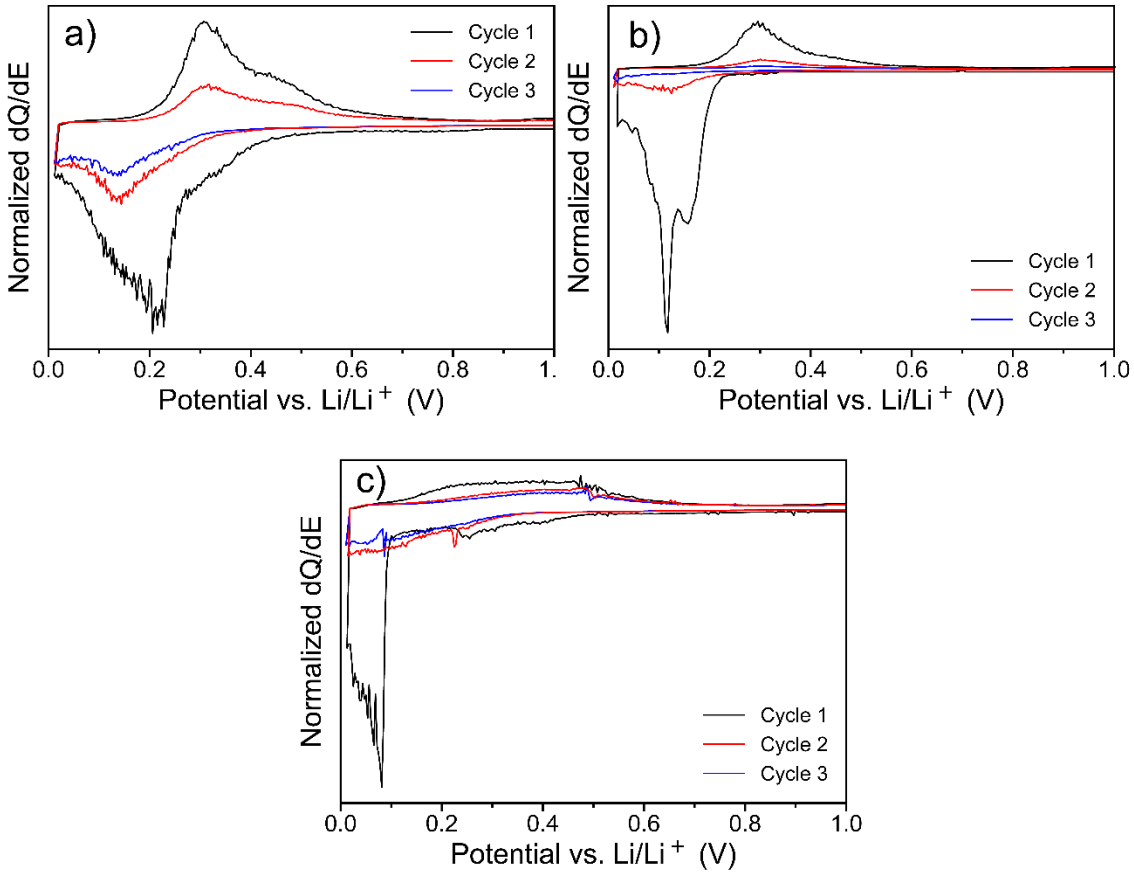

Figure A.6 Differential capacity plots derived from galvanostatic cycling (25 mA/g) for the first 3 cycles of (a) BM-Al0 (b) HG-Al0 and (c) HG-Al16

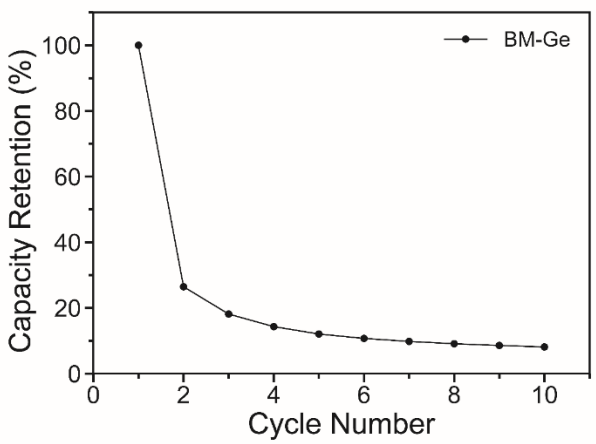

Figure A.7 Capacity retention of BM-Ge electrodes showing that the capacity decay is similar to that in the Ge clathrates. Initial charge capacity is equal to 875 mAh/g.

Table A.3 Theoretical conversion capacities and number of Li per formula unit (f.u.) assuming a final product of $Li_{4.4}Ge$. The values are compared with the experimentally observed lithiation (top) and delithiation (bottom) values and Coulombic efficiency (CE%). The number of Li per formula unit for the experimental results are calculated assuming each electron corresponds to a Li^+ inserted, with no charge loss to side reactions (e.g. SEI formation).

y in $Ba_8Al_yGe_{46-y}$	Theoretical		Experimental					
			Hand Ground Samples			Ball-Milled Samples		
	Capacity (mAh/g)	# of Li per f.u.	Capacity (mAh/g)	# of Li per f.u.	CE %	Capacity (mAh/g)	# of Li per f.u.	CE%
0	1201	189	1098	173	62	1248	197	69
			683	108		858	133	
4	1163	184	896	142	68	1087	173	69
			607	96		751	119	
8	1100	167	883	134	51	879	134	62
			451	68		548	83	
12	1030	149	558	81	59	702	102	61
			329	48		431	63	
16	954	132	518	72	56	651	90	61
			289	40		397	55	

A.6. Electrochemical Impedance Spectroscopy

Electrochemical impedance spectroscopy (EIS) measurements were performed on the HG-Al0, BM-Al0, HG-Al16, and BM-Al16 electrodes in pouch cells with Li metal as the counter electrode at different states of charge (SOC) and depths of discharge (DOD). The explored frequency range was from 1 MHz to 1 mHz under an AC stimulus with 10 mV of amplitude. Galvanostatic pulses (25 mA/g) were used to vary the SOC during lithiation and DOD during delithiation. Each EIS spectrum was collected at the end of the corresponding galvanostatic step after a long relaxation period (15 h) at the open circuit voltage condition so that the electrode was probed at close to equilibrium conditions[317]. The voltage vs. time plots obtained for each electrode using this protocol are shown in Figure A.8. The obtained Nyquist plots are shown in Figure A.9, Figure A.10 and Figure A.11. Bode plots for the lithiation steps are displayed in Figure 3.1.7.

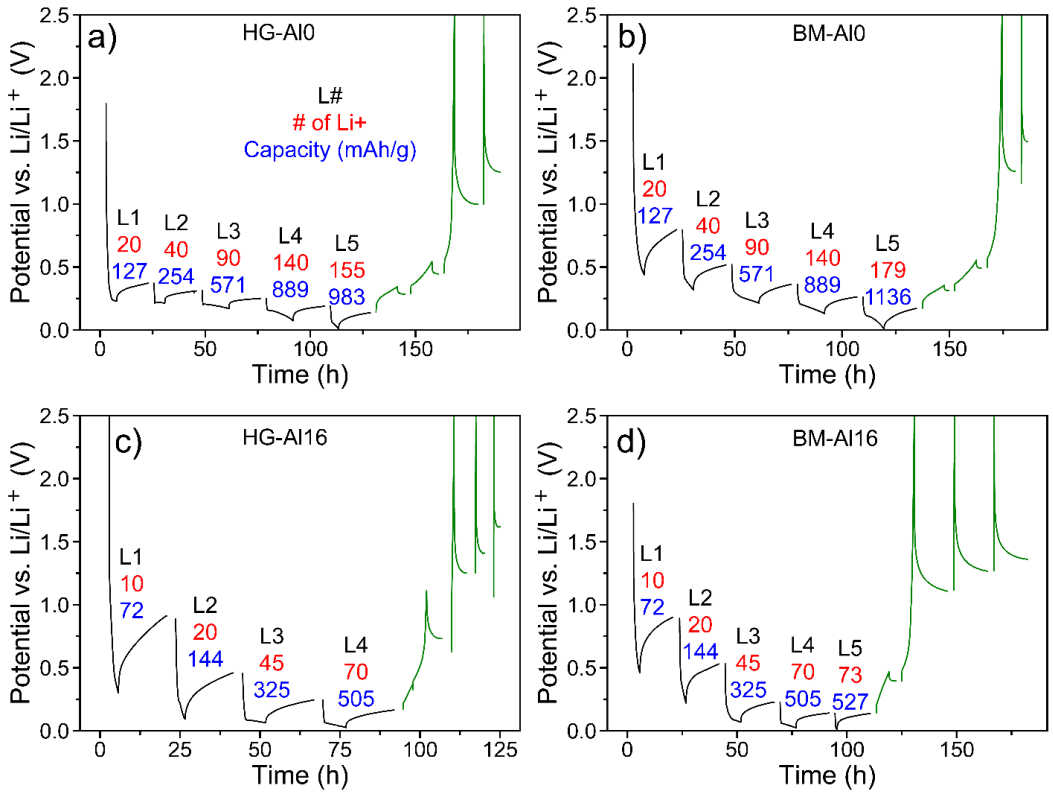

Figure A.8 Voltage profile of galvanostatic testing procedures applied to sample (a) HG-Al0, (b) BM-Al0, (c) HG-Al16, and (d) BM-Al16 for the EIS measurements (black = lithiation, green = delithiation). The total capacity inserted into the electrode after each lithiation step and equivalent # of Li per f.u. are indicated below each step (L1 = first lithiation step, L2 = second lithiation step, etc.).

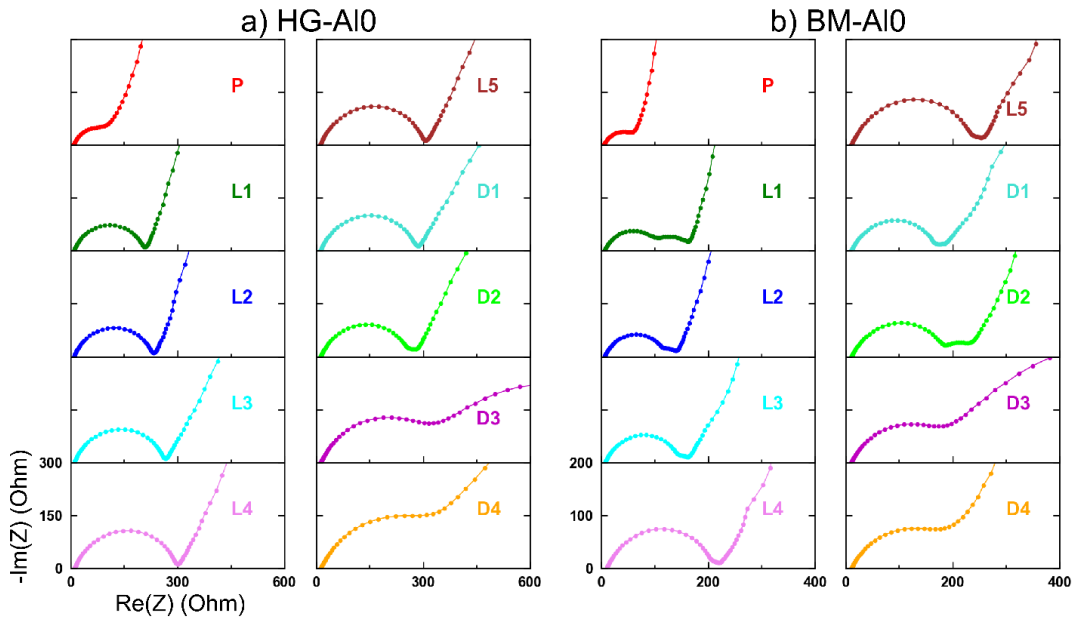

Figure A.9 Nyquist plots for (a) HG-Al0 and (b) BM-Al0. (P = pristine, L1 = first lithiation step, L2 = second lithiation, D1 = first delithiation etc. as described in Figure A.8).

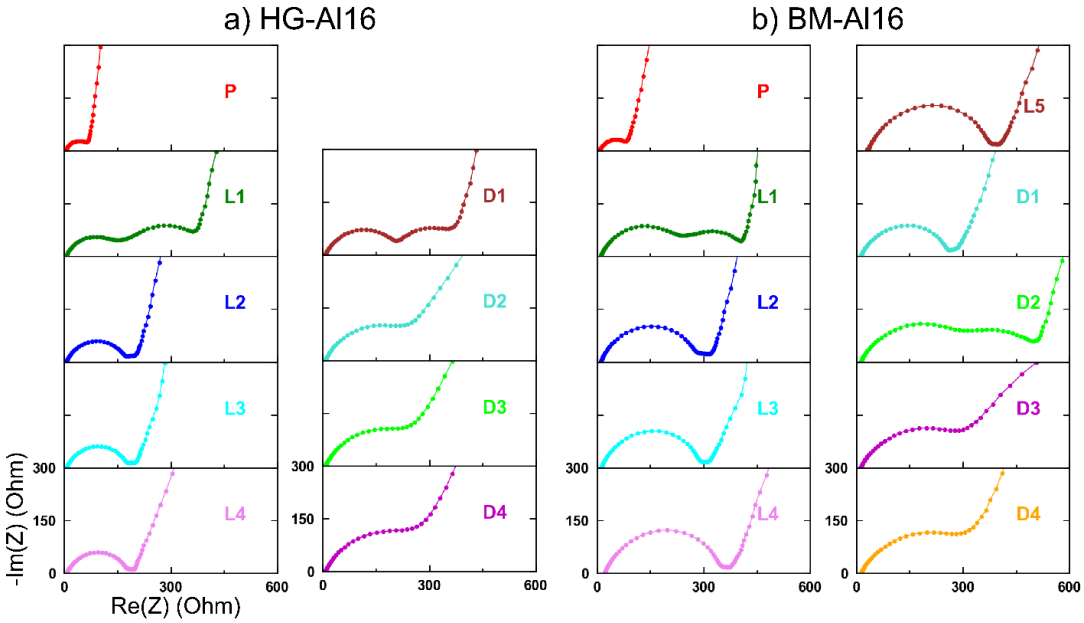

Figure A.10 Nyquist plots of (a) HG-Al16 and (b) BM-Al16. (P = pristine, L1 = first lithiation step, L2 = second lithiation, D1 = first delithiation etc. as described in Figure A.8).

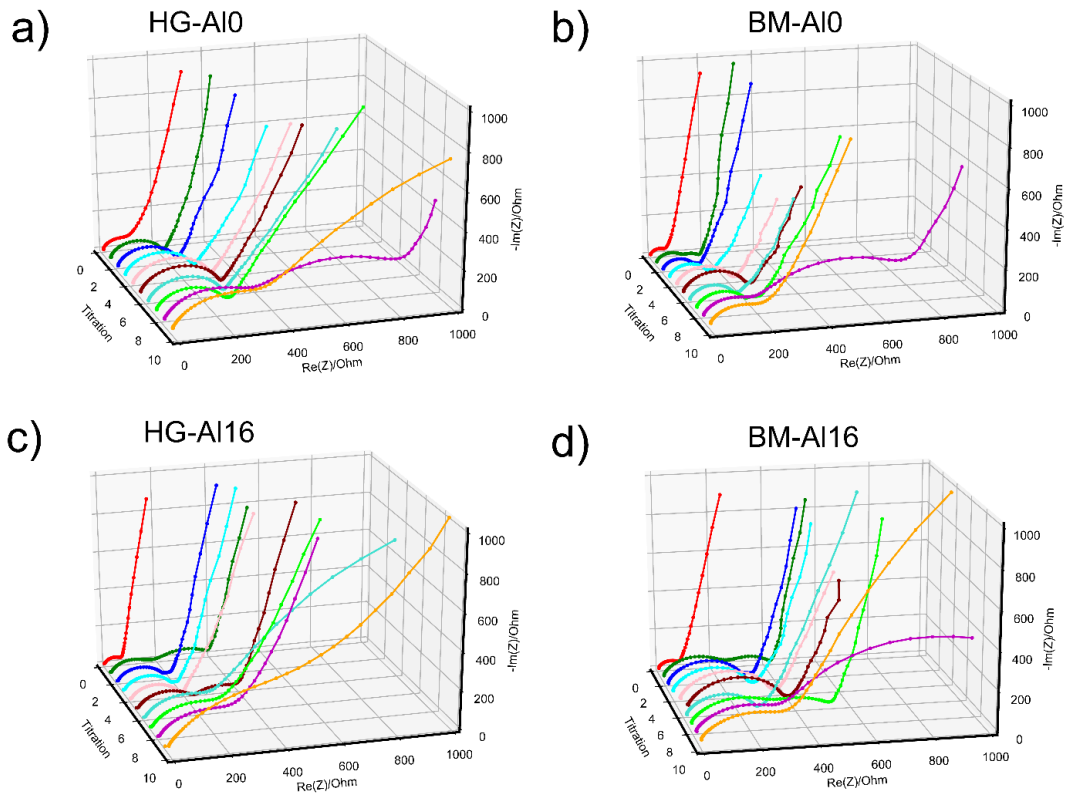

Figure A.11 Expanded view of Nyquist plots for (a) HG-Al0, (b) BM-Al0, (c) HG-Al16, and (d) BM-Al16. Titrations 0, 1, 2, 3, 4 correspond to P, L1 ,L2 ,L3 etc, as described in Figure A.8 using the same color coding as in Figure A.9 and Figure A.10.

A.7. Computational Methods

The first-principles density-functional theory (DFT) calculations were performed in a similar manner to our previous work[55]. The calculations were performed using the VASP code[77,78]. The PBE functional[73] and projector augmented wave (PAW) potentials with a plane wave basis set. In the PAW potentials, the Ge 4p and 3d, Ba 5s, 5p, and 6s, Al 3s and 3p, and Li 1s and 2s electrons were treated as valence electrons. The energy cutoff for the plane wave basis set was 400 eV and the reciprocal space was sampled with Monkhorst pack meshes 3 x 3 x 3 centered at gamma. The convergence criteria for energy and force were set to be 0.01 and 0.1 meV, respectively. The geometric optimization was performed in two steps. First the cell was optimized without the constraint of cubic symmetry and then that optimized volume was used in a second step where only ionic relaxation was allowed using the optimized volume of the previous step under cubic symmetry constraint. The lattice parameters of the 2nd step are reported. The formation energies, Gibbs free energy change, and average lithiation voltage were calculated as described previously[55]. Gibbs free energy changes and voltages were calculated with the unlithiated compound and bcc Li as the reactants, except for $Ba_8Ge_{43}Li_3Li_1$ (Li in three 6c sites and one 6b site), in which case $Ba_8Ge_{43}Li_3$ was used as the reactant. The elemental energies used were -4.621 eV for diamond cubic Ge, -1.904 eV for bcc Li, -1.922 eV for bcc Ba, and -3.746 eV for fcc Al.

The climbing image nudged elastic band (NEB) method was used to calculate the Li diffusion barriers[85] from one 6c vacancy site to another in Ba_8Ge_{43}. All NEB calculations were calculated with the same conditions as described above. Several intermediate images were used between the starting and end points and the linear interpolation of the initial and final structures was used as the initial band. The images were converged until the force on each image was below 0.03 eV/Å.

For Path 2, seven intermediate images were adopted between the starting and end points and the linear interpolation of the start and end structures was performed to generate the initial band. For Path 1, the complete NEB pathway was formed in two separate NEB calculations. The first step was a linear interpolation of a Li position in the vacancy and a Li position off a pentagon adjacent to another Ge_{24} cage. The second step

was a linear interpolation of two Li positions on each side of this pentagon, where the Li would pass through the pentagon to reach the other Ge_{24} cage. Finishing the path to the vacancy is symmetrical to the first step that was described so that these two steps comprise the full vacancy to vacancy path. The images were converged until the force on each image was below 0.03 eV/Å.

All crystal model figures were generated with Diamond 3.2.

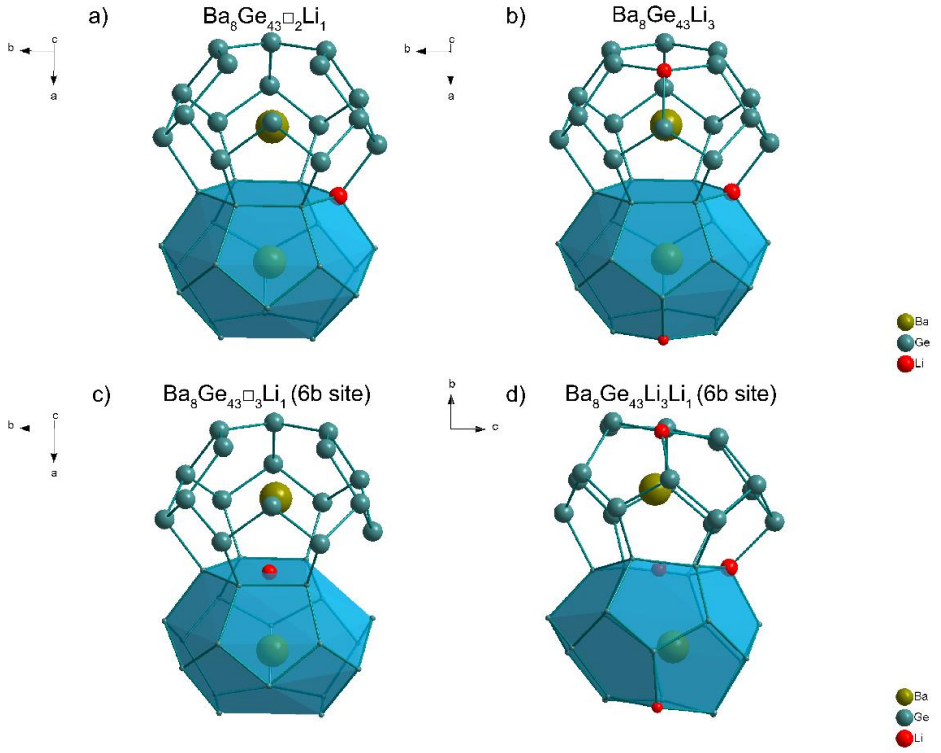

Figure A.12 Crystal model schematics showing two Ge_{24} cages from the lithiated compounds shown in Table 3.1.2 (a) $Ba_8Ge_{43}\square_2Li_1$, (b) $Ba_8Ge_{43}Li_3$, (c) $Ba_8Ge_{43}\square_3Li_1$, and (d) $Ba_8Ge_{43}Li_3Li_1$.

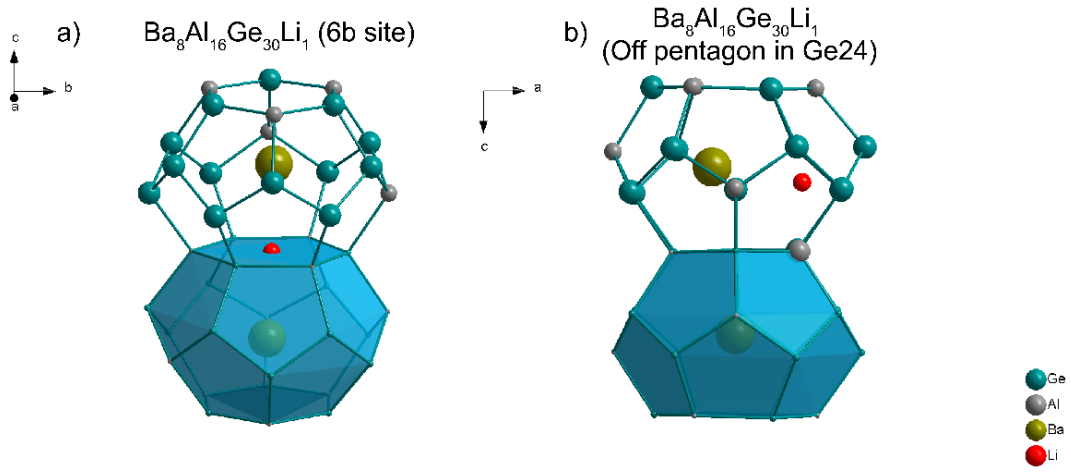

Figure A.13 Crystal model schematics showing two Ge_{24} cages from the lithiated compounds shown in Table 3.1.2 (a) $Ba_8Al_{16}Ge_{30}Li_1$ (6b) and (b) $Ba_8Al_{16}Ge_{30}Li_1$ (Off pentagon in Ge_{24})

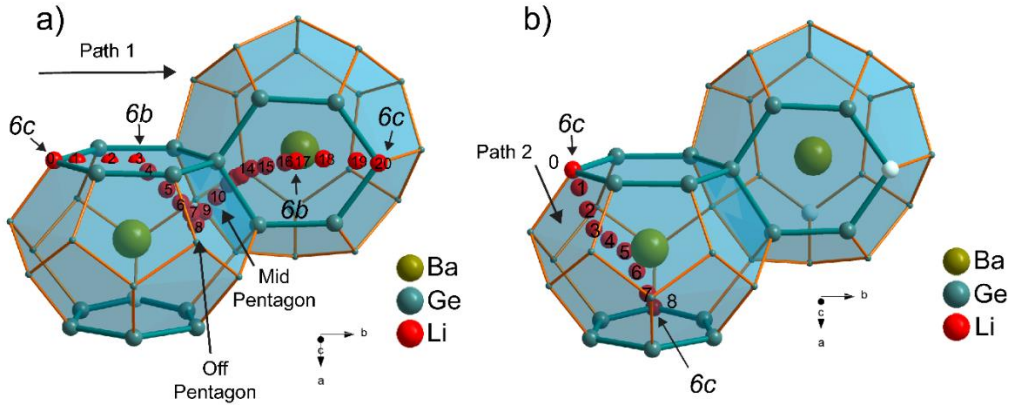

Figure A.14 Li diffusion (a) Path 1 and (b) Path 2, with each image labelled according to the reaction coordinate.White atoms indicate unfilled vacancies.

APPENDIX B

SUPPORTING INFORMATION FOR CHAPTER 3.2

B.1. List of Tables

Table B.1 Calculated shortest Li-Tt distances and lattice parameters for the Tt_{46} structures presented in Figure 3.2.2 after relaxation with Li in the four positions.

Clathrate	Position	Description	Li-Tt Distance (Å)	Lattice Parameter (Å)
Si_{46}	1	Si_{24} Cage Center	3.43	10.224
	2	Si_{20} Cage Center	3.25	10.226
	3	Off Hex	2.81	10.226
	4	Off Pent	2.92	10.227
Ge_{46}	1	Ge_{24} Cage Center	3.60	10.742
	2	Ge_{20} Cage Center	3.41	10.751
	3	Off Hex	2.90	10.758
	4	Off Pent	2.81	10.757
Sn_{46}	1	Sn_{24} Cage Center	4.17	12.411
	2	Sn_{20} Cage Center	3.93	12.405
	3	Off Hex	2.90	12.426
	4	Off Pent	2.93	12.417

Table B.2 Calculated Li-Tt bond lengths for the initial and transition states, and the energy of the highest energy image from NEB results in Figure 3.2.3a-b. These bond lengths for $LiSi_{46}$ are illustrated in the crystal structures in Figure B.3b.

Face	Clathrate Composition	Li-Tt Bond Length (Å)		Energy (eV)
		Initial State	Transition State	
Hexagonal	Si	2.814	2.415	0.35
	Ge	2.900	2.540	0.09
Pentagonal	Si	3.029	2.203	2.05
	Ge	2.900	2.306	1.28
	Sn	2.930	2.645	0.54

Table B.3 Calculated shortest Na-Tt distances and lattice parameters for the Tt_{46} structures presented in Figure 3.2.6 after relaxation with Na in the four positions.

Clathrate	Position	Description	Na-Tt Distance (Å)	Lattice Parameter (Å)
Si_{46}	1	Si_{24} Cage Center	3.44	10.228
	2	Si_{20} Cage Center	3.26	10.231
	3	Off Hex	3.44	10.228
	4	Off Pent	3.44	10.228
Ge_{46}	1	Ge_{24} Cage Center	3.65	10.748
	2	Ge_{20} Cage Center	3.44	10.762
	3	Off Hex	3.59	10.748
	4	Off Pent	3.63	10.746
Sn_{46}	1	Sn_{24} Cage Center	4.16	12.403
	2	Sn_{20} Cage Center	3.94	12.414
	3	Off Hex	4.01	12.405
	4	Off Pent	3.50	12.417

Table B.4 Calculated Na-Tt bond lengths for the initial and transition states, and the energy of the highest energy image, from the NEB results in Figure 3.2.7a-b. The bond lengths for $NaGe_{46}$ are illustrated in the crystal structures in Figure B.3a.

Face	Clathrate Composition	Na-Tt Bond Length (Å)		Energy (eV)
		Initial State	Transition State	
Hexagonal	Si	3.440	2.521	2.42
	Ge	3.650	2.632	1.48
	Sn	3.600	2.983	0.45
Pentagonal	Sn	3.605	2.732	2.22

B.2. List of Figures

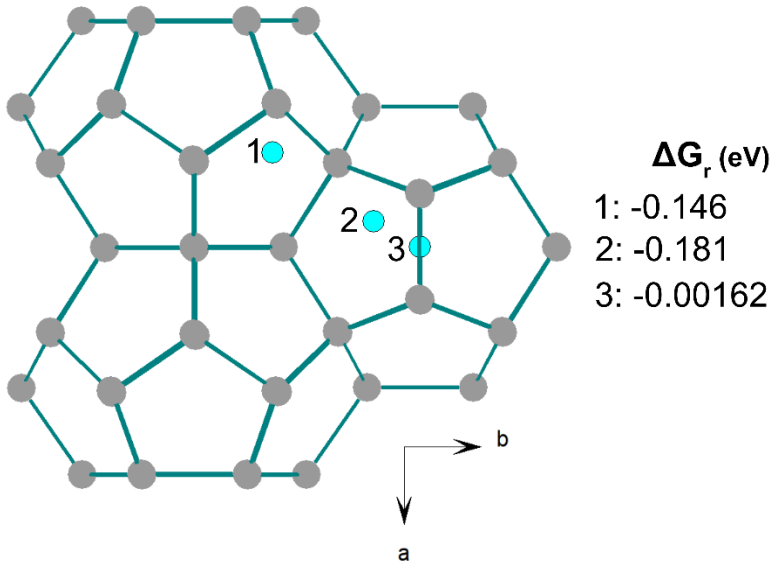

Figure B.1 Crystal model schematic of Sn_{46} (Sn = grey, Li = cyan) and Gibbs free energy change of reaction (ΔG_r) showing Off-Pent Li positions 1 and 2 in comparison to the centered position 3 in Sn_{20}. It is more favorable for Li to occupy the off-center position 2 in the Sn_{20} cage as demonstrated by the lower energy for ΔG_r.

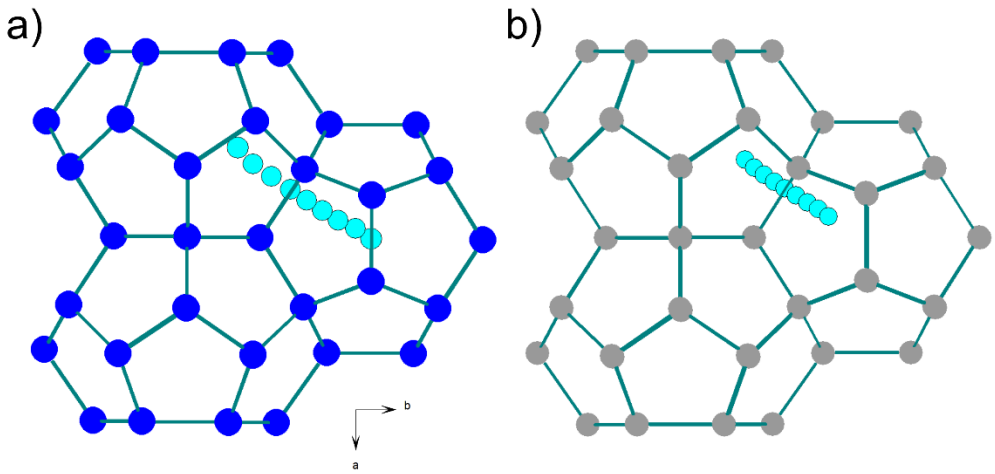

Figure B.2 Crystal model schematic of NEB pathway for pentagonal migration of Li (Figure 3.2.3b) in a) Ge_{46} and b) Sn_{46}. Li = cyan, Ge = blue, Sn = grey.

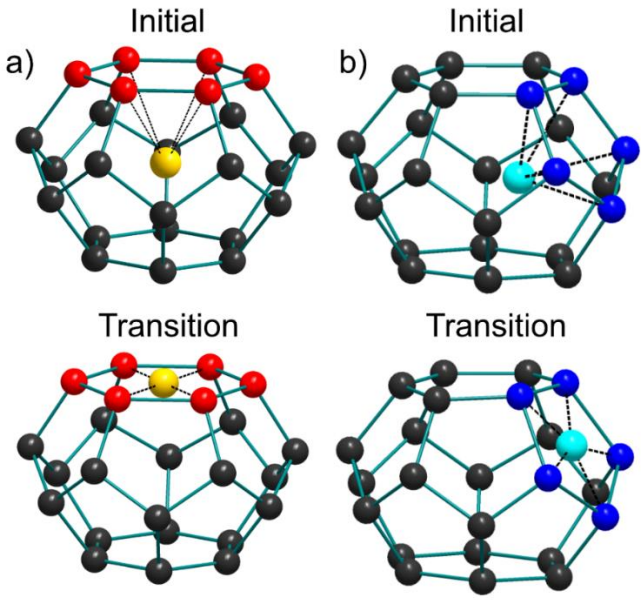

Figure B.3 Crystal structures of a single Tt_{24} cage showing examples of the initial and transition states for Na (yellow atom) or Li (cyan atom) during migration through a) a hexagonal (red) face (shown for $NaGe_{46}$) and b) pentagonal (blue) face (shown for $LiSi_{46}$). The dashed lines indicate the bond lengths that are reported in Table B.2 and Table B.4. The black atoms represent other Tt atoms in the framework.

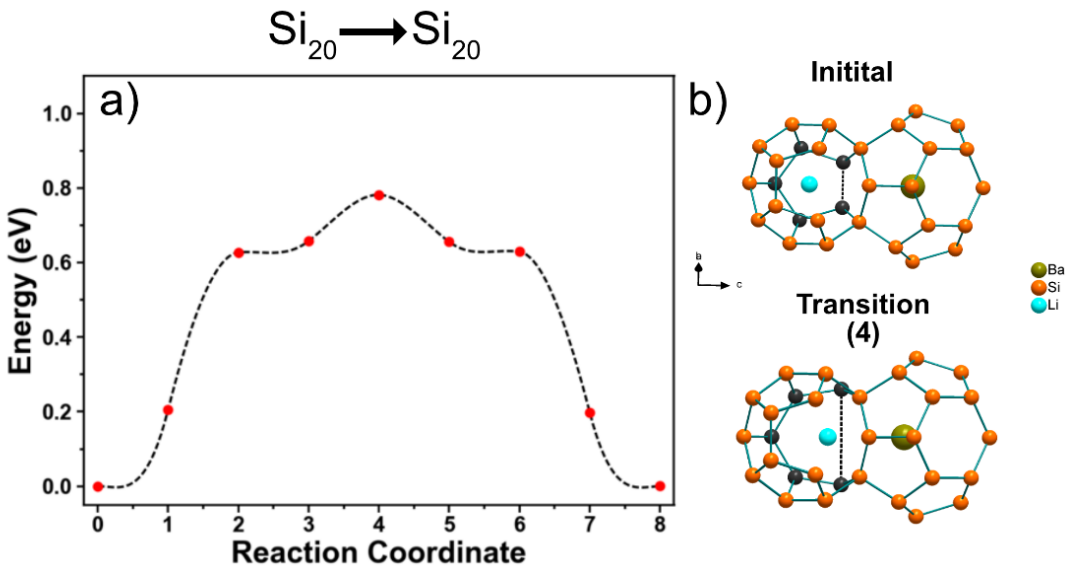

Figure B.4 NEB minimum energy path for $LiBa_8Si_{136}$ (type II Si clathrate) for Li migration between two Si_{20} cages. Instead of going through the center of the Si pentagon, Li breaks a Si-Si bond. b) Crystal structures for the initial and transition states of the Li migration pathway. The black atoms indicate Si atoms that comprise the pentagon that share the broken bond. The calculation was performed using the conventional Ba_8Si_{136} unit cell and a 2 × 2 × 2 K-point grid.

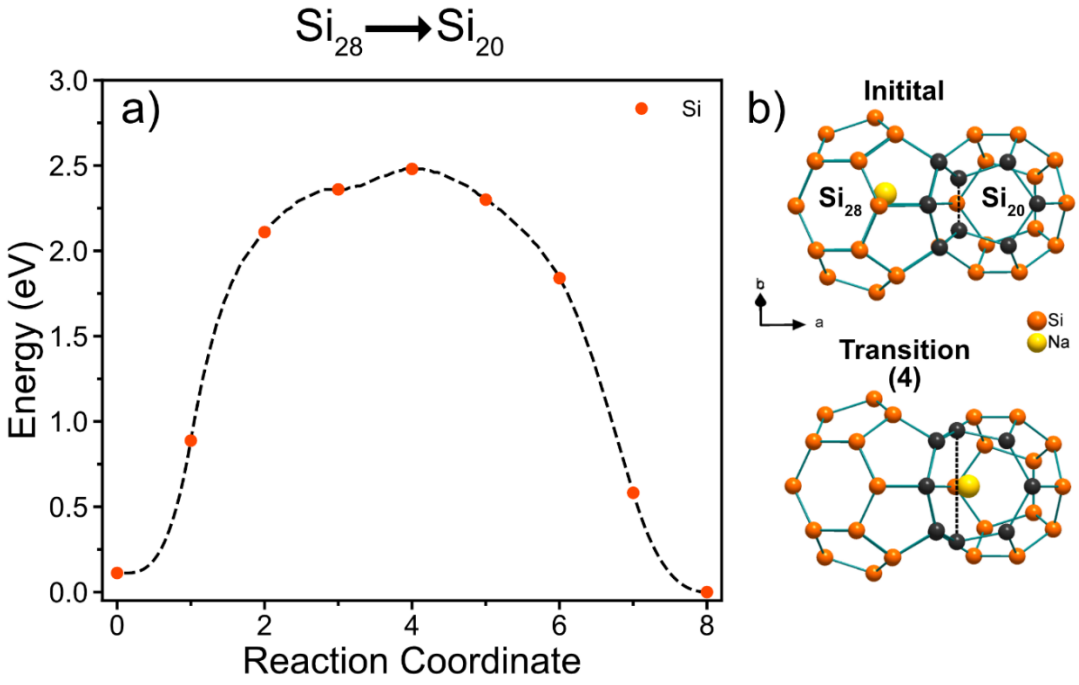

Figure B.5 a) NEB minimum energy path for the Na migration in $NaSi_{136}$ (type II Si clathrate) between the Si_{28} and Si_{20} cages. Instead of going through the center of the Si pentagon, the Na breaks a Si-Si bond. b) Crystal models of the initial and transition states of the migration pathway for Na. The black atoms indicate Si atoms that comprise the pentagons which share the broken bond. The calculation was performed using the conventional Si_{136} cubic unit cell and a 2 × 2 × 2 K-point grid mesh.

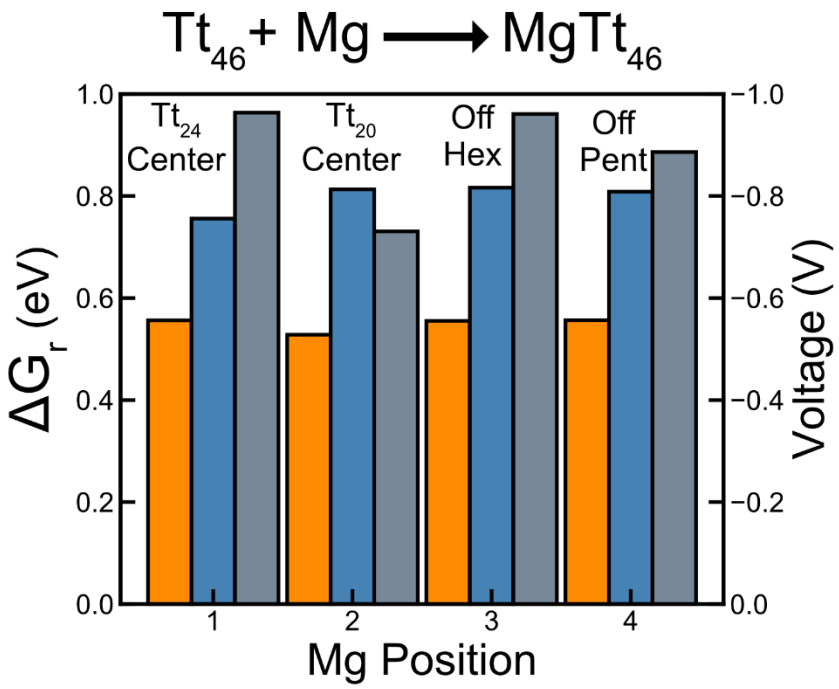

Figure B.6 Gibbs free energy change of reaction (ΔG_r) and voltage vs. Mg/Mg^+ for the reaction Tt_{46} + Mg → $MgTt_{46}$, where Tt = Si, Ge, Sn, for each of the 4 Mg positions. An energy of -1.594 eV/atom from the bulk hexagonal phase of Mg was used for the elemental energy of Mg metal.

APPENDIX C

SUPPORTING INFORMATION FOR CHAPTER 3.3

C.1. Experimental and Computational Procedures

C.1.1 Synthesis of type II silicon clathrates

The synthesis of the type II Si clathrate was carried out by the thermal decomposition of Na_4Si_4 under vacuum. The Na_4Si_4 precursor was synthesized by combining Na and Si in 1.2 : 1 molar ratio in a Nb tube in an argon-filled glove box. The Nb tube was taken out of the glovebox and arc-welded shut under an argon atmosphere. The Nb tube was then sealed in a stainless-steel reactor in an argon-filled glovebox with copper gaskets. The stainless-steel reactor was taken out of the argon glove box and heated in a tube furnace. The Na-Si mixture was heated at 650 °C for 48 hours and then cooled down over 4 hours to room temperature. The Nb tube was opened in the glovebox and the large crystals were hand ground to a fine black powder with a mortar and pestle. Powder XRD of the Na_4Si_4 confirmed the phase purity of the precursor.

For the type II clathrate synthesis, a stainless-steel tube reactor was used to carry out the thermal decomposition of Na_4Si_4 under vacuum (Figure C.1). The stainless-steel tube had 2.75-inch conflat flanges welded to the ends which allowed the tube to be sealed with copper gaskets. One side of the stainless-steel tube had a water cooled finger which provides a cold surface for Na condensation during the thermal decomposition[155]. The other side of the tube was connected to a gate valve which was connected to a turbomolecular pump. The type II clathrates were synthesized by loading 400-500 mg of the hand ground Na_4Si_4 powder into a Ta boat and placing it in the center of the stainless-steel tube inside an argon-filled glovebox. The gate valve was sealed, and the reactor was taken out of the glovebox to the tube furnace and connected to the turbomolecular pump.

. The water-cooled finger was connected to a water chiller and water was circulated through the finger at a temperature of 5°C. Prior to heating, both the water cooling and dynamic vacuum were operational. To synthesize $Na_{0.9}Si_{136}$ (Na1), Na_4Si_4 was heated to 370 °C in 3.5 hours and held at 370 °C for 48 hours. Then, the temperature was increased to 425 °C in 30 minutes and held for an additional 72 hours and then cooled to room temperature. The sample with a composition of $Na_{10.7}Si_{136}$ was heated to 370°C in 3.5 hours, held for 30 hours, and then cooled to room temperature. After the reactions, the stainless-steel reactor was taken back into the argon-filled glovebox and opened to obtain the reaction products.

To remove any residual Na_4Si_4, the powder was taken out of the glovebox and transferred to a fume hood, where ~10 mL ethanol was introduced rapidly to the powder from a wash bottle. Rapid bubbling would indicate the reaction of Na_4Si_4 with ethanol, since silicon clathrates are stable in air and water[155]. *Note: Extreme care must be taken and appropriate personal protective equipment must be used when working with Na_4Si_4 in ambient conditions due to its high reactivity to both air and water. After 5 minutes of reaction with the ethanol, the powder was then immersed in an ultrasonic bath to break up agglomerates. After the bubbling decreased in intensity, de-ionized water (~10 mL) was introduced to the powder and the resulting suspension was sonicated for additional time. *Caution: Do not add water directly to the powder containing Na_4Si_4 as it could lead to a fire. After all the bubbling had completed, the powder was recovered using vacuum filtration and then dried. The powder was then used for electrochemical experiments without any further processing.

C.1.2. Electrochemical measurements

The obtained clathrate powder was prepared into slurries by mixing the clathrate sample with 10 wt% carbon black (to serve as conducting additive) and 10 wt% polyvinylidene difluoride (PVDF) (to serve as binder) in N-methyl pyrrolidone (NMP) as solvent. The slurries were stirred overnight and coated onto Cu foil current collectors using a Meyer rod, and then heated at 120 ^{o}C to remove the solvent. The clathrate composite electrodes were evaluated in pouch cells with Li metal as the counter electrode, Celgard 2500 as separator, and 1 M $LiPF_6$ in EC/DMC/DEC (4:3:3 v/v) with VC additive (LBC3015B, MTI) as electrolyte. For long term cycling experiments of Na1 (Figure 3.3.9), CR2032 coin cells were assembled using Li metal as a counter electrode. For the cycling experiments, an electrolyte of 1 M $LiPF_6$ (Sigma Aldrich) in fluoroethylene carbonate and diethyl carbonate electrolyte (Sigma Aldrich) (1: 1 by vol) was used, which showed better cycling performance than the EC/DMC/DEC electrolyte. Electrochemical testing was performed using a Biologic VMP3 galvanostat/potentiostat. Galvanostatic measurements were performed at 10 – 25 mA/g from 0.01 – 2.5 V vs. Li/Li^+. To provide enough lithiated powder for synchrotron characterization, samples from 2–3 cells were prepared and electrochemically lithiated in the same manner were combined.

C.1.3. Sample preparation for synchrotron measurements

After the electrochemical lithiation was complete, the pouch cell was taken into the argon-filled glovebox and opened. The electrode was then immersed in 10 mL of dimethyl carbonate for 30 seconds to wash off any excess battery electrolyte. After the

electrode was dry, the lithiated powder was scraped off the copper current collector using a knife. The extracted powder was then crushed in a mortar and pestle to break up any agglomeration. The powder was sealed in a 2 mL centrifuge tube and then sealed under argon in a polyfoil bag before shipping to the synchrotron facility.

C.1.4. Powder X-ray diffraction (XRD)

High-resolution synchrotron powder diffraction data were collected using beamline 11-BM at the Advanced Photon Source (APS), Argonne National Laboratory, using wavelengths of 0.41284 and 0.412781 Å for the unlithiated samples and lithiated samples, respectively. Discrete detectors covering an angular range from $-6 < 2\theta < 16^{o}$ were scanned over a 34º range in 2θ, with data points collected every 0.001º 2θ and scan speed of 0.01º/s. Samples were placed in Kapton capillaries and sealed with wax. Additional synchrotron XRD was performed at the P02.1 Powder Diffraction and Total Scattering Beamline at PETRA III at the Deutsches Elektronen-Synchrotron (DESY) with 60 keV X-rays at a wavelength of 0.20733 Å. A Perkin Elmer XRD1621 was used as the X-ray detector. The lithiated samples were loaded into 0.8 mm borosilicate capillaries in an argon-filled glovebox and sealed with wax. Laboratory powder XRD data were collected using a Panalytical X'pert Pro diffractometer with CuKα radiation operating at 40 kV/40 mA.

Rietveld refinement was performed with Jana2006[64] taking the initial type II Si clathrate coordinates from Beekman et al[186] The peak shapes were described by the pseudo-Voigt function and the background was modeled with Legendre polynomials. To avoid correlations with the occupancies, the isotropic atomic displacement parameters for

all Na and Li atoms were fixed to ten times the average equivalent isotropic displacement parameter for the Si sites, based on the values reported for other type II clathrates[186]. Changing the ratio $\langle U_{eq}(Si)\rangle$/Uiso(Na/Li) in the range 1–10 had a negligible effect on the refined occupancies.

C.1.5. Electron microscopy

Scanning electron microscopy (SEM) imaging was performed using a Nova 200 Nanolab microscope and a 10 kV electron beam. The electrodes were cut from copper foil and mounted on SEM stubs with carbon tape. Transmission electron microscopy (TEM) was performed using an aberration correction FEI Titan operated at 300 kV. Powdered samples were dispersed into methanol with ultrasonication for 5 minutes and then dropped onto a copper TEM grid with holey carbon support (Pacific Grid Tech). After all the methanol was evaporated, the grid was loaded onto a single-tilt sample holder and taken into the microscope for examination. The samples were not covered with any conductive coatings. Images and diffraction patterns were recorded using a Gatan UltraScan CCD and Fast Fourier Transforms (FFT) were performed using Gatan Digital Micrograph software.

C.1.6. Density-functional theory (DFT) calculations

The first-principles DFT calculations were performed to explore Li insertion and migration in type II Si clathrate using a similar manner as in our previous work[55,152,179]. The calculations were carried out using the VASP code[77,78], the PBE functional[73], and projector augmented wave (PAW) potentials with a plane wave basis set[78]. In the PAW potentials, the Si 3s and 3p and Li 1s and 2s electrons were treated as valence electrons.

The kinetic energy cutoff for the plane wave basis set was chosen to be 400 eV and the reciprocal space was sampled with the Monkhorst pack meshes 3 × 3 × 3 centered at Γ. The cubic Si_{136} unit cell ($Fd\bar{3}m$ space group)[186] was used in all calculations. The convergence criteria for the electronic and ionic relaxations were set to be 0.01 and 0.1 meV, respectively. These criteria resulted in relaxed structures with residual forces below 0.03 eV/Å. The geometric optimization was performed in two steps. First, the unit cell volume was optimized without the constraint of the cubic symmetry. Then the relaxed lattice constant, taken from the relaxed volume, was used in a second step where only ionic relaxation was allowed under the cubic symmetry constraint. The crystal structures with the ionic positions of the second step are reported.

The Gibbs free energy change of reaction (ΔG_r) and the average voltage were calculated as described previously[55,152,179]. The formulas used for calculating the Gibbs free energy change and average voltage for insertion of Li in Si_{136}, for example, are shown in equation (1) and (2), respectively:

$$\Delta G_r = E(Li_xSi_{136}) - E\left(Li_ySi_{136}\right) - (x-y)E(Li) \qquad (1)$$

$$V(x) = -\frac{\Delta G_r}{(x-y)}, x, y = \#\text{ of Li} \qquad (2)$$

where $E(Li_xSi_{136})$ and $E\left(Li_ySi_{136}\right)$ are the total free energies for the clathrate systems with different amounts of Li atoms, and $E(Li)$ is the energy per atom in Li metal. The calculated values for $E(Li)$ is -1.904 eV/atom. A negative ΔG_r (i.e. positive voltage) represents a spontaneous reaction relative to Li metal, suggesting the feasibility of

lithiation in a half cell with Li metal as the counter electrode. All crystal structure figures were created with Diamond 4.5.3.

The climbing image nudged elastic band (NEB) method was used to calculate the Li migration barriers[85]. For the NEB calculations Monkhorst pack meshes 2 × 2 × 2 centered at Γ were used. All NEB calculations used a linear interpolation as the starting band with 7 intermediate images between the beginning and ending images. The images were converged until the force on each image was below 0.03 eV/Å.

C.2. List of Tables

Table C.1 Atomic coordinates, occupancies, and atomic displacement parameters for $Na_{0.9(1)}Si_{136}$ (Na1) corresponding to the Rietveld refinement in Figure 3.3.2a.

$Na_{0.9(1)}Si_{136}$		Lattice Parameter:	14.6460(1) Å			
Atom	Site	x/a	y/b	z/c	Occ.	$U_{iso/eq}$ (Å^2)[a]
Na1	8b	3/8	3/8	3/8	0.044(9)	0.0556
Na2	32e	0.023(7)	x	x	0.018(4)	0.0556
Si1	8a	1/8	1/8	1/8	1	0.0041(4)
Si2	32e	0.21717(8)	x	x	1	0.0059(3)
Si3	96g	0.06723(5)	x	0.37072(9)	1	0.0063(3)

[a]U_{iso} for all Na sites was set to $10\times\langle U_{eq}(Si)\rangle$. The Si atoms were refined anisotropically.

Table C.2 Atomic coordinates, occupancies, and atomic displacement parameters for $Na_{10.7(1)}Si_{136}$ (Na11) corresponding to the Rietveld refinement in Figure 3.3.2b.

$Na_{10.7(1)}Si_{136}$		Lattice Parameter:	14.6544(2) Å			
Atom	Site	x/a	y/b	z/c	Occ.	U_{iso} (Å^2)
Na1	8b	3/8	3/8	3/8	0.913(9)	0.122(4)
Na2	16c	0	0	0	0.216(5)	0.010(5)
Si1	8a	1/8	1/8	1/8	1	0.0044(7)
Si2	32e	0.21765(6)	x	x	1	0.0080(5)
Si3	96g	0.06692(4)	x	0.37092(6)	1	0.0080(3)

Table C.3 Atomic coordinates, occupancies, and atomic displacement parameters for the lithiated Na1 sample corresponding to the Rietveld refinement in Figure 3.3.4b.

$Na_{0.9}Li_{22(1)}Si_{136}$		Lattice Parameter:	14.6570(2) Å			
Atom	Site	x/a	y/b	z/c	Occ.[a]	$U_{iso/eq}$ (Å^2)[b]
Na1	8b	3/8	3/8	3/8	0.044	0.0595
Na2	32e	0.008(2)	x	x	0.018	0.0595
Li1	32e	0.434(2)	x	x	0.34(2)	0.0595
Li2[c]	32e	0.008	x	x	0.33(2)	0.0595
Si1	8a	1/8	1/8	1/8	1	0.0064(6)
Si2	32e	0.21733(10)	x	x	1	0.0055(4)
Si3	96g	0.06736(6)	x	0.37078(11)	1	0.0070(4)

[a]Occupancies of the Na positions were fixed to the values determined for the unlithiated clathrate. [b]U_{iso} for all Na and Li sites was set to $10\times\langle U_{eq}(Si)\rangle$. The Si atoms were refined anisotropically. [c]The coordinates of Li2 were fixed to those of Na2.

Table C.4 Atomic coordinates, occupancies, and atomic displacement parameters for the pristine Na1 corresponding to Figure C.3b.

$Na_{1.4(2)}Si_{136}$		Lattice Parameter:	14.6480(4) Å			
Atom	Site	x/a	y/b	z/c	Occ.	$U_{iso/eq}$ ($Å^2$)[a]
Na1	8b	3/8	3/8	3/8	0.111(13)	0.0633
Na2	32e	0.020(12)	x	x	0.016(6)	0.0633
Si1	8a	1/8	1/8	1/8	1	0.0035(9)
Si2	32e	0.21733(15)	x	x	1	0.0075(6)
Si3	96g	0.06701(9)	x	0.37058(16)	1	0.0080(7)

[a]U_{iso} for all Na and Li sites was set to $10\times\langle U_{eq}(Si)\rangle$. The Si atoms were refined anisotropically.

Table C.5 Atomic coordinates, occupancies, and atomic displacement parameters for the lithiated Na1 corresponding to Figure C.3c.

$Na_{1.4}Li_{16(3)}Si_{136}$		Lattice Parameter:	14.6576(6) Å			
Atom	Site	x/a	y/b	z/c	Occ.[a]	$U_{iso/eq}$ ($Å^2$)[b]
Na1	8b	3/8	3/8	3/8	0.111	0.0620
Na2	32e	0.011(5)	x	x	0.016	0.0620
Li1	32e	0.434(6)	x	x	0.20(5)	0.0620
Li2[c]	32e	0.011	x	x	0.29(4)	0.0620
Si1	8a	1/8	1/8	1/8	1	0.0049(14)
Si2	32e	0.2176(2)	x	x	1	0.0071(10)
Si3	96g	0.06707(13)	x	0.3705(2)	1	0.0081(11)

[a]Occupancies of the Na positions were fixed to the values determined for the unlithiated clathrate. [b]U_{iso} for all Na and Li sites was set to $10\times\langle U_{eq}(Si)\rangle$. The Si atoms were refined anisotropically. [c]The coordinates of Li2 were fixed to those of Na2.

C.3. List of Figures

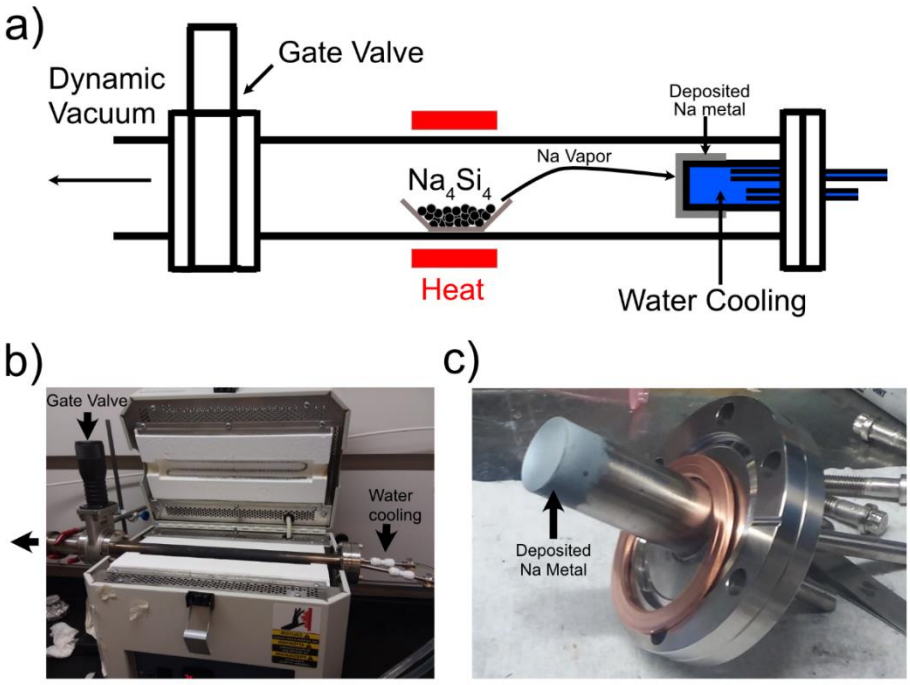

Figure C.1 (a) Schematic of stainless-steel tube reactor with water cooling used for the thermal decomposition of Na_4Si_4 under vacuum. (b) Photograph of the reactor and tube furnace used for the thermal decomposition of Na_4Si_4. (c) Photograph of the water-cooling element with Na evaporated on to it.

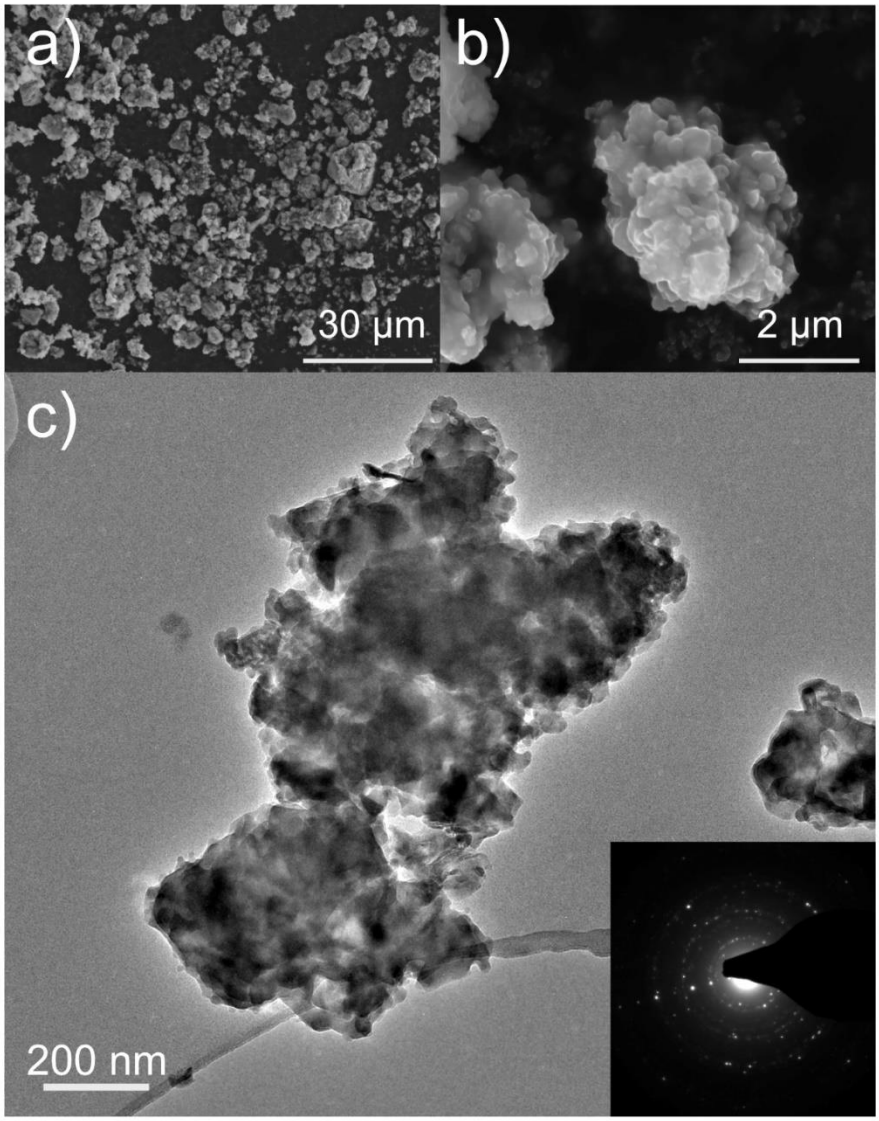

Figure C.2 (a) Low magnification SEM micrograph of type II clathrate with low Na content (Na1) (b) High magnification SEM micrograph of Na1. (c) Low magnification TEM image of type II Si clathrate, Na1, with selected area electron diffraction pattern of the particle in the inset.

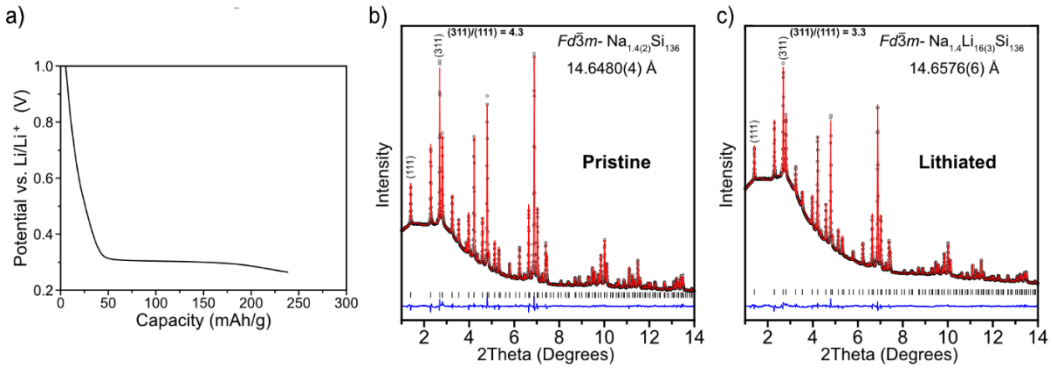

Figure C.3 (a) Galvanostatic voltage profile of a Na1.4 sample lithiated at 10 mA/g. Synchrotron PXRD (λ=0.20733 Å) of the (a) pristine type II Si clathrate and (b) lithiated type II Si clathrate shown in (a). The black circles are the observed data, red trace is the simulated data, the blue trace is the difference curve; the black tick marks are the reflection positions of the type II Si clathrate. The ratio of the (311) and (111) reflection are given to demonstrate how the (111) reflection increases in intensity after electrochemical lithiation, which is an indication of Li occupation in the Si_{20} cages.

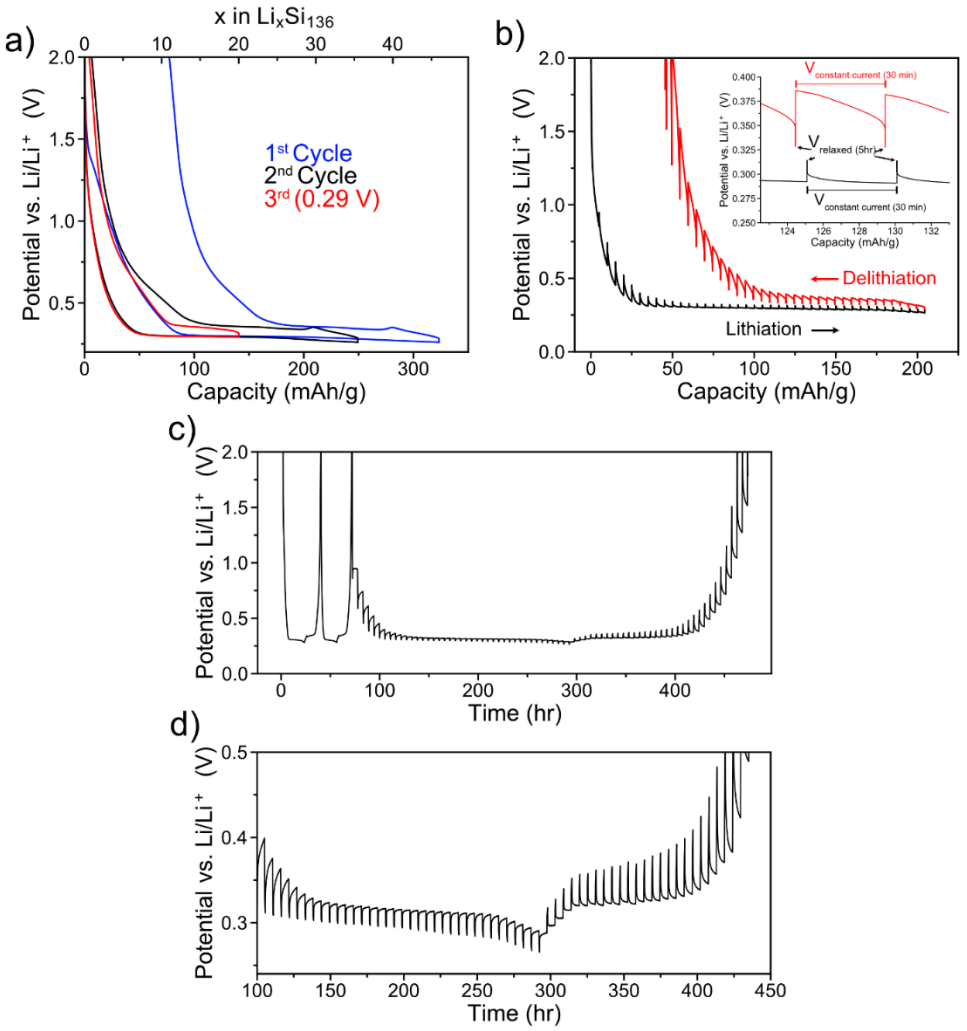

Figure C.4 (a) The lithiation and delithiation voltage profile of Na1 cycled between 0.26–2.5 V (Cycle 1 and 2) and 0.29–2.5V (Cycle 3) at 25 mA/g. (b) GITT profile of the lithiation and delithiation of Na1 at a current density of 10 mA/g with 30 min pulses and 5 hour relaxation times. The cell was cycled 2 times from 0.27–2.5 V prior to the GITT experiment. The height of lines labeled "$V_{relaxed}$" indicate the voltage after the 5 hour relaxation time, while the intervals labeled "$V_{constant\ current}$" represent the voltage during the 30 minute current pulse. (c) The full GITT profile in terms of time showing the first two cycles prior to the GITT experiment. (d) Zoom in of the GITT profile in terms of time.

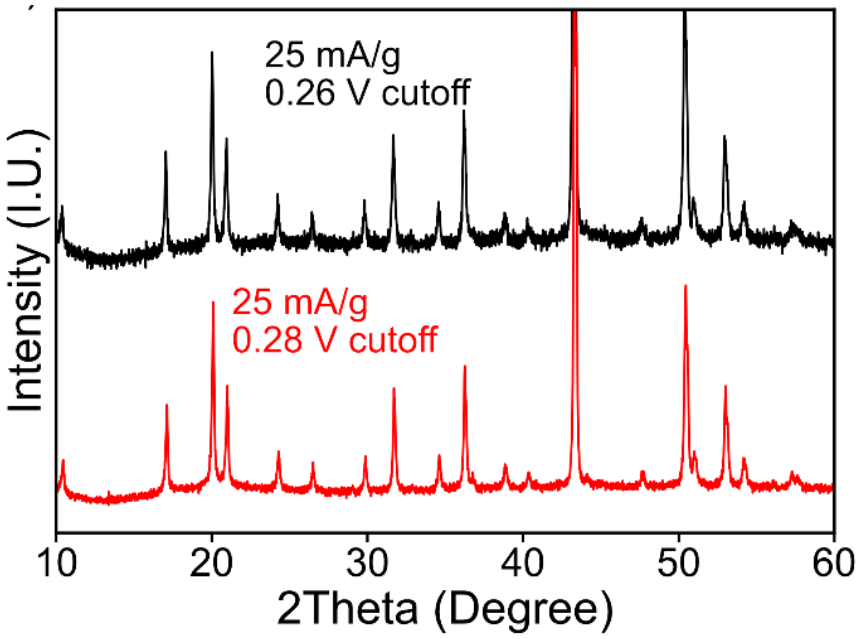

Figure C.5 Laboratory PXRD (Cu Kα) of the cycled electrodes after 50 cycles. The reflections at 2θ = 43° and 51° correspond to the copper current collector of the electrodes.

APPENDIX D

SUPPORTING INFORMATION FOR CHAPTER 4.1

D.1. Experimental Procedures

D.1.1. Synthesis of type I Ge clathrates

The synthesis of Ba_8Ge_{43} and $Ba_8Al_{16}Ge_{30}$ was prepared in a similar manner as described in our previous work.[152] Metals of Ba, and Al and Ge (commercial grade materials with stated purity 99.9% wt) were weighed in an Ar-filled glove box (controlled O_2 and moisture atmosphere). An extra amount (5%) of Ba was loaded since Ba is more volatile than other elements. The total weight of the starting materials was ca. 600 mg. Then, the materials were quickly transferred to the chamber of a custom-made arc-melter, which was evacuated to ca. 10^{-4} Torr and backfilled with high purity argon. After the initial melting, the formed ingot was taken out and turned over. The melting process was repeated three times to ensure good homogeneity. The ingot was hand ground in a mortar and pestle prior to electrochemical testing.

D.1.2. Electrochemical measurements

The clathrate powder was prepared into slurries by mixing the clathrate sample with 10 wt% carbon black (to serve as conducting additive) and 10 wt% polyvinylidene difluoride (PVDF) (to serve as binder) in N-methyl pyrrolidone (NMP) as solvent. Hand ground 100 mesh Ge powder (Sigma Aldrich 99.999%) was used to prepare electrodes for comparison to the clathrate samples. The slurries were stirred overnight and coated onto Cu foil current collectors using a Meyer rod, and then heated at 120 ^oC to remove the solvent. Electrodes were cut into circles 18mm in diameter and typically had an area mass loading of 4-4.5 $mg/cm^{2.}$ The clathrate composite electrodes were evaluated in pouch cells with Li metal as the counter electrode, Celgard 2500 as separator, and 1 M

$LiPF_6$ in ethylene carbonate and ethyl methyl carbonate (3: 7 by vol) (LBC3015B, MTI) as electrolyte. Electrochemical testing was performed using a Biologic VMP3 galvanostat/potentiostat. Galvanostatic measurements were performed at 25 mA/g from 0.01 – 2.5 V vs. Li/Li^+. After the cell was lithiated to the desired composition, it was allowed to relax at open circuit for 5 hours prior to disassembly. To provide sufficient lithiated powder for structural characterization, samples from 2-3 cells prepared and electrochemically lithiated in the same manner were combined.

D.1.3. Sample preparation for synchrotron measurements

After the electrochemical lithiation was complete, the pouch cell was taken into the argon-filled glovebox and opened. The electrode was then immersed in 10 mL of dimethyl carbonate for 30 seconds to wash off any excess battery electrolyte. After the electrode was dry, the lithiated powder was scraped off of the copper current collector using a knife. The extracted powder was then crushed in a mortar and pestle to break up any agglomeration. The powder was sealed in a 2 mL centrifuge tube and then sealed under argon in a polyfoil bag before shipping to the synchrotron facility.

D.1.4. Pair distribution function (PDF) analysis

Lithiated powders were loaded into 0.8 mm diameter borosilicate capillaries and sealed with wax and superglue inside an argon-filled glovebox, while pristine powders were loaded into the capillaries in ambient conditions. PDF measurements were performed at Diamond Light Source (Didcot, United Kingdom) at the I15-I dedicated PDF beamline with 76 keV X-rays (wavelength of 0.161669 Å) and 2D PerkinElmer image plate detectors. The detector geometry allowed collection of total scattering data to

Q = 30 Å^{-1}. Ex situ PDF measurements were carried out at room temperature. The in situ PDF heating measurements were carried out from 300 – 450 K (temperature interval of 10 K) using an Oxford Instruments Cryojet 5. After reaching each hold temperature, there was a 1.5 min equilibration period and then the scattering data were collected with a 10 minute collection time. For the $Li_{3.75}Ge$ heating experiments, a 5 minute collection time was used due to time constraints.

PDFs were generated from the total scattering data using PDFgetx3[221] within the xPDFsuite software package,[222] wherein the measured total scattering intensities, $I(Q)$, are corrected to obtain the coherent scattering, $I_c(Q)$ and transformed into the structure function, $S(Q)$, according to equation 1,[221]

$$S(Q) = \frac{I_c(Q) - \langle f(Q)^2 \rangle + \langle f(Q) \rangle^2}{\langle f(Q) \rangle^2}$$

where $f(Q)$ is the atomic scattering factor, which is averaged over all atom types in the sample. The PDF, $G(r)$, is obtained from the Fourier transform of $S(Q)$ as shown in equation 2:

$$G(r) = \frac{2}{\pi} \int_{Q_{min}}^{Q_{max}} Q[S(Q) - 1] \sin(Qr)\, dQ$$

To generate the PDFs, the following parameters were used: Q_{min} = 0.5 Å^{-1}, Q_{max} = 25 Å,$^{-1}$ r_{step} = 0.1 Å, and r_{poly}= 0.9. The nominal composition for lithiated samples was obtained from the charge passed during the electrochemical measurements.

PDF refinements were carried out using PDFgui[68]. No attempts were made to consider the presence of binder, carbon black, or SEI components in the samples. Previous reports

have shown that these components add negligible contribution to the PDF data.[318] PDF refinements were performed using Q_{damp} = 0.0247 and Q_{broad} = 0.0151 (obtained from refinement of a NIST Si standard). To refine a PDF pattern, the major phase of the pattern was first selected and then scale factor and lattice parameter were refined. Then the atomic displacement parameters (ADP) for each element (initially set to 0.03 $Å^2$) and the linear atomic scale factor (delta1) were allowed to be refined. If this resulted in an insufficient fit, possible secondary phases were added and refined in a similar way. In some cases, the Li ADP refined to very large values (0.5 – 1 $Å^2$). If this occurred, the Li ADP was fixed to a lower value. Unphysical ADPs for Li have been reported previously and is an indication of disorder/partial occupancy or atomic substitution[319].

The refinements were conducted using the following structures for the fittings: Ba_8Ge_{43} ($Pm\bar{3}m$, ICSD-97480)[90], α-Ge ($Fd\bar{3}m$, ICSD-44841)[320], Li_9Ge_4 (Cmcm, ICSD-25308)[228], Li_7Ge_2 (Cmmm, ICSD-42063)[227], $Li_{15}Ge_4$ ($I\bar{4}3d$, ICSD-43235)[224], and Li_7Ge_3 ($P3_212$), Li_5Ge_2 ($R\bar{3}m$), and $Li_{13}Ge_5$ ($P\bar{3}m1$) (predicted from first principles calculations by Morris et. al.[223]

D.1.5. Powder X-ray diffraction (XRD)

Synchrotron XRD was performed at the P02.1 Powder Diffraction and Total Scattering Beamline at PETRA III at the Deutsches Elektronen-Synchrotron (DESY) with 60 keV X-rays at a wavelength of 0.20733 Å. A Perkin Elmer XRD1621 was used as the X-ray detector. The lithiated samples were loaded into 0.8 mm borosilicate capillaries in an argon-filled glovebox and sealed with wax. In situ heating experiments were conducted in borosilicate capillaries and heated with an Oxford Cryostream cooler.

For the in situ measurements, 3 scans were taken every 2 minutes with a total hold time of 6 minutes at the temperature. A temperature interval of 20 K was used starting at 300 K and going to 480 K.

Rietveld refinement was performed with Jana2006[64]. The peak shapes were described by the pseudo-Voigt function, background fit with Legendre polynomials, and atomic displacement parameters were modeled as isotropic. In some cases, the Li ADP refined to very large values (0.5 – 1 $Å^2$). If this occurred, the Li ADP was fixed to a lower value. Unphysical ADPs for Li have been reported previously and is an indication of disorder/partial occupancy or atomic substitution[319].

Laboratory powder X-ray diffraction was performed with a Bruker D8 diffractometer with Cu X-rays operated at 40 kV and 40 mA with standard Bragg-Brentano diffraction geometry. For air-sensitive samples, the sample was covered with a Kapton film in an argon-filled glovebox prior to diffraction measurements. The Kapton film resulted in a broad amorphous background from $15 < 2\theta < 25$.

Obtained XRD patterns were compared to the same reference patterns indicated in the previous section, as well as the following: LiGe ($I4_1/a$, ICSD-42062)[321], Ba_2LiGe_3 (Fddd, ICSD-404705)[322], Li_4Ge_1 (Cmcm, ICSD-427231)[323], $Li_{17}Ge_4$ ($F\bar{4}3m$, ICSD-427232)[323].

D.1.6. Scanning electron microscopy

Scanning electron microscopy (SEM) imaging was performed using an XL 30 ESEM-FEG microscope and a 20 kV electron beam. The electrodes were cut from copper foil and mounted on SEM stubs with carbon tape

D.2. List of Tables

Table D.1 The measured voltages and corresponding capacity for each sample after electrochemical lithiation to different Li/Ge ratios.

Electrode	# of Li inserted per Ge atom	Voltage (V vs. Li/Li^+)	Capacity (mAh/g)
Ba_8Ge_{43}	1.75	0.175	478
	2.75	0.11	752
	3.75	0.01	1025
α-Ge	1.75	0.28	647
	2.75	0.17	1017
	3.75	0.01	1386

Table D.2 Refined atomic positions, lattice parameters, and atomic displacement parameters for the $Li_{1.75}Ge$ sample. The refinement plot can be found in Figure D.2a. *The atomic displacement parameters for Li were fixed to 0.05 due to refining to unphysical values.

Ge	$Fd\bar{3}m$	Lattice Parameter:	5.65735(8) Å			
Atom	Site	x/a	y/b	z/c	Occ.	U_{iso} ($Å^2$)
Ge1	8b	0	0	0	1	0.0071(3)
Li_5Ge_2	$R\bar{3}m$	Lattice Parameter:	a= 4.46774(18) Å	c= 18.3973(14) Å		
Atom	Site	x/a	y/b	z/c	Occ.	U_{iso} ($Å^2$)
Li1	3a	0	0	1/2	1	0.05*
Li2	6c	0	0	0.350712	1	0.05*
Li3	6c	0	0	0.191734	1	0.05*
Ge1	6c	0	0	0.06795(11)	1	0.0112(7)

Table D.3 Refined atomic positions, lattice parameters, and atomic displacement parameters for the $Li_{3.75}Ge$ sample. The refinement plot can be found in Figure D.2b. *The atomic displacement parameters for Li were fixed to 0.03 due to refining to unphysical values.

$Li_{15}Ge_4$	$I\bar{4}3d$	Lattice Parameter:	10.7763(4) Å			
Atom	Site	x/a	y/b	z/c	Occ.	U_{iso} ($Å^2$)
Li1	48e	0.0349(17)	0.3727(13)	0.1515(13)	1	0.008(4)
Li2	12a	3/8	0	1/4	1	0.03*
Ge1	16c	0.20975(10)	x	x	1	0.0168(6)

Table D.4 PDFgui refinement parameters for pristine α-Ge and the $Li_{1.75}Ge$ sample fit to different phase combinations. Plot of the pristine α-Ge and the sample refined with Ge and Li_5Ge_2 is presented in Figure D.3ab.

	Pristine α-Ge	$Li_{1.75}Ge$		$Li_{1.75}Ge$		$Li_{1.75}Ge$	
Phase	Ge $Fd\bar{3}m$	Ge $Fd\bar{3}m$	Li_7Ge_3 $P3_212$	Ge $Fd\bar{3}m$	Li_5Ge_2 $R\bar{3}m$	Ge $Fd\bar{3}m$	Li_9Ge_4 Cmcm
Mol Fraction	1	0.096	0.904	0.094	0.906	0.093	0.907
Lattice Parameters (Å)	a= 5.655	a = 5.652	a = 7.723 c = 18.470	a = 5.652	a = 4.464 c = 18.435	a = 5.649	a = 4.453 b = 7.700 c = 24.808
Delta 1	1.937	1.724	2.397	2.444	1.045	1.748	2.419
ADP*	0.008	Ge: 0.011	Li: 0.204 Ge: 0.022	Ge: 0.011	Li: 0.280 Ge: 0.027	Ge: 0.0086	Li: 0.129 Ge: 0.031
R_w	0.082	0.197		0.191		0.229	

*Atomic displacement parameters (U_{11}= U_{22}= U_{33}, $Å^2$)

Table D.5 PDFgui refinement parameters for $Li_{2.75}Ge$ sample fit to different phase combinations. Plot of the sample refined with $Li_{13}Ge_5$ and Li_7Ge_2 is presented in Figure D.3c.

	$Li_{2.75}Ge$		$Li_{2.75}Ge$	$Li_{2.75}Ge$
Phase	$Li_{13}Ge_5$ $P\bar{3}m1$	Li_7Ge_2 Cmmm	Li_7Ge_3 $P3_212$	Li_5Ge_2 $R\bar{3}m$
Mol Fraction	0.643	0.357	1	1
Lattice Parameters (Å)	a = 4.452 c = 16.122	a = 9.106 b = 13.233 c = 4.532	a = 7.735 c = 18.678	a = 4.470 c = 18.645
Delta 1	1.977	1.856	2.334	2.334
ADP*	Li: 0.086 Ge: 0.016	Li: 0.03** Ge: 0.018	Li: 0.062 Ge: 0.021	Li: 0.083 Ge: 0.023
R_w	0.195		0.255	0.268

*Atomic displacement parameters (U_{11}= U_{22}= U_{33}, $Å^2$)
** Note: Refinement of the ADPs for Li in the Li_7Ge_2 phase resulted in unreasonably high values so it was fixed at 0.03.

Table D.6 PDFgui refinement parameters for $Li_{3.75}Ge$ sample fit to different phase combinations. Plot of the sample refined with $Li_{15}Ge_4$ and Li_7Ge_3 is presented in Figure D.3d.

	$Li_{3.75}Ge$	$Li_{3.75}Ge$		$Li_{3.75}Ge$	
Phase	$Li_{15}Ge_4$ $I\bar{4}3d$	$Li_{15}Ge_4$ $I\bar{4}3d$	Li_7Ge_3 $P3_212$	$Li_{15}Ge_4$ $I\bar{4}3d$	Li_5Ge_2 $R\bar{3}m$
Mol Fraction	1	0.857	0.143	0.862	0.138
Lattice Parameters (Å)	a = 10.784	a = 10.763	a = 7.728 c = 18.814	a = 10.763	a = 4.471 c = 18.751
Delta 1	0.763	1.724	1.929	1.799	1.045
ADP*	Li: 0.064 Ge: 0.016	Li: 0.105 Ge: 0.013	Li: 0.045 Ge: 0.015	Li: 0.107 Ge: 0.013	Li: 0.044 Ge: 0.016
R_w	0.229	0.118		0.127	

*Atomic displacement parameters (U_{11}= U_{22}= U_{33}, Å^2)

Table D.7 PDFgui refinement parameters for the pristine Ba_8Ge_{43} and $Li_{1.75}Ba_{0.19}Ge$ PDF plots in Figure D.6.

	Pristine Ba_8Ge_{43}		$Li_{1.75}Ba_{0.19}Ge$	$Li_{1.75}Ba_{0.19}Ge$ (10-30 Å)
Phase	Ba_8Ge_{43} $Pm\bar{3}n$	Ge $Fd\bar{3}m$	Ba_8Ge_{43} $Pm\bar{3}n$	Ba_8Ge_{43} $Pm\bar{3}n$
Mol Fraction	0.956	0.044	1	1
Lattice Parameter (Å)	a = 10.658	a = 5.652	a = 10.652	a = 10.646
Delta 1	2.285	n/a	2.432	2.432
ADP*	Ba: 0.050 Ge: 0.027	Ge: 0.007	Ba: 0.027 Ge: 0.025	Ba: 0.022 Ge: 0.022
R_w	0.130		0.587	0.290

*Atomic displacement parameters (U_{11}= U_{22}= U_{33}, Å^2)

Table D.8 PDFgui refinement parameters for pristine $Ba_8Al_{16}Ge_{30}$ and $Li_{1.9}Ba_{0.17}Al_{0.35}Ge_{0.65}$ PDF plots in Figure D.8bc.

	Pristine $Ba_8Al_{16}Ge_{30}$	$Li_{1.9}Ba_{0.17}Al_{0.35}Ge_{0.65}$
Phase	$Ba_8Al_{16}Ge_{30}$ $Pm\bar{3}n$	$Ba_8Al_{16}Ge_{30}$ $Pm\bar{3}n$
Mol Fraction	1	1
Lattice Parameter (Å)	a = 10.854	a = 10.836

Delta 1	1.489	2.0
ADP*	Ba: 0.05 Ge/Al: 0.014	Ba: 0.023 Ge/Al: 0.01
R_w	0.095	0.674

*Atomic displacement parameters (U_{11}= U_{22}= U_{33}, Å^2)

Table D.9 PDFgui refinement parameters for PDFs of $Li_{2.75}Ba_{0.19}Ge$ and $Li_{3.75}Ba_{0.19}Ge$ after heating to 450 K and 420 K, respectively. Plots of these refinements can be found in Figure D.11.

	$Li_{2.75}Ba_{0.19}Ge$	$Li_{2.75}Ba_{0.19}Ge$ (6-30 Å)	$Li_{3.75}Ba_{0.19}Ge$
Phase	Li_7Ge_2 Cmmm	Li_7Ge_2 Cmmm	$Li_{15}Ge_4$ $I\bar{4}3d$
Mol Fraction	1	1	1
Lattice Parameters (Å)	a = 9.315 b = 13.154 c = 4.561	a = 9.317 b = 13.174 c = 4.55	a = 10.826
Delta 1	2.569	2.569	1.040
ADP*	Li: 0.1** Ge: 0.027	Li: 0.1** Ge: 0.025	Li: 0.1** Ge: 0.018
R_w	0.550	0.286	0.389

*Atomic displacement parameters (U_{11}= U_{22}= U_{33}, Å^2)
*Refinement of the ADP for Li in both cases resulted in unreasonably high values so it was fixed.

D.3. List of Figures

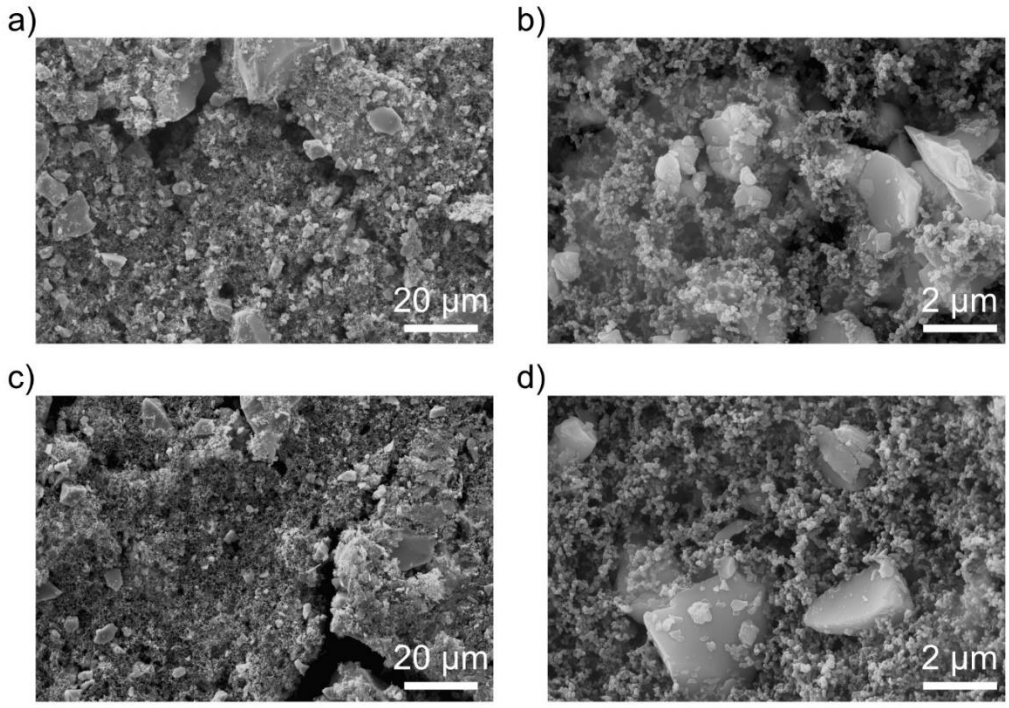

Figure D.1 SEM images of the (a,b) Ba_8Ge_{43} and (c,d) α-Ge electrodes prior to electrochemical cycling. The small, nanosized particles are the carbon black conducting additive used to improve electronic conductivity throughout the composite electrode.

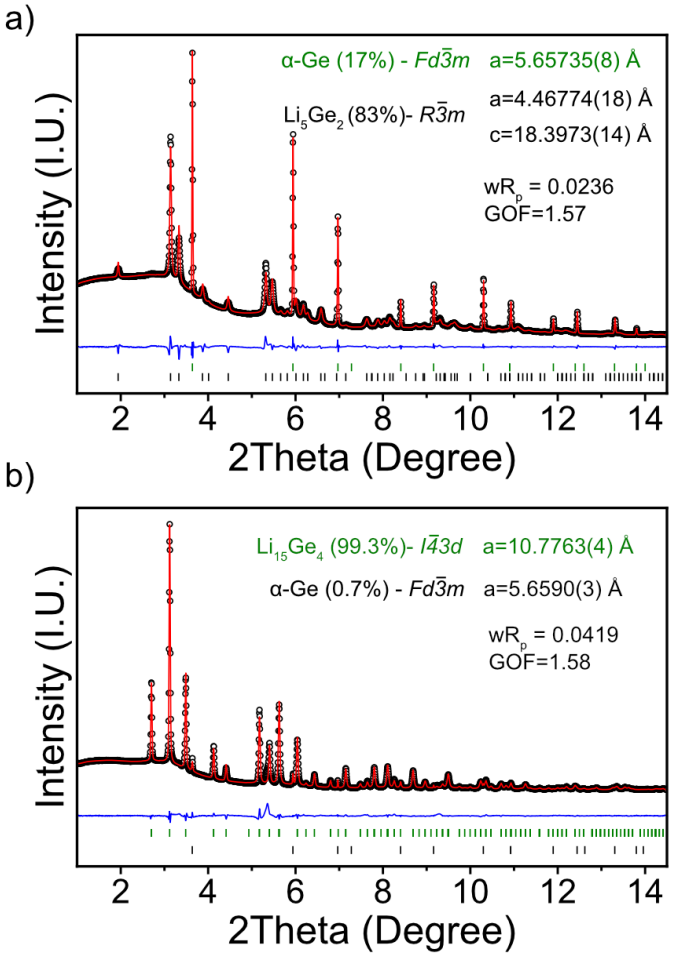

Figure D.2 Rietveld refinement of the PXRD patterns of the (a) $Li_{1.75}Ge$ and (b) $Li_{3.75}Ge$ samples. The black circles represent the experimental pattern, the red curve represents the calculated pattern, and the blue curve represents the difference curve. The phase fractions are in mol%. The refined atomic positions, occupancies, and atomic displacement parameters can be found in Table D.2-3.

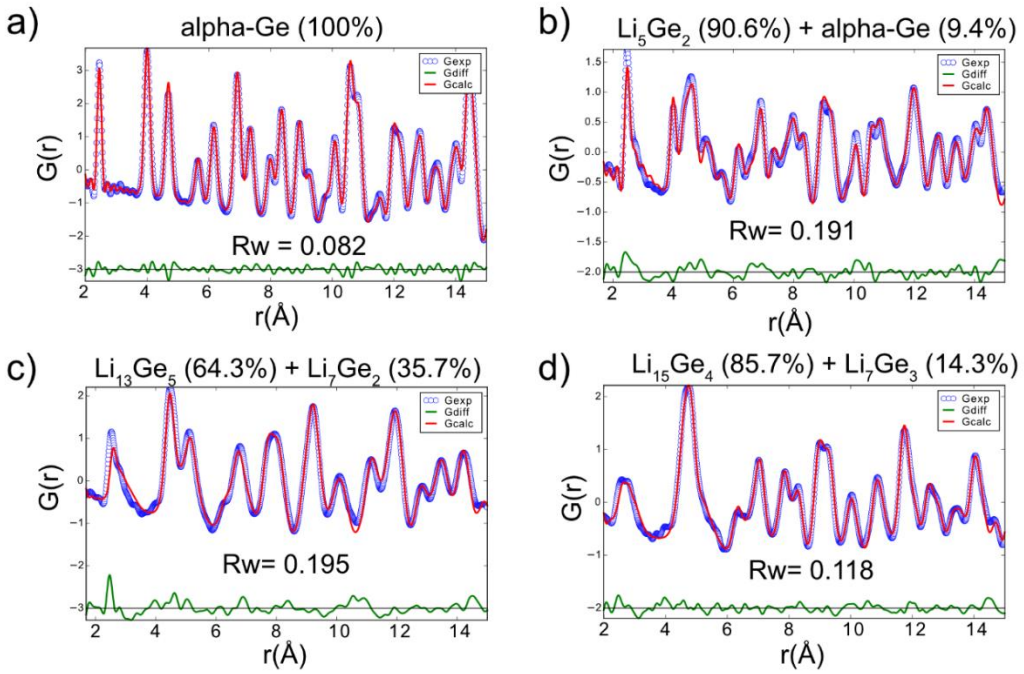

Figure D.3 Refinements of the α-Ge PDF patterns at compositions of (a) pristine α-Ge (b) $Li_{1.75}Ge$, (c) $Li_{2.75}Ge$ and (d) $Li_{3.75}Ge$. Phase amounts indicated in mol%. The sources for the reference structures are included in Section D.1.4 of Appendix D.

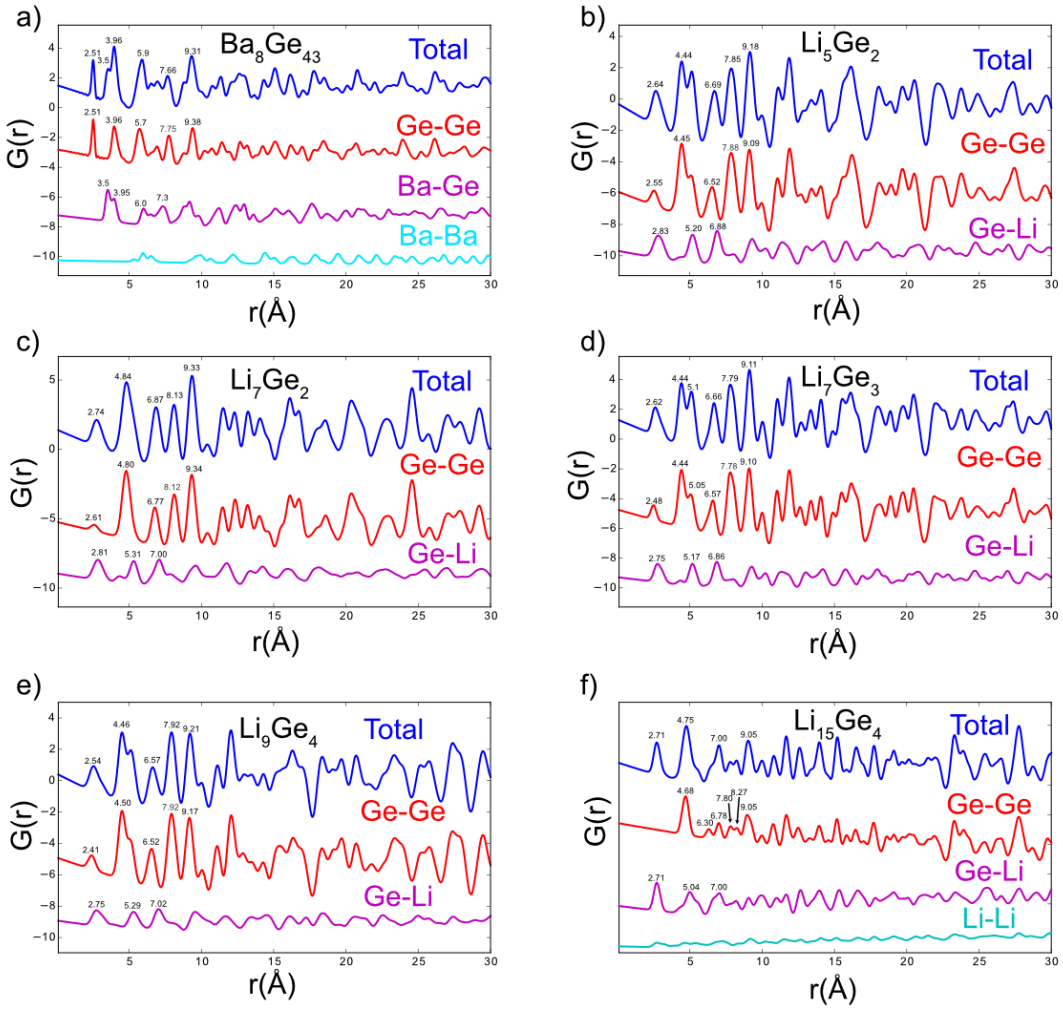

Figure D.4 Calculated total and partial PDF patterns for (a) Ba_8Ge_{43}, (b) Li_5Ge_2, (c) Li_7Ge_2, (d) Li_7Ge_3, (e) Li_9Ge_4, and (f) $Li_{15}Ge_4$. The sources for the reference structures are included in D.1.4 of Appendix D except for the structure of Ba_8Ge_{43}, which came from our previous study.[152]

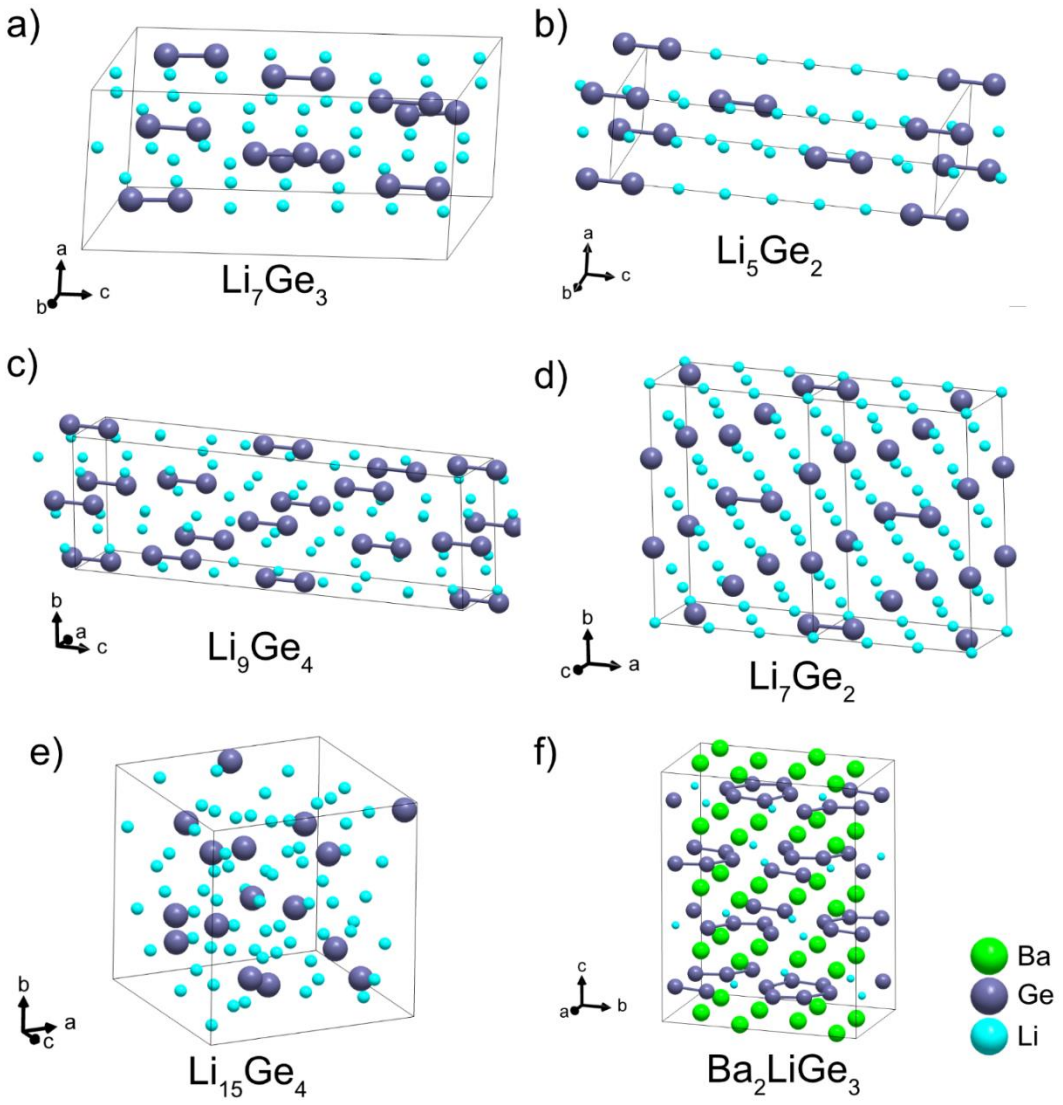

Figure D.5 Crystal structures of (a) Li_7Ge_3, (b) Li_5Ge_2, (c) Li_9Ge_4, (d) Li_7Ge_2 (e) $Li_{15}Ge_4$, and (f) Ba_2LiGe_3. The sources for the reference structures are included in D.1.4 and 1.5 of Appendix D.

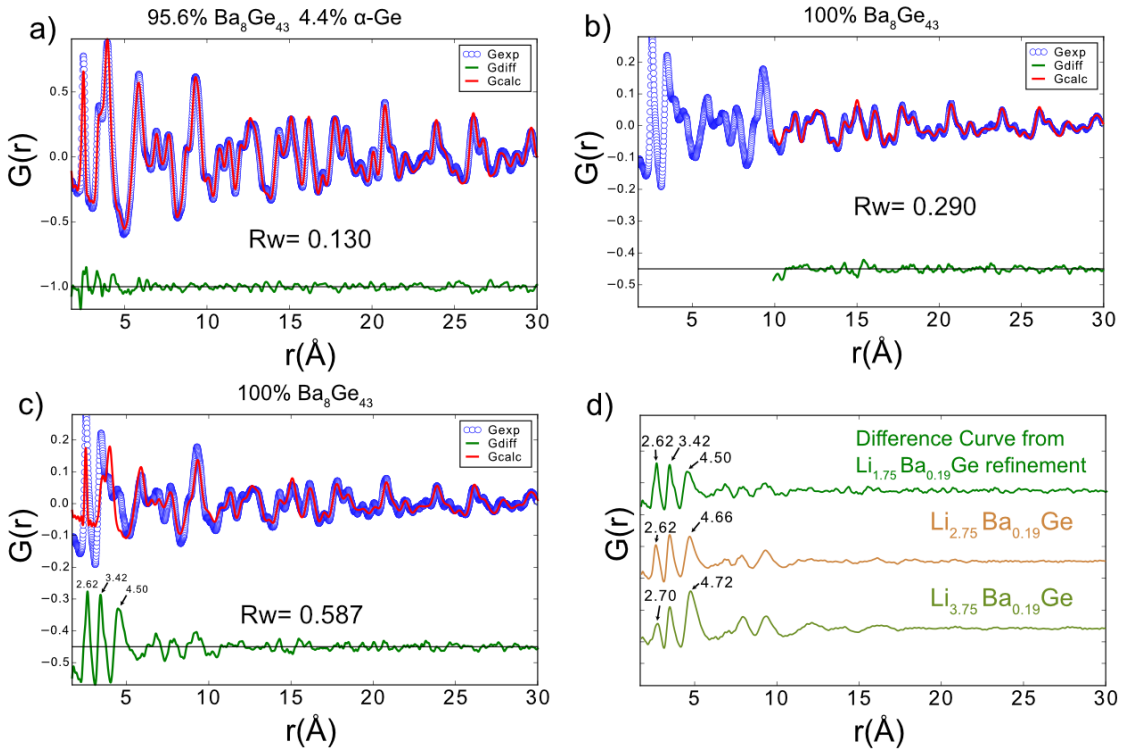

Figure D.6 PDF refinements for (a) pristine Ba_8Ge_{43}, (b) Ba_8Ge_{43} after lithiation to a composition of $Li_{1.75}Ba_{0.19}Ge$ and (c) $Li_{1.75}Ba_{0.19}Ge$ (fit range restricted to 10 – 30 Å). (d) Comparison of the amorphous phase from the difference curve of the refinement for $Li_{1.75}Ba_{0.19}Ge$ in (c) with the PDFs of $Li_{2.75}Ba_{0.19}Ge$ and $Li_{3.75}Ba_{0.19}Ge$ (y-offset for clarity). The sources for the reference structures are included in D.1.4 of Appendix D.

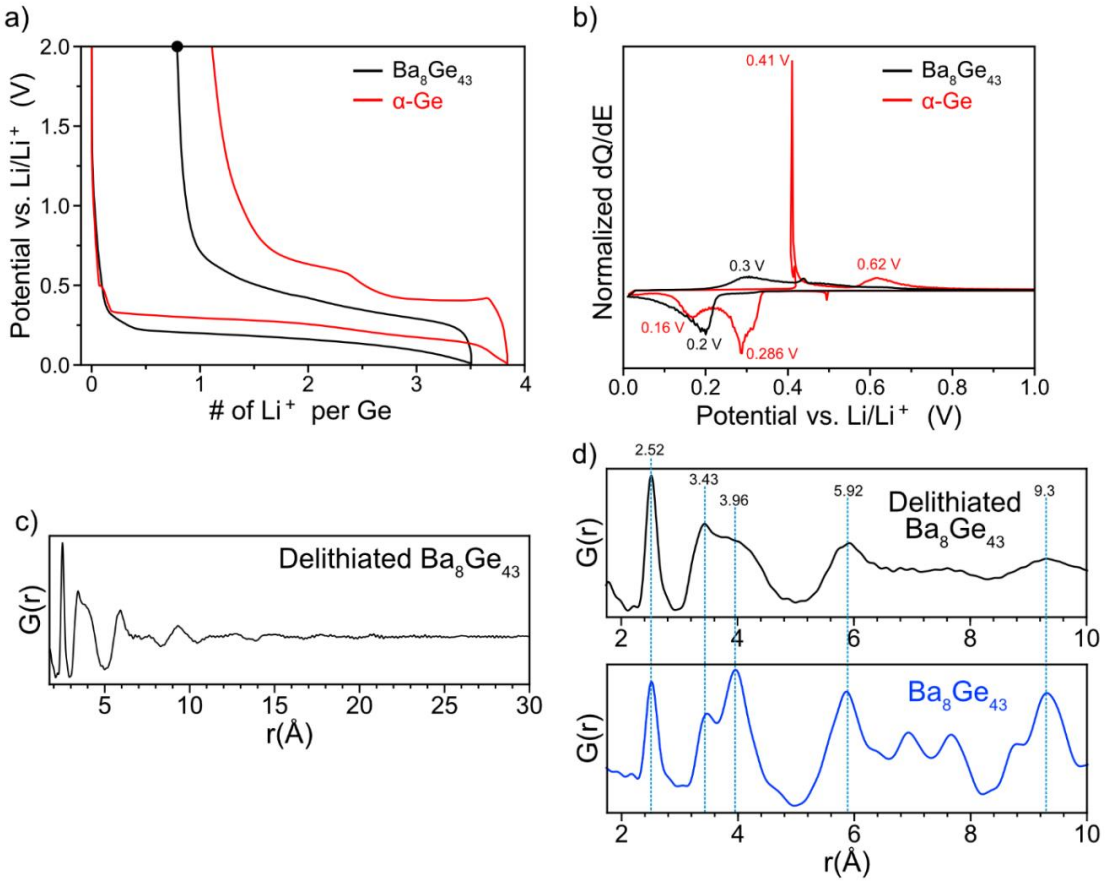

Figure D.7 (a) Voltage profile of the lithiation and delithiation of Ba_8Ge_{43} and α-Ge using 25 mA/g; the # of Li^+ is referenced to the amount of Ge atoms in each compound. (b) Corresponding dQ/dE plot of the voltage profiles. (c) PDF plot of the Ba_8Ge_{43} after one full lithiation/delthiation cycle ("delithiated Ba_8Ge_{43}") taken from the point indicated by the black dot in the voltage profile in (a). (d) Comparison of PDFs from delithiated Ba_8Ge_{43} (amorphous) and the crystalline Ba_8Ge_{43}. The position of the peaks in the PDFs are similar, suggesting that the delithiated Ba_8Ge_{43} might have a similar local structure as the crystalline Ba_8Ge_{43}.

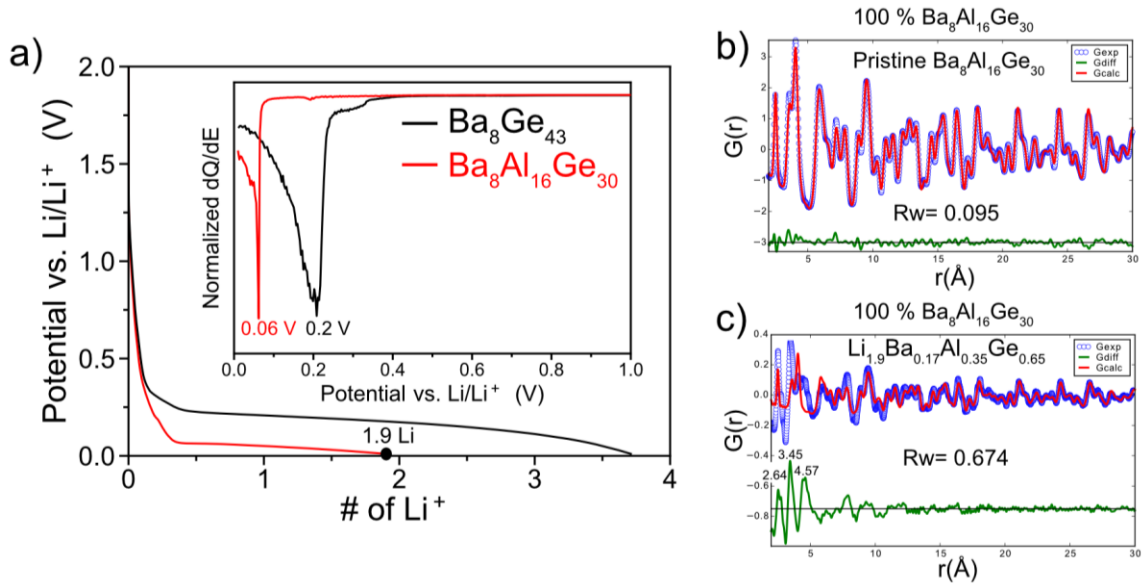

Figure D.8 (a) Voltage profile and corresponding dQ/dE plot of the lithiation of Ba_8Ge_{43} and $Ba_8Al_{16}Ge_{30}$ using 25 mA/g; the # of Li^+ is referenced to the amount of (Al + Ge) atoms in each compound. (b) PDF refinement of the pristine $Ba_8Al_{16}Ge_{30}$ clathrate, using structure from ref.[152] (c) PDF refinement of the lithiated $Ba_8Al_{16}Ge_{30}$ ($Li_{1.9}Ba_{0.17}Al_{0.35}Ge_{0.65}$) to the $Ba_8Al_{16}Ge_{30}$ structure from ref.[152] The difference curve reveals the presence of an amorphous phase with similar correlation positions as those found in $Li_{1.75}Ba_{0.19}Ge$ (Figure D.6c).

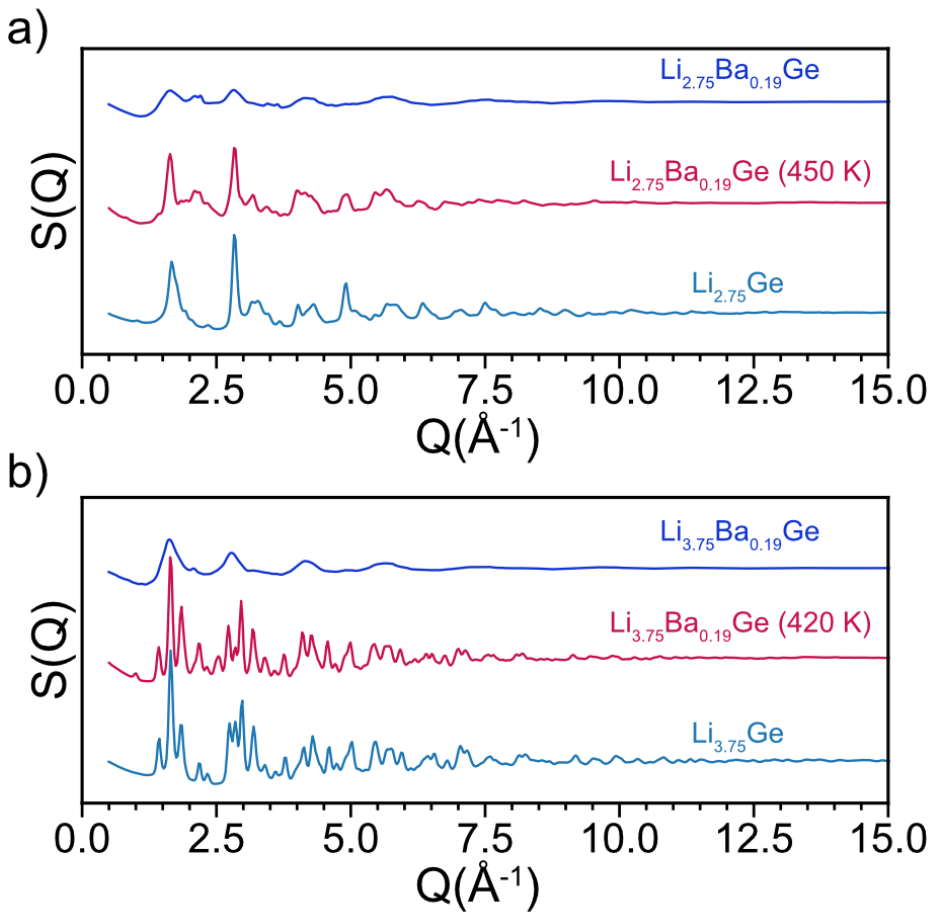

Figure D.9 Comparison of total scattering structure function, S(Q), with intensities normalized by the average scattering factors and corrected by a polynomial fit of (a) $Li_{2.75}Ba_{0.19}Ge$: unheated (blue), heated to 450 K (pink), and lithiated α-Ge (light blue); (b) $Li_{3.75}Ba_{0.19}Ge$: unheated (blue), heated to 420 K (pink), and lithiated α-Ge (light blue).

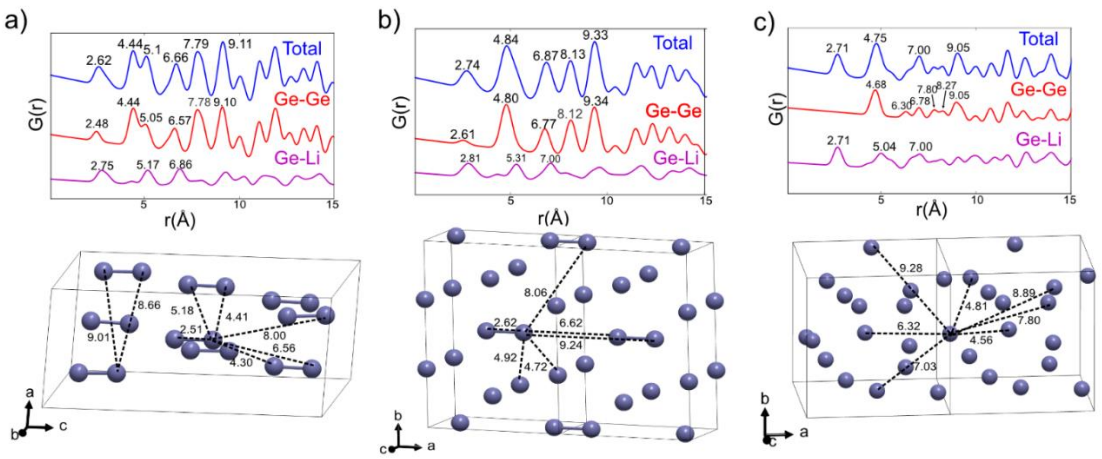

Figure D.10 Assignment of Ge-Ge correlation distances found in the calculated PDF to distances between Ge atoms for (a) Li_7Ge_3 (b) Li_7Ge_2 and (c) $Li_{15}Ge_4$. Note that this is not an exhaustive assignment of the atomic correlations but serves to give an idea of the types of atom-atom distances corresponding to the correlations in the PDFs. The sources for the reference structures are included in D.1.4 of Appendix D.

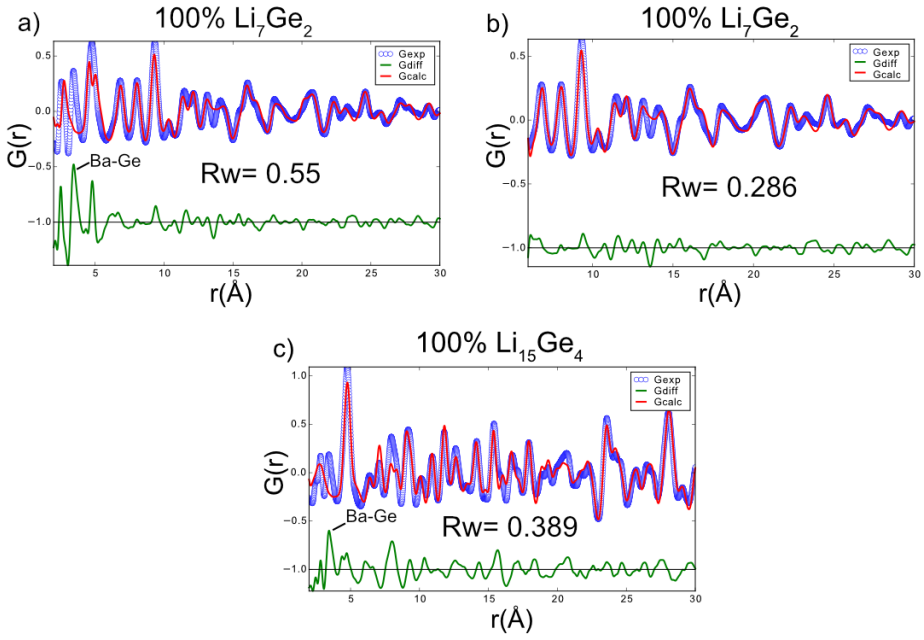

Figure D.11 Refinements of the PDF from $Li_{2.75}Ba_{0.19}Ge$ after heating to 450 K, fit to Li_7Ge_2 (a) from 2 – 30 Å, and (b) from 6 – 30 Å. (c) Refinement of the PDF for $Li_{3.75}Ba_{0.19}Ge$ heated to 420 K, fit to $Li_{15}Ge_4$. The sources for the reference structures are included in D.1.4 of Appendix D.

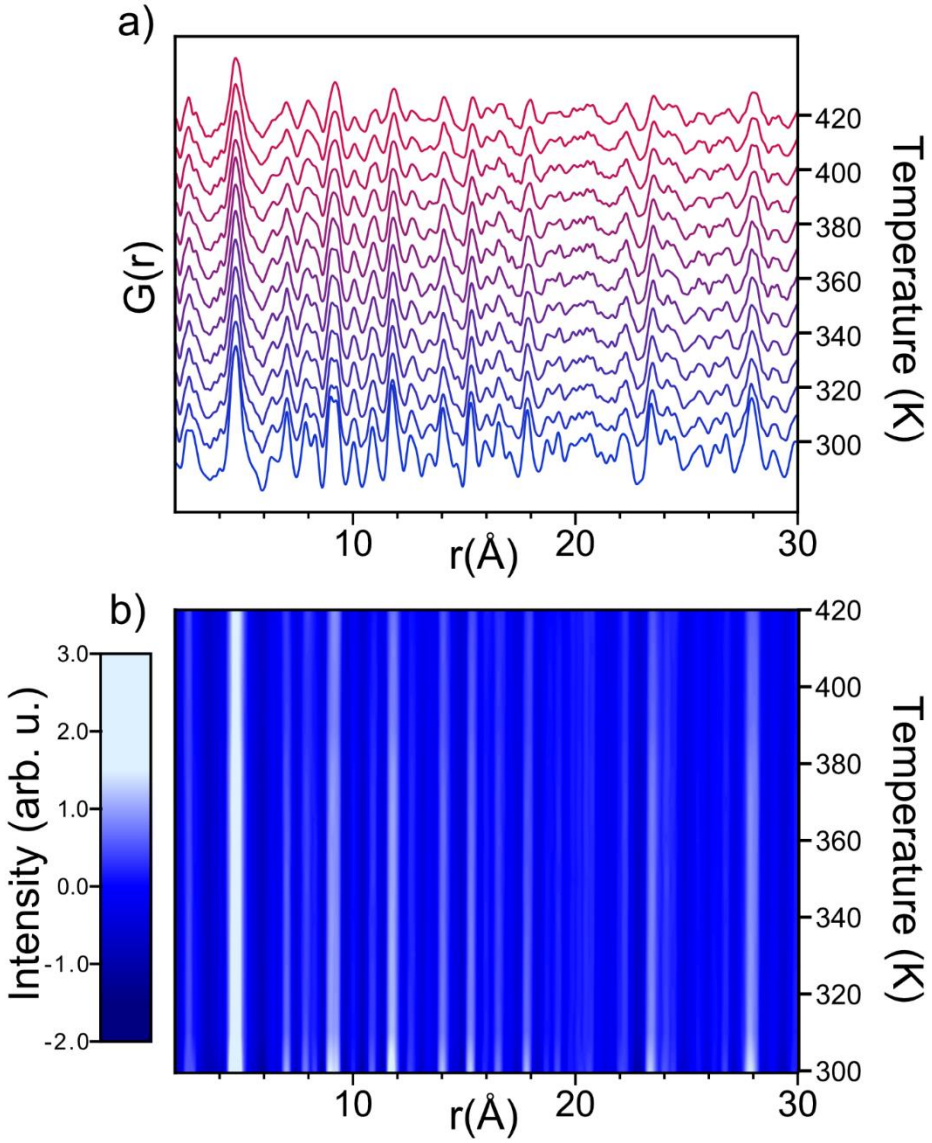

Figure D.12 (a) Variable temperature PDF during in situ heating from 310 – 420 K for fully lithiated α-Ge ($Li_{3.75}Ge$). Intervals of 10 K and 10 minute holds at each temperature were used. (b) Corresponding false colormaps of the PDF data; a linear interpolation was between measured data points.

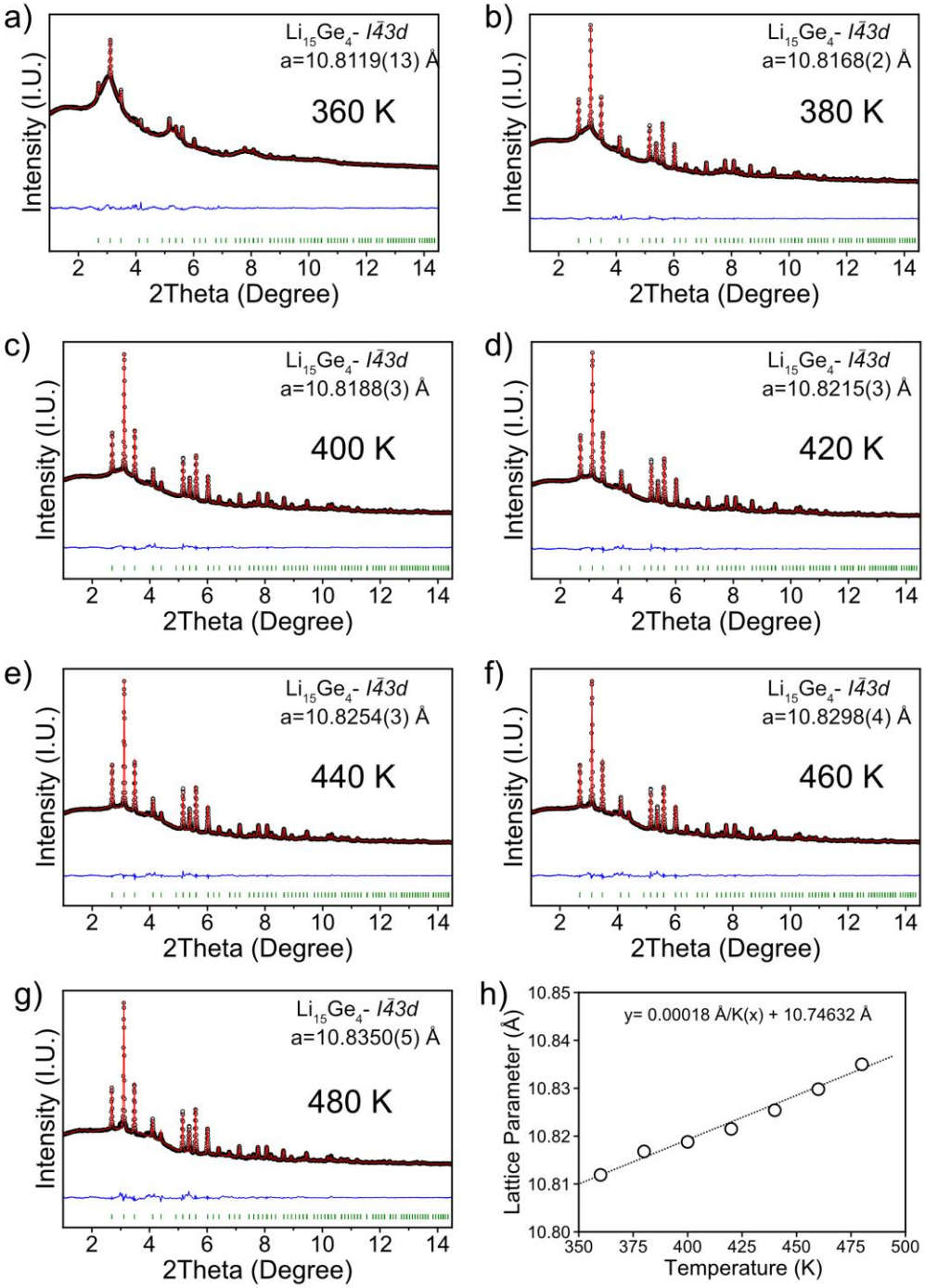

Figure D.13 (a)-(g) Rietveld refinements for the in situ heating of $Li_{3.75}Ba_{0.19}Ge$ to the $Li_{15}Ge_4$ structural model from 360-480 K (h) Lattice parameter vs temperature plot with a linear regression model for the dependence.

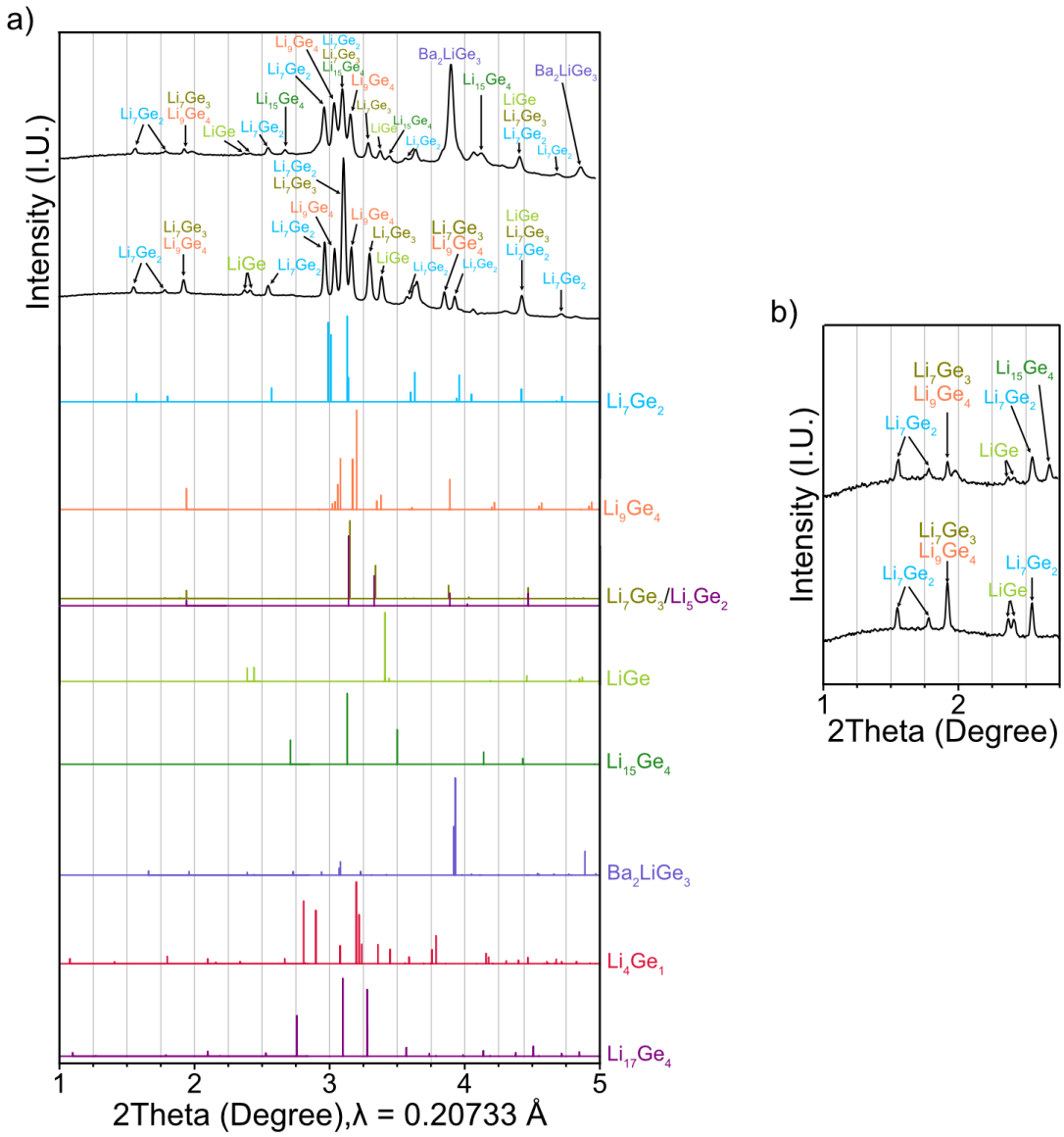

Figure D.14 (a) XRD patterns of $Li_{3.75}Ba_{0.19}Ge$ and $Li_{3.75}Ge$ after heating to 480 K with the simulated XRD patterns of possible Li/Ge/Ba phases for identification. (b) Zoom in of the low angle peaks and their identification. The sources for the reference structures are included in D.1.4 and 1.5 of Appendix D.

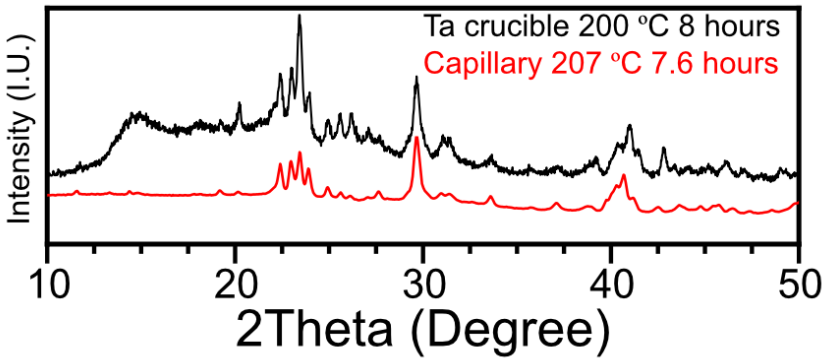

Figure D.15 Ex situ lab powder XRD pattern of $Li_{3.75}Ba_{0.19}Ge$ after heating at 200 ºC for 8 hours under argon in a Ta boat (red) compared to the synchrotron in situ XRD heating pattern taken from $Li_{3.75}Ba_{0.19}Ge$ after heating at 480 K for 6.6 hours in a borosilicate capillary (black). Note that the XRD pattern for the sample heated in the Ta boat was taken at room temperature while the XRD pattern from the capillary was taken at 480 K (207 ºC). The background from $15 < 2\theta < 25$ in the black trace is from the Kapton film that was used to protect the sample from oxidation during the measurement. The similarity in the XRD patterns suggests that the use of the glass capillary did not have any effect on the formation of the reaction products.

APPENDIX E

SUPPORTING INFORMATION FOR CHAPTER 4.2

E.1. Experimental and Computational Procedures

E.1.1. Synthesis of Type VIII Clathrate $Ba_8Ga_{15}Sn_{31}$

The synthesis was done in a manner, similar to a previous work.[171] Large crystals of the type VIII clathrate with refined composition $Ba_8Ga_{\sim 15}Sn_{\sim 31}$ were grown by Ga/Sn flux reaction. Elemental Ba, Ga, and Sn (commercial grade materials with stated purity 99.9% wt or greater) were combined in a 8:40:65 molar ratio to a 2 cm^3 alumina crucible that was subsequently flamed-sealed in an evacuated fused silica tube. The sample was heated to 500 ºC (20 ºC/hr) then held at 500 ºC for 500 hrs. After cooling to 400 ºC (-5 ºC/hr), the Ga/Sn flux was removed by centrifugation. The large crystals were then hand ground prior to electrochemical testing.

E.1.2. Single Crystal X-ray Diffraction

Single-crystal X-ray diffraction measurements were performed on a Bruker APEX-II CCD diffractometer stocked with a sealed-tube Mo Kα ($\lambda = 0.71073$ Å) source. Proper single crystals were selected under an optical microscope, covered in Paratone-N oil and placed onto a holder loop made of low-background plastic. The holder was transported to the goniometer head, where a cold stream of nitrogen gas was used to harden the oil and to prevent oxidation/decomposition over the span of the data collection. The temperature was kept at 200(2) K throughout the experiment. Data acquisition was performed with Bruker-provided software. Measurements were collected in batch runs with a frame width of 0.8° in ω and θ. Data reduction and scaling were managed using SAINT.[127] Absorption correction was implemented using SADABS software program.[324] The structure was solved using ShelXT[325] in Olex2[326] and refined

with the full-matrix least squares method on F^2, as implemented in SHELXL[327]. Atomic coordinates were standardized using STRUCTURE TIDY[328] and tables were generated using ReportPlus.

E.1.3. Electrochemical Measurements

The clathrate powder was prepared into slurries by mixing the clathrate sample with 10 wt% carbon black (to serve as conducting additive) and 10 wt% polyvinylidene difluoride (PVDF) (to serve as binder) in N-methyl pyrrolidone (NMP) as solvent. β-Sn powder (Sigma Aldrich, 10 microns, 99%) was used as-received and prepared with using 5 wt% carbon black and 5 wt% PVDF for comparison to the clathrate samples. The slurries were stirred overnight and coated onto Cu foil current collectors using a Meyer rod, followed by heating at 120 ^{o}C to remove the solvent.

For cycling experiments, the electrodes were evaluated in CR2302 coin cells with Li metal as the counter electrode, Celgard 2500 as separator, and 1 M $LiPF_6$ in EC:DMC:DEC, 4:3:3 by volume, with VC additive (LBC3051C, MTI) as the electrolyte. Electrochemical testing was performed using a Biologic VMP3 galvanostat/potentiostat. Galvanostatic measurements were performed from 0.01 – 2.5 V vs. Li/Li^+. After the cell was lithiated to the desired amount, it was allowed to relax at open circuit for 5 hours prior to disassembly. Two to three repeats of a single electrochemical experiment were conducted to provide enough lithiated powder for structural characterization.

For preparing lithiated samples for total scattering measurements, the composite electrodes were evaluated in pouch cells rather than coin cells. After the electrochemical lithiation was complete, the pouch cell was taken into an argon-filled glovebox and

opened. The electrode was then immersed in 10 mL of dimethyl carbonate for 30 seconds to wash off any excess battery electrolyte. After the electrode was dry, the lithiated powder was scraped off the copper current collector using a knife. The extracted powder was then crushed in a mortar with a pestle to break up any agglomeration. The powder was sealed in a 2 mL centrifuge tube and then sealed under argon in a polyfoil bag before shipping to the synchrotron facility.

E.1.4. Pair Distribution Function (PDF) Analysis

Lithiated powders were loaded into 0.8 mm diameter borosilicate capillaries and sealed with wax and superglue inside an argon-filled glovebox, while pristine powders were loaded into the capillaries in ambient conditions. PDF measurements were performed at Diamond Light Source (Didcot, United Kingdom) at the I15-I dedicated PDF beamline with 76 keV X-rays (wavelength of 0.161669 Å) and 2D PerkinElmer image plate detectors. The detector geometry allowed collection of total scattering data to $Q = 30$ Å^{-1}. Ex situ PDF measurements were carried out at room temperature. The in situ PDF heating measurements were carried out from 300 – 450 K (temperature interval of 10 K) using an Oxford Instruments Cryojet 5. After reaching each hold temperature, there was a 1.5 min equilibration period and then the scattering data were collected with a 5 minute collection time. The heating temperature was limited to 450 K to avoid decomposition of the PVDF binder in the composite electrodes.

PDFs were generated from the total scattering data using PDFgetx3[221] within the xPDFsuite software package,[222] wherein the measured total scattering intensities, I(Q),

are corrected to obtain the coherent scattering, $I_c(Q)$, and transformed into the structure function, $S(Q)$, according to equation 1,[221]

$$S(Q) = \frac{I_c(Q) - \langle f(Q)^2 \rangle + \langle f(Q) \rangle^2}{\langle f(Q) \rangle^2} \quad (1)$$

where $f(Q)$ is the atomic scattering factor, which is averaged over all atom types in the sample. The PDF, $G(r)$, is obtained from the Fourier transform of $S(Q)$ as shown in equation 2:

$$G(r) = \frac{2}{\pi} \int_{Q_{min}}^{Q_{max}} Q[S(Q) - 1] \sin(Qr)\, dQ \quad (2)$$

To generate the PDFs, the following parameters were used: Q_{min} = 0.5 Å^{-1}, Q_{max} = 25 Å,$^{-1}$ r_{step} = 0.1 Å, and r_{poly} = 0.9. The nominal composition for lithiated samples was obtained from the charge passed during the electrochemical measurements.

PDF refinements were carried out using PDFgui.[68] No attempts were made to consider the presence of binder, carbon black, or SEI components in the samples. Previous reports have shown that these components add negligible contribution to the PDF data.[318] PDF refinements were performed using Q_{damp} = 0.0247 and Q_{broad} = 0.0151 (obtained from refinement of a NIST Si standard). To refine a PDF pattern, the major phase of the pattern was first selected and then scale factor and lattice parameter were refined. Then the atomic displacement parameters (ADP) for each element (initially set to 0.03 Å^2) and the linear atomic scale factor (delta1) were allowed to be refined. If this resulted in an insufficient fit, possible secondary phases were added and refined in a similar way. In some cases, the Li ADP refined to very large values (0.5 – 1 Å^2). If this occurred, the Li ADP was fixed to a lower value. Unphysical ADPs for Li have been

reported previously and is an indication of disorder/partial occupancy or atomic substitution.[319] The refinements were conducted using the following structures for the fittings: $Ba_8Ga_{14.9}Sn_{31.1}$ ($I\bar{4}3m$), β-Sn ($I4_1/amd$, ICSD-252800),[329] LiSn (P2/m, ICSD-104782),[246] Li_7Sn_3 ($P2_1/m$, ICSD-104785),[254] and Li_7Sn_2 (Cmmm, ISCD-104784).[330]

E.1.5. Powder X-ray Diffraction (XRD)

Powder X-ray diffraction was performed with a Bruker D8 diffractometer with Cu X-ray source operated at 40 kV and 40 mA with standard Bragg-Brentano diffraction geometry. For air-sensitive samples, the sample was covered with a Kapton film in an argon-filled glovebox prior to diffraction measurements. The Kapton film resulted in a broad amorphous background from $15^o < 2\theta < 25^o$.

E.1.6. Scanning Electron Microscopy

Scanning electron microscopy (SEM) imaging was performed using an XL 30 ESEM-FEG microscope and a 20 kV electron beam. The electrodes were cut from copper foil and mounted on SEM stubs with carbon tape.

E.1.7. Density Functional Theory (DFT) Calculations

The first-principles DFT calculations were performed to explore Li insertion and migration in the type VIII clathrate using a similar manner as in our previous work[55,152,179]. The calculations were carried out using the VASP code[77,78], the PBE functional[73], and projector augmented wave (PAW) potentials with a plane wave basis set[78]. In the PAW potentials, the Sn 5p and 4d, Ba 5s, 5p, and 6s, Ga 4p and 3d and Li 1s and 2s electrons were treated as valence electrons. The kinetic energy cutoff for the plane

wave basis set was chosen to be 400 eV and the reciprocal space was sampled with the Monkhorst pack meshes 3 × 3 × 3 centered at Γ. The $Ba_8Ga_{15}Sn_{31}$ structure was created by starting with the Ba_8Sn_{46} using the atomic positions obtained from the single crystal refinement. Then, the Sn atoms were replaced with Ga using the fractional occupancies derived from the single crystal refinement. The distribution of Ga on the four Wyckoff sites (24g : 12d : 8c : 2a) was chosen to be 7 : 3 : 5 : 0 while minimizing Ga–Ga bonds. The convergence criteria for the electronic and ionic relaxations were set to be 0.01 and 0.1 meV, respectively. The geometric optimization was performed in two steps. First, the unit cell volume was optimized without the constraint of the cubic symmetry. Then the relaxed lattice constant, taken from the relaxed volume, was used in a second step where only ionic relaxation was allowed under the cubic symmetry constraint. The crystal structures with the ionic positions of the second step are reported.

The formation energy was calculated as described previously.[53,152] The energies used for the elemental energies of Ba, Sn, and Ga were –1.923 eV/atom, –3.972 eV/atom, and –3.0281 eV/atom, respectively. The formation energy was determined using equation 3:

$$E_{form} = \frac{E(Ba_xGa_ySn_z) - xE(Ba) - yE(Ga) - zE(Sn)}{x+y+z} \qquad (3)$$

where $E(Ba_xGa_ySn_z)$ is the calculated energy of the Ba-Ga-Sn clathrate, $E(Ba)$ $E(Ga)$ and $E(Sn)$ are the total energy per atom of bulk Ba, Ga, and Sn, respectively. The Gibbs free energy change of reaction (ΔG_r) and the average voltage were calculated as described previously.[55,152,179] The formulas used for calculating the Gibbs free energy

change and average voltage for insertion of a single Li atom into $Ba_8Ga_{15}Sn_{31}$ are shown in equation (4) and (5), respectively:

$$\Delta G_r = E(LiBa_8Ga_{15}Sn_{31}) - E(Ba_8Ga_{15}Sn_{31}) - E(Li) \qquad (4)$$

$$V(x) = -\Delta G_r \qquad (5)$$

where $E(LiBa_8Ga_{15}Sn_{31})$ and $E(Ba_8Ga_{15}Sn_{31})$ are the total free energies for the lithiated and unlithiated clathrate systems and $E(Li)$ is the energy per atom in Li metal. The calculated values for $E(Li)$ is –1.904 eV/atom. A negative ΔG_r (i.e. positive voltage) represents a spontaneous reaction relative to Li metal, suggesting the feasibility of lithiation in a half cell with Li metal as the counter electrode. All crystal structure figures were created with Diamond 4.5.3.

The climbing image nudged elastic band (NEB) method was used to calculate the Li migration barriers[85]. For the NEB calculations Monkhorst pack meshes 3 × 3 × 3 centered at Γ were used. All NEB calculations used a linear interpolation as the starting configurations with 7 intermediate images between the beginning and ending images. The images were converged until the force on each image was below 0.03 eV/Å.

E.1.8. Synthesis and Characterization of Type I Clathrate $K_8Li_xGe_{46-x}$

The $K_8Li_xGe_{46-x}$ clathrate was synthesized using Liang's method.[143] The as-made sample was ground by hand and then washed three times with water. After heating overnight at 50 °C under vacuum to remove the moisture, the powder was prepared into slurries with 10 wt% carbon black and 10 wt% PVDF in NMP solvent. The slurries were stirred overnight and coated onto Cu foil current collectors using a Meyer rod, and then

heated at 120 °C to remove the solvent. Half-cells were assembled using Li metal as the counter electrode in the glovebox. Electrochemical testing was performed using a Biologic VMP3 galvanostat/potentiostat. Galvanostatic measurements were performed from 0.01 – 2.5 V vs. Li/Li^+ range using a current density of 25 mA/g, while potentiostatic measurements were performed within the same voltage range using a current density of 100 mA/g.

E.2. List of Tables

Table E.1 Crystallographic data for $Ba_8Ga_{14.9}Sn_{31.1}$ from single crystal XRD

Empirical Formula	$Ba_8Ga_{14.9}Sn_{31.1(1)}$
Formula Weight	5829.30
Temperature (K)	200(2)
Radiation, λ	MoK_a, 0.71073Å
Crystal System	Cubic
Space Group, Z	$I\bar{4}3m$ (no. 217), Z = 1
a/Å	11.5887(9)
V/Å^3	1556.3(4)
$\rho_{calc.}$/ g cm^{-3}	6.22
m/cm^{-1}	234.9
R_1 ($I>2\sigma_I$)[a]	0.0192
wR_2 ($I>2\sigma_I$)[a]	0.0330
R_1 (all data)	0.0216
wR_2 (all data)	0.0335
Largest diff. Peak & hole / e$^-$ Å^{-3}	0.65 / -0.55
Goodness of Fit (Gof)	1.143

[a] $R_1 = \sum||F_o| - |F_c||/\sum|F_o|$; $wR_2 = [\sum[w(F_o^2 - F_c^2)^2]/\sum[w(F_o^2)^2]]^{1/2}$, where $w = 1/[\sigma^2F_o^2 + (0.0084\cdot P)^2 + (2.831\cdot P)]$, and $P = (F_o^2 + 2F_c^2)/3$. CIF has been deposited with the CCDC database with a reference number 2071610.

Table E.2 Atomic coordinates, occupancies, and equivalent isotropic displacement parameters (U_{eq}[a]) of $Ba_8Ga_{14.9}Sn_{31.1}$ from single crystal XRD refinement

Atom	Wyckoff Site	x	y	z	Occupancy	U_{eq} (Å^2)
Ba	8c	0.31513(7)	x	x	1	0.0345(5)
Sn1	24g	0.08429(5)	x	0.35137(6)	0.70(1)	0.0141(2)
Ga1	24g	0.08429(5)	x	0.35137(6)	0.30(1)	0.0141(2)
Sn2	12d	1/4	1/2	0	0.85(2)	0.0182(4)
Ga2	12d	1/4	1/2	0	0.15(2)	0.0182(4)
Sn3	8c	0.13423(7)	x	x	0.33(2)	0.0126(5)
Ga3	8c	0.13423(7)	x	x	0.67(2)	0.0126(5)
Sn4	2a	0	0	0	0.78(3)	0.0100(8)
Ga4	2a	0	0	0	0.22(3)	0.0100(8)

[a] U_{eq} is defined as one third of the trace of the orthogonalized U_{ij} tensor.

Table E.3 Refinement parameters for PDF refinement of pristine clathrate sample fit to Type VIII $Ba_8Ga_{15}Sn_{31}$ and β-Sn. The refinement plot is presented in Figure 4.2.2c.

	Pristine $Ba_8Ga_{15}Sn_{31}$	
Phase	Type VIII $Ba_8Ga_{15}Sn_{31}$	β-Sn
Space Group	$I\bar{4}3m$	$I4_1/amd$
Phase Fraction	0.976	0.024
Lattice Parameters (Å)	a = 11.596	a = 5.767 c = 3.160
Delta 1	1.83	2.00*
Atomic displacement parameters (U_{11}= U_{22}= U_{33}, Å^2)	Ba = 0.044 Ga/Sn = 0.019	Sn = 0.014*
R_w	0.151	

*These parameters were fixed during the refinement due to resulting in unphysical values if not fixed.

Table E.4 The voltage and capacity corresponding to the lithiated type VIII $Ba_8Ga_{15}Sn_{31}$ and β-Sn samples used for PDF measurements (corresponding to the points indicated in Figure 4.2.3). The number of Li inserted was normalized to the amount of Sn or (Ga + Sn) in the starting compound.

Electrode	# of Li inserted	Voltage (V vs. Li/Li^+)	Capacity (mAh/g)
$Ba_8Ga_{15}Sn_{31}$	1.5 Li	0.213	320
	2.0 Li	0.171	427
	3.2 Li	0.010	683
β-Sn	1.5 Li	0.440	338
	2.0 Li	0.387	451
	2.5 Li	0.236	584
	3.4 Li	0.010	767

Table E.5 PDF refinement parameters of best fits for β-Sn, $Li_{1.5}Sn$, $Li_{2.0}Sn$, $Li_{2.5}Sn$, $Li_{3.4}Sn$ samples. Plots of the refinements are presented in Figure E.4-5.

	Pristine	$Li_{1.5}Sn$		$Li_{2.0}Sn$		$Li_{2.5}Sn$	$Li_{3.4}Sn$	
Phase	β-Sn $I4_1/amd$	LiSn $P2/m$	Li_7Sn_3 $P2_1/m$	LiSn $P2/m$	Li_7Sn_3 $P2_1/m$	Li_7Sn_3 $P2_1/m$	Li_7Sn_3 $P2_1/m$	Li_7Sn_2 $Cmmm$
Phase Fraction	1	0.735	0.265	0.182	0.818	1	0.526	0.474
Lattice Parameters (Å)	a = 5.833 c = 3.180	a = 5.192 b = 3.176 c = 7.717	a = 8.516 b = 4.728 c = 9.446	a = 5.180 b = 3.190 c = 7.702	a = 8.587 b = 4.709 c = 9.457	a = 8.600 b = 4.704 c = 9.436	a = 8.557 b = 4.707 c = 9.479	a = 9.783 b = 13.885 c = 4.724
Delta 1	2.17	1.80	1.53	2.18	2.47	2.37	1.12	2.84
Atomic displacement parameters (U_{11}= U_{22}= U_{33}, $Å^2$)	Sn = 0.023	Li = 0.023 Sn = 0.016	Li = 0.076 Sn = 0.011	Li = 0.044 Sn = 0.013	Li = 0.238 Sn = 0.017	Li = 0.249 Sn =0.019	Li = 0.1* Sn = 0.018	Li = 0.1* Sn = 0.023
R_w	0.102	0.159		0.115		0.139	0.199	

*Refinement of the ADP for Li in both cases resulted in unreasonably high values so it was fixed.

Table E.6 PDF refinement parameters of fits for the lithiated clathrate samples to different phase combinations. Plots of the refinements are presented in Figure E.6.

	$Li_{1.5}Ba_{0.17}Ga_{0.33}Sn_{0.67}$		$Li_{2.0}Ba_{0.17}Ga_{0.33}Sn_{0.67}$	$Li_{3.2}Ba_{0.17}Ga_{0.33}Sn_{0.67}$
Phase	Type VIII $Ba_8Ga_{15}Sn_{31}$ $I\bar{4}3m$	Li_7Sn_3 $P2_1/m$	Li_7Sn_3 $P2_1/m$	Li_7Sn_3 $P2_1/m$
Phase Fraction	0.306	0.694	1	1
Lattice Parameters (Å)	a = 11.593	a = 8.518 b = 4.685 c = 9.469	a = 8.435 b = 4.697 c = 9.513	a = 8.456 b = 4.685 c = 9.603
Delta 1	2.12	2.00*	2.00*	2.00*
Atomic displacement parameters (U_{11}= U_{22}= U_{33}, Å^2)	Ba = 0.04 Ga/Sn = 0.0236	Li = 0.05* Sn = 0.025*	Li = 0.02* Sn = 0.02*	Li = 0.02* Sn = 0.02*
R_w	0.493		0.820	0.855

*These parameters were fixed during the refinement due to resulting in unphysical values if not fixed.

E.3. List of Figures

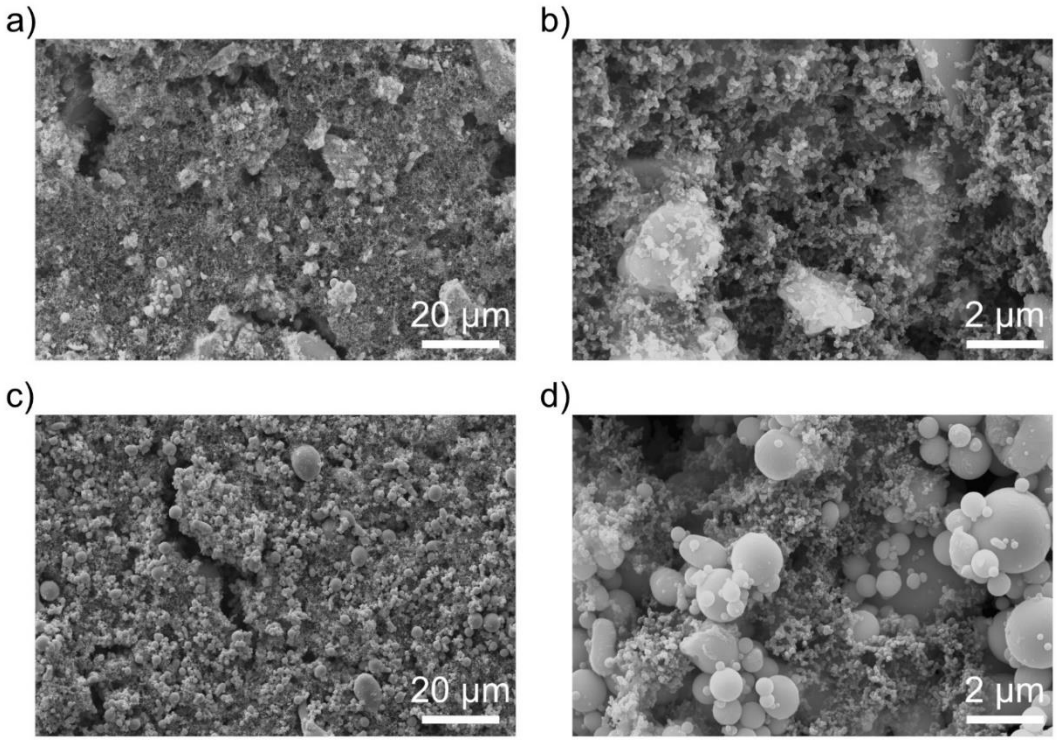

Figure E.1 SEM images of the composite electrodes made from (a,b) type VIII $Ba_8Ga_{15}Sn_{31}$ clathrate, and (c,d) β-Sn prior to electrochemical lithiation. The small, nanosized particles are the carbon black conducting additive used to improve electronic conductivity throughout the composite electrode.

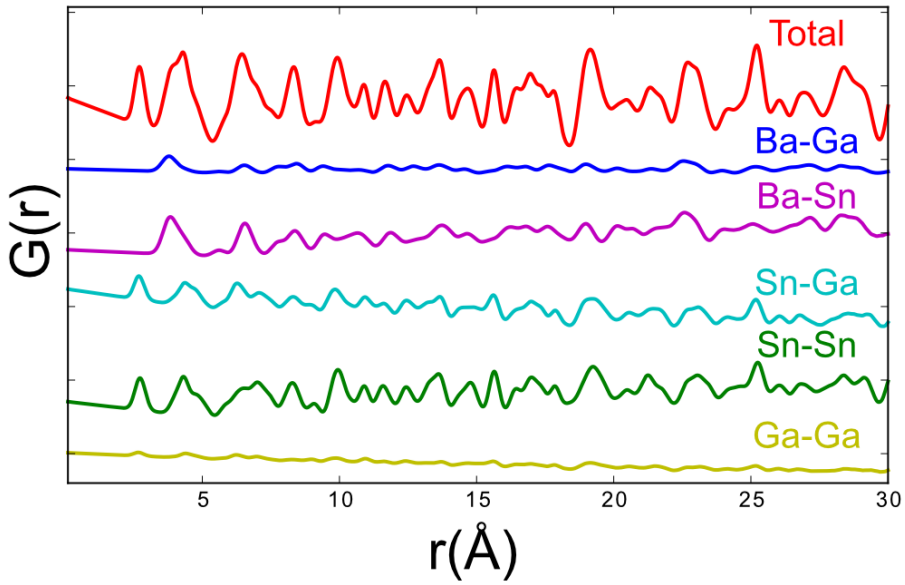

Figure E.2 Calculated total and partial PDF patterns for type VIII clathrate $Ba_8Ga_{15}Sn_{31}$.

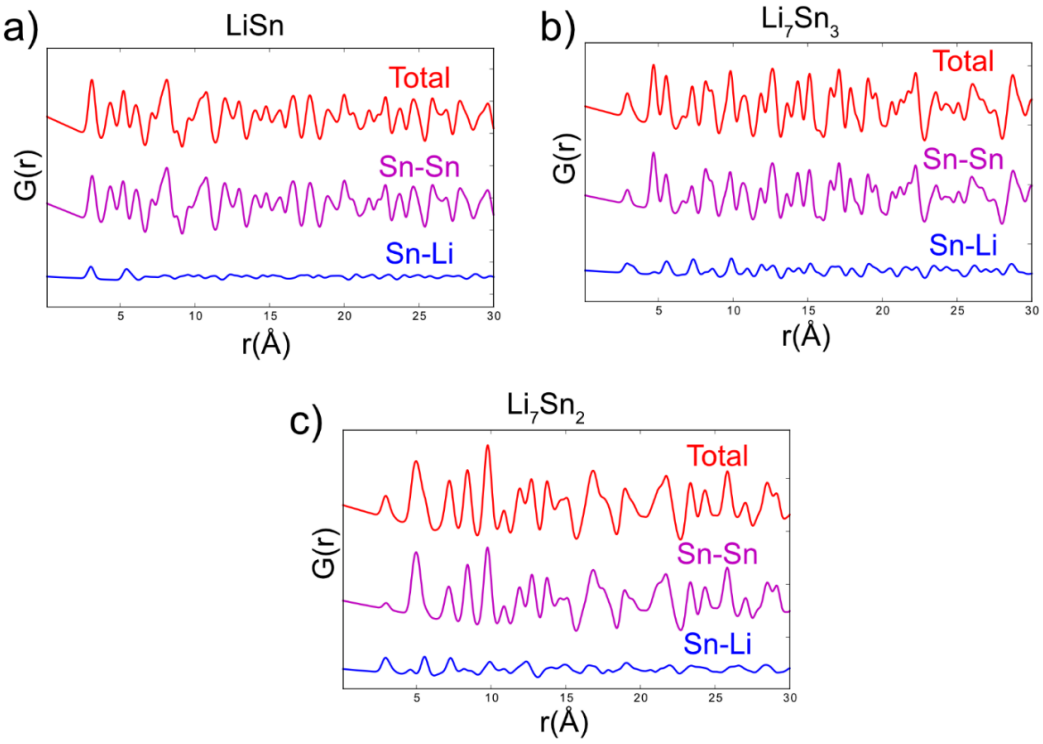

Figure E.3 Calculated total and partial PDF patterns for (a) LiSn, (b) Li_7Sn_3, and (c) Li_7Sn_2.

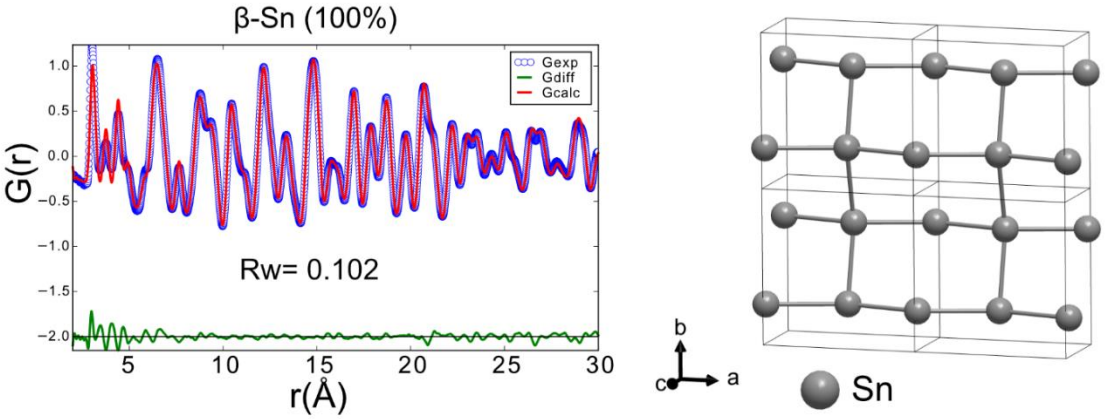

Figure E.4 PDF refinement and crystal structure of pristine β-Sn

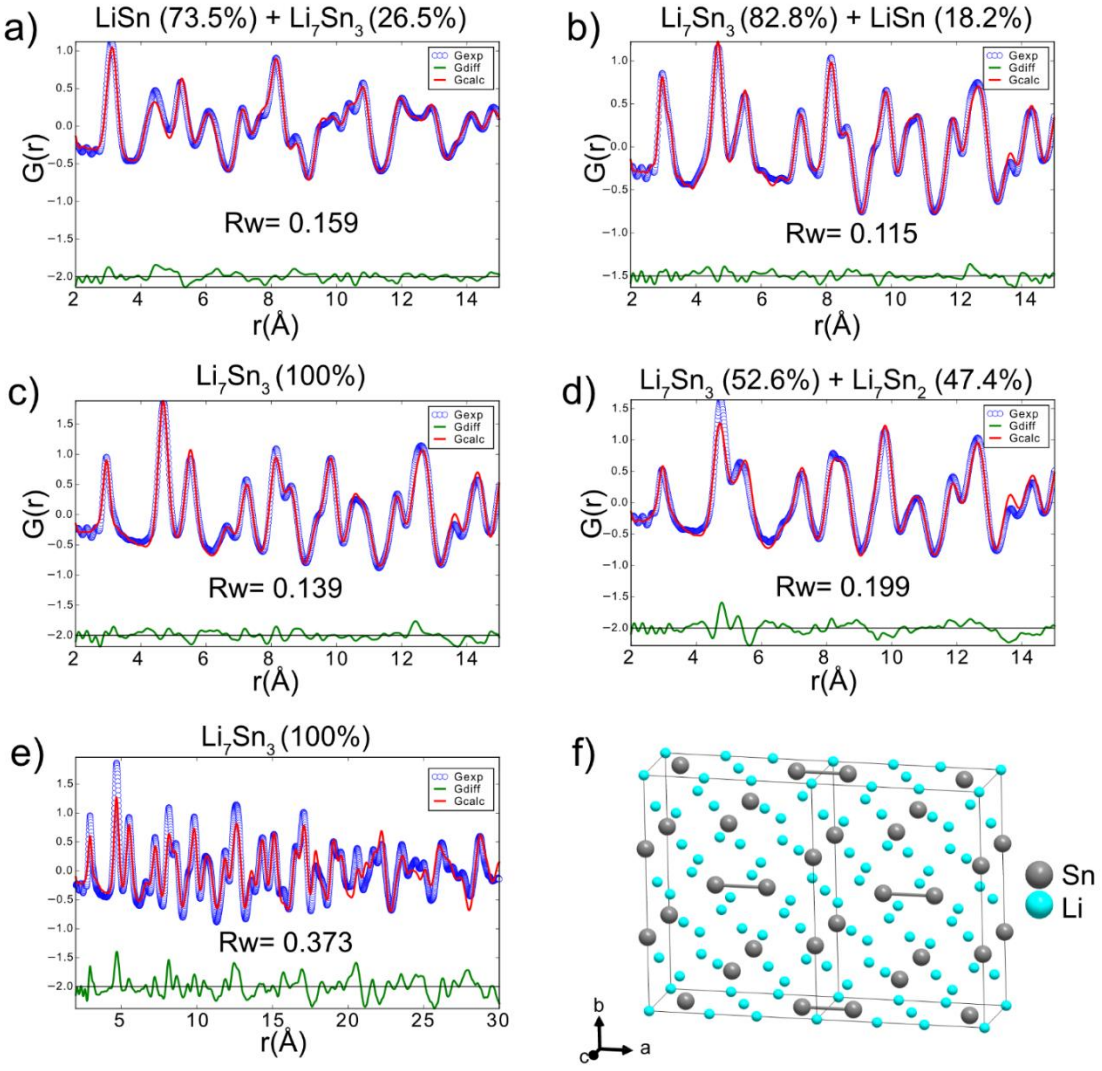

Figure E.5 PDF refinements of the lithiated β-Sn PDF patterns at compositions of (a) $Li_{1.5}Sn$ (b) $Li_{2.0}Sn$, (c) $Li_{2.5}Sn$ and (d) $Li_{3.4}Sn$. (e) $Li_{2.5}Sn$ fit from 2 – 30 Å. The phases used in the fitting and corresponding mol% from the refinements are shown above each plot. (f) Crystal structure of Li_7Sn_2.

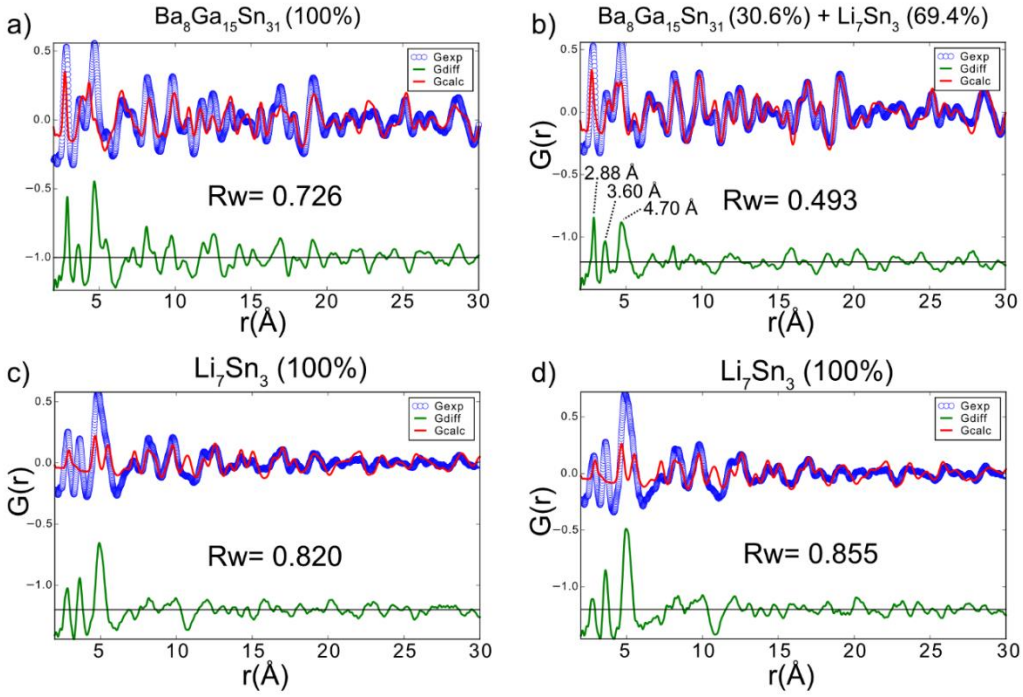

Figure E.6 PDF refinements of the lithiated type VIII clathrate PDF patterns at composition of (a),(b) $Li_{1.5}Ba_{0.17}Ga_{0.33}Sn_{0.67,}$ (b) $Li_{2.0}Ba_{0.17}Ga_{0.33}Sn_{0.67}$, and (c) $Li_{3.2}Ba_{0.17}Ga_{0.33}Sn_{0.67}$. The phases used in the fitting and corresponding mol% from the refinements are shown above each plot.

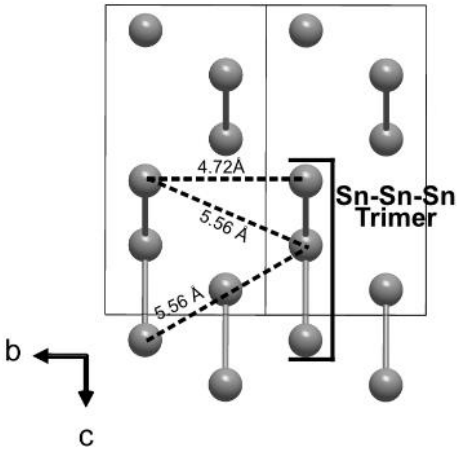

Figure E.7 Crystal models schematic of Li_7Sn_3 showing only the Sn atoms viewed down the [100] direction. The dashed lines show the distances that correspond to the two split peaks in the PDF of Li_7Sn_3.

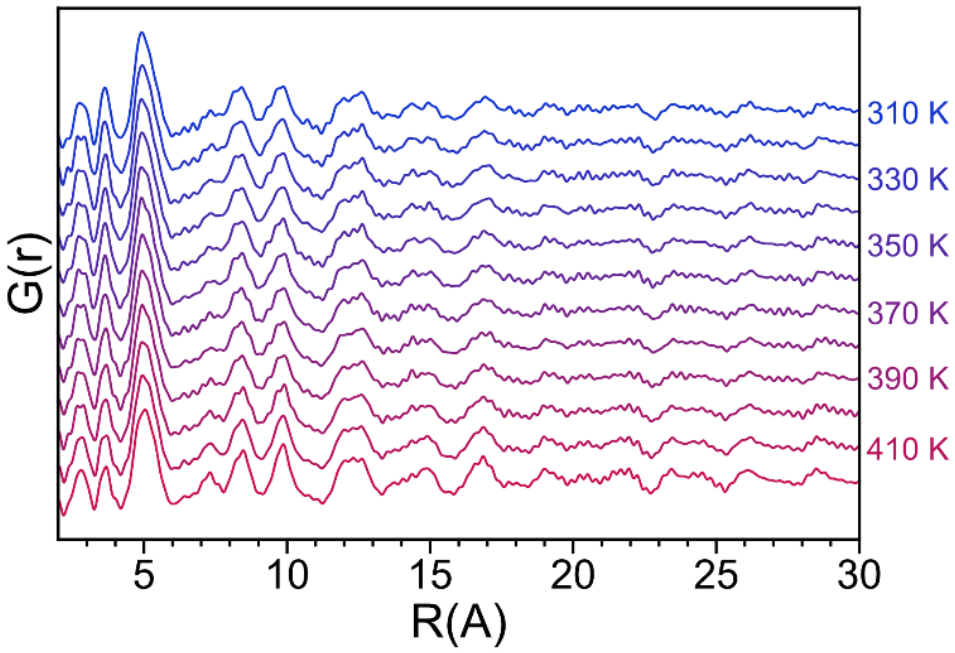

Figure E.8 Variable temperature (310 K- 420 K) PDF of the fully lithiated type VIII clathrate ($Li_{3.2}Ba_{0.17}Ga_{0.33}Sn_{0.67}$). An interval of 10 K and a 5 minute hold at each temperature was used.

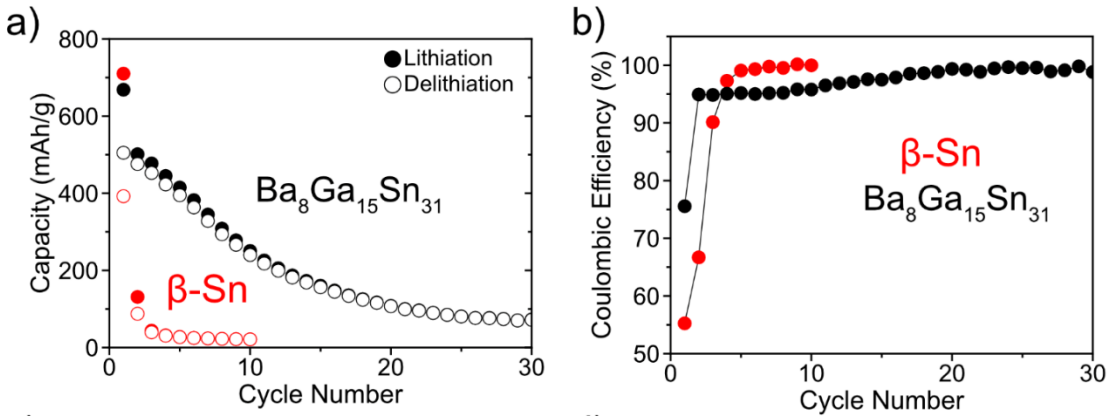

Figure E.9 (a) Capacity and (b) Coulombic efficiency vs. cycle number for β-Sn and type VIII $Ba_8Ga_{15}Sn_{31}$ clathrate electrodes in half-cells cycled at 12.5 mAh/g with a voltage range of 0.01 – 2.5 V vs. Li/Li^+.

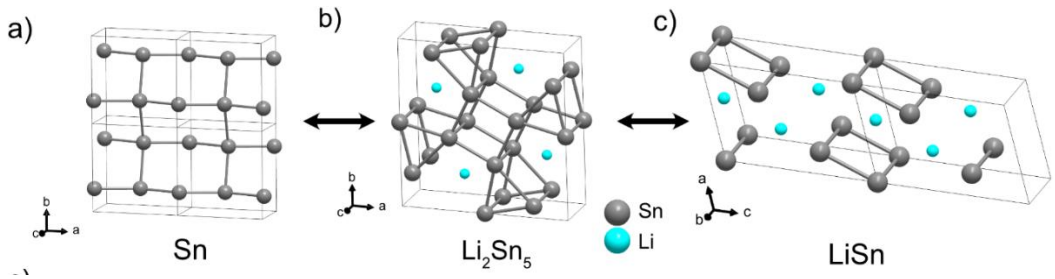

Figure E.10 Crystal structures of (a) β-Sn, (b) Li_2Sn_5 and (c) LiSn. The common square Sn unit between the three structures has been suggested to make these phase transformations kinetically facile.

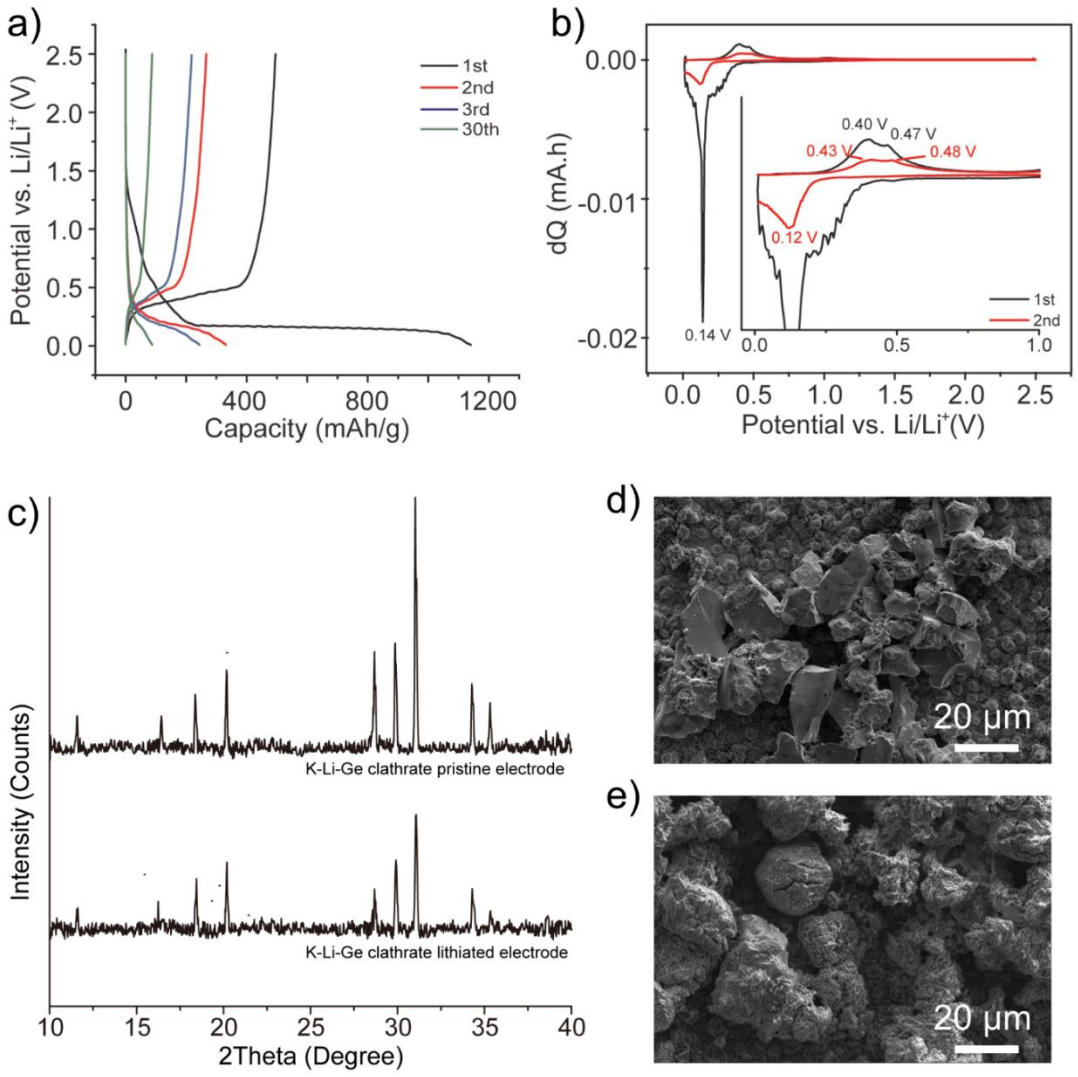

Figure E.11 (a) Galvanostatic cycling of $K_8Li_xGe_{46-x}$ electrodes at 25 mA/g. (b) dQ plot derived from potentiostatic measurements with a current limit of a 100 mA/g. (c) PXRD of the clathrate electrodes before and after full lithiation. SEM images of the clathrate electrode (d) before and (e) after lithiation.

APPENDIX F

SUPPORTING INFORMATION FOR CHAPTER 4.3

F.1. Experimental Procedures

F.1.1 Synthesis of type II silicon clathrates

The synthesis of the type II Si clathrate was carried out by the thermal decomposition of Na_4Si_4 under vacuum using the sampe procedure as our previous report.[244] The Na_4Si_4 precursor was synthesized by combining Na and Si in 1.2 : 1 molar ratio in a Nb tube in an argon-filled glove box. The Nb tube was taken out of the glovebox and arc-welded shut under an argon atmosphere. The Nb tube was then sealed in a stainless-steel reactor in an argon-filled glovebox with copper gaskets. The stainless-steel reactor was taken out of the argon glove box and heated in a tube furnace. The Na-Si mixture was heated at 650 °C for 48 hours and then cooled down over 4 hours to room temperature. The Nb tube was opened in the glovebox and the large crystals were hand ground to a fine black powder with a mortar and pestle. Powder XRD of the Na_4Si_4 confirmed the phase purity of the precursor.

For the type II clathrate synthesis, a stainless-steel tube reactor was used to carry out the thermal decomposition of Na_4Si_4 under vacuum. The stainless-steel tube had 2.75-inch conflat flanges welded to the ends which allowed the tube to be sealed with copper gaskets. One side of the stainless-steel tube had a water cooled finger which provides a cold surface for Na condensation during the thermal decomposition[155]. The other side of the tube was connected to a gate valve which was connected to a turbomolecular pump. The type II clathrates were synthesized by loading 400-500 mg of the hand ground Na_4Si_4 powder into a Ta boat and placing it in the center of the stainless-steel tube inside an argon-filled glovebox. The gate valve was sealed, and the reactor was taken out of the

glovebox to the tube furnace and connected to the turbomolecular pump. The water-cooled finger was connected to a water chiller and water was circulated through the finger at a temperature of 5°C. Prior to heating, both the water cooling and dynamic vacuum were operational. To synthesize $Na_{0.3(1)}Si_{136}$, Na_4Si_4 was heated to 370 °C in 3.5 hours and held at 370 °C for 48 hours. Then, the temperature was increased to 425 °C in 30 minutes and held for an additional 72 hours and then cooled to room temperature.

To remove any residual Na_4Si_4, the powder was taken out of the glovebox and transferred to a fume hood, where ~10 mL ethanol was introduced rapidly to the powder from a wash bottle. Rapid bubbling would indicate the reaction of Na_4Si_4 with ethanol, since silicon clathrates are stable in air and water[155]. *Note: Extreme care must be taken and appropriate personal protective equipment must be used when working with Na_4Si_4 in ambient conditions due to its high reactivity to both air and water. After 5 minutes of reaction with the ethanol, the powder was then immersed in an ultrasonic bath to break up agglomerates. After the bubbling decreased in intensity, de-ionized water (~10 mL) was introduced to the powder and the resulting suspension was sonicated for additional time. *Caution: Do not add water directly to the powder containing Na_4Si_4 as it could lead to a fire. After all the bubbling had completed, the powder was recovered using vacuum filtration and then dried. The powder was then used for electrochemical experiments without any further processing.

F.1.2. Electrochemical measurements

The clathrate powder was prepared into slurries by mixing the clathrate sample with 10 wt% carbon black (to serve as conducting additive) and 10 wt% polyvinylidene difluoride (PVDF) (to serve as binder) in N-methyl pyrrolidone (NMP) as solvent. Hand ground 100 mesh Si powder (Sigma Aldrich 99.999%) was used to prepare electrodes for comparison to the clathrate samples. The slurries were stirred overnight and coated onto Cu foil current collectors using a Meyer rod, and then heated at 120 ^{o}C to remove the solvent. Electrodes were cut into circles 18mm in diameter and typically had a mass loading of 4-4.5 mg/cm$^{2.}$ The clathrate composite electrodes were evaluated in pouch cells with Li metal as the counter electrode, Celgard 2500 as separator, and 1 M $LiPF_6$ in EC:DMC:DEC, 4:3:3 by volume, with VC additive (LBC3051C, MTI) as the electrolyte. Electrochemical testing was performed using a Biologic VMP3 galvanostat/potentiostat. Galvanostatic measurements were performed at 25 mA/g from 0.01 – 2.5 V vs. Li/Li^{+}. To provide sufficient lithiated powder for structural characterization, samples from 2-3 cells prepared and electrochemically lithiated in the same manner were combined.

F.1.3. Sample preparation for synchrotron measurements

After the electrochemical lithiation was complete, the pouch cell was taken into the argon-filled glovebox and opened. The electrode was then immersed in 10 mL of dimethyl carbonate for 30 seconds to wash off any excess battery electrolyte. After the electrode was dry, the lithiated powder was scraped off the copper current collector using a knife. The extracted powder was then crushed in a mortar and pestle to break up any agglomeration. The powder was sealed in a 2 mL centrifuge tube and then sealed under argon in a polyfoil bag before shipping to the synchrotron facility.

F.1.4. Pair distribution function (PDF) analysis

Lithiated powders were loaded into 0.8 mm diameter borosilicate capillaries and sealed with wax and superglue inside an argon-filled glovebox, while pristine powders were loaded into the capillaries in ambient conditions. PDF measurements were performed at Diamond Light Source (Didcot, United Kingdom) at the I15-I dedicated PDF beamline with 76 keV X-rays (wavelength of 0.161669 Å) and 2D PerkinElmer image plate detectors. The detector geometry allowed collection of total scattering data to $Q = 30$ Å^{-1}. Ex situ PDF measurements were carried out at room temperature.

PDFs were generated from the total scattering data using PDFgetx3[221] within the xPDFsuite software package,[222] wherein the measured total scattering intensities, $I(Q)$, are corrected to obtain the coherent scattering, $I_c(Q)$ and transformed into the structure function, $S(Q)$, according to equation 1,[221]

$$S(Q) = \frac{I_c(Q) - \langle f(Q)^2 \rangle + \langle f(Q) \rangle^2}{\langle f(Q) \rangle^2}$$

where $f(Q)$ is the atomic scattering factor, which is averaged over all atom types in the sample. The PDF, $G(r)$, is obtained from the Fourier transform of $S(Q)$ as shown in equation 2:

$$G(r) = \frac{2}{\pi} \int_{Q_{min}}^{Q_{max}} Q[S(Q) - 1] \sin(Qr)\, dQ$$

To generate the PDFs, the following parameters were used: $Q_{min} = 0.5$ Å^{-1}, $Q_{max} = 18$ Å,$^{-1}$ $r_{step} = 0.1$ Å, and $r_{poly} = 0.9$. Although the detector allowed for a higher Q_{max}, 18 Å^{-1} was chosen to generate the PDFs to minimize the noise due to the low signal originating

from the low atomic number Li-Si samples. The nominal composition for lithiated samples was obtained from the charge passed during the electrochemical measurements.

PDF refinements were carried out using PDFgui[68]. No attempts were made to consider the presence of binder, carbon black, or SEI components in the samples. Previous reports have shown that these components add negligible contribution to the PDF data.[318] PDF refinements were performed using Q_{damp} = 0.0247 and Q_{broad} = 0.0151 (obtained from refinement of a NIST Si standard). To refine a PDF pattern, the major phase of the pattern was first selected and then scale factor and lattice parameter were refined. Then the atomic displacement parameters (ADP) for each element (initially set to 0.03 $Å^2$) and the linear atomic scale factor (delta1) were allowed to be refined. If this resulted in an insufficient fit, possible secondary phase were added and refined in a similar way. In some cases, the nanoparticle amplitude correction parameter (Spdiameter) was incorporated to improve the fit. For the refinement of 10 mV electrodes that contained $Li_{15}Si_4$, the residual Si-Si bonds were incorporated into the refinement by using an α-Si phase with a Spdiameter of 4 Å. The refinements were conducted using the following structures for the fittings: $Na_{11.2}Si_{136}$ ($Fd\bar{3}m$, Na occupancy set to 1)[190], α-Si ($Fd\bar{3}m$),[277] $Li_{15}Si_4$ ($I\bar{4}3d$)[231].

F.1.5. Powder X-ray diffraction (XRD)

Synchrotron XRD was performed at the P02.1 Powder Diffraction and Total Scattering Beamline at PETRA III at the Deutsches Elektronen-Synchrotron (DESY) with 60 keV X-rays at a wavelength of 0.20733 Å. A Perkin Elmer XRD1621 was used

as the X-ray detector. The lithiated samples were loaded into 0.8 mm borosilicate capillaries in an argon-filled glovebox and sealed with wax.

Rietveld refinement was performed with Jana2006[64]. The peak shapes were described by the pseudo-Voigt function, background fit with Legendre polynomials, and atomic displacement parameters were modeled as isotropic. The starting structures for the refinement were: $Na_{11.2}Si_{136}$ ($Fd\bar{3}m$)[190] and Na_8Si_{46} ($Pm\bar{3}n$).[190] The Na atoms were refined by setting the isotropic displacement parameter based on previous literature value for each site. The Na1 (8b) site was set to 0.125 $Å^2$ while the Na2 (16c) was set to 0.02 $Å^2$.[186,290] Then the occupancies were refined. In the case of Na2, the occupancy was very close to 0 and therefore was set to 0 for the refinement.

F.2. List of Tables

Table F.1 Atomic coordinates and atomic displacement parameters for refinement of as-prepared clathrate sample (Na_1Si_{136}) corresponding to Figure F.1.

$Na_{0.3(1)}Si_{136}$		Lattice Parameter:	14.6484(8) Å			
Atom	Site	x/a	y/b	z/c	Occ.	U_{iso} ($Å^2$)
Na1	8b	3/8	3/8	3/8	0.034(8)	0.125
Na2	-	-	-	-	-	-
Si1	8a	1/8	1/8	1/8	1	0.0026(8)
Si2	32e	0.21771(8)	x	x	1	0.0088(6)
Si3	96g	0.06704(4)	x	0.37092(6)	1	0.0094(3)

Table F.2 Lithiation capacity and voltage for each electrode prepared for PDF analysis (corresponding to the points on the voltage profile in Figure 4.3.2.

α-Si			Na_1Si_{136} Type II Clathrate		
x in Li_xSi	Capacity (mAh/g)	Voltage (V vs. Li/Li^+)	x in Li_xSi	Capacity (mAh/g)	Voltage (V vs. Li/Li^+)
1.05	1000	0.094	1.05	1000	0.222
2.10	2000	0.071	2.10	2000	0.076
2.77	2650	0.055	2.60	2484	0.055
3.35	3201	0.010	3.26	3118	0.10

Table F.3 PDFgui refinement parameters for the pristine α-Si, 1000 mAh/g, 2000 mAh/g, 55 mV and 10 mV. The refinement plots can be found in Figure F.3 and 5.

	Pristine α-Si	1000 mAh/g	2000 mAh/g	55 mV	10 mV	
Phase	α-Si $Fd\bar{3}m$	α-Si $Fd\bar{3}m$	α-Si $Fd\bar{3}m$	α-Si $Fd\bar{3}m$	$Li_{15}Si_4$ $I\bar{4}3d$	α-Si $Fd\bar{3}m$
Mol Fraction	1	1	1	1	0.565	0.434
Lattice Parameter (Å)	a = 5.430	a = 5.427	a = 5.427	a = 5.426	a= 10.713	a = 5.306
Delta 1	2.05	2.03*	2.00*	2.0*	2.04	n/a
ADP*	Si: 0.006	Si: 0.005	Si: 0.005	Si: 0.005	Si: 0.018 Li: 0.057	Si: 0.007*
Spdiameter (Å)	n/a	n/a	n/a	n/a	95.53	4
R_w	0.091	0.213	0.354	0.775	0.254	

*Fixed during the refinement

Table F.4 PDFgui refinement parameters for the pristine Na_1Si_{136}, 1000 mAh/g, 2000 mAh/g and 10 mV. The refinement plots can be found in Figure F.3 and 5.

	Pristine Na_1Si_{136}	1000 mAh/g	2000 mAh/g	10 mV	
Phase	Si_{136} $Fd\bar{3}m$	Si_{136} $Fd\bar{3}m$	Si_{136} $Fd\bar{3}m$	$Li_{15}Si_4$ $I\bar{4}3d$	α-Si $Fd\bar{3}m$
Mol Fraction	1	1	1	0.491	0.509
Lattice Parameter (Å)	a = 14.636	a = 14.640	a = 14.650	a= 10.867	a = 5.371
Delta 1	1.93	n/a	n/a	2.97	n/a
ADP*	Si: 0.007	Si: 0.005	Si: 0.002	Si: 0.021 Li: 0.053	Si: 0.007*
Spdiameter (Å)	101.34	42.20	44.8	69.37	4
R_w	0.096	0.570	0.917	0.312	

*Fixed during the refinement.

F.3. List of Figures

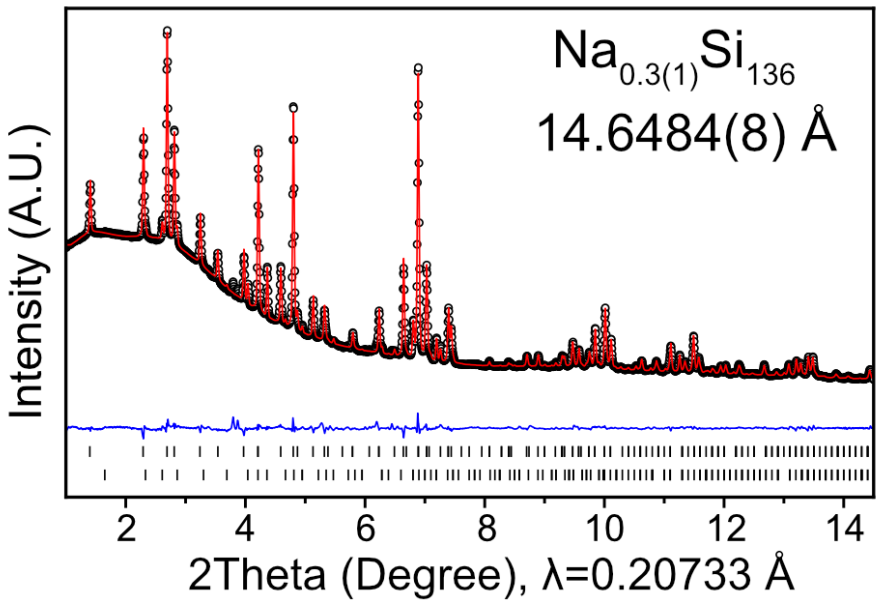

Figure F.1 Rietveld refinement of the PXRD patterns of the as-prepared clathrate (Na_1Si_{136}) sample investigated with ex situ total scattering measurements. The black circles represent the experimental pattern, the red curve represents the calculated pattern, and the blue curve represents the difference curve. The refined atomic positions, occupancies, and atomic displacement parameters can be found in Table F.1. The top tick marks represent the reflections corresponding to $Na_{0.3(1)}Si_{136}$ (94.59(12) wt%) and the bottom tick marks represent the impurity Na_8Si_{46} (5.41(10) wt%) phase. Refinement residuals: χ^2= 1.06, R_p= 0.012, and wR_p= 0.017.

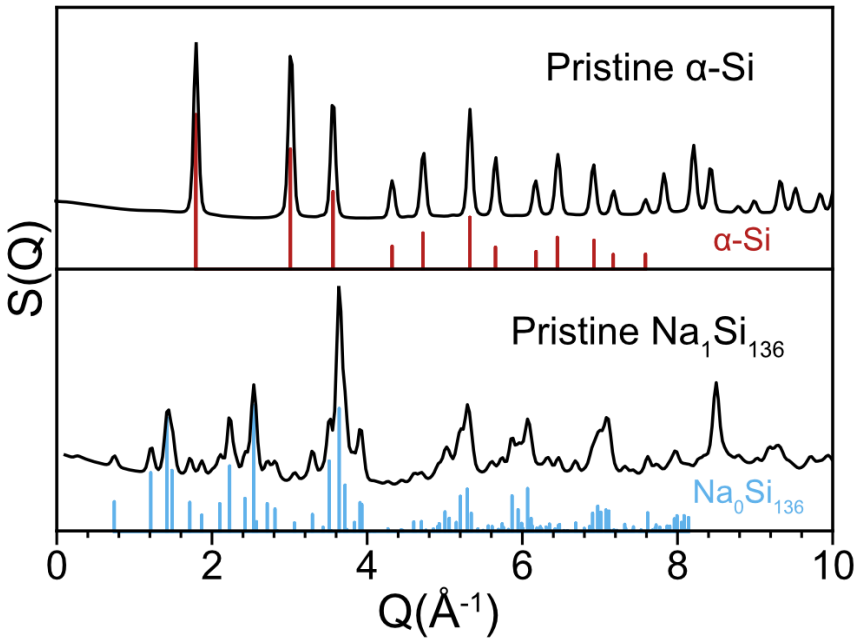

Figure F.2 Comparison of structure function plots for pristine α-Si and Na_1Si_{136} clathrate with their reference patterns.

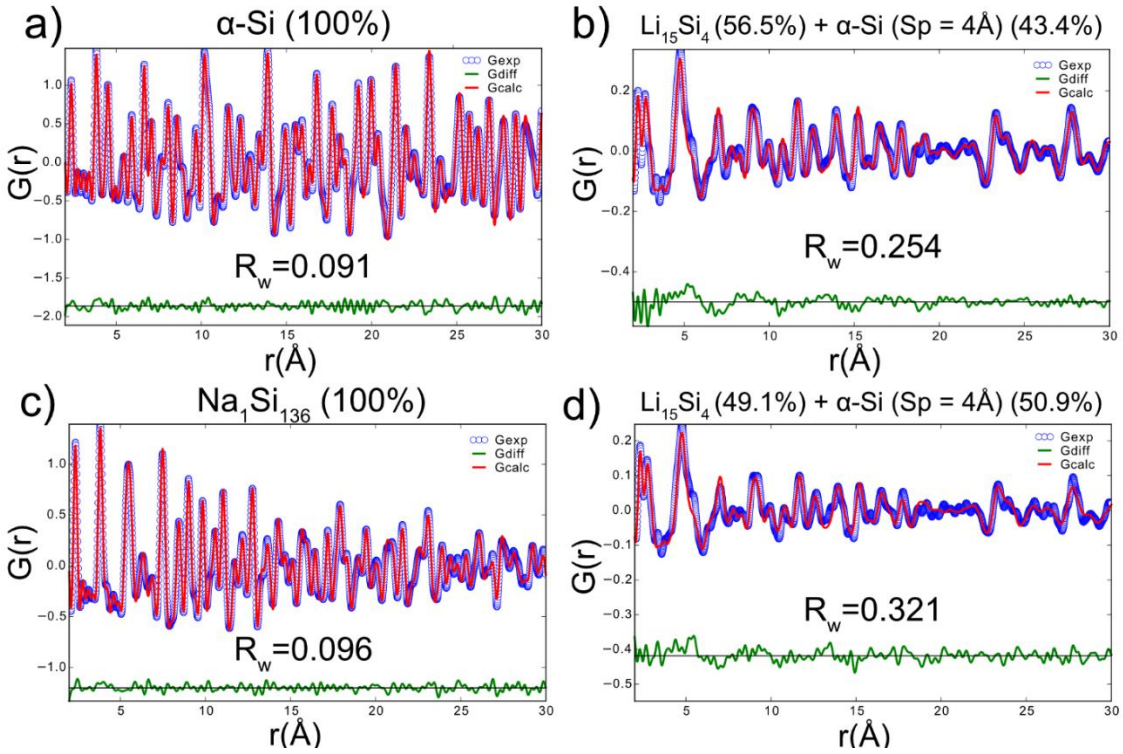

Figure F.3 (a) PDF refinement of pristine α-Si and (b) α-Si after lithiation to 10 mV vs. Li/Li^+ fit to $Li_{15}Si_4$. (c) PDF refinement of pristine type II Na_1Si_{136} clathrate and (d) Na_1Si_{136} clathrate after lithiation to 10 mV vs. Li/Li^+ fit to $Li_{15}Si_4$. To incorporate the residual Si-Si bonds in the refinements with $Li_{15}Si_4$, the nanoparticle amplitude correction factor (Sp parameter) was set to 4 Å, which only models the first Si-Si correlation of α-Si.

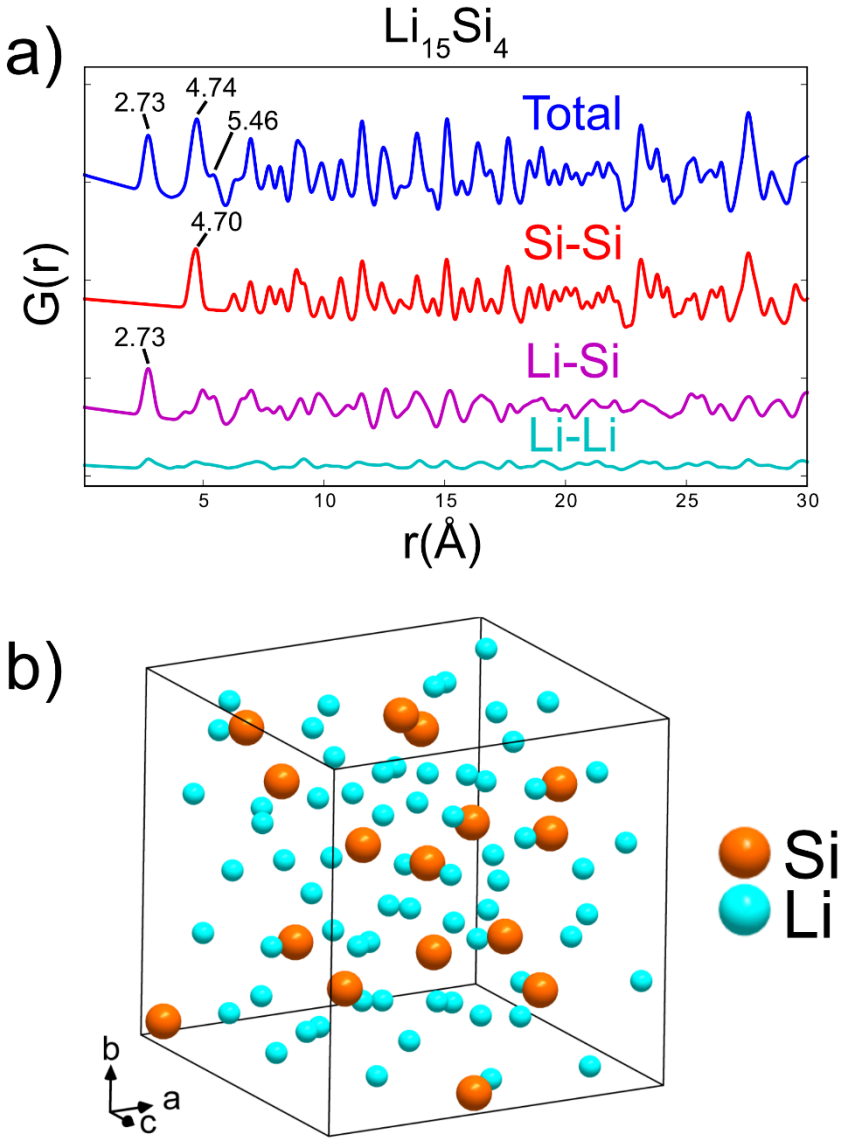

Figure F.4 (a) Calculated total and partial PDF patterns for $Li_{15}Si_4$. (b) Crystal structure of $Li_{15}Si_4$.

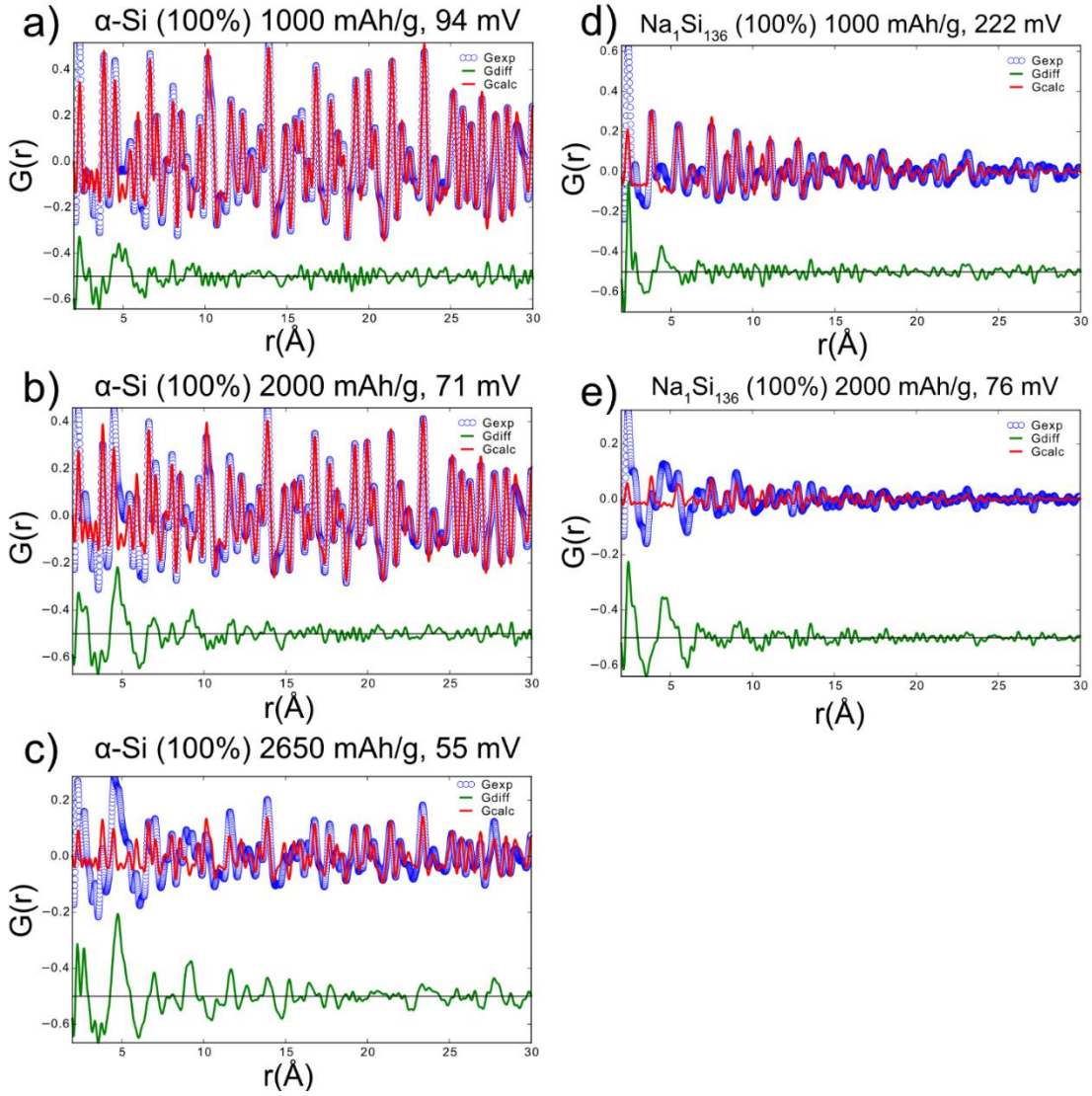

Figure F.5 Refinements of the PDFs from α-Si and type II Na_1Si_{136} clathrate after lithiation to different points in the two-phase region of the voltage profile. α-Si lithiated to (a) 1000 mAh/g (94 mV), (b) 2000 mAh/g (71 mV), (c) 2650 Ah/g (55 mV) with refinement fit to α-Si. Clathrate lithiated to (d) 1000 mAh/g (222 mV), (e) 2000 mAh/g (76 mV) with refinement fit to the type II structure. Voltages are referenced to Li/Li^+.

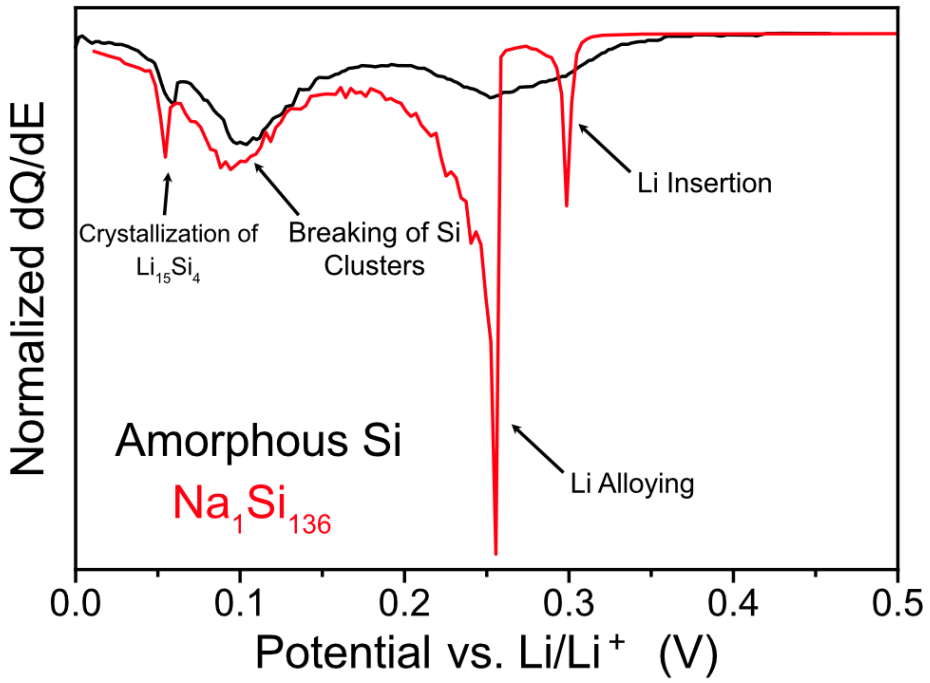

Figure F.6 Comparison of the dQ/dE plots of amorphous Si (black) and the type II Si clathrate, Na_1Si_{136} (red). The dQ/dE plot for amorphous Si* shows a broad peak from 0.35 – 0.2 V vs. Li/Li^+ associated with Li insertion into the amorphous Si to form an amorphous lithium silicide phase. The broad peak at 90 – 100 mV is attributed to the breaking up of larger Si clusters in favor of smaller Si units such as Si-Si dumbbells and single atoms.[35,117,279] The peak at 45 – 50 mV is attributed to the crystallization of the amorphous Li_xSi phase to crystalline $Li_{15}Si_4$.[117,276] In the first lithiation of the type II Si clathrate, the dQ/dE plot shows a sharp peak at 0.30 V associated with topotactic Li insertion into the clathrate cages to form $Li_{32}Si_{136}$,[244] and then another sharp peak at 0.25 V assigned to the Li alloying reaction associated with conversion of the $Li_{32}Si_{136}$ to an amorphous lithium silicide phase. After the $Li_{32}Si_{136}$ is completely consumed, the electrode is completely composed of amorphous lithium silicide and behaves analogously to the amorphous Si electrode, which is evident by the similar shape of the dQ/dE plots below 0.2 V. *The dQ/dE plot for the amorphous Si comes from the second lithiation cycle of α-Si reproduced from Li et al.[33] After the first lithiation/delithiation cycle of α-Si, the fully delithated electrode comprises amorphous Si (i.e., α-Si is not reformed after lithium extraction); therefore the second lithiation cycle of α-Si shows the behavior of lithium insertion into amorphous Si.

APPENDIX G

SUPPORTING INFORMATION FOR CHAPTER 5.1

G.1. List of Tables

Table G.1 Refinement results for the sample synthesized at 450 °C with the Na counter electrode. The refined atomic positions, occupancies, and atomic displacement parameters for the refinement to Na_8Si_{46} ($Pm\bar{3}n$). Atomic sites are described using Wyckoff symmetry notation. The refinement plot can be found in Figure G.6.

Na_8Si_{46}		Lattice Parameter:	10.2045(6) Å			
Atom	Site	x/a	y/b	z/c	Occ.	U_{iso} (Å^2)
Na1	6d	1/4	1/2	0	1	0.0455(15)
Na2	2a	0	0	0	1	0.028(2)
Si1	24k	0	0.30822(11)	0.11754(11)	1	0.0114(5)
Si2	16i	0.18454(9)	x	x	1	0.0098(5)
Si3	6c	1/4	0	1/2	1	0.0045(8)

Table G.2 Refinement results for the sample synthesized at 450 °C with the Sn counter electrode. The refined atomic positions, occupancies, and atomic displacement parameters for the refinement to Na_8Si_{46} ($Pm\bar{3}n$). Atomic sites are described using Wyckoff symmetry notation. The refinement plot can be found in Figure G.7.

Na_8Si_{46}		Lattice Parameter:	10.2002(4) Å			
Atom	Site	x/a	y/b	z/c	Occ.	U_{iso} (Å^2)
Na1	6d	1/4	1/2	0	1	0.0523(13)
Na2	2a	0	0	0	1	0.0322(17)
Si1	24k	0	0.30844(9)	0.11729(9)	1	0.0149(4)
Si2	16i	0.18452(8)	x	x	1	0.0164(4)
Si3	6c	1/4	0	1/2	1	0.0105(7)

Table G.3 Refinement results for the sample synthesized at 550 °C with the Na counter electrode. The refined atomic positions, occupancies, and atomic displacement parameters for the refinement to Na_8Si_{46} ($Pm\bar{3}n$). Atomic sites are described using Wyckoff symmetry notation. The refinement plot can be found in Figure G.8.

Na_8Si_{46}		Lattice Parameter:	10.2032(4) Å			
Atom	Site	x/a	y/b	z/c	Occ.	U_{iso} (Å^2)
Na1	6d	1/4	1/2	0	1	0.0371(13)
Na2	2a	0	0	0	1	0.038(2)
Si1	24k	0	0.30902(11)	0.11757(11)	1	0.0102(4)
Si2	16i	0.18491(8)	x	x	1	0.0079(5)
Si3	6c	1/4	0	1/2	1	0.0062(8)

Table G.4 Summary of the experimental masses of the working electrode and the theoretical and experimental capacities for the different oxidation conditions.

Counter Electrode	Temperature (°C)	Mass of Na_4Si_4 (mg)	Theoretical capacity to form Na_8Si_{46} (mAh)	Observed Experimental Capacity (mAh)	% of Theoretical capacity to form Na_8Si_{46}
Na	450	160.0	69.1	82.0	119
Na	550	114.0	49.3	75.0	152
Sn	450	107.0	46.2	39.0	84
Sn	550	107.0	46.2	46.0	99

G.2. List of Figures

Figure G.1 Photograph of the stainless-steel housing used for the electrochemical cell. The housing consists of a standard 2.75-inch half nipple with the hole on the bottom welded shut with a stainless-steel cap. The top is comprised of a high voltage feedthrough made of stainless steel that is insulated from the flange with alumina. A copper gasket was placed in between the half nipple and feedthrough. The reactions were carried out in a furnace inside an argon glovebox to mitigate the oxidation of the stainless-steel housing at high temperatures.

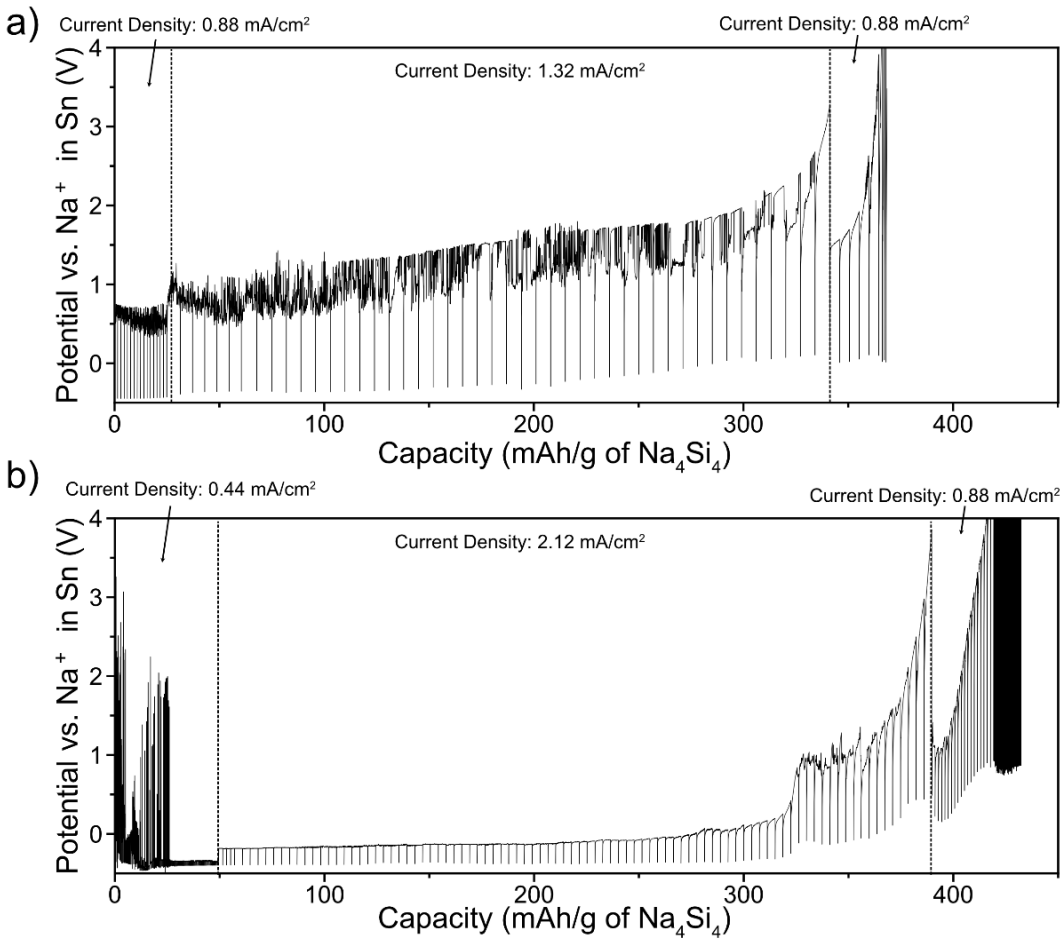

Figure G.2 GITT profile for oxidation of Na_4Si_4 using a Sn metal counter electrode. GITT profile showing the voltage versus the capacity for the reaction at (a) 450 ºC (30 min current pulse, 1.5 min relaxation time) and (b) 550 ºC (10 min current pulse, 0.5 min relaxation time).

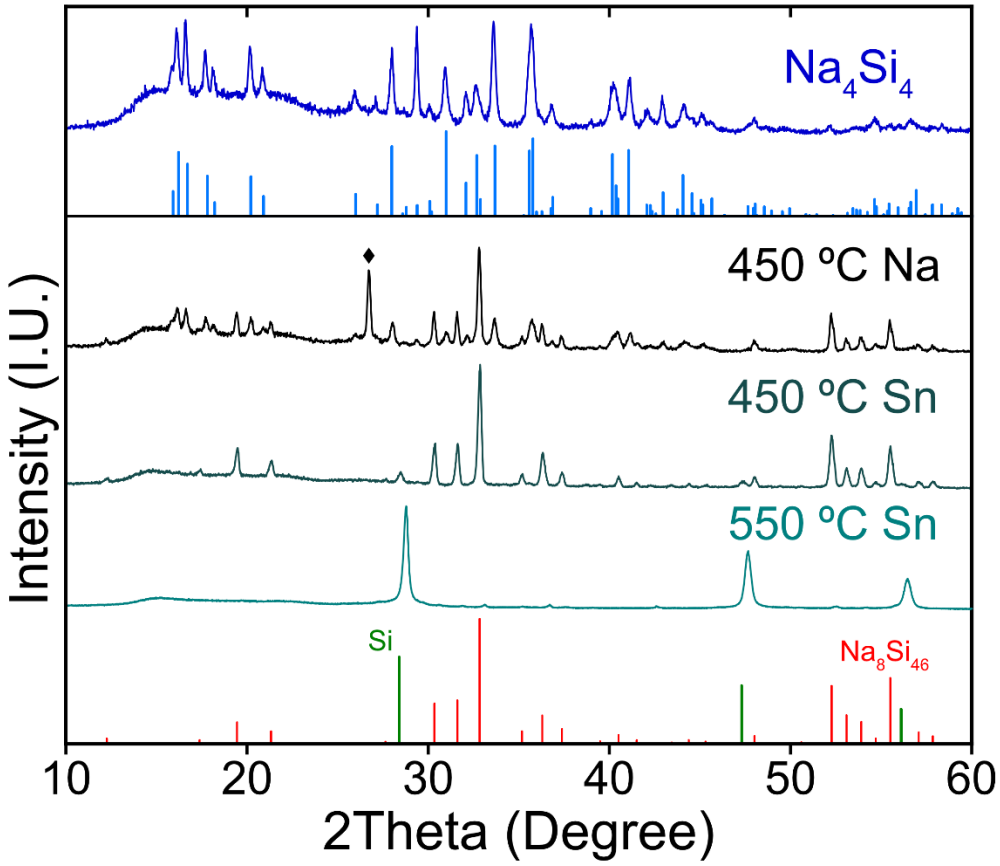

Figure G.3 PXRD patterns of as-recovered reaction products after the oxidation of Na_4Si_4 prior to washing with ethanol and water. The reaction temperature and counter electrode used are indicated above each pattern. The PXRD pattern of the synthesized Na_4Si_4 precursor and Na_4Si_4 reference pattern are shown in the top. The background from $15° < 2\theta < 25°$ is from the Kapton film that was used to protect the sample from oxidation during the measurement. The reflection marked with a diamond is of unknown origin and was not seen in any other samples.

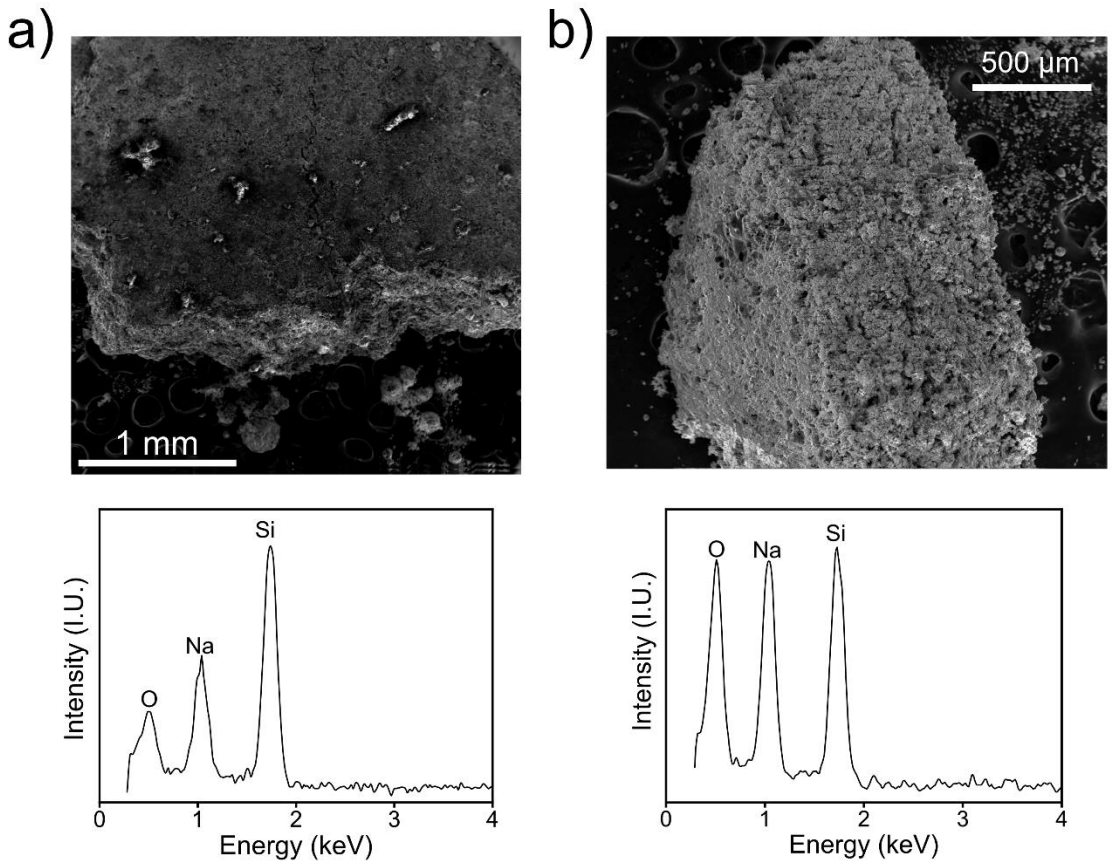

Figure G.4 SEM and EDS of pellets after electrochemical oxidation with the Na electrode. (a) Plan-view SEM micrograph of the pellet after electrochemical oxidation at 450 ºC and corresponding EDS spectrum below; (b) Cross-sectional SEM micrograph of the pellet after electrochemical oxidation at 550 ºC and corresponding EDS spectrum below. These data were acquired without washing the pellet after the reaction. The high oxygen content in the EDS spectra is likely from the rapid oxidation of residual Na_4Si_4 during transfer of the samples to the SEM chamber (30 – 60 seconds).

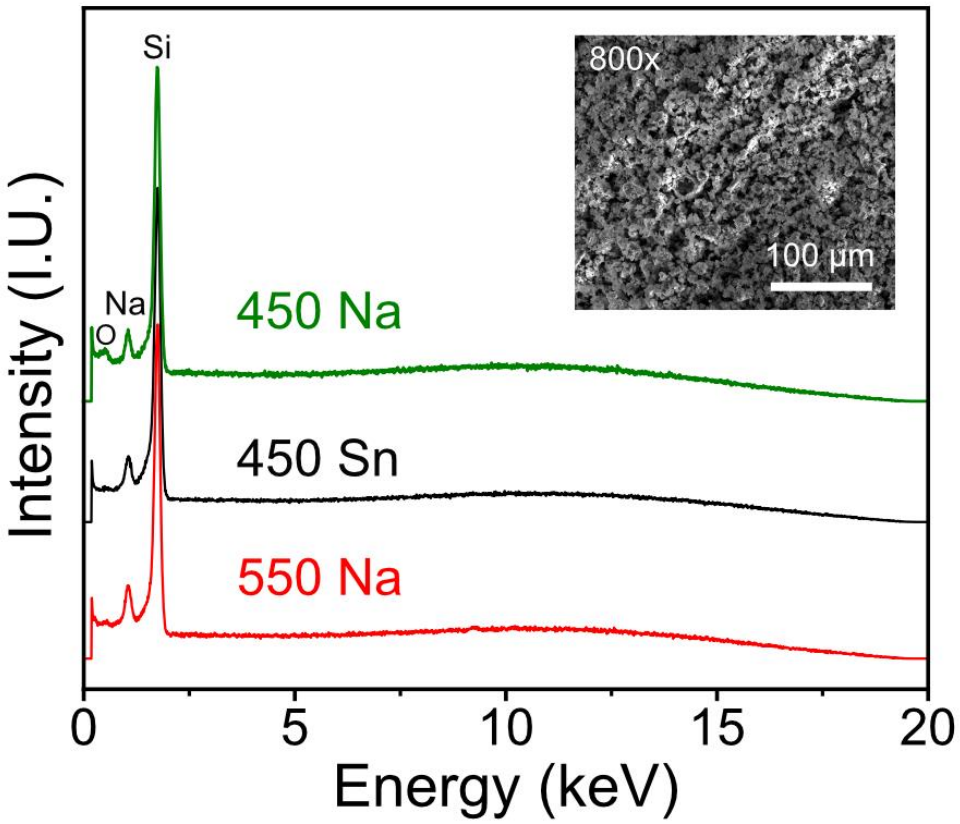

Figure G.5 EDS spectra taken in an SEM for the synthesized type I Na_8Si_{48} powders after washing with ethanol and water. Accelerating voltage = 20 kV, 800x magnification. Inset SEM image is a representative example of the powder morphology where the EDS spectra were collected (from the sample synthesized at 550 °C with Na CE).

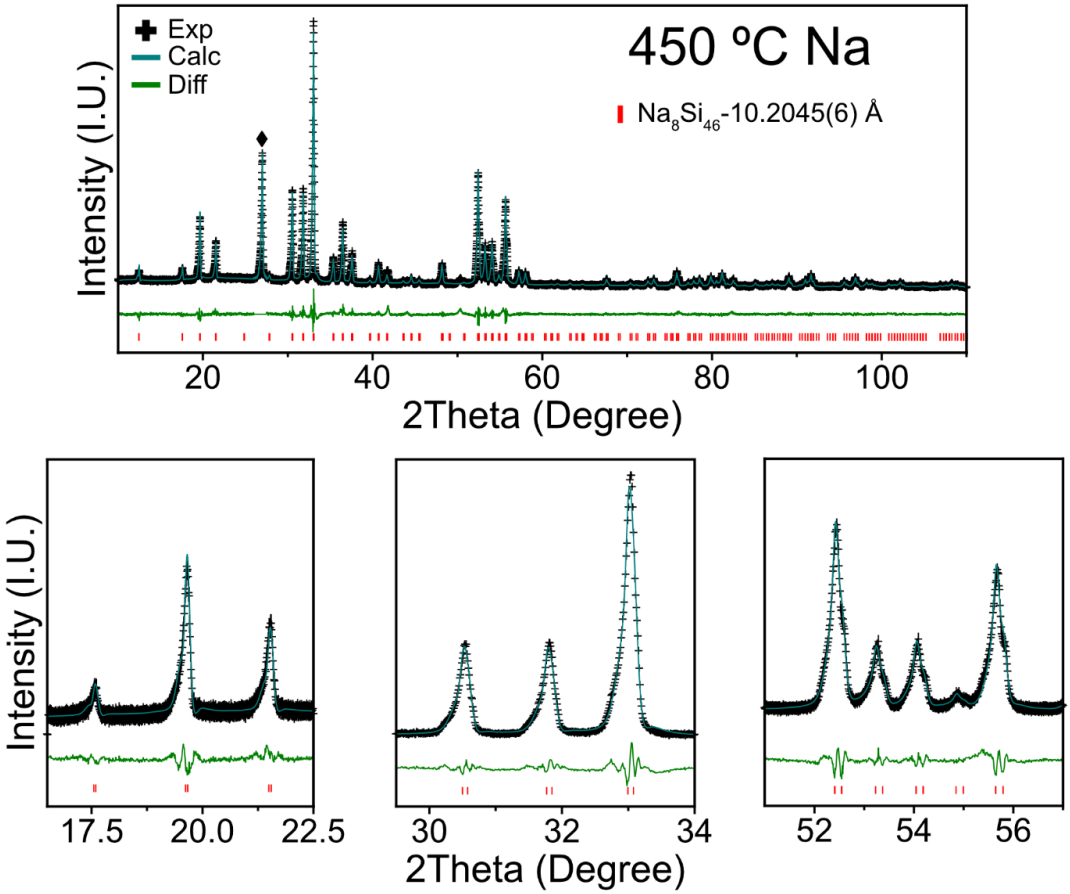

Figure G.6 Rietveld refinement of the PXRD pattern from the clathrate sample synthesized using a Na counter electrode at 450 °C. The black crosses represent the experimental pattern, the teal curve represents the calculated pattern, and the green curve represents the difference curve. The red tick marks represent the reflections corresponding to Na_8Si_{46}. The bottom set of plots show zoomed-in areas of the full refinement plot. Refinement residuals are: χ^2= 1.84, R_p= 0.0619, and wR_p= 0.0826. The reflection marked with a diamond symbol at 27° was excluded from the refinement. The refined atomic positions, occupancies, and atomic displacement parameters can be found in Table G.1.

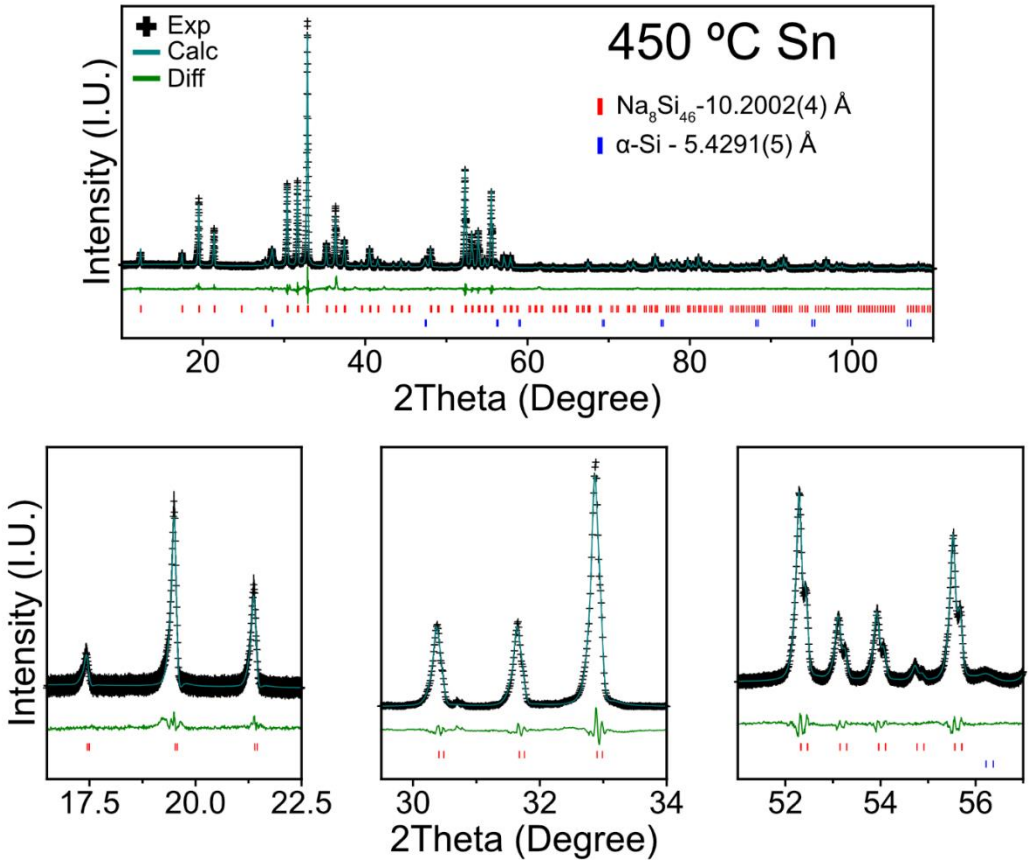

Figure G.7 Rietveld refinement of the PXRD pattern from the clathrate sample synthesized using a Sn counter electrode at 450 °C. The black crosses represent the experimental pattern, the teal curve represents the calculated pattern, and the green curve represents the difference curve. The red tick marks represent the reflections corresponding to Na_8Si_{46} (94.71(11) wt%) and the blue ticks represent the α-Si (5.29(11) wt%) phase. The bottom set of plots show zoomed-in areas of the full refinement plot. Refinement residuals are: χ^2= 1.84, R_p= 0.0596, and wR_p= 0.0809. The refined atomic positions, occupancies, and atomic displacement parameters can be found in Table G.2.

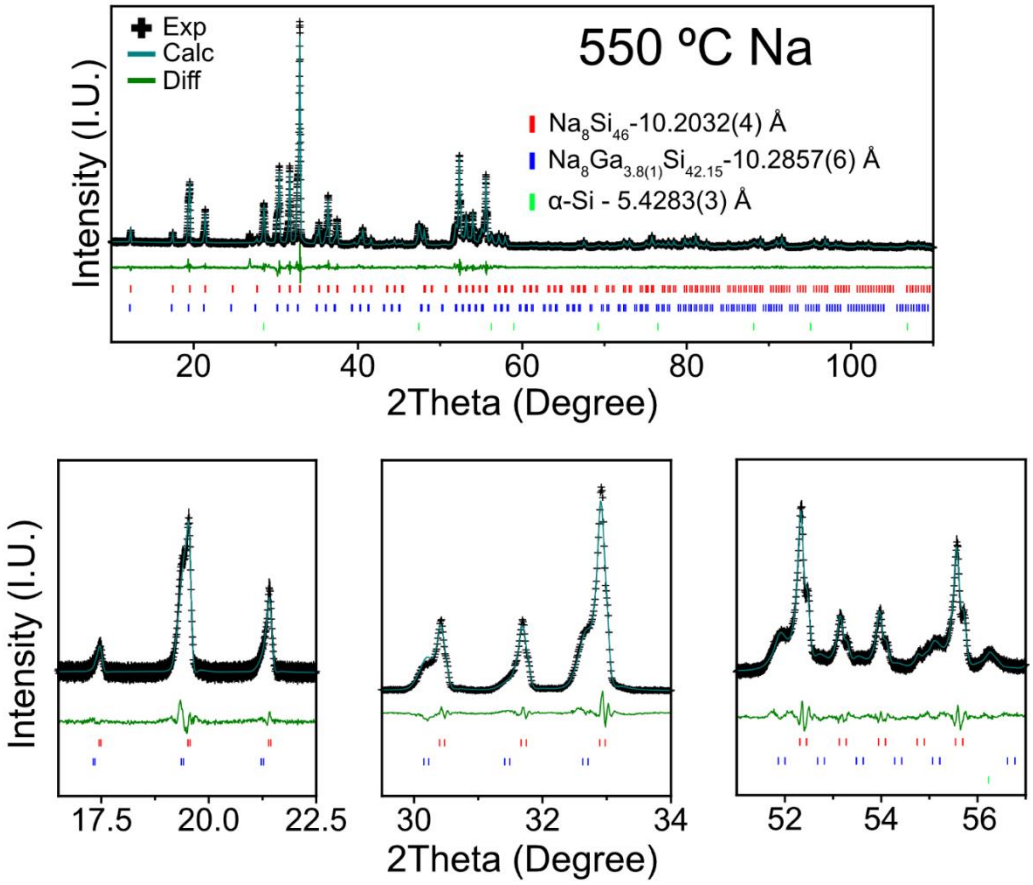

Figure G.8 Rietveld refinement of the PXRD pattern of the clathrate sample synthesized using a Na counter electrode at 550 °C. The black crosses represent the experimental pattern, the teal curve represents the calculated pattern, and the green curve represents the difference curve. The red tick marks represent the reflections corresponding to Na_8Si_{46} (71.3(3) wt%), the blue ticks represent the Ga-substituted type I clathrate phase ($Na_8Ga_{3.85(5)}Si_{42.15}$) (20.5(3) wt%) and orange tick marks represent the α-Si (8.12(10) wt%) phase. The bottom set of plots show zoomed-in areas of the full refinement plot. Refinement residuals are: χ^2= 1.67, R_p= 0.058, and wR_p= 0.0762. The refined atomic positions, occupancies, and atomic displacement parameters can be found in Table G.3.

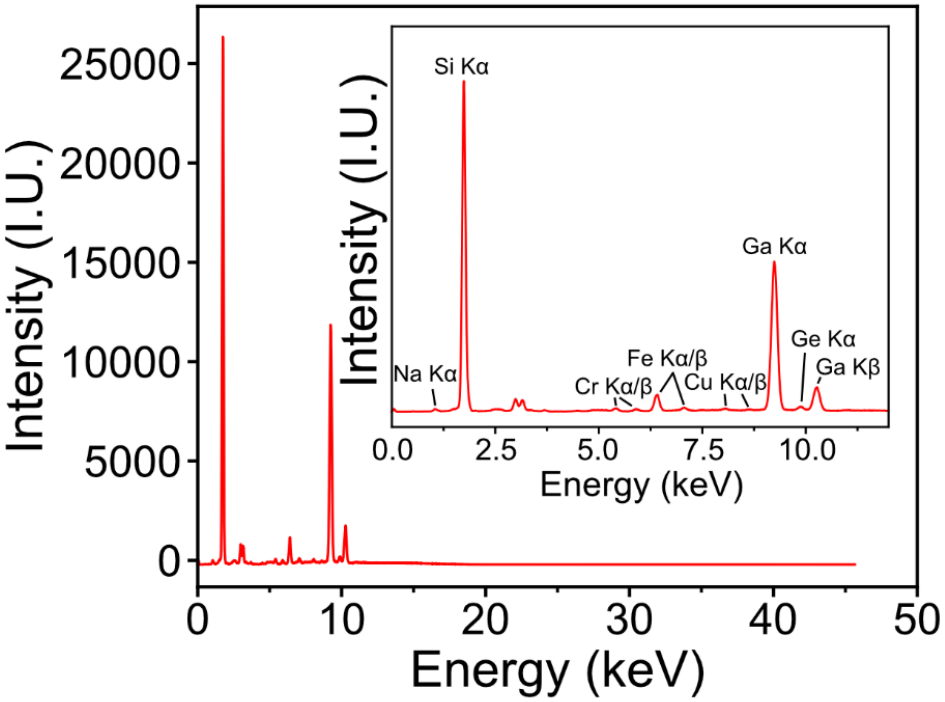

Figure G.9 XRF spectra of the powder obtained at 550 °C with the Na counter electrode. The inset shows the identified elemental constituents. Notably, Ga appears in a significant quantity along with transition metal ions. The amount of Ga is estimated to be around 6 wt%, but due to low sample amounts obtained in the synthesis (~20 – 40 mg), the exact compositions cannot be extracted with confidence. The origin of the transition metal atoms could be from the XRF instrument or from the powder's prolonged exposure to the stainless-steel reactor housing.

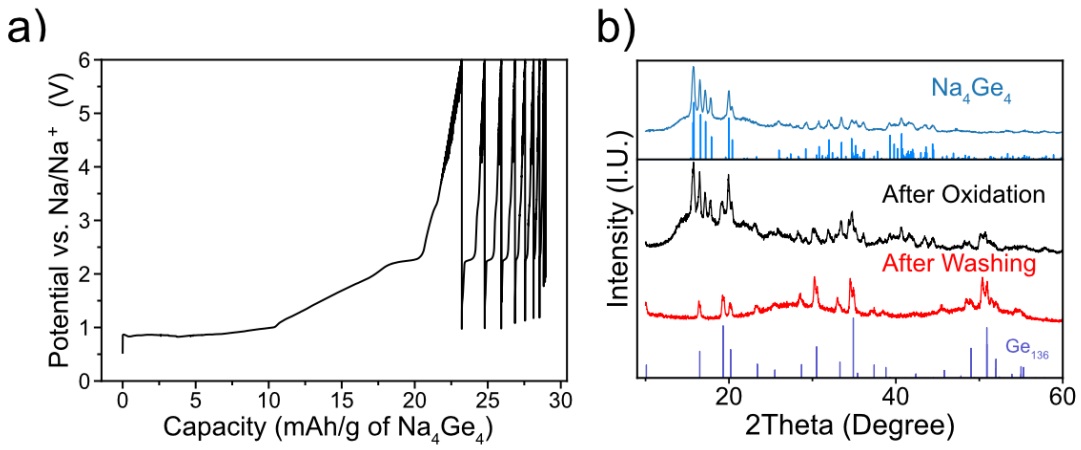

Figure G.10 Synthesis of type II Ge clathrate from electrochemical oxidation of Na_4Ge_4. (a) Voltage profile of the desodiation of a Na_4Ge_4 pellet (37 mg, 7 mm diameter) working electrode at a constant current of 0.61 mA/cm^2 at 350 ºC. The theoretical capacity to remove all Na from Na_4Ge_4 is 280 mAh/g of Na_4Ge_4. (b) PXRD of the Na_4Ge_4 precursor, product after electrochemical oxidation, and after washing with ethanol and water. The reference pattern in blue is for Na_4Ge_4 and the reference pattern in purple is for the guest free type II clathrate (Ge_{136}). We note the possibility of Na occupation of the clathrate cages (Na_xGe_{136}) however due to the very small amount of sample obtained after washing (~5mg), a detailed structural characterization cannot be carried out. Future work will be devoted to understanding the synthesis of Ge clathrates in more detail using the electrochemical oxidation approach.

APPENDIX H

SUPPORTING INFORMATION FOR CHAPTER 5.2

H.1. List of Tables

Table H.1 Atomic coordinates and atomic displacement parameters for refinement of product synthesized at 350ºC corresponding to Figure 5.2.6

$Na_{3.4(1)}Si_{34}Ge_{102}$		Lattice Parameter:	15.1186(4) Å			
Atom	Site	x/a	y/b	z/c	Occ.	U_{iso} (Å^2)
Na1	16a	1/2	1/4	1/4	0.079(12)	0.033(2)
Na2	32e	0.319(4)	x	-0.069(4)	0.067(17)	0.033(2)
Si1	8a	3/8	3/8	3/8	0.25	0.033(2)
Si2	32e	0.28268(13)	x	x	0.25	0.0236(14)
Si3	96g	0.31716(7)	x	0.12946(13)	0.25	0.0170(8)
Ge1	8a	3/8	3/8	3/8	0.75	0.033(2)
Ge2	32e	0.28268(13)	x	x	0.75	0.0236(14)
Ge3	96g	0.31716(7)	x	0.12946(13)	0.75	0.0170(8)

H.2. List of Figures

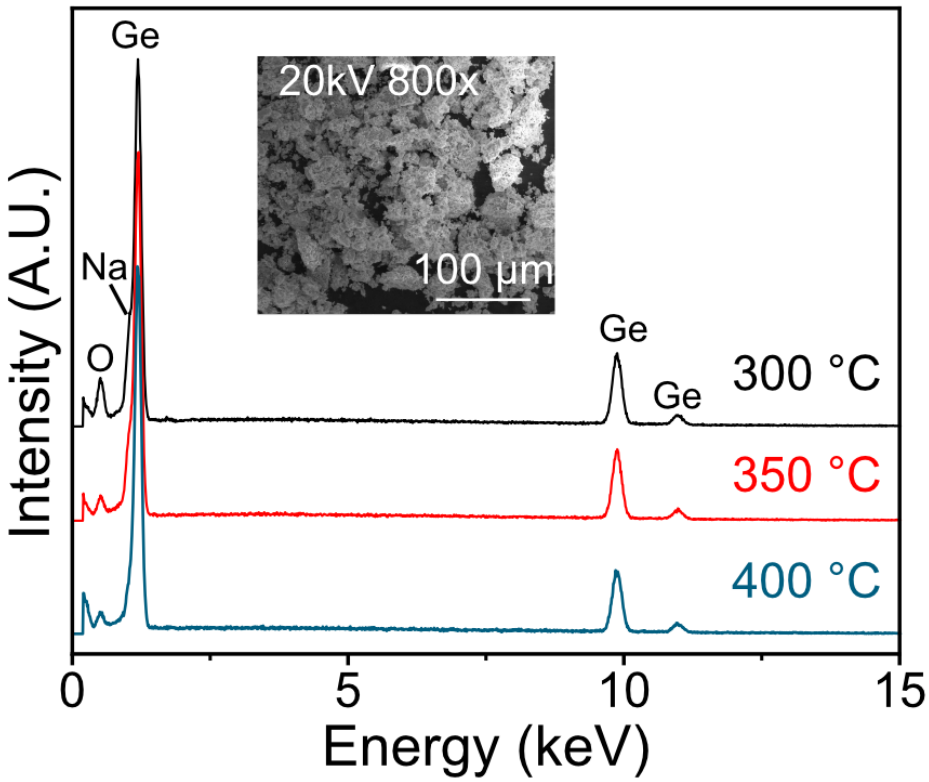

Figure H.1 EDS spectra of the products taken at 20kV and 800x of the electrochemical oxidation of Na_4Ge_4 after exposure to air. The SEM image shows a representative area that the spectra were collected.

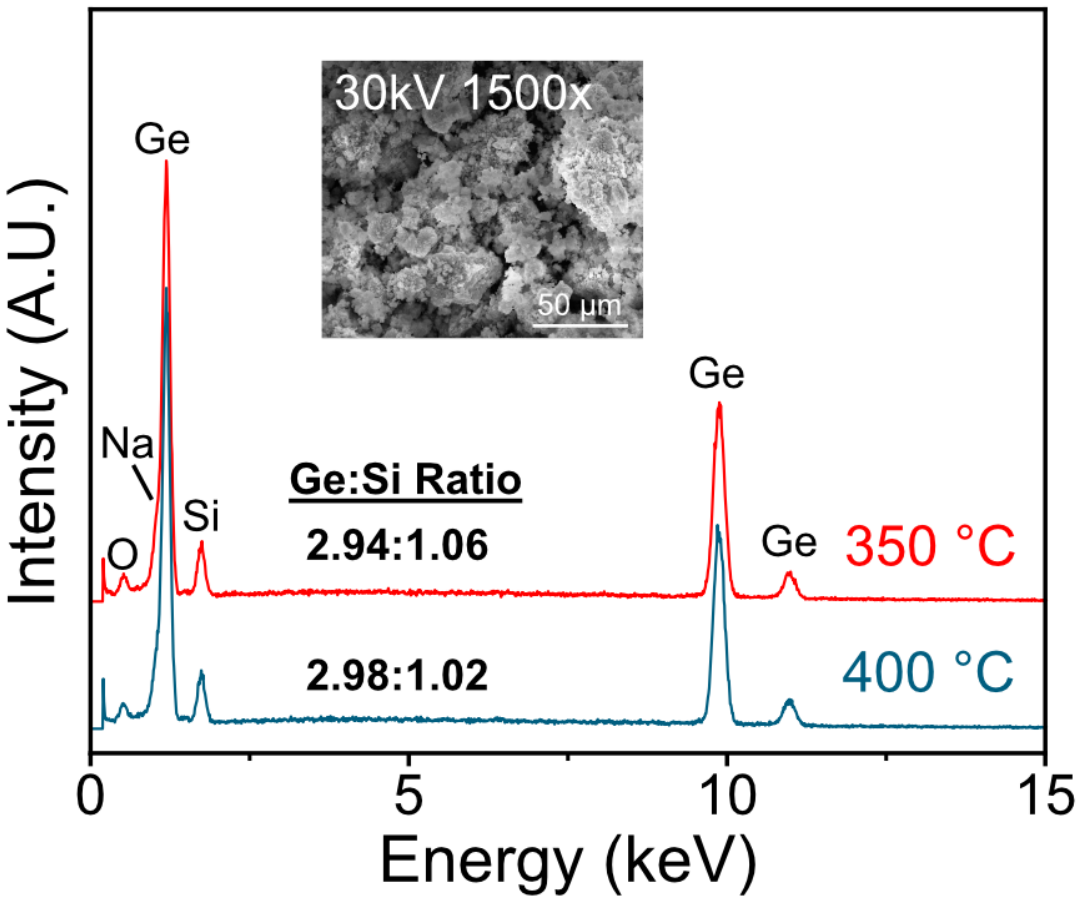

Figure H.2 EDS spectra of the products taken at 30kV and 1500x of the electrochemical oxidation of $Na_4Ge_3Si_1$ after exposure to air. The SEM image shows a representative area that the spectra were collected. The Ge:Si ratios are from the reported composition from the EDS software fit.

APPENDIX I

SUPPORTING INFORMATION FOR CHAPTER 5.3

I.1. List of Figures

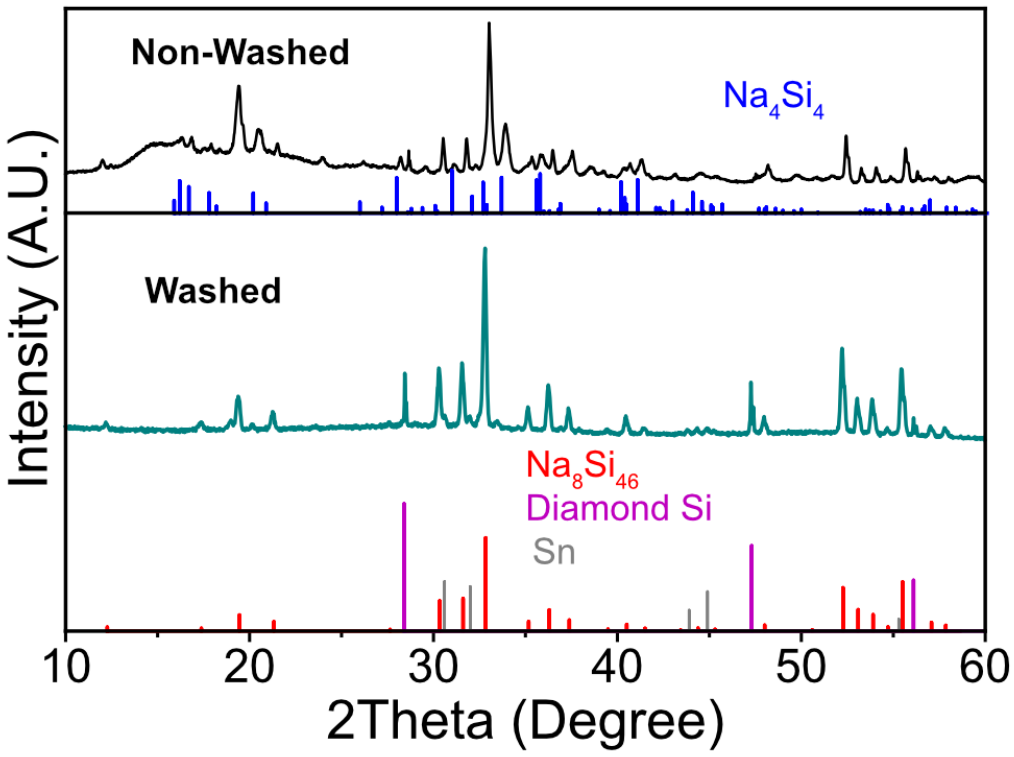

Figure I.1 PXRD of the non-washed and washed powder of the products of the Na-NaSi reaction shown in Figure 5.3.3c

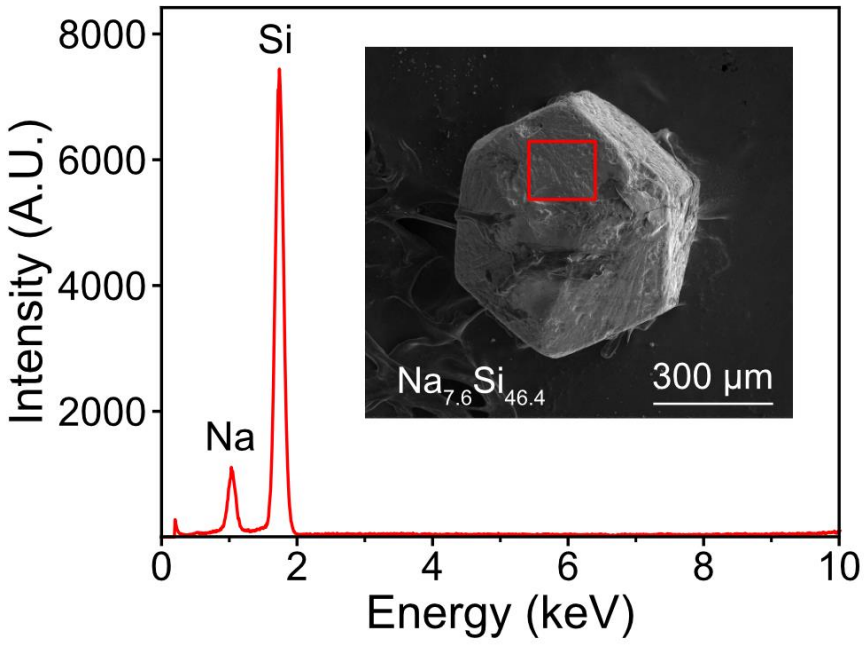

Figure I.2 SEM EDS (20 kV) taken from the box marked in red from the face of a Na_8Si_{46} single crystal. The composition in white is calculated from the EDS software.